HELICOPTER FLIGHT DYNAMICS SIMULATION WITH REFINED AERODYNAMIC MODELING

by

Colin Rhys Theodore

Dissertation submitted to the Faculty of the Graduate School of the
University of Maryland, College Park in partial fulfillment
of the requirements for the degree of
Doctor of Philosophy
2000

Advisory Committee:

Associate Professor Roberto Celi, Chair/Advisor
Professor Inderjit Chopra
Professor Sung W. Lee
Professor J. Gordon Leishman
Associate Professor Balakumar Balachandran, Dean's Representative

Abstract

Title of Dissertation: HELICOPTER FLIGHT DYNAMICS SIMULATION
WITH REFINED AERODYNAMIC MODELING

Colin Rhys Theodore, Doctor of Philosophy, 2000

Dissertation directed by: Dr. Roberto Celi, Associate Professor
Department of Aerospace Engineering

This dissertation describes the development of a coupled rotor-fuselage flight dynamic simulation that includes a maneuvering free wake model and a coupled flap-lag-torsion flexible blade representation. This mathematical model is used to investigate effects of main rotor inflow and blade modeling on various flight dynamics characteristics for both articulated and hingeless rotor helicopters. The inclusion of the free wake model requires the development of new numerical procedures for the calculation of trim equilibrium positions, for the extraction of high-order, constant coefficient linearized models, and for the calculation of the free flight responses to arbitrary pilot inputs.

The free wake model, previously developed by other investigators at the University of Maryland, is capable of modeling the changes in rotor wake geometry resulting from maneuvers, and the effects of such changes on the main rotor inflow. The overall flight dynamic model is capable of simulating the helicopter behavior

during maneuvers that can be arbitrarily large. The combination of sophisticated models of rotor wake and blade flexibility enables the flight dynamics model to capture the effects of maneuvers with unprecedented accuracy for simulations based on first principles: this is the main contribution of the research presented in this dissertation.

The increased accuracy brought about by the free wake model significantly improves the predictions of the helicopter trim state for both helicopter configurations considered in this study. This is especially true in low speed flight and hover. The most significant improvements are seen in the predictions of the main rotor collective and power required by the rotor, which can be significantly underpredicted using traditional linear inflow models.

Results show that the free-flight on-axis responses to pilot inputs can be predicted with good accuracy with a relatively unsophisticated models that do not include either a free wake nor a refined flexible blade model. It is also possible to predict the off-axis response from first principles, that is, without empirically derived correction factors and without assumptions on the wake geometry. To do so, however, requires much more sophisticated modeling. Both a free wake model that includes the wake distortions caused by the maneuver and a refined flexible blade model must be used. Most features of the off-axis response can be captured by using a simpler dynamic inflow theory extended to account for maneuver-induced wake distortions, and for a fraction of the cost of using a free wake model. The most cost-effective strategy, for typical flight dynamic analyses, and if vibratory loads are not required, is probably to calibrate such a theory using the more accurate free wake-based model, and then use it in all further calculations.

Acknowledgements

This research was supported by the National Rotorcraft Technology Center under the Rotorcraft Center of Excellence program. Detailed configuration parameters for the BO-105 were provided by Dr. A. Desopper of ONERA, France. Flight test data for the BO-105 were provided by Dr. C. Ockier of DLR, Germany . Flight test data for the UH-60A were provided by Dr. M. Tischler of NASA Ames. I would like to thank Drs. Ashish Bagai and J. Gordon Leishman for providing a copy of the maneuvering free wake code and for many useful discussions.

I would also like to thank the members of my dissertation committee for their valuable feedback: Drs. Balakumar Balachandran, Inderjit Chopra, Sung W. Lee and J. Gordon Leishman. I especially would like to thank Dr. Roberto Celi, my dissertation director, for his guidance and support during my graduate studies and his invaluable assistance while I was writing this dissertation.

I would like to thank current and past colleagues at the Rotorcraft Center, who helped me gain a better understanding of helicopter anaysis and made my time at the University of Maryland more enjoyable, particularly fellow flight dynamicists Chris Jones, Vineet Sahasrabudhe, Anne Spence, Steve Turnour and Rendy Cheng. I would especially like to thank Ashish Bagai for his time and help with the free wake code.

I appreciate the love, support and encouragement my family provided me. Their emails, faxes, phone calls and packages have meant a lot to me. Finally, I thank my wife, Alisse, for all of her love and support in keeping me focused on a goal and helping me to get this dissertation written.

Table of Contents

List of Tables

List of Figures

Nomenclature

a	Lift-curve slope
$\mathbf{a}$	Acceleration vector
$\mathbf{A}$	State matrix
b	Semi-chord length
$\mathbf{B}$	Control matrix
c	Blade section chord length
C_L, C_D, C_M	Blade section lift, drag and pitching moment coefficients
C_Γ	Ratio of tip vortex strength to maximum bound circulation
E	Young's Modulus, acceleration coupling matrix
e_1	Hinge offset of main rotor blade
$\mathbf{e}_T$, $\mathbf{e}_P$, $\mathbf{e}_R$	Unit vectors of local airflow velocity reference frame
$\hat{\mathbf{e}}_x$, $\hat{\mathbf{e}}_y$, $\hat{\mathbf{e}}_z$	Unit vectors of undeformed preconed blade reference frame
$\hat{\mathbf{e}}'_x$, $\hat{\mathbf{e}}'_y$, $\hat{\mathbf{e}}'_z$	Unit vectors of deformed blade reference frame
g	Acceleration due to gravity
G	Shear modulus
$\mathbf{G}$	Blade deformed section basis vectors
$\mathbf{H}$	Hermite interpolation polynomials
i_θ, i_ϕ	Longitudinal and lateral shaft tilt angles
$\mathbf{i}, \mathbf{j}, \mathbf{k}$	Unit vectors of hub rotating reference frame
$\mathbf{i}_\mathrm{B}, \mathbf{j}_\mathrm{B}, \mathbf{k}_\mathrm{B}$	Unit vectors of body-fixed reference frame

$\mathbf{i}_{\mathrm{F}}, \mathbf{j}_{\mathrm{F}}, \mathbf{k}_{\mathrm{F}}$	Unit vectors of rotating blade reference frame
$\mathbf{i}_{\mathrm{G}}, \mathbf{j}_{\mathrm{G}}, \mathbf{k}_{\mathrm{G}}$	Unit vectors of global wake reference frame
$\mathbf{i}_{\mathrm{I}}, \mathbf{j}_{\mathrm{I}}, \mathbf{k}_{\mathrm{I}}$	Unit vectors of inertial reference frame
$\mathbf{i}_{\mathrm{P}}, \mathbf{j}_{\mathrm{P}}, \mathbf{k}_{\mathrm{P}}$	Unit vectors of free wake blade preconed reference frame
$\mathbf{i}_{\mathrm{S}}, \mathbf{j}_{\mathrm{S}}, \mathbf{k}_{\mathrm{S}}$	Unit vectors of shaft reference frame
$\mathbf{i}_{\mathrm{W}}, \mathbf{j}_{\mathrm{W}}, \mathbf{k}_{\mathrm{W}}$	Unit vectors of wind reference frame
$\mathbf{i}$	Unit vector
I_{xx}, I_{yy}, I_{zz}	Aircraft mass moments of inertia about body axes
I_{xy}, I_{xz}, I_{yz}	Aircraft products of inertia
$\mathbf{j}$	Unit vector
$\mathbf{k}$	Unit vector
$\mathbf{K}$	Linear portion of stiffness matrix
K_R	Wake distortion parameter
L, M, N	Components of total applied moments about body axes
m_o	Reference blade mass per unit length
M	Mach number
$\mathbf{M}$	Linear portion of mass matrix
N_{b}	Number of blades
N_{e}	Number of finite elements
N_{h}	Number of harmonics of each blade mode
N_{m}	Number of blade modes
p	Roll rate of aircraft
$\mathbf{p}$	Blade section applied force vector
q	Pitch rate of aircraft, blade generalized coordinate, dynamic pressure
$\mathbf{q}$	Blade section applied moment vector

r	Yaw rate of aircraft
r_c	Viscous core radius
R	Main rotor radius
$\mathbf{B}$	Position vector
t	Time (sec)
T_{AP}	Transformation matrix from undeformed preconed frame to blade section aerodynamic frame
T_{BI}	Transformation matrix from inertial frame to body-fixed frame
T_{DP}	Transformation matrix from undeformed preconed frame to deformed blade frame
T_{FG}	Transformation matrix from global wake-fixed frame to rotating blade frame
T_{GB}	Transformation matrix from body-fixed frame to global wake-fixed frame
T_{PG}	Transformation matrix from global wake-fixed frame to undeformed preconed frame
T_{PR}	Transformation matrix from hub-rotating frame to undeformed preconed frame
T_{RS}	Transformation matrix from shaft-fixed frame to hub-rotating frame
T_{SB}	Transformation matrix from body-fixed frame to shaft-fixed frame
T_{TS}	Transformation matrix from shaft-fixed frame to tip path plane
T_{WB}	Transformation matrix from body-fixed frame to wind reference frame
u	Forward speed of the aircraft, axial deflection of a point on the blade

$\mathbf{u}$	Control vector
v	Lateral speed of the aircraft, lagwise elastic deflection of a point on the blade
$\mathbf{V}$	Velocity vector, modal coordinate transformation matrix
$\mathbf{y}$	State vector
$\mathbf{y}_n$	Finite element degrees of freedom vector
w	Vertical speed of the aircraft, flapwise elastic deflection of a point on the blade
X, Y, Z	Components of total applied forces along body axes
$\mathbf{x}$	Trim vector
x_0, y_0, z_0	Location of a point on the blade in local coordinates
x_A	Aerodynamic center offset from elastic axis

Greek Symbols

α	Aircraft angle of attack
α_S	Longitudinal shaft tilt
α_Y	Blade section angle of attack
β	Fuselage sideslip angle, local flap slope of blade elastic axis
β_0	Blade coning angle
β_{1c}, β_{1s}	Tip path plane longitudinal and lateral tilt angles
β_p	Blade precone angle
Γ	Tail rotor cant angle, circulation
γ	Flight path angle
γ_{xy}	Coherence
γ_I	Blade section local flow yaw angle
ϵ	Component of strain

Δ_{SP}	Swashplate phase angle
$\Delta\psi$	Azimuth discretization resolution, wake resolution
$\Delta\zeta$	Vortex filament discretization resolution
δ	Perturbation size, turbulent velocity coefficient
ζ	Local lag slope of the blade elastic axis
η	Coordinates of a point on a blade section in local coordinates
θ	Aircraft pitch attitude Euler angle, blade pitch angles associated with geometric rotation
$\theta_0, \theta_{1c}, \theta_{1s}, \theta_{0t}$	Collective, lateral, longitudinal cyclic pitch and tail rotor collective
θ_G	Total geometric pitch of blade section
θ_{TW}	Build-in blade twist
ζ	vortex age
κ_y, κ_z	Beam curvature
$\lambda_0, \lambda_c, \lambda_s$	Steady, cosine and sine portions of main rotor inflow
λ_t	Tail rotor inflow
μ	Main rotor advance ratio
ν	Kinematic viscosity
ρ	Air density
σ	Stress components
τ	Elastic twist of deformed blade section
ϕ	Aircraft roll attitude Euler angle, blade section elastic deformation
χ	Wake skew angle
ψ	Aircraft yaw attitude Euler angle, rad, blade azimuth angle, rad

ω	Vector of angular rates
Ω	Main rotor speed

Superscripts and Subscripts

$(\dot{\ })$	Derivative with respect to time
$(\ddot{\ })$	Second partial derivative with respect to time
$(\ )^\top$	Transpose
$(..)_{,x}$	Partial derivative with respect to x spatial coordinate
$(\ )_\mathrm{A}$	Aerodynamic
$(..)_\mathrm{B}$	Body-fixed reference frame
$(..)_\mathrm{CG}$	Center of mass
$(..)_\mathrm{D}$	Lag damper
$(..)_\mathrm{F}$	Fuselage reference frame, fuselage
$(..)_\mathrm{G}$	Global wake reference frame
$(\ )_\mathrm{H}$	Horizontal tail
$(..)_h$	Harmonics
$(..)_\mathrm{I}$	Inertial reference frame, inertia
$(\ )_\mathrm{MR}$	Main rotor
$(..)_\mathrm{P}$	Free wake blade preconed reference frame
$(..)_\mathrm{S}$	Shaft reference frame, structural
$(..)_\mathrm{T}$	Tension
$(..)_\mathrm{TPP}$	Tip path plane
$(\ )_\mathrm{tr}$	Tail rotor
$(\ )_\mathrm{V}$	Vertical tail
$(..)_\mathrm{W}$	Wind reference frame

Chapter 1

Introduction and Literature Review

1.1 Introduction

In recent years, there has been increased interest in improving the accuracy of flight dynamics mathematical models of helicopters. There have been a number of factors that have contributed to this interest. For example, the increasingly stringent handling qualities requirements set forth in Ref. [2] require high levels of dynamic stability and reduced control cross-coupling in helicopters. Furthermore, advances in design and construction technologies are producing increasingly lightweight and more maneuverable helicopters. This is apparent from the recent increase in the number of hingeless and bearingless rotor configurations. Also, the reliable design of high-gain, high-authority flight control systems requires increasingly more accurate mathematical models in both the time and frequency domains. A fourth reason is the traditional problem of lack of accuracy in the off-axis response calculations with flight dynamics models, to the extent that such calculations are often predicted in the opposite direction to experimental results. This is because of the lack of understanding of the physical mechanisms associated with the rotor and aerodynamics that results in specific helicopter response characteristics. The aeroelastic stabil-

ity characteristics of advanced rotor helicopters are difficult to calculate accurately with current models, especially in the lag direction. With the development of more highly maneuverable helicopters, coupled with the development of advanced rotor systems, the task of analyzing the handling qualities, rotor/body stability characteristics and response of these helicopters has become increasingly more difficult. All of these aspects of helicopter flight dynamics analysis require increasingly more accurate mathematical models describing the dynamics of the coupled rotor/body system.

Flight dynamics simulation is the task of analyzing the dynamic response of the aircraft as a whole, and, in particular, aircraft response during unsteady transient conditions. The task of flight dynamics analysis involves two key ingredients. The first ingredient is to describe the dynamics of the various components of the helicopter problem in an appropriate mathematical form. This involves the definition and construction of mathematical models for the individual components, and when coupled together, hopefully describe the dynamics of the system as a whole. These models include (with some examples): 1. A fuselage model (rigid, elastic). 2. A blade lift model (steady, quasi-steady, unsteady, dynamic stall). 3. A blade structural model (rigid-blade, elastic-blade, small or large deformations). 4. An inflow model (uniform, linear, prescribed wake, free wake, maneuvering free wake). Additional models may include the dynamics of the tail rotor, empennage, control linkages and actuators, engine, control system, etc. The second ingredient of a flight dynamic simulation involves the coupling of the individual component mathematical models to form a complete model that describes the dynamics of the aircraft as a whole. Then to use this complete model for the calculation of trim equilibrium conditions, linearized models through analytical or numerical perturbations, and time history responses to arbitrary pilot control inputs. The task of coupling the individ-

ual component models together for the calculation of the required solutions is often the most difficult task in flight dynamics analysis. This is compounded by the fact that the individual component models may require different solution techniques. In addition, the types of results that can be obtained are often limited by the fact that some of the individual components may be incompatible for one or more of the flight dynamics solutions required.

The flight dynamics simulation model used in this research study evolved originally from the GENHEL helicopter model of Howlett [3]. In this original model, the rotor was modeled with rigid blades that were hinged in both flap and lag and blade torsional dynamics were included using a simple empirically based dynamic twist model. The fuselage was modeled as a rigid body with the aerodynamic characteristics of the fuselage and empennage being provided via look-up tables of empirically measured aerodynamic coefficients. This model contributes much of the modeling of the fuselage, empennage and tail rotor to the current model, or essentially any parts of the model not related to the main rotor. The GENHEL model was extended by Ballin [4] who made a number of changes to increase the fidelity of the model, especially with respect to the modeling of the engine. Kim [5] added the dynamic modeling of the main rotor inflow using the Pitt-Peters dynamic inflow model [6, 7]. A new trim procedure was also developed. The equations of motion were represented in rigorous first-order form. This allowed for the development of methods to calculate linear, constant coefficient equations of motion that describe the small perturbation dynamics about an equilibrium position, where the linear model includes the dynamics of individual blades, of the main and tail rotor inflow, and of the propulsion system. The model developed by Kim was termed UM-GENHEL. Turnour [8] extended the modeling of the rotor blades by including a fully numerical structural formulation [9] that includes coupled elastic flap, lag and torsional de-

grees of freedom. A finite element analysis was used along with a modal coordinate transformation to reduce the number of blade degrees of freedom. Turnour also considered the inflow modeling by adding a higher order dynamic inflow model [10, 11] that includes the effects of trailed as well as shed wake and added the Leishman-Nguyen [12] state-space unsteady aerodynamics model. The mathematical model, termed FLEXUM, is specialized for the UH-60A articulated rotor helicopter, and this model is composed of a set of first order differential equations that represent the dynamics of the bare-airframe. From this mathematical model, trim, linearization and time history results can be obtained. This FLEXUM model represents the starting point for the formulation of the current flight dynamics simulation model.

Recently the aerodynamic modeling of the main rotor has come under increased scrutiny. Various research studies have concluded that increasing the fidelity of aerodynamic and inflow models can correspondingly increase the fidelity of the complete aircraft model and lead to improvements in the accuracy of flight dynamics analysis. In general, flight dynamics models that have included inflow dynamics have used the Pitt-Peters dynamic inflow model [6] or more recently the Peters-He finite state wake model [11]. The use of these dynamic inflow models involves a number of key assumptions about the aerodynamic environment of the main rotor. The first assumption is that the rotor wake has a cylindrical structure that is skewed with forward speed. This prescribed wake structure then forms the basis of the calculation of the main rotor inflow. Second, it is assumed that changes in the main rotor aerodynamics occur slowly, indicating the low-frequency nature of these dynamic inflow models. With these assumptions in mind, it has been reported that dynamic inflow models, in general, give good results in hover and high speed forward flight, but accuracy has been lacking at moderate speeds in the transitional flight regime. An alternative to these dynamic inflow models that prescribe the geometry of the

rotor wake are the free wake models where the wake structure itself becomes part of the solution and no a priori assumptions are made about the wake structure. The use of these free wake models results in more physically realistic wake structures.

The development of more sophisticated models to examine the aerodynamic environment of the main rotor disk, including free wake models, has been made possible with advances in computer architecture and technology. One of these free wake models, which has been used to develop the new flight dynamics model in the current study, is the Maryland Free Wake model (MFW) [1], which is also known as the Bagai-Leishman free wake model. This inflow model uses a relaxation technique to solve the numerically the governing wake equations for an assumed steady flight condition. This leads to the positions of the individual vortex filaments that make up the wake structure. With the addition of maneuvering effects [13] to the Bagai-Leishman free wake inflow model, the resulting inflow model has the ability to capture the effects of steady pitch and roll rates on the wake as encountered during maneuvers. This ability to capture maneuvering effects is fairly unique as far as free wake models are concerned. Unlike dynamic inflow models, the free wake model does not make any assumptions about the positions of the vortex wake filaments. This ability to capture the effects of maneuvers on the inflow distribution is not included in traditional dynamic inflow models. A review of inflow modeling used in flight dynamics applications and the effect that these models have on various flight dynamics results is presented in Section 1.2.3.

The current analysis focuses on the modeling of hingeless rotor helicopters, (although the UH-60A articulated rotor helicopter is also considered), and the effect that main rotor aerodynamic modeling, particularly the inflow, has on the various flight dynamic results. The modeling of hingeless rotor helicopters (in particular the BO-105) required altering portions of the fuselage, empennage and tail rotor math-

ematical models of the original FLEXUM code to enable the available BO-105 data to be used. The major contribution of the present study, however, is to the modeling of the main rotor aerodynamic environment. A two-dimensional quasi-steady aerodynamics model [14] is included to calculate the blade sectional aerodynamic loads, where this model takes into account the shed wake effects associated with variations in aerodynamic loads with respect to time. The trailed wake effects associated with radial variations in the aerodynamic loads are taken into account by using various inflow models. The most significant of these inflow models is the maneuvering free wake model of Bagai and Leishman [1] that is used to calculate the distribution of inflow over the main rotor. Results with the free wake inflow model are compared to results obtained with the traditional Pitt-Peters dynamic inflow model as well as with results obtained by using an extended momentum-based dynamic inflow model. This model, proposed by Keller and Curtiss [15, 16] and Arnold *et al.* [17], includes wake distortion effects from pitch and roll rates on a linear inflow distribution.

An important aspect of the new flight dynamics model is that it has the capability of accurately modeling helicopter behavior during maneuvers where the excursions from trim need not be small. This provides an accuracy range beyond that of linearized models. However, the deviations from trim are not arbitrary and they must be within the validity of the Euler angle definitions. The free wake model, being of a maneuvering type, also captures the effects of maneuvers on the wake geometry and on the inflow distribution. Therefore, both the flight dynamics and free wake models can, at least in principle, capture the effects of maneuvers on the helicopter response. This ability to capture the maneuver effects is not present in the Pitt-Peters dynamic inflow model and while it is present in the extended dynamic inflow model [15, 16, 17], there are a number of assumptions used in this model that may limit it usefulness in general flight dynamics work (see Section 1.2.3). The types

of maneuvers considered include the analysis of the helicopters in steady turns, as well as the analysis of the response resulting from arbitrary control inputs.

The general objective of this dissertation is to couple the Bagai-Leishman maneuvering free wake inflow model with a comprehensive flight dynamics model. Then to use this new flight dynamics model to investigate the effects on inflow modeling on flight dynamics. As previously discussed, these results include trim solutions in straight and level flight as well as in steady coordinated turns, stability of the rotor/body system as well as the aeroelastic stability of the rotor system, and the response to pilot inputs, which include harmonic inputs for frequency responses and arbitrary pilot inputs for time history responses. Results are presented for both articulated and hingeless rotor helicopters and the various results generated with the new flight dynamics model that includes the maneuvering free wake model are compared with a baseline flight dynamics model with the Pitt-Peters inflow model and also with flight test data where such data are available.

Particular attention is given to the long-standing problem in flight dynamics of predicting the off-axis response of the helicopter to pilot inputs, and especially the pitch and roll cross-coupling. This off-axis response problem has received a fair amount of attention of late with a number of possible explanations presented by various researchers. However, at present, there is no definitive explanation for the lack of accurate prediction of the off-axis response or the requirements to improve the predictions in flight dynamics analyses. The present study looks at the effect of inflow modeling on off-axis response predictions and examines the level of sophistication required in the various components of the flight dynamics model that allow for an improvement in the off-axis response predictions.

1.2 Literature Review

This section presents a survey of various publications that are relevant to the current study. This section is divided into five parts. The first part surveys current "comprehensive" rotorcraft simulation models and emphasizes the modeling of the main rotor aerodynamic environment. The next reviews aeromechanical stability analyses and the effect that inflow modeling has on aeromechanical stability predictions. The third part is comprised of a review of inflow models suitable for flight dynamics modeling, including dynamic and free wake inflow models. The fourth part reviews the analysis of helicopters in steady coordinated turns. The final part reviews some recent publications that address the prediction of off-axis response characteristics of helicopters.

1.2.1 Flight dynamic simulation modeling

The requirements of accurate modeling of helicopters, particularly in the design phase, has prompted the development of quite a number of simulation models that describe the dynamic behavior of the helicopter as a whole. With advances in computer architecture, larger and more sophisticated simulation models are being developed and these models can be used to calculate wider ranges of flight simulation results. These so-called "comprehensive" rotorcraft codes generally include sophisticated models for the various components of the helicopter and they allow for a variety of solutions to be generated. There are quite a few comprehensive rotorcraft codes in current use that include some or all of the ingredients required for flight dynamics simulation work. Most of these current codes are developed in-house or are only available commercially. For this reason, there is little that has been published on the specifics of the individual component models or the solution

techniques used, especially with respect to the most recent versions of these codes. Publications generally focus on the comparison of results generated with these codes with flight test data and results generated by using other such codes in an endeavor to validate the codes and gain additional knowledge of specific rotorcraft modeling problems. In general, an overview of the modeling techniques is all that is presented with little or no details of the techniques and issues related to coupling the individual component models together. Or of the solution techniques used for the calculation of the specific flight dynamics results.

With these problems in mind, this section presents a brief survey of some of the comprehensive rotorcraft codes that are in current use. First a general overview of the component modeling is presented, with a focus on the specifics of the aerodynamic modeling of the main rotor environment because this aspect of the modeling is the focus of the current research study. Next, the types of solutions that are available from each of these codes is looked at including some brief details about the techniques used in making the calculations. This is followed by a discussion of the validation of these codes and some examples of these validation studies that are available in the literature. Finally the validation of the various stages of the development of the GENHEL, UM-GENHEL and FLEXUM codes is examined.

The comprehensive rotorcraft codes considered in this survey are the following: 1. The Second Generation Comprehensive Helicopter Analysis System (2GCHAS) [18] developed by the ARMY/AMES. 2. The COmprehensive Program for Theoretical Evaluation of Rotorcraft (COPTER) [19] developed by Bell. 3. CAMRAD [20, 21] collectively refers to the family of comprehensive helicopter codes CAMRAD, CAMRAD/JA and CAMRAD II developed by Johnson Aeronautics. 4. The Technology One program (TECH-01) [22] developed by Boeing. 5. FLIGHTLAB that was originally developed by DuVal [23] as a coupling of the flexible rotor model of the

REXOR aeroelastic analysis with the GENHEL aircraft model of Howlett [3]. 6. The University of Maryland Advanced Rotorcraft Code (UMARC) [24, 25] developed at the University of Maryland.

All of the comprehensive rotorcraft codes considered include the modeling of the coupled rotor/fuselage problem. With respect to modeling of the fuselage, all of the codes include a rigid fuselage model, while the 2GCHAS, COPTER, TECH-01 and UMARC codes allow for a NASTRAN modal representation of the elastic fuselage. All of the codes include the flexibility of modeling different types of rotor hub configurations, including articulated, hingeless, and bearingless hubs. Being of the second generation of codes, a finite element analysis of the main rotor blade elasticity is used in all cases. This finite element basis allows for the dynamic analysis of rigid and elastic blades, with fully coupled flap, lag and torsional degrees of freedom being included in the 2GCHAS, COPTER, CAMRAD and UMARC codes. TECH-01 models the blade by using coupled flap/pitch dynamics and uncoupled lag dynamics. FLIGHTLAB uses coupled flap/lag and uncoupled torsional dynamics.

With respect to the modeling of the main rotor inflow characteristics, a number of inflow modeling options associated with each of the comprehensive rotorcraft codes are available. A simple uniform inflow model using momentum theory is available in the 2GCHAS, CAMRAD and UMARC codes. A linear inflow distribution is available using the Pitt-Peters [6, 7] three-state dynamic inflow model can be selected in the TECH-01 and UMARC codes. The Drees [26] dynamic inflow model is available in the TECH-01 and UMARC codes. There are also a number of vortex wake models that can be used for inflow calculations in each of the codes. All of the codes allow for the vortex geometries to be prescribed based on parameters including the flight condition, motion of the rotor blades, blade loading distribution, etc. The first free wake model to be used in flight dynamics simulation work was the Scully

free wake model [27] and the inclusion of this model is an option in the 2GCHAS, COPTER, CAMRAD and UMARC codes. The Johnson free wake model [20] is a modification of the Scully free wake model for use in the CAMRAD family of codes, and, this is also available in the COPTER and UMARC codes. MFW is the Maryland Free Wake model [1], and, this is available in the 2GCHAS and UMARC codes.

There are no current comprehensive codes that include a maneuvering free wake model to capture the direct aerodynamic effects of maneuvers, including pitch and roll rate maneuvers on the vortex wake geometries and subsequent inflow distributions. It should be mentioned that 2GCHAS does have the ability to capture maneuvering effects on the vortex wake geometry, but this is only available through a prescribed wake model and it is not clear from the published literature how this is achieved.

With respect to trim calculations, each of the codes allows for free-flight and wind-tunnel trim conditions to be calculated, with CAMRAD being the only code that is reported to have the capability of calculating trim conditions of helicopters during steady maneuvers, such as coordinated turns and descending and climbing flight. There are some differences in the procedures used to calculate the trim conditions. 2GCHAS uses a *periodic* trim procedure that enforces periodicity as the basis for the trim calculations where UMARC uses an *algebraic* trim where a trim equilibrium condition is enforced by satisfying a set of equations. CAMRAD has the ability to use both types of trim procedures to calculate trim conditions.

All of the comprehensive codes have the capability of extracting a set of linear equations from the non-linear equations that make up the mathematical models. Because of the complexity of the non-linear mathematical models, the linearized models in each case have to be calculated numerically by using a perturbation anal-

ysis. The basis of the linearized model calculations is a trim equilibrium position. For the cases where the equations of motion are formulated in the rotating frame of reference, the resulting linear models have periodic coefficients and require the use of analytical techniques that can handle periodic coefficients, such as Floquet Theory [28, 29]. These codes also allow for constant coefficient linear models to be calculated in the non-rotating frame using a multi-blade coordinate transformation.

Because each of the codes allows for the extraction of linearized models about a trim equilibrium condition, time histories can be calculated in response to pilot inputs by using the linear model. With the exception of UMARC, the comprehensive codes allow for the calculation of free-flight responses to arbitrary pilot inputs by using the full non-linear mathematical model. The time history responses to pilot inputs are calculated by numerically integrating the equations of motion. Only FLIGHTLAB can calculate free-flight responses in real-time and this is achieved through the use of parallel processing.

Most of the published validations are made with the comprehensive codes that are used in government (2GCHAS) and educational (UMARC) research institutions and those available commercially (CAMRAD, FLIGHTLAB,). There has been less published in the literature regarding the codes that are developed by companies for in-house use with their own products, namely the COPTER code developed by Bell and the TECH-01 code developed by Boeing. Although these comprehensive codes contain some or all of the ingredients required for flight dynamics work, the actual number of studies and publications that deal with the specifics of flight dynamics simulation are limited.

The FLIGHTLAB real-time flight dynamics simulation code has been used in a number of studies that look at some of the specifics of flight dynamics work. The study of He and Lewis [30] contains a validation study with the UH-60A for both

trim and dynamic time history results. The modeling included elastic blades and the Peters-He finite state dynamic inflow model [10, 11]. Trim results were presented in straight and level flight with the sideslip angle set to zero for the entire speed range. These results showed a fair degree of accuracy when compared to flight test data, although the main rotor collective was significantly underpredicted. Time history results in hover were calculated for a lateral step input and compared to flight test data. The results showed an over-prediction of the roll rate response with uniform inflow dynamics that was not seen with the addition of non-uniform inflow dynamics. The off-axis, pitch rate response was initially predicted in the opposite direction to flight test data and the correlation was not improved by using elastic blades or higher-harmonic inflow dynamics. Similar results for a longitudinal stick maneuver showed a good correlation with flight test data for the on-axis response, but not for the off-axis response.

Another study using the FLIGHTLAB code, performed by Choi, He and Du Val [31], also focused on the modeling of the UH-60A helicopter. This study modeled the main rotor blades as rigid beams that were hinged in the flap and lag directions and the inflow was modeled using a three-state dynamic inflow model. Validation was performed by comparing the simulation results to flight test data for a variety of maneuvers. Results showed that the primary, or on-axis response was in good agreement with flight test data, while the cross-coupling, or off-axis response predictions were not satisfactory for most cases.

With respect to the GENHEL [3] model, which forms the basis for the current model, there have been a number of validation studies that have been performed on various versions of this model. Ballin [32] performed a validation of a real-time version of the original GENHEL simulation code with the UH-60A helicopter. Comparisons were made between simulation results and flight test data for trim in

straight and level flight, climbs and descents and 1-g coordinated turns. Comparisons were also made for dynamic time history results for a variety of maneuvers. The dynamic time history results presented in this study showed a general accurate prediction of the on-axis characteristics following control inputs, however the off-axis response characteristics were poorly predicted.

Kim, Celi and Tischler [5] focused on the extraction of linearized models with the UM-GENHEL model to represent the linearized dynamics of the UH-60A in different flight conditions. All of the results presented here were in the frequency domain and the validation study showed that, at least in hover, there was a good correlation between calculated results and flight test data for the on-axis response from 0.5 rad/sec to 15 rad/sec, which is the frequency range that is generally the most important for flight dynamics work. There were no results presented for the off-axis response calculations. Turnour and Celi [8] extended the model to include a coupled flap-lag-torsion elastic rotor formulation. Frequency response results presented for the UH-60A in hover and forward flight were shown to improve the accuracy of the calculated results to include the frequency range from about 0.5 rad/sec to 50 rad/sec with the addition of the flexible blade model. Turnour [33] also looked at the effects of including the finite state wake model and an unsteady aerodynamics model on the results in the frequency domain. The correlation between calculated results and flight test data showed a favorable correlation for the on-axis results and some improvement in the magnitude of the off-axis response was seen in certain frequency ranges. Yet the phase of the off-axis response was not improved.

1.2.2 Aeromechanical models and comprehensive analyses

Aeroelasticity is the study of dynamic characteristics of the helicopter body/rotor system that considers the coupling between the aerodynamic, structural and inertial

contributions. There has been quite a bit of activity in the field of rotorcraft aeroelasticity, especially with the advent of advanced rotor systems including hingeless and bearingless rotor helicopters. Some comprehensive reviews of the aeromechanical characteristics related to hingeless rotor helicopters include studies by Johnson [34], Ormiston *et al.* [35], Friedmann [36], and Chopra [37]. These are particularly relevant since the soft-in-plane hingeless rotor helicopter, which is studied in the current research, is susceptible to a number of resonance conditions, including ground and air resonances.

As mentioned in the previous section, many aeroelastic studies are made with the comprehensive rotorcraft codes that are currently available. An example is the study of Millott *et al.* [38] who presented a comparison of trim variables, aeroelastic stability and response of hingeless rotor blades in forward flight obtained with 2GCHAS and two other aeroelastic codes. The 2GCHAS results were obtained with the Greenberg quasi-steady aerodynamics model [39] and a uniform inflow distribution. A further example was the study of Ganguli *et al.* [40] that looked at the prediction of vibratory hub loads with the UMARC comprehensive rotorcraft code, and a free wake model [41]. This study compared the results with a number of aerodynamic and inflow models, including linear and free wake inflow models, with quasi-steady and unsteady aerodynamic models. While the use of the unsteady aerodynamic model caused only minor changes in the results, the use of the non-linear inflow modeling was critical to the prediction of the rotor hub loads, both in the low and high speed flight regimes. The study of Milgram and Chopra [42] looked at the analysis of rotors with trailing edge flaps and compared results obtained with the UMARC and CAMRAD/JA codes to wind tunnel data, where the UMARC code used in this study included the Maryland Free Wake model [1]. A conclusion of this study was that a free wake model is required for the correct prediction of the

vibratory loads, particularly at low advance ratios.

The use of three-dimensional wake modeling is often used for the calculation of loads and vibrational characteristics of rotors but are not as common in the aeroelastic stability analysis of rotors. The study of Chunduru *et al.* [43] examined the effects of main rotor aerodynamic modeling on the stability characteristics of a small scale isolated hingeless rotor. Particular attention was paid to the prediction of the lag damping, which is difficult to predict for hingeless rotor helicopters. The inclusion of a dynamic stall model and the finite state wake inflow model improved the overall predictions when compared to results using a quasi-steady stall theory. With respect to the prediction of the lag damping, the results obtained with the dynamic stall and finite state wake models in general improved the overall lag damping predictions. Nagabhushanam and Gaonkar [44] also used a finite state wake inflow model in the study of aeromechanical stability prediction of hingeless rotor helicopters. Hover and forward flight conditions were examined for air resonance, as well as with the helicopter in ground contact for ground resonance predictions. This study again shows that improvements in lag damping predictions for hingeless rotor helicopters could be obtained by using the finite state wake model. The best correlations with test data were obtained with a high number of azimuthal harmonics and radial shape functions indicating that the use of a non-linear inflow may be required to improve the various stability predictions.

The UMARC code with the free wake model from CAMRAD was used by Torok and Chopra [45] to study aeroelastic stability. While this study used a variable free wake geometry in the calculation of the trim state of the helicopter, the wake geometry was fixed for the stability analysis. Thus, the wake distortion effects resulting from perturbations in the trim state were not included in the calculation of the stability characteristics.

1.2.3 Wake and inflow models suitable for flight dynamics work

An important component of any flight dynamics analysis is the modeling of the aerodynamic environment of the main rotor. As described in Section 1.2.1, there are a number of rotorcraft comprehensive codes that are in current use in the rotorcraft community, and that there are also quite a number of inflow models that are used within these comprehensive codes. With respect to flight dynamics modeling, each of these inflow models has specific strength and weaknesses in calculating specific flight dynamic simulation results. Many of the simple dynamic inflow models that have been around for a number of years are still in extensive use today in calculating many types of flight simulation results. There are a number of reasons for this including the fact that they have been extensively used and validated and they are reliable and accurate for many types of analyses. One reason is that they are generally computationally inexpensive and they are in the form required to be coupled to existing comprehensive codes. Another reason is that many of these inflow models are formulated in first order form and fit quite easily into the formulation and solution methodologies of existing mathematical models. In the simplest form, the dynamic inflow models would be formulated as a set of first order ordinary differential equations with a number of associated states and an equal number of equations. This allows for the integration of these equations and states by simply appending them to the current mathematical models. The Pitt-Peters dynamic inflow model is an example where the linear distribution of inflow over the rotor disk is represented by three inflow coefficients, and the inflow dynamics is modeled by three first-order ordinary differential equations. The more recent finite state wake models, which have a variable number of states, are not limited to a linear inflow distribution, but rather allow for higher order polynomials representing the radial variation of inflow

and higher harmonic variations of inflow around the azimuth. This is achieved while still retaining the first order nature of the model, with the number of dynamic inflow equations being equal to the number of coefficients required to describe the inflow distribution over the main rotor disk. Thus this particular form of dynamic inflow model can have its equations appended to the first order mathematical model describing the dynamics of the rest of the helicopter.

There are however a number of drawbacks of using these for flight dynamics work. The first of these drawbacks is that the inflow distributions are limited to the mathematical representation that is defined by the model. For instance, the Pitt-Peters dynamic inflow model limits the inflow to a linear radial variation with only the first harmonic azimuthal variation, resulting in a linear inflow distribution over the rotor disk. The finite state wake models improve this by allowing for a higher-order representation of inflow variation along the radius and higher-harmonic variations around the azimuth, but the same problem occurs where there are restrictions put on the types of inflow distributions that are allowed. The second drawback is that these dynamic inflow models are based on assumptions about the structure of the wake geometry that is used to calculate the inflow distribution. For instance, the Pitt-Peters dynamic inflow models is based on an undistorted helical structure that is skewed with forward speed. Similar assumptions about the wake structures are also made in other dynamic inflow models of this type. These inflow models have been shown to give fair degrees of accuracy in low speed flight, including hover, and for high speed flight, but accuracy is limited at moderate forward speeds and in the transitional flight regime. A third drawback is the inherent low-frequency nature of the dynamic inflow models and the inability to accurately predict high-frequency events. The type of results that are of interest here would include higher-harmonic blade loading and high-frequency vibration loads on the helicopter. There are a

number of studies [46, 45] that have concluded that the accurate prediction of various blade loads and helicopter vibrations cannot be performed by using traditional linear dynamic inflow models.

Some comprehensive reviews of inflow modeling and its use in flight dynamics analyses include those conducted by Gaonkar and Peters [47], Gaonkar [48] and Chen [49]. At this time the limitations on model complexity that could be reasonable included in flight dynamics codes have limited the modeling of inflow to relatively simple models. One of the most widely used of these early dynamic inflow models is the Pitt-Peters dynamic inflow model [6] that is a linear, unsteady theory that relates the transient rotor loads (thrust, roll moment and pitch moment) to the overall transient response of the rotor induced-velocity field and the equations themselves are derived using an unsteady actuator-disk theory.

The next level of sophistication of inflow models would be where the inflow distribution over the rotor disk is calculated based on a prescribed vortex wake. Using the Biot-Savart law, the induced velocity at any point on the rotor disk is calculated as the combined influence of all of the modeled vortices associated with the wake. There are no predefined limitations placed on the types of inflow distributions that can be obtained, as with fixed state dynamic inflow models. As with dynamic inflow models, there are a number of drawbacks associated with inflow models of this type. The first is that the wake geometry is prescribed and requires knowledge of the appropriate wake structure to use for the specific flight condition and rotor and blade configuration. This requires an extensive knowledge of the wake structures and factors that effect the wake structures to accurately model the wake geometry. A second drawback is that with these prescribed wake models is that all inflow dynamics are lost since the inflow distribution is calculated with the wake geometry at a specific instant in time. The inflow is calculated from a prescribed

wake geometry that does not include the effects of time variations in the inflow or the blade loading. The third drawback is that the inflow cannot in general be represented by a set of first order equations. This means that the equations related to the prescribed wake inflow models cannot be simply appended to the flight dynamics models and treated the same as dynamic inflow models. This creates difficulties for various aspects of flight dynamics analyses, including the calculation of linearized models, that are in general calculated numerically, as there are no states associated with the wake geometry or inflow distribution that can be perturbed independently of the rest of the model. This means that when any of the states are perturbed, the results include or are contaminated by the changes in the inflow associated with the states perturbations.

The next step from prescribed wake models is to use free wake models to generate the rotor inflow distributions used in the flight dynamics simulation model. With free wake models, the rotor wake structure is not prescribed and it is allowed to distort under the influence of the flight condition, blade loading and self-induced interaction to become a part of the solution. The study of Bagai [50] contains an excellent review of free wake models, including their development, types of free wake model currently used, solutions techniques and associated problems with the formulation and use. With respect to flight dynamics simulation modeling, the use of free wake inflow models includes the least amount of assumptions of any of the types of inflow models considered here and, in principle, should produce the most realistic wake structure among the inflow models. However, this comes at a cost as there are a number of drawbacks associated with the use of free wake models to provide the inflow used in flight dynamics work. The first two of these drawbacks are also associated with prescribed wake models and are the lack of inflow dynamics associated with the use of the free wake model and the lack of defined states

associated with the inflow model. A third drawback is the computational expense associated with the use of free wake models. This is particularly true when the free wake model is coupled to a flight dynamics model where the free wake model, may be required to be evaluated quite a number of times in the course of calculating the required flight dynamics results.

A fourth drawback is that while the use of free wake inflow models is based on less assumptions than the other types of inflow models, there are still a number of assumptions that have to be made. These assumptions include: 1. How the rotor wake is to be modeled (single tip vortex, vortex sheet, etc). 2. The structure of the individual vortex filaments including the vortex core size and velocity profile through the vortex. 3. The initial strength of the vortex filaments and how the dissipation and diffusion of the vortices are to be modeled. 4. The radial release point of the vortices from the blades and how the roll up of the vorticity in the tip region is handled. 5. The specifics of the discretization of the vortex wake and the age of the individual vortex filaments before they are assumed to no longer influence the main rotor inflow. While all of these aspects of the use of the free wake models are function of the free wake model itself, they will influence the coupling with the flight dynamics model and are thus discussed here.

The study of Landgrebe [51] looked at the correlation of free wake model wake geometries with experimental results. While this study did not include any flight dynamics effects or effects of the free wake model on flight dynamics results it did attempt to validate the wake geometries generated with a free wake model. The study also investigated the effects of various rotor parameters on wake geometries and compared them to experimental data. The various rotor design parameters were the following: number of blades, blade twist, aspect ratio, tip speed, and ground height. This is important since the amount of test data is limited, and any

validation of free wake geometries with test data is important, especially with respect to maneuvering forward flight applications. The study showed that, for hover, there was a good overall agreement between the predicted free wake geometries and those obtained from experiments.

Miller and Bliss [52] introduced a free wake model that calculates the wake geometry by direct inversion of a linear system. This model enforces periodicity of the wake as a boundary condition and is thus steady-state in nature. The wake was modeled as a single tip vortex released from each blade and held for four rotor turns by using a 15 degree azimuthal resolution. Results for low and high speed showed good correlations with results obtained by using traditional time-marching free wake models and indicated that no loss of accuracy was seen.

There are few studies that have focused on the validation of specific components of the mathematical models that make up the comprehensive codes, namely comparisons of predicted and experimental wake geometries, vortex strength and structure characteristics and the subsequent inflow distributions over the rotor disk. This is because of the limited amount of experimental data that is available due to the difficulties in making the required measurements in an experimental setting. However there are some studies that deal with the validation of the inflow and wake characteristics.

For instance the study of Hoad, Althoff and Elliott [53] looked at a validation of the inflow distributions predicted by using a number of analytical models, which included the CAMRAD code with the Scully free wake model [27]. The validation was performed by comparing the inflow distributions calculated in the simulation models at various advance ratios with experimental data measured on a reduced-scale rotor model in a wind tunnel. The test apparatus was a four-bladed fully articulated rotor where all blades were of a rectangular planform with NACA0012

airfoil section, -8 degrees of linear twist, 33.8 inch radius and 2.6 inch chord. The inflow measurements were made by using laser velocimetry at a vertical distance of approximately one chord length above the rotor. This vertical spacing resulted from difficulties in making velocity measurements within or close to the plane of the rotor. This also required that the induced velocity distributions used for comparison from the CAMRAD code also had to be calculated at the same vertical spacing above the plane of the rotor. The experimental and simulation inflow distributions were comparable at advance ratios below about $\mu = 0.15$ with some significant differences being observed at higher speeds. Most notably of these differences was the measured induced upflow region at the front of the rotor disk that enlarged from the forward most 20% of the rotor disk at $\mu = 0.15$ to almost the complete forward half of the rotor disk at $\mu = 0.30$, that was significantly under-predicted in extent by the CAMRAD model at high advance ratios.

The study by Ghee and Elliott [54] involved a validation of the wake geometries calculated using the CAMRAD code with the Scully free wake model [27] against experimental data. The test apparatus was the same as that used in the study of Hoad, Althoff and Elliott [53], which used a reduced scale, four-bladed fully articulated rotor. The visualization of the vortex wake geometry was performed by using a combination of a laser light sheet that was pulsated at the rotor speed to visualize a stationary wake and smoke was injected in the flow so that the flow structures were visible with the laser sheet. This study looked at a number of the physical aspects of the vortex wake, including the wake geometries, the apparent vortex trajectories near the rotor disk that gave an indication of the induced velocities and the characteristics of the vortex core. This study showed that the overall wake geometries were predicted well for the advance ratios of 0.15 and 0.23 considered in these studies. Although there were a number of areas in which the predictions did not agree with

the experimental data, including the trajectory of the tip vortices created near the leading edge of the disk that resulted in inaccuracies in the prediction of the upwash there.

1.2.4 Helicopter analysis in coordinated turns

One aspect of flight dynamics analysis that has not received much attention is the analysis of helicopters in turning flight. To this end, the current research study includes the analysis of articulated and hingeless rotor helicopters in level coordinated turns. The flight condition is also assumed to be steady by setting the linear and angular components of the body acceleration to zero. Coordinated turns are considered by enforcing the condition of zero resultant lateral force on the body. The focus of the present study is on the effect that inflow and blade modeling have on the trim and aeroelastic stability characteristics in steady coordinated turns at various forward speeds.

Chen and Jeske [55] formulated a set of exact kinematic equations that describe the motions of helicopters in steady helical turns. An important finding of this study was that the sideslip angle during steady coordinated turns has a strong influence on the trim equilibrium position. It was shown that the sideslip angle has a strong influence on the pitch attitude and roll rate of the helicopter. The effect of the angle of attack of the body on the helicopter attitudes and rates was also examined.

Ballin [32] looked at trim results for the UH-60A in descending and climbing steady coordinated turns and compared results generated with the GENHEL flight dynamics simulation model with flight test data. Kim [56] performed a similar comparison with the UM-GENHEL model and also presented some results in the frequency domain that compared frequency responses in straight flight with frequency responses in 1-g turns. There have been very few studies that deal with

articulated rotor, in particular the UH-60A helicopter, in steady coordinated turns, and none that deal with the aeroelasticity characteristics.

Aeroelastic studies of hingeless rotor helicopters in turning flight are very limited, and there is no experimental data with which to validate simulation results. Chen [57] has examined the stability and control characteristics of different rotor configurations by using the set of kinematic relations developed in Ref. [55]. The rotor was modeled by using a rigid blade with root springs, undergoing flap motion only. This study examined the factors that effect the stability in turns, including the effects of the direction of the turn and effects of forward speed.

Spence and Celi [58] looked at the aeromechanical stability of a soft-in-plane hingeless rotor helicopter in coordinated steady turns. An elastic blade model was used, including nonlinearities from moderately large elastic deflections. The Pitt-Peters dynamic inflow model was used to represent the inflow dynamics. The aeromechanical stability was assessed by starting from a trim state and linearizing the equations of motion. The resulting linear system has periodic coefficients and the stability characteristics was assessed by using Floquet theory. In this study, the effects of turn rate, aircraft speed and flight path angle on the stability in turns was examined. It was shown that the effect of level turns is to stabilize the lag mode. There were no comparisons with flight test data because there is no such data available that addresses aeromechanical stability in turning flight.

The studies of Celi [59, 60] have examined the aeroelastic stability of soft-in-plane hingeless rotor helicopters in steady "high-g" turns. The rotor model included coupled flap, lag and torsional degrees of freedom. The Dress wake model was used to describe the non-linear inflow distribution over the rotor disk. The study [59] focused on the effects of steady stall and compressibility effects associated with the use of a quasi-steady aerodynamics model and airfoil coefficients obtained from look-

up tables as functions of angle of attack and Mach number. It was shown that the effect of compressibility increased the damping of the lag mode.

1.2.5 Helicopter cross-coupling

A long-standing problem in helicopter flight dynamics has been the inability to accurately predict the off-axis response to pilot inputs. This is especially true of the pitch and roll cross-coupling. Until recently, the prediction of the off-axis response (e.g., the pitch response to a lateral cyclic pilot input) were inaccurate, to the point of sometimes having the wrong sign when compared to the results of flight tests. The cause of the discrepancies has come under recent scrutiny with a number of theories being presented as to the correct physical explanation of the off-axis response phenomena. Some of these explanations include the following: wake curvature, wake stacking, wake swirl, wake inertia, unsteady wake effects, blade flexibility, inaccurate modeling of rotor/fuselage interactions, and a number of other theories. At this stage, there is still no definitive explanation as to the precise physical causes of specific off-axis response observed on actual helicopters, nor is there a definitive mathematical theory that can be used in a flight dynamics simulation mode to accurately predict helicopter cross-coupling over a broad range of applications.

The first major contribution to the understanding of the off-axis response problem has come from the work of Rosen and Isser [61], who were the first to point out the importance of vortex spacing on the inflow distribution over the rotor disk during steady pitch and roll rate maneuvers. Steady pitch and roll motions of the rotor shaft alter the rotor wake spacing by decreasing the spacing on one side of the rotor disk and increasing the spacing on the opposite side. The distortions of the wake geometry resulting from maneuvers modifies the inflow distribution at the rotor disk. This change in inflow distribution causes changes in blade flapping, which

in turn changes the aerodynamic pitch and roll moments from the rotor. This study showed that, in hover, the inclusion of the wake distortion from a steady pitching motion of the shaft resulted in a sign change of the lateral flapping. Similar results were observed for rolling motions. A "specially developed" prescribed wake model was used to take into account the wake distortion effects caused by pitch and roll maneuvers. For the UH-60A and AH-64 helicopters, this new model was found to improve the prediction of cross-coupling pitch and roll derivatives. The mechanism is that for a steady nose-up shaft pitch rate, the wake vertical spacing is increased at the front of the disk and decreased at the rear of the disk, bringing the tip vortices closer to the rotor disk. This causes a decrease in inflow and increase in lift over the front of the disk and corresponding inflow increase and lift decrease over the rear. The change in longitudinal lift distribution results in a lateral change in blade flapping, which contributes to the off-axis response. While this study shows the importance of pitch rate effects on the wake geometry and subsequent inflow distributions, and that improvements in off-axis response predictions can be achieved, there are a number of limitations of this study that make it difficult to apply the theory to a general rotorcraft problem. First, the wake geometry and wake perturbations from steady shaft rates are prescribed, requiring an a priori knowledge of wake structures. Second, the analysis is performed in hover and it would be difficult to generalize to forward flight. Finally, the effects of wake geometry and inflow changes were examined on the lateral flapping only, and not on the lateral response of a helicopter in a general case.

Following Rosen and Isser's work, other investigations have developed simple inflow models that capture the inflow changes from a maneuver through the use of correction coefficients. Keller [15] developed a so called extended momentum theory that contains simple additional terms proportional to pitch and roll rates. The

additional terms contain correction coefficients that account for the wake geometry distortions from pitch and roll angular rates on the main rotor inflow, the numerical values of which are determined based on a vortex ring analysis. Results generated with the new inflow model were compared to flight test data for the UH-60A in hover, and they showed a significant improvement in the prediction of the off-axis response. The helicopter motion model included linear rotor/fuselage equations of motion that were specialized for hover. The fuselage and empennage aerodynamic forces were neglected as was the tail rotor. The rigid blade model was used with flap and lag hinges. Blade torsion was not included. The applicability of this model to general rotorcraft problems suffers from the same limitations as the study of Rosen and Isser [61], where the wake distortions resulting from angular rates are prescribed and the study is limited to the hover flight condition. Although since this new model is based on a simple three-state dynamic inflow model, its integration into existing flight dynamics simulation models is straight forward with no increase in execution time.

The wake geometry changes resulting from a maneuver have been modeled by Basset [62] and by Basset and Tchen-Fo [63] by using a dynamic vortex wake model. In this model, the wake is represented by vortex rings. The vortex rings were arranged into vortex groups where each contained a number of planar and concentric vortex rings. One vortex group was released from the rotor for each rotor revolution of time. The center of each vortex group was convected at the local velocity, that is a combination of the rotor trajectory and the inflow calculated from the mean aerodynamic load. While each vortex group remains planar, the effect of pitch and roll rate maneuvers alters the attitude of the planar vortices with respect to the rotor. In a flight dynamic simulation model, this wake model is used to calculate two wake distortion coefficients that relate the longitudinal inflow change to pitch

rate, K_q, and the lateral inflow change to the roll rate, K_p. The coefficients are then used in the Pitt-Peters dynamic inflow model [6, 7] to couple the angular rates to the inflow distribution. Results presented showed that K_q and K_p are non-linear functions of advance ratio and that the longitudinal and lateral values were different. Substantial improvements in the prediction of the hover off-axis response for the BO-105 were obtained. This study extends the work of Keller [15] to forward flight, and shows how the wake distortion correction coefficients vary with advance ratio.

The studies of Rosen and Isser [61], Keller [15] and Basset and Tchen-Fo [63] have made the assumption that there is a linear relationship between the change in inflow and the imposed angular rate. For instance the assumption is made that the longitudinal change in inflow is directly proportional to the magnitude of the pitch rate of the rotor disk, including the shaft pitch rate. This leads to the K_R factor [15] being independent of the angular rate for the hover cases considered.

A maneuvering free wake model was used by Bagai *et al.* [13] to study the effects of steady angular rates on inflow distributions. The free wake model used was the Maryland Free Wake model [1] with the addition of maneuvering effects [13]. The rotor was modeled as an isolated rotor and only flap dynamics were considered. The results of this study showed an essentially linear relationship between the angular rates and the longitudinal and lateral inflow changes. However, it was also shown that in low speed forward flight the proximity of the tip vortices to the rotor results in non-linear changes in the inflow distributions indicating that a simple superposition of inflow changes resulting from maneuvers may not be possible for this flight condition. Another important conclusion was the dependence of the results on the advance ratio, where the steady pitch and roll rates affect the longitudinal and lateral inflow differently, and show non-linear variations with advance ratio. These results with advance ratio compare favorably with similar results generated

by Basset [62, 63].

A completely different explanation for the discrepancies of off-axis predictions has been offered by von Grünhagen [64]. A "virtual inertia effect" was proposed that accounts for the in-plane, or swirl components of the rotor wake that increases the inertia of the main rotor and contributes to the overall equilibrium of the helicopter. In this analysis, the rotor wake was assumed to have a stationary angular momentum that is fixed to the rotor disk and moves with the rotor. In essence, the rotor wake adds a *virtual inertia* to the rotor that induces a reaction moment directly to the aircraft when angular rates of the rotor hub are present. The additional reaction moments are applied directly to the moment equilibrium equations of the fuselage, whereas the studies of Rosen and Isser [61], Keller [15] and Basset [62, 63] introduce changes to the inflow equations to account for wake distortion. This new theory can be easily added to an existing flight dynamics model as, in essence, a feedback of the aircraft angular rates on the moment equilibrium equations. This results in simple correction terms that can be added to a flight dynamics model, and has been shown to improve considerably the off-axis predictions for the BO-105 in hover and forward flight. This theory does not try to model the aerodynamic environment of the rotor in detail, but rather to present an overall effect that can be used within a flight dynamics simulation model to assist in the prediction of helicopter cross-coupling over a wide range of flight conditions.

All of the previous studies have attempted to improve the correlation of off-axis response through refined theoretical models. A different approach has been proposed by Mansur and Tischler [65]. Corrected lift and drag coefficients of the blade airfoils were obtained from the instantaneous, baseline values through a first-order filter, the time constant of which is selected in terms of an equivalent aerodynamic phase lag. This phase lag is then determined from flight test data by using system identification

techniques. This approach was spured by the fact that linear models extracted from flight test data do accurately capture the off-axis response phenomena, while linear models generated from simulation models are lacking in off-axis response predictions. The technique was applied to the analysis of the AH-64 and substantially improved the off-axis response predictions in both hover and forward flight. The dependence of the technique on experimental data limits its applicability to general helicopter problems. This is especially the case where appropriate test data in the required flight condition is not available. While this model was shown to improve the off-axis flight response prediction capability of flight simulation models for specific cases, it does not contribute significantly to the physical understanding of helicopter cross-coupling.

A review of three aerodynamic models that have been proposed to improve off-axis response predictions was made by Arnold [17]. The aerodynamic models are as follows: 1. Momentum theory extended to include the effects of wake distortion on the inflow distribution [15]. 2. A first-order aerodynamic lag model that his in general equivalent to a lift deficiency function where τ_L is an aerodynamic phase lag that is used in the equation for the aerodynamic lift. 3. An aerodynamic phase correction, that essentially produces a phase shift in the aerodynamic flapping moment, where ψ_a is the aerodynamic phase angle that is defined by this theory. Comparisons between the different models were made with the UH-60A helicopter in hover by using a simple helicopter model and with blade degrees of freedom in flap only. Results showed that when the theoretical values of the coefficients were used in each of the models, there were significant improvements in off-axis predictions. Yet the best agreement with test data was obtained with coefficient values that were higher than their theoretical values. This indicates that, in each case, the theoretical analyses capture some but not all of the effects required to give the best agreement

with test data.

1.3 Objectives of Study

The primary motivation for the present research is that current flight dynamics simulation capabilities are inadequate in a number of areas. As a consequence, for example, flight control law design based only on analytical predictions of helicopter dynamics is still unsatisfactory, and extensive tuning of the flight control laws on the actual aircraft is usually needed. Reasonably accurate results have been obtained by taking advantage of flight test results, or through specific assumptions on the behavior of the aircraft. This requires that the actual aircraft be available for testing, and limits the range of validity of the results. An especially challenging example is the prediction of the off-axis response of helicopters to pilot inputs, which has traditionally been predicted inaccurately (particularly roll-to-pitch and pitch-to-roll cross-coupling), to the extent of sometimes being predicted in the opposite direction to test data.

More sophisticated representations of the aerodynamics and dynamics of the main rotor have the potential of increasing the accuracy and the generality of the predictions. To obtain accurate, first principle based predictions, a coupled flap, lag and torsional elastic blade model and a maneuvering free vortex wake model are probably necessary, but no flight dynamic simulation model with such a level of refinement is currently available.

In light of the literature review presented in the previous section, and the motivations listed above, the main objectives of this study are:

1. To develop a mathematical model that includes flexible blades, arbitrary hub motions and a maneuvering free vortex wake model for flight dynamics ap-

plications. This will be accomplished by coupling the Bagai-Leishman maneuvering free wake with an existing flight dynamic simulation that already includes flexible blade modeling.

2. To develop methods for the calculation of trim equilibrium conditions, linear models and free-flight dynamics time responses, as needed by the introduction of the free wake, and to validate these results with test data.

3. To identify issues related to the use of the free vortex wake model for various flight dynamics calculations and determine the validity and limitations of assumptions made in this the new mathematical model and in the solution procedures.

4. To study the effects of aerodynamic modeling, particularly inflow modeling, and blade modeling on various types of flight dynamics predictions.

5. To investigate helicopter cross-coupling (particularly roll-to-pitch and pitch-to-roll cross-coupling) characteristics and mechanisms of articulated and hingeless rotor helicopters, and to assess the effects of inflow and blade modeling on the cross-coupling predictions.

6. To validate the new simulation model through comparisons with flight test data.

Additionally, the original flight dynamics model, which was specialized for the Sikorsky UH-60A Blackhawk, will be extended to include a detailed configuration of the Eurocopter BO-105. This will allow the validation of the model with two different sets of flight test data. The validation with the BO-105 data will be especially significant, because this hingeless rotor helicopter exhibits strong couplings between

roll and pitch dynamics, and blade flexibility plays an important role in its flight dynamic characteristics.

Chapter 2

Mathematical Model

This chapter describes the main features of the mathematical model of the helicopter used in this research. A brief overview of the main mathematical features of the model is followed by a detailed description of the aircraft coordinate systems and reference frames. A list of the main assumptions used in the formulation of the mathematical model, and in the solution methods is provided next. The chapter continues with the formulation of the main rotor equations of motion, including the components of the equations, the finite element discretization of the equations, and the modal coordinate transformation. Then the formulation of the rigid fuselage equations, including complete descriptions of all of the components of the applied loads. Followed by the formulation of the equation representing tail rotor inflow dynamics and the transformation of the equations of motion into rigorous first order, state space form. Finally, the main rotor inflow models are briefly described: first, the dynamic inflow models, in the versions with and without the modeling of maneuvering effects, and then, the maneuvering free vortex wake model.

2.1 Overview

The mathematical model used in this study describes the rigid body dynamics of the aircraft, the coupled flap-lag-torsion-axial dynamics of each main rotor blade, and the inflow dynamics for the main rotor and the tail rotor. With the exception of the free wake, the mathematical model is formulated as a system of first order, coupled, non-linear ordinary differential equations of the form:

$$\dot{\mathbf{y}} = \mathbf{f}(\mathbf{y}, \mathbf{u}; t) \tag{2.1}$$

where $\mathbf{y}$ is a vector of states, $\mathbf{u}$ is a vector of controls and t is time.

The maneuvering free wake model is implemented as a set of nonlinear algebraic equations. These equations result from the finite difference discretization of a hyperbolic partial differential equation (PDE), namely the vorticity transport equation [66]. Because the free wake finite difference equations are solved using a relaxation technique, the solution is a steady state wake geometry and inflow distribution appropriate for a steady flight condition. Therefore, although the governing equations contain the ingredients required to describe time-accurate wake dynamics, the free wake model of Ref. [13] used in this research is rigorously valid only for a trimmed flight condition.

The wake partial differential equations are simultaneously discretized in space and in time, and there is no intermediate stage where the partial differential equations are converted into a set of ordinary differential equations with time as the independent variable. Therefore, the wake model does not contribute any additional dynamic equations to the basic flight dynamics model, nor does it change the basic first order form of the equations of motion from Eqn. (2.1). This mismatch between the mathematical forms of the wake and of the rest of the aircraft model raises a number of issues concerning the incorporation of the free wake model into

the flight dynamic analysis, especially in the extraction of a linearized model and in the calculation of the transient response to pilot inputs. These issues will be addressed in detail in the following chapters.

When a dynamic inflow model, rather than the free wake, is used to describe the main rotor inflow, the state vector $\mathbf{y}$ takes the form (for a four-bladed rotor):

$$\begin{aligned}\mathbf{y}(\psi_i) &= [u\ v\ w\ p\ q\ r\ \phi_F\ \theta_F\ \psi_F\ \lambda_t\ \lambda_0\ \lambda_c\ \lambda_s\ q_1^1\ q_2^1\ q_3^1\ q_4^1\ \dot{q}_1^1\ \dot{q}_2^1\ \dot{q}_3^1\ \dot{q}_4^1 \\ &\quad \ldots q_1^{N_h}\ q_2^{N_h}\ q_3^{N_h}\ q_4^{N_h}\ \dot{q}_1^{N_h}\ \dot{q}_2^{N_h}\ \dot{q}_3^{N_h}\ \dot{q}_4^{N_h}] \end{aligned} \tag{2.2}$$

in which u, v, w, p, q, and r are the velocities and rates in the body fixed coordinate system; ϕ_F, θ_F, and ψ_F are the Euler angles of the fuselage; λ_0, λ_c, and λ_s are respectively the uniform, cosine and sine coefficients of the dynamic inflow model; λ_t is the tail rotor inflow; and q_i^k and $\dot{q}_i^k$ are the generalized displacement and velocity coordinates for the i-th blade and the k-th normal mode in the rotating frame at the azimuth angle ψ_i.

When the inflow distribution over the main rotor is calculated using the free wake model, the dynamic inflow states (λ_0, λ_c, and λ_s) are removed from the state vector and the dynamic inflow equations are removed from the first-order model. The state vector then takes the form:

$$\begin{aligned}\mathbf{y}(\psi) &= [u\ v\ w\ p\ q\ r\ \phi_F\ \theta_F\ \psi_F\ \lambda_t\ q_1^1\ q_2^1\ q_3^1\ q_4^1\ \dot{q}_1^1\ \dot{q}_2^1\ \dot{q}_3^1\ \dot{q}_4^1 \\ &\quad \ldots q_1^{N_h}\ q_2^{N_h}\ q_3^{N_h}\ q_4^{N_h}\ \dot{q}_1^{N_h}\ \dot{q}_2^{N_h}\ \dot{q}_3^{N_h}\ \dot{q}_4^{N_h}] \end{aligned} \tag{2.3}$$

The control vector, $\mathbf{u}$ is defined as:

$$\mathbf{u} = [\theta_0\ \theta_{1c}\ \theta_{1s}\ \theta_t\ \dot{\theta}_0\ \dot{\theta}_{1c}\ \dot{\theta}_{1s}] \tag{2.4}$$

where θ_0 and θ_t are the main and tail rotor collective controls, θ_{1c} and θ_{1s} are the lateral and longitudinal cyclic controls and $\dot{\theta}_0$, $\dot{\theta}_{1c}$ and $\dot{\theta}_{1s}$ are the time derivatives

of the pitch controls. The time derivatives of the pitch controls are required only in special cases, such as, for example, in the modeling of the lag damper used on the Sikorsky UH-60A [3, 5].

2.2 Coordinate Systems

The coordinate systems required for the formulation of the equations can be divided into three groups, namely:

1. *Body coordinate systems*, which are used to describe the overall motion of the helicopter.

2. *Main rotor coordinate systems*, which are used to formulate the equations of motion of the rotor blades, including the calculation of the aerodynamic and inertia loads, and the elastic deformations of the blades.

3. *Free wake coordinate systems*, which are used to describe the geometry of the vortex wake with respect to the main rotor blades.

2.2.1 Body coordinate systems

The three main coordinate systems that are used to describe the overall motion of the aircraft are the inertial, body-fixed, and wind coordinate systems. The frames of reference of these coordinate systems and the transformations from one system to another are as follows:

Inertial coordinate system

The inertial coordinate system has its origin at the center of mass of the helicopter, with the z-axis aligned parallel to the direction of gravity. The actual directions of the x and y axes are not important in the present study, because the results are not

a function of the course followed by the aircraft. If such information was important, the x and y axes could be selected as pointing North and East respectively. The axes of this coordinate system are x_I, y_I, z_I with corresponding unit vectors $\mathbf{i}_\mathrm{I}$, $\mathbf{j}_\mathrm{I}$, $\mathbf{k}_\mathrm{I}$. This coordinate system is shown in Figure 2.1.

Body-fixed coordinate system

The body-fixed coordinate system has its origin at the center of mass of the helicopter, and axes that rotate with the fuselage. This system will also be referred to as the "fuselage" coordinate system. Its axes are x_B, y_B, z_B, and point forward, to starboard, and downward respectively. The corresponding unit vectors are $\mathbf{i}_\mathrm{B}$, $\mathbf{j}_\mathrm{B}$, $\mathbf{k}_\mathrm{B}$. The $x_B - z_B$ plane is a plane of symmetry, or quasi-symmetry of the helicopter. This system is illustrated in Figure 2.1.

The transformation from inertial to body-fixed frames of reference is based on the Euler angles ϕ, θ and ψ which represent the roll, pitch and yaw attitudes of the aircraft. This transformation by the Euler angles is illustrated in Figure 2.2. The transformation from inertial frame to body-fixed frame is given by the matrix [67]:

$$[T_{\mathrm{BI}}] = \begin{bmatrix} \cos\theta\cos\psi & \sin\psi\cos\theta & -\sin\theta \\ \sin\phi\sin\theta\cos\psi - \cos\phi\sin\psi & \sin\phi\sin\theta\sin\psi + \cos\phi\cos\psi & \sin\phi\cos\theta \\ \cos\phi\sin\theta\cos\psi + \sin\phi\sin\psi & \cos\phi\sin\theta\sin\psi - \sin\phi\cos\psi & \cos\phi\cos\theta \end{bmatrix} \tag{2.5}$$

so that:

$$\begin{Bmatrix} \mathbf{i}_\mathrm{B} \\ \mathbf{j}_\mathrm{B} \\ \mathbf{k}_\mathrm{B} \end{Bmatrix} = [T_{\mathrm{BI}}] \begin{Bmatrix} \mathbf{i}_\mathrm{I} \\ \mathbf{j}_\mathrm{I} \\ \mathbf{k}_\mathrm{I} \end{Bmatrix} \tag{2.6}$$

Helicopter manufacturers often identify longitudinal, lateral, and vertical reference lines, and define points on the helicopter with reference to these axes; the distances along these lines are called stations, buttlines and waterlines, respectively

(e.g., see Ref. [3]). Then the x, y and z body-axes are parallel to the longitudinal, lateral, and vertical reference lines, respectively.

2.2.2 Wind coordinate system

The wind coordinate system has its origin at the center of mass of the helicopter and is defined with respect to the freestream airflow experienced by the helicopter. For the hovering flight condition, where there is no freestream airflow, the wind coordinate system becomes undefined. To overcome this problem, the hover is considered in this study to be at a forward speed of 1 knot.

The x_W-axis of the wind coordinate system is aligned with the freestream velocity, and points forward. The y_W and z_W axes point to the right and down respectively. The wind and body-fixed frames are related by the aircraft angles of attack α_F and sideslip β_F (the subscript "F" has been added to prevent confusion with the aerodynamic angle of attack of the blade cross-sections and the blade flapping angle respectively). As customary [67] the angle of attack α_F is defined as the angle that the projection of the freestream velocity vector onto the x_B-z_B plane makes with the x_B body axis; the angle is positive for a relative airflow coming from below. The sideslip angle β_F is defined as the angle that the airflow makes with the x_B-z_B plane, and is positive with the relative airflow coming from the right. The unit vectors of this coordinate system are $\mathbf{i}_\mathrm{W}$, $\mathbf{j}_\mathrm{W}$, $\mathbf{k}_\mathrm{W}$ along x_W, y_W, and z_W respectively.

As shown in Figure 2.3, the transformation from body-fixed to wind reference frames is obtained by a rotation of the sideslip angle β_F about the z_B-axis, followed by a rotation of the angle of attack α_F about the y-axis (which is the y_B-axis after the β_F rotation). This transformation from body-fixed to wind coordinate systems

is given by the matrix:

$$[T_{\mathrm{WB}}] = \begin{bmatrix} \cos\alpha_F \cos\beta_F & -\cos\alpha_F \sin\beta_F & -\sin\alpha_F \\ \sin\beta_F & \cos\beta_F & \\ \sin\alpha_F \cos\beta_F & -\sin\alpha_F \sin\beta_F & \cos\alpha_F \end{bmatrix} \tag{2.7}$$

so that:

$$\begin{Bmatrix} \mathbf{i}_{\mathrm{W}} \\ \mathbf{j}_{\mathrm{W}} \\ \mathbf{k}_{\mathrm{W}} \end{Bmatrix} = [T_{\mathrm{WB}}] \begin{Bmatrix} \mathbf{i}_{\mathrm{B}} \\ \mathbf{j}_{\mathrm{B}} \\ \mathbf{k}_{\mathrm{B}} \end{Bmatrix} \tag{2.8}$$

2.2.3 Main rotor coordinate systems

Shaft coordinate system

To relieve steady loads in flight, main rotor shafts are not usually mounted parallel to the z_B body axis, but instead their axes make small angles with it. The angles that the shaft makes with the y_B-z_B and with the x_B-z_B plane are defined as the longitudinal and lateral shaft tilt respectively, and are denoted with i_θ and i_ϕ. The shaft coordinate system takes these angles into account. This is a non-rotating coordinate system that has its origin at the rotor hub. Its orientation depends on the tilt of the main rotor shaft relative to the body-fixed coordinate system. Its axes are x_S, y_S, z_S with corresponding unit vectors $\mathbf{i}_{\mathrm{S}}$, $\mathbf{j}_{\mathrm{S}}$, $\mathbf{k}_{\mathrm{S}}$. The transformation from body-fixed to shaft-fixed reference frames is defined by a rotation of i_θ about the body-fixed y-axis followed by a rotation of i_ϕ about the x-axis.

The transformation from body-fixed to shaft-fixed frame is illustrated in Figure 2.4 and is described by the following matrix:

$$\{T_{\mathrm{SB}}] = \begin{bmatrix} \cos i_\theta & \sin i_\theta \sin i_\phi & \sin i_\theta \cos i_\phi \\ 0 & \cos i_\phi & -\sin i_\phi \\ -\sin i_\theta & \cos i_\theta \sin i_\phi & \cos i_\theta \cos i_\phi \end{bmatrix} \tag{2.9}$$

so that:

$$\begin{Bmatrix} \mathbf{i}_{\mathrm{S}} \\ \mathbf{j}_{\mathrm{S}} \\ \mathbf{k}_{\mathrm{S}} \end{Bmatrix} = [T_{\mathrm{SB}}] \begin{Bmatrix} \mathbf{i}_{\mathrm{B}} \\ \mathbf{j}_{\mathrm{B}} \\ \mathbf{k}_{\mathrm{B}} \end{Bmatrix} \tag{2.10}$$

Hub rotating coordinate system

The hub rotating coordinate system has its origin at the hub; the system rotates about the z-axis with a speed equal to the main rotor speed. Its axes are x, y, z and the corresponding unit vectors are $\mathbf{i}$, $\mathbf{j}$, $\mathbf{k}$. The z-axis is aligned parallel with the shaft and points upwards, in the opposite direction to z_S. The x-axis lies in a vertical plane passing through the elastic axis of the undeformed blade. The y-axis is orthogonal to the x-z plane and points in the blade lead direction. Each blade has its own set of hub rotating coordinates. The relationship between the hub rotating coordinate system and the shaft coordinate system is illustrated in Figure 2.5.

The transformation from shaft non-rotating coordinates to hub rotating coordinates is defined by the blade azimuth angle, which is positive in the direction of rotation with the advancing blade on the starboard side of the rotor, and is zero when the blade is over the tail. The transformation from the shaft non-rotating to the hub rotating reference frames is given by the matrix:

$$\{T_{\mathrm{RS}}\} = \begin{bmatrix} -\cos\psi & \sin\psi & 0 \\ \sin\psi & \cos\psi & 0 \\ 0 & 0 & -1 \end{bmatrix} \tag{2.11}$$

so that:

$$\begin{Bmatrix} \mathbf{i} \\ \mathbf{j} \\ \mathbf{k} \end{Bmatrix} = [T_{\mathrm{RS}}] \begin{Bmatrix} \mathbf{i}_{\mathrm{S}} \\ \mathbf{j}_{\mathrm{S}} \\ \mathbf{k}_{\mathrm{S}} \end{Bmatrix} \tag{2.12}$$

Undeformed preconed blade coordinate system

The undeformed preconed blade coordinate system is a rotating coordinate system with origin at the blade root. Its unit vectors are $\hat{\mathbf{e}}_x$, $\hat{\mathbf{e}}_y$, $\hat{\mathbf{e}}_z$, defined such that $\hat{\mathbf{e}}_x$ points outboard, $\hat{\mathbf{e}}_y$ points in the blade lead direction and $\hat{\mathbf{e}}_z$ points upwards perpendicular to the blade elastic axis. The transformation from the hub rotating coordinate system to the undeformed preconed blade coordinate system is defined

by the blade precone angle β_p. The transformation is given by the matrix:

$$T_{\mathrm{PR}} = \begin{bmatrix} \cos\beta_p & 0 & \sin\beta_p \\ 0 & 1 & 0 \\ -\sin\beta_p & 0 & \cos\beta_p \end{bmatrix} \tag{2.13}$$

so that:

$$\begin{Bmatrix} \hat{\mathbf{e}}_x \\ \hat{\mathbf{e}}_y \\ \hat{\mathbf{e}}_z \end{Bmatrix} = [T_{\mathrm{PR}}] \begin{Bmatrix} \mathbf{i} \\ \mathbf{j} \\ \mathbf{k} \end{Bmatrix} \tag{2.14}$$

For the case in which there is no precone, the hub rotating and undeformed preconed blade coordinate systems are coincident. This is the coordinate system in which the equations of motion of the blade are written.

Deformed blade coordinate system

The deformed blade coordinate system is a rotating coordinate system with origin at any point on the deformed elastic axis of the blade. Its unit vectors are $\hat{\mathbf{e}}'_x$, $\hat{\mathbf{e}}'_y$, $\hat{\mathbf{e}}'_z$ where $\hat{\mathbf{e}}'_x$ points outboard along the tangent to the elastic axis at the origin point. The $\hat{\mathbf{e}}'_y$ axis is aligned with the blade chord perpendicular to the elastic axis and is positive in the blade lead direction. The $\hat{\mathbf{e}}'_z$ is normal to the $\hat{\mathbf{e}}'_x$-$\hat{\mathbf{e}}'_y$ plane and is defined as positive up.

The transformation from undeformed to deformed blade coordinates is given by the matrix [68]:

$$T_{\mathrm{DP}} = \begin{bmatrix} S_{11} & S_{12} & S_{13} \\ S_{21} & S_{22} & S_{23} \\ S_{31} & S_{32} & S_{33} \end{bmatrix} \tag{2.15}$$

where

$$\begin{aligned} S_{11} &= \cos\theta_y \cos\theta_z \\ S_{12} &= \cos\theta_y \sin\theta_z \\ S_{13} &= -\sin\theta_y \\ S_{21} &= \sin\theta_x \sin\theta_y \cos\theta_z - \cos\theta_x \sin\theta_z \end{aligned}$$

$$
\begin{aligned}
S_{22} &= \cos\theta_x \cos\theta_z - \sin\theta_x \sin\theta_y \sin\theta_z \\
S_{23} &= \sin\theta_x \cos\theta_y \\
S_{31} &= \cos\theta_x \sin\theta_y \cos\theta_z + \sin\theta_x \sin\theta_z \\
S_{32} &= -(\sin\theta_x \cos\theta_z - \cos\theta_x \sin\theta_y \sin\theta_z) \\
S_{33} &= \cos\theta_x \cos\theta_y
\end{aligned}
$$

and where,

$$
\begin{aligned}
\theta_x &= \phi \\
\sin\theta_y &= -\frac{w_{,x}}{\sqrt{1 + 2u_{,x} + {u_{,x}}^2 + {v_{,x}}^2 + {w_{,x}}^2}} \\
\cos\theta_y &= -\frac{\sqrt{1 + 2u_{,x} + {u_{,x}}^2 + {v_{,x}}^2}}{\sqrt{1 + 2u_{,x} + {u_{,x}}^2 + {v_{,x}}^2 + {w_{,x}}^2}} \\
\sin\theta_z &= \frac{v_{,x}}{\sqrt{1 + 2u_{,x} + {u_{,x}}^2 + {v_{,x}}^2 + {w_{,x}}^2}} \\
\cos\theta_z &= \frac{1 + u_{,x}}{\sqrt{1 + 2u_{,x} + {u_{,x}}^2 + {v_{,x}}^2 + {w_{,x}}^2}}
\end{aligned}
$$

The transformation from the undeformed, preconed blade coordinate system to the deformed blade coordinate system is given by:

$$
\left\{ \begin{array}{c} \hat{\mathbf{e}}'_x \\ \hat{\mathbf{e}}'_y \\ \hat{\mathbf{e}}'_z \end{array} \right\} = [T_{\mathrm{DP}}] \left\{ \begin{array}{c} \hat{\mathbf{e}}_x \\ \hat{\mathbf{e}}_y \\ \hat{\mathbf{e}}_z \end{array} \right\} \tag{2.16}
$$

The relationships between the hub rotating coordinate system and the undeformed and deformed preconed blade coordinate systems are illustrated in Figure 2.6.

Tip path plane coordinate system

The tip path plane coordinate system is a nonrotating coordinate system used in the formulation of the dynamic inflow model [7]. Its unit vectors are $\mathbf{i}_{\mathrm{TPP}}$, $\mathbf{j}_{\mathrm{TPP}}$, $\mathbf{k}_{\mathrm{TPP}}$. The z-axis of this coordinate system is perpendicular to the plane defined

by the first-harmonic flapping motion of the blade tips and points downward. The transformation from the shaft reference frame to the tip path plane reference frame is illustrated in Figure 2.7 and is given by the matrix:

$$[T_{\mathrm{TS}}] = \begin{bmatrix} \cos\beta_{1c} & \sin\beta_{1c}\sin\beta_{1s} & \sin\beta_{1c}\cos\beta_{1s} \\ 0 & \cos\beta_{1s} & -\sin\beta_{1s} \\ -\sin\beta_{1c} & \cos\beta_{1c}\sin\beta_{1s} & \cos\beta_{1c}\cos\beta_{1s} \end{bmatrix} \tag{2.17}$$

where β_{1c} and β_{1s} are multiblade coordinates defined as follows:

$$\beta_{1c} = \frac{2}{N_{\mathrm{b}}} \sum_{j=1}^{N_{\mathrm{b}}} \frac{w_{\mathrm{tip}j}}{R-e} \cos\psi_j \tag{2.18}$$

$$\beta_{1s} = \frac{2}{N_{\mathrm{b}}} \sum_{j=1}^{N_{\mathrm{b}}} \frac{w_{\mathrm{tip}j}}{R-e} \sin\psi_j \tag{2.19}$$

where N_{b} is the number of blades, e is the hinge offset and $w_{\mathrm{tip}j}$ is the elastic deflection of the tip of the jth blade.

The unit vectors of the tip path plane and shaft-fixed systems are related by:

$$\begin{Bmatrix} \mathbf{i}_{\mathrm{TPP}} \\ \mathbf{j}_{\mathrm{TPP}} \\ \mathbf{k}_{\mathrm{TPP}} \end{Bmatrix} = [T_{\mathrm{TS}}] \begin{Bmatrix} \mathbf{i}_{\mathrm{S}} \\ \mathbf{j}_{\mathrm{S}} \\ \mathbf{k}_{\mathrm{S}} \end{Bmatrix} \tag{2.20}$$

Blade sectional aerodynamics coordinate system

The blade sectional aerodynamics coordinate system is a rotating coordinate system with its origin at any point on the elastic axis of the blade. This is the coordinate system in which the local airflow velocity components at the blade section are represented. Its unit vectors are $\mathbf{e}_T$, $\mathbf{e}_P$ and $\mathbf{e}_R$, defined such that $\mathbf{e}_T$ points aft in the blade lag direction, $\mathbf{e}_P$ points outboard along the tangent to the elastic axis at the origin point and $\mathbf{e}_R$ is normal to the $\mathbf{e}_T$-$\mathbf{e}_P$ plane and is defined as positive up.

The total airflow velocity at a blade section used in the calculation of the sectional aerodynamic loads in the blade sectional aerodynamics coordinate is represented as:

$$\mathbf{V}_A = U_T\mathbf{e}_T + U_P\mathbf{e}_P + U_R\mathbf{e}_R \tag{2.21}$$

and the absolute velocity of the blade section in the undeformed preconed blade coordinate system is represented as:

$$\mathbf{V}_P = V_x\hat{\mathbf{e}}_x + V_y\hat{\mathbf{e}}_y + V_z\hat{\mathbf{e}}_z \tag{2.22}$$

The transformation of the absolute velocity of the blade section in the undeformed preconed blade coordinate system to the total airflow velocity in the blade sectional aerodynamics coordinate system is given by the matrix:

$$[T_{\mathrm{AP}}] = \begin{bmatrix} -\sin\zeta & \cos\zeta & 0 \\ \sin\beta\cos\zeta & \sin\beta\sin\zeta & -\cos\beta \\ -\cos\beta\cos\zeta & -\cos\beta\sin\zeta & -\sin\beta \end{bmatrix} \tag{2.23}$$

where β and ζ are the local flap and lag slopes of the blade elastic axis with reference to the undeformed preconed blade coordinate system and are given by:

$$\beta = \frac{\partial w}{\partial x} \tag{2.24}$$

$$\zeta = \frac{\partial v}{\partial x} \tag{2.25}$$

where w and v represent the flap and lag displacements of the elastic axis.

The unit vectors of the blade sectional aerodynamics and undeformed preconed blade coordinate systems are related by:

$$\begin{Bmatrix} \mathbf{e}_T \\ \mathbf{e}_P \\ \mathbf{e}_R \end{Bmatrix} = [T_{\mathrm{AP}}] \begin{Bmatrix} \hat{\mathbf{e}}_x \\ \hat{\mathbf{e}}_y \\ \hat{\mathbf{e}}_z \end{Bmatrix} \tag{2.26}$$

2.2.4 Free wake coordinate systems

The free wake model [1] used in this study is formulated in a wind axis system. The trim conditions used for wake geometry and inflow calculations are consistent with a wind tunnel trim methodology. Therefore, the shaft tilt angle with respect to the freestream flow is fixed and the trim controls, θ_0, θ_{1c}, θ_{1s} are determined to provide a thrust vector of prescribed magnitude and aligned parallel to the rotor

shaft. This alignment of the thrust vector is obtained when the tip path plane is parallel to the rotor hub plane, which implies that there is no cyclic variation in the blade flapping angle. Therefore, only a rotor coning angle is considered in the free wake calculations. The free wake formulation leads to the following coordinate systems:

Global wake coordinate system

The global wake coordinate system is a wind axis system in which the free wake model is formulated. The x-axis is aligned with the freestream flow and is positive aft, the y-axis points to starboard and the z-axis points up. For a wind tunnel trim problem, the x-axis is aligned with the longitudinal axis of the wind tunnel.

As illustrated in Figure 2.8, the angle that the z-axis makes with the rotor shaft is the longitudinal shaft tilt α_S, and also indicates the angle of attack of the rotor hub with respect to the freestream flow. Because there is no cyclic variation in rotor flapping, the longitudinal shaft tilt α_S is also the angle of attack of the rotor tip path plane with respect to the freestream flow. The longitudinal shaft tilt α_S is defined as positive with the shaft tilted aft so that the thrust vector is also tilted in the aft direction. The axes of the global coordinate system are x_G, y_G, z_G, with corresponding unit vectors $\mathbf{i}_\mathrm{G}$, $\mathbf{j}_\mathrm{G}$, $\mathbf{k}_\mathrm{G}$.

Rotating blade coordinate system

The rotating blade coordinate system has its origin at the hub, with the x-axis aligned with the blade elastic axis and pointing outboard. The free wake model assumes that the blade is rigid in flap, lag and torsion and has a single flap hinge located at the axis of rotation. The y-axis of this coordinate system is perpendicular to the blade and points forward in the direction of the lead motion of the blade.

The z-axis points upwards perpendicular to the x-y plane. This is the coordinate system in which the local blade aerodynamic environment is defined for the free wake model. The axes of this coordinate system are x_F, y_F, z_F with corresponding unit vectors $\mathbf{i}_\mathrm{F}$, $\mathbf{j}_\mathrm{F}$, $\mathbf{k}_\mathrm{F}$.

The transformation from the global coordinate system to the rotating blade coordinate system requires a rotation by the longitudinal shaft tilt α_S about the y_G-axis, followed by a rotation of the azimuth angle ψ about the new z-axis that is aligned with the tilted rotor shaft, and a rotation of the blade coning angle β_0 about the new y-axis which is normal to the shaft and points in the blade lead direction. The coning angle used here is the sum of the coning due to blade flapping and of any built-in precone angle if present.

The transformation from the global coordinate system to the rotating blade coordinate system is given by the matrix:

$$[T_\mathrm{FG}] = \begin{bmatrix} \cos\alpha_S \cos\psi \cos\beta_0 \\ \quad + \sin\alpha_S \sin\beta_0 & \sin\psi\cos\beta_0 & -\sin\alpha_S\cos\psi\cos\beta_0 \\ & & \quad + \cos\alpha_S \sin\beta_0 \\ -\cos\alpha_S \sin\psi & \cos\psi & \sin\alpha_S \sin\psi \\ -\cos\alpha_S\cos\psi\sin\beta_0 & -\sin\psi\sin\beta_0 & \sin\alpha_S\cos\psi\sin\beta_0 \\ \quad + \sin\alpha_S\cos\beta_0 & & \quad + \cos\alpha_S\cos\beta_0 \end{bmatrix} \tag{2.27}$$

so that:

$$\begin{Bmatrix} \mathbf{i}_\mathrm{F} \\ \mathbf{j}_\mathrm{F} \\ \mathbf{k}_\mathrm{F} \end{Bmatrix} = [T_\mathrm{FG}] \begin{Bmatrix} \mathbf{i}_\mathrm{G} \\ \mathbf{j}_\mathrm{G} \\ \mathbf{k}_\mathrm{G} \end{Bmatrix} \tag{2.28}$$

Free wake blade preconed coordinate system

The free wake blade preconed coordinate system has its origin at the hub; its unit vectors are $\mathbf{i}_\mathrm{P}$, $\mathbf{j}_\mathrm{P}$, $\mathbf{k}_\mathrm{P}$ with the x-axis pointing outboard along the blade, the y-axis pointing in the blade lead direction and the z-axis pointing up. The induced velocities calculated in the free wake model are returned to the flight dynamics

model in this reference frame.

The transformation from the global-fixed frame to the free wake blade preconed rotating frame is defined by a rotation of the longitudinal shaft tilt α_S about the global fixed y_G-axis, followed by a rotation of the azimuth angle ψ about the new z-axis that is aligned with the tilted rotor shaft, and a rotation of the precone angle β_P about the new y-axis which is normal to the rotor shaft and points in the blade lead direction.

The transformation from global-fixed to blade preconed reference frames is given by the matrix:

$$T_{\mathrm{PG}} = \begin{bmatrix} \cos\alpha_S \cos\psi \cos\beta_p & \sin\psi \cos\beta_p & -\sin\alpha_S \cos\psi \cos\beta_p \\ +\sin\alpha_S \sin\beta_p & & +\cos\alpha_S \sin\beta_p \\ -\cos\alpha_S \sin\psi & \cos\psi & \sin\alpha_S \sin\psi \\ -\cos\alpha_S \cos\psi \sin\beta_p & -\sin\psi \sin\beta_p & \sin\alpha_S \cos\psi \sin\beta_p \\ +\sin\alpha_S \cos\beta_p & & +\cos\alpha_S \cos\beta_p \end{bmatrix} \tag{2.29}$$

so that:

$$\begin{Bmatrix} \mathbf{i}_{\mathrm{P}} \\ \mathbf{j}_{\mathrm{P}} \\ \mathbf{k}_{\mathrm{P}} \end{Bmatrix} = [T_{\mathrm{PG}}] \begin{Bmatrix} \mathbf{i}_{\mathrm{G}} \\ \mathbf{j}_{\mathrm{G}} \\ \mathbf{k}_{\mathrm{G}} \end{Bmatrix} \tag{2.30}$$

2.2.5 Coupling of the flight dynamic and the free wake coordinate systems

Because the coordinate systems used in the free wake model are slightly different from those used in the rest of the flight dynamic model, it is necessary to define appropriate transformations between the two sets.

The first such transformation is required because the freestream velocity and body rates calculated in the flight dynamic coordinate systems need to be provided to the free wake model. This requires a conversion from the body-fixed axis system (Section 2.2.1) to the global wake axis system (Section 2.2.4).

The second transformation is required when the inflow distribution calculated in the free wake model needs to be provided to the rest of the flight dynamic model.

This requires a conversion from the rotating blade coordinate system used in the free wake model (Section 2.2.4) to a reformulated free wake blade preconed coordinate system (from that of Section 2.2.4).

Body-fixed to global wake coordinate systems

The conversion from the body-fixed coordinate system used in the flight dynamic model to the global wake system used in the free wake model requires some consideration of the trim procedures for which each model was intended. For instance, for wind tunnel trim calculations, the x-axis of the global wake coordinate system is aligned with the freestream and results in a fixed angle of attack of the rotor disk. For free-flight trim calculations this is not the case because the pitch and roll attitudes of the body are variable, and because the cyclic variation in blade flapping change the angle of attack of the rotor disk with respect to the freestream.

Therefore, to define the transformation between the two systems, the axes of the free wake global wake coordinate system are assumed to be aligned with the body-fixed axes system. This results in a global wake coordinate system that is no longer aligned with the freestream flow but rather with the aircraft body and that also rotates with the body. Using this convention, any changes in the angles of attack or sideslip in the flight dynamics model will be treated as changes in the velocity components, u, v, w used by the free wake model. Using this assumption the transformation from the body-fixed to the wake global wake reference frames is simply given by the following matrix:

$$T_{\mathrm{GB}} = \begin{bmatrix} -1 & 0 & 0 \\ 0 & 1 & 0 \\ 0 & 0 & -1 \end{bmatrix} \tag{2.31}$$

so that:

$$\begin{Bmatrix} \mathbf{i}_{\mathrm{G}} \\ \mathbf{j}_{\mathrm{G}} \\ \mathbf{k}_{\mathrm{G}} \end{Bmatrix} = [T_{\mathrm{GB}}] \begin{Bmatrix} \mathbf{i}_{\mathrm{B}} \\ \mathbf{j}_{\mathrm{B}} \\ \mathbf{k}_{\mathrm{B}} \end{Bmatrix} \tag{2.32}$$

Using this transformation, the velocity components of the body can be converted from the body-fixed system to the global wake axis system as follows:

$$\left\{ \begin{array}{c} u_G \\ v_G \\ w_G \end{array} \right\} = \left\{ \begin{array}{c} -u_B \\ v_B \\ -w_B \end{array} \right\} \tag{2.33}$$

and the body pitch and roll rates are converted as follows:

$$\left\{ \begin{array}{c} p_G \\ q_G \end{array} \right\} = \left\{ \begin{array}{c} -p_B \\ q_B \end{array} \right\} \tag{2.34}$$

This transformation also implies that the angle of attack of the rotor disk α_S used in the free wake model is equal to the longitudinal shaft tilt i_θ in the flight dynamics model.

Blade flap angle transformation

In the free wake model formulation the blade flap angle is assumed to be constant [66], and therefore longitudinal and lateral flapping are not explicitly included. Therefore, the free wake model needs to be slightly modified, so that the blade flap angle is a function of the azimuth angle and not simply equal to a constant coning angle.

A further assumption made in the free wake model is that the blade is straight and has a flap hinge at the axis of rotation. Because in the present study the blades may be flexible and have hinges not exactly on the axis of rotation, an "equivalent" blade flap angle needs to be defined, for use in the free wake calculations. This flap angle β represents the angle between the hub plane and a straight blade hinged at the axis of rotation that has the same tip flap displacement as the elastic blade. This is illustrated in Figure 2.9, which shows that the tip flap locations are the same for the straight and elastic blades. The "equivalent" blade flapping angle is given by the following equation:

$$\beta(\psi) = \frac{w_{\text{tip}}(\psi)}{R} + \beta_p \tag{2.35}$$

where w_{tip} is the flapping displacement of the elastic blade from the undeformed preconed blade coordinate system in the flight dynamics model and β_p is the blade precone angle. The blade flapping angle $\beta(\psi)$ therefore includes contributions from both the blade precone angle and the elastic deformation of the blade. The calculation of the tip flap displacement within the flight dynamic model is discussed in Section 3.2.2.

The transformation from the global wake coordinate system to the free wake rotating blade coordinate system given in Equation (2.27) is now defined by a rotation by the longitudinal shaft tilt i_θ followed by the azimuth angle ψ and the flapping angle β as follows:

$$T_{\text{FG}} = \begin{bmatrix} \cos i_\theta \cos\psi \cos\beta \\ + \sin i_\theta \sin\beta \\ - \cos i_\theta \sin\psi \\ - \cos i_\theta \cos\psi \sin\beta \\ + \sin i_\theta \cos\beta \end{bmatrix} \begin{matrix} \sin\psi \cos\beta \\ \\ \cos\psi \\ \\ - \sin\psi \sin\beta \end{matrix} \begin{bmatrix} - \sin i_\theta \cos\psi \cos\beta \\ + \cos i_\theta \sin\beta \\ \sin i_\theta \sin\psi \\ \sin i_\theta \cos\psi \sin\beta \\ + \cos i_\theta \cos\beta \end{bmatrix} \tag{2.36}$$

so that:

$$\begin{Bmatrix} \mathbf{i}_{\text{F}} \\ \mathbf{j}_{\text{F}} \\ \mathbf{k}_{\text{F}} \end{Bmatrix} = [T_{\text{FG}}] \begin{Bmatrix} \mathbf{i}_{\text{G}} \\ \mathbf{j}_{\text{G}} \\ \mathbf{k}_{\text{G}} \end{Bmatrix} \tag{2.37}$$

For completeness, the transformation from the global fixed to free wake blade preconed reference frames given in Equation (2.29) is also reformulated as:

$$T_{\text{PG}} = \begin{bmatrix} \cos i_\theta \cos\psi \cos\beta_p \\ + \sin i_\theta \sin\beta_p \\ - \cos i_\theta \sin\psi \\ - \cos i_\theta \cos\psi \sin\beta_p \\ + \sin i_\theta \cos\beta_p \end{bmatrix} \begin{matrix} \sin\psi \cos\beta_p \\ \\ \cos\psi \\ \\ - \sin\psi \sin\beta_p \end{matrix} \begin{bmatrix} - \sin i_\theta \cos\psi \cos\beta_p \\ + \cos i_\theta \sin\beta_p \\ \sin i_\theta \sin\psi \\ \sin i_\theta \cos\psi \sin\beta_p \\ + \cos i_\theta \cos\beta_p \end{bmatrix} \tag{2.38}$$

so that:

$$\begin{Bmatrix} \mathbf{i}_{\text{P}} \\ \mathbf{j}_{\text{P}} \\ \mathbf{k}_{\text{P}} \end{Bmatrix} = [T_{\text{PG}}] \begin{Bmatrix} \mathbf{i}_{\text{G}} \\ \mathbf{j}_{\text{G}} \\ \mathbf{k}_{\text{G}} \end{Bmatrix} \tag{2.39}$$

It should be mentioned that it is assumed within the free wake model that the blade does not have lag and torsion degrees of freedom. Thus lag and torsion effects are not included in these transformations.

2.3 Main assumptions

The main assumptions made in the formulation of the mathematical model used in this research are listed below.

1. The undeformed blade is straight with no sweep, droop or torque offsets.

2. The wind velocity is zero.

3. The airframe is a rigid body with a constant mass and a uniform mass distribution; the x-z plane is a plane of symmetry.

4. For the Sikorsky UH-60 configuration the pitch angle of the horizontal stabilizer is fixed for a given flight condition, and the control logic for the automatic positioning of the stabilizer is not modeled.

5. The fuselage and tail surface aerodynamics are derived from wind tunnel tests without the main rotor. The aerodynamic coefficients are provided in the form of look-up tables as functions of angle of attack and sideslip, which are not necessarily small angles. Stall, compressibility, and unsteady aerodynamic effects are neglected for the fuselage and tail.

6. For the Eurocopter BO-105 configuration, the blade is cantilevered at the hub and its feathering axis is preconed by the angle β_P.

7. For the Sikorsky UH-60 configuration, the blade is assumed to be rigid in flap, lag and torsion inboard of the flap and lag hinges.

8. The flap, lag and pitch hinges (when they are present) are coincident.

9. The blade cross sections are symmetric with respect to the major principal axes.

10. The lines connecting the blade cross-sectional centers of gravity (CG), aerodynamic centers (AC), and elastic axes (EA) need not be coincident. The blade cross-sectional area centroid and elastic axes are coincident, meaning that the tension center is coincident with the elastic axis.

11. Blade chord, built-in twist, stiffness and mass properties, and cross-sectional offsets are defined at discrete spanwise stations, and vary linearly in between.

12. The blade is built of an isotropic, linearly elastic material.

13. Bernoulli-Euler beam theory is used, implying that plane cross sections remain plane and perpendicular to the elastic axis during deformations. The effects of shear deformation are neglected.

14. The blade undergoes moderate deflections implying small strains and finite rotations.

15. Structural damping forces are of a viscous type.

16. Without the free wake inflow model, a two-dimensional quasi-steady aerodynamics model is used to calculate the main rotor aerodynamics loads. The unsteady aerodynamics of the main rotor is modeled by a dynamic inflow model. The tip losses due to 3D effects are approximated by considering the outboard 3% of the blade to be ineffective aerodynamically.

17. The aerodynamic coefficients of the main rotor blade sections are provided in the form of look-up tables derived from wind tunnel tests. The lift, drag and moment coefficients are tabulated as a function of angle of attack, for Mach numbers ranging from 0.3 to 1 in increments of 0.1. The aerodynamic coefficients vary linearly between angle of attack and Mach number data points.

18. The effects of dynamic stall are not included. Static stall is reflected in the empirical lift, drag and moment coefficients. Below stall the unsteady aerodynamic includes circulatory effects and the acceleration type non-circulatory effects are neglected with the exception of the pitch damping.

19. Aerodynamic forces and moments on the blade section are based on the airflow velocity at the elastic axis of the blade.

20. All blades are assumed to have identical mass, stiffness, and geometric properties.

21. The blades rotate at a constant angular speed, Ω. Engine and engine control system dynamics are neglected.

22. The blade pitch control system, including the actuators, is infinitely stiff. Freeplay in the control linkages is not modeled. The swashplate and tail rotor collective control are attached rigidly to the pilot controls.

The following assumptions are made when coupling the free wake model to the rest of the flight dynamic model:

1. Blade trailed vorticity is characterized by a single vortex released from the blade elastic axis at the blade tip.

2. The initial tip vortex strength is taken to be a percentage of the maximum bound circulation along the blade. The percentage value used is determined empirically. The same value is used at all azimuth angles.

3. Within the free wake model, it is assumed that the blade is rigid and straight with a single flap hinge at the axis of rotation. An "equivalent" flap angle is defined as indicated in Section 2.2.5.

4. The free wake model provides all three spatial components of the induced velocity in the free wake blade preconed coordinate system (see Section 2.2.4), however the x and y components are set to zero and only the z component (i.e., the component along the z_P axis) is used for the calculation of the aerodynamic loads.

5. For the purpose of calculating all the aerodynamic properties, the bound circulation and blade control points are located at the 1/4-chord station. This implies that the Weissinger-L model [69], which locates the blade control points at the 3/4-chord station, is not used.

2.4 Main rotor equations of motion

This section contains a brief description of the mathematical model of the rotor system. The basic formulation and solution of the equations is unchanged with respect to previous work (see Section 1.1 for a description of the evolution of the model), and therefore only the most important modeling features are summarized here.

The dynamics of the main rotor blades are treated individually in the rotating frame where equations for each blade are formulated independently, rather than considering the dynamics of the rotor system as a whole and formulating the equations in the non-rotating frame. This modeling of individual blades by separate (although coupled) equations allows for the analysis of rotor systems with dissimilar blades. So this analysis can model rotor systems where conceivably all of the blades are tracked differently and thus have different dynamics, or an extreme case where the blade control is ineffective through the failure of a pitch link. However, for all of the results in this study, the blades are assumed to be identical and follow the same

track.

The main rotor blades are modeled as flexible beams undergoing coupled flap, lag, torsion, and axial motion. They are attached to a hub that may have large amplitude linear and angular motions. The blade equations of motion are nonlinear, coupled, partial differential equations with periodic coefficients. These equations are transformed into a system of nonlinear, coupled, *ordinary* differential equations using a finite element discretization to eliminate the spatial variable. The discretization is based on Galerkin's method of weighted residuals. The resulting beam finite element has 15 nodal degrees of freedom, namely: flap and lag bending displacements and slopes at the ends of the element, for a total of 8 degrees of freedom; torsional rotations at the ends of the element and at the element mid-point; and axial displacements at four equally spaced nodes within the element, including the two end points. The aerodynamic, structural, tensile and inertial load vectors are calculated numerically, using Gaussian integration.

A modal coordinate transformation, is used to reduce the number of degrees of freedom and consequently the number of equations that describe the dynamics of each rotor blade. Coupled, rotating blade mode shapes are used in the transformation. The result is a system of nonlinear, coupled, second order ordinary differential equations with time-varying coefficients, which is converted to first-order form and is coupled to the rest of the mathematical model.

This section summarizes the formulation of the main rotor equations of motion. The derivation of the distributed aerodynamic, inertial, structural, and tension loads is described first. Next is a description of the finite element modeling procedure including the degrees of freedom within each element, the calculation of the element load vectors, and the assembly of the local element properties into a global blade finite element model. This is followed by a description of the calculation of the blade

mode shapes, of the modal coordinate transformation, and of the final conversion to first order form.

2.4.1 Main rotor aerodynamic loads

A key ingredient for the calculation of the aerodynamic forces and moments is the absolute velocity of a point on the elastic axis of the blade, which is the derivative with respect to time of the position vector of a point on the elastic axis of the blade relative to a fixed point. The position vector is given by:

$$\mathbf{R}_P = \mathbf{R}_{CG} + \mathbf{R}_H + \mathbf{R}_B \tag{2.40}$$

where $\mathbf{R}_{CG}$ is the position vector of the body center of gravity with respect to a fixed point, $\mathbf{R}_H$ is the position vector of the hub with respect to the center of gravity and $\mathbf{R}_B$ is the position vector of the point P, on the elastic axis of the blade, with respect to the hub.

The position vector of the hub as referenced from the center of gravity, $\mathbf{R}_H$, is given by:

$$\mathbf{R}_H = x_H \mathbf{i}_\mathrm{B} + y_H \mathbf{j}_\mathrm{B} + z_H \mathbf{k}_\mathrm{B} \tag{2.41}$$

where x_H, y_H and z_H are the components of the position vector from the center of gravity of the body to the hub.

The position vector of the point on the elastic axis as referenced from the hub, $\mathbf{R}_B$, is given by:

$$\mathbf{R}_B = e\mathbf{i} + (x_0 + u)\hat{\mathbf{e}}_x + v\hat{\mathbf{e}}_y + w\hat{\mathbf{e}}_z \tag{2.42}$$

where e is the offset of the blade flap, lag and pitch hinges (where present) from the axis of rotation. This also marks the radial location of the blade root, where the elastic portion of the blade begins; the portion of the blade inboard of the hinge is assumed to be rigid, but may still produce aerodynamic loads if the actual

configuration requires it. The quantity x_0 is the distance from the blade root (start of elastic portion) to the point P on the elastic axis of the undeformed section in the $\hat{\mathbf{e}}_x$ direction and u, v and w are the components of the elastic deflections of the point from the undeformed blade frame. Using the coordinate transformation presented in Eqn. (2.13), this position vector can be expressed in terms of the undeformed preconed coordinate system as

$$\mathbf{R}_B = (e\cos\beta_p + x_0 + u)\hat{\mathbf{e}}_x + v\hat{\mathbf{e}}_y + (w - \sin\beta_p)\hat{\mathbf{e}}_z \tag{2.43}$$

where β_p is the blade precone angle.

The absolute velocity of the point on the elastic axis is given by:

$$\mathbf{V}_P = \frac{d\mathbf{R}_P}{dt} = \frac{d\mathbf{R}_{CG}}{dt} + \frac{d\mathbf{R}_H}{dt} + \frac{d\mathbf{R}_B}{dt} \tag{2.44}$$

where

$$\frac{d\mathbf{R}_H}{dt} = \frac{\partial\mathbf{R}_H}{\partial t} + \boldsymbol{\omega}\times\mathbf{R}_H \tag{2.45}$$

$$\frac{d\mathbf{R}_B}{dt} = \frac{\partial\mathbf{R}_B}{\partial t} + \boldsymbol{\omega}\times\mathbf{R}_B \tag{2.46}$$

where $\boldsymbol{\omega}$ is the angular velocity vector of the body and is

$$\boldsymbol{\omega} = p\mathbf{i}_\mathrm{B} + q\mathbf{j}_\mathrm{B} + r\mathbf{k}_\mathrm{B} \tag{2.47}$$

where p, q and r are respectively the roll, pitch and yaw rates.

Because the fuselage is rigid, the derivative $\partial\mathbf{R}_H/\partial t$ is zero. The component $\partial\mathbf{R}_B/\partial t$ is the velocity vector of the point as seen by an observer that moves with the body-fixed axes. Therefore, it is given by

$$\frac{\partial\mathbf{R}_B}{\partial t} = \left(\frac{\partial\mathbf{R}_B}{\partial t}\right)_R + \boldsymbol{\Omega}\times\mathbf{R}_B \tag{2.48}$$

where $\left(\frac{\partial\mathbf{R}_B}{\partial t}\right)_R$ represents the velocity vector of the point relative to the hub in the rotating frame and $\boldsymbol{\Omega}$ is the angular velocity vector of the main rotor

$$\boldsymbol{\Omega} = \Omega\mathbf{k}_\mathrm{S} \tag{2.49}$$

where Ω is the rotor speed.

The body components of the velocity are

$$\frac{d\mathbf{R}_{CG}}{dt} = u\mathbf{i}_{\mathrm{B}} + v\mathbf{j}_{\mathrm{B}} + w\mathbf{k}_{\mathrm{B}} \tag{2.50}$$

where u, v and w are the linear velocity components in the body-fixed axes system and should not be confused with the blade elastic deflections in Eqn. 2.43.

The absolute velocity $\mathbf{V}_P$ (from Eqn. 2.44) is given by:

$$\mathbf{V}_P = \frac{d\mathbf{R}_{CG}}{dt} + \left(\frac{\partial \mathbf{R}_B}{\partial t}\right)_R + \boldsymbol{\Omega} \times \mathbf{R}_B + \boldsymbol{\omega} \times [\mathbf{R}_H + \mathbf{R}_B] \tag{2.51}$$

The total velocity $\mathbf{V}_T$ of the generic point is given by

$$\mathbf{V}_T = \mathbf{V}_P - \mathbf{V}_I \tag{2.52}$$

where $\mathbf{V}_I$ is the velocity induced at the generic point by the rotor wake. In the undeformed preconed blade coordinate system, the components of the velocity $\mathbf{V}_P$ can be written in the form

$$\mathbf{V}_P = V_{11}\hat{\mathbf{e}}_x + V_{12}\hat{\mathbf{e}}_y + V_{13}\hat{\mathbf{e}}_z \tag{2.53}$$

where $\hat{\mathbf{e}}_x$, $\hat{\mathbf{e}}_y$ and $\hat{\mathbf{e}}_z$ are the unit vectors of the undeformed preconed blade coordinate system and V_{11}, V_{12} and V_{13} are the velocity components in each of these directions. The second term in Eqn. (2.52) can similarly be written as

$$\mathbf{V}_I = \lambda_x\hat{\mathbf{e}}_x + \lambda_y\hat{\mathbf{e}}_y + \lambda_z\hat{\mathbf{e}}_z \tag{2.54}$$

where λ_x, λ_x and λ_x are the x, y and z components in the undeformed preconed blade coordinate system of the induced velocity. With the dynamic inflow model, only the z component of the induced velocity is available, but with the free wake inflow model, all three inflow components are available. However in this study only

the z component of $\mathbf{V}_I$ will be considered even when the free wake inflow model is used.

Including only the z component of the induced velocity, the total velocity is

$$\begin{aligned} \mathbf{V}_T &= V_{11}\hat{\mathbf{e}}_x + V_{12}\hat{\mathbf{e}}_y + (V_{13} - \lambda_z)\hat{\mathbf{e}}_z \quad (2.55) \\ &= V_x\hat{\mathbf{e}}_x + V_y\hat{\mathbf{e}}_y + V_z\hat{\mathbf{e}}_z \quad (2.56) \end{aligned}$$

where V_x, V_y and V_z are the velocity components in the undeformed preconed blade coordinate system.

Using the coordinate transformation presented in Eqn. (2.23), which takes into account the local flap and lag angles of the blade section elastic axis, this total velocity can be expressed in terms of the airflow velocity components in the blade sectional aerodynamics coordinate system

$$\mathbf{V}_A = U_T\mathbf{e}_T + U_P\mathbf{e}_P + U_R\mathbf{e}_R \quad (2.57)$$

where $\mathbf{V}_A$ is the resultant velocity of the airflow at the 1/4-chord location. The U_T and U_R components follow the usual sign conventions by which U_T is positive for an airflow coming toward the leading edge of the airfoil and U_R is positive for an outboard flow. The component U_P is defined as positive for a flow coming from below.

The yaw angle of the flow γ_I is shown in Figure 2.10 and is defined in terms of the velocity components as

$$\gamma_I = \cos^{-1}\left[\frac{|U_T|}{\sqrt{U_T^2 + U_R^2}}\right] \quad (2.58)$$

so that

$$\cos\gamma_I = \frac{|U_T|}{\sqrt{U_T^2 + U_R^2}} \quad (2.59)$$

so that $\cos\gamma_I$ is always a number between 0 and 1. This implies that $\cos\gamma_I$ is positive regardless of the sign of the U_T component of the flow.

The angle of attack at the blade section α_Y (also shown in Figure 2.10) is given by:

$$\alpha_Y = \tan^{-1}\left[\frac{(U_T\tan\theta_G + U_P)\cos\gamma_I}{U_T - U_P\tan\theta_G\cos^2\gamma_I}\right] \tag{2.60}$$

where θ_G is the total geometric pitch of the blade section, defined as

$$\theta_G = \theta_0 + \theta_{1c}\cos(\psi + \Delta_{SP}) + \theta_{1s}\sin(\psi + \Delta_{SP}) + \theta_{TW} + \phi \tag{2.61}$$

where ψ is the blade azimuth angle, θ_{TW} is the built-in twist, Δ_{SP} is the swashplate phasing angle and ϕ is the elastic rotating of the blade section about the elastic axis.

The blade section lift, drag and moment coefficients are obtained from data look-up tables as a function of the local angle of attack and Mach number, that is

$$C_L = C_L(\alpha_Y, M) \tag{2.62}$$

$$C_D = C_D(\alpha_Y, M) \tag{2.63}$$

$$C_M = C_M(\alpha_Y, M) \tag{2.64}$$

The blade section force and moment calculations are based on two-dimensional quasi-steady aerodynamics [14]. The basic expressions for the distributed lift L and pitching moment M are [14]:

$$L = L_Q + \frac{1}{2}a\rho(bR)^2\left[\ddot{h} + V_0\dot{\alpha} - \left(x_A - \frac{1}{2}bR\right)\ddot{\alpha}\right] \tag{2.65}$$

$$\begin{aligned} M = {} & L_Q x_A + \frac{1}{2}a\rho(bR)^2\left(x_A - \frac{1}{2}bR\right)\left[\ddot{h} - \left(x_A - \frac{1}{2}bR\right)\ddot{\alpha}\right] \\ & -\frac{1}{2}a\rho V_0\dot{\alpha}(bR - x_A)(bR)^2 - \left(\frac{a}{16}\right)\rho(bR)^4\ddot{\alpha} \end{aligned} \tag{2.66}$$

where a is the lift-curve slope, ρ is the air density, b is the non-dimensional semi-chord length, R is the blade radius, α is the total pitch angle of the blade section

, h, $\dot{h}$ and $\ddot{h}$ are the heave displacement, velocity and acceleration respectively, V_0 is the oncoming freestream flow, x_A is the blade cross-sectional aerodynamic center offset from the elastic axis (positive for aerodynamic center forward of the elastic axis). $\dot{\alpha}$ is the time rate of change of the total blade pitch angle and is

$$\dot{\alpha} = \dot{\theta}_G = -\theta_{1c}\sin(\psi + \Delta_{SP}) + \theta_{1s}\cos(\psi + \Delta_{SP}) + \dot{\phi} \tag{2.67}$$

The quasi-steady lift L_Q is given by:

$$L_Q = a\rho bRV_0^2\left[\alpha + \frac{\dot{h}}{V_0} + \frac{\dot{\alpha}}{V_0}(bR - x_A)\right] \tag{2.68}$$

The acceleration terms $\ddot{h}$ and $\ddot{\alpha}$ in Eqs. (2.65) and (2.66) will be neglected in the present study. They represent non-circulatory or apparent mass terms, together with the $\dot{\alpha}$ term that instead will be retained. With this simplification, the expression for the quasi-steady lift remains unchanged, whereas the expressions for the total lift and the aerodynamic pitching moment reduce to

$$L = L_Q + \frac{1}{2}a\rho(bR)^2V_0\dot{\alpha} \tag{2.69}$$

$$M = L_Q x_A - \frac{1}{2}a\rho V_0\dot{\alpha}(bR - x_A)(bR)^2 \tag{2.70}$$

In Eqn. (2.68) the term $\alpha + \frac{\dot{h}}{V_0}$ represents the angle of attack α_Y, which is used in the data tables to obtain the lift coefficient. Thus the current implementation of the quasi-steady lift equation is

$$L_Q = \frac{1}{2}C_L\rho V_0^2 c + \frac{1}{2}a\rho V_0 c\left(\frac{c}{2} - x_A\right)\dot{\alpha} \tag{2.71}$$

$$= \frac{1}{2}\rho V_0^2 c\left[C_L + \frac{a\dot{\alpha}}{V_0}\left(\frac{c}{2} - x_A\right)\right] \tag{2.72}$$

where c is the local blade chord.

The lift equation (Eqn. (2.69)), with the chord c substituted for the semi-chord b, becomes

$$L = L_Q + \frac{1}{8}a\rho_A V_0 c^2\dot{\alpha} \tag{2.73}$$

The aerodynamic drag is given by:

$$D = C_D \frac{1}{2} \rho_A V_0^2 c \tag{2.74}$$

where C_D is the steady drag coefficient obtained from look-up tables.

The aerodynamic lift L and drag D forces have to be transformed to the local blade sectional aerodynamics coordinate system. The aerodynamic force components are f_P in the direction of the $\mathbf{e}_P$ axis, f_T in the direction of the $\mathbf{e}_R$ axis and f_R in the direction of the $\mathbf{e}_R$ axis. The transformation of the aerodynamics forces is given by:

$$f_P = \frac{1}{V_0} \left[L \frac{U_T}{\cos \gamma_I} + D U_P \right] \tag{2.75}$$

$$f_T = \frac{1}{V_0} \left[D U_T - L U_P \cos \gamma_I \right] \tag{2.76}$$

$$f_R = \frac{1}{V_0} \left[D U_R - L \frac{U_P \cos \gamma_I U_R}{U_T} \right] \tag{2.77}$$

For convenience the total pitching moment is separated into three components as follows:

$$M = M_S + M_Q + M_{\dot{\alpha}} \tag{2.78}$$

where M_S the a steady component resulting from the steady pitching moment coefficient C_M, M_Q is the component from Eqn. (2.70) resulting from the quasi-steady lift and $M_{\dot{\alpha}}$ is the component from Eqn. (2.70) that represents the non-circulatory pitch damping contribution. These components are written as follows:

$$M_S = \frac{1}{2} C_M \rho V_0^2 c^2 \tag{2.79}$$

$$M_Q = f_P \frac{L_Q}{L} x_A \cos \theta_G + f_T \frac{L_Q}{L} x_A \sin \theta_G \tag{2.80}$$

$$M_{\dot{\alpha}} = -\frac{1}{8} a \rho V_0 c^2 \dot{\alpha} \left(\frac{c}{2} - x_A \right) \tag{2.81}$$

where the ratio $\frac{L_Q}{L}$ is required to scale the force components f_P and f_T which

contain the total lift and not just the quasi-steady lift component that is required in Eqn. (2.80).

The distributed aerodynamic loads are calculated in the undeformed preconed blade coordinate system by converting the force components in the blade sectional aerodynamics coordinate system f_P, f_T and f_R using the inverse of the coordinate transformation matrix presented in Eqn. (2.23). The distributed aerodynamic forces are

$$\begin{aligned}
\mathbf{p}_{\mathrm{A}} &= \left(f_P \cos\zeta \sin\beta - f_T \sin\zeta - f_R \cos\zeta \cos\beta\right) \hat{\mathbf{e}}_x \\
&\quad + \left(f_P \sin\zeta \sin\beta + f_T \cos\zeta - f_R \sin\zeta \cos\beta\right) \hat{\mathbf{e}}_y \\
&\quad + \left(-f_P \cos\beta - f_R \sin\beta\right) \hat{\mathbf{e}}_z \\
&= p_{\mathrm{A}x}\hat{\mathbf{e}}_x + p_{\mathrm{A}y}\hat{\mathbf{e}}_y + p_{\mathrm{A}z}\hat{\mathbf{e}}_z
\end{aligned} \tag{2.82}$$

The distributed aerodynamic moments are

$$\begin{aligned}
\mathbf{q}_{\mathrm{A}} &= -M\cos\zeta\cos\beta\hat{\mathbf{e}}_x - M\sin\zeta\cos\beta\hat{\mathbf{e}}_y - M\sin\beta\hat{\mathbf{e}}_z \\
&= q_{\mathrm{A}x}\hat{\mathbf{e}}_x + q_{\mathrm{A}y}\hat{\mathbf{e}}_y + q_{\mathrm{A}z}\hat{\mathbf{e}}_z
\end{aligned} \tag{2.83}$$

2.4.2 Main rotor inertial loads

In the formulation of the main rotor equations of motion, the distributed loads due to blade inertia are required. These inertia loads are dependent on the absolute acceleration of a point on the rotor blade, $\mathbf{a}_P$. The inertia forces and moments per unit span are respectively given by

$$\begin{aligned}
\mathbf{p}_{\mathrm{I}} &= -\int_A \rho(\mathbf{a}_P + g\mathbf{k}_{\mathrm{I}})dA \\
&= p_{\mathrm{I}x}\hat{\mathbf{e}}_x + p_{\mathrm{I}y}\hat{\mathbf{e}}_y + p_{\mathrm{I}z}\hat{\mathbf{e}}_z
\end{aligned} \tag{2.84}$$

$$\begin{aligned}
\mathbf{q}_{\mathrm{I}} &= -\int_A \rho\left[(y_0\hat{\mathbf{e}}'_x + z_0\hat{\mathbf{e}}'_y) \times (\mathbf{a}_P + g\mathbf{k}_{\mathrm{I}})\right] dA \\
&= q_{\mathrm{I}x}\hat{\mathbf{e}}_x + q_{\mathrm{I}y}\hat{\mathbf{e}}_y + q_{\mathrm{I}z}\hat{\mathbf{e}}_z
\end{aligned} \tag{2.85}$$

where ρ is the mass density of the blade, y_0 and z_0 are the coordinates of the generic mass point of the cross section A (see Figure 2.6) and $g\mathbf{k_I}$ is the contribution due to gravity ($\mathbf{k_I}$ is the z-component of the inertial coordinate system (see Section 2.2.1)).

The absolute acceleration of the point on the rotor blade ($\mathbf{a}_P$ in Eqs. (2.84) and (2.85)) is obtained by taking the second derivative with respect to time of the position vector of the point. The formulation of the position vector $\mathbf{R}_P$ for the calculation of the inertial loads is the same as that in Eqn. (2.40) with some additions since the point P refers to a general point on the deformed blade section, whereas for the aerodynamic loads calculations P was on the elastic axis. With reference to Eqn. (2.42) the position vector of the point with respect to the hub is represented by

$$\mathbf{R}_B = e\mathbf{i} + (x_0 + u)\hat{\mathbf{e}}_x + v\hat{\mathbf{e}}_y + w\hat{\mathbf{e}}_z \underline{+ y_0\hat{\mathbf{e}}'_y + z_0\hat{\mathbf{e}}'_z} \tag{2.86}$$

where the underlined terms have been added to Eqn. (2.42). Using the coordinate transformations presented in Eqs. (2.13) and (2.15), this position vector can be expressed in terms of the undeformed preconed coordinate system as

$$\begin{aligned} \mathbf{R}_B &= \left[(e\cos\beta_p + u) + x_0 \underline{+ S_{21}y_0 + S_{31}z_0}\right]\hat{\mathbf{e}}_x + \\ &\quad \left[v \underline{+ S_{22}y_0 + S_{32}z_0}\right]\hat{\mathbf{e}}_y + \left[w - \sin\beta_{\mathrm{P}} \underline{+ S_{23}y_0 + S_{33}z_0}\right]\hat{\mathbf{e}}_z \end{aligned} \tag{2.87}$$

where the underlined terms are the additions to Eqn. (2.43) for the generic point on the deformed blade section.

The absolute velocity of the point is the same as that in Eqn. (2.51)

$$\mathbf{V}_P = \frac{d\mathbf{R}_{CG}}{dt} + \left(\frac{\partial \mathbf{R}_B}{\partial t}\right)_R + \boldsymbol{\Omega} \times \mathbf{R}_B + \boldsymbol{\omega} \times [\mathbf{R}_H + \mathbf{R}_B] \tag{2.88}$$

where each of the components are the same as those defined in Section 2.4.1 with the exception of the $\mathbf{R}_B$ vector which is defined in Eqn. (2.87).

The acceleration of the point on the blade relative to a fixed point is

$$\begin{aligned}\mathbf{a}_P &= \frac{d^2\mathbf{R}_{CG}}{dt^2} + \frac{\partial^2\mathbf{R}_B}{\partial t^2} + 2\boldsymbol{\omega} \times \frac{\partial \mathbf{R}_B}{\partial t} + \dot{\boldsymbol{\omega}} \times (\mathbf{R}_B + \mathbf{R}_H) + \\ &\quad \boldsymbol{\omega} \times [\boldsymbol{\omega} \times (\mathbf{R}_B + \mathbf{R}_H)] \end{aligned} \tag{2.89}$$

where

$$\frac{\partial^2\mathbf{R}_B}{\partial t^2} = \left(\frac{\partial^2\mathbf{R}_B}{\partial t^2}\right)_R + \dot{\boldsymbol{\Omega}} \times \mathbf{R}_B + 2\boldsymbol{\Omega} \times \left(\frac{\partial \mathbf{R}_B}{\partial t}\right)_R + \boldsymbol{\Omega} \times (\boldsymbol{\Omega} \times \mathbf{R}_B) \tag{2.90}$$

The body components of the acceleration are

$$\frac{d^2\mathbf{R}_{CG}}{dt^2} = \dot{u}\mathbf{i}_\mathrm{B} + \dot{v}\mathbf{j}_\mathrm{B} + \dot{w}\mathbf{k}_\mathrm{B} \tag{2.91}$$

where $\dot{u}$, $\dot{v}$ and $\dot{w}$ are the linear acceleration components in the body fixed axes system.

Combining Eqs. (2.48), (2.89) and (2.90) gives the final expression for the absolute acceleration of a point on the blade

$$\begin{aligned}\mathbf{a}_P &= \frac{d^2\mathbf{R}_{CG}}{dt^2} + \dot{\boldsymbol{\omega}} \times \mathbf{R}_H + \boldsymbol{\omega} \times (\boldsymbol{\omega} \times \mathbf{R}_H) + \left(\frac{\partial^2\mathbf{R}_B}{\partial t^2}\right)_R + \dot{\boldsymbol{\Omega}} \times \mathbf{R}_B + \\ &\quad 2\boldsymbol{\Omega} \times \left(\frac{\partial \mathbf{R}_B}{\partial t}\right)_R + \boldsymbol{\Omega} \times (\boldsymbol{\Omega} \times \mathbf{R}_B) + \dot{\boldsymbol{\omega}} \times \mathbf{R}_B + \\ &\quad 2\boldsymbol{\omega} \times \left[\left(\frac{\partial \mathbf{R}_B}{\partial t}\right)_R + \boldsymbol{\Omega} \times \mathbf{R}_B\right] + \boldsymbol{\omega} \times (\boldsymbol{\omega} \times \mathbf{R}_B) \end{aligned} \tag{2.92}$$

The acceleration in Eqn. (2.92) is substituted into Eqs. (2.84) and (2.85) to give the distributed forces and moments per unit span at the particular blade section. The expansion of the acceleration terms is further detailed by Turnour [33].

2.4.3 Main rotor structural loads

The structural terms in the main rotor blade equations of motion are derived using Bernoulli-Euler theory for homogeneous, isotropic beams undergoing deflections in

flap, lag, torsion, and axial directions. A fully numerical formulation [9] is used: the mathematical expressions of the various components of the structural model are not expanded symbolically, but are instead assembled numerically as part of the solution process. The formulation does not require the use of ordering schemes. The starting point for the structural model was a theory [68] that was limited to moderately large deflections because an ordering scheme had to be used to reduce the mathematical complexity of the model. The numerical implementation of the same theory used in the present study, however, is not limited to moderately large deflections because the ordering scheme is no longer used (see Ref. [9] for further details).

The numerical implementation is based on the fact that the numerical values of the displacements and of their space and time derivatives are always available as part of the solution process, as explained in Section 2.4.6. Therefore, they can be used directly to calculate the numerical values of the structural loads [9].

A set of strain-displacement relations are used to calculate the strain components within the blade section. The strain components for a point on the blade section are determined using:

$$\epsilon_{xx} = \frac{1}{2}\left(\mathbf{G}_x \cdot \mathbf{G}_x - 1\right) \tag{2.93}$$

$$\epsilon_{yy} = \frac{1}{2}\left(\mathbf{G}_y \cdot \mathbf{G}_y - 1\right) \tag{2.94}$$

$$\epsilon_{zz} = \frac{1}{2}\left(\mathbf{G}_z \cdot \mathbf{G}_z - 1\right) \tag{2.95}$$

$$\epsilon_{xy} = \frac{1}{2}\left(\mathbf{G}_x \cdot \mathbf{G}_y\right) \tag{2.96}$$

$$\epsilon_{xz} = \frac{1}{2}\left(\mathbf{G}_x \cdot \mathbf{G}_z\right) \tag{2.97}$$

$$\epsilon_{yz} = \frac{1}{2}\left(\mathbf{G}_y \cdot \mathbf{G}_z\right) \tag{2.98}$$

where the vectors $\mathbf{G}_x$, $\mathbf{G}_y$ and $\mathbf{G}_z$ represent the spatial derivatives of the position

vector of the generic point on the deformed blade section (Eqn. (2.86)). With the assumption that the cross-section is rigid, the expressions for $\mathbf{G}_x$, $\mathbf{G}_y$ and $\mathbf{G}_z$ are:

$$\begin{aligned}\mathbf{G}_x = \frac{\partial \mathbf{R}_B}{\partial x} &= (1+u_{,x})\hat{\mathbf{e}}_x + v_{,x}\hat{\mathbf{e}}_y + w_{,x}\hat{\mathbf{e}}_z + \\ &\quad y_0(-\kappa_y\hat{\mathbf{e}}'_x + \tau\hat{\mathbf{e}}'_z) + z_0(-\kappa_z\hat{\mathbf{e}}'_x + \tau\hat{\mathbf{e}}'_y) \qquad (2.99)\\ \mathbf{G}_y = \frac{\partial \mathbf{R}_B}{\partial y} &= \hat{\mathbf{e}}'_y \qquad (2.100)\\ \mathbf{G}_z = \frac{\partial \mathbf{R}_B}{\partial z} &= \hat{\mathbf{e}}'_z \qquad (2.101)\end{aligned}$$

where κ_y and κ_z are the blade curvatures and τ is the elastic twist of the deformed blade section, and these are given by:

$$\begin{aligned}\kappa_y &= -\hat{\mathbf{e}}'_x \cdot \hat{\mathbf{e}}'_{y,x} = -(S_{11}S_{21,x} + S_{12}S_{22,x} + S_{13}S_{23,x}) \qquad (2.102)\\ \kappa_z &= -\hat{\mathbf{e}}'_x \cdot \hat{\mathbf{e}}'_{z,x} = -(S_{11}S_{31,x} + S_{12}S_{32,x} + S_{13}S_{33,x}) \qquad (2.103)\\ \tau &= -\hat{\mathbf{e}}'_y \cdot \hat{\mathbf{e}}'_{y,x} = -(S_{21}S_{21,x} + S_{22}S_{22,x} + S_{23}S_{23,x}) \qquad (2.104)\end{aligned}$$

where the S operators are given in Eqn. (2.15).

The stress-strain relationship is given by:

$$\begin{Bmatrix}\sigma_{xx}\\ \sigma_{yy}\\ \sigma_{zz}\\ \sigma_{xy}\\ \sigma_{xz}\\ \sigma_{yz}\end{Bmatrix} = [Q]\begin{Bmatrix}\epsilon_{xx}\\ \epsilon_{yy}\\ \epsilon_{zz}\\ \epsilon_{xy}\\ \epsilon_{xz}\\ \epsilon_{yz}\end{Bmatrix} \qquad (2.105)$$

where for a linear elastic and isotropic material

$$[Q] = \begin{bmatrix} E & 0 & 0 & 0 & 0 & 0\\ 0 & E & 0 & 0 & 0 & 0\\ 0 & 0 & E & 0 & 0 & 0\\ 0 & 0 & 0 & 2G & 0 & 0\\ 0 & 0 & 0 & 0 & 2G & 0\\ 0 & 0 & 0 & 0 & 0 & 2G \end{bmatrix} \qquad (2.106)$$

where E is Young's Modulus and G is the shear modulus of the material.

The final ingredient is the stress-force relationship that produces the structural forces and moments at the blade section. The stress-force relationship is

$$\mathbf{F} = T\hat{\mathbf{e}}'_x + V_y\hat{\mathbf{e}}'_y + V_z\hat{\mathbf{e}}'_z = \int\int_A \mathbf{t}dA \tag{2.107}$$

$$\mathbf{M} = M_x\hat{\mathbf{e}}'_x + M_y\hat{\mathbf{e}}'_y + M_z\hat{\mathbf{e}}'_z = \int\int_A \mathbf{d}\times\mathbf{t}dA \tag{2.108}$$

where

$$\mathbf{d} = y_0\hat{\mathbf{e}}'_y + z_0\hat{\mathbf{e}}_z \tag{2.109}$$

$$\mathbf{t} = \sigma_{xx}\hat{\mathbf{e}}'_x + \tau_{xy}\hat{\mathbf{e}}'_y + \tau_{xz}\hat{\mathbf{e}}'_y \tag{2.110}$$

Because the equations of motion are written in the *undeformed* preconed blade coordinate system, the structural operators required to calculate the structural nodal loads, Eqn. (2.154), need to be transformed to that coordinate system. The resulting structural operators associated with the lag, flap and torsion equations of motion are given by:

$$p_{\mathrm{S}y} = \left[M_{z,x} + S_{13,x}M_x + (S_{23,x} - S_{13}S_{21,x})M_y - S_{32}M_{y,x}\right]_{,x} \tag{2.111}$$

$$p_{\mathrm{S}z} = \left[M_{y,x} + S_{12,x}M_x + (S_{32,x} - S_{12}S_{31,x})M_z - S_{23}M_{z,x}\right]_{,x} \tag{2.112}$$

$$q_{\mathrm{S}x} = M_{x,x} + (S_{21,x} + S_{13}S_{23,x})M_y + (S_{31,x} + S_{12}S_{32,x})M_z \tag{2.113}$$

The vector of nodal structural loads (Eqn. (2.154)) requires the derivatives of the structural operators with respect to the spanwise coordinate. The required operators are:

$$p^{II}_{\mathrm{S}y} = M_z - S_{32}M_y \tag{2.114}$$

$$p^{II}_{\mathrm{S}z} = -(M_y - S_{23}M_z) \tag{2.115}$$

$$p^{I}_{\mathrm{S}y} = -S_{13,x}M_x - (S_{23,x} - S_{13}S_{21,x})M_y - S_{32,x}M_y \tag{2.116}$$

$$p^{I}_{\mathrm{S}z} = S_{12,x}M_x + (S_{32,x} - S_{12}S_{31,x})M_y + S_{23,x}M_y \tag{2.117}$$

$$q^{I}_{\mathrm{S}x} = M_x \tag{2.118}$$

where the superscripts $(\ )^I$ and $(\ )^{II}$ indicate that the structural load contributions to the modal loads are expressed as operators on the first and second derivatives respectively with respect to the spanwise coordinate of the mode shape.

2.4.4 Lag damper loads

A mechanical damper, if present, is modeled by introducing viscous damping into the blade motion at the blade root in the lag direction. The viscous damping model has a non-linear force-velocity relationship that is implemented through the use of look-up tables [3]. The lag damper is considered to produce a pure moment at the root of the blade (hinge). The moment $\mathbf{M}_{\mathrm{D}}$ generated by the damper is given by:

$$\mathbf{M}_{\mathrm{D}} = M_{\mathrm{D}x}\hat{\mathbf{e}}_x + M_{\mathrm{D}y}\hat{\mathbf{e}}_y + M_{\mathrm{D}z}\hat{\mathbf{e}}_z \tag{2.119}$$

The details of the implementation of the lag damper model as coupled to the fully numerical blade elastic model are provided in Ref. [33].

2.4.5 Tension-induced loads

The tension in the blade, primarily from centrifugal loads, contributes to two types of blade loads. The first type of loads are the tension contributes to the axial dynamics of the blade. However since the current study does not include axial degrees of freedom, axial dynamics are not considered. The second are pure bending moments that originate from the curvature of the blade in combination with the axial tension. This effective stiffening is included in this study, and the associated loads will be termed "tension-induced loads".

The tension-induced loads must be calculated after all of the other distributed loads since the blade tension is dependent on the aerodynamic, inertial and structural loads. The calculation of the tension-induced distributed loads is started at the blade tip where the axial tension is zero and proceeds inboard to the blade root.

The tension-induced loads are calculated based on the equations of equilibrium of a deformed rod [68]:

$$\begin{aligned} P_{\mathrm{T}}^{I} &= TS_{12}\hat{\mathbf{e}}_y + TS_{13}\hat{\mathbf{e}}_z \\ &= p_{\mathrm{T}y}^{I}\hat{\mathbf{e}}_y + p_{\mathrm{T}z}^{I}\hat{\mathbf{e}}_z \end{aligned} \tag{2.120}$$

where S_{12} and S_{13} are elements of transformation matrix from undeformed to deformed coordinates (Eqn. (2.15)), T is the tension load at the particular blade section, and the superscript $(\ )^I$ indicates that the tension-induced loads contribution to the modal loads is expressed as an operator on the first derivative with respect to spanwise coordinate of the mode shape.

2.4.6 Finite element analysis

A finite element analysis is used to convert the governing partial differential equations of motion of the blade to ordinary differential equations, by eliminating the spanwise variable. The finite element representation is based on the Galerkin method of weighted residuals [70].

Figure 2.11 illustrates the nodal degrees of freedom in each element. The total number of degrees of freedom is 11: displacements and slopes in flap and lag bending at the two end points of the element, for a total of 8 degrees of freedom; and torsional rotations at the two ends of the element and at a mid-element point. In Figure 2.11, ϕ, v and w denote respectively the torsion, lag and flap degrees of freedom. It should be noted that the study of Turnour [33] also included four degrees of freedom representing the displacements in the axial direction. However in this study axial dynamics are not considered.

The lag degrees of freedom are represented as

$$\mathbf{y}_v = \{\ v_0\ v_{x,0}\ v_1\ v_{x,1}\}^{\mathrm{T}} \tag{2.121}$$

where v_0 and $v_{x,0}$ are the lag displacement and rotation at the inboard end and v_1 and $v_{x,1}$ are the lag displacement and rotation at the outboard end. Similarly for the flap degrees of freedom

$$\mathbf{y}_w = \{\ w_0\ w_{x,0}\ w_1\ w_{x,1}\}^{\mathrm{T}} \tag{2.122}$$

and for torsion

$$\mathbf{y}_\phi = \left\{\ \phi_0\ \phi_{\frac{1}{2}}\ \phi_1\ \right\}^{\mathrm{T}} \tag{2.123}$$

where ϕ_0 is the torsional rotation at the inboard end, $\phi_{\frac{1}{2}}$ is the twist at the center of the element and ϕ_1 at the outboard end. The vector of degrees of freedom for a single element (the i-th element) is arranged as:

$$\mathbf{y}_i = \left\{ \begin{array}{c} \mathbf{y} \\ \mathbf{y}_w \\ \mathbf{y}_\phi \end{array} \right\} \tag{2.124}$$

The elemental degrees of freedom are combined into global degrees of freedom as shown in Figure 2.12, which also shows the blade discretized into four finite elements. With the eleven degree of freedom elements used, the total number of degrees of freedom for the blade, N_y, is $5 + 6N_e$ where N_e is the number of finite elements used. With the application of the root constraints, the number of actual degrees of freedom is reduced. For an articulated rotor, N_y is reduced by three with the flap, lag and torsional displacements being zero at the inboard end. For a hingeless rotor, N_y is reduced by five with the flap and lag rotations being zero as well as the flap, lag and torsional displacements being zero at the inboard end. It should be noted that this formulation does not require equal-sized elements, but just that the elements form a continuous beam so that compatibility at the element boundaries is retained.

The degrees of freedom are contained in the vector, $\mathbf{y}_n$, which is ordered as

follows:

$$\mathbf{y}_n = \begin{bmatrix} \mathbf{v}_n \\ \mathbf{w}_n \\ \boldsymbol{\phi}_n \end{bmatrix} \tag{2.125}$$

where

$$\mathbf{v}_n = \begin{bmatrix} v_0 \\ v_{0,x} \\ v_1 \\ v_{1,x} \\ \vdots \\ v_{N_e} \\ v_{N_e,x} \end{bmatrix} \tag{2.126}$$

$$\mathbf{w}_n = \begin{bmatrix} w_0 \\ w_{0,x} \\ w_1 \\ w_{1,x} \\ \vdots \\ w_{N_e} \\ w_{N_e,x} \end{bmatrix} \tag{2.127}$$

$$\boldsymbol{\phi}_n = \begin{bmatrix} \phi_0 \\ \phi_1 \\ \vdots \\ \phi_{2N_e} \end{bmatrix} \tag{2.128}$$

The displacements and blade twist at any point in the element can be calculated from the nodal degrees of freedom using Hermite interpolation polynomials. For flap and lag the polynomials, or shape functions, are

$$\mathbf{H}_v(x_e) = \mathbf{H}_w(x_e) = \left\{ \begin{array}{c} 1 - 3\eta^2 + 2\eta^3 \\ \eta(1 - 2\eta + \eta^2)l \\ 3\eta^2 - 2\eta^3 \\ \eta(-\eta + \eta^2)l \end{array} \right\}^{\mathrm{T}} \tag{2.129}$$

where l is the length of the element and $\eta = x_e/l$ with x_e being the distance from the inboard end of the element. Thus $\eta = 0$ represents the inboard end and $\eta = 1$ represents the outboard end of the element.

The shape functions for torsion are

$$\mathbf{H}_{\phi}(x_e) = \left\{ \begin{array}{c} 1 - 3\eta + 2\eta^2 \\ 4\eta - 4\eta^2 \\ -\eta + 2\eta^2 \end{array} \right\}^{\mathrm{T}} \tag{2.130}$$

Therefore, the flap, lag and torsion deflections at any point inside the element are given by

$$v(x_e) = \mathbf{H}_v(x_e)\mathbf{y}_v(t) \tag{2.131}$$

$$w(x_e) = \mathbf{H}_w(x_e)\mathbf{y}_w(t) \tag{2.132}$$

$$\phi(x_e) = \mathbf{H}_{\phi}(x_e)\mathbf{y}_{\phi}(t) \tag{2.133}$$

Using this formulation, the derivatives of the displacements with respect to spanwise location and time are easily found. This results from the fact that the shape functions are only a function of spanwise coordinates and the nodal displacement quantities are only a function of time. Therefore, the derivative with respect to the spanwise coordinate requires the differentiation of the shape function only and the derivative with respect to time requires the differentiation of nodal degrees of freedom only.

The derivatives of the Hermite polynomials with respect to spanwise coordinates are

$$\mathbf{H}_{v,x}(x_e) = \mathbf{H}_{w,x}(x_e) = \frac{1}{l}\left\{ \begin{array}{c} -6\eta + 6\eta^2 \\ (1 - 4\eta + 3\eta^2)l \\ 6\eta - 6\eta^2 \\ (-2\eta + 3\eta^2)l \end{array} \right\}^{\mathrm{T}} \tag{2.134}$$

$$\mathbf{H}_{v,xx}(x_e) = \mathbf{H}_{w,xx}(x_e) = \frac{1}{l^2}\left\{ \begin{array}{c} -6 + 12\eta \\ (-4 + 6\eta)l \\ 6 - 12\eta \\ (-2 + 6\eta)l \end{array} \right\}^{\mathrm{T}} \tag{2.135}$$

and those with respect to the torsional shape functions are

$$\mathbf{H}_{\phi,x}(x_e) = \frac{1}{l}\left\{ \begin{array}{c} -3 + 4\eta \\ 4\eta - 8\eta \\ -1 + 4\eta \end{array} \right\}^{\mathrm{T}} \tag{2.136}$$

Using these expressions, the derivatives of the displacement quantities with respect to spanwise distance are

$$v_{,x}(x_e) = \mathbf{H}_{v,x}(x_e)\mathbf{y}_v(t) \tag{2.137}$$

$$v_{,xx}(x_e) = \mathbf{H}_{v,xx}(x_e)\mathbf{y}_v(t) \tag{2.138}$$

$$w_{,x}(x_e) = \mathbf{H}_{w,x}(x_e)\mathbf{y}_w(t) \tag{2.139}$$

$$w_{,xx}(x_e) = \mathbf{H}_{w,xx}(x_e)\mathbf{y}_w(t) \tag{2.140}$$

$$\phi_{,x}(x_e) = \mathbf{H}_{\phi,x}(x_e)\mathbf{y}_\phi(t) \tag{2.141}$$

Similarly, the derivatives of the displacements with respect to time are

$$\dot{v}(x_e) = \mathbf{H}_v(x_e)\dot{\mathbf{y}}_v(t) \tag{2.142}$$

$$\ddot{v}(x_e) = \mathbf{H}_v(x_e)\ddot{\mathbf{y}}_v(t) \tag{2.143}$$

$$\dot{w}(x_e) = \mathbf{H}_w(x_e)\dot{\mathbf{y}}_w(t) \tag{2.144}$$

$$\ddot{w}(x_e) = \mathbf{H}_w(x_e)\ddot{\mathbf{y}}_w(t) \tag{2.145}$$

$$\dot{\phi}(x_e) = \mathbf{H}_\phi(x_e)\dot{\mathbf{y}}_\phi(t) \tag{2.146}$$

$$\ddot{\phi}(x_e) = \mathbf{H}_\phi(x_e)\ddot{\mathbf{y}}_\phi(t) \tag{2.147}$$

The displacements and derivatives are used in the calculation of the distributed aerodynamic, inertial, tensile and structural loads for the blade, as well as the moment from the lag damper. So, the distributed blade loading can be calculated at any point along the span of the blade.

The distributed nodal loads are calculated using the displacement quantities. The formulation is based on the Galerkin finite element method [70]. The element inertia load vector is calculated using

$$\mathbf{p}_{\mathrm{I}i} = \int_0^{l_i} \left\{ \begin{array}{c} p_{\mathrm{I}y}\mathbf{H}_v\left(x_e\right) \\ p_{\mathrm{I}z}\mathbf{H}_w\left(x_e\right) \\ q_{\mathrm{I}x}\mathbf{H}_\phi\left(x_e\right) \end{array} \right\} dx \tag{2.148}$$

where $p_{\mathrm{I}y}$, $p_{\mathrm{I}z}$ and $q_{\mathrm{I}x}$ are components of the distributed inertial loads $\mathbf{p}_{\mathrm{I}}$ and $\mathbf{p}_{\mathrm{I}}$ are defined in Eqs. (2.84) and (2.85) in Section 2.4.2. The vector of distributed nodal loads for the i-th element is arranged as follows:

$$\mathbf{p}_{\mathrm{I}i} = \left\{ \begin{array}{c} \mathbf{p}_{\mathrm{I}i_v} \\ \mathbf{p}_{\mathrm{I}i_w} \\ \mathbf{p}_{\mathrm{I}i_\phi} \end{array} \right\} \tag{2.149}$$

where $\mathbf{p}_{\mathrm{I}i_v}$, $\mathbf{p}_{\mathrm{I}i_w}$ and $\mathbf{p}_{\mathrm{I}i_\phi}$ are the nodal load vectors for the elemental lag, flap and torsional degrees of freedom respectively. The individual nodal load vector for the lag loads is arranged as follows:

$$\mathbf{p}_{\mathrm{I}i_v} = \int_0^{l_i} p_{\mathrm{I}y}\mathbf{H}_v\left(x_e\right) dx = \left\{ \begin{array}{c} p_{\mathrm{I}v_0} \\ p_{\mathrm{I}v_{0,x}} \\ p_{\mathrm{I}v_1} \\ p_{\mathrm{I}v_{1,x}} \end{array} \right\} \tag{2.150}$$

where $p_{\mathrm{I}v_0}$ and $p_{\mathrm{I}v_{0,x}}$ are the lag force and moment at the inboard end of the element and $p_{\mathrm{I}v_1}$ and $p_{\mathrm{I}v_{1,x}}$ are the lag force and moment at the outboard end of the element. Similarly, for the flap nodal loads

$$\mathbf{p}_{\mathrm{I}i_w} = \int_0^{l_i} p_{\mathrm{I}z}\mathbf{H}_w\left(x_e\right) dx = \left\{ \begin{array}{c} p_{\mathrm{I}w_0} \\ p_{\mathrm{I}w_{0,x}} \\ p_{\mathrm{I}w_1} \\ p_{\mathrm{I}w_{1,x}} \end{array} \right\} \tag{2.151}$$

and for torsion

$$\mathbf{p}_{\mathrm{I}i_\phi} = \int_0^{l_i} q_{\mathrm{I}x}\mathbf{H}_\phi\left(x_e\right) dx = \left\{ \begin{array}{c} p_{\mathrm{I}\phi_0} \\ p_{\mathrm{I}\phi_{\frac{1}{2}}} \\ p_{\mathrm{I}\phi_1} \end{array} \right\} \tag{2.152}$$

where $p_{\mathrm{I}\phi_0}$ is the torsional load at the inboard end, $p_{\mathrm{I}\phi_{\frac{1}{2}}}$ is the torsional load the the center of the element and $p_{\mathrm{I}\phi_1}$ at the outboard end.

The aerodynamic nodal loads, $\mathbf{p}_A$, associated with the ith element are calculated using

$$\mathbf{p}_{\mathrm{A}i} = \int_0^{l_i} \left\{ \begin{array}{c} p_{\mathrm{A}y}\mathbf{H}_v\left(x_e\right) \\ p_{\mathrm{A}z}\mathbf{H}_w\left(x_e\right) \\ q_{\mathrm{A}x}\mathbf{H}_\phi\left(x_e\right) \end{array} \right\} dx \tag{2.153}$$

where $p_{\mathrm{A}y}$, $p_{\mathrm{A}z}$ and $q_{\mathrm{A}x}$ are the components of the blade section aerodynamic loads $\mathbf{p}_{\mathrm{A}}$ and $\mathbf{q}_{\mathrm{A}}$ in the undeformed blade rotating coordinate system. This system is used since it is the system in which the main rotor equations of motion are to be represented. The distributed aerodynamic loads were defined in Eqs. (2.82) and (2.83) in Section 2.4.1. The arrangement of the elements of the aerodynamic elemental load vector is similar to that of the inertial load vector (Eqs. (2.149)-(2.152)).

The structural nodal load vector for the i-th element is given as

$$\mathbf{p}_{\mathrm{S}i} = \int_0^{l_i} \left\{ \begin{array}{c} p^I_{\mathrm{S}y}\mathbf{H}_{v,x}\left(x_e\right) + p^{II}_{\mathrm{S}y}\mathbf{H}_{v,xx}\left(x_e\right) \\ p^I_{\mathrm{S}z}\mathbf{H}_{w,x}\left(x_e\right) + p^{II}_{\mathrm{S}z}\mathbf{H}_{w,xx}\left(x_e\right) \\ q_{\mathrm{S}x}\mathbf{H}_{\phi}\left(x_e\right) + q^I_{\mathrm{S}x}\mathbf{H}_{\phi,x}\left(x_e\right) \end{array} \right\} dx \tag{2.154}$$

where the structural operators $p^I_{\mathrm{S}y}$, $p^{II}_{\mathrm{S}y}$, $p^I_{\mathrm{S}z}$, $p^{II}_{\mathrm{S}z}$, $q_{\mathrm{S}x}$ and $q^I_{\mathrm{S}x}$ are defined in the undeformed blade coordinate system according to Eqs. (2.113) through (2.118) in Section 2.4.3. The arrangement of the elements of the structural elemental load vector is similar to that of the inertial load vector (Eqs. (2.149)-(2.152)).

Finally the tension load vector for the i-th finite element is given by:

$$\mathbf{p}_{\mathrm{T}i} = \int_0^{l_i} \left\{ \begin{array}{c} p^I_{\mathrm{T}y}\mathbf{H}_{v,x}\left(x_e\right) \\ p^I_{\mathrm{T}z}\mathbf{H}_{w,x}\left(x_e\right) \\ 0 \end{array} \right\} dx \tag{2.155}$$

where the distributed tension-induced loads are defined in Eqn. (2.120) in Section 2.4.5. The arrangement of the elements of the tension-induced elemental load vector is similar to that of the inertial load vector (Eqs. (2.149)-(2.152)).

The integration of the distributed loads to obtain the nodal load vectors for each element is performed numerically using an 8-point Gaussian integration formula. Thus the total number of Gauss points for the blade is $8N_e$, and once the blade is separated into N_e elements, the Gauss points do not change. This is an important

point to consider when the flight dynamics model is coupled to the free wake model, as the spanwise distribution of the Gauss points must be known and held fixed throughout the analysis.

The final contribution to the elemental nodal load vector is associated with the moments produced by the lag damper. The lag damper applies a concentrated moment, $\mathbf{M}_{\mathrm{D}}$, to the inboard end of the inboard-most element. These root moments are applied directly to the nodal load vector in the undeformed blade coordinate system

$$\mathbf{p}_{\mathrm{D}_1} = \{\ 0\ M_{\mathrm{D}y}\ 0\ 0\ 0\ M_{\mathrm{D}z}\ 0\ 0\ M_{\mathrm{D}x}\ 0\ 0\ \}^{\mathrm{T}} \tag{2.156}$$

where the subscript $(\ )_1$ applied to the nodal load vector indicates that this is for the inboard most element only. The quantities $M_{\mathrm{D}x}$, $M_{\mathrm{D}y}$ and $M_{\mathrm{D}z}$ are the components of the lag damper moment (Eqn. (2.119)).

2.4.7 Blade mode shapes

A modal coordinate transformation, which is based on a set of blade mode shapes, is performed to reduce the number of rotor degrees of freedom. This set of blade mode shapes and corresponding natural frequencies is calculated using the rotating blade in a vacuum with no damping. The problem of finding the mode shapes and natural frequencies is written as

$$[M]\,\ddot{\mathbf{y}}_n + [K]\,\mathbf{y}_n = \mathbf{0} \tag{2.157}$$

where $[M]$ is the linear portion of the mass matrix, $[K]$ is the linear portion of the stiffness matrix and $\mathbf{y}_n$ is the vector of nodal displacements from the finite element model. The mass and stiffness matrices must be calculated using a finite difference approximation as the mass and stiffness matrices are non-linear and are never built explicitly. In fact the inertial, structural and tension loads are non-

linear functions of the blade displacements and their implementation is based on a numerical formulation.

The calculation of the linear portion of the mass matrix is obtained from the inertial loads acting on the blade. The vector of nodal inertial loads acting on the blade is ordered as follows:

$$\mathbf{p}_{\mathrm{I}} = \left\{ \begin{array}{c} \mathbf{p}_{\mathrm{I}_v} \\ \mathbf{p}_{\mathrm{I}_w} \\ \mathbf{p}_{\mathrm{I}_\phi} \end{array} \right\} \tag{2.158}$$

where

$$\mathbf{p}_{\mathrm{I}_v} = \left\{ \begin{array}{c} p_{\mathrm{I}_{v1}} \\ p_{\mathrm{I}_{v1,x}} \\ p_{\mathrm{I}_{v2}} \\ p_{\mathrm{I}_{v2,x}} \\ \vdots \\ p_{\mathrm{I}_{vN_e+1}} \\ p_{\mathrm{I}_{vN_e+1,x}} \end{array} \right\} \tag{2.159}$$

$$\mathbf{p}_{\mathrm{I}_w} = \left\{ \begin{array}{c} p_{\mathrm{I}_{w1}} \\ p_{\mathrm{I}_{w1,x}} \\ p_{\mathrm{I}_{w2}} \\ p_{\mathrm{I}_{w2,x}} \\ \vdots \\ p_{\mathrm{I}_{wN_e+1}} \\ p_{\mathrm{I}_{wN_e+1,x}} \end{array} \right\} \tag{2.160}$$

$$\mathbf{p}_{\mathrm{I}_\phi} = \left\{ \begin{array}{c} p_{\mathrm{I}_{\phi 1}} \\ p_{\mathrm{I}_{\phi 2}} \\ \vdots \\ p_{\mathrm{I}_{\phi 2N_e+1}} \end{array} \right\} \tag{2.161}$$

The i-th column of the mass matrix is obtained by perturbing the i-th component of the nodal acceleration vector of each displacement, with all of the other accelerations held to zero. If the blade inertial load vector (Eqn. (2.158)) is represented symbolically as $\mathbf{p}_{\mathrm{I}}(\ddot{\mathbf{y}}_n, \dot{\mathbf{y}}_n, \mathbf{y}_n)$ then the calculation of the i-th column of the mass matrix can be written as

$$\mathbf{M}_i = \frac{\mathbf{p}_{\mathrm{I}}(\ddot{\mathbf{y}}_i, \mathbf{0}, \mathbf{0}) - \mathbf{p}_{\mathrm{I}}(\mathbf{0}, \mathbf{0}, \mathbf{0})}{\delta} \tag{2.162}$$

where $\ddot{\mathbf{y}}_i = \delta \mathbf{e}_i$, δ is the perturbation size and $\mathbf{e}_i$ is a vector that contains a one in the i-th element and zero in all other elements. The entire mass matrix is obtained column by column by perturbing each successive element of the nodal acceleration vector.

The stiffness matrix is obtained from a combination of the structural, inertial and tension contributions. The nodal load vectors for the structural and tension-induced loads are calculated in the same way as the inertial nodal load vector (Eqn. (2.158)-(2.161)). The i-th column of the stiffness matrix is obtained by perturbing the i-th component of the nodal displacement vector which is represented as

$$\begin{aligned} \mathbf{K}_i \quad = \quad & \frac{\mathbf{p}_{\mathrm{I}}(\mathbf{0},\mathbf{0},\mathbf{y}_i) - \mathbf{p}_{\mathrm{I}}(\mathbf{0},\mathbf{0},\mathbf{0})}{\delta} + \\ & \frac{\mathbf{p}_{\mathrm{S}}(\mathbf{0},\mathbf{0},\mathbf{y}_i) - \mathbf{p}_{\mathrm{S}}(\mathbf{0},\mathbf{0},\mathbf{0})}{\delta} + \\ & \frac{\mathbf{p}_{\mathrm{T}}(\mathbf{0},\mathbf{0},\mathbf{y}_i) - \mathbf{p}_{\mathrm{T}}(\mathbf{0},\mathbf{0},\mathbf{0})}{\delta} \end{aligned} \tag{2.163}$$

The blade mode shapes are calculated by solving the eigen equation

$$\omega^2 [M] \bar{\mathbf{y}}_n + [K] \bar{\mathbf{y}}_n = 0 \tag{2.164}$$

where $\bar{\mathbf{y}}_n$ are the eigenvectors which form the columns of the modal transformation matrix, $[V]$.

The square roots of the eigenvalues are the natural frequencies of vibration ω, with the i-th element of ω being the natural frequency of the i-th mode described by the i-th eigenvector.

In looking at the eigenvectors, in all but a few cases, it is generally seen that there is a combination of flap, lag and torsion in the mode shape itself, indicating the coupled nature of the flexible blade modes. It is customary to define each mode depending on the dominant tip response, whether in the flap, lag or torsional degrees of freedom. Thus a mode where w_{tip} is the largest component of the mode shape

is identified as a 'flap' mode; if v_{tip} is largest, then the mode is identified as a 'lag' mode; and if ϕ_{tip} is largest then the mode is identified as a 'torsion' mode.

These definitions are not strict because, all of the blade modes are usually coupled and can contain flap, lag and torsional components. The exceptions to this are the lowest frequency flap and lag modes of an articulated rotor, which are rigid body modes, and have a linear spanwise distribution of displacements in the corresponding degree of freedom.

The mode shapes are scaled so that the tip deflection of the dominating displacement quantity is equal to 1. Using this scheme, the RMS value of the tip deflection will always be greater than or equal to 1

$$\left(w_{tip}^2 + v_{tip}^2 + \phi_{tip}^2\right)^{\frac{1}{2}} \geq 1 \tag{2.165}$$

2.4.8 Modal coordinate transformation

The number of nodal degrees of freedom representing the blade motion is $N_D = 5+6N_e$, which results in N_D second order, non-linear ordinary differential equations representing the dynamics of each rotor blade.

To reduce the number of degrees of freedom and equations a modal coordinate transformation is used. The vector of finite element degrees of freedom, $\mathbf{y}_n$, defined in Eqn. (2.125) is written as the product of a modal coordinate transformation matrix $[V]$ and a vector of modal coefficients, $\mathbf{q}$, as

$$\mathbf{y}_n = [V]\,\mathbf{q} \tag{2.166}$$

The columns of $[V]$ contain normal modes of the blade. Therefore, if N_m modes are used in the modal coordinate transformation, the matrix $[V]$ had N_D rows and N_m columns, usually with $N_m \ll N_D$. The vector $\mathbf{q}$ becomes the vector of blade generalized coordinates for the problem.

It should be mentioned that, with the exception of the calculation of the main rotor blade mode shapes, the vector of the finite element degrees of freedom $\mathbf{y}_n$ is not built explicitly. Instead the degrees of freedom for each element are extracted in turn, as follows:

$$\mathbf{y}_i = [V_i]\,\mathbf{q} \tag{2.167}$$

where $\mathbf{y}_i$ contains the degrees of freedom of the i-th element (Eqn. (2.124)) and $[V_i]$ is the portion of the $[V]$ matrix corresponding to the i-th element.

The nodal load vectors for each element, defined in Eqs. (2.148) and (2.153) through (2.156) are transformed into modal load vectors using the same modal coordinate transformation used to reduce the number of degrees of freedom. The transformation of the individual elemental nodal load vectors to modal loads vectors is as follows

$$\mathbf{F}_{\mathrm{A}} = \sum_{i=1}^{N_e} [V_i]^{\mathrm{T}}\,\mathbf{p}_{\mathrm{A}i} \tag{2.168}$$

$$\mathbf{F}_{\mathrm{I}} = \sum_{i=1}^{N_e} [V_i]^{\mathrm{T}}\,\mathbf{p}_{\mathrm{I}i} \tag{2.169}$$

$$\mathbf{F}_{\mathrm{S}} = \sum_{i=1}^{N_e} [V_i]^{\mathrm{T}}\,\mathbf{p}_{\mathrm{S}i} \tag{2.170}$$

$$\mathbf{F}_{\mathrm{T}} = \sum_{i=1}^{N_e} [V_i]^{\mathrm{T}}\,\mathbf{p}_{\mathrm{T}i} \tag{2.171}$$

$$\mathbf{F}_{\mathrm{D}} = \sum_{i=1}^{N_e} [V_i]^{\mathrm{T}}\,\mathbf{p}_{\mathrm{D}i} \tag{2.172}$$

This transformation of the load vectors leads to the governing equations representing the blade dynamics. These ordinary differential equations are represented as

$$\mathbf{0} = \mathbf{F}_{\mathrm{A}} + \mathbf{F}_{\mathrm{I}} + \mathbf{F}_{\mathrm{S}} + \mathbf{F}_{\mathrm{T}} + \mathbf{F}_{\mathrm{D}} \tag{2.173}$$

where the total number of modal equations is obtained by multiplying the number of

blades, N_b, by the number of mode shapes in the modal coordinate transformation, N_m.

2.5 Fuselage equations of motion

The non-linear equations of motion of the fuselage are formulated in the body fixed coordinate system. The assumption is made that the aircraft body is rigid. The three force and moment equilibrium equations are written as follows:

$$X\frac{R}{m_0} = m\dot{u} + m(qw - rv) + mg\sin\theta_F \tag{2.174}$$

$$Y\frac{R}{m_0} = m\dot{v} + m(ru - pw) - mg\cos\theta_F\sin\phi_F \tag{2.175}$$

$$Z\frac{R}{m_0} = m\dot{w} + m(pv - qu) - mg\cos\theta_F\cos\phi_F \tag{2.176}$$

$$\begin{aligned} L\frac{R^3}{m_0} &= I_{xx}\dot{p} - I_{xy}\dot{q} - I_{xz}\dot{r} - I_{yz}(q^2 - r^2) - I_{xz}pq + I_{xy}pr \\ &\quad -(I_{yy} - I_{zz})qr \end{aligned} \tag{2.177}$$

$$\begin{aligned} M\frac{R^3}{m_0} &= I_{yy}\dot{q} - I_{xy}\dot{p} - I_{yz}\dot{r} - I_{xz}(r^2 - p^2) - I_{xy}qr + I_{yz}pq \\ &\quad -(I_{zz} - I_{xx})pr \end{aligned} \tag{2.178}$$

$$\begin{aligned} N\frac{R^3}{m_0} &= I_{zz}\dot{r} - I_{xz}\dot{p} - I_{yz}\dot{q} - I_{xy}(p^2 - q^2) - I_{yz}pr + I_{xz}qr \\ &\quad -(I_{xx} - I_{yy})pq \end{aligned} \tag{2.179}$$

The terms on the left hand side of Eqs. (2.174)-(2.179) are the externally applied loads at the center of gravity of the body. These terms would include contributions from the main and tail rotors, as well as aerodynamic loads applied directly to the fuselage. The terms on the right hand side represent the rigid body motion of the fuselage in response to the applied loading.

The mass and inertia terms are non-dimensionalized with respect to the main

rotor radius and a reference blade mass, as follows:

$$\overline{m} = \frac{mR}{m_0} \tag{2.180}$$

$$\overline{I}_{xx} = I_{xx}\frac{R^3}{m_0} \tag{2.181}$$

where m_0 is a reference mass per unit length of the blade and R is the main rotor radius. The mass m and inertia I_{xx} quantities include the entire helicopter with the exception of the main rotor blades which are included as the $g\mathbf{k}_I$ terms in the equations for the main rotor inertial loads (Eqs. (2.84) and (2.85)). These main rotor mass and inertia loads are dependent on the linear and angular accelerations of the body and are taken into account in the left hand side of the Eqs. (2.174)-(2.179) as applied forces and moments to the center of gravity of the body.

The applied forces and moments are the sum of contributions from the main rotor, tail rotor, fuselage and empennage and are written as follows:

$$X = X_{MR} + X_{TR} + X_F + X_V + X_H \tag{2.182}$$

$$Y = Y_{MR} + Y_{TR} + Y_F + Y_V + Y_H \tag{2.183}$$

$$Z = Z_{MR} + Z_{TR} + Z_F + Z_V + Z_H \tag{2.184}$$

$$L = L_{MR} + L_{TR} + L_F + L_V + L_H \tag{2.185}$$

$$M = M_{MR} + M_{TR} + M_F + M_V + M_H \tag{2.186}$$

$$N = N_{MR} + N_{TR} + N_F + N_V + N_H \tag{2.187}$$

where the subscript MR denotes the main rotor, TR the tail rotor, F the fuselage, H and V the horizontal and vertical tail loads.

Another three equations are obtained from the relationship between the aircraft rates and Euler angles. There equations are as follows:

$$\dot{\phi}_F = p + q\tan\theta_F \sin\phi_F + r\tan\theta_F \cos\psi_F \tag{2.188}$$

$$\dot{\theta}_F = q\cos\phi_F - r\sin\phi_F \tag{2.189}$$

$$\dot{\psi}_F = r\frac{\cos\psi_F}{\cos\theta_F} + q\frac{\sin\phi_F}{\cos\theta_F} \tag{2.190}$$

The components of the external forces and moments applied to the center of gravity of the body are now treated in turn.

2.5.1 Main rotor loads

The contributions to the fuselage loads from the main rotor are of inertial and aerodynamic origin. The distributed aerodynamic and inertial loads are integrated along the span of the span of the blade to obtain the loads at the hub for a hingeless rotor, or at the hinge for an articulated rotor. Since the equations of motion of the main rotor blades are formulated in the undeformed preconed coordinate system (Section 2.2.3), the integrated loads are also formulated in this reference frame. These forces and moments are given by

$$\mathbf{F}_R = \int_e^1 (\mathbf{p}_\mathrm{A} + \mathbf{p}_\mathrm{I}) dx_0 \tag{2.191}$$

$$\mathbf{M}_R = \int_e^1 \mathbf{R}_C \times (\mathbf{p}_\mathrm{A} + \mathbf{p}_\mathrm{I}) dx_0 + \mathbf{M}_\mathrm{D} \tag{2.192}$$

where $\mathbf{p}_\mathrm{A}$, $\mathbf{p}_\mathrm{I}$ and $\mathbf{M}_\mathrm{D}$ are defined by Eqs. (2.82), (2.84) and (2.119), respectively. These loads are in the rotating frame at the hinge for an articulated rotor, or at the axis of rotation for a hingeless rotor (in this case the hinge offset e is zero). Also $\mathbf{R}_C$ is the position vector of the deflected elastic axis from the hub in the undeformed preconed coordinate system, and is given by:

$$\mathbf{R}_C = x_0\hat{\mathbf{e}}_x + u\hat{\mathbf{e}}'_x + v\hat{\mathbf{e}}'_y + w\hat{\mathbf{e}}'_z \tag{2.193}$$

The main rotor loads have to be converted to equivalent loads at the center of gravity of the body in the body fixed axes system (x_B, y_B, z_B). This transformation

depends on the rotor type because no flap and lag moments are transferred through the hinge for an articulated rotor configuration.

For a hingeless rotor configuration, the main rotor forces resolved at the center of gravity of the body for a single blade are given by:

$$\mathbf{F}_{MR} = \left\{ \begin{array}{c} X_{MR} \\ Y_{MR} \\ Z_{MR} \end{array} \right\} = [T_{SB}]^{-1}[T_{RS}]^{-1}[T_{PR}]^{-1} \left\{ \begin{array}{c} \int_0^1 (p_{\mathrm{A}x} + p_{\mathrm{I}x}) dx_0 \\ \int_0^1 (p_{\mathrm{A}y} + p_{\mathrm{I}y}) dx_0 \\ \int_0^1 (p_{\mathrm{A}z} + p_{\mathrm{I}z}) dx_0 \end{array} \right\} \tag{2.194}$$

where distributed aerodynamic and inertial load components are given in Eqs. (2.82) and (2.84) respectively; $[T_{PR}]^{-1}$ transforms the loads from the preconed to non-preconed coordinate systems (Eqn. (2.13)); $[T_{RS}]^{-1}$ transforms from the rotating to non-rotating reference frames (Eqn. (2.11)); and finally $[T_{SB}]^{-1}$ transforms from the shaft to body fixed axes systems (Eqn. (2.9)).

The moment vector from the main rotor loads resolved at the center of gravity of the body for a single blade is given by:

$$\begin{aligned} \mathbf{M}_{MR} = \left\{ \begin{array}{c} L_{MR} \\ M_{MR} \\ N_{MR} \end{array} \right\} &= [T_{SB}]^{-1}[T_{RS}]^{-1}[T_{PR}]^{-1} \left\{ \begin{array}{c} \int_0^1 (q_{\mathrm{A}x} + q_{\mathrm{I}x}) dx_0 + M_{\mathrm{D}x} \\ \int_0^1 (q_{\mathrm{A}y} + q_{\mathrm{I}y}) dx_0 + M_{\mathrm{D}y} \\ \int_0^1 (q_{\mathrm{A}z} + q_{\mathrm{I}z}) dx_0 + M_{\mathrm{D}z} \end{array} \right\} \\ &+ [T_{SB}]^{-1}[T_{RS}]^{-1}[T_{PR}]^{-1} \left\{ \int_0^1 \mathbf{R}_C \times (\mathbf{p}_{\mathrm{A}} + \mathbf{p}_{\mathrm{I}}) \, dx_0 \right\} \\ &+ \mathbf{R}_H \times \mathbf{F}_{MR} \end{aligned} \tag{2.195}$$

where the distributed aerodynamic and inertial loads are given in Eqs. (2.83) and (2.85) and the lag damper moments are given in Eqn. (2.119) and $\mathbf{R}_H$ is the position vector of the hub relative the center of gravity of the body (Eqn. (2.41)).

For an articulated rotor configuration, there are no aerodynamic or inertial blade moments in the flap and lag directions are transferred through the hinge. The forces generated by the rotor are obtained by integrating the aerodynamic and inertial distributed loads over the elastic portion of the blade and. For a single rotor blade,

it is

$$\mathbf{F}_{MR} = \left\{ \begin{array}{c} X_{MR} \\ Y_{MR} \\ Z_{MR} \end{array} \right\} = [T_{SB}]^{-1}[T_{RS}]^{-1}[T_{PR}]^{-1} \left\{ \begin{array}{c} \int_e^1 (p_{\mathrm{A}x} + p_{\mathrm{I}x}) dx_0 \\ \int_e^1 (p_{\mathrm{A}y} + p_{\mathrm{I}y}) dx_0 \\ \int_e^1 (p_{\mathrm{A}z} + p_{\mathrm{I}z}) dx_0 \end{array} \right\} \tag{2.196}$$

The moment vector from the main rotor loads resolved at the center of gravity of the body, for a single blade, is

$$\begin{aligned} \mathbf{M}_{MR} = \left\{ \begin{array}{c} L_{MR} \\ M_{MR} \\ N_{MR} \end{array} \right\} &= [T_{SB}]^{-1}[T_{RS}]^{-1}[T_{PR}]^{-1} \left\{ \begin{array}{c} M_{\mathrm{D}x} \\ M_{\mathrm{D}y} \\ \int_0^1 (q_{\mathrm{A}z} + q_{\mathrm{I}z}) dx_0 + M_{\mathrm{D}z} \end{array} \right\} \\ &+ [T_{SB}]^{-1}[T_{RS}]^{-1}[T_{PR}]^{-1} \{\mathbf{R}_C \times \mathbf{F}_R\} \\ &+ \mathbf{R}_H \times \mathbf{F}_{MR} \end{aligned} \tag{2.197}$$

where the first term indicates that all of the lag damper moments but only the pitching moments of the distributed inertial and aerodynamic loads are transferred through the hinge. The second term transforms the forces at the blade hinge into moments at the hub by considering the position vector from the hub to the hinge in the rotating frame, $\mathbf{R}_C$, where $\mathbf{R}_C$ is

$$\mathbf{R}_C = e\hat{\mathbf{e}}_x \tag{2.198}$$

The final term in Eqn. (2.197) transforms the forces at the hub into moments at the center of gravity of the body; the moment arm is the distance $\mathbf{R}_H$ of the hub from the aircraft center of gravity (Eqn. (2.41)).

2.5.2 Fuselage aerodynamic loads

The forces and moments acting directly on the fuselage are of aerodynamic origin and are obtained from non-linear data tables of aerodynamic coefficients. These aerodynamic loads are based on the freestream velocity at the fuselage aerodynamic reference point, with a correction factor to take into account interference of the main

rotor

$$u_F = u_B + y_f r_B - z_f q_B + u_{in_f} \tag{2.199}$$

$$v_F = v_B + z_f p_B - x_f r_B + v_{in_f} \tag{2.200}$$

$$w_F = w_B + x_f q_B - y_f p_B + w_{in_f} \tag{2.201}$$

where x_f, y_f and z_f are the components of the position vector from the center of gravity of the body to the aerodynamic reference point of the fuselage; u_{in_f}, u_{in_f} and u_{in_f} are the interference velocities that are based on the main rotor downwash, tip speed and wake skew angle, and are based on experimental results. These interference components are only used for the UH-60A and not for the BO-105.

For the UH-60A

$$u_{in_f} = v_0 \nu_{x_{wf}}(\beta_{1c}, \chi) \tag{2.202}$$

$$v_{in_f} = 0 \tag{2.203}$$

$$w_{in_f} = v_0 \nu_{z_{wf}}(\beta_{1c}, \chi) \tag{2.204}$$

where β_{1c} is the longitudinal tilt of the tip path plane, given in Eqn. (2.18); v_0 is the main rotor downwash; and χ is the rotor wake skew angle, given by

$$\chi = \tan^{-1} \frac{u_S}{|v_0 - w_S|} + \beta_{1c} \tag{2.205}$$

where u_S and w_S are the freestream velocity components taken in the shaft fixed coordinate system. The functions $\nu_{x_{wf}}(\beta_{1c}, \chi)$ and $\nu_{z_{wf}}(\beta_{1c}, \chi)$ are provided in the form of look-up tables.

The angles of attack and sideslip of the fuselage are

$$\alpha_F = \tan^{-1} \frac{w_F}{|u_F|} \tag{2.206}$$

$$\beta_F = \tan^{-1} \frac{v_F}{\sqrt{v_F^2 + w_F^2}} \tag{2.207}$$

where α_F is defined as positive nose up and β_F is defined as positive nose right.

The dynamic pressure is

$$\bar{q}_F = \frac{1}{2}\rho\frac{R^2}{m_0}(u_F^2 + v_F^2 + w_F^2) \tag{2.208}$$

The representation of the fuselage aerodynamic data for the BO-105 and UH-60A differ in that the UH-60A data used in the present study were provided in the wind axes system while the BO-105 data were provided in the body fixed axes system.

For the UH-60A, non-linear fuselage aerodynamic coefficients are defined in the wind-axes system

$$\begin{aligned}
C_{Df} &= C_{D_\alpha f}(\alpha_F) + C_{D_\beta f}(\beta_F) && (2.209)\\
C_{Yf} &= C_{Yf}(|\beta_F|) && (2.210)\\
C_{Lf} &= C_{L_\alpha f}(\alpha_F) + C_{L_\beta f}(-\beta_F) && (2.211)\\
C_{Rf} &= -\frac{\beta_F}{|\beta_F|}C_{Rf}(|\beta_F|) && (2.212)\\
C_{Mf} &= C_{M_\alpha f}(\alpha_F) - \frac{\beta_F}{|\beta_F|}C_{Mf}(|\beta_F|) && (2.213)\\
C_{Nf} &= C_{Nf}(-\beta_F) && (2.214)
\end{aligned}$$

The non-dimensional fuselage aerodynamic loads in the wind axes system are

$$\begin{aligned}
\mathbf{F}_{wF} &= -\bar{q}_F C_{Df}\mathbf{i}_\mathrm{F} - \bar{q}_F C_{Yf}\mathbf{j}_\mathrm{F} - \bar{q}_F C_{Lf}\mathbf{k}_\mathrm{F} && (2.215)\\
\mathbf{M}_{wF} &= \bar{q}_F C_{Rf}\mathbf{i}_\mathrm{F} - \bar{q}_F C_{Mf}\mathbf{j}_\mathrm{F} + \bar{q}_F C_{Nf}\mathbf{k}_\mathrm{F} && (2.216)
\end{aligned}$$

The transformation of the loads from the wind axes system to the body axes system is made by considering the angles of attack and sideslip at the aerodynamic reference point of the fuselage. The transformation is similar to the transformation from wind axes system to body fixed system (Eqn. (2.7)) and is

$$T_\mathrm{FB} = \begin{bmatrix} \cos\alpha_F\cos\beta_F & \cos\alpha_F\sin\beta_F & -\sin\alpha_F \\ \sin\beta_F & \cos\beta_F & \\ \sin\alpha_F\cos\beta_F & -\sin\alpha_F\sin\beta_F & \cos\alpha_F \end{bmatrix} \tag{2.217}$$

so that

$$\left\{ \begin{array}{c} \mathbf{i}_{\mathrm{B}} \\ \mathbf{j}_{\mathrm{B}} \\ \mathbf{k}_{\mathrm{B}} \end{array} \right\} = [T_{\mathrm{FB}}]^{-1} \left\{ \begin{array}{c} \mathbf{i}_{\mathrm{F}} \\ \mathbf{j}_{\mathrm{F}} \\ \mathbf{k}_{\mathrm{F}} \end{array} \right\} \tag{2.218}$$

The forces and moments due to the fuselage aerodynamics, resolved at the center of gravity of the body, are:

$$\mathbf{F}_F = \left\{ \begin{array}{c} X_F \\ Y_F \\ Z_F \end{array} \right\} = [T_{FB}]^{-1} \mathbf{F}_{wF} = [T_{FB}]^{-1} \left\{ \begin{array}{c} -\bar{q}_F C_{Df} \\ -\bar{q}_F C_{Yf} \\ -\bar{q}_F C_{Lf} \end{array} \right\} \tag{2.219}$$

and

$$\mathbf{M}_F = \left\{ \begin{array}{c} L_F \\ M_F \\ N_F \end{array} \right\} = [T_{FB}]^{-1} \mathbf{M}_{wF} + \mathbf{x}_F \times \mathbf{F}_F \tag{2.220}$$

where $\mathbf{x}_F$ is the position vector of the fuselage aerodynamic reference point from the center of gravity of the body

$$\mathbf{x}_F = x_f \mathbf{i}_{\mathrm{B}} + y_f \mathbf{j}_{\mathrm{B}} + z_f \mathbf{k}_{\mathrm{B}} \tag{2.221}$$

For the BO-105 the non-linear fuselage aerodynamic coefficients are represented in the body fixed axes system and are functions of the angles of attack and sideslip at the aerodynamic reference point:

$$C_{Xf} = C_{Xf}(\alpha_F, \beta_F) \tag{2.222}$$

$$C_{Yf} = C_{Yf}(\alpha_F, \beta_F) \tag{2.223}$$

$$C_{Zf} = C_{Zf}(\alpha_F, \beta_F) \tag{2.224}$$

$$C_{Lf} = C_{Lf}(\alpha_F, \beta_F) \tag{2.225}$$

$$C_{Mf} = C_{Mf}(\alpha_F, \beta_F) \tag{2.226}$$

$$C_{Nf} = C_{Nf}(\alpha_F, \beta_F) \tag{2.227}$$

The non-dimensional aerodynamic forces at the center of gravity in the body axes system are:

$$\mathbf{F}_F = \left\{ \begin{array}{c} X_F \\ Y_F \\ Z_F \end{array} \right\} = \left\{ \begin{array}{c} \bar{q}_F C_{Xf} \\ \bar{q}_F C_{Yf} \\ \bar{q}_F C_{Zf} \end{array} \right\} \tag{2.228}$$

The fuselage aerodynamic moment vector is

$$\mathbf{M}_F = \left\{ \begin{array}{c} L_F \\ M_F \\ N_F \end{array} \right\} = \left\{ \begin{array}{c} \bar{q}_F C_{Lf} \\ \bar{q}_F C_{Mf} \\ \bar{q}_F C_{Nf} \end{array} \right\} + \mathbf{x}_F \times \mathbf{F}_F \tag{2.229}$$

where $\mathbf{x}_F$ is given by Eqn. (2.221).

2.5.3 Empennage aerodynamic loads

The load contributions from the empennage are the result of aerodynamic loads acting on the horizontal and vertical tail surfaces. The loads are based on the resultant velocities at the horizontal and vertical tail aerodynamic reference points:

$$\mathbf{u}_H = K_H \mathbf{u}_B + \mathbf{x}_H \times \omega + \mathbf{u}_{in_H} \tag{2.230}$$

$$\mathbf{u}_V = K_V \mathbf{u}_B + \mathbf{x}_V \times \omega + \mathbf{u}_{in_V} \tag{2.231}$$

where K_H and K_V are empirical factors that define the extent of the dynamic pressure losses at the horizontal and vertical tails respectively; $\mathbf{x}_H \times \omega$ and $\mathbf{x}_V \times \omega$ are the velocity components due to the rotation of the body; $\mathbf{u}_{in_H}$ and $\mathbf{u}_{in_V}$ are the interference velocity components due to the presence of the main rotor and fuselage, based on wind tunnel test data and are defined for the UH-60A only. For the BO-105 the interference velocities are assumed to be zero.

For the UH-60A, the interference velocities are non-linear functions of the main rotor downwash, tip speed and rotor wake skew angle:

$$\mathbf{u}_{in_H} = v_0 \nu_{x_w H}(\beta_{1c}, \chi)\mathbf{i}_{\mathrm{H}} + v_0 \nu_{z_w H}(\beta_{1c}, \chi)\mathbf{k}_{\mathrm{H}} \tag{2.232}$$

$$\mathbf{u}_{in_V} = v_0 \nu_{x_w V}(\beta_{1c}, \chi)\mathbf{i}_{\mathrm{V}} + v_0 \nu_{z_w V}(\beta_{1c}, \chi)\mathbf{k}_{\mathrm{V}} \tag{2.233}$$

where v_0, β_{1c} and χ are defined in the same way as the quantities in Section 2.5.2, that is v_0 is the main rotor downwash, β_{1c} is the longitudinal tilt of the tip path

plane and χ is the rotor wake skew angle. The functions $\nu_{x_wH}(\beta_{1c}, \chi)$, $\nu_{z_wH}(\beta_{1c}, \chi)$, $\nu_{x_wV}(\beta_{1c}, \chi)$ and $\nu_{z_wV}(\beta_{1c}, \chi)$ are provided in the form of look-up tables.

The dynamic pressures at the tail surfaces are

$$\bar{q}_H = \frac{1}{2}\rho\frac{R^2}{m_0}(u_H^2 + v_H^2 + w_H^2) \tag{2.234}$$

$$\bar{q}_V = \frac{1}{2}\rho\frac{R^2}{m_0}(u_V^2 + v_V^2 + w_V^2) \tag{2.235}$$

The angles of attack and sideslip at the tail surfaces are given by:

$$\alpha_H = \tan^{-1}\frac{w_H}{|u_H|} + \theta_{0\mathrm{H}} \tag{2.236}$$

$$\beta_H = \tan^{-1}\frac{v_H}{\sqrt{v_H^2 + w_H^2}} \tag{2.237}$$

$$\alpha_V = \tan^{-1}\frac{w_V}{|u_V|} \tag{2.238}$$

$$\beta_V = \tan^{-1}\frac{v_V}{\sqrt{v_V^2 + w_V^2}} \tag{2.239}$$

where the angles of attack are defined as positive nose up, the angle of sideslip are defined as positive nose right and $\theta_{0\mathrm{H}}$ is the variable pitch angle of the horizontal tail, for the UH-60A only, that is adjusted by the flight control system as a function of the flight speed.

The aerodynamic loads acting on the empennage of the UH-60A and BO-105 are calculated differently: as the UH-60A aerodynamic coefficients are defined in the local wind axes system, while the BO-105 aerodynamic coefficients are defined in the body axes system.

For the UH-60A, the lift and drag aerodynamic coefficients at the tail surfaces are given by:

$$C_{LH} = C_{LH}(\alpha_H) \tag{2.240}$$

$$C_{DH} = C_{DH}(|\alpha_H|) \tag{2.241}$$

$$C_{LV} = C_{LV}(\beta_V) \tag{2.242}$$

$$C_{DV} = C_{DV}(|\beta_V|) \tag{2.243}$$

The aerodynamic loads in the local wind axes systems of the horizontal and vertical tails are:

$$\mathbf{F}_{wH} = -C_{DH}\bar{q}_H S_H \mathbf{i}_{\mathrm{H}} - C_{LH}\bar{q}_H S_H \mathbf{k}_{\mathrm{H}} \tag{2.244}$$

$$\mathbf{F}_{wV} = -C_{DV}\bar{q}_V S_V \mathbf{i}_{\mathrm{V}} + C_{LV}\bar{q}_V S_V \mathbf{j}_{\mathrm{V}} \tag{2.245}$$

where S_H and S_V are the surface areas of the horizontal and vertical tails respectively.

These forces are converted from the local wind axes system of the horizontal ($\mathbf{i}_{\mathrm{H}}$, $\mathbf{j}_{\mathrm{H}}$, $\mathbf{k}_{\mathrm{H}}$) and vertical ($\mathbf{i}_{\mathrm{V}}$, $\mathbf{j}_{\mathrm{V}}$, $\mathbf{k}_{\mathrm{V}}$) tails to the body fixed system using transformations similar to Eqn. (2.217). The transformation from horizontal tail wind axes system to the body fixed system is

$$T_{\mathrm{HB}} = \begin{bmatrix} \cos(\alpha_H - \theta_{0\mathrm{H}})\cos\beta_H & \cos(\alpha_H - \theta_{0\mathrm{H}})\sin\beta_H & -\sin(\alpha_H - \theta_{0\mathrm{H}}) \\ \sin\beta_H & -\cos\beta_H & 0 \\ \sin(\alpha_H - \theta_{0\mathrm{H}})\cos\beta_H & \sin(\alpha_H - \theta_{0\mathrm{H}})\sin\beta_H & \cos(\alpha_H - \theta_{0\mathrm{H}}) \end{bmatrix} \tag{2.246}$$

so that:

$$\begin{Bmatrix} \mathbf{i}_{\mathrm{B}} \\ \mathbf{j}_{\mathrm{B}} \\ \mathbf{k}_{\mathrm{B}} \end{Bmatrix} = [T_{\mathrm{HB}}]^{-1} \begin{Bmatrix} \mathbf{i}_{\mathrm{H}} \\ \mathbf{j}_{\mathrm{H}} \\ \mathbf{k}_{\mathrm{H}} \end{Bmatrix} \tag{2.247}$$

The aerodynamic forces and moments of the horizontal tail, resolved at the center of gravity of the body are given by

$$\mathbf{F}_H = \begin{Bmatrix} X_H \\ Y_H \\ Z_H \end{Bmatrix} = [T_{\mathrm{HB}}]^{-1}\mathbf{F}_{wH} \tag{2.248}$$

and

$$\mathbf{M}_H = \begin{Bmatrix} L_H \\ M_H \\ N_H \end{Bmatrix} = \mathbf{x}_H \times \mathbf{F}_H \tag{2.249}$$

where $\mathbf{x}_H$ is the position vector of the horizontal tail aerodynamic reference point with respect to the center of gravity of the body

$$\mathbf{x}_H = x_H \mathbf{i}_\mathrm{B} + y_H \mathbf{j}_\mathrm{B} + z_H \mathbf{k}_\mathrm{B} \tag{2.250}$$

For the vertical tail

$$T_\mathrm{VB} = \begin{bmatrix} \cos\alpha_V \cos\beta_V & \cos\alpha_V \sin\beta_V & -\sin\alpha_V \\ \sin\beta_V & -\cos\beta_V & 0 \\ \sin\alpha_V \cos\beta_V & \sin\alpha_V \sin\beta_V & \cos\alpha_V \end{bmatrix} \tag{2.251}$$

so that

$$\begin{Bmatrix} \mathbf{i}_\mathrm{B} \\ \mathbf{j}_\mathrm{B} \\ \mathbf{k}_\mathrm{B} \end{Bmatrix} = [T_\mathrm{VB}]^{-1} \begin{Bmatrix} \mathbf{i}_\mathrm{V} \\ \mathbf{j}_\mathrm{V} \\ \mathbf{k}_\mathrm{V} \end{Bmatrix} \tag{2.252}$$

And the forces and moments at the center of gravity of the body are:

$$\mathbf{F}_V = \begin{Bmatrix} X_V \\ Y_V \\ Z_V \end{Bmatrix} = [T_\mathrm{VB}]^{-1} \mathbf{F}_{wV} \tag{2.253}$$

and:

$$\mathbf{M}_V = \begin{Bmatrix} L_V \\ M_V \\ N_V \end{Bmatrix} = \mathbf{x}_V \times \mathbf{F}_V \tag{2.254}$$

where the position vector from the center of gravity of the aircraft to the vertical tail reference points $\mathbf{x}_V$ is

$$\mathbf{x}_V = x_V \mathbf{i}_\mathrm{B} + y_V \mathbf{j}_\mathrm{B} + z_V \mathbf{k}_\mathrm{B} \tag{2.255}$$

For the BO-105, the aerodynamic coefficients are defined in the body axes system

$$C_{XH} = C_{XH}(\alpha_H, \beta_H) \tag{2.256}$$

$$C_{YH} = C_{YH}(\alpha_H, \beta_H) \tag{2.257}$$

$$C_{ZH} = C_{ZH}(\alpha_H, \beta_H) \tag{2.258}$$

$$C_{LH} = C_{LH}(\alpha_H, \beta_H) \tag{2.259}$$

$$C_{MH} = C_{MH}(\alpha_H, \beta_H) \tag{2.260}$$

$$C_{NH} = C_{NH}(\alpha_H, \beta_H) \tag{2.261}$$

$$C_{XV} = C_{XV}(\alpha_H, \beta_V) \tag{2.262}$$

$$C_{YV} = C_{YV}(\alpha_H, \beta_V) \tag{2.263}$$

$$C_{ZV} = C_{ZV}(\alpha_H, \beta_V) \tag{2.264}$$

$$C_{LV} = C_{LV}(\alpha_H, \beta_V) \tag{2.265}$$

$$C_{MV} = C_{MV}(\alpha_H, \beta_V) \tag{2.266}$$

$$C_{NV} = C_{NV}(\alpha_H, \beta_V) \tag{2.267}$$

For the horizontal tail

$$\mathbf{F}_H = \begin{Bmatrix} X_H \\ Y_H \\ Z_H \end{Bmatrix} = \begin{Bmatrix} \bar{q}_H S_H C_{XH} \\ \bar{q}_H S_H C_{YH} \\ \bar{q}_H S_H C_{ZH} \end{Bmatrix} \tag{2.268}$$

$$\mathbf{M}_H = \begin{Bmatrix} L_H \\ M_H \\ N_H \end{Bmatrix} = \begin{Bmatrix} \bar{q}_H S_H C_{LH} \\ \bar{q}_H S_H C_{MH} \\ \bar{q}_H S_H C_{NH} \end{Bmatrix} + \mathbf{x}_H \times \mathbf{F}_H \tag{2.269}$$

and for the vertical tail

$$\mathbf{F}_V = \begin{Bmatrix} X_V \\ Y_V \\ Z_V \end{Bmatrix} = \begin{Bmatrix} \bar{q}_V S_V C_{XV} \\ \bar{q}_V S_V C_{YV} \\ \bar{q}_V S_V C_{ZV} \end{Bmatrix} \tag{2.270}$$

$$\mathbf{M}_V = \begin{Bmatrix} L_V \\ M_V \\ N_V \end{Bmatrix} = \begin{Bmatrix} \bar{q}_V S_V C_{LV} \\ \bar{q}_V S_V C_{MV} \\ \bar{q}_V S_V C_{NV} \end{Bmatrix} + \mathbf{x}_V \times \mathbf{F}_V \tag{2.271}$$

2.5.4 Tail rotor loads

The tail rotor is modeled based on a modification of the simplified closed-form Bailey solution [71]. The velocity vector of the airflow at the tail rotor in the body fixed axes system is given by

$$\mathbf{u}_{tr} = \mathbf{u}_B + \mathbf{x}_{TR} \times \omega + \mathbf{u}_{in_{tr}} \tag{2.272}$$

where $\mathbf{u}_{in_{tr}}$ is the interference velocity due to the fuselage and main rotor wake and is a function of the main rotor downwash, tip speed and wake skew angle:

$$\mathbf{u}_{in_{tr}} = v_0 \nu_{x_w tr}(\beta_{1c}, \chi)\mathbf{i}_{\mathrm{TR}} + v_0 \nu_{z_w tr}(\beta_{1c}, \chi)\mathbf{k}_{\mathrm{TR}} \tag{2.273}$$

where the functions $\nu_{x_w tr}(\beta_{1c}, \chi)$ and $\nu_{z_w tr}(\beta_{1c}, \chi)$ are provided in the form of look-up tables.

The position vector from the center of gravity of the body to the hub of the tail rotor, $\mathbf{x}_{TR}$, is:

$$\mathbf{x}_{TR} = x_{tr}\mathbf{i}_{\mathrm{B}} + y_{tr}\mathbf{j}_{\mathrm{B}} + z_{tr}\mathbf{k}_{\mathrm{B}} \tag{2.274}$$

Expressing the velocity components at the tail rotor hub in the body fixed coordinate system

$$u_{tr} = u_B + y_{tr} r_B - z_{tr} q_B + u_{in_{tr}} \tag{2.275}$$

$$v_{tr} = v_B + z_{tr} p_B - x_{tr} r_B + v_{in_{tr}} \tag{2.276}$$

$$w_{tr} = w_B + x_{tr} q_B - y_{tr} p_B + w_{in_{tr}} \tag{2.277}$$

A coordinate transformation is applied to these velocity components to obtain the velocity components in the local tail rotor coordinate system. This transformation consists of two rotations. The first about the x_B axis by the tail rotor cant angle, Γ, and the second about the new z axis by the tail rotor yaw angle, Λ. The coordinate transformation matrix is given by:

$$T_{\mathrm{TB}} = \begin{bmatrix} \cos\Lambda & -\sin\Gamma\sin\Lambda & \cos\Gamma\sin\Lambda \\ 0 & \cos\Gamma & \sin\Gamma \\ -\sin\Lambda & -\sin\Gamma\cos\Lambda & \cos\Gamma\cos\Lambda \end{bmatrix} \tag{2.278}$$

The velocity components in the local tail rotor coordinate system are:

$$\begin{Bmatrix} u_{\mathrm{tl}} \\ v_{\mathrm{tl}} \\ w_{\mathrm{tl}} \end{Bmatrix} = [T_{\mathrm{TB}}] \begin{Bmatrix} u_{tr} \\ v_{tr} \\ w_{tr} \end{Bmatrix} \tag{2.279}$$

where the subscript (tl) indicates the velocity components in the local tail rotor coordinate system.

Using the Bailey analysis, the final expression for the non-dimensional tail rotor thrust is:

$$T_{\mathrm{tl}} = 2\rho\left(\pi\bar{R}_{\mathrm{t}}\right)^2 \nu_{\mathrm{t}} v_{T\mathrm{t}} \left(\bar{\Omega}_{\mathrm{t}}\bar{R}_{\mathrm{t}}\right)^2 K_{blk}\left[\frac{R^2}{m_0}\right] \tag{2.280}$$

where $\bar{R}_{\mathrm{t}}$ and $\bar{\Omega}_{\mathrm{t}}$ are the non-dimensional tail rotor radius and rotational speed respectively, ν_{t} is the tail rotor induced velocity, $v_{T\mathrm{t}}$ is the total speed of the airflow at the tail rotor hub and K_{blk} is the empirical tail rotor blockage factor to account for the presence of the vertical tail.

The total speed of the airflow is given by:

$$v_{T\mathrm{tl}} = \sqrt{\mu_{\mathrm{t}}^2 + \lambda_{\mathrm{t}}^2} \tag{2.281}$$

where

$$\mu_{\mathrm{tl}} = \sqrt{u_{\mathrm{tl}}^2 + v_{\mathrm{tl}}^2} \tag{2.282}$$

$$\lambda_{\mathrm{t}} = w_{\mathrm{tl}} - \nu_{\mathrm{t}} \tag{2.283}$$

The non-dimensional torque produced by the tail rotor is given by:

$$Q_{\mathrm{tl}} = \frac{1}{2}\rho\left(\bar{\Omega}_{\mathrm{t}}\bar{R}_{\mathrm{t}}\right)^2 \pi\bar{R}_{\mathrm{t}}^3\left[\frac{R^2}{m_0}\right] \tag{2.284}$$

The only forces and moments considered in the present study will be the thrust and torque loads in the local tail rotor coordinate system, that is:

$$\mathbf{F}_{\mathrm{tl}} = -T_{\mathrm{tl}}\mathbf{j}_{\mathrm{t}} \tag{2.285}$$

$$\mathbf{M}_{\mathrm{tl}} = -Q_{\mathrm{tl}}\mathbf{j}_{\mathrm{t}} \tag{2.286}$$

The resultant tail rotor loads at the center of gravity of the body are obtained using the transformation from tail rotor coordinate system to body fixed system

(Eqn. (2.278)), and the position vector, $\mathbf{x}_{\mathrm{t}}$, of the tail rotor hub with respect to the center of gravity of the aircraft,

$$\mathbf{F}_{TR} = \left\{ \begin{array}{c} X_{TR} \\ Y_{TR} \\ Z_{TR} \end{array} \right\} = [T_{\mathrm{TB}}]^{-1}\mathbf{F}_{\mathrm{tl}} \tag{2.287}$$

$$\mathbf{M}_{TR} = \left\{ \begin{array}{c} L_{TR} \\ M_{TR} \\ N_{TR} \end{array} \right\} = [T_{\mathrm{TB}}]^{-1}\mathbf{M}_{\mathrm{tl}} + \mathbf{x}_{TR} \times \mathbf{F}_{TR} \tag{2.288}$$

2.6 Tail rotor inflow dynamics

The tail rotor inflow dynamics are based on the dynamic inflow theory of Pitt-Peters [6], with the sine and cosine components of the tail rotor inflow assumed to be zero. This reduces the dynamic inflow of the tail rotor to a single equation

$$\frac{1}{\Omega_t}\tau_t\dot{\nu}_t + \nu_t = L_t C_{T_t} \tag{2.289}$$

where

$$\tau_t = \frac{1}{v_{T_t}}\frac{4}{3\pi} \tag{2.290}$$

$$\text{Ł}_t = \frac{1}{2v_{T_t}} \tag{2.291}$$

and v_{T_t} is the total induced velocity at the tail rotor, defined as:

$$v_{T_t} = \sqrt{(u_t^2 + \lambda_t^2)} \tag{2.292}$$

The thrust coefficient of the tail rotor, C_{T_t} is given by:

$$C_{T_t} = \frac{T_{\mathrm{tl}} m_0 \Omega^2 R^2}{\rho\pi\Omega_t^2 R_t^4} \tag{2.293}$$

where Ω_t is the tail rotor rotational speed, R_t is the tail rotor radius and T_{tl} is the non-dimensional tail rotor thrust (Eqn. (2.280)).

2.7 Dynamic inflow model

Two dynamic inflow models are used to provide the main rotor inflow for the baseline configuration when the free wake model is not included. The first dynamic inflow model used is the Pitt-Peters model [6]; the corresponding equations can be found in Ref. [7]. This is a three state model that consists of a uniform inflow component, v_0, and sine and cosine inflow components, v_s and v_c, respectively. They represent an inflow distribution that has a first-harmonic azimuthal distribution and a linear radial distribution. It should be mentioned that this inflow model takes into account the effects of the trailed wake only and thus does not conflict with the quasi-steady aerodynamics model (Section 2.4.1), used for the calculation of sectional aerodynamic loads, which considers the effects of shed wake alone.

The dynamic inflow equations relate the inflow dynamics to the aerodynamic loads in a linear, first-order fashion. Represented in the wind reference coordinate system of the tip path plane, the dynamic inflow equations are

$$\frac{1}{\Omega}\mathbf{M}\left\{\begin{array}{c}\dot{v}_0\\ \dot{v}_s\\ \dot{v}_c\end{array}\right\}+\mathbf{L}_{nl}^{-1}\left\{\begin{array}{c}v_0\\ v_s\\ v_c\end{array}\right\}=\left\{\begin{array}{c}C_T\\ -C_L\\ -C_M\end{array}\right\}_{aero} \tag{2.294}$$

where $\mathbf{M}$ is the matrix of mass terms which represents the time delay effects due to the unsteady wake; $\mathbf{L}_{nl}$ is the non-linear version of the inflow gain matrix [7]; and C_T, C_L and C_M are the instantaneous rotor thrust, rolling moment and pitching moment coefficients respectively, in the wind axis system.

$$\left\{\begin{array}{c}C_T\\ -C_L\\ -C_M\end{array}\right\}_{aero}=\left[\begin{array}{ccc}1 & 0 & 0\\ 0 & \cos\beta_F & \sin\beta_F\\ 0 & -\sin\beta_F & \cos\beta_F\end{array}\right]\left\{\begin{array}{c}C_T\\ C_1\\ -C_2\end{array}\right\}_{aero} \tag{2.295}$$

$$\left\{\begin{array}{c}v_0\\ v_s\\ v_c\end{array}\right\}_{aero}=\left[\begin{array}{ccc}1 & 0 & 0\\ 0 & \cos\beta_F & \sin\beta_F\\ 0 & -\sin\beta_F & \cos\beta_F\end{array}\right]\left\{\begin{array}{c}\lambda_0\\ \lambda_s\\ \lambda_c\end{array}\right\}_{aero} \tag{2.296}$$

In the non-rotating hub-fixed coordinate system, Eqn. (2.294) becomes

$$\frac{1}{\Omega}[\tau]\begin{Bmatrix}\dot{\lambda}_0\\ \dot{\lambda}_s\\ \dot{\lambda}_c\end{Bmatrix}+\begin{Bmatrix}\lambda_0\\ \lambda_s\\ \lambda_c\end{Bmatrix}=\mathbf{L}_{nl}\begin{Bmatrix}C_T\\ C_1\\ -C_2\end{Bmatrix}_{aero} \tag{2.297}$$

where

$$[\tau]=\mathbf{L}_{nl}\mathbf{M} \tag{2.298}$$

The matrix of apparent mass terms $\mathbf{M}$ is

$$\mathbf{M}=\begin{bmatrix}\frac{8}{3\pi} & 0 & 0\\ 0 & \frac{16}{45\pi} & 0\\ 0 & 0 & \frac{16}{45\pi}\end{bmatrix} \tag{2.299}$$

and for twisted rotors, $M_{11}=\frac{128\pi}{75}$.

The inflow gain matrix $\mathbf{L}_{nl}$ is

$$\mathbf{L}_{nl}=\begin{bmatrix}\frac{1}{2v_T} & 0 & \frac{15\pi}{64v_m}\tan\frac{\chi}{2}\\ 0 & \frac{-4}{v_m(1+\cos\chi)} & 0\\ \frac{15\pi}{64v_T}\tan\frac{\chi}{2} & 0 & \frac{-4\cos\chi}{v_m(1+\cos\chi)}\end{bmatrix} \tag{2.300}$$

where χ is the wake skew angle, v_T is the normalized total velocity at the center of the rotor and v_m is the mass flow parameter, and these are given by:

$$\chi = \tan^{-1}\left(\frac{u_s}{|\lambda|\Omega R}\right)+\beta_{1c} \tag{2.301}$$

$$v_T = \sqrt{(\mu^2+\lambda^2)} \tag{2.302}$$

$$v_m = \frac{[\mu^2+\lambda(\lambda+\nu_0)]}{v_T} \tag{2.303}$$

Finally the matrix $[\tau]$ is found from $\mathbf{M}$ and $\mathbf{L}_{nl}$ and is

$$[\tau]=\begin{bmatrix}\frac{1}{v_T}\frac{4}{3\pi} & 0 & \frac{-1}{12v_m}\tan\frac{\chi}{2}\\ 0 & \frac{64}{45\pi v_m(1+\cos\chi)} & 0\\ \frac{5}{8v_T}\tan\frac{\chi}{2} & 0 & \frac{64\cos\chi}{45\pi v_m(1+\cos\chi)}\end{bmatrix} \tag{2.304}$$

The force and moment coefficients in the non-rotating hub plane (Eqn. (2.295)) are based only on the rotor aerodynamic loads and are calculated by integrating the distributed aerodynamic forces, $\mathbf{p}_{\mathrm{A}}$ (Eqn. (2.82)) and moments $\mathbf{q}_{\mathrm{A}}$ (Eqn. 2.83)). These aerodynamic load coefficients are

$$C_T = \int_0^1 p_{\mathrm{A}z} dx \tag{2.305}$$

$$C_1 = \int_0^1 (q_{\mathrm{A}x} \cos\psi - q_{\mathrm{A}y} \sin\psi) dx \tag{2.306}$$

$$-C_2 = \int_0^1 (-q_{\mathrm{A}y} \cos\psi - q_{\mathrm{A}x} \sin\psi) dx \tag{2.307}$$

The inflow at a given radial station r and azimuth angle ψ is calculated from the inflow coefficients as follows:

$$\lambda(r, \psi) = \lambda_0 + \lambda_s r \sin\psi + \lambda_c r \cos\psi \tag{2.308}$$

where r is the non-dimensional spanwise coordinate.

The inflow is inserted into the aerodynamics model in the undistorted preconed blade coordinate system (see Section 2.2.3), which requires a transformation by the precone angle β_P

$$\lambda_z(r, \psi) = \cos\beta_P(\lambda_0 + \lambda_s r \sin\psi + \lambda_c r \cos\psi) \tag{2.309}$$

This inflow is inserted into the aerodynamics model in Eqn. (2.55).

The second dynamic inflow model used to provide the main rotor inflow is the extended momentum theory model proposed by Keller and Curtiss [15, 16] and Arnold *et al.* [17]. This inflow model includes wake distortion effects from pitch and roll rates of the tip path plane on the linear inflow distribution. This is a three state model that consists of a uniform inflow component, λ_0, and sine and cosine inflow components, λ_s and λ_c, respectively. For the hover flight condition, the

equations governing the inflow dynamics in the non-rotating hub-fixed coordinate system Eqn. (2.294) are

$$\frac{1}{\Omega}[\tau]\left\{\begin{array}{c}\dot{\lambda}_0\\ \dot{\lambda}_s\\ \dot{\lambda}_c\end{array}\right\}+\left\{\begin{array}{c}\lambda_0\\ \lambda_s\\ \lambda_c\end{array}\right\} = \mathbf{L}_{nl}\left\{\begin{array}{c}C_T\\ C_1\\ -C_2\end{array}\right\}_{aero} \underline{+K_T\left[\begin{array}{ccc}0&0&0\\0&\mu_y&0\\0&0&\mu_x\end{array}\right]} \underline{+K_R\left[\begin{array}{ccc}0&0&0\\0&p+b_1'&0\\0&0&q+a_1'\end{array}\right]} \tag{2.310}$$

where the underlined terms are those added to Eqn. (2.297) with the extended momentum theory model. The matrices $[\tau]$ and $\mathbf{L}_{nl}$ are calculated in hover from Eqs. (2.304) and (2.300) with $\mu = 0$ and $\chi = 0$. The term K_T arises from the "blow back" of the wake due to translation. For this study it is assumed that $K_T = 0$. The term K_R arises from the curvature of the wake due to the pitch and roll rates of the rotor. The quantities q and p are the pitch and roll rates and a_1' and b_1' are the longitudinal and lateral flap rates.

The inflow at a given radial station r and azimuth angle ψ is calculated using Eqn. (2.308) and converted to the undistorted preconed blade coordinate system (see Section 2.2.3) using Eqn. (2.309). The inflow is then inserted into the aerodynamics model in Eqn. (2.55).

2.8 Assembly of equations of motion

The equations of motion that describe the dynamics of the complete aircraft have been derived in previous sections, namely the main rotor equations in Section 2.4, the fuselage equations in Section 2.5, and the dynamic inflow equations for the baseline case (in which the free wake model is not used) in Section 2.7. These equations have been formulated to be in first-order, ODE form

$$\dot{\mathbf{y}} = \mathbf{g}(\dot{\mathbf{y}}, \mathbf{y}, \mathbf{u}\,; t) \tag{2.311}$$

However this representation of the equations of motion introduces complications when linear models or time histories are to be calculated because of the presence of state derivatives on the right hand side of the equation. The terms containing the state derivatives that appear in the right hand side of Eqn. (2.311) must be identified and grouped on the left hand side, resulting in a system of equations that are in rigorous first-order, ODE form.

The right hand side derivative terms result from the acceleration-dependent portions of the main rotor and fuselage equations. Specifically, for the main rotor these terms are associated with main rotor inertia. Acceleration-dependent terms of structural or aerodynamic origin are neglected [33]. The state derivatives that appear on the right hand side are collected into the following vector (for the baseline case with the dynamic inflow model)

$$\begin{aligned} \dot{\mathbf{y}} \;=\; & [\dot{u}\ \dot{v}\ \dot{w}\ \dot{p}\ \dot{q}\ \dot{r}\ \dot{\phi}\ \dot{\theta}\ \dot{\psi}\ \dot{\lambda}_0\ \dot{\lambda}_s\ \dot{\lambda}_c\ \dot{\lambda}_t\ \dot{q}_1^1\ \dot{q}_2^1\ \dot{q}_3^1\ \dot{q}_4^1\ \ddot{q}_1^1\ \ddot{q}_2^1\ \ddot{q}_3^1\ \ddot{q}_4^1 \\ & \ldots\ \dot{q}_1^{N_\mathrm{h}}\ \dot{q}_2^{N_\mathrm{h}}\ \dot{q}_3^{N_\mathrm{h}}\ \dot{q}_4^{N_\mathrm{h}}\ \ddot{q}_1^{N_\mathrm{h}}\ \ddot{q}_2^{N_\mathrm{h}}\ \ddot{q}_3^{N_\mathrm{h}}\ \ddot{q}_4^{N_\mathrm{h}}]^\top \end{aligned} \tag{2.312}$$

where $\dot{u}$, $\dot{v}$, $\dot{w}$, $\dot{p}$, $\dot{q}$, $\dot{r}$, $\dot{\phi}$, $\dot{\theta}$ and $\dot{\psi}$ are the linear and angular accelerations and the angular velocities at the center of gravity of the aircraft, λ_0, λ_s, λ_c and λ_t are the time derivatives of the main and tail rotor dynamic inflow coefficients and $\dot{q}_i^k$ and $\ddot{q}_i^k$ are the generalized velocity and acceleration coefficients of the i-th blade for the k-th normal mode.

The equation resulting from the removal of the acceleration-dependent terms from the equations $\mathbf{g}$ is

$$\dot{\mathbf{y}} = \mathbf{g}_I(\dot{\mathbf{y}}\,; t) + \mathbf{g}_N(\mathbf{y}, \mathbf{u}\,; t) \tag{2.313}$$

in which

$$\mathbf{g}_I(\dot{\mathbf{y}}\,; t) = \mathbf{E}_C \dot{\mathbf{y}} \tag{2.314}$$

where $\mathbf{E}_C$ is an inertial coupling matrix that is calculated numerically using a perturbation analysis and $\mathbf{g}_N$ is the equations of motion with the acceleration-dependent terms removed. This is substituted into Eqn. (2.313) to give

$$\dot{\mathbf{y}} = \mathbf{E}_C \dot{\mathbf{y}} + \mathbf{g}_N(\mathbf{y}, \mathbf{u}\,; t) \tag{2.315}$$

from which the required first order form can be easily obtained

$$\dot{\mathbf{y}} = (I - \mathbf{E}_C)^{-1} \mathbf{g}_N(\mathbf{y}, \mathbf{u}\,; t) \tag{2.316}$$

or

$$\dot{\mathbf{y}} = \mathbf{f}(\mathbf{y}, \mathbf{u}\,; t) \tag{2.317}$$

which is the form of the equations of motion described in Eqn. (2.1).

Using this formulation, the generalized acceleration coefficients $\ddot{\mathbf{q}}$ have been moved to the left hand side of the second-order ODEs governing the blade dynamics (Eqn. (2.173)). This results in the ODEs governing the blade motion taking the form,

$$\ddot{\mathbf{q}} = \mathbf{f}_q(\dot{\mathbf{q}}, \mathbf{q}) \tag{2.318}$$

2.9 Free wake model

The free wake model used in the current study is the Bagai-Leishman free wake model that is implemented as the Maryland Free-Wake Code (MFW) (Ref. [1]) with minor modifications required to interface it with the rest of the flight dynamics model. This section summarizes the main features of the free wake model.

This model uses a relaxation scheme to calculate a steady-state wake geometry that defines the induced velocity distribution at the rotor disk consistent with the blade loads. This inflow is used to calculate the aerodynamic loads within the flight dynamics model. A relaxation scheme is used so the model cannot produce a

time accurate solution because any wake and inflow transients are removed by the relaxation strategy.

This free wake model belongs to a general set of wake methods known as free vortex methods in which the rotor wake is modeled as a set of vortex filaments and/or vortex sheets. The combined influence, or induced effects, of the individually modeled vortices can be calculated at any point in the flow field or at points on the blades themselves for the case of the inflow.

In the Bagai-Leishman model, the rotor wake is modeled using a set of "free" vortices that are allowed to distort. The "free" vortices distort under the self and mutual influence of all of the modeled vortices, as well as the bound circulation. The geometry and strength of the wake vortices are used to calculate the induced velocity distribution at the rotor disk.

The trailed wake from each blade is modeled by a single "tip" vortex. The initial strength and radial release point are supplied as an input to the model. For the results in this study the assumption is made that the tip vortices are released from the blade quarter-chord at the blade tip. An additional assumption is that the strengths of the tip vortices are given as a function of the bound circulation distribution along the blade at each individual azimuth angle. For an azimuth angle, ψ, the tip vortex strength is

$$\Gamma_{tip}(\psi) = C_\Gamma \max_{i=1,N} [\Gamma_b(r_i, \psi)] \tag{2.319}$$

where $\Gamma_{tip}(\psi)$ is the tip vortex strength and C_Γ is an empirical factor determined experimentally that represents the ratio of the initial tip vortex strength to the maximum bound circulation along the blade. $\Gamma_b(r_i, \psi)$ (Eqn. (3.45)) is the bound circulation at a blade section at a radius r_i and an azimuth angle ψ.

For the study of Bagai [50] it was assumed that the sum of the blade bound

vorticity outboard of the maximum is trailed into the tip vortex. This implies that the initial tip vortex strength is equal to the maximum bound circulation over the span of the blade at a particular azimuth angle. The same assumption is nominally used for this study. Experimental studies [72, 73] have determined that the tip vortex strength is lower than the maximum bound circulation along the blade span, so the effects of including a value of C_Γ that is consistent with experimental measurements is also investigated.

In the free wake model it is possible to include a "secondary" vortex that is associated with a vortex released from the blade root. The initial vortex strength and radial release point of this vortex would be supplied as input to the model. The current study does not look at the effects of the inclusion of this "secondary" vortex.

Additionally, the model includes provisions for a number of rigid trailed vortices that are prescribed and not allowed to distort. The number, lengths, radial locations and strengths of these "trailers" must be supplied as an input to the model. The geometry of these rigid inboard trailers is an undistorted helix and their inclusion attempts to account for the vorticity that is trailed behind the blade inboard of the tip region, due to the radial change in the bound circulation in this region. The results presented in this study will not include these additional inboard trailers.

A free vortex model of this type is governed by the vorticity transport equation, which states that the vortices are convected downstream of the rotor at the local flow field velocity,

$$\frac{\partial \vec{r}(\psi,\zeta)}{\partial \psi} + \frac{\partial \vec{r}(\psi,\zeta)}{\partial \zeta} = \frac{1}{\Omega}\vec{V}\left(\vec{r}(\psi,\zeta)\right) \tag{2.320}$$

where $\vec{r}$ is the position vector of a point on a vortex filament, ψ is the azimuth angle of the blade from which the vortex filament is released, ζ is the azimuthal distance along the vortex filament to the point, $\vec{V}$ is the local velocity vector at the point

$\vec{r}(\psi, \zeta)$ and includes the induced effects from the circulation of the modeled vortices and the bound circulation, as well as any freestream contributions. This velocity vector did not originally include any maneuvering effects on the free vortices and this capability was added for the current analysis in accordance with the method presented by Bagai *et al.* [13], which is described later in this section.

The first step in solving the vorticity transport equation (Eqn. (2.320)) to find the wake geometry is to discretize the equation using finite differences. The first discretization is with respect to the distance along the vortex filament, ζ. This is done by discretizing the tip vortex filament into a number of straight line vortex segments that are joined at a set of collocation points to form a continuous vortex filament. The set of collocation points describes the geometry of the rotor wake. The azimuthal distance between each successive collocation point is the vortex filament discretization resolution, $\Delta\zeta$. The length of each tip vortex filament is an input to the free wake model, and is given in terms of a maximum wake age, ζ_{max}. Therefore the total number of straight line vortex segments in each filament is,

$$N_s = \frac{\zeta_{max}}{\Delta\zeta} \tag{2.321}$$

and the total number of collocation points for a single vortex filament is,

$$N_\zeta = \frac{\zeta_{max}}{\Delta\zeta} + 1 \tag{2.322}$$

The overall free wake geometry is characterized by the positions of the collocation points corresponding to a number of trailed vortex filaments, each of which is generated at a discrete azimuth angle. This leads to the second, or azimuthwise, discretization where the resolution $\Delta\psi$ of the discretization is the azimuthal distance between the release point of each successive vortex filament. The total number of vortex filaments representing the tip vortex geometries at the entire set of azimuth

angles is,

$$N_\psi = \frac{2\pi}{\Delta\psi} \tag{2.323}$$

The free wake model for the azimuthal discretization resolution $\Delta\psi$ need to be equal to the vortex discretization resolution $\Delta\zeta$, but they are equal for the current study. These parameters are collectively referred to the wake resolution $\Delta\psi$.

Figure 2.13 shows the conventions used for the discretization in the ζ and ψ directions. When considering the locations of the collocation points, the index j is used as a reference to the azimuth angle ψ and the index k references the location of the collocation point in the vortex filament ζ.

A pseudo-implicit predictor-corrector method is used to solve Eqn. (2.320) numerically using a relaxation technique. The details of the implementation of the numerical scheme have been presented in Refs. [1], [66], [74]. The partial differential equation, Eqn. (2.320), is first order in ψ and ζ. The solution requires the specification of two boundary conditions, one in the ψ direction and one in the ζ direction. The first boundary condition, with respect to ψ, enforces periodicity of the wake, that is

$$\vec{r}(\psi,\zeta) = \vec{r}(\psi + 2\pi,\zeta) \tag{2.324}$$

The second boundary condition, with respect to ζ, ensures that the trailed vortex filaments are attached to the blade at each azimuth angle, i.e.,

$$\begin{aligned}
\vec{r}(\psi,0) &= r_v\left(\cos\beta\cos\psi\cos\alpha_s + \sin\beta\sin\alpha_s\right)\mathbf{i}_\mathrm{G} \\
&+ r_v\cos\beta\sin\psi\mathbf{j}_\mathrm{G} \\
&+ r_v\left(\sin\beta\cos\alpha_s - \cos\beta\cos\psi\sin\alpha_s\right)\mathbf{k}_\mathrm{G}
\end{aligned} \tag{2.325}$$

where α_s is the longitudinal shaft tilt and is positive aft, $r_v(\psi)$ is the radial release point of the vortex filaments (assumed to be at the blade tip for the current study,

i.e., $r_v = 1.0$) and $\beta(\psi)$ is the rigid blade flapping angle based on an equivalent straight blade with a flap hinge at the axis of rotation (see Section 3.2.2 for further details).

The velocity contributions on the right hand side of Eqn. (2.320) is given as

$$\vec{V}\left(\vec{r}(\psi,\zeta)\right) = \vec{V}_\infty + \vec{V}_{ind}\left(\vec{r}(\psi,\zeta)\right)\Big[\ + \vec{V}_e\left(\vec{r}(\psi,\zeta)\right)\ \Big] \tag{2.326}$$

where $\vec{V}_\infty$ is the freestream velocity which is uniform through the flow field (see Section 3.2.2) and $\vec{V}_{ind}$ contains the induced effects of all of the modeled vortices as well as the effects of the bound circulation. The vector $\vec{V}_e$ is an external velocity profile that results from outside influences that produce non-uniform flow-field velocities, such as gusts and maneuvers. This terms is enclosed in square brackets to indicate that it was not part of the original free wake model and was added for this analysis.

The external velocity profile with the inclusion of maneuver-induced effects is given by [13],

$$\vec{V}_e\left(\vec{r}(\psi,\zeta)\right) = (-q_G z)\mathbf{i}_\mathrm{G} + (p_G z)\mathbf{j}_\mathrm{G} + (q_G x - p_G y)\mathbf{k}_\mathrm{G} \tag{2.327}$$

where these velocity components are resolved in the free wake global fixed coordinate system at the position given by x_G, y_G and z_G, also in the global fixed coordinate system (see Section 2.2.4). The quantities p_G and q_G are the roll and pitch rates at the hub in the same coordinate system.

Before the induced velocities can be calculated, consideration must be given to the vortex model used to represent the free vortices released from the blade tips (and the prescribed inboard trailers when they are present). Two aspects of the vortex model that are important here. These are the tangential velocity profile (i.e., the velocity profile normal to the vortex centerline) and the diffusion of the vortex along its length.

The tangential velocity profile is characterized by an inner viscous region which consists of a "solid-body" rotation and an outer region that simulates a potential vortex profile. Ref [75] shows that the tangential velocity profile of the rotor tip vortices can be closely approximated by

$$v_\theta(r) = \frac{\Gamma r}{2\pi\sqrt{r_c^4 + r^4}} \tag{2.328}$$

where Γ is the vortex circulation strength and r_c is the vortex viscous core radius, which is typically 10-15% of the blade chord.

The diffusion of the vortex is incorporated as a variation in the viscous core radius r_c in which the core radius grows as function of the vortex age in a manner consistent with the decay of a Lamb-Oseen vortex [76]

$$r_c(\zeta) = 2.24\sqrt{\nu\delta\frac{\zeta}{\Omega}} \tag{2.329}$$

where ν is the kinematic viscosity of air, ζ is the vortex age in radians, Ω is the rotational speed of the rotor, and δ is an "eddy" or turbulent velocity coefficient that determines the rate at which the vortex core grows with time, and is determined empirically [50].

It should be noted that while vortex diffusion is taken into account as an increase in core radius with vortex age, there is no modeling of vortex dissipation where the vortex circulation strength would decrease with vortex age. Instead it is assumed that the vortex strength is constant along length.

The contributions to the vorticity transport equation from the induced induced ($\vec{V}_{ind}$ in Eqn. (2.326)) are comprised of the instantaneous velocity contributions of all of the vortex filaments in the wake. The Biot-Savart law is used to calculate the velocity induced at a point located at position $\vec{r}$ relative to the vortex element $d\vec{l}$,

and takes the form,

$$\vec{V}_{ind} = \frac{\Gamma}{4\pi} \int \frac{d\vec{l} \times \vec{r}}{|\vec{r}|^3} \tag{2.330}$$

Incorporating the tangential velocity profile model (Eqn. (2.328)) and vortex diffusion (Eqn. (2.329)) into the Biot-Savart law, the induced velocity due to the vortex element becomes,

$$\vec{V}_{ind} = \frac{\Gamma h}{2\pi\sqrt{r_c^4 + h^4}} \int \frac{d\vec{l} \times \vec{r}}{|\vec{r}|^3} \tag{2.331}$$

where h is the perpendicular distance of the evaluation point from the influencing vortex element. The total induced velocity at a point in the flow field is the combined effect of all of the influencing vortices.

The pseudo-implicit predictor-corrector scheme is an iterative procedure on the geometry of the "free" vortices, in which a new vortex wake geometry is the result of each iteration. Thus there is a change in wake geometry from one iteration to the next, which can be quantified by considering the L_2 norm of the wake geometry change between successive iterations. The root mean square (RMS) change in the wake structure is calculated using [50],

$$RMS = \frac{1}{j_{max} k_{max}} \sqrt{\sum_{\psi:j=1}^{j_{max}} \sum_{\zeta:k=1}^{k_{max}} (\vec{r}_{j,k}^{\,n} - \vec{r}_{j,k}^{\,n-1})^2} \tag{2.332}$$

where j_{max} is the number of blade azimuthal steps in one revolution, with $j_{max} = N_\psi$, and k_{max} is the number of collocation points used to describe each of the trailed vortex filaments, with $k_{max} = N_\zeta$.

In the Bagai-Leishman free wake model, the iterative process defining the wake geometry is started by assuming an undistorted helical wake structure. The convergence criterion for the iterative process is based on the RMS change in the wake geometry for the current iteration in comparison with the RMS change in wake

geometry from the first iteration. Or more specifically, the wake geometry is considered converged when the ratio of the RMS change for the current iteration to the RMS change of the first iteration falls below a certain threshold. This can be written as

$$\frac{(RMS)_n}{(RMS)_1} < \epsilon \tag{2.333}$$

where ϵ is the threshold for convergence, $(RMS)_n$ is the RMS change in wake geometry of the nth iteration, $(RMS)_1$ is the RMS change of the first iteration started from an undistorted helical wake. In the present study the convergence criterion was slightly modified, and based on the absolute RMS change in wake geometry, rather than the relative change, as detailed later in Section 3.2.3.

Finally, the converged wake is used to calculate the local induced velocity at specified points along the blade span and around the azimuth. These local velocities only contain contributions from the bound and wake circulations and represent only the induced velocity, $\vec{V}_{ind}(\vec{r}(\psi, \zeta))$ from Eqn. (2.326). The free stream and kinematic contributions to the local blade aerodynamic profile are included internally in the flight dynamics code.

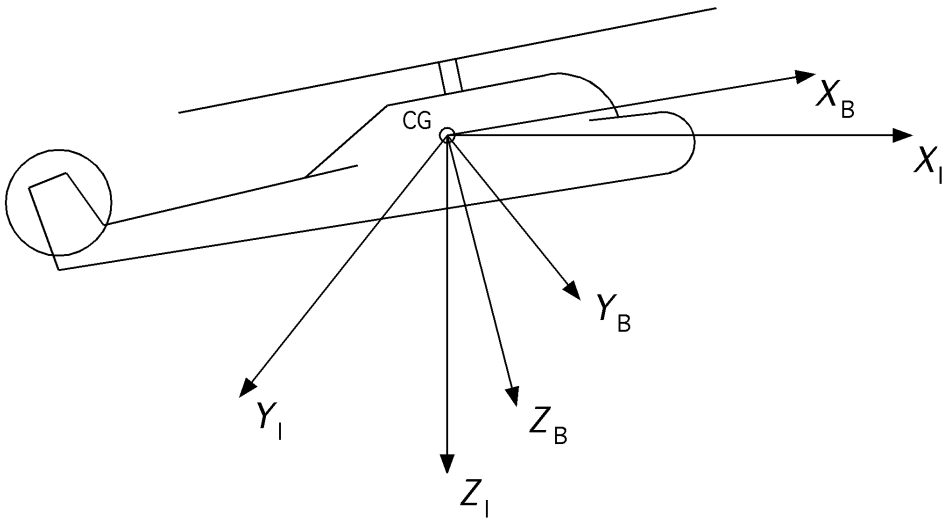

Figure 2.1: Inertial and fuselage coordinate systems.

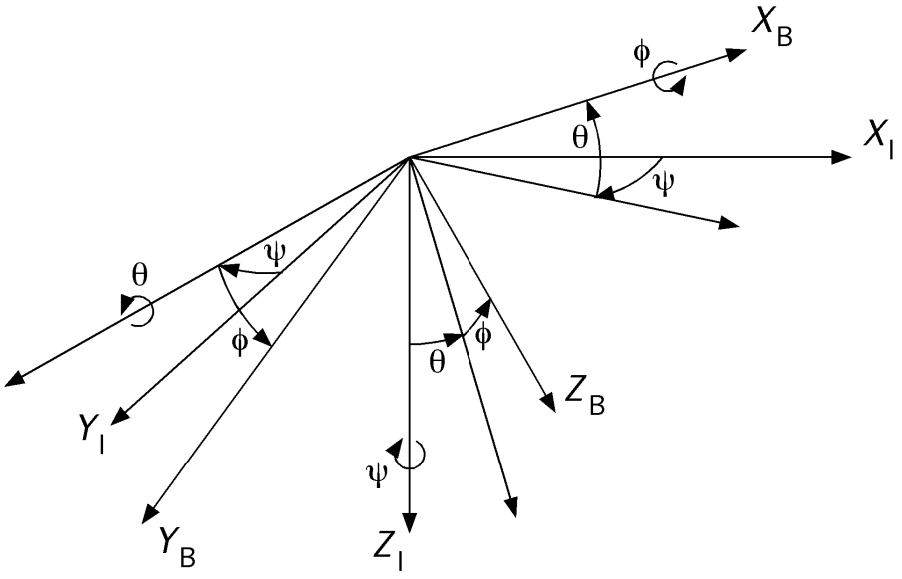

Figure 2.2: Euler rotations from the inertial to fuselage coordinate systems. Sequence of rotations: $\psi \longrightarrow \theta \longrightarrow \phi$.

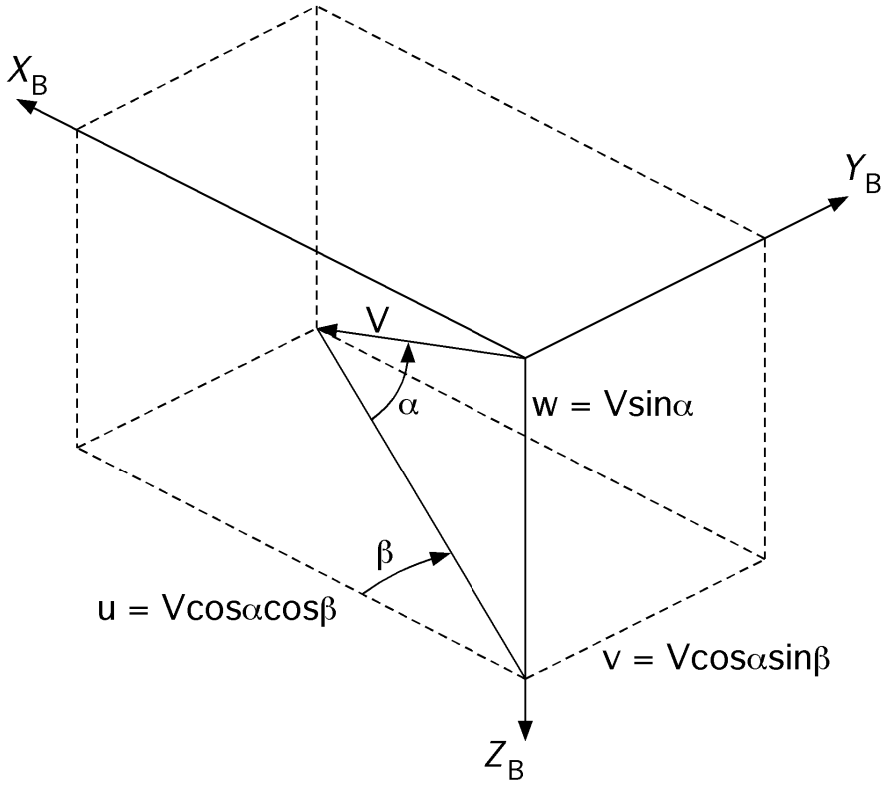

Figure 2.3: Relationship between velocity vector and fuselage coordinate system.

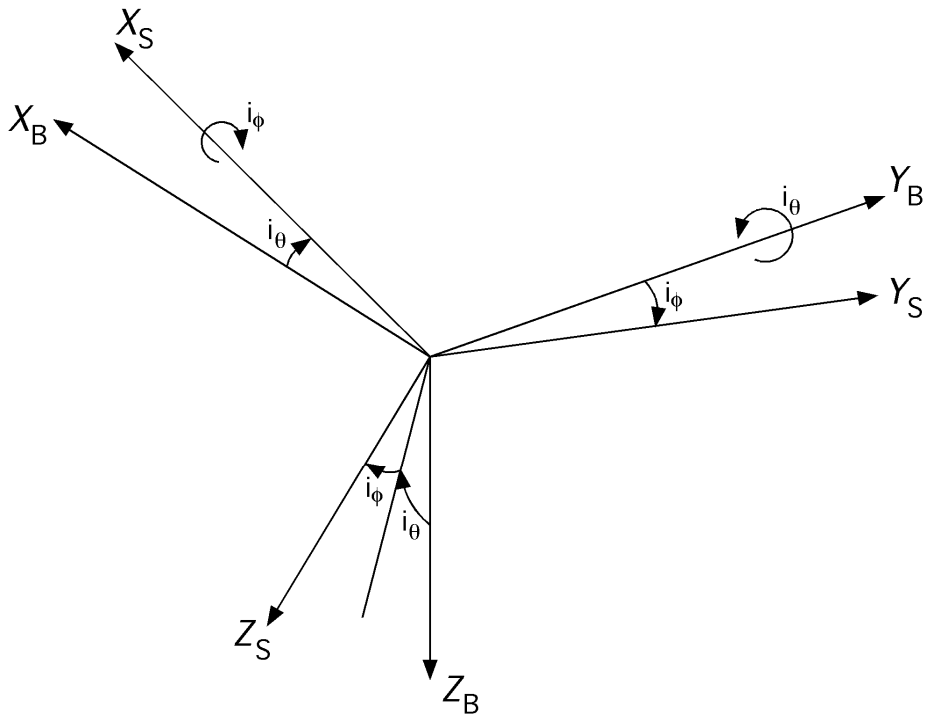

Figure 2.4: Transformation from fuselage and shaft coordinate systems. Sequence of rotations: $i_\theta \longrightarrow i_\phi$.

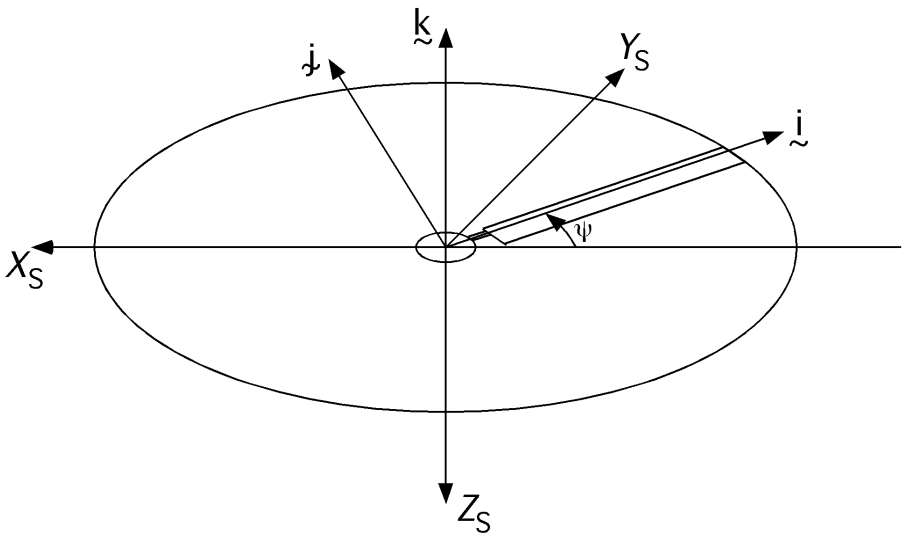

Figure 2.5: Hub-fixed rotating and shaft-fixed non-rotating coordinate systems.

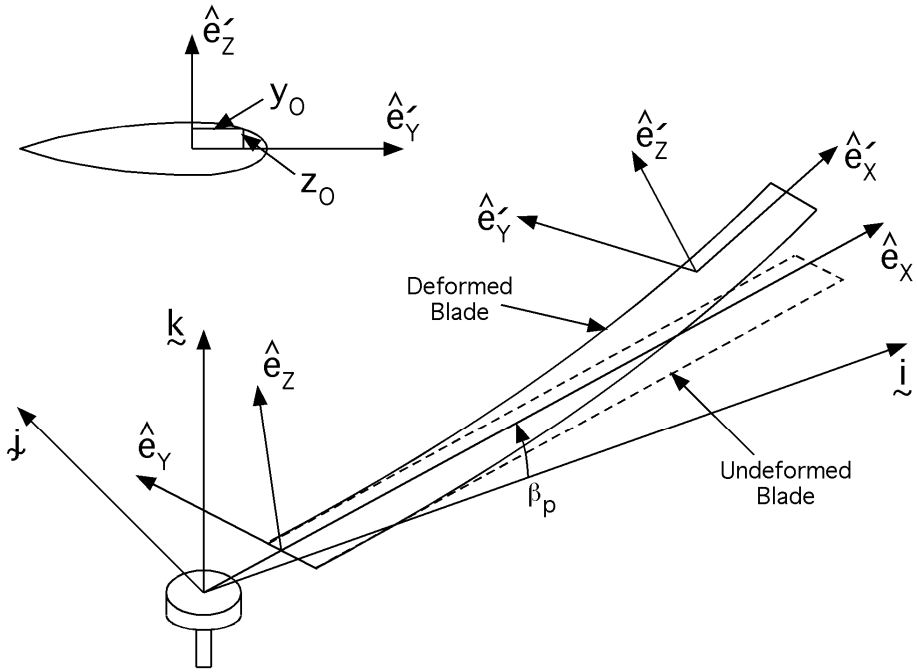

Figure 2.6: Blade deformed and undeformed coordinate systems.

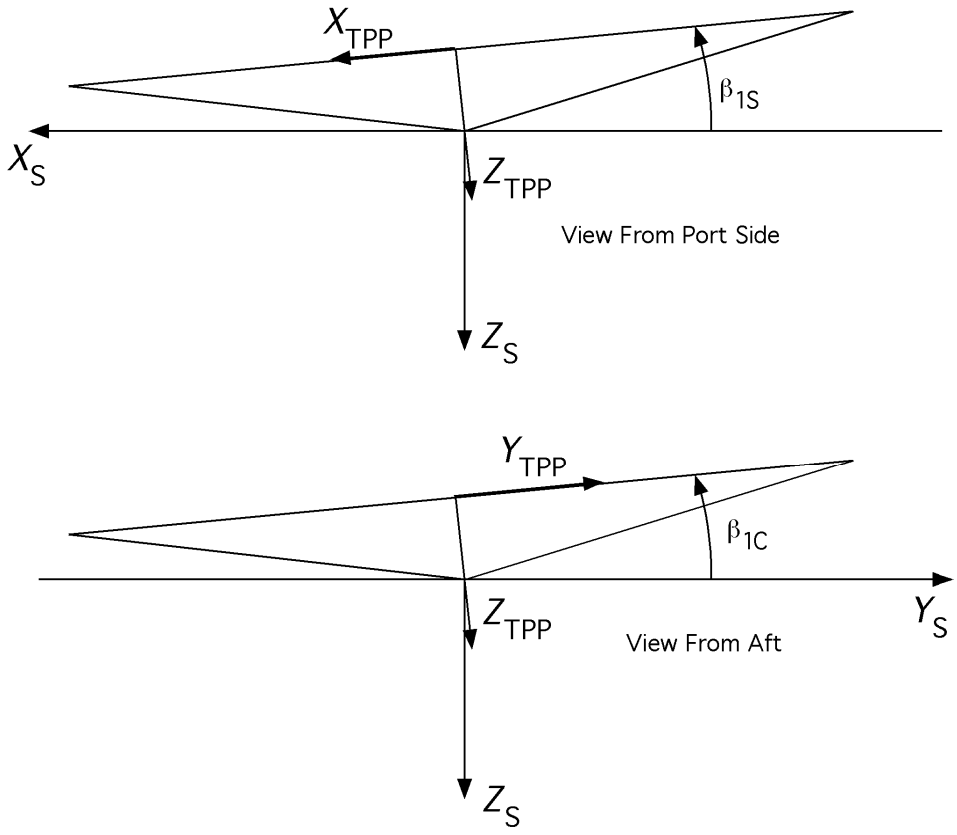

Figure 2.7: Transformation from shaft to tip path plane coordinate systems.

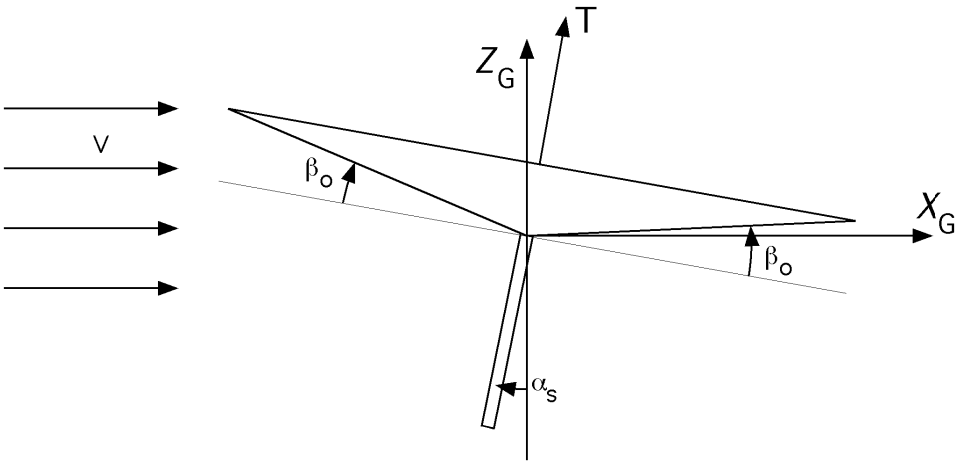

Figure 2.8: Global-fixed coordinate system for free wake model.

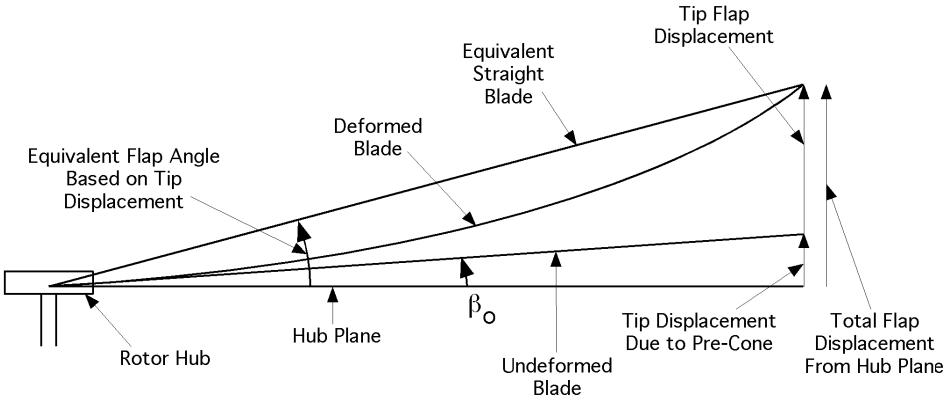

Figure 2.9: Definition of tip flapping angles for the flight dynamics and free wake models.

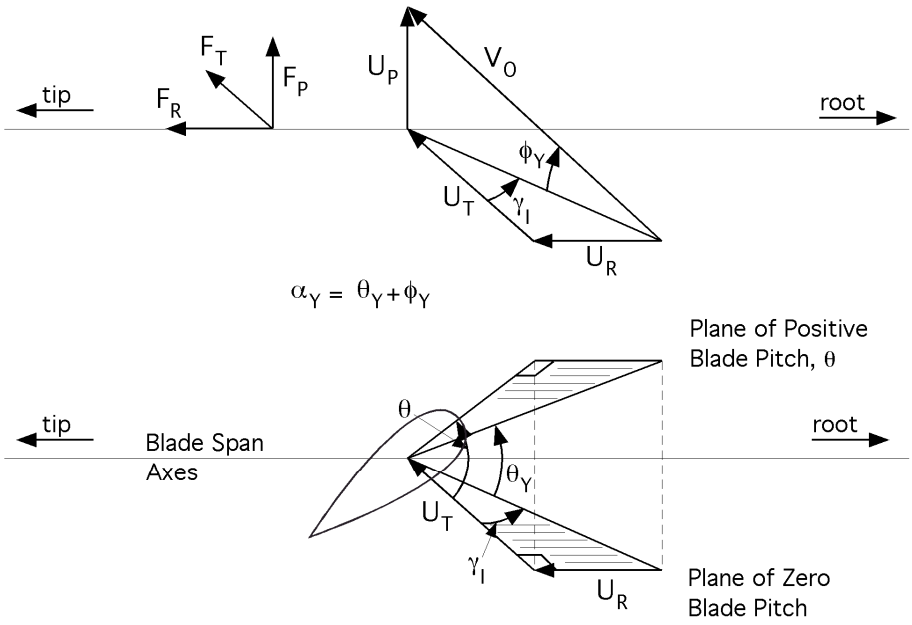

Figure 2.10: Definition of blade section yaw angle γ_I and angle of attack ϕ_Y.

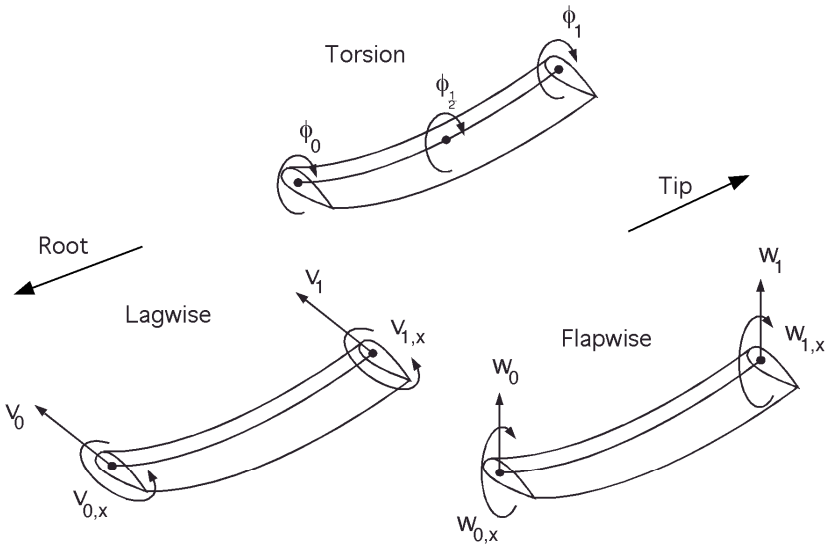

Figure 2.11: Finite element nodes and degrees of freedom.

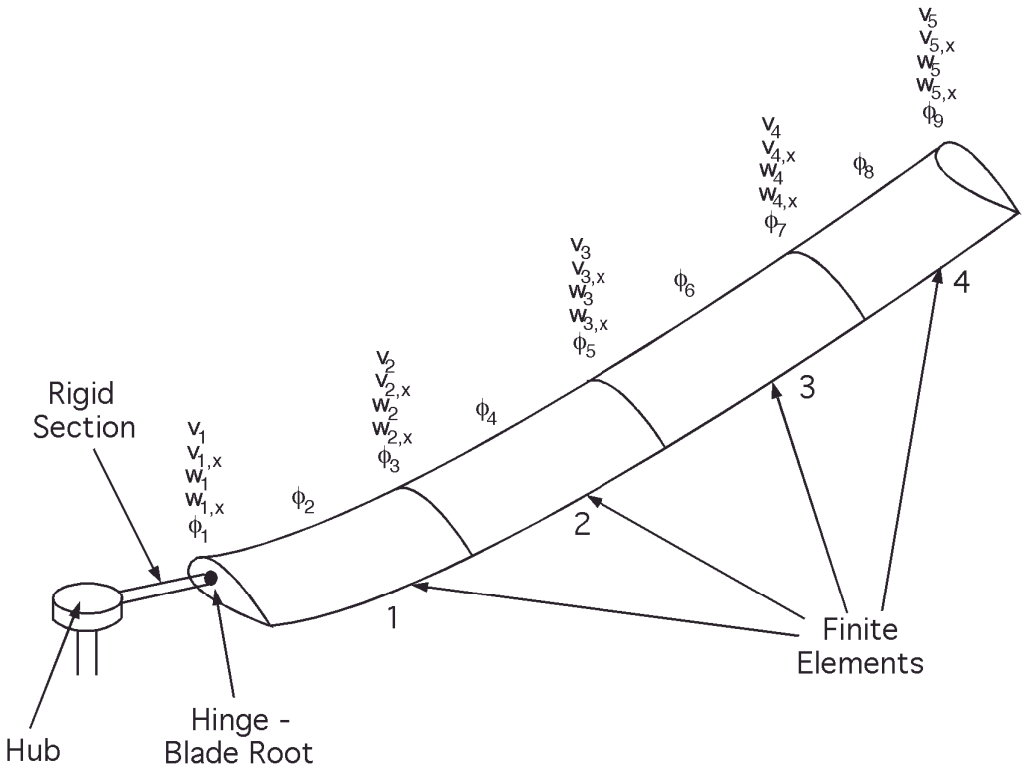

Figure 2.12: Blade degrees of freedom using four finite elements.

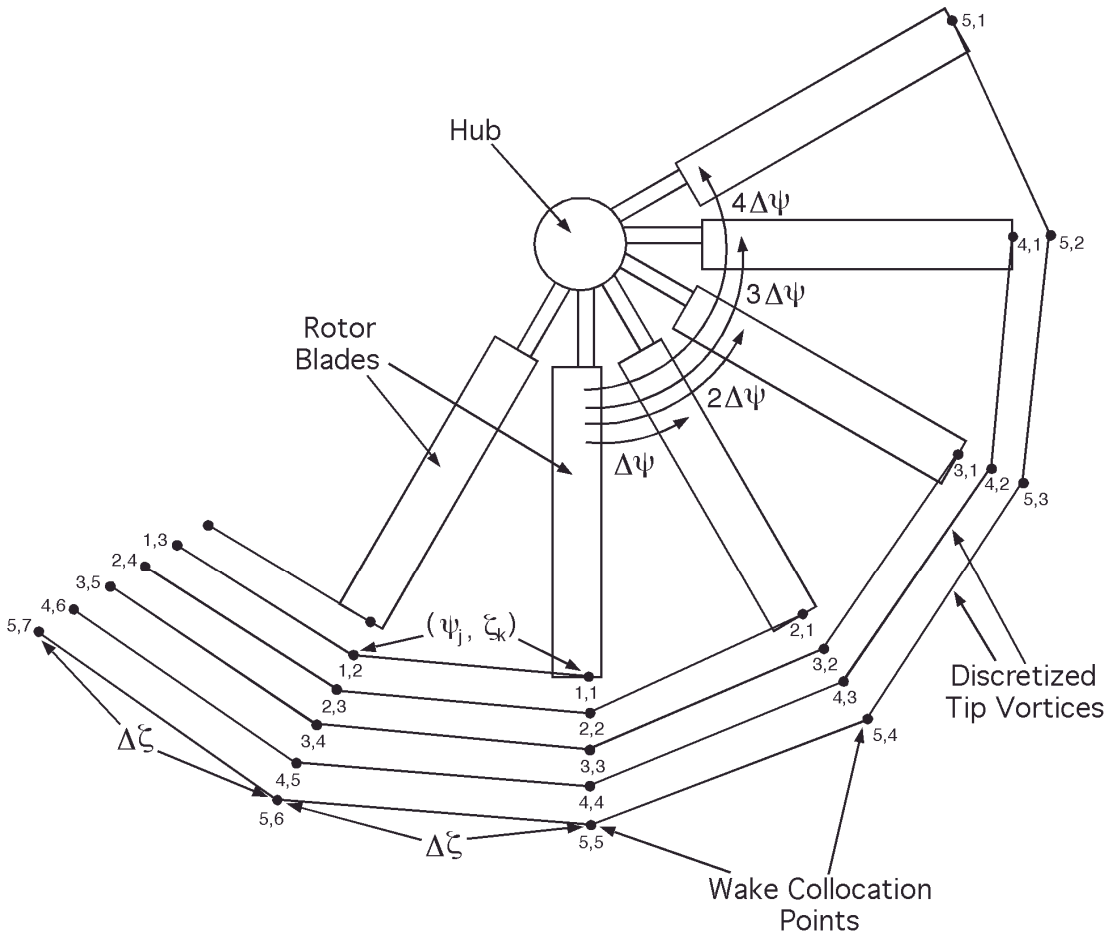

Figure 2.13: Discretized physical domain for free wake [1].

Chapter 3

Solution Methods: Trim

This chapter presents the methods used to calculate the trim state of the helicopter. The generic flight condition assumed is a steady, coordinated, helical turn. Straight and level flight is treated as a special case of turn with the flight path angle and turn rate equal to zero.

This chapter is divided into two main parts. The first describes the baseline trim procedure, for the case in which a free wake model is not included. The second describes in detail the changes in the formulation and solution methods required by the incorporation of the free wake model into the trim procedure. A third section describes how to reconstruct the state vector corresponding to the trim solution.

3.1 Baseline trim procedure

This section describes the baseline trim procedure for the case in which the free wake model is not included. The baseline flight condition is described first, followed by a description of the unknowns of the problem, the equations that make up the trim problem, and the solution process. The basic trim procedure is essentially the same as that described in Refs. [60] and [77], which extend the original formulation by Chen and Jeske [55].

3.1.1 Definition of the flight condition

The trim state is calculated for a coordinated, steady, helical turn defined by the following parameters:

1. the velocity V along the trajectory;
2. the flight path angle γ, positive for climbing flight; and
3. the turn rate $\dot{\psi}$, positive for a turn to the right, or clockwise when seen from above.

The geometry of the trim problem for a coordinated turn is shown in Figure 3.1.

Straight and level flight is treated as a special case of turn with $\dot{\psi} = \gamma = 0$. For hover it should also be $V = 0$. However, a zero speed would introduce zeros in the denominator of some trim expressions, and therefore a very small number sufficient to avoid numerical singularities is used instead. This eliminates the need for two different sets of equations for zero and nonzero values of V, and has no practical repercussions on the accuracy of the final results.

3.1.2 Unknowns of the trim problem

The unknowns of the trim problem are grouped into a vector $\mathbf{x}$ that is partitioned into a rigid body part, a main rotor part and an inflow part as follows:

$$\mathbf{x} = \left\{ \begin{array}{c} \mathbf{x}_B \\ \mathbf{x}_R \\ \mathbf{x}_I \end{array} \right\} \tag{3.1}$$

The $\mathbf{x}_B$ partition contains the unknowns of the trim procedure associated with the overall trim of the helicopter:

$$\mathbf{x}_B = [\ \theta_0\ \theta_{1c}\ \theta_{1s}\ \theta_t\ \alpha_F\ \beta_F\ \phi_F\ \theta_F\ \lambda_t\ ]^\top \tag{3.2}$$

where θ_0, θ_{1c}, θ_{1s} and θ_t are the trim control settings of the main and tail rotors; α_F and β_F are the angles of attack and sideslip of the fuselage; ϕ_F and θ_F are the roll and pitch Euler angles of the fuselage; and λ_t is the constant tail rotor inflow, and is included in the $\mathbf{x}_B$ partition for convenience. The subscript $(\ )_F$ is used to indicate that the quantity is related to the fuselage.

Once the angle of attack α_F and the sideslip β_F are known, the velocities u, v, and w along the body axes can be obtained from

$$u = V \cos\alpha_F \cos\beta_F \tag{3.3}$$

$$v = V \sin\beta_F \tag{3.4}$$

$$w = V \sin\alpha_F \cos\beta_F \tag{3.5}$$

The angular velocities p, q, and r about the body axes can be obtained from

$$p = -\dot{\psi} \sin\theta_F \tag{3.6}$$

$$q = \dot{\psi} \sin\phi_F \cos\theta_F \tag{3.7}$$

$$r = \dot{\psi} \cos\phi_F \cos\theta_F \tag{3.8}$$

The $\mathbf{x}_R$ partition contains the Fourier series expansion coefficients of each of the blade modes retained for trim (see Section 2.4.8 for further details on the modal coordinate transformation). In the trim condition, the blade motion is periodic and the generalized coordinate of each of the blade modes is approximated by a truncated Fourier series. The coefficients of these Fourier expansions become the unknowns of the trim problem:

$$q^k(\psi) \approx q^k_{app}(\psi) = q^k_0 + \sum_{j=1}^{N_\mathrm{h}} (q^k_{jc} \cos j\psi + q^k_{js} \sin j\psi) \tag{3.9}$$

where q^k_0 is the constant coefficient in the expansion of the k-th mode, and q^k_{jc} and q^k_{js} are respectively the coefficients of the j-th harmonic cosine and sine for the k-th

mode. Also, N_h is the number of harmonics included in the expansion for each mode and N_m is the number of main rotor modes retained for the trim procedure.

It should be mentioned that the generalized coordinates q^k and their Fourier series approximations q^k_{app} are periodic functions of the azimuth angle ψ where the Fourier series expansion coefficients q^k_0, q^k_{jc} and q^k_{js} are constant for a particular trim vector and are not a function of azimuth angle.

The coefficients of the Fourier series expansion make up the $\mathbf{x}_R$ partition, which is arranged as follows:

$$\begin{aligned}\mathbf{x}_R = \; [\;\; & q^1_0 \; q^1_{1c} \; q^1_{1s} \; q^1_{2c} \; q^1_{2s} \ldots q^1_{N_h c} \; q^1_{N_h s} \ldots \\ & \ldots q^{N_\mathrm{m}}_0 \; q^{N_\mathrm{m}}_{1c} \; q^{N_\mathrm{m}}_{1s} \; q^{N_\mathrm{m}}_{2c} \; q^{N_\mathrm{m}}_{2s} \ldots q^{N_\mathrm{m}}_{N_\mathrm{h} c} \; q^{N_\mathrm{m}}_{N_\mathrm{h} s} \;]^\top \end{aligned} \tag{3.10}$$

The assumption is made that the blades are identical, and perform identical motions in trim. Therefore, the dynamics of only one blade need be taken into account.

Finally, the $\mathbf{x}_I$ partition contains the constant trim values of the dynamic inflow coefficients representing the main rotor inflow (see Section 2.7 for further details on the inflow model):

$$\mathbf{x}_I = [\; \lambda_0 \; \lambda_s \; \lambda_c \;]^\top \tag{3.11}$$

where λ_0 is the uniform inflow component, and λ_s and λ_c are the sine and cosine inflow components, respectively. Thus the total number of trim variables associated with the dynamic inflow model is 3.

The partitions $\mathbf{x}_B, \mathbf{x}_R$, and $\mathbf{x}_I$ contain respectively 9, $N_\mathrm{m}(2N_\mathrm{h}+1)$, and 3 unknowns. Therefore, the total number of trim variables is $12 + N_\mathrm{m}(2N_\mathrm{h}+1)$.

3.1.3 Formulation of the trim problem

The trim problem is formulated as a system of coupled nonlinear algebraic equations symbolically written as

$$\mathbf{F}(\mathbf{x}) = \mathbf{0} \tag{3.12}$$

The vector $\mathbf{F}$ of equations is composed of three partitions

$$\mathbf{F} = \left\{ \begin{array}{c} \mathbf{F}_B \\ \mathbf{F}_R \\ \mathbf{F}_I \end{array} \right\} \tag{3.13}$$

where $\mathbf{F}_B$ represents the set of equations that enforce overall force and moment equilibrium on the fuselage, and includes some geometric and dynamic conditions that have to be satisfied in the turn. An equation for the average tail rotor inflow is also included in this vector. These equations will be collectively referred to as "fuselage equations." The second partition, $\mathbf{F}_R$, contains the equations that enforce the periodicity of main rotor blade dynamics. The final partition, $\mathbf{F}_I$, contains the trim equations related to the main rotor inflow model; they enforce the requirement that the derivatives of the harmonics of the main rotor inflow be zero when averaged over one rotor revolution. Each of these sets of equations will now be considered in turn.

Fuselage equations

The fuselage trim equations consist of a set of nine algebraic equations describing the trim state of the entire aircraft and the tail rotor inflow. These equations are defined by the following conditions:

1. *Force and moment equilibrium.* These six equations require that the linear and angular accelerations of the aircraft be equal to zero when averaged over

one rotor revolution.

$$\int_0^{2\pi} \dot{u}\, d\psi = 0 \tag{3.14}$$

$$\int_0^{2\pi} \dot{v}\, d\psi = 0 \tag{3.15}$$

$$\int_0^{2\pi} \dot{w}\, d\psi = 0 \tag{3.16}$$

$$\int_0^{2\pi} \dot{p}\, d\psi = 0 \tag{3.17}$$

$$\int_0^{2\pi} \dot{q}\, d\psi = 0 \tag{3.18}$$

$$\int_0^{2\pi} \dot{r}\, d\psi = 0 \tag{3.19}$$

Eqs. (3.14)-(3.16) are equivalent to enforcing force equilibrium along the body axes, whereas Eqs. (3.17)-(3.19) enforce moment equilibrium about the body axes. The derivatives $\dot{u}, \ldots, \dot{r}$ are given in Eqs. 2.174 through 2.179 respectively.

2. *Equation for turn coordination.* The turn coordination equation requires that the Y force component be equal to zero when averaged over one rotor revolution, that is:

$$\int_0^{2\pi} \left[\sin\phi_F - \frac{\dot{\psi} V}{g} (\cos\alpha_F \cos\phi_F + \sin\alpha_F \tan\theta_F) \cos\beta_F \right] d\psi = 0 \tag{3.20}$$

In straight flight $\dot{\psi} = 0$, and Eqn. (3.20) becomes:

$$\int_0^{2\pi} \sin\phi_F\, d\psi = 0$$

This means that the turn coordination equation implies that in straight flight the average roll angle is zero *regardless of the flight speed.* At high speed this is a reasonable assumption if the helicopter has a vertical tail, because large lateral forces and yaw moments can be generated by the tail. As the speed decreases the vertical tail becomes less effective, and to achieve lateral force

equilibrium along the y_B body axis it is necessary to generate lateral weight components through the roll angle ϕ_F. Therefore, at hover and low speeds, $\phi_F = 0$ may not be a good assumption. In reality there is a trade-off between ϕ_F and β_F, which leaves part of the trim problem undetermined for the straight flight case. Mathematically this means that when $\dot{\psi} = 0$ the solution of Eqn. (3.20) is only one of an infinite number of possible combinations of ϕ_F and β_F.

To eliminate the ambiguity, the turn coordination equation, Eqn. (3.20) is used for straight flight only at advance ratios above $\mu = 0.1$. This implies a zero trim roll angle, which is a reasonable assumption. For advance ratios below $\mu = 0.1$ the turn coordination equation is replaced by another, which enforces a zero average sideslip angle:

$$\int_0^{2\pi} \beta_F d\psi = 0 \tag{3.21}$$

and trim is achieved through a variable, usually nonzero, *bank* angle ϕ_F.

3. *Relationship between angle of attack and Euler pitch angle.* This equation corresponds to a kinematic relation between the flight path angle, γ, and angle of attack, sideslip angle, roll angle, and pitch angle:

$$\int_0^{2\pi} [\cos\alpha_F \cos\beta_F \sin\theta_F - (\sin\beta_F \sin\phi_F + \sin\alpha_F \cos\beta_F \cos\phi_F) \cos\theta_F - \sin\gamma]\, d\psi = 0 \tag{3.22}$$

$$\tag{3.23}$$

4. *Tail rotor inflow.* This equation requires that the tail rotor inflow be constant on average over one rotor revolution:

$$\int_0^{2\pi} \dot{\nu}_t \, d\psi = 0 \tag{3.24}$$

Blade Trim Equations

A Galerkin technique is used to transform the governing blade ordinary differential equations into a set of non-linear algebraic equations. The motion of the blade is assumed to be periodic. The generalized coordinates and their derivatives can be obtained from their truncated Fourier series expansions, Eqn. (3.9):

$$q^k(\psi) \approx q^k_{app}(\psi) = q^k_0 + \sum_{j=1}^{N_\mathrm{h}} (q^k_{jc} \cos j\psi + q^k_{js} \sin j\psi) \tag{3.25}$$

$$\dot{q}^k(\psi) \approx \dot{q}^k_{app}(\psi) = \Omega \sum_{j=1}^{N_\mathrm{h}} (-q^k_{jc} \sin j\psi + q^k_{js} \cos j\psi) \tag{3.26}$$

$$\ddot{q}^k(\psi) \approx \ddot{q}^k_{app}(\psi) = -\Omega^2 \sum_{j=1}^{N_\mathrm{h}} (q^k_{jc} \cos j\psi + q^k_{js} \sin j\psi) \tag{3.27}$$

where the superscript k refers to the k-th mode in the modal coordinate transformation and N_h is the highest harmonic in the truncated Fourier series for the approximation to the generalized coordinates.

The generalized coordinates for each mode are assembled into a vector

$$\mathbf{q} = \left\{ \begin{array}{c} q^1 \\ q^2 \\ \vdots \\ q^{N_\mathrm{m}} \end{array} \right\} \tag{3.28}$$

and similarly

$$\dot{\mathbf{q}} = \left\{ \begin{array}{c} \dot{q}^1 \\ \dot{q}^2 \\ \vdots \\ \dot{q}^{N_\mathrm{m}} \end{array} \right\} \tag{3.29}$$

$$\ddot{\mathbf{q}} = \left\{ \begin{array}{c} \ddot{q}^1 \\ \ddot{q}^2 \\ \vdots \\ \ddot{q}^{N_\mathrm{m}} \end{array} \right\} \tag{3.30}$$

Similar vectors are also defined for the approximations to the generalized coordinates and to their derivatives calculated from the Fourier series expansions of

Eqs. (3.25) through (3.27):

$$\mathbf{q}_{app} = \left\{ \begin{array}{c} q^1_{app} \\ q^2_{app} \\ \vdots \\ q^{N_{\rm m}}_{app} \end{array} \right\} \tag{3.31}$$

$$\dot{\mathbf{q}}_{app} = \left\{ \begin{array}{c} \dot{q}^1_{app} \\ \dot{q}^2_{app} \\ \vdots \\ \dot{q}^{N_{\rm m}}_{app} \end{array} \right\} \tag{3.32}$$

$$\ddot{\mathbf{q}}_{app} = \left\{ \begin{array}{c} \ddot{q}^1_{app} \\ \ddot{q}^2_{app} \\ \vdots \\ \ddot{q}^{N_{\rm m}}_{app} \end{array} \right\} \tag{3.33}$$

The ODEs governing the motion of a single blade have been written in the form (see Eqn. (2.318))

$$\ddot{\mathbf{q}} = \mathbf{f}_{\rm q}(\dot{\mathbf{q}}, \mathbf{q}) \tag{3.34}$$

where it is implied that the generalized coordinates, their derivatives and the set of equations are given as a function of the azimuth angle.

In general, if the approximate solutions for $\mathbf{q}$, Eqs. (3.25)-(3.27) are substituted in Eqn. (3.34), the equation will not be exactly satisfied. There will usually be a nonzero residual vector $\boldsymbol{\varepsilon}$, defined as:

$$\boldsymbol{\varepsilon}(\psi) = \ddot{\mathbf{q}}_{app} - \mathbf{f}_{\rm q}(\dot{\mathbf{q}}_{app}, \mathbf{q}_{app}) \tag{3.35}$$

where the vector of residuals $\boldsymbol{\varepsilon}$, contains one element for each of the blade modes used in the modal coordinate transformation.

According to the Galerkin method, the choice of q^j_0, q^j_{kc}, and q^j_{ks} that minimizes

on average the residual vector $\boldsymbol{\varepsilon}$ is that which satisfies the following equations [60]

$$\begin{cases} \displaystyle\int_0^{2\pi} \boldsymbol{\varepsilon}^k(\psi)\, d\psi = 0 \\ \displaystyle\int_0^{2\pi} \boldsymbol{\varepsilon}^k(\psi) \cos j\psi\, d\psi = 0 \quad j = 1, \ldots, N_\mathrm{h} \\ \displaystyle\int_0^{2\pi} \boldsymbol{\varepsilon}^k(\psi) \sin j\psi\, d\psi = 0 \quad j = 1, \ldots, N_\mathrm{h} \end{cases} \tag{3.36}$$

This formulation yields a set of $1 + 2N_\mathrm{h}$ vector algebraic equations, and a total of $(1 + 2N_\mathrm{h})N_\mathrm{m}$ scalar equations if N_m modes are used in the modal coordinate transformation. These equations make up the partition $\mathbf{F}_R$ of the vector of trim equations, Eqn. (3.13).

Dynamic Inflow Trim Equations

The dynamic inflow models have been described in Section 2.7. The treatment of both dynamic inflow models is the same since they are both represented in first order form. The corresponding trim equations enforce the requirement that the average over one rotor revolution of the derivative of each dynamic inflow coefficient be zero, that is:

$$\int_0^{2\pi} \dot{\lambda}_0\, d\psi = 0 \tag{3.37}$$

$$\int_0^{2\pi} \dot{\lambda}_s\, d\psi = 0 \tag{3.38}$$

$$\int_0^{2\pi} \dot{\lambda}_c\, d\psi = 0 \tag{3.39}$$

The number of main rotor inflow trim equations is 3 and these equations make up the partition $\mathbf{F}_I$ of the vector of trim equations, Eqn. (3.13).

Summary of trim equations and unknowns for the baseline case

The complete set of trim equations for the baseline case is composed of:

- 3 force equilibrium equations, Eqs. (3.14)-(3.16)
- 3 moment equilibrium equations, Eqs. (3.17)-(3.19)
- 1 equation for turn coordination, Eqn. (3.20), or, for straight flight at $\mu \leq 0.1$, zero average sideslip, Eqn. (3.21)
- 1 kinematic relation for the flight path angle, Eqn. (3.23)
- 1 tail rotor inflow equation, Eqn. (3.24)
- $(1 + 2N_{\mathrm{h}})N_{\mathrm{m}}$ equations for periodic blade motion, Eqs. (3.36)
- 3 equations for the main rotor inflow, Eqs. (3.37)-(3.39)

for a total of $12 + (1 + 2N_{\mathrm{h}})N_{\mathrm{m}}$ equations.

The vector $\mathbf{x}$ of unknowns of the baseline trim procedure is composed of:

$$\begin{aligned} \mathbf{x}_{trim} &= [\theta_0\ \theta_{1c}\ \theta_{1s}\ \theta_{0t}\ \alpha_F\ \beta_F\ \theta_F\ \phi_F\ \lambda_t\ q_0^1\ q_{1c}^1\ q_{1s}^1\ q_{2c}^1\ q_{2s}^1 \dots q_{N_{\mathrm{h}}c}^1\ q_{N_{\mathrm{h}}s}^1 \dots \\ &\quad \dots q_0^{N_{\mathrm{m}}}\ q_{1c}^{N_{\mathrm{m}}}\ q_{1s}^{N_{\mathrm{m}}}\ q_{2c}^{N_{\mathrm{m}}}\ q_{2s}^{N_{\mathrm{m}}} \dots q_{N_{\mathrm{h}}c}^{N_{\mathrm{m}}}\ q_{N_{\mathrm{h}}s}^{N_{\mathrm{m}}}\ \lambda_0\ \lambda_s\ \lambda_c\ ]^\top \end{aligned} \tag{3.40}$$

where the unknowns are:

- Collective pitch θ_0, lateral and longitudinal cyclic pitch θ_{1c} and θ_{1s} of the main rotor; collective pitch θ_{0t} of the tail rotor
- Angles of attack α_F and sideslip β_F of the fuselage
- Pitch angle θ_F and roll angle ϕ_F of the fuselage
- Tail rotor inflow λ_t
- Modal coefficients of the main rotor blade motion, q_0^k, q_{jc}^k and q_{js}^k with k being the mode number

- Uniform, sine and cosine coefficients of the dynamic inflow model λ_0, λ_s and λ_c

for a total of $12 + (1 + 2N_{\mathrm{h}})N_{\mathrm{m}}$ unknowns.

3.1.4 Solution of baseline trim equations

The set of trim equations is solved using a standard nonlinear algebraic equation solver. In the present study, the equations were solved using the code HYBRD [78], which implements a quasi-Newton method. It is useful to recall some aspects of the solution process that will be important in the coupling of the free wake model.

The code HYBRD requires that the system of trim equations be written in the form

$$\mathbf{F}(\mathbf{x}) = \mathbf{r} \tag{3.41}$$

where $\mathbf{r}$ is the vector of residual obtained by substituting a tentative trim solution $\mathbf{x}$ into the system of equations $\mathbf{F}$. In other words, it is only necessary to calculate the residuals $\mathbf{r}$ of the trim equations for *given* values of pitch settings, blade motions, fuselage velocities, attitudes and rates, and steady inflow, regardless of whether such values actually correspond to a trimmed solution. The equation solver then adjusts the values of $\mathbf{x}$ to reduce the norm of $\mathbf{r}$ below a certain tolerance, and therefore solve the trim problem. Figure 3.2 shows a block diagram that summarizes the baseline trim procedure.

3.2 Trim Procedure with Free Wake Inflow Model

This section presents the procedure for the calculation of the trim solution when the dynamic inflow model is replaced by the maneuvering free wake model. The basic differences between the two trim formulations are outlined first.

3.2.1 Formulation of the trim problem with the free wake

The definition of the flight condition is the same as that of the baseline trim. Therefore, the velocity V along the trajectory, the turn rate $\dot{\psi}$, and flight path angle γ, completely define the problem.

When the free wake model provides the main rotor inflow, there are no explicit trim unknowns associated with the main rotor inflow. With reference to Eqn. (3.1), the vector of trim unknowns is now partitioned only into a rigid body part $\mathbf{x}_B$ and a main rotor part $\mathbf{x}_R$ as follows:

$$\mathbf{x} = \left\{ \begin{array}{c} \mathbf{x}_B \\ \mathbf{x}_R \end{array} \right\} \tag{3.42}$$

Therefore, the vector $\mathbf{x}$ of unknowns of the modified trim procedure with the free wake model is smaller than the corresponding vector for the baseline trim, and is given by:

$$\begin{aligned} \mathbf{x}_{trim} \;\; = \;\; & [\theta_0 \; \theta_{1c} \; \theta_{1s} \; \theta_{0t} \; \alpha_F \; \beta_F \; \theta_F \; \phi_F \; \lambda_t \; q_0^1 \; q_{1c}^1 \; q_{1s}^1 \; q_{2c}^1 \; q_{2s}^1 \ldots q_{N_{\rm h}c}^1 \; q_{N_{\rm h}s}^1 \ldots \\ & \ldots q_0^{N_{\rm m}} \; q_{1c}^{N_{\rm m}} \; q_{1s}^{N_{\rm m}} \; q_{2c}^{N_{\rm m}} \; q_{2s}^{N_{\rm m}} \ldots q_{N_{\rm h}c}^{N_{\rm m}} \; q_{N_{\rm h}s}^{N_{\rm m}}]^\top \end{aligned} \tag{3.43}$$

When the inflow is calculated using the free wake, the trim equations associated with the dynamic inflow model are omitted. Therefore, with reference to Eqn. (3.13), the system of trim equations reduces to:

$$\mathbf{F} = \left\{ \begin{array}{c} \mathbf{F}_B \\ \mathbf{F}_R \end{array} \right\} \tag{3.44}$$

that is, the trim equations are now:

- 3 force equilibrium equations, Eqs. (3.14)-(3.16)
- 3 moment equilibrium equations, Eqs. (3.17)-(3.19)

- 1 equation for turn coordination, Eqn. (3.20), or, for straight flight at $\mu \leq 0.1$, zero average sideslip, Eqn. (3.21)
- 1 kinematic relation for the flight path angle, Eqn. (3.23)
- 1 tail rotor inflow equation, Eqn. (3.24)
- $(1 + 2N_{\mathrm{h}})N_{\mathrm{m}}$ equations for periodic blade motion, Eqs. (3.36)

for a total of $9 + (1 + 2N_{\mathrm{h}})N_{\mathrm{m}}$ equations.

3.2.2 Calculation of Main Rotor Inflow

Figure 3.3 shows schematically how the maneuvering free wake model is coupled to the remaining flight dynamics model. Specifically the figure shows that the flight dynamics model provides the maneuvering free wake model with:

1. the bound circulation distribution, $\Gamma_b(r, \psi)$
2. the equivalent rigid blade flapping angles, $\beta(\psi)$
3. the pitch and roll rates, (p_G, q_G)
4. the freestream velocity components, (V_{Gx}, V_{Gy}, V_{Gz})

In turn, the free wake model provides the main rotor inflow distribution $\lambda_z(r, \psi)$. Details of the treatment of each of these items will be presented below.

Bound circulation distribution

Within the free wake model, the bound circulation is required for two different types of calculations, namely: (i) to initialize the strengths of the tip vortices released from the blade tips, and (ii) to calculate the wake vortex propagation due to the bound circulation distribution.

The value of the bound circulation is calculated in the flight dynamics model at a given blade station r and azimuth angle ψ using the following equation:

$$\Gamma_b(r,\psi) = \frac{1}{2}\, L(r,\psi)\, V(r,\psi)\, c(r) \tag{3.45}$$

where r is the spanwise coordinate, ψ is the azimuth angle, L is the non-dimensional total lift from the quasi-steady aerodynamic model (Eqn. (2.73)), V is the local velocity at the blade section (Eqn. (2.52)), and c is the local blade chord.

The radial stations used in the flight dynamics model are those necessary to calculate the generalized aerodynamic loads for the finite element representation of the blade. The calculation is performed using an 8-point Gauss quadrature formula over each finite element. Therefore, if N_E finite elements are used to model the blade, the quantities required to calculate the bound circulation will be available at $8N_E$ non-equidistant radial stations.

The azimuth angles used in the calculation of the trim solution are those required to calculate integrals such as those of Eqs. (3.36). The integration for one full rotor revolution is broken up into N_A equal sized azimuthal sections and an azimuthal integration is performed for each section. An 8-point Gauss quadrature integration technique is used for each of the azimuthal segments. Therefore, if N_A azimuthal sections are used in the integration over the rotor disk, the quantities required to calculate the bound circulation will be available at $8N_A$ non-equidistant azimuth angles.

The free wake model does not require the bound circulation at any specific number or distribution of spanwise coordinates. Therefore for simplicity the number and distribution of spanwise locations used in the free wake model are chosen to be the same as those used in the flight dynamics model, with a total of $8N_E$ non-equidistant radial stations.

The same is not true, however, for the azimuth angles, because the free wake model requires that the bound circulation be provided at a set of equally spaced azimuth angles. The number of equidistant azimuth angles used in the free wake model is given in Eqn. (2.323), and is dependent on the azimuthal discretization resolution $\Delta\psi$. Because the azimuthal locations where the bound circulation is required for the free wake model are different from those of the flight dynamics model, some form of interpolation is required. At each blade radial station a simple one-dimensional linear interpolation is used to obtain the bound circulation values at the free wake azimuthal points from the values at the flight dynamics azimuthal points.

Rigid blade flapping angles

Within the free wake model the precise flap displacements of the blade tips with respect to the hub plane are required, as these flap displacements define the initial release points of the vortex filaments. For this study the wake is modeled by a single vortex filament released from the tip of each blade.

As discussed in Section 2.2.5, the assumption is made within the free wake model that the blades are straight and are allowed to flap about a single flap hinge located at the axis of rotation. An "equivalent" flapping angle of the rigid blade is defined that is sufficient to locate the blade tip in the flap direction.

In the flight dynamics model, the tip flap displacement is given as a function of the azimuth angle and is

$$w_{tip}(\psi) = \sum_{k=1}^{N_{\mathrm{m}}} \phi^k(R) q^k_{app}(\psi) \tag{3.46}$$

where $w_{tip}(\psi)$ is the flap displacement of the blade tip in the undeformed preconed blade coordinate system, N_{m} is the number of normal modes used in the modal

coordinate transformation, ϕ^k is the displacement in the k-th normal mode and q^k_{app} is the modal coefficient for the k-th mode (Eqn. (3.25)).

The "equivalent" blade flapping angle (Eqn. (2.35)) includes the effects of blade precone and is given by:

$$\beta(\psi) = \frac{w_{tip}(\psi)}{R} + \beta_P \tag{3.47}$$

where β_P is the precone angle of the blade.

Equations (3.46) and (3.47) imply two minor assumptions, namely: (i) that the tip displacements due to lag and axial deformations are small enough to be neglected, and (ii) that the tip vortex is released from a point on the elastic axis at the blade tip.

The "equivalent" blade flap angles are calculated at the same non-equidistant azimuth angles as the bound circulation. Therefore, a linear interpolation is required to convert the flapping angles from the flight dynamics model non-equidistant azimuth angles to the free wake model equidistant azimuth angles.

Pitch and roll rates

The pitch and roll rates are required in the free wake model to provide the varying flow field velocities due to the maneuver. These pitch and roll rates produce a velocity profile that varies through the flow field, which in turn gives the free wake model the ability to capture the effects of maneuvers on the resulting wake geometry (Eqn. (2.327)). The free wake model requires the pitch and roll rates in the global fixed coordinate system (see Section 2.2.4) in which the free wake model equations are formulated.

The pitch and roll angular velocities about the body axes system are calculated from the turn rate $\dot{\psi}$ and the pitch θ_F and roll ϕ_F Euler angles using Eqs. (3.6) and (3.7). These angular rates are then converted from the body fixed axes system

to the global, fixed axes system using the coordinate transformation T_{GB}, according to Eqn. (2.32). This gives the pitch q_G and roll p_G rates in the global, fixed coordinate system. The result of the transformation of the rates is:

$$p_G = -p_B \tag{3.48}$$

$$q_G = q_B \tag{3.49}$$

Freestream velocity components

The values of the freestream velocity components in the global, fixed coordinate system are required by the free wake model to define the uniform velocity field around the rotor and wake. This uniform flow field comes from the translational velocities at the center of mass of the aircraft.

The translational velocities of the aircraft in the body axes system are calculated for the flight speed V and the angles of attack α_F and sideslip β_F using Eqs. (3.3)-(3.5). These body velocity components are transformed to translational velocity components in the global, fixed coordinate system using the transformation T_{GB}, according to Eqn. (2.32). Since the velocity components of the freestream as experienced by the body are required, the negative of the translational velocities is taken, as follows:

$$\left\{ \begin{array}{c} V_{Gx} \\ V_{Gy} \\ V_{Gz} \end{array} \right\} = \left\{ \begin{array}{c} -u_G \\ -v_G \\ -w_G \end{array} \right\} = \left\{ \begin{array}{c} u_B \\ -v_B \\ w_B \end{array} \right\} \tag{3.50}$$

where V_{Gx}, V_{Gz} and V_{Gz} are the freestream velocity components that are passed to the free wake model.

Inflow distribution from free wake

Once a converged solution for the free wake geometry is obtained, the inflow distribution is calculated using the modified Biot-Savart law (Eqn. (2.331)) which includes

the effects of the viscous vortex core and vortex diffusion. These calculations are made in the global, fixed coordinate system which results in the x, y and z-induced velocity components at each of the blade radial stations and azimuth angles used in the free wake model [50].

The inflow is required in the flight dynamics model in the blade preconed coordinate system (Eqn. (2.55)), so the free wake induced velocity components must be transformed to this frame. This involves rotations by the shaft tilt i_θ, azimuth angle ψ and blade precone angle β_P, with the resulting transformation being T_{PG}, Eqn. (2.29). Even though the x, y and z components of the inflow are available from the free wake model, only the z component is used in the current study.

A one-dimensional linear interpolation is used to convert the values of the inflow from the equidistant azimuthal locations used in the free wake model to the non-equidistant azimuthal locations used in the flight dynamics model. As with the bound circulation, no interpolation is required in the radial direction, as the radial stations used in the free wake model are the same as those of the flight dynamics model.

Once the linear interpolation of the inflow has been performed, the z-component of the inflow is inserted into Eqn. (2.55), which represents the total velocity of the blade section.

3.2.3 Solution of Trim Equations with Free Wake Model

The basic aspects of the solution of the trim equations with the free wake model are the same as those of the baseline case, in the sense that the trim procedure still consists of the solution of a coupled set of nonlinear algebraic equations. However, the procedure differs in some important details.

Figure 3.4 shows a schematic of the modified trim procedure with the free wake

model providing the main rotor inflow. Mathematically, the problem can still be written in the form of Eqn. (3.41). As with the baseline case, the trim procedure is started by supplying an initial guess of the trim state to the algebraic equations solver HYBRD. The equation solver iterates to reduce the vector of residuals **r** (Eqn. (3.41)) below a certain tolerance, at which point the trim solution is reached.

When the free wake model is included, the trim process takes the form of a triple nested loop (shown in Figure 3.4). The outermost loop is associated with the basic solution of the trim equations and is called the *trim loop*. The two inner loops are the *circulation loop* and the *wake geometry loop* and these are associated with the free wake solution. These three nested loops are now described in turn.

Trim Loop

The outermost loop is called the *trim loop* and consists of the solution of Eqn. (3.41). This is the same as in the baseline case except that the inflow equations and the corresponding inflow unknowns have been removed. At every iteration, the algebraic equation solver provides a tentative value of the trim vector **x**. All the subsequent calculations are performed with this value of **x**, and therefore with given values of pitch settings, fuselage velocities, attitudes and rates, and harmonics of blade motion, regardless of whether or not these values correspond to an actual trim condition. This trim vector **x** is then passed to the inner loops. The output from these inner loops is the free wake inflow distribution that corresponds to the trim vector **x** and this is used to evaluate the trim equations to get a set of equation residuals **r**. The trim loop is terminated when the norm of the residual vector **r** in Eqn. (3.41) becomes smaller than a preassigned tolerance; at that point the trim solution has been found.

Circulation Loop

The second loop involves an iteration on the bound circulation and inflow distributions and is called the *circulation loop*. This loop is shown in Figure 3.4 and is started by assuming an initial inflow distribution. This initial inflow is taken to be the final inflow distribution from the previous evaluation of the circulation loop, if such an inflow distribution is available. The very first time that the circulation loop is evaluated, the initial inflow is chosen to be uniform at a value of 0.05. This initial inflow is, in fact, arbitrary and does not affect the final inflow at the conclusion of the circulation loop, but does affect the number of iterations required for convergence, and thus the computational time. So, for maximum computational efficiency, the initial inflow should be chosen to be as close as possible to the converged inflow. For this reason the inflow distribution resulting from the previous evaluation of the circulation loop is used to start the current evaluation.

The inflow distribution is used to evaluate the main rotor aerodynamic loads, including the bound circulation distribution (Eqs. (2.54) and (3.45)). This bound circulation, along with the rigid blade flap angles, the body pitch and roll rates and the freestream velocity components, are passed to the free wake model. It should be pointed out that of all the inputs to the free wake model, Figure 3.3, the bound circulation is the only one that is dependent on the inflow distribution and thus is the only free wake input which varies during the circulation loop. The other inputs, namely the blade motion, body rates and aircraft velocities are given directly from the tentative trim vector $\mathbf{x}$.

The free wake model iterates on the wake geometry and returns a new inflow distribution generated by the innermost loop. This new inflow is used to re-evaluate the aerodynamic loads, bound circulation and wake geometry to continue the circula-

tion loop. The circulation loop is terminated when the inflow distribution converges, that is when the L_2 norm of the difference between the current inflow distribution and that of the previous iteration falls below a preassigned tolerance. The L_2 norm of the inflow change is given by:

$$\|\Delta\lambda\|_2^n = \frac{1}{8N_A 8N_E}\sqrt{\sum_{\psi:j=1}^{8N_A}\sum_{r:k=1}^{8N_E}\left(\lambda_{j,k}^n - \lambda_{j,k}^{n-1}\right)^2} \tag{3.51}$$

where $8N_A$ and $8N_E$ are the number of azimuth angles and blade radial stations respectively where the inflow values are available. When the value of the L_2 norm falls below a certain tolerance, then the loop has converged. The final free wake inflow distribution is returned to the trim loop for the evaluation of the trim equations.

Wake Geometry Loop

The third and innermost loop is called the *wake geometry loop*, and adjusts the geometry of the vortex wake to make it consistent with the free wake inputs. As illustrated in Figure 3.4 this loop is entirely contained within the free wake model and consequently all of the inputs to the free wake model, including the bound circulation, are held fixed within this loop.

The initial wake geometry used to start the loop is taken as the final wake geometry from the previous time the loop was evaluated. For the very first iteration of the wake geometry loop in the calculation of a trim solution, the vortex wake is taken to have an undistorted helical structure. A better strategy is to used the final wake geometry from a previous trim case at a similar speed, if such a wake geometry is available.

The convergence criterion for this loop has been slightly modified, compared with that of Ref. [74] and mentioned in Section 2.9. The free wake model originally used an undistorted helical wake as its starting point and used the change in wake

geometry over the first iteration as the basis for convergence. Thus the wake was considered converged when the ratio of the wake geometry change for the current iteration to that of the first iteration fell below a certain tolerance (Eqn. (2.333)). This is not appropriate for the current application as it would be computationally very expensive to start the wake geometry loop with an undistorted helical wake each time.

The convergence criterion which is currently used is based on the absolute value of the change in wake geometry for the current iteration. This is more appropriate than the previous convergence criteria since the starting wake geometry is different each time the loop is evaluated and may already represent a converged wake solution. The root mean square (RMS) change in the wake geometry between successive wake geometry iterations, as calculated in the free wake model, is given by Eqn. (2.332):

$$(RMS)_n = \frac{1}{j_{max} k_{max}} \sqrt{\sum_{\psi:j=1}^{j_{max}} \sum_{\zeta:k=1}^{k_{max}} (\vec{r}_{j,k}^{\,n} - \vec{r}_{j,k}^{\,n-1})^2} \tag{3.52}$$

where j_{max} is the number of blade azimuthal steps in one rotor revolution and k_{max} is the number of collocation points used to describe each of the trailed vortex filaments.

The loop is considered converged when the value of $(RMS)_n$ falls below a pre-assigned tolerance. Finally the inflow distribution is calculated with the converged wake geometry and returned to the circulation loop.

3.3 State vector corresponding to the trim solution

Once the trim solution has been determined using the non-linear equation solver, the vectors of states and controls can be calculated. Both of these vectors are calculated using a combination of the trim solution $\mathbf{x}$ and the flight condition from which the trim was defined. The vectors of states and controls are required as the

starting point for the calculation of time histories by direct numerical integration of the equations of motion and for the extraction of the linearized models.

Since the equations of motion are formulated in the rotating frame of reference, the state vector is also required in the rotating frame. The calculation of the state vector in the rotating frame is thus defined with respect to a reference azimuth angle, ψ_{REF}. This angle is taken to be the azimuthal location of a reference blade and is termed the reference azimuth angle. The locations of all other blades can be determined from this reference azimuth angle.

For the baseline case when the free wake model is not included, the state vector includes information about the inflow distribution over the main rotor disk, as well as about the blade and body motions. The state vector in the rotating frame can be partitioned into a rigid body part, an inflow part and a main rotor part, as follows:

$$\mathbf{y} = \left\{ \begin{array}{c} \mathbf{y}_B \\ \mathbf{y}_I \\ \mathbf{y}_R \end{array} \right\} \tag{3.53}$$

The rigid body part of the state vector $\mathbf{y}_B$ contains the state variables associated with the motion of the rigid body of the aircraft and are not dependent on the reference azimuth angle at which the state vector is defined. As with the rigid body portion of the trim vector, the tail rotor inflow is included in the rigid body portion of the state vector for convenience. This rigid body part takes the form:

$$\mathbf{y}_B = [u\ v\ w\ p\ q\ r\ \phi_F\ \theta_F\ \psi_F\ \lambda_t]^\top \tag{3.54}$$

These components are determined from the rigid body part of the trim vector, $\mathbf{x}_R$ and the flight condition from which the trim solution was calculated, namely the velocity, V, the flight path angle, γ, and the turn rate, $\dot{\psi}$. The velocity components along the body axes are obtained from

$$u \;=\; V \cos\alpha_F \cos\beta_F \tag{3.55}$$

$$v = V \sin \beta_F \tag{3.56}$$

$$w = V \sin \alpha_F \cos \beta_F \tag{3.57}$$

the angular velocities p, q, and r about the body axes can be obtained

$$p = -\dot{\psi} \sin \theta_F \tag{3.58}$$

$$q = \dot{\psi} \sin \phi_F \cos \theta_F \tag{3.59}$$

$$r = \dot{\psi} \cos \phi_F \cos \theta_F \tag{3.60}$$

The pitch and roll Euler angles of the fuselage in the state vector, θ_F, ϕ_F, are the same as those in the trim vector and are directly available. As for the Euler yaw angle, ψ_F, the value is arbitrary since it is defined with respect to the inertial coordinate system; in the present study it is taken to be zero. The value of the tail rotor inflow, λ_t, in the state vector is the same as that in the trim vector.

The main rotor portion of the state vector $\mathbf{y}_R$ contains modal coefficients for the individual main rotor blades and their time derivatives; these are dependent on the azimuth angle. For a four-bladed rotor, the main rotor portion of the state vector takes the form:

$$\begin{aligned} \mathbf{y}(\psi_i)_R = [&q_1^1 \; q_2^1 \; q_3^1 \; q_4^1 \; \dot{q}_1^1 \; \dot{q}_2^1 \; \dot{q}_3^1 \; \dot{q}_4^1 \\ &\ldots q_1^{N_\mathrm{m}} \; q_2^{N_\mathrm{m}} \; q_3^{N_\mathrm{m}} \; q_4^{N_\mathrm{m}} \; \dot{q}_1^{N_\mathrm{m}} \; \dot{q}_2^{N_\mathrm{m}} \; \dot{q}_3^{N_\mathrm{m}} \; \dot{q}_4^{N_\mathrm{m}}]^\top \end{aligned} \tag{3.61}$$

in which q_i^k and $\dot{q}_i^k$ are the generalized displacement and velocity coefficients of the i-th blade for the k-th normal mode in the rotating frame at azimuth angle, ψ_i.

These states are reconstructed from the Fourier series expansions at trim, that is:

$$q_i^k = q_0^k + \sum_{j=1}^{N_\mathrm{h}} (q_{jc}^k \cos j\psi_i + q_{js}^k \sin j\psi_i) \quad k = 1, 2, \ldots, N_m \tag{3.62}$$

$$\dot{q}_i^k = \Omega \sum_{j=1}^{N_\mathrm{h}} (-q_{jc}^k \sin j\psi_i + q_{js}^k \cos j\psi_i) \quad k = 1, 2, \ldots, N_m \tag{3.63}$$

where the superscript k refers to the k-th mode in the modal coordinate transformation and the subscript i is the blade number. It should be mentioned that the q_i and $\dot{q}_i$ quantities referring to the displacement and velocity modal quantities of the i-th blade, and shown in the left hand side of Eqs. (3.62) and (3.63), are a function of the azimuth angle of the blade, whereas the q_0, q_{jc} and q_{js} quantities referring to the Fourier series coefficients of the expansion of the generalized modal coordinates, and shown in the right hand side of Eqs. (3.62) and (3.63), are constant for a given trim solution and are not a function of azimuth angle.

The calculation of the blade states depends on the azimuth angle of the blade under consideration. The azimuth angle of the current blade, the i-th blade, is calculated with respect to the reference azimuth angle using:

$$\psi_i = \psi_{REF} + \frac{2\pi(i-1)}{N_\mathrm{b}} \tag{3.64}$$

where the reference blade is blade number 1 and the other blades are numbered 2, 3 and 4 in the counter clockwise direction. N_b is the number of main rotor blades.

The inflow part of the state vector $\mathbf{y}_I$ contains the inflow coefficients for the dynamic inflow model, which are not a function of the azimuth angle at which the state vector is defined. Further the inflow coefficients in the state vector are the same in number and distribution as those in the inflow portion of the trim vector $\mathbf{x}_I$ (Eqn. (3.11)). So the inflow portion of the state vector is as follows:

$$\mathbf{y}_I = \mathbf{x}_I = \left\{ \begin{array}{c} \lambda_0 \\ \lambda_s \\ \lambda_c \end{array} \right\} \tag{3.65}$$

For the modified flight dynamics model, the free wake is used to provide the vortex wake geometry and main rotor inflow. The state vector no longer contains the inflow part and is made up of only a rigid body part and a main rotor part, as

follows:

$$\mathbf{y} = \left\{ \begin{array}{c} \mathbf{y}_B \\ \mathbf{y}_R \end{array} \right\} \tag{3.66}$$

The rigid body and main rotor parts of this state vector are the same as those for the baseline case with the dynamic inflow model. Thus the state vector for the modified flight dynamics model is smaller than for the baseline case since it does not include any inflow coefficients.

The vector of controls is the same for the baseline case and the case with the free wake model and is as follows:

$$\mathbf{u} = [\theta_0 \; \theta_{1c} \; \theta_{1s} \; \theta_t \; \dot{\theta}_0 \; \dot{\theta}_{1c} \; \dot{\theta}_{1s}]^\top \tag{3.67}$$

The main and tail rotor controls in the control vector are the same as those in the rigid body portion of the trim vector. The derivatives of the controls in the control vector are taken to be zero for trim since the controls themselves are fixed for trim.

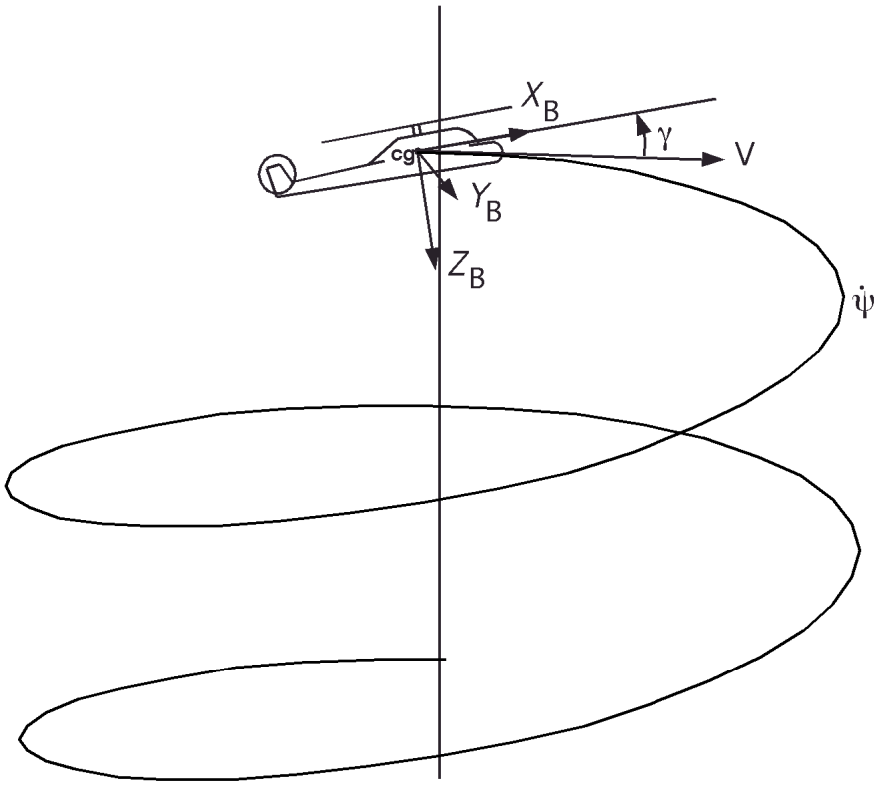

Figure 3.1: Geometry of a helicopter in a steady coordinated turn.

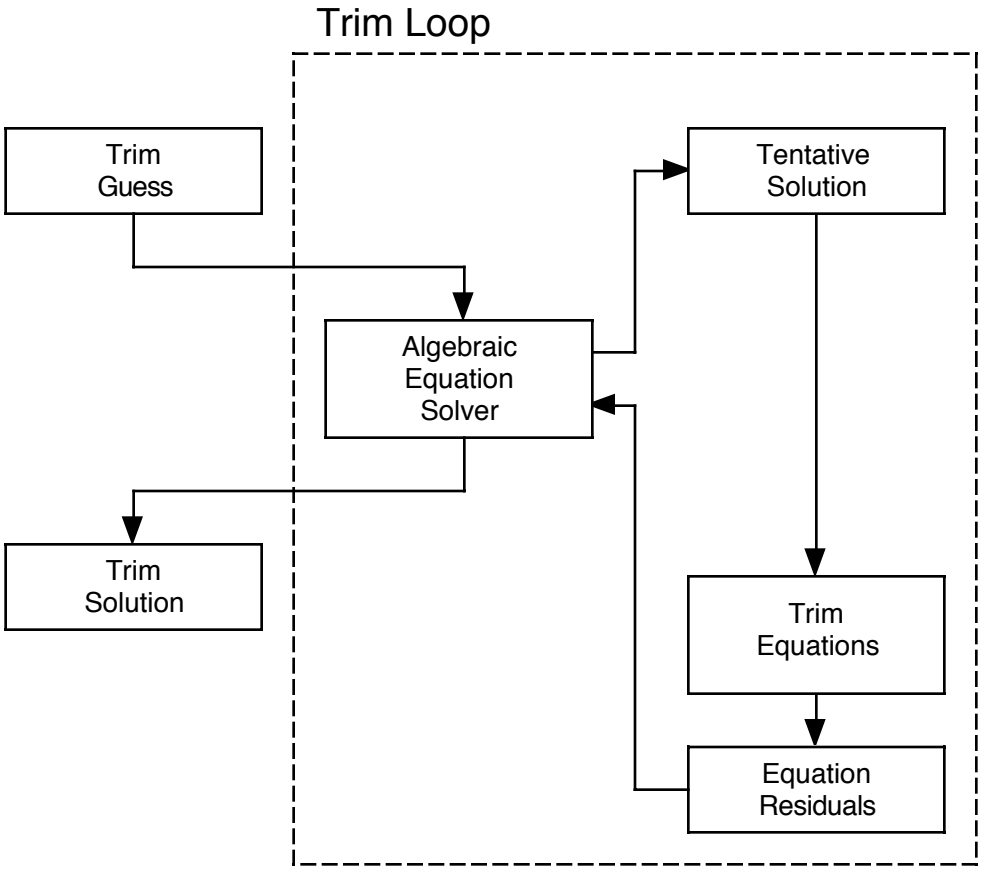

Figure 3.2: Schematic of the baseline trim procedure with the dynamic inflow model included.

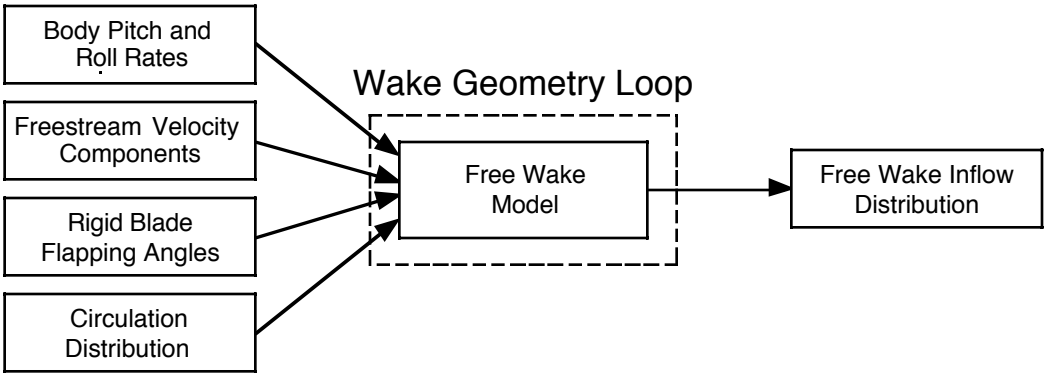

Figure 3.3: Inputs and outputs of the free wake model.

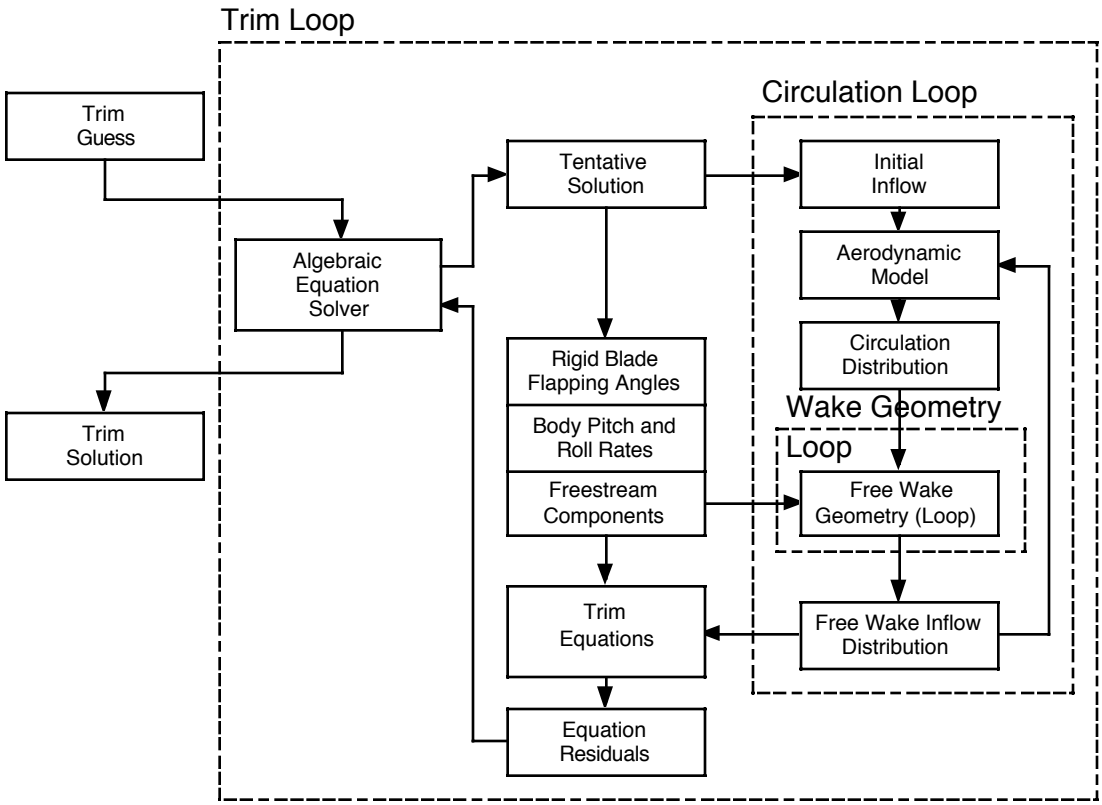

Figure 3.4: Schematic of the trim procedure with the free wake model used to provide the main rotor inflow.

Chapter 4

Solution Methods: Linearization of the Equations of Motion

This chapter presents the methods used to extract a linearized model of the coupled rotor-fuselage system. The linear model describes the small perturbation motion about a given equilibrium position. Although the procedure is valid for a linearization about an arbitrary flight condition, only trimmed equilibrium conditions are used in this study.

When the free wake model is not included, the state vector consists of velocities, attitudes and angular rates of the helicopter, generalized coordinates that describe rotor dynamics, and main rotor and tail rotor inflow states. When the free wake model is included, the main rotor inflow states are dropped. Therefore, inflow and wake dynamics are neglected.

This chapter is divided into two main parts. The first describes the baseline linearization procedure for the case in which a free wake model is not included. The second describes in detail the changes in the formulation and solution methods required by the incorporation of the free wake model into the linearization procedure.

4.1 Linearization of baseline equations of motion

The linearized model is based on a first-order Taylor series expansion of the non-linear system $\mathbf{f}$ of differential equations about a trimmed equilibrium position. The equilibrium position is defined by appropriate values of the state vector $\mathbf{y}_{trim}$ and of the control vector $\mathbf{u}_{trim}$. Because of the inclusion of rotor dynamics, the state vector $\mathbf{y}_{trim}$ in the rotating frame has time-varying coefficients, even in steady, straight flight. This is also true in hover as there is some time variation due to the small amounts of longitudinal and lateral cyclic pitch necessary to maintain trim. The state and control vectors are obtained from the trim solution as described in Section 3.3. The state vector is in the rotating frame and is thus defined with respect to an azimuth angle ψ_k.

The Taylor series expansion of the non-linear equations $\mathbf{f}$ about a trim condition is

$$\Delta\dot{\mathbf{y}} = \left[\frac{\partial \mathbf{f}}{\partial \mathbf{y}}\right]_{\mathbf{y}=\mathbf{y}_{trim}} \Delta\mathbf{y} + \left[\frac{\partial \mathbf{f}}{\partial \mathbf{u}}\right]_{\mathbf{u}=\mathbf{u}_{trim}} \Delta\mathbf{u} + O\left(\|\Delta\mathbf{y}\|^2, \|\Delta\mathbf{u}\|^2\right) \tag{4.1}$$

where the perturbation state and control vectors are defined as follows:

$$\Delta\dot{\mathbf{y}} = \dot{\mathbf{y}} - \dot{\mathbf{y}}_{trim} \tag{4.2}$$

$$\Delta\mathbf{y} = \mathbf{y} - \mathbf{y}_{trim} \tag{4.3}$$

$$\Delta\mathbf{u} = \mathbf{u} - \mathbf{u}_{trim} \tag{4.4}$$

The perturbation matrices in Equation (4.1) are obtained using finite difference approximations:

$$\left[\frac{\partial \mathbf{f}}{\partial \mathbf{y}}\right]_{\mathbf{y}=\mathbf{y}_{trim}} \approx \left[\frac{\Delta \mathbf{f}}{\Delta \mathbf{y}}\right]_{\mathbf{y}=\mathbf{y}_{trim}} = \mathbf{A} \tag{4.5}$$

$$\left[\frac{\partial \mathbf{f}}{\partial \mathbf{u}}\right]_{\mathbf{u}=\mathbf{u}_{trim}} \approx \left[\frac{\Delta \mathbf{f}}{\Delta \mathbf{u}}\right]_{\mathbf{u}=\mathbf{u}_{trim}} = \mathbf{B} \tag{4.6}$$

Therefore the linearized model in the rotating frame has the form:

$$\Delta\dot{\mathbf{y}} = \mathbf{A}\Delta\mathbf{y} + \mathbf{B}\Delta\mathbf{u} \tag{4.7}$$

The state matrix $\mathbf{A}$ and the control matrix $\mathbf{B}$ are calculated using central difference approximations. The generic element a_{ij} of the matrix $\mathbf{A}$ at azimuth ψ_k is given by:

$$a_{ij}(\psi_k) = \frac{f_i(\mathbf{y}_{trim}(\psi_k) + \delta\mathbf{y}_j, \mathbf{u}_{trim}, \psi_k) - f_i(\mathbf{y}_{trim}(\psi_k) - \delta\mathbf{y}_j, \mathbf{u}_{trim}, \psi_k)}{2\delta y_j} \tag{4.8}$$

where $\delta\mathbf{y}_j$ is a vector that contains all zeros, except for the j-th element which contains the value of a small perturbation δy_j. Similarly, the generic element b_{ij} of the control matrix $\mathbf{B}$ at azimuth ψ_k is given by:

$$b_{ij}(\psi_k) = \frac{f_i(\mathbf{y}_{trim}(\psi_k), \mathbf{u}_{trim} + \delta\mathbf{u}_j, \psi_k) - f_i(\mathbf{y}_{trim}(\psi_k), \mathbf{u}_{trim} - \delta\mathbf{u}_j, \psi_k)}{2\delta u_j} \tag{4.9}$$

where $\delta\mathbf{u}_j$ is a vector that contains all zeros, except for the j-th element which contains the value of the small perturbation δu_j.

It should be noted that the rotor equations of motion (Eqn. (3.12)) are formulated in a rotating frame, namely the hub fixed, rotating coordinate system. Thus, the rotor portions of the vectors $\mathbf{y}$ and $\dot{\mathbf{y}}$, of their perturbations $\Delta\mathbf{y}$ and $\Delta\dot{\mathbf{y}}$, and of the state and control matrices $\mathbf{A}$ and $\mathbf{B}$ are also defined in a rotating frame at a specific azimuth angle ψ_k.

The rotor portions of the state vector and of the linearized matrices are transformed to the body fixed non-rotating frame, resulting in a linearized system that is written entirely in a non-rotating system. This system can be indicated with the following notation:

$$\Delta\dot{\mathbf{y}}_{NR} = \mathbf{A}_{NR}\Delta\mathbf{y}_{NR} + \mathbf{B}_{NR}\Delta\mathbf{u} \tag{4.10}$$

where the state $\mathbf{A}_{NR}$ and control $\mathbf{B}_{NR}$ matrices in the non-rotating frame are calculated using the multiblade coordinate transformation according to Eqs. A.10 and A.11 for azimuth angle ψ_k.

The control vector is already defined in a fixed system and needs no further transformation. The state vector in the non-rotating frame $\mathbf{y}_{NR}$ is defined for a four-bladed rotor as:

$$\begin{aligned}\mathbf{y}_{NR}(\psi) &= [u\ v\ w\ p\ q\ r\ \phi_F\ \theta_F\ \psi_F\ \lambda_0\ \lambda_s\ \lambda_c\ \lambda_t\ q_0^1\ q_{1c}^1\ q_{1s}^1\ q_2^1\ \dot{q}_0^1\ \dot{q}_{1c}^1\ \dot{q}_{1s}^1\ \dot{q}_2^1 \\ &\quad \ldots q_0^{N\mathrm{m}}\ q_{1c}^{N\mathrm{m}}\ q_{1s}^{N\mathrm{m}}\ q_2^{N\mathrm{m}}\ \dot{q}_0^{N\mathrm{m}}\ \dot{q}_{1c}^{N\mathrm{m}}\ \dot{q}_{1s}^{N\mathrm{m}}\ \dot{q}_2^{N\mathrm{m}}]^\top \end{aligned} \quad (4.11)$$

where $q_0^k, q_{1c}^k, q_{1s}^k$, and q_2^k are respectively the collective, longitudinal, lateral, and differential portion of the generalized coordinate of the k-th rotor mode. It is also:

$$\Delta\mathbf{y}_{NR} = \mathbf{y}_{NR} - \mathbf{y}_{NR_{trim}} \quad (4.12)$$

$$\Delta\dot{\mathbf{y}}_{NR} = \dot{\mathbf{y}}_{NR} - \dot{\mathbf{y}}_{NR_{trim}} \quad (4.13)$$

In transforming the linearized model from the rotating frame to the non-rotating frame, the multiblade coordinate transformation reduces the time dependency but does not completely remove it. For this reason, the matrices $\mathbf{A}_{NR}$ and $\mathbf{B}_{NR}$ are calculated over one rotor revolution, at a number of equidistant azimuth angles, and then averaged to obtain a linear, time-invariant system.

The choice of azimuth angles, ψ_k, depends on the helicopter configuration. For the case with four dissimilar blades, averaging over a full rotor revolution is required for the calculation of the linearized model. However, for the case with four identical blades considered in this study, the linearization need only be carried out over one quadrant. Therefore, the azimuth angles are chosen as,

$$\psi_k = \frac{k\pi}{2N} \quad (4.14)$$

where N is the total number of linearized models calculated in the rotating frame.

This final linearized system is represented by the matrices $\mathbf{A}_{avg}$ and $\mathbf{B}_{avg}$ as follows:

$$\Delta\dot{\mathbf{y}}_{NR} = \mathbf{A}_{avg}\Delta\mathbf{y}_{NR} + \mathbf{B}_{avg}\Delta\mathbf{u} \tag{4.15}$$

The procedure for the calculation of the state $\mathbf{A}_{avg}$ and control $\mathbf{B}_{avg}$ matrices, (Eqn. (4.15)) is shown schematically in Figure 4.1. The various steps of the procedure are listed below, to allow a comparison with the procedure used when the free wake is present:

1. The calculation of the linearized model is started from a trim vector $\mathbf{x}$ corresponding to the flight condition about which the linearization is desired. This trim vector need not represent an actual trim solution; however, for all of the results in the present study trimmed flight conditions are used. So the trim vector used for a given flight condition is that resulting from the baseline trim procedure described in Section 3.1.

2. For the current azimuth angle ψ_k in the azimuthal loop, the state $\mathbf{y}(\psi_k)$ and control $\mathbf{u}$ vectors are obtained from the trim vector $\mathbf{x}$ as described in Section 3.3. The reference azimuth angle ψ_{REF} used in the calculation of the state vector is taken to be ψ_k, representing the azimuthal location of Blade 1.

3. Calculate the state matrix $\mathbf{A}(\psi_k)$ in the rotating frame using finite difference approximations as shown in Eqn. (4.8). This involves a loop where each element of the state vector in the rotating frame is positively and negatively perturbed to build the state matrix column by column as the loop progresses. The state matrix is entirely defined after the positive and negative perturbations of all of the state variables are made.

4. Convert the perturbation matrix $\mathbf{A}(\psi_k)$ to the fixed frame using a multiblade coordinate transformation (Eqn. (A.10)) to obtain $\mathbf{A}_{NR}(\psi_k)$.

5. Calculate the control matrix $\mathbf{B}(\psi_k)$ in the rotating frame using finite difference approximations as shown in Eqn. (4.9). This involves a loop where each element of the control vector is positively and negatively perturbed to build the control matrix column by column as the loop progresses. The control matrix is entirely defined after the positive and negative perturbations of all of the control variables are made.

6. Convert the perturbation matrix $\mathbf{B}(\psi_k)$ to the fixed frame using a multiblade coordinate transformation (Eqn. (A.11)) to obtain $\mathbf{B}_{NR}(\psi_k)$.

7. Repeat Steps 2 through 6 for each azimuth angle ψ_k. The result is a set of state and control matrices in the non-rotating frame, one at each of the azimuth angles used.

8. The state perturbation matrices $\mathbf{A}_{NR}(\psi_k)$ in the non-rotating frame are averaged element by element to obtain the final linearized state matrix, $\mathbf{A}_{avg}$, for the desired flight condition. The control perturbation matrices $\mathbf{B}_{NR}(\psi_k)$ are also averaged element by element to obtain the final linearized control matrix, $\mathbf{A}_{avg}$, for the same flight condition.

It should be noted that this linearization procedure is slightly different from that presented earlier in Refs. [5, 33]. The difference is in the way that the state vector is calculated at each azimuth angle used in the averaging of the state and control matrices. Previously, the linearization procedure started from the state vector in the rotating frame at a reference azimuth angle of zero, and the state vector was updated at each successive azimuth angle by integrating the equations of motion

in time to the new reference azimuth angle. There are two reasons why this was changed in favor of calculating the state vector at each azimuth angle directly from the trim vector. The first is that the ODE solver used in the time integration here cannot easily be adapted during the linearization when the free wake model is used to provide the main rotor inflow. Second, as the time integration is performed, the state vector no longer strictly represents a trimmed condition, since the equations of motion may be unstable in certain flight conditions. This is not an issue when a true trim condition is used to start the linearization procedure since the deviation from trim after integrating for one rotor revolution will be negligible. However if we were analyzing a flight condition that did not represent trim, then the change in the state vector after integrating for one rotor revolution may significantly change the results.

4.2 Linearization of equations of motion with free wake model

The maneuvering free wake model used in this study is a quasi-steady model that is rigorously valid only in steady, i.e., trimmed, flight conditions. In fact, it is based on the assumption that the blade motion is periodic, and that the hub moves with constant linear and angular velocities. When the rotor or the hub motions are perturbed from the trimmed position, as is the case in the linearization process, the wake vortices do "move" to positions consistent with the new rotor or hub motion, but this apparent transient behavior is due to the relaxation algorithm, and therefore it is of a numerical, rather than a physical nature.

Because the wake is quasi-steady, it does not include inflow dynamics and does not add states to the linearized system. As a consequence, it does not add poles or zeros to the small perturbation dynamics as the dynamic inflow model does. It

does, however, modify the state and control matrices by modifying the aerodynamic loads. Furthermore, by changing trim, it changes the equilibrium position about which the governing equations are linearized. This causes an additional change in the state and control matrices because the equations are nonlinear.

With the free wake model used to supply the main rotor inflow, the circulation loop, described for trim, must be evaluated each time a state or control is perturbed. If the method used was the same as for the baseline case, where perturbations are made in the rotating frame, the total number of evaluations of the circulation loop would be $2(N_y + N_u)N$ if central differencing is used. The quantity N is the number of azimuthal locations, N_y is the number of states and N_u is the number of controls.

An alternative to the expense of making the perturbations in the rotating frame and evaluating the circulation loop each time is to make the perturbations in the fixed frame. In the fixed frame, each state and control variable is perturbed only once positively and once negatively in the calculation of the linearized model. Because the circulation loop is evaluated only when a variable is perturbed, the number of circulation loop evaluations required is reduced to $2(N_y + N_u)$ from $2(N_y + N_u)N$. Since the evaluation of the circulation loop is the most computationally expensive portion of the model, the total time to obtain the linearized model is essentially reduced by a factor of about N.

The circulation loop used in the calculation of the linearized model is essentially the same as that for trim, but with a couple of changes. For trim, the azimuth angles in the flight dynamics model are obtained using a Gaussian distribution since an azimuthal integration is used. For the linearization, there is no restriction on the azimuth angles or azimuthal spacing, so these are chosen to be the same as those used with the free wake model. Thus no interpolation is required to convert the bound circulation or rigid blade flapping angles from the flight dynamics model to

the free wake model or to convert the inflow from the free wake model to the flight dynamics model. This makes the inflow-circulation loop a little simpler, but does not decrease the computational time required for the loop.

The procedure for the calculation of the state matrix $\mathbf{A}_{avg}$ (Eqn. (4.15)) is shown schematically in Figure 4.2. The various steps of the procedure with the free wake model included are as follows:

1. Reconstruct from the trim vector $\mathbf{x}$ the state vector in the non-rotating frame $\mathbf{y}_{NR}$ and the control vector $\mathbf{u}$.

2. This is the start of the state variable loop where the state number is indicated by the variable j. Initially $j = 1$, indicating that the loop starts at the first state variable.

3. A positive perturbation is made to the j-th state. $\mathbf{y}_{NR}^{j+}$ indicates that the j-th state variable is perturbed in the positive direction with all other state variables remaining unchanged.

4. With the current state vector in the non-rotating frame $\mathbf{y}_{NR}^{j+}$, the wake geometry and corresponding inflow distribution is calculated using the circulation loop previously described. This gives the inflow distribution over the entire rotor disk corresponding to the positively perturbed state vector.

5. This is the azimuth angle loop, where each of the azimuth angles ψ_k at which the inflow is available are treated in-turn. At the k-th azimuth angle, the multiblade coordinate transformation is used to calculate the state vector in the rotating frame as follows:

$$\mathbf{y}_R^{j+}(\psi_k) = \mathbf{T}(\psi_k)\mathbf{y}_{NR}^{j+} \tag{4.16}$$

where the subscript R is added to clearly indicate that the vector, $\mathbf{y}_R^{j+}(\psi_k)$, is in the rotating frame, although the addition of this subscript is not strictly necessary. $\mathbf{T}(\psi_k)$ is the multiblade coordinate transformation matrix (A.5).

This perturbed state vector in the rotating frame $\mathbf{y}_R^{j+}(\psi_k)$ is used to evaluate the equation of motions using the inflow distribution corresponding to the perturbed state vector at azimuth angle ψ_k. This provides the time derivative of the state vector in the rotating frame, which is represented as follows:

$$\mathbf{f}_R^{j+}(\psi_k) = \mathbf{f}(\mathbf{y}_R^{j+}(\psi_k), \mathbf{u}; \psi_k) \tag{4.17}$$

This derivative vector is converted to the non-rotating frame by applying the multiblade coordinate transformation given in Eqn. A.14 as follows:

$$\mathbf{f}_{NR}^{j+}(\psi_k) = \mathbf{T}_{d1}\mathbf{f}_R^{j+}(\psi_k) + \mathbf{T}_{d2}\mathbf{y}_R^{j+}(\psi_k) \tag{4.18}$$

where $\mathbf{f}_{NR}^{j+}(\psi_k)$ is the derivative state vector in the non-rotating frame at the k-th azimuth angle for a positive perturbation in the j-th state variable. $\mathbf{T}_{d1}$ and $\mathbf{T}_{d2}$ are the multiblade coordinate transformation matrices given by Eqs. (A.15) and (A.16) respectively.

The result of this azimuth angle loop is a set of derivative state vectors corresponding to the positive perturbation of the j-th state variable, one at each azimuth angle ψ_k.

6. Apply a negative perturbation to the j-th state $\mathbf{y}_{NR}^{j-}$ in the non-rotating frame and calculate the inflow distribution using the circulation loop with the new state vector. This step is similar to Steps 3 and 4 combined, but with a negative perturbation of the j-th state instead of a positive perturbation. This step produces the inflow distribution over the rotor disk corresponding to the negatively perturbed state vector.

7. Loop through the azimuth angles ψ_k at which the inflow is available, computing the derivative vector in the non-rotating frame $\mathbf{f}_{NR}^{j-}(\psi_k)$ at each. The procedure is the same as that in Step 5 but with the negatively perturbed state vector.

   At each azimuth angle, the rotating frame state vector is calculated

$$\mathbf{y}_R^{j-}(\psi_k) = \mathbf{T}(\psi_k)\mathbf{y}_{NR}^{j-} \tag{4.19}$$

   and the equations of motion are evaluated to obtain the vector of derivatives

$$\mathbf{f}_R^{j-}(\psi_k) = \mathbf{f}(\mathbf{y}_R^{j-}(\psi_k), \mathbf{u}; \psi_k) \tag{4.20}$$

   and finally the derivative vector is calculated in the non-rotating frame using a coordinate transformation

$$\mathbf{f}_{NR}^{j-}(\psi_k) = \mathbf{T}_{d1}\mathbf{f}_R^{j-}(\psi_k) + \mathbf{T}_{d2}\mathbf{y}_R^{j-}(\psi_k) \tag{4.21}$$

   The result of this azimuth angle loop is a set of derivative state vectors corresponding to the negative perturbation of the j-th state variable, one at each of the azimuth angles ψ_k.

8. The j-th column of the average state vector in the non-rotating frame $\mathbf{A}_{avg}$ is calculated using the derivative vectors for the positive and negative perturbations. This column corresponds to the number of the state variable that is being perturbed. Considering the j-th state variable, the j-th column of the state matrix is given by:

$$\mathbf{A}_{avg}^{j} = \frac{1}{N}\sum_{k=1}^{N}\frac{\mathbf{f}_{NRk}^{+}(\psi_k) - \mathbf{f}_{NRk}^{-}(\psi_k)}{2\delta y_j} \tag{4.22}$$

   where $\mathbf{A}_{avg}^{j}$ represents the j-th column of the state perturbation matrix in the non-rotating frame.

9. The variable j is incremented and Steps 3 through 8 are repeated, each time producing one column of the state perturbation matrix $\mathbf{A}_{avg}^{j}$. This loop is continued until the entire state perturbation matrix $\mathbf{A}_{avg}$ has been constructed.

The control perturbation matrix is calculated in the same way as the state perturbation matrix except that the controls are perturbed instead of states in Steps 3 and 6. Also the control perturbation matrix in the non-rotating frame is build one column at a time in Step 8 as follows:

$$\mathbf{B}_{avg}^{j} = \frac{1}{N}\sum_{k=1}^{N}\frac{\mathbf{f}_{NRk}^{+}(\psi_k) - \mathbf{f}_{NRk}^{-}(\psi_k)}{2\delta u_j} \tag{4.23}$$

The results of this procedure is a linearized model that has the effects of the free wake model on the inflow distribution included implicitly. The linearized model has the form:

$$\Delta\dot{\mathbf{y}}_{NR} = \mathbf{A}_{avg}\Delta\mathbf{y}_{NR} + \mathbf{B}_{avg}\Delta\mathbf{u} \tag{4.24}$$

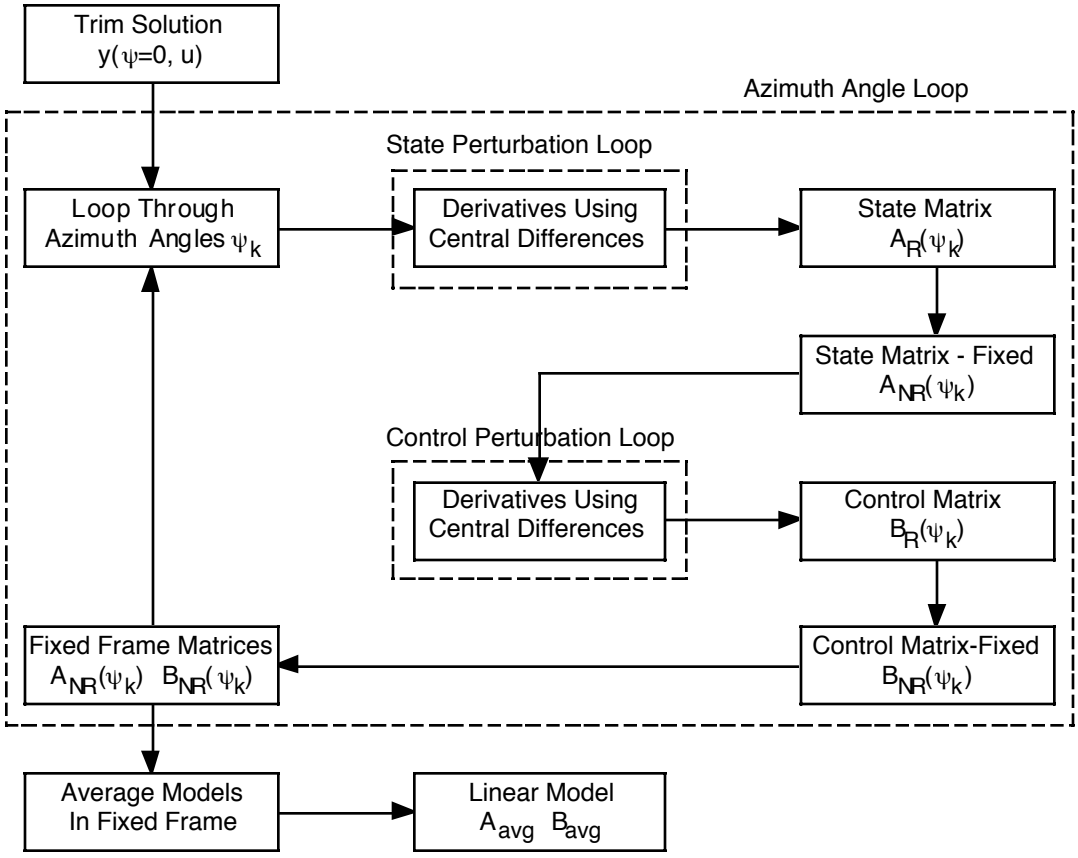

Figure 4.1: Schematic of the baseline linear model extraction procedure with the dynamic inflow model.

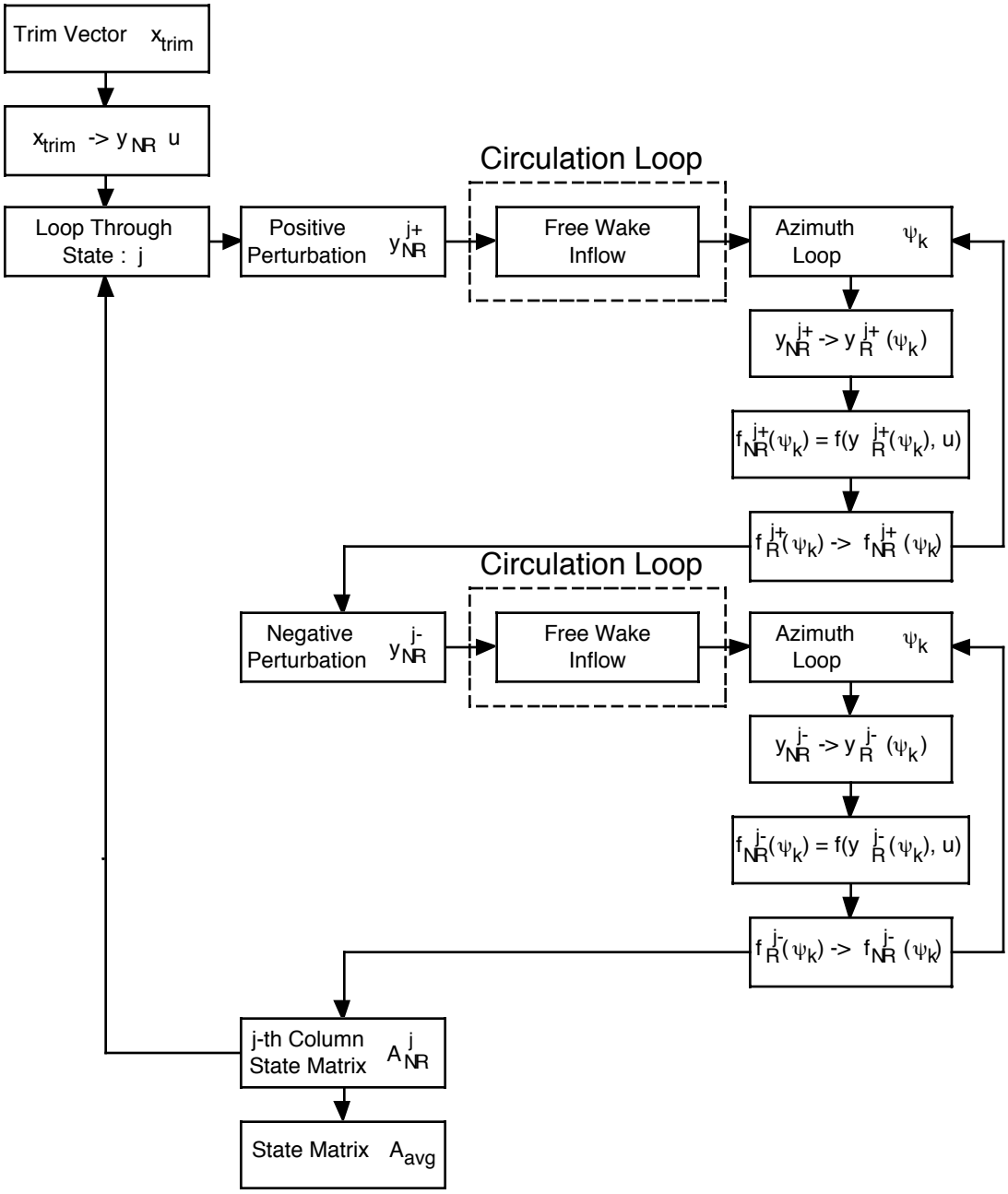

Figure 4.2: Schematic of linearization procedure with the free wake model used to provide the inflow distribution.

Chapter 5

Solution Methods: Time Integration

5.1 Time integration of baseline equations of motion

The time integration of the baseline equations of motion involves the calculation of the dynamic response results for a given set of initial conditions and controls that are applied during the integration. There are two methods by which the time histories are calculated. The first is to integrate the full set of non-linear equations with respect to time. The second is a simpler approach where the time history is calculated by performing the integration using the linearized equations of motion, which is calculated at the flight condition from which the time history is required; in this case the results are obviously only valid for small perturbation motion about a trimmed condition.

5.1.1 Integration of non-linear equations of motion

As the equations of motion are represented in first-order state space form,

$$\dot{\mathbf{y}} = \mathbf{f}(\mathbf{y}, \mathbf{u}; t) \tag{5.1}$$

an ordinary differential equation solver is used to integrate the non-linear equations numerically. A variable step, variable order Adams-Bashforth ordinary differential equation solver is used for this numerical integration. In this study, the system of equations is integrated from an initial condition corresponding to a trimmed helicopter state. This procedure is shown schematically in Figure 5.1. The simulation is started from the trim condition and the non-linear equations of motion are integrated with respect to time until the simulation is complete. This figure also shows that internally, the ordinary differential equation solver evaluates the equations of motion with a variable step size.

The integration is performed with respect to time and produces the time histories of all of the state variables for a prescribed set of control inputs. Typically the control inputs would include the time histories of one or more of the pilot or swashplate controls. In addition to prescribing the controls, the time histories of one or more of the state variables themselves can be specified. For instance in a lateral maneuver, the actual flight test roll rate could be prescribed along with the controls, when looking at the pitch rate, or the off-axis response, of the helicopter.

5.2 Time integration of equations of motion with free wake

With the free wake model included, the system of Eqs. (5.1) no longer contains equations for inflow dynamics. Instead a steady-state main rotor inflow is provided by the free wake model at various stages of the time integration. The same two methods that were used in the baseline case are used here to calculate the time histories with the free wake model; namely integration of the full non-linear equations of motion and integration of a linearized set of equations.

5.2.1 Numerical integration of the non-linear equations of motion

Again the Adams-Bashforth variable step, variable order ordinary differential equation solver is used to integrate the equations of motion, with the free wake model now providing the inflow distribution for the main rotor.

The variable step Adams-Bashforth algorithm must be able to evaluate the equations of motion at any azimuth angle. The specific values of azimuth angle used are selected by the integration algorithm itself and are not known prior to the integration. This raises an issue with the free wake model since the inflow is only available at a specific set of azimuth angles. For the trim calculations, the azimuthal points are given at the points required by Gaussian quadrature, and although the step size is not uniform, the points are known in advance and the inflow is interpolated accordingly. For the linearized model calculations, the equations of motion are evaluated at a set of evenly spaced azimuth angles which are the same as the azimuth angles used in the free wake model and no interpolation is required. This issue does not arise with dynamic inflow since the dynamic inflow equations are formulated in the rotating frame and can be evaluated at any azimuth angle. With the free wake model used in the time integration, a linear interpolation of the inflow is performed as a function of the azimuth angle.

The free wake model used in this study is a steady-state wake model based on a relaxation technique, so it is strictly only valid for steady-state trim conditions. This means that when the free wake model is used to calculate the inflow at a certain point in the maneuver, this point is assumed to represent a steady-state condition. The free wake model iterates to find a steady-state wake geometry and uses this to calculate a steady-state inflow distribution. Therefore there are no dynamics associated with the wake or inflow, and whenever the free wake model is

evaluated there is an instantaneous change in the wake geometry and subsequent inflow distribution.

With respect to the time integration, this lack of inflow dynamics with the free wake means that the inflow can only be updated at specific points in the maneuver. The question is: how often should the inflow be updated during the time integration? At one extreme, the free wake inflow distribution is calculated only at the start of the time integration from the trim condition and is held fixed for the entire maneuver. Thus the maneuver-induced wake distortions and their subsequent effect on the inflow are not present in the calculated dynamic response. At the other extreme, a new inflow distribution is calculated at each time step of the integration. Thus any changes in the state variables or controls during the maneuver would lead to instantaneous changes in the wake geometries and inflow. This scheme would also be prohibitively expensive as far as CPU time is concerned because of the number of times the inflow distribution would have to be calculated for a realistic maneuver.

For the dynamic response results presented in this study the inflow distribution is updated using the free wake model at the start of each rotor revolution. Therefore, the total number of times that the inflow is calculated is equal to the total number of rotor revolutions for the particular maneuver. This method is illustrated in Figure 5.2 and the procedure is as follows:

1. The simulation is started from a trimmed flight condition that is represented by the trim vector $\mathbf{x}_{trim}$ (Eqn. (3.40)). The state vector in the rotating frame at an azimuth angle of zero $\mathbf{y}(\psi_{REF} = 0)$ is calculated using the method presented in Section 3.3.

2. The current states and controls of the helicopter are used to evaluate the circulation loop, to give the steady-state inflow distribution over the main

rotor disk. This implies that the current state of the helicopter is assumed to represent a steady-state condition. The circulation loop is the modified loop that was described in Section 4.2 for the calculation of a linearized set of equations.

3. The inflow distribution is now held fixed and used to integrate the non-linear equations of motion for a single rotor revolution, using the prescribed control inputs during the particular rotor revolution. During this rotor revolution control inputs and changes in helicopter states have no effect on the wake geometry because the inflow is held fixed and consequently on the inflow distribution.

4. Using the new state of the helicopter, Steps 2 and 3 are repeated for each rotor revolution until the simulation is complete.

As with the baseline case, the time histories of one or more states in addition to the controls can be prescribed for the time integration.

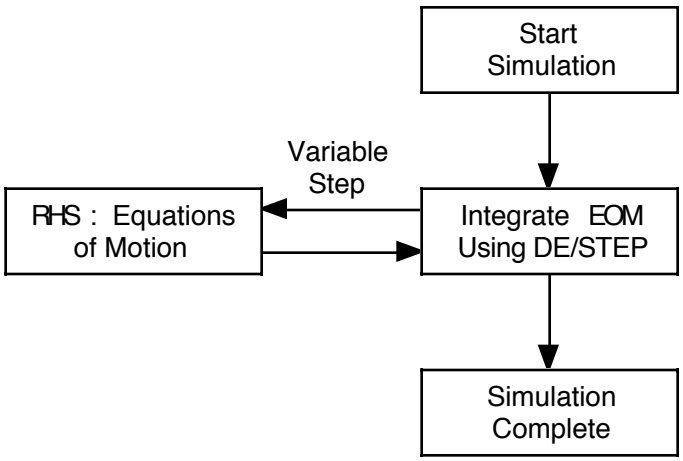

Figure 5.1: Schematic of the baseline time integration procedure with the dynamic inflow model.

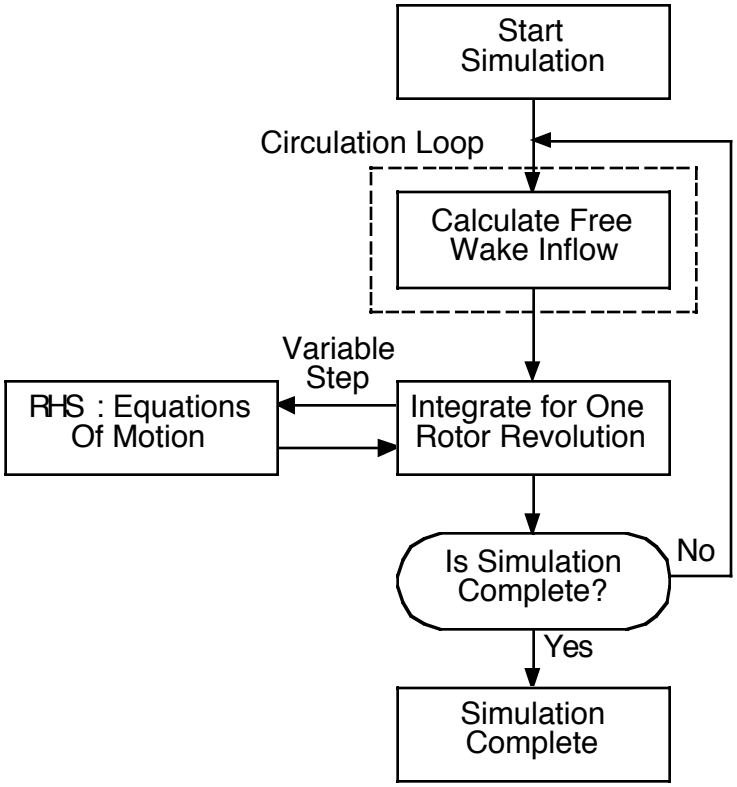

Figure 5.2: Schematic of the time integration procedure with the free wake model included.

Chapter 6

Aircraft Modeling Configurations

Two aircraft configurations are used in this study. The first is the Eurocopter BO-105 that incorporates a hingeless rotor system. The second is the Sikorsky UH-60A that uses an articulated rotor system. This section describes the general physical attributes of these helicopters and the modeling configurations used in the current study.

6.1 BO-105 configuration

The BO-105 has a hingeless soft in-plane main rotor. This configuration results in an equivalent hinge offset of about 14%, which produces a high control power and bandwidth, making the helicopter highly maneuverable. The high relative hinge offset also contributes to high cross couplings between the longitudinal and lateral-directional dynamics of the helicopter. The results presented in this study for the BO-105 helicopter are with the flight control system turned off (bare airframe configuration).

Table 6.1 contains the configuration of the BO-105 soft-in-plane hingeless rotor helicopter used in this study. Results are presented for a gross weight of 4,850 lbs. and at altitudes of 250 and 3000 feet. Assuming a standard atmosphere, these

altitudes correspond to C_T/σ values of 0.070 and 0.076 respectively.

The main rotor blades are modeled using a set of natural mode shapes that are calculated using the finite element technique as detailed in Section 2.4.7. In the calculation of the normal modes the geometric pitch angle at the root of the blade is set to zero. The cross-sectional centers of gravity and shear of the blade are coincident at the quarter-chord location, which effectively decouples torsion from the flap and lag degrees of freedom when considering the structural and inertial contributions. The presence of the small amount of structural twist of the blade introduces a small coupling between the flap and lag bending modes. Four finite elements of equal spanwise length are nominally used in the calculation of the natural blade modes, although the effect of the number of finite elements is investigated with the use of eight finite elements in some specific calculations. The mass and stiffness distributions of the blade are assumed to be uniform, and their values are chosen so that the fundamental flap, lag and torsion frequencies match those presented in Ref. [79]. Table 6.3 lists the modes that are included in the current analysis for the BO-105, generated using four and eight finite elements, including the modal natural frequencies for the current analysis and those from Ref. [79] (which are based on the true, nonuniform mass and stiffness distributions), and the type of the mode. Figures 6.1 through 6.7 show the seven lowest frequency natural mode shapes for the BO-105, generated with four finite elements and uniform mass and stiffness distributions.

The numerical results for the BO-105 generated for this study are obtained with two different blade models. The first is a *simple* blade model that includes only the fundamental elastic flap mode that has a natural frequency of 1.1253/rev and is shown in Figure 6.2. The second blade model is a *refined* blade model that includes the first seven elastic blade modes with the lowest natural frequencies. This refined

blade model includes three flap modes, two lag modes and two torsional modes (Figs. 6.1-6.7).

Figures 6.8 through 6.14 show a comparison between the first seven elastic blade modes with four and eight finite elements. These figures show that there is very little difference between the two sets of blade modes with the different numbers of finite elements. The effect of the number of finite elements on the trim results for the BO-105 is investigated in Section 7.1.6.

6.2 UH-60A configuration

The UH-60A Black Hawk helicopter has a fully-articulated 4-bladed rotor with a radius of 26.83 feet and a forward shaft tilt of 3 degrees. The blade airfoil section is the SC 1095 and the tip is swept by 20 degrees over the outboard most 1.90 feet of the radius, although the swept tip region is not included in this study and the blade is assumed to be straight. The hinge offset is 1.25 feet and the cuff extends outboard another 3.83 feet. The blade has a chord length of 1.75 feet and an equivalent linear twist of about -18 degrees, although the blade is twisted only outboard of cuff. The actual blade twist from the root to tip is -14 degrees (without the inclusion of the swept tip). Its design rotor speed is 27 rad/sec or 260 RPM. The tail rotor has a cant angle of 20 degrees, and therefore it generates relatively strong couplings between longitudinal and lateral directional dynamics. It uses the same airfoil section and blade twist as the main rotor, but with a smaller radius (5.5 feet) and a smaller chord (0.81 feet). The horizontal stabilizer uses the NACA 0014 airfoil. Its incidence is adjustable by the flight control system as a function of speed. It has an area of 45 square feet and an aspect ratio of 4.6. The vertical stabilizer uses the NACA 0021 airfoil. It has a surface area of 32.3 square feet and an aspect ratio of 1.92.

Table 6.2 contains the configuration of the UH-60A articulated rotor helicopter used in this study. Results are presented at a gross weight of 16,000 lbs. and at an altitude of 5250 feet. Many of the UH-60 specific parameters and non-linear functions have been adapted for use with this model from an existing UH-60 simulation model [3]. Further details of the implementation of the UH-60A helicopter can be found in the GENHEL theory manual [3].

For the numerical results for the UH-60A generated for this study, two blade models are used. The first is a *simple* blade model that includes the rigid lag mode of frequency 0.2680/rev (Fig. 6.15) and the rigid flap mode of frequency 1.0352/rev (Fig. 6.16). The second blade model is a *refined* blade model that includes the first six blade modes, shown in Figures 6.15 through 6.20, together with the corresponding natural frequencies.

MAIN ROTOR	
Number of blades	4
Radius R, ft	16.12
Blade chord c, ft	0.89
Rotational speed Ω, rad/sec	44.4
Tip speed V_{tip}, ft/sec	715.73
Longitudinal mast tilt i_θ, deg	-3.0
Airfoil section	NACA23012
First airfoil section, ft	3.61
Blade precone β_P, deg	2.5
Linear blade twist θ_{TW}, deg	-6.2
Solidity σ	0.07
Lock number γ at 250 feet	5.54
Lock number γ at 3000 feet	5.11
Control phase shift Δ_{SP},deg	-10.0
FUSELAGE	
Gross weight w, lbs	4850.17
Pitch inertia I_{yy}, lbs-ft^2	3667.92
Roll inertia I_{xx}, lbs-ft^2	1056.17
Yaw inertia I_{zz}, lbs-ft^2	3023.20
I_{xz}, lbs-ft^2	486.80
CG below hub, ft	3.15
TAIL ROTOR	
Number of blades	2
Radius R_{tr}, ft	3.18
Blade chord c_{tr}, ft	0.59
Rotational speed Ω_{tr}, rad/sec	233.0
Tip speed, ft/sec	726.21
Rotor shaft tilt, deg	-4.2

Table 6.1: Main parameters of the BO-105 helicopter configuration.

MAIN ROTOR	
Number of blades	4
Radius R, ft	26.83
Blade chord c, ft	1.75
Rotational speed Ω, rad/sec	27.0
Tip speed V_{tip}, ft/sec	724.41
Longitudinal mast tilt i_θ, deg	-3.0
Airfoil section	SC 1095
First airfoil section, ft	5.08
Blade precone β_P, deg	0.0
Linear blade twist θ_{TW}, deg	-18.0
Solidity σ	0.083
Lock number γ	5.11
Control phase shift Δ_{SP},deg	-9.7
FUSELAGE	
Gross weight w, lbs	16000.00
Pitch inertia I_{yy}, lbs-ft^2	38512.0
Roll inertia I_{xx}, lbs-ft^2	4659.0
Yaw inertia I_{zz}, lbs-ft^2	36796.0
I_{xz}, lbs-ft^2	1882.0
TAIL ROTOR	
Number of blades	4
Radius R_{tr}, ft	5.5
Blade chord c_{tr}, ft	0.81
Rotational speed Ω_{tr}, rad/sec	124.62
Tip speed, ft/sec	685.41
Rotor shaft cant angle, deg	20.0

Table 6.2: Main parameters of the UH-60A Black Hawk helicopter configuration.

Mode Number	Mode Type	Frequency (/rev)		
		Ref. [79]	4 FEMs	8 FEMs
1	1st lag	0.732	0.7316	0.7312
2	1st flap	1.125	1.1253	1.1247
3	1st torsion	3.176	3.1806	3.1805
4	2nd flap	2.780	3.4141	3.4108
5	2nd lag	4.510	4.4860	4.4820
6	3rd flap	5.007	7.6743	7.6342
7	2nd torsion	6.349	9.1375	9.1269

Table 6.3: BO-105 blade natural frequencies

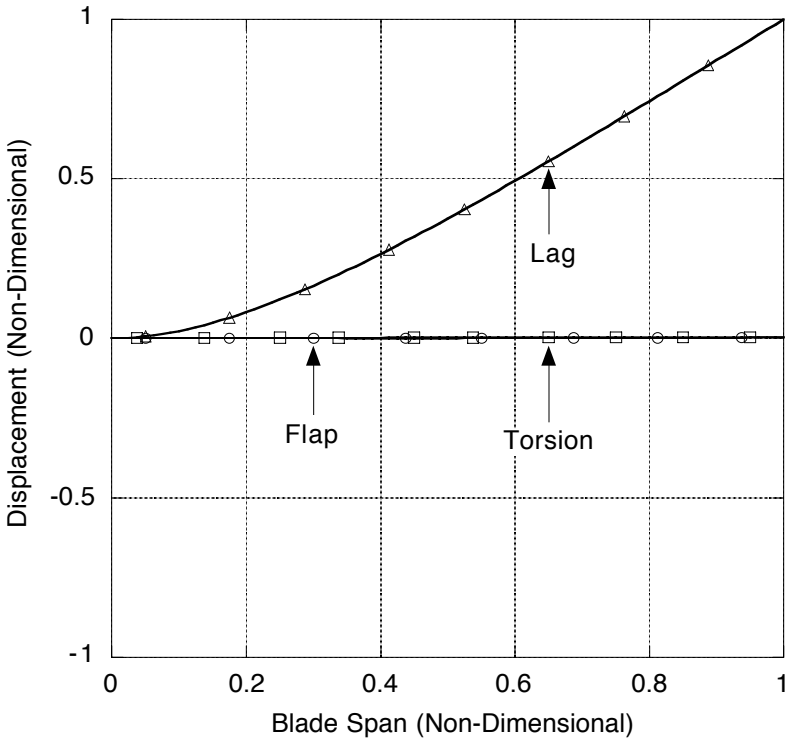

Figure 6.1: BO-105 first elastic lag mode. Frequency = 0.7316/rev.

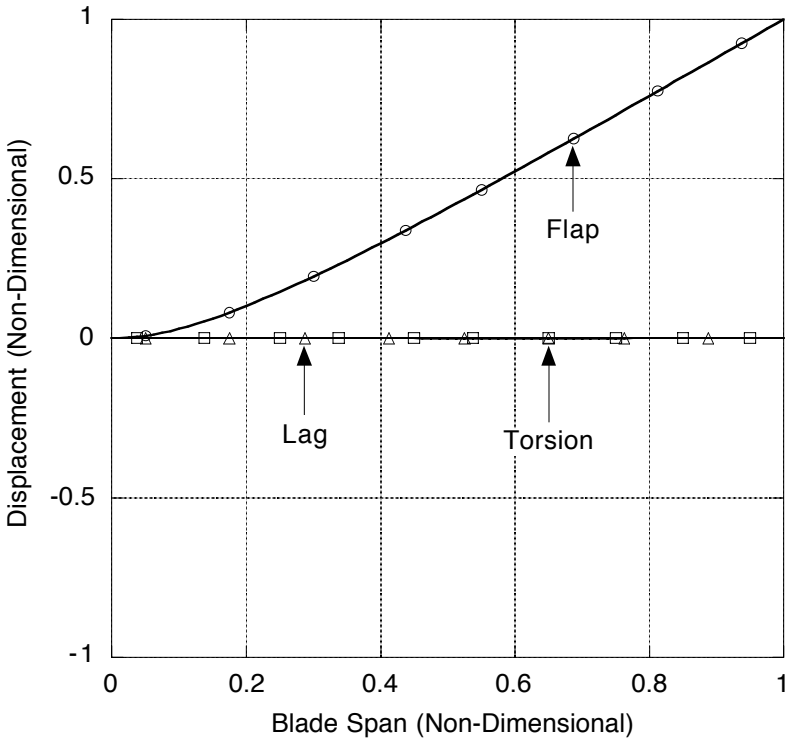

Figure 6.2: BO-105 first elastic flap mode. Frequency = 1.1253/rev.

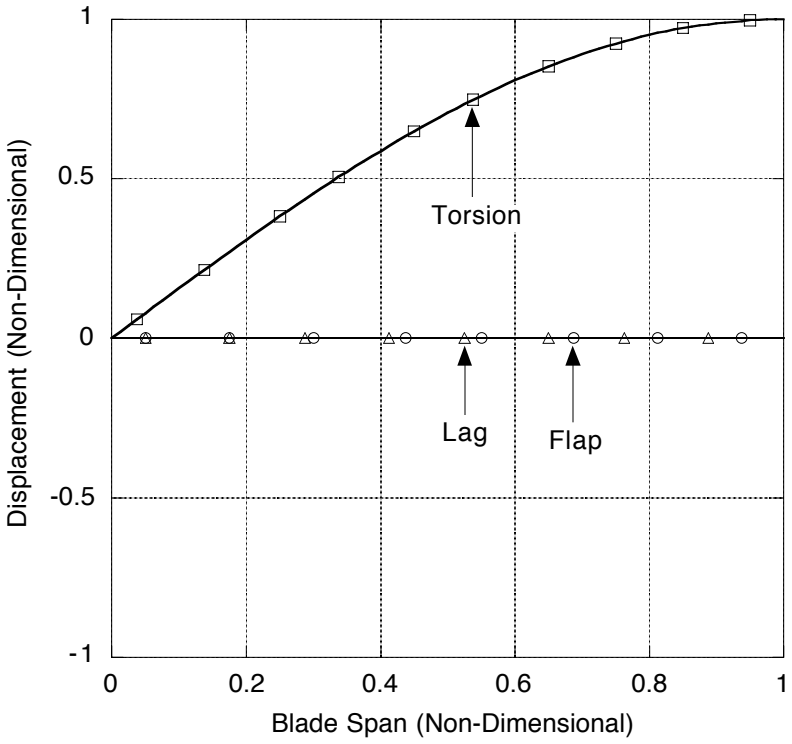

Figure 6.3: BO-105 first elastic torsional mode. Frequency = 3.1806/rev.

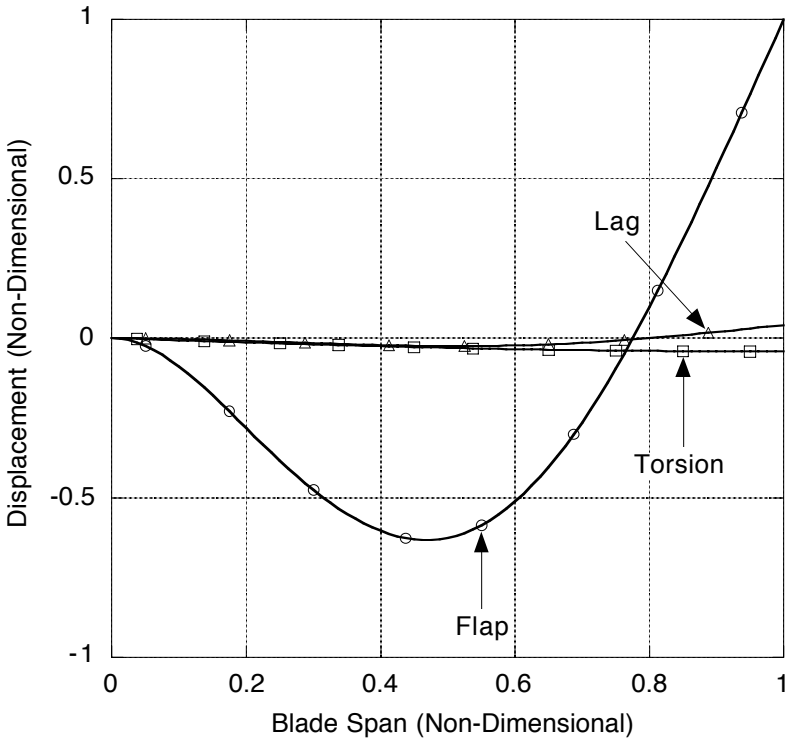

Figure 6.4: BO-105 second elastic flap mode. Frequency = 3.4141/rev.

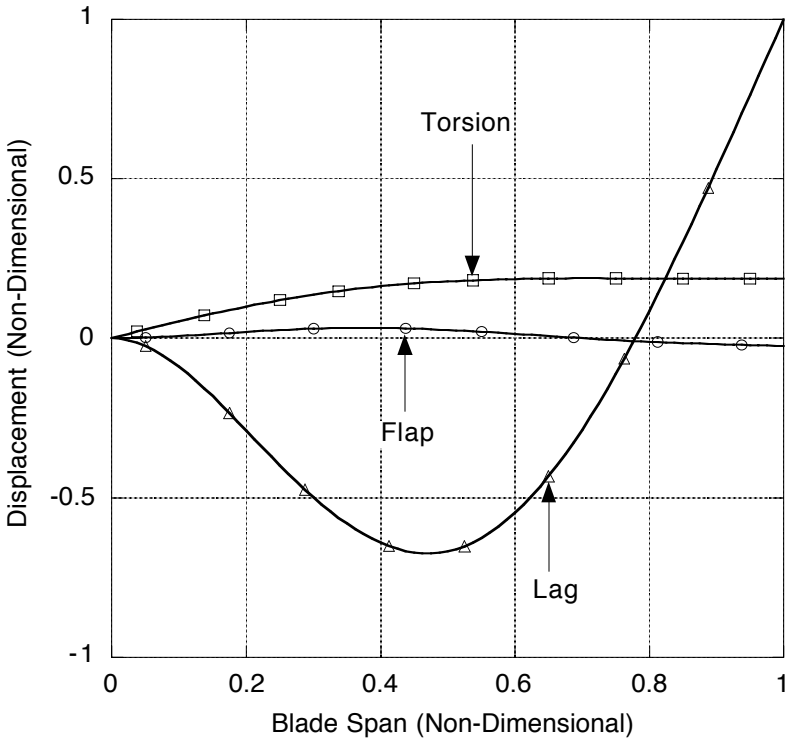

Figure 6.5: BO-105 second elastic lag mode. Frequency = 4.4860/rev.

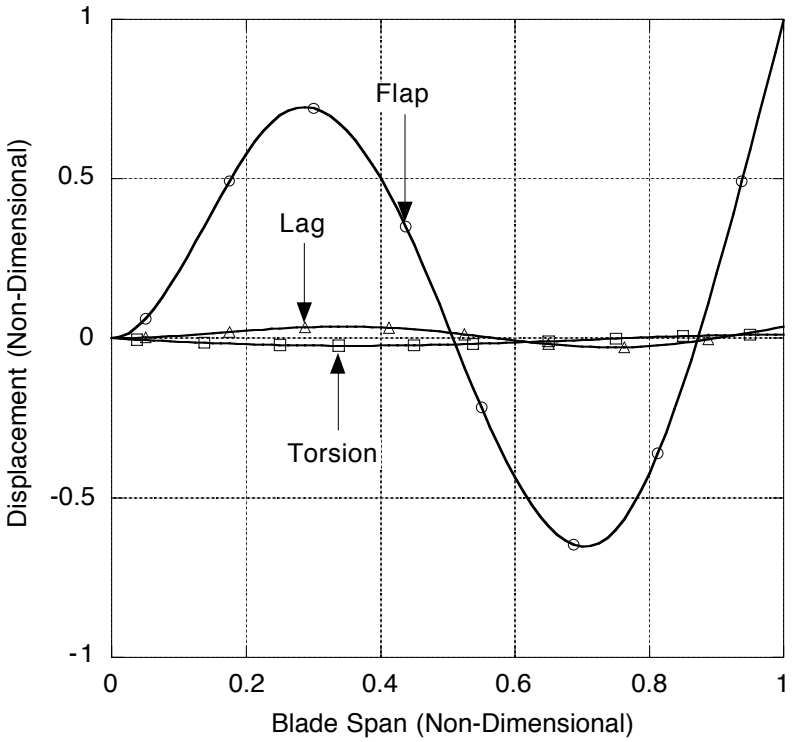

Figure 6.6: BO-105 third elastic flap mode. Frequency = 7.6743/rev.

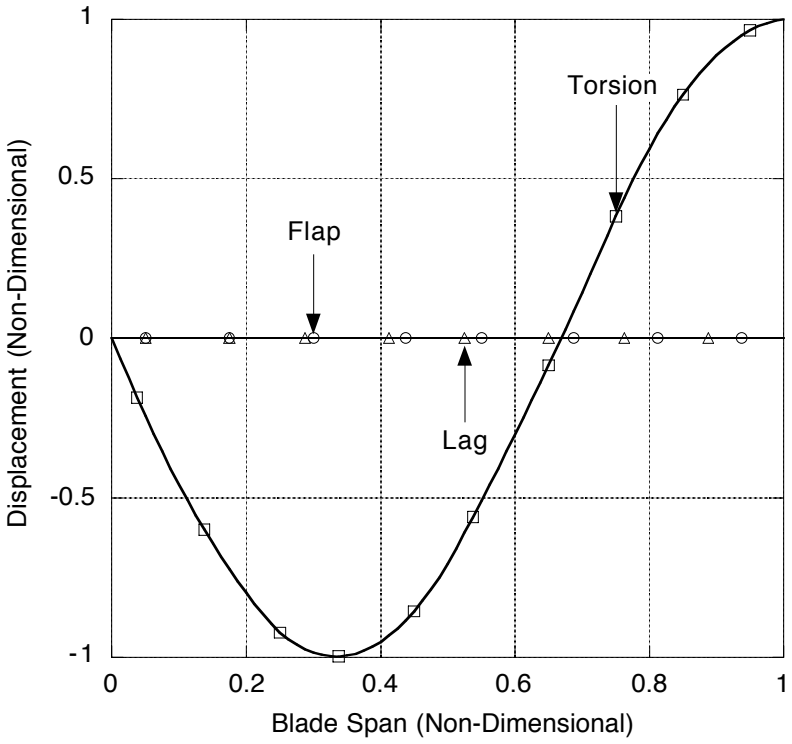

Figure 6.7: BO-105 second elastic torsional mode. Frequency = 9.1375/rev.

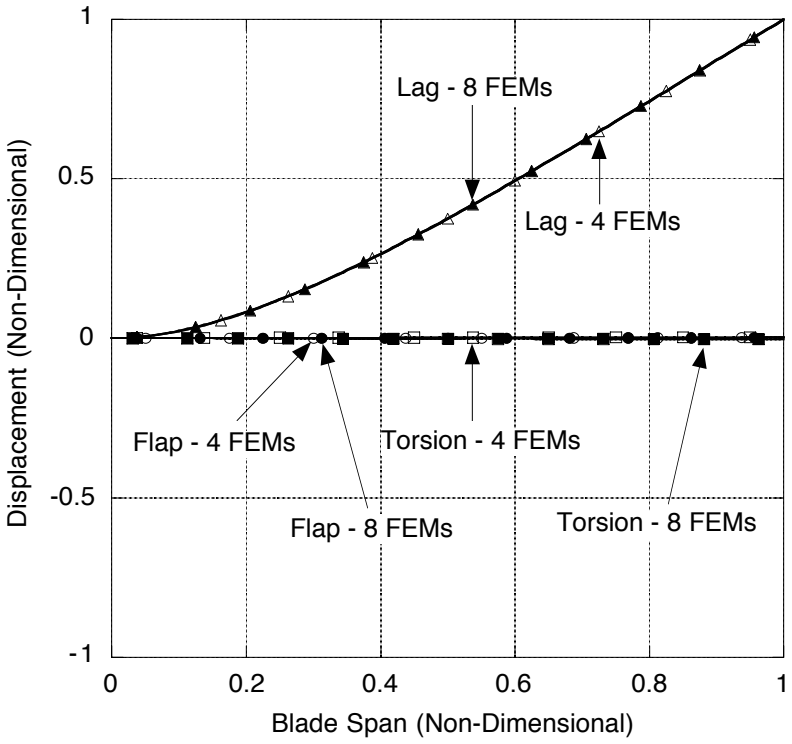

Figure 6.8: BO-105 first elastic lag mode. Frequency = 0.7316/rev.

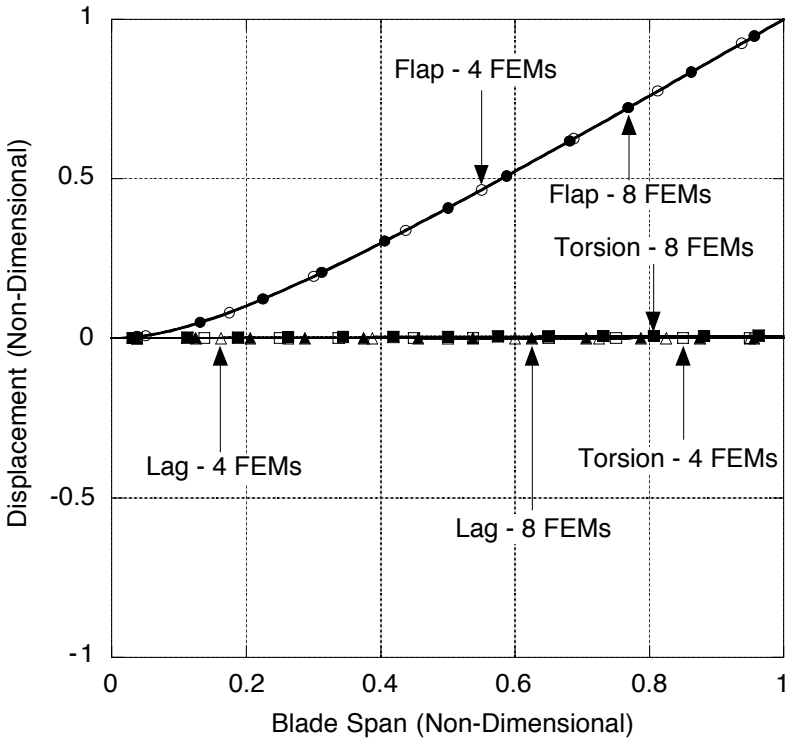

Figure 6.9: BO-105 first elastic flap mode. Frequency = 1.1253/rev.

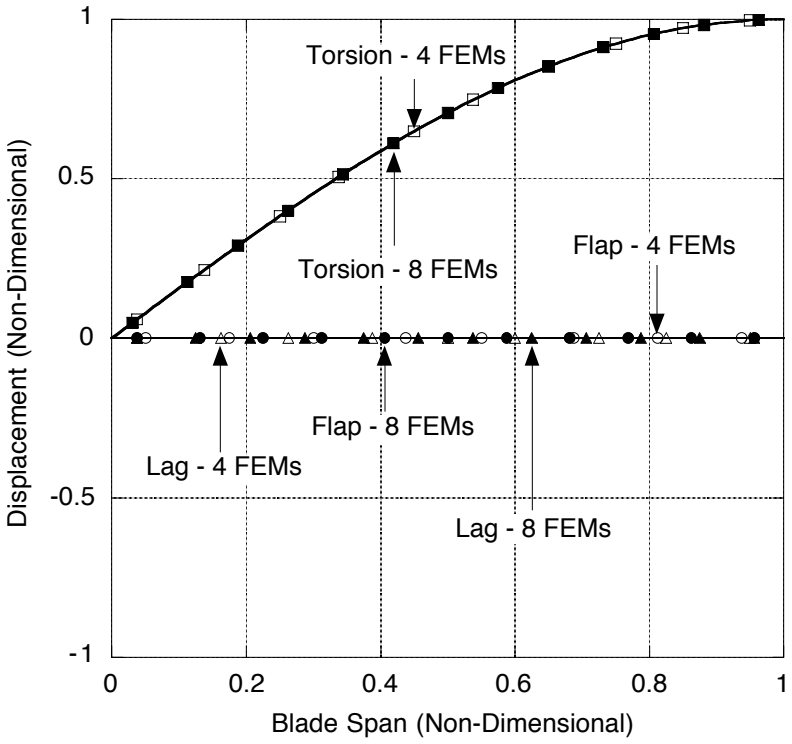

Figure 6.10: BO-105 first elastic torsional mode. Frequency = 3.1806/rev.

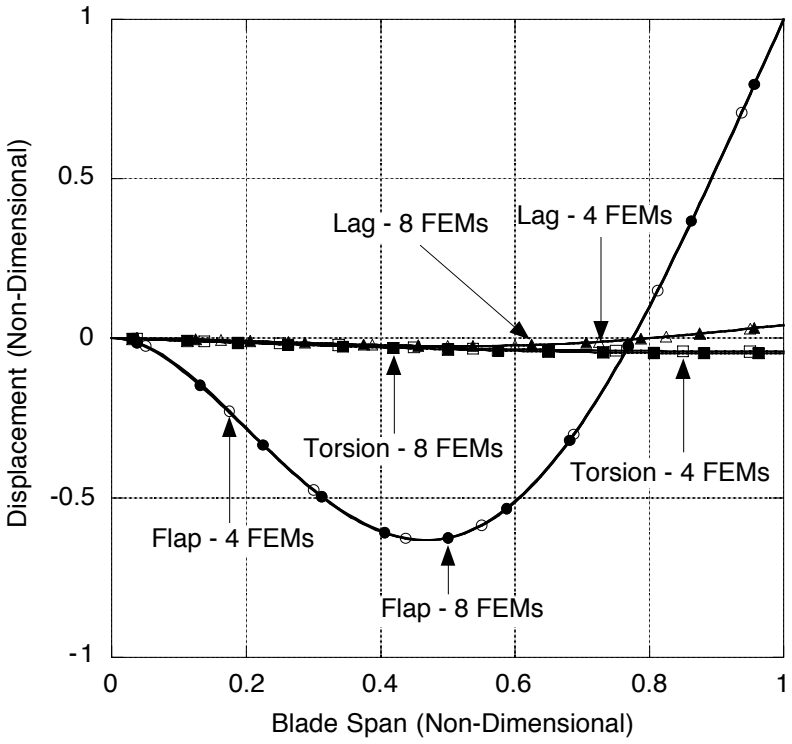

Figure 6.11: BO-105 second elastic flap mode. Frequency = 3.4141/rev.

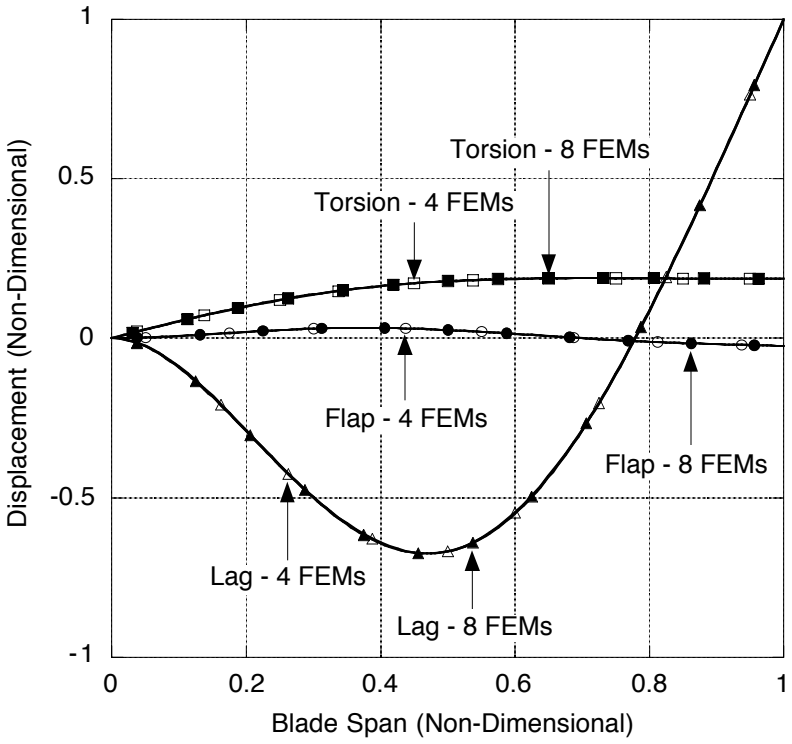

Figure 6.12: BO-105 second elastic lag mode. Frequency = 4.4860/rev.

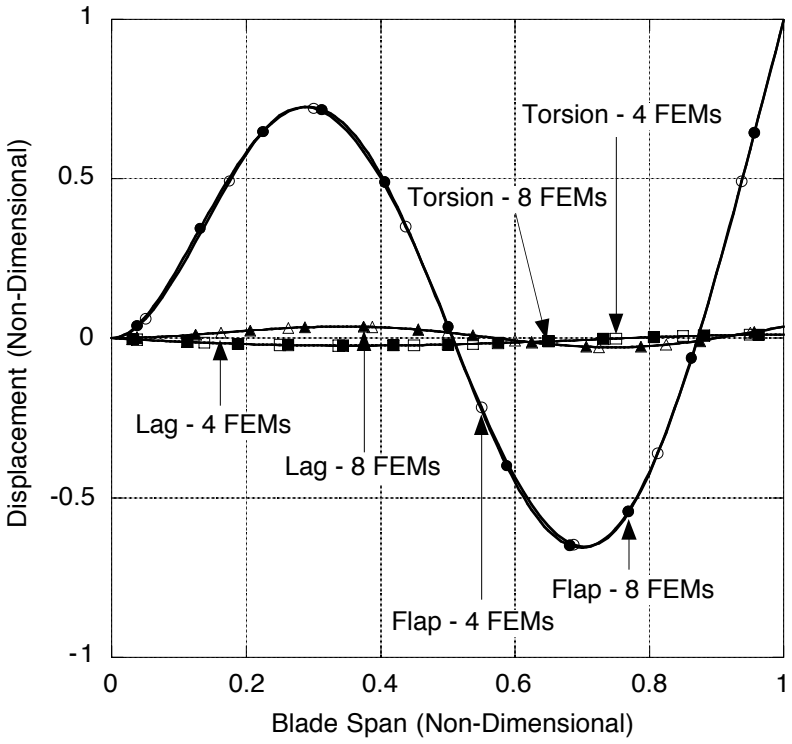

Figure 6.13: BO-105 third elastic flap mode. Frequency = 7.6743/rev.

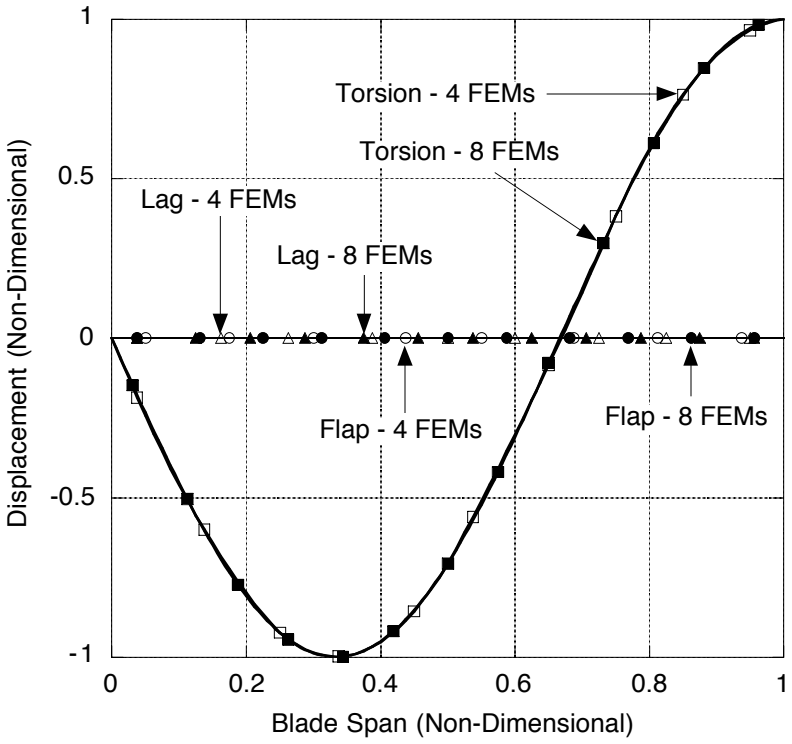

Figure 6.14: BO-105 second elastic torsional mode. Frequency = 9.1375/rev.

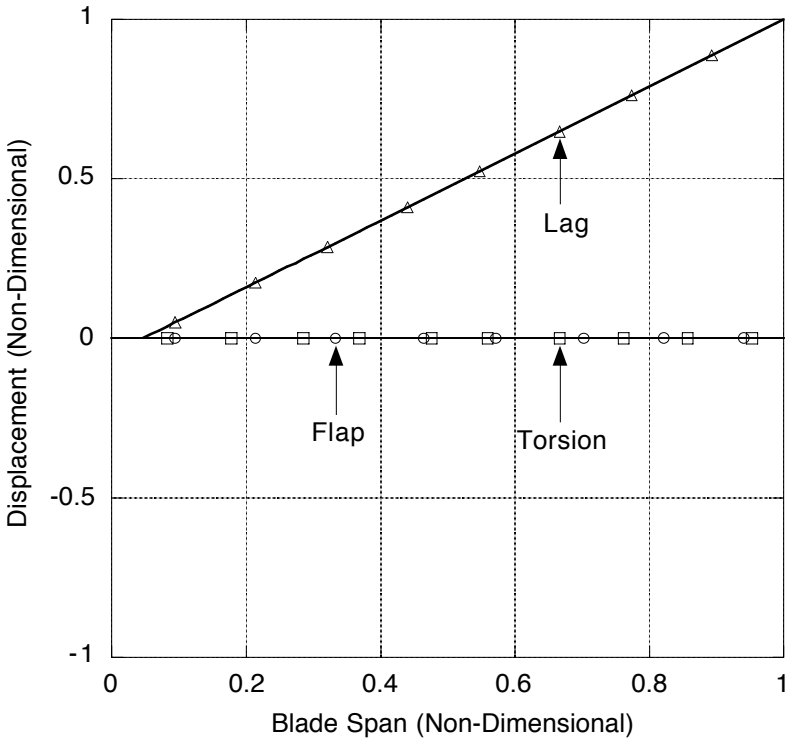

Figure 6.15: UH-60A first natural mode shape. Frequency = 0.2680/rev.

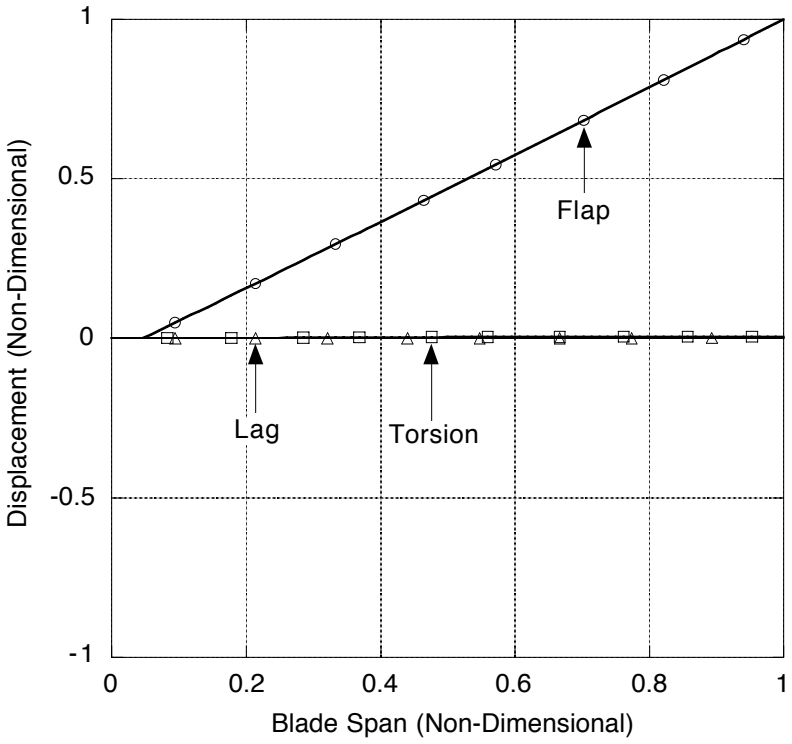

Figure 6.16: UH-60A second natural mode shape. Frequency = 1.0352/rev.

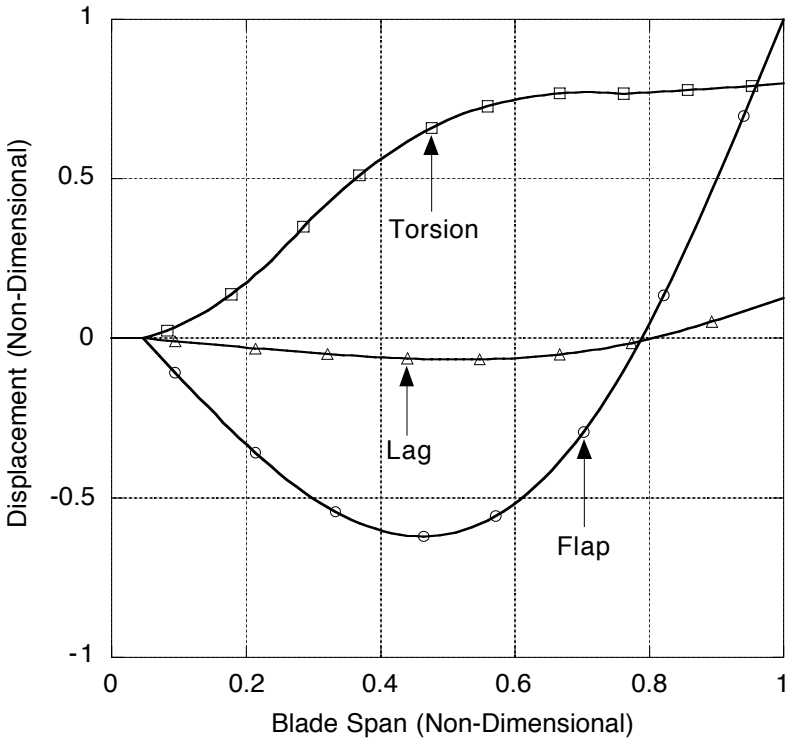

Figure 6.17: UH-60A third natural mode shape. Frequency = 2.8187/rev.

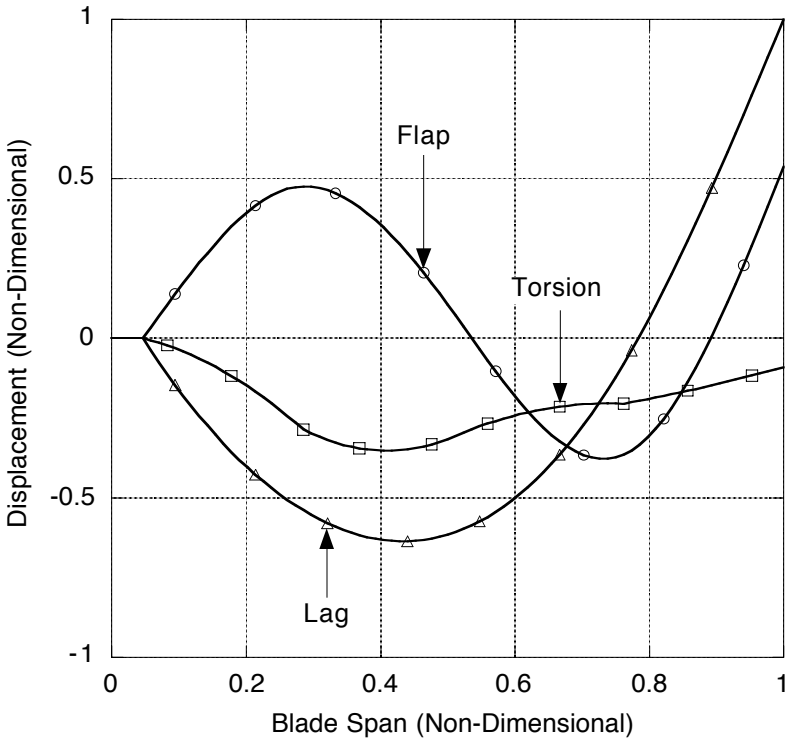

Figure 6.18: UH-60A fourth natural mode shape. Frequency = 4.6516/rev.

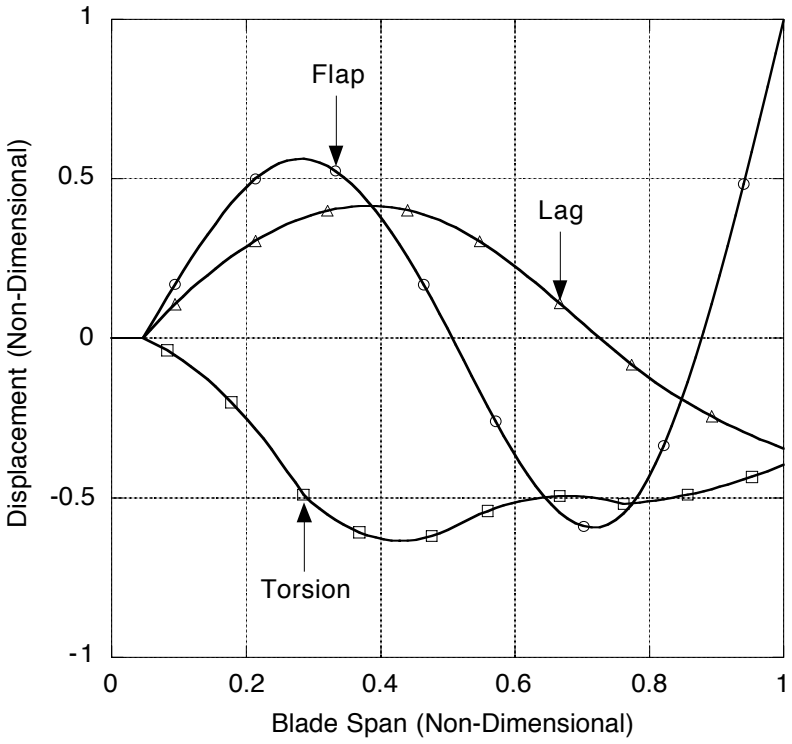

Figure 6.19: UH-60A fifth natural mode shape. Frequency = 5.1797/rev.

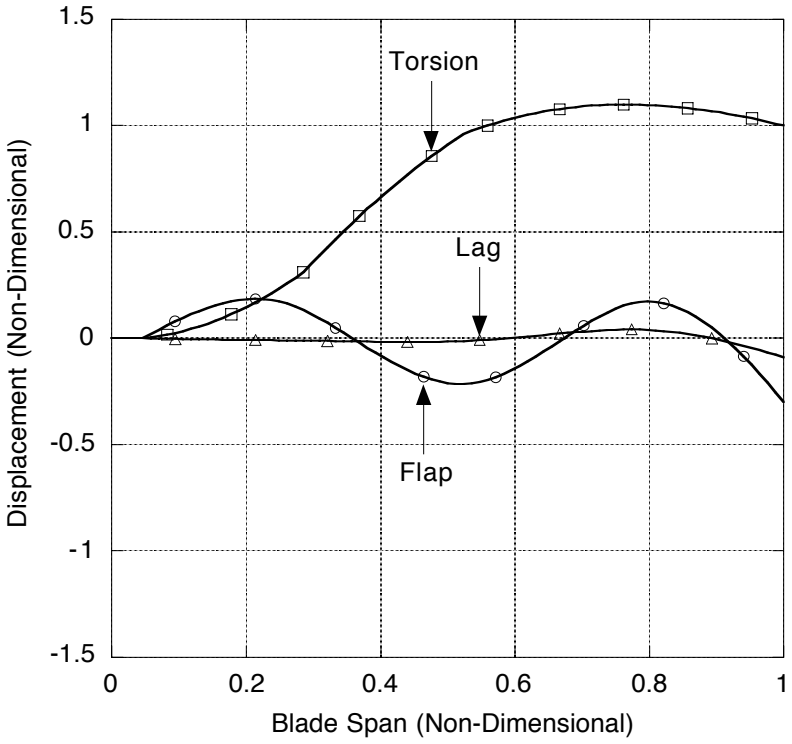

Figure 6.20: UH-60A sixth natural mode shape. Frequency = 7.8886/rev.

Chapter 7

Trim Results

This chapter presents the trim results in straight and level flight for the BO-105 and UH-60A helicopters and in steady turning flight for the UH-60A. A free-flight trim procedure that considers the dynamics of the entire helicopter is used for the numerical results presented in this chapter. The simulation results are compared with flight test data where such data are available.

7.1 BO-105 Trim Results

The trim results presented in this section refer to the BO-105 helicopter with the flight control system turned off (bare airframe configuration). The two blade modeling configurations for the BO-105 described in Section 6.1 are used to represent blade motion and flexibility. These are the *simple* blade model that includes only the first elastic flap mode and the *refined* blade model that includes the first seven blade modes with the lowest natural frequencies. It should be recalled that these modes are calculated by assuming that the mass and stiffness distributions of the blade are uniform and the center of gravity offset from the elastic axis of the blade section is zero along the blade span. This effectively uncouples the torsional degrees of freedom from the flap and lag degrees of freedom for the calculation of the blade

modes in the absence of aerodynamic loads. The quasi-steady aerodynamic model used for the calculation of main rotor aerodynamic loads does, however, introduce pitch-flap coupling. The mutual interactions between the main rotor and fuselage aerodynamic environments are neglected with both the dynamic inflow and free wake models, although a simple model of main rotor downwash on the horizontal tail is included with the dynamic inflow model in Section 7.1.5.

The flight test data used for comparison have been obtained from Ref. [80] and were measured at an altitude of 3000 feet with a gross vehicle weight of 4850 pounds.

7.1.1 Effect of inflow and blade modeling

The effect of inflow and blade flexibility modeling on the various trim results are shown in Figures 7.1 through 7.8. The results with the baseline flight dynamics model are denoted with the "Dyn. inflow" legend indicating that the Pitt-Peters model is used for the representation of inflow dynamics; recall that the inflow of the Pitt-Peters model has a linear variation over the rotor disk. The results with the new flight dynamics model that use the free wake inflow are denoted with the "Free wake" legend. For these results, the resolution of the vortex wake $\Delta\psi$ is 5 degrees, the total length of each vortex filament is 720 degrees, and the initial tip vortex strength is assumed to be equal to the maximum bound circulation along the blade ($C_\Gamma = 1.0$). The two blade models used in the generation of the numerical trim results are the *simple* blade model with the first elastic flap mode only, denoted with the "1 mode" legend and the *refined* blade model with the first seven elastic blade modes, denoted by the "7 modes" legend.

Figure 7.1 shows the correlation for the collective pitch as a function of forward speed. Considering first the results with the dynamic inflow model, with only the first elastic flap mode to model blade flexibility, the main rotor collective is under-

predicted by about three to five degrees over the entire speed range. This is typical of results with the Pitt-Peters dynamic inflow model, which tends to underpredict the collective. With the refined blade model and dynamic inflow, the results are significantly improved with a one degrees underprediction of the collective in the low speed region which stretches to a two to three degree difference in the high speed region. In looking at the effects of blade modeling, it is seen that the inclusion of the refined blade model increases the main rotor collective required by about two to three degrees over the entire speed range. This difference can be explained when considering the blade elastic twist that is present with the refined blade model, but not with the simple blade model. Figure 7.9 shows the elastic twist angle at the blade tip as a function of azimuth angle in hover and at forward speeds of 60 and 120 knots. The dynamic inflow and refined blade models are used. The blade tip twist using the simple blade model is not shown because no torsional degrees of freedom are included, so the twist is zero. This figure shows that in hover there is a two degree nose down elastic twist that is nearly independent of azimuth angle. This nose down elastic twist requires an increase in the root collective pitch setting to recover the same thrust as in the torsionally rigid rotor. As the speed increases, the azimuthal variation in tip elastic twist becomes larger because of cyclic variations in the blade aerodynamic environment. The average tip twist is, however, between -2 and -3 degrees at each of the speeds considered, accounting for the 2 to 3 degree higher collective required with the refined blade model over the simple blade model. Notice that the baseline (or dynamic inflow) results include a tip loss correction, according to which the outboard 3% of the blade does not generate aerodynamic lift.

The results in Figure 7.1 are generated with the free wake model. In the low speed region, the introduction of the free wake inflow model improves the correlation

with flight test data with the simple blade model, however, with the refined blade model the collective is over-predicted by between two and three degrees. As with the dynamic inflow results, the differences in the free wake results with the simple and refined blade models can be explained by the presence or absence of elastic twist in the blade model. Figure 7.10 shows the blade elastic twist at the blade tip as a function of azimuth angle, using the refined blade model in hover and at forward speeds of 63 and 127 knots. The increase in collective associated with the refined blade model again results from the blade tip twist. There is only a small variation in the average tip twist with forward speed. At speeds above 40 knots, the results with the free wake model and the simple blade model underpredict the main rotor collective, as do the results with the refined blade model.

Now the dynamic inflow and free wake model results can be compared, and the largest differences between the predicted results are seen in hover. With the refined blade model, there is a three to four degree difference in the collective in hover, which decreases to less than one degree in high speed flight. The same trend is observed in the results with the simple blade model. This indicates that the effect of inflow modeling is greatest in hover and low speed flight, decreases as the speed increases, and only plays a minor roll at high speed.

Figure 7.2 shows the correlation for the main rotor power required for trim versus forward speed. The dynamic inflow results underpredict the power over the entire speed range, while power is over-predicted with the free wake model in the low speed region up to about 60 knots, and under-predicted in the high speed range. This figure also shows that the power required is essentially independent of blade modeling for the entire speed range considered. As expected the results with the two different inflow models converge at high speed where the aerodynamic modeling of the fuselage plays a more significant role and the wake vortices are quickly swept

away from the disk. The differences between the simulation results and the flight test data in the high speed region seem to indicate that there may be some deficiencies in the fuselage aerodynamic model which are evident at high speeds but not at low speeds. A similar underprediction of the main rotor collective is seen in Figure 7.1, which also indicates some problem with the fuselage aerodynamic model. The effects of fuselage aerodynamic model on the trim results of the BO-105 are examined in Section 7.1.4.

The largest difference between the predicted power with the dynamic inflow and free wake models is seen in hover. Here, most of the power required by the main rotor is induced power, and therefore will be directly dependent on the inflow distribution. Figure 7.11 shows a comparison of the longitudinal variation in inflow generated with the dynamic inflow and free wake models in hover with the refined blade model. With dynamic inflow, the inflow is essentially uniform with a value of between 0.05 and 0.06 over the entire rotor disk. With the free wake, the inflow over the inner 80% of the rotor disk is between 0.1 and 0.12 and drops to zero in the tip region. Comparing these inflow distributions shows that the free wake inflow values are significantly higher than the dynamic inflow values over most of the rotor disk. The effect of this higher inflow is to increase the main rotor power required. This can be clearly seen in Figure 7.2 which shows that the predicted power required to hover using the free wake inflow model is over 50% higher than the power required using the dynamic inflow model. Another effect that this has is to increase the induced angle of attack of the blade sections, which requires an increase in the main rotor collective to increase the blade pitch so that the rotor system will produce the same amount of thrust. The over-prediction of the inflow generated with the free wake model is dealt with further in Section 7.1.2.

Figure 7.3 shows the correlation for the longitudinal cyclic pitch. The agreement

with flight test data is generally good for both inflow models over the entire speed range. Below 40 knots there is essentially no difference in the results with inflow model or with blade model. This figure also illustrates the differences in the definition of the trim procedure above and below an advance ratio of 0.1 (42 knots). Up to an advance ratio of 0.1, the trim is based on the assumption that the sideslip angle is zero, where for $\mu \geq 0.1$ the assumption of coordinated turn is maintained. Recall that in straight flight this assumption leads to $\sin\phi\cos\theta = 0$, which implies that the roll angle ϕ is close to zero. In the region from 40 to 80 knots, using the free wake model leads to an overprediction of forward cyclic.

Figure 7.4 shows the correlation with the lateral cyclic pitch. The simulation results show good agreement with the flight test data over the entire speed range, with the exception of the free wake inflow results in the region from 30 to 40 knots.

Figure 7.5 shows the correlation for the tail rotor collective setting. The simulation results in general show an overprediction of the tail rotor collective. This can be attributed in part to the relatively simple way in which the tail rotor thrust is calculated with the Bailey solution [71], which is based on momentum theory and so is limited to the uniform inflow assumption. With the free wake model, the tail rotor collective is higher because the rotor power is overpredicted, and so is main rotor torque. To balance this additional torque, the tail rotor thrust must be higher, requiring a higher tail rotor collective.

Figure 7.6 shows the correlation for the fuselage pitch attitude. In this case the agreement is good for both inflow models over most of the speed range and the simulations results are not altered by the blade model. For speeds between about 20 and 35 knots both models fail to predict a pitch-up behavior. This is likely because the aerodynamic interaction between the main rotor wake and horizontal tail and rear of the fuselage has been neglected. Therefore the entrance of the horizontal tail

into the rotor wake, and its subsequent exit as the speed increases, is not included in these results. Section 7.1.5 examines the effect of including a simple model of main rotor downwash on the horizontal tail on the trim results to explain the failure of the simulation models to predict the nose-up pitch in the 20 to 35 knot speed range.

Figure 7.7 shows the effect of inflow modeling on the roll attitude. There were no flight test data available to allow a comparison with the simulation results. This figure clearly shows the differences in trim calculations above and below an advance ratio of 0.1, where the bank angle is variable below $\mu = 0.1$ and is zero above $\mu = 0.1$. The bank angle shown here is not affected by the refinement of the blade model. With the free wake inflow model a higher bank angle to the left is predicted, compared with the dynamic inflow case. This is a direct result of the higher roll moments caused by the overprediction of tail rotor thrust at low speed.

Figure 7.7 shows the effect of inflow modeling on the sideslip angle. The trim is performed to a variable sideslip angle for speeds above $\mu = 0.1$. The modeling of the blade does not affect the prediction of the sideslip angle. In the speed range from 40 to about 70 knots, there are significant differences in the sideslip angle prediction with the free wake model predicting a significantly higher nose left sideslip angle.

The results presented in this section showed the effect of inflow and blade modeling on the trim predictions of the BO-105 helicopter. These results raise some issues regarding the use of the free wake model and the modeling of the BO-105. With respect to inflow predictions using the free wake model, the effect of the initial tip vortex strength is examined in Section 7.1.2 and the effect of the wake resolution is examined in Section 7.1.3. These results show that there may be some deficiencies with the specific modeling of the BO-105. The effect of fuselage modeling is examined in Section 7.1.4, and a simple model for the downwash of the main rotor on the horizontal tail is examined in Section 7.1.5.

7.1.2 Effect of tip vortex strength

The free wake model trim results shown in Figures 7.1 through 7.8 were calculated based on the assumption that the initial tip vortex strength at each azimuth angle is equal to the maximum bound circulation along the blade at the particular azimuth angle. This was found to lead to an over-prediction of the main rotor collective and power required, particularly in hover and low speed flight. The effect of the initial tip vortex strength on the calculated trim results is investigated in this section.

Bagai [50] uses essentially the same free wake model as the current study and assumes that 100% of the vorticity outboard of the peak bound circulation rolls up into the tip vortex. This led to an overprediction of the hover inflow by about 50% when compared to that generated using a momentum theory analysis. The experimental studies of Dosanjh *et al.* [73] and Bhagwat and Leishman [72] related measurements of tip vortex characteristics to bound circulation and showed that the tip vortex strengths are lower than the maximum bound circulation. Dosanjh *et al.* [73] experimented with a rectangular untwisted wing in a wind tunnel and found that only 58% of the peak bound circulation rolls up into the tip vortex. This value was calculated by dividing the measured tip vortex strength by the theoretical maximum bound circulation calculated using lifting-line theory. For this fixed wing case, the peak bound circulation was observed at the semi-span point and dropped to zero at the wing tips. Bhagwat and Leishman [72] used LDV measurements on one and two-bladed hovering rotors to conclude that 85% of the peak bound circulation is contained in the trailed tip vortex filaments. The blades were rectangular and untwisted so that the lift distribution was biased towards the blade tip with the point of peak bound circulation close to the tip. At present the physical mechanisms involved in the formation of the trailed tip vortices are not fully understood and it

is not clear how the physical characteristics (planform, twist, aspect ratio, etc.) or the operational characteristics (circulation distribution, thrust coefficient, advance ratio, etc.) effect the trailed vortices. The parameter C_Γ, which is the ratio of the initial tip vortex strength to the maximum bound circulation must therefore be derived empirically.

Figures 7.12 through 7.19 show the effects of variations in the tip vortex strength on the trim results generated with the free wake inflow model and the simple and refined blade models. The calculation of the initial tip vortex strength is given as a fraction of the maximum bound circulation along the blade at a particular azimuth angle (Eqn. (2.319)), where C_Γ is the ratio of the initial tip vortex strength to the maximum bound circulation along the blade. The values of C_Γ used in these figures are 1.00 and 0.70, which represent 100 and 70 percent respectively of the initial tip vortex strength to the maximum bound circulation. By lowering the initial tip vortex strength, the inflow distribution is affected in essentially two ways. First the inflow is calculated based on the influence of the tip vortices and since the tip vortex strengths are decreased, the inflow will also be decreased. Second the wake geometry itself will be changed by changes in the tip vortex strength, which will also affect the inflow.

Figure 7.12 shows the correlation for the collective pitch as a function of forward speed. The effect of lowering the initial tip vortex strength is to decrease the main rotor collective in hover by about two degrees, which significantly improves the correlation between the free wake results with the refined blade model and the flight test data. The initial tip vortex strength has less effect as the speed increases as the collective pitch becomes more a function of the fuselage aerodynamic modeling than inflow modeling. This also shows that the changes in the initial tip vortex strengths do not improve the predictions of the main rotor collective at high speeds.

Figure 7.13 shows the effect of tip vortex strength on the prediction of the main rotor power required. By assuming that the initial tip vortex strength is 70% of the maximum bound circulation, the power predictions are substantially improved for speeds up to about 50 knots compared with flight test data. In hover, where almost all of the power required is induced, there is a good quantitative agreement between the results with $C_\Gamma = 0.70$ and the flight test data. This seems to indicate that the inflow distribution, or at least the mean inflow, is being predicted with good accuracy. As with the main rotor collective, the power is under-predicted for speeds above 50 knots and changes in the tip vortex strengths do not effect this result.

The longitudinal variation in the hover inflow distributions generated with varying tip vortex strengths is shown in Figure 7.20. The curves are generated with $C_\Gamma = 1.00$ and $C_\Gamma = 0.70$. The decrease in the tip vortex strength with $C_\Gamma = 0.70$ results in a corresponding decrease in the inflow values. This decreased inflow results in a decrease in the power required to hover because most of the power in hover is induced.

The longitudinal cyclic predictions are shown in Figure 7.14, where the correlation between simulation and flight test results are improved by decreasing the tip vortex strength. This is particularly true at about 40 knots where the over-prediction of the forward stick with $C_\Gamma = 1.00$ is reduced with $C_\Gamma = 0.70$. Again the results beyond 50 knots seem to suggest a problem with the aerodynamic model of the fuselage. The lateral cyclic predictions shown in Figure 7.15 show a better agreement between simulation results and flight test data with reduced tip vortex strength for speeds below 40 knots. The agreement also improved above 50 knots, although these results have to be considered with care because there are some issues with the aerodynamic model of the fuselage.

Figure 7.16 shows the correlation for the tail rotor collective. With the reduced

tip vortex strengths, the magnitude of inflow over the rotor disk is reduced, which in-turn reduces the main rotor power required and the main rotor torque. A lower tail rotor thrust and thus lower tail rotor collective is required to balance the lower main rotor torque. In hover, essentially all of the main rotor torque has to be balanced by the thrust from the tail rotor and because the main rotor torque decreases by decreasing the tip vortex strengths, there is a corresponding decrease in the tail rotor collective required. This improves the correlation between the simulation results and the flight test data, however, the tail rotor collective is over-predicted by a couple of degrees. This is probably related to the simple uniform inflow model used for the analysis of the tail rotor.

Figure 7.17 shows that the prediction of the fuselage pitch attitude is not significantly affected by the reduction in the tip vortex strengths. The same is true of the fuselage roll attitude shown in figure 7.18 where the predicted results are only slightly affected by the tip vortex strength. Figure 7.19 shows the effect of the tip vortex strength on the prediction of the sideslip angle required for trim. The only differences in the predicted results are in the range from 40 to 70 knots where the lower value of the tip vortex strengths results in a lower value of the fuselage sideslip angle. Because the fuselage sideslip angle is strongly coupled to the lateral cyclic and the tail rotor collective, the lower value of the predicted tail rotor collective also results in a lower value of the fuselage sideslip angle.

The results of this section show the effect of tip vortex strength on the trim results for the BO-105. The parameter that governs the strength of the free tip vortices is C_Γ, which is the ratio of the tip vortex strength to the maximum bound circulation along the blade at a particular azimuth angle. By decreasing C_Γ from 1.00 to 0.70, the corresponding reduction in the inflow results in lower trim values of the main rotor collective and power required. This is particularly evident in hover

where the inflow has the greatest effect. These results show that the trim predictions for the BO-105 are significantly improved with $C_\Gamma = 0.70$, or only 70% of the bound circulation from the blade tip to the peak circulation along the blade is rolled up into the tip vortex.

7.1.3 Effect of vortex wake resolution

The vortex wake used in the free wake model is represented by a single vortex filament released from the 1/4-chord location at the tip of each blade. There are three important parameters associated with the modeling of these tip vortices. These are: the initial tip vortex strength, the resolution of the vortex wake and the total length of the vortex filament. The effect of the initial tip vortex strength has been examined in the previous section. The total length of each vortex filament corresponds to two revolutions of the main rotor, or 720 degrees for all of the numerical results in this study. This leaves the free wake resolution, which is the focus of this section.

As described in Section 2.9, the wake resolution is characterized by two parameters, namely, the azimuthal discretization resolution $\Delta\psi$ and the vortex filament discretization resolution $\Delta\zeta$. For this study these parameters are equal and are referred to collectively as the wake resolution $\Delta\psi$. This wake resolution does not directly affect the trim calculations, in the sense that the azimuthal points at which the equations are evaluated are determined by the Gaussian quadrature used for the azimuthwise integrals (see Section 3.1.3). This is because the azimuthal points where the equations of motion are evaluated are given be a Gaussian distribution and so are not a function of the wake resolution. Within the free wake model, the wake resolution has essentially three effects. The first is with respect to computational efficiency. In fact, by halving the value of $\Delta\psi$, the computer time required for each iteration of the wake geometry loop increases four fold. Second, the inflow

distribution is affected as the wake geometry used to calculate the inflow will be somewhat dependent on the wake resolution. The effect that these inflow differences have on the trim results is investigated in this section. The third effect is with respect to the convergence of the free wake model. The convergence characteristics of the free wake model are not investigated in this study, however, there are some conditions in which the wake geometry loop of the free wake model fails to converge. These regions are pointed out in this section.

Figures 7.21 through 7.26 show the trim results calculated with the free wake model with wake resolutions $\Delta\psi$ of 5 and 10 degrees and compare these predicted results with flight test data. Both the simple and refined blade models are used with $C_\Gamma = 0.70$.

These figures show that the wake resolution has only a small influence on the trim solution. This same trend is seen with all of the trim variables. It is also seen that no trim condition could be found with $\Delta\psi = 10^o$ for speeds below 40 knots. This is caused by the failure of the wake geometry loop within the free wake model to converge.

These results indicate, for the wake resolutions considered, that the predicted trim results are not dependent on the wake resolution. However, it is not always possible to obtain trim results with the coarse wake resolution because the free wake geometry loop may fail to converge at low speeds.

7.1.4 Effect of fuselage aerodynamic modeling

It has been suggested in previous sections that a possible cause of the discrepancies between the simulation results and the flight test data in the high speed range is the aerodynamic model of the fuselage. In this section, a simple fuselage aerodynamic drag model is used to generate additional trim results for the BO-105. This simple

fuselage drag model has the aerodynamic drag calculated based on an estimate of the fuselage parasitic equivalent wetted or flat-plate area, f, of 20 ft^2. The resulting drag force is assumed to act in the direction of the freestream flow at the aerodynamic reference point of the fuselage. The aerodynamic loads from the empennage are still present and are not effected by the inclusion of the simple fuselage drag model.

Figure 7.27 shows the effect of fuselage modeling on the main rotor collective required for trim and compares the simulation results with flight test data. The numerical results are calculated with the refined blade model and the free wake model with $\Delta\psi = 5^o$ and $C_\Gamma = 0.70$. For speeds up to 50 knots, the fuselage aerodynamic model has essentially no effect on the prediction of the collective pitch as the low dynamic pressure in this region results in low fuselage aerodynamic loads. As the speed increases from 50 knots, the fuselage aerodynamic model has an increasing influence on the results. The simple fuselage drag model produces an improvement in the correlation of the main rotor collective with the flight test data in the high speed range where the fuselage aerodynamic model has the greatest influence.

Figure 7.28 shows the correlation with the main rotor power required. Again, the fuselage aerodynamic model does not effect the results at low speed below 50 knots and the use of the simple fuselage drag model produces an improvement in the prediction of the main rotor power above 50 knots. As the power required in high speed forward flight is predominantly a function of the fuselage drag, the higher drag associated with the simple model produces a higher power at high speeds and an improved correlation with flight test data.

Figure 7.29 shows the effect of fuselage modeling on the longitudinal cyclic required for trim. At high speed, the correlation with the flight test data is improved with the simple fuselage drag model when compared with the results using the non-

linear fuselage aerodynamic model. However, the correlation worsens in the speed range from 40 to 80 knots where an over-prediction of the forward stick is predicted. Figure 7.30 shows the effect of fuselage modeling on the lateral cyclic. The simple aerodynamic model improves the correlation with flight test data, except in the range from 40 to 70 knots. This is probably because the simple fuselage drag model does not include yawing and pitching moment responses from non-zero pitch and yaw attitudes.

Figure 7.31 shows the effect of fuselage modeling on the tail rotor collective. For the speed range of hover to 40 knots, there is no difference in the tail rotor collective as in this speed range the sideslip angle is set to zero as part of the trim procedure. The simple fuselage model contributes only a drag force and no yawing moments with sideslip angle are produced. The lack of yawing moments from the fuselage aerodynamics is the reason for the increase in the tail rotor collective for speeds above 40 knots where the sideslip angle is not zero. Without the yawing moments from the fuselage, a higher tail rotor thrust is required to compensate, resulting in a higher tail rotor collective.

Figures 7.32, 7.33 and 7.34 show the effect of fuselage aerodynamic modeling on the pitch, roll and sideslip angles of the fuselage respectively for trim. The correlation of the pitch attitude is improved in the high speed region with the simple fuselage drag model, although this fuselage aerodynamic model does not include any pitching moments resulting from pitch attitude that would be present on the actual helicopter. The roll attitudes are non-zero below 40 knots and are not significantly effected by the fuselage aerodynamic model in this region. The largest difference between the results with the two fuselage models are with respect to the sideslip angle. With the simple fuselage drag model the main rotor torque is balanced entirely from the thrust of the tail rotor and the lateral forces produced

by the vertical tail. Because the lateral force is dependent on the sideslip angle, a higher vertical tail lateral force required a higher sideslip angle.

These results show that improvements in the predictions of the main rotor collective and power required can be achieved using the simple fuselage aerodynamic drag model. This seems to indicate that the discrepancies at high speed with the non-linear fuselage aerodynamic model are due to an underestimation of the fuselage drag. The predictions of the tail rotor collective and sideslip angle are, however, less satisfactory because the simple drag model does not include yawing moments produced with non-zero sideslip angle for $\mu \geq 0.1$. Any improvement in the correlation of the predicted trim state of the BO-105 with flight test data would require further validation and improvement in the fuselage aerodynamic model.

7.1.5 Effect of downwash on horizontal tail

This section presents results obtained with the inclusion of a simple model for the downwash from the main rotor onto the horizontal tail, and describes the effects that this modification has on the trim results. It was observed in Figure 7.6 that there were discrepancies between the simulation results and the flight test data in the speed range from 15 to 40 knots where the nose up pitch attitude changes observed in the flight test data were not captured. The nose-up attitude in the flight test data is probably a result of the interaction between the main rotor downwash and the horizontal tail. The downwash from the main rotor would contribute to a download on the horizontal tail, which in-turn would produce a nose-up pitch of the fuselage. The effect of including a simple model of the downwash on the horizontal tail is examined in this section.

In the simple interaction model, the downwash from the main rotor contributes to the velocity profile at the horizontal tail in the speed range from 15 to 40 knots.

Within this speed range, it is assumed that the horizontal tail is immersed in the far wake of the main rotor, and that the rotor wake has contracted to half the disk area. The downwash velocity at the horizontal tail is, therefore, twice the downwash at the rotor disk. Only results with the dynamic inflow model were obtained, and the average downwash over the rotor is used in the calculation of this aerodynamic interaction.

Figures 7.35 and 7.36 show the effect of the inclusion of the aerodynamic interaction on the longitudinal cyclic and fuselage pitch attitude respectively. The numerical results are generated with the refined blade model and dynamic inflow. These figures show that the predicted longitudinal cyclic and pitch attitude are only slightly effected in the speed range from 15 to 40 knots and that the inclusion of the simple aerodynamic interaction model has only a small effect. A more nose-up pitch attitude is observed with the aerodynamic interaction included, which is in the correct direction to improve the correlation with flight test data but it too small to make much of an improvement.

It should be remembered that this simple aerodynamic interaction model includes the downwash from the main rotor onto the horizontal tail and not the fuselage. The results suggest that the interactions between the main rotor downwash and the fuselage and empennage are complicated and to accurately capture the physical effects a more refined aerodynamic interaction model would be required. The prediction of the pitch attitude (Fig. 7.36) in hover agrees well with the flight test data, however as the speed increases towards 40 knots, the model predicts a decreasing nose-up pitch attitude while the flight test data shows that the nose-up attitude increases. As seen in the flight test data, as the speed increases from hover to 40 knots the increasing nose-up attitude is probably a result of the influence of the main rotor downwash moving further aft along the fuselage causing a more nose-up

attitude with speed. This would be in addition to the downwash on the horizontal tail. As the speed increases from about 40 knots, the fuselage is no longer immersed in the main rotor downwash and the nose-up pitch attitudes are no longer seen.

These results suggest that a more refined model for the aerodynamic interactions between the main rotor downwash and fuselage and empennage is required to more fully capture the longitudinal dynamics of the helicopter at low speed.

7.1.6 Effect of the number of finite elements

Figures 6.8 through 6.14 have shown that the number of finite elements used in the generation of the main rotor natural mode shapes had only a small effect on the mode shapes themselves and the corresponding natural frequencies. This section examines the effect of the number of finite elements used in the mode shape calculations on the predicted trim results. The numerical results are generated with the dynamic inflow model and four and eight finite elements. For both sets of results the refined blade model is used with seven modes used in the modal coordinate transformation.

Figures 7.37 through 7.42 show the effect of the number of finite elements on the predicted trim results and the correlation with flight test data. It is shown that the number of finite elements has a negligible effect on the prediction of the trim condition. However, it should be remembered that the blade properties used for the modeling of the BO-105 main rotor blades are uniform along the span. More finite elements may be needed to describe the behavior of the actual blade, which has highly nonuniform properties, especially in the root section, and it may also be necessary to include more blade modes in the modal coordinate transformation.

7.2 UH-60A trim results - straight and level flight

The trim results presented in this section refer to the UH-60A helicopter with the flight control system turned off (base airframe configuration). The two blade modeling configurations for the UH-60A described in Section 6.2 are used to represent blade motion and flexibility. These are the *simple* blade model that includes the rigid flap and lag modes and the *refined* blade model that includes the first six blade modes with the lowest natural frequencies. The flight test data used for comparison have been obtained from Ref. [81] and were measured at an altitude of 5250 feet with a vehicle gross weight of 16000 pounds.

The effect of inflow and blade modeling on the various trim results are shown in Figures 7.43 through 7.50. The results with the baseline flight dynamics model are denoted with the "Dyn. inflow" legend indicating that the Pitt-Peters model is used for the representation of inflow dynamics. The results with the new flight dynamics model that uses the free wake inflow are denoted with the "Free wake" legend. For these results, the vortex filament discretization resolution $\Delta\zeta$ of the wake is 5 degrees, the total length of each vortex filament is 720 degrees, and the initial tip vortex strength is assumed to be equal to the maximum bound circulation along the blade ($C_\Gamma = 1.0$). The two blade models used in the generation of the numerical trim results are the *simple* blade model with the rigid flap and lag modes, denoted with the "2 modes" legend and the *refined* blade model with the first six elastic blade modes, denoted by the "6 modes" legend.

Figure 7.43 shows the correlation for the collective stick input as a function of forward speed. The units on the vertical axis of this figure are the percentages of the control excursion, with 0% corresponding to the lowest collective pitch and 100% corresponding to the highest. Consider first the simulation results with the dynamic

inflow model. The predicted values of the collective stick agree well with the flight test data for speeds greater than about 50 knots, or $\mu \geq 0.1$, however, at lower speeds the collective is underpredicted. This is typical of results generated using a dynamic inflow model, where at advance ratios less than 0.1 the calculated collective pitch is significantly less than that calculated with a more accurate vortex wake model. The results also show very little effect of blade modeling on the predicted main rotor collective stick, most likely because of the structural and aerodynamic coupling between the flap, lag and torsional degrees of freedom. With the free wake inflow model, the prediction of the main rotor collective stick (Fig. 7.43) is considerable improved below 50 knots. This is a results of the higher inflow predicted by the free wake model, compared with that predicted by the dynamic inflow model. For speeds from 50 to about 100 knots, the collective stick is slightly overpredicted with the free wake model.

The correlation for the main rotor power required is shown in Figure 7.44. The trends here are similar to those of the prediction of the collective stick, where below 50 knots, or $\mu \geq 0.1$, the power is significantly underpredicted using the dynamic inflow model while the predictions are significantly improved using the free wake model. In this speed range the majority of the main rotor power required results from induced effects. Because the free wake inflow values are generally higher than those of the dynamic inflow model, a higher power is predicted when using the free wake model. For speeds above 50 knots, the prediction of the power is improved using the free wake model. As with the prediction of the collective stick, the modeling of the blades does not significantly affect the prediction of the main rotor power required.

Figures 7.45 and 7.46 show the correlation of the longitudinal stick input and fuselage pitch attitude for trim respectively. The accurate prediction of the pitching behavior at low speeds is difficult because of the complex aerodynamic interactions

between the main rotor wake and the fuselage and horizontal tail. These aerodynamic interactions are not modeled in this study. With this in mind, both the dynamic inflow and free wake models show a reasonable prediction of the longitudinal stick position over the entire speed range. Both models, however, fail to predict the forward stick required between 20 and 50 knots, which is probably a results of the aerodynamic interactions previously discussed. For the UH-60A, the incidence of the horizontal tail is variable, and is changed by the flight control system as a function of speed. For the current study, the horizontal tail incidence angle is set based on the forward speed. The pitch attitude of the fuselage is predicted well above about 80 knots but is overpredicted by a couple of degrees below this speed.

Figure 7.47 shows the correlation of the lateral stick input for trim. This figure shows only a small influence of the inflow and blade modeling on the prediction of the lateral stick position for trim. The numerical predictions are good for speeds above about 50 knots, however right stick is required for trim in the low speed region below 50 knots and is not captured in the simulation results.

Figure 7.48 shows the predicted pedal position. This quantity is usually coupled to the lateral stick and the required main rotor power. The units on the vertical axis of this figure correspond to the pedal input: 0% is a full left pedal and a high value of tail rotor collective, while 100% is a full right pedal and a low value of tail rotor collective. The prediction of pedal position is improved in the low speed region with the inclusion of the free wake model. This is a result of the higher main rotor torque (and power) predicted with the free wake model, that is balanced by a higher thrust from the tail rotor. This figure also shows that the pedal is predicted more to the right, corresponding to a lower tail rotor collective, over the entire speed range when compared to the flight test data. This is due to the relatively simple way in which the tail rotor is modeled. The Bailey solution [71] (see Section 2.5.4) used

is based on momentum theory and a uniform inflow distribution that leads to an underprediction of the collective pitch required to generate the required tail rotor thrust. This may help to explain the underprediction of the tail rotor collective at all speeds.

Figures 7.49 and 7.50 show the correlation of the fuselage roll attitude and sideslip angle respectively. For $\mu \leq 0.1$, corresponding to $V \leq 45$ knots, the sideslip angle is zero and the trim is performed to a variable roll attitude. A higher fuselage roll attitude to the left is predicted with the free wake model because of the higher tail rotor thrust required to balance the main rotor torque in the low speed region. Both the dynamic inflow and free wake model results for the roll attitude agree well with the flight test data. For speeds above 45 knots, $\mu \geq 0.1$, the roll attitude is zero and the trim is performed to a variable sideslip angle. The prediction of the fuselage sideslip angle is, in general, improved with the free wake model, although in the speed range from 50 to 70 knots, the sideslip angle to the right is overpredicted with the free wake model. This is a result of the higher main rotor torque associated with the free wake model.

7.3 UH-60A trim results - turning flight

The analysis of helicopters in maneuvering flight has become more important as helicopters become more maneuverable with advanced hub designs and higher control power. In particular the analysis of helicopter performance, stability and control in maneuvering flight has been receiving increased attention. The focus of this section is the trim analysis of helicopters in steady coordinated level turns.

The current flight dynamic model is capable of modeling helicopter behavior in maneuvering flight where the deviations from trim need not be small. In addition,

the calculation of the trim equilibrium position in steady coordinated turns, as well as in climbing and descending flight is possible. The free wake model used in the current study is of a maneuvering type and has the ability to capture the effects of steady maneuvers on the wake geometry and subsequent inflow distribution. In particular, the wake distortions associated with pitch and roll rates encountered during steady turns are captured by the free wake model. The baseline flight dynamics model, which uses a dynamic inflow model, does not include wake distortion effects in the inflow model and so cannot fully capture the pitch and roll rate effects during steady maneuvering flight.

The trim results presented in this section refer to the UH-60A in steady coordinated turning flight at a constant altitude and a forward speed of 100 knots. The refined blade model for the UH-60A, as described in Section 6.2, is used to represent the blade motion and flexibility. This blade model includes the first six blade modes with the lowest natural frequencies. The flight test data used for comparison have been obtained from Ref. [81] and were measured at an altitude of 5250 feet with a gross vehicle weight of 16000 pounds.

Figures 7.51 through 7.56 show the trim quantities for the UH-60A in a level coordinated turn at a forward speed of 100 knots. The numerical results are obtained as a function of the prescribed turn rate $\dot{\psi}$ and then plotted as a function of the bank angle ϕ_F. In these figures, the curves marked "Free wake inflow" are calculated with the flight dynamics model that includes the maneuvering free wake model and the curves marked "Dynamic inflow" are calculated using the baseline flight dynamics model that includes dynamic inflow.

Figure 7.51 shows the trim pitch attitude θ_F versus roll attitude ϕ_F and compares the simulation results with flight test data. For turns to the right, where the roll attitude of the fuselage is positive, the prediction of the pitch attitude is

improved with the free wake model. However for turns to the left, where the roll attitude is negative, the predictions with dynamic inflow correlate better with the test data. For left turns the pitch attitude is underpredicted by about two degrees with the free wake model where the fuselage pitches to a lower nose-up attitude. The study of Chen and Jeske [55] showed that the pitch attitude is very sensitive to the aircraft sideslip angle in turning flight, which contributes to the discrepancies in the prediction of the pitch attitude. For the calculation of the numerical results, turn coordination is assumed where the average lateral acceleration over one rotor revolution is zero. This turn coordination assumption will effect the prediction of the sideslip angle, and based on the work of Chen and Jeske [55], also the predicted pitch attitude. Figure 7.54 shows the longitudinal stick position required for trim versus roll attitude. The numerical results show that the free wake model predicts a more aft stick position then with dynamic inflow and that the offset between the two sets of results is virtually independent of the roll attitude. The more aft stick required with the free wake model causes a more aft tilt of the tip path plane which compensates for the lower nose-up pitch attitude associated with the free wake pitch results.

The predicted values of the main rotor power required and collective pitch agree well with the flight test data as shown in Figures 7.56 and 7.52, with the free wake model predictions showing a better accuracy for all bank angles. As expected there is an increase in the rotor thrust and power requirements as the helicopter negotiates a tighter turn. The figures also indicate that the thrust required for turns to the right is greater than for turns to the left, although the differences are fairly small. The reason for this is that the yaw rates associated with turning flight reduce the effective rotor speed for right turns and increase it for left turns.

Comparisons for the predictions of the pedal and lateral stick positions are shown

in Figures 7.55 and 7.53. The inflow model has little effect on the prediction of the pedal input and the simulation results underpredict the right pedal when compared to flight test data for all turn rates. The differences between the flight test and simulation results are probably a result of the relatively simple way in which the tail rotor thrust is calculated. Another contributing factor would be the prediction of the sideslip angle, which will also effect the thrust of the tail rotor. Improvements in the prediction of the fuselage sideslip angle and in the modeling of the tail rotor should lead to improvements in the pedal predictions. The lateral stick predictions show an excellent agreement with flight test data and the predictions are also virtually independent of the inflow model.

Figures 7.57 and 7.58 show a comparison of the free wake geometries in straight and level and turning flight conditions at 100 knots. In particular, rear and side views of the wake geometries in left and right turns at a turn rate of 15 deg/sec are compared with those obtained in straight and level flight. Looking at the figures showing the wake geometries from the retreating side, the positive (nose-up) pitch rate associated with both left and right turns causes the wake to be swept back more in the plane of the rotor, and not as much below the rotor as in the straight flight case. The figures also show that the positive roll rates for right turns and negative roll rates for left turns do not have a significant effect on the wake geometries. This is evident in looking at the views of the wake geometries from the rear, which show only slight differences in the wake geometries for the positive and negative roll rates associated with right and left turns. Any differences in the wake geometries resulting from the different roll rates should be most visible in the rear views of the wake geometries, however only small differences are observed. This indicates that the wake geometry changes due to pitch rate, which are similar for both right and left turns, are more significant than those of the roll rate, which have opposite sign

for left and right turns.

7.4 Discussion of trim results

This section contains a further discussion of the trim results for the BO-105 and UH-60A helicopters presented earlier in this chapter.

The BO-105 trim results indicate that there is an issue related to the aerodynamic modeling of the fuselage. Figures 7.1 and 7.2 show that the main rotor collective and power required are significantly underpredicted when compared with flight test data in the high speed range where the effects of fuselage modeling are strongest. The aerodynamic forces and moments on the fuselage are calculated from aerodynamic coefficients that are presented in look-up tables as functions of the angles of attack and sideslip. The coefficients themselves were obtained from wind tunnel data. The underprediction of the main rotor collective and power required suggests that the fuselage aerodynamic drag is being under-predicted. The results of Section 7.1.4 show that the collective and power predictions are significantly improved with a simple fuselage drag model with an equivalent flat-plate area of 20 ft^2 for the fuselage aerodynamic drag calculations. This simple model does not include yawing and pitching moments due to angles of attack and sideslip and correspondingly worsens the predictions of the pitch attitude and sideslip angle.

With respect to the effect of blade modeling on the trim calculations, the numerical results presented in this chapter are generated using two different blade models are used for both the BO-105 and UH-60A. These are a simple blade model that includes a minimum number of blade modes, and a refined blade model that includes additional blade mode shapes with additional degrees of freedom. For the UH-60A there was essentially no difference in the trim results with the two blade models.

However, for the BO-105 the results showed a number of differences. The most significant of these was to the main rotor collective where the use of the refined blade model predicted a two to three degree increase in the collective when compared with the simple blade model predictions. This difference is fairly uniform over the entire speed range. The increase in collective is attributed to the blade elastic twist that is present with the refined blade model but not with the simple blade model that does not include torsional degrees of freedom. While the elastic twist is dependent on the forward speed and blade azimuth angle, a nose down elastic twist of between two and five degrees is consistently observed (Figs. 7.9 and 7.10). This translates into an increase in the main rotor collective required to produce the required thrust for trim. The BO-105 main rotor blades are modeled with uniform mass and stiffness distributions and the sectional center of gravity is coincident with the elastic axis along the blade which results in no structural pitch-flap or pitch-lag coupling. The quasi-steady aerodynamics model does however introduce aerodynamic pitch-flap coupling in the form of pitching moments due to flap rate. In hover, the cyclic variations in blade section aerodynamic environment and flapping are small, so the pitching moments due to aerodynamic pitch-flap coupling will likewise be small. Here the nose down elastic twist is therefore almost entirely due to the non-zero pitching moments coefficients that act about the 1/4-chord location and are fundamental to the airfoil. If these steady pitching moment coefficients were assumed to be zero, then the large nose down elastic tip twist would not be present and the prediction of the collective would be considerably different. In addition to this a non-zero offset between the sectional center of gravity and elastic axis would introduce structural pitch-flap coupling which would further alter the torsional dynamics, including the blade elastic twist and thus the prediction of the main rotor collective.

The use of the free wake model to calculate the main rotor inflow improves the

correlation of the trim predictions with flight test data for both the BO-105 and UH-60A. The two free wake parameters that were investigated in this chapter were the resolution of the wake and the initial tip vortex strength. The results of Section 7.1.3 show that the wake resolution does not effect the trim results but for speeds below about 50 knots no trim condition could be reached. This is characterized by the failure of the wake geometry loop, within the free wake model, to converge.

The second free wake parameter investigated in this chapter was the amount of bound vorticity that is assumed to roll up into the trailed tip vortex. The initial strength of the tip vortex is given as a percentage of the maximum bound circulation along the blade at each azimuth angle. Considering the hover flight condition, the initial tip vortex strength is particularly important as there is an almost direct relationship between this tip vortex strength and the resulting inflow. There is also an almost direct relationship between the inflow and the power required because in hover almost all of the power required by the rotor is induced in nature. Figures 7.2 and 7.44 show the power predictions for the BO-105 and UH-60A helicopters respectively, and that with dynamic inflow in hover, the power is under-predicted. This is because, in hover, the use of momentum theory leads to an under-prediction of the inflow and so the power.

The use of the free wake model produces a hover power prediction that is significantly higher than that predicted with dynamic inflow, mainly as a result of the higher inflow values associated with the free wake model. By assuming that all of the vorticity outboard of the peak value is contained in the tip vortex, an excellent agreement is found between the numerical predictions and flight test data for the UH-60A (Fig. 7.44) over the entire speed range. For the BO-105 the power required (Fig. 7.2) to hover is significantly over-predicted with $C_\Gamma = 1.00$. However if it is assumed that only 70% ($C_\Gamma = 0.70$) of the peak bound circulation ends up in the

tip vortex, then the power prediction for the BO-105 is improved (Fig. 7.13). A possible source of the differences between the BO-105 and UH-60A results is related to the blade structural twist, which significantly effects the blade loading and circulation distributions. For the UH-60A, the rotor is optimized for low speed and hovering flight and thus includes a high amount of structural twist (-14.0^o from root to tip) which has the effect of producing a more uniform lift distribution and a more linear circulation distribution. For the BO-105, the small amount of blade twist (-6.2^o from root to tip) produces a more linear lift distribution and a more parabolic circulation distribution. It is not clear how these differences in lift and circulation distributions effect the characteristics of the tip vortices. For modeling purposes, it may be more appropriate to use an average, or weighted average bound circulation to define the tip vortex characteristics rather than the peak value.

The effect of inflow modeling on trim predictions in level coordinated turns was investigated for the UH-60A at a forward speed of 100 knots. The simulation results showed that inflow modeling has a more significant effect on the trim quantities related to the longitudinal dynamics than those related to the lateral-directional dynamics. The predictions of the lateral stick and pedal positions were not significantly effected by inflow modeling, however, noticeable differences were observed in the predictions of the pitch attitude and of the longitudinal stick position. The calculation of the simulation results involves the assumption of turn coordination, which ensures that the lateral acceleration is zero when averaged over one rotor revolution, and this assumption significantly effects the prediction of the sideslip angle. Because the pitch attitude is very sensitive to the sideslip angle in turning flight, small changes in the sideslip angle can have noticeable effects on the prediction of the pitch attitude and of the longitudinal stick position because these two quantities are related.

The main rotor collective, power required and lateral cyclic were predicted with good accuracy using both inflow model, however, the results with the free wake inflow model showed a slightly better agreement with the flight test data. The extent of the right pedal was underpredicted with both inflow models and these inaccuracies can be attributed to the relatively simple model used for the tail rotor thrust calculations. Wake geometries for varying turn rates showed that the magnitude of the turn rate has a more significant effect on the wake geometry than the direction of the turn, which has only a small effect. The pitch rate, which is positive for both left and right turns, has a large effect on the wake geometry, while the roll rate, which is positive for right turns and negative for left turns, has only a small effect on the wake geometries. This indicates that the pitch rate effects are more significant than the roll rate effects on the wake geometries and inflow distributions.

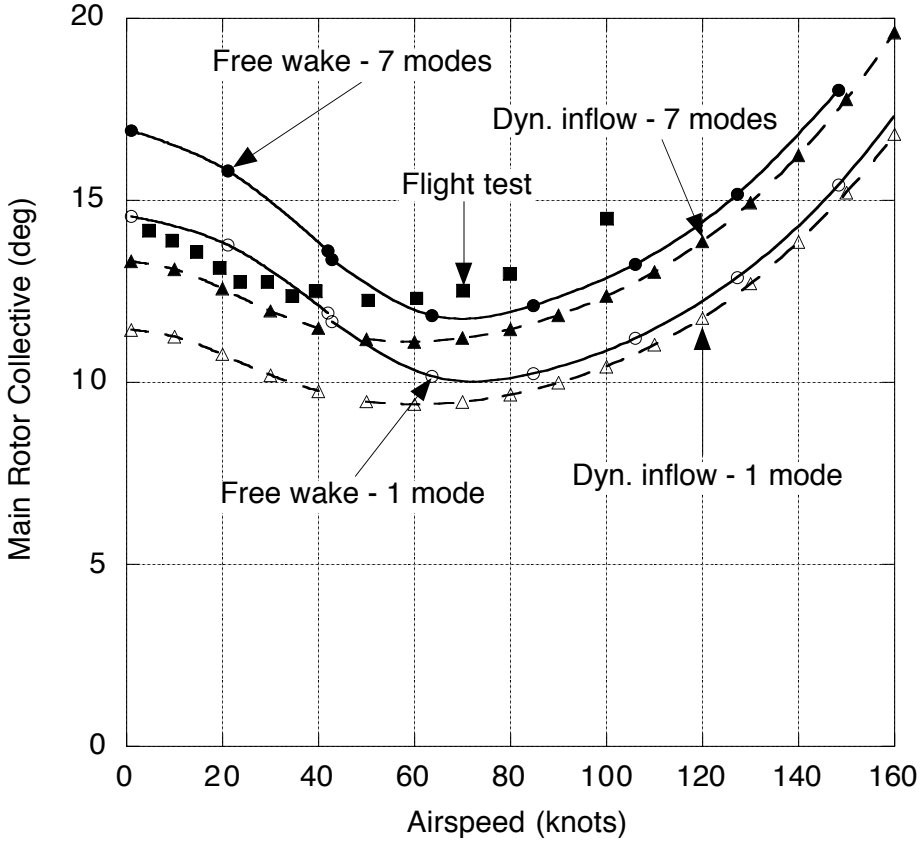

Figure 7.1: Effect of inflow models and blade modeling on main rotor collective pitch required for trim versus airspeed for the BO-105 in straight and level flight.

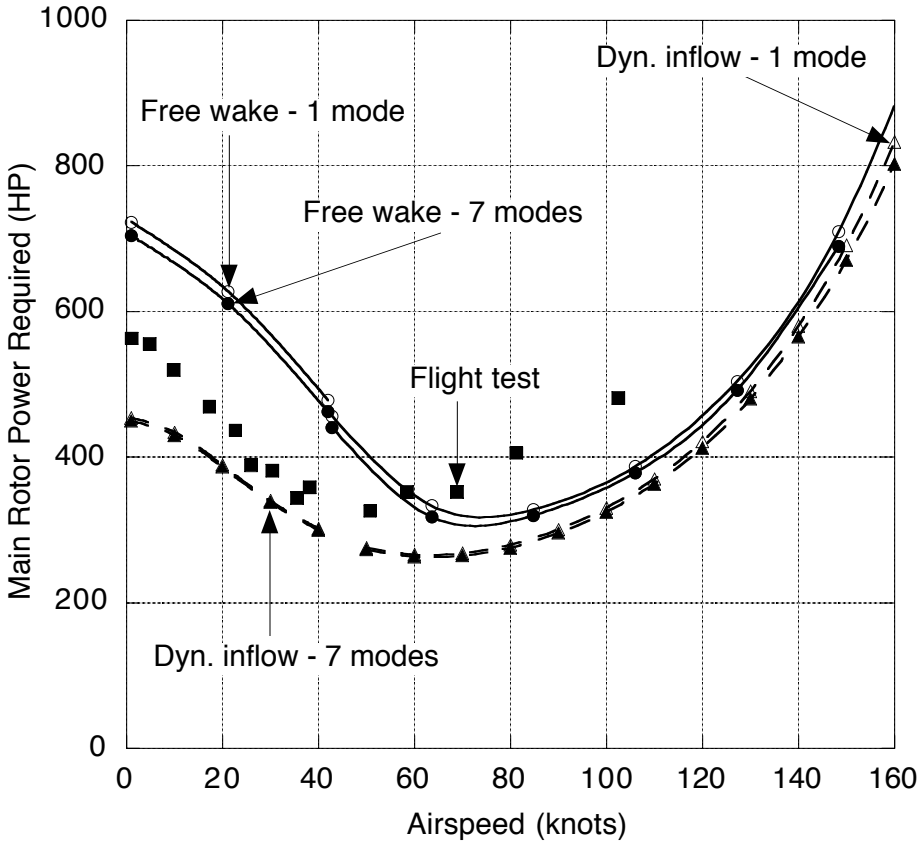

Figure 7.2: Effect of inflow models and blade modeling on main rotor power required for trim versus airspeed for the BO-105 in straight and level flight.

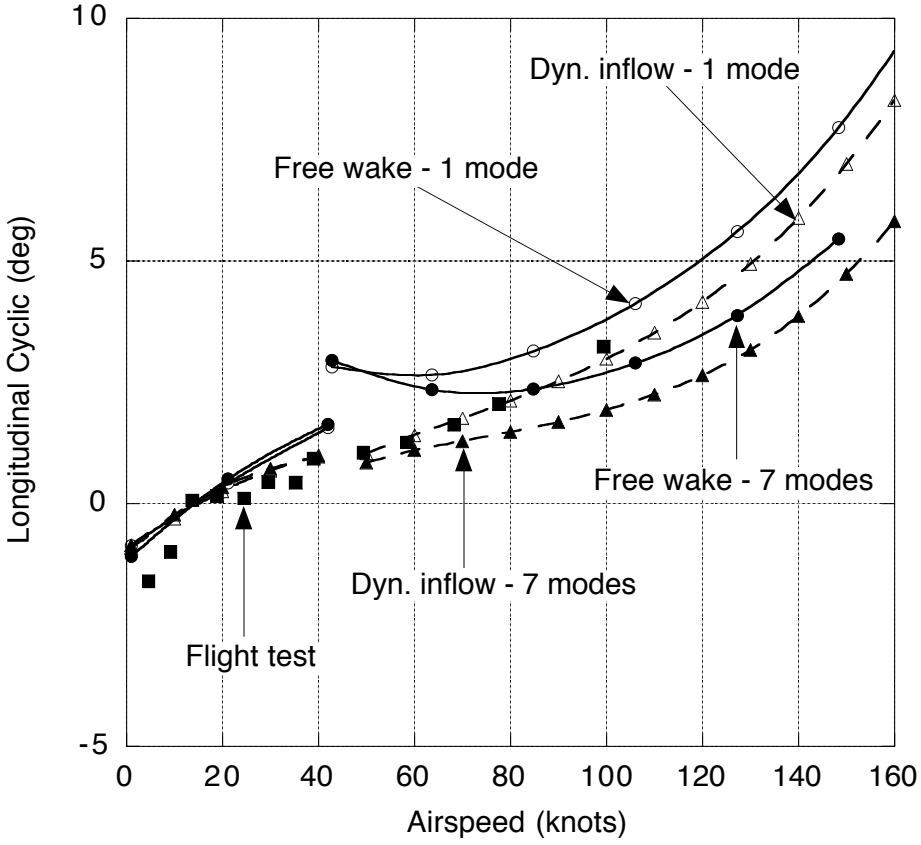

Figure 7.3: Effect of inflow models and blade modeling on longitudinal cyclic pitch required for trim versus airspeed for the BO-105 in straight and level flight.

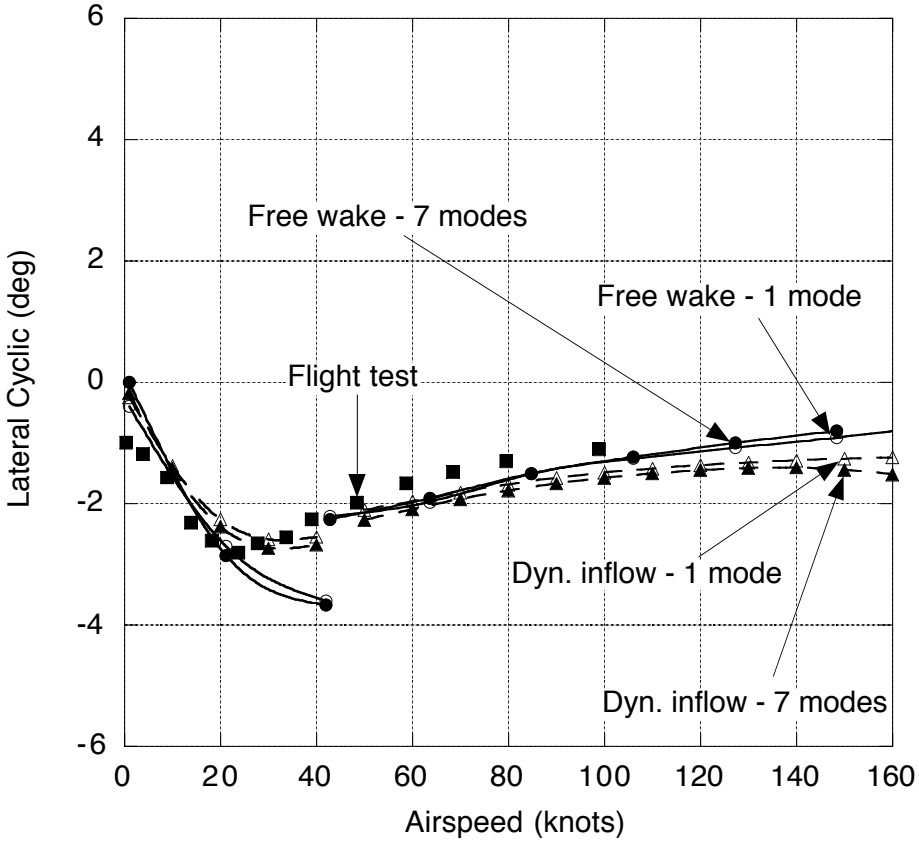

Figure 7.4: Effect of inflow models and blade modeling on lateral cyclic pitch required for trim versus airspeed for the BO-105 in straight and level flight.

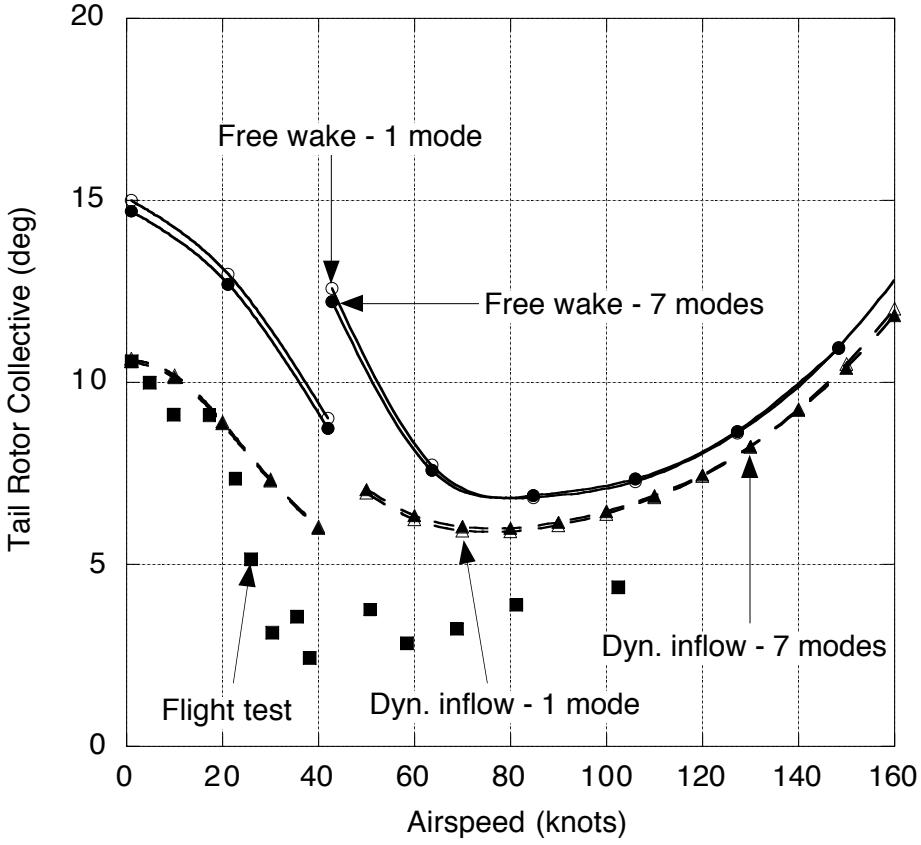

Figure 7.5: Effect of inflow models and blade modeling on tail rotor collective pitch required for trim versus airspeed for the BO-105 in straight and level flight.

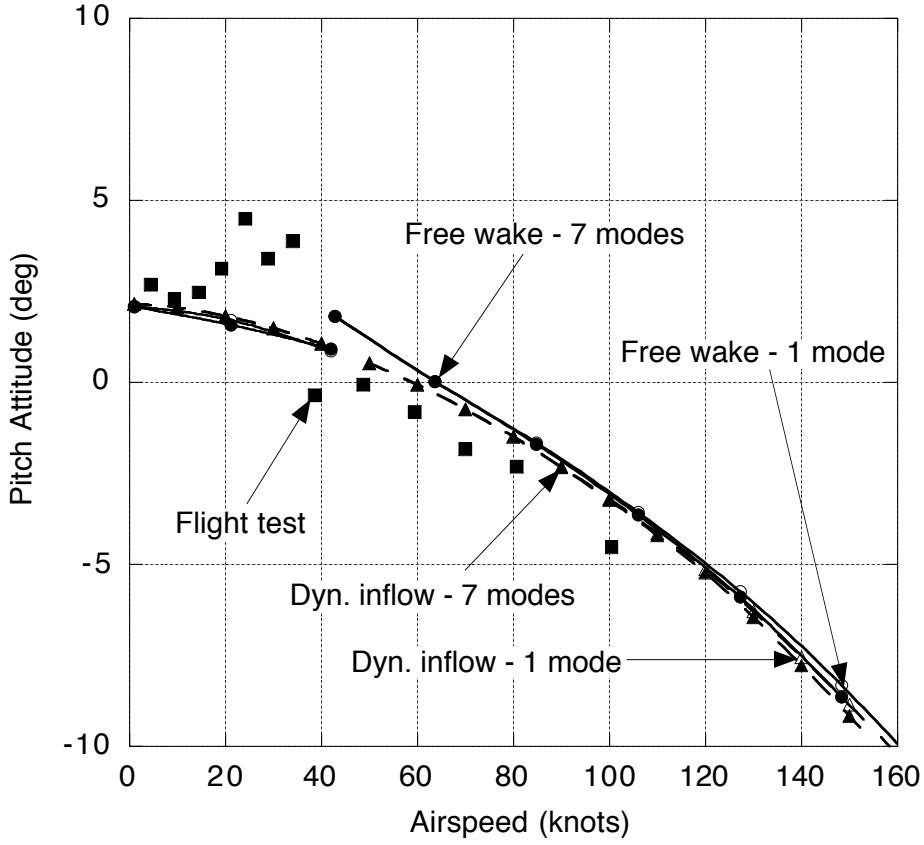

Figure 7.6: Effect of inflow models and blade modeling aircraft pitch attitude for trim versus airspeed for the BO-105 in straight and level flight.

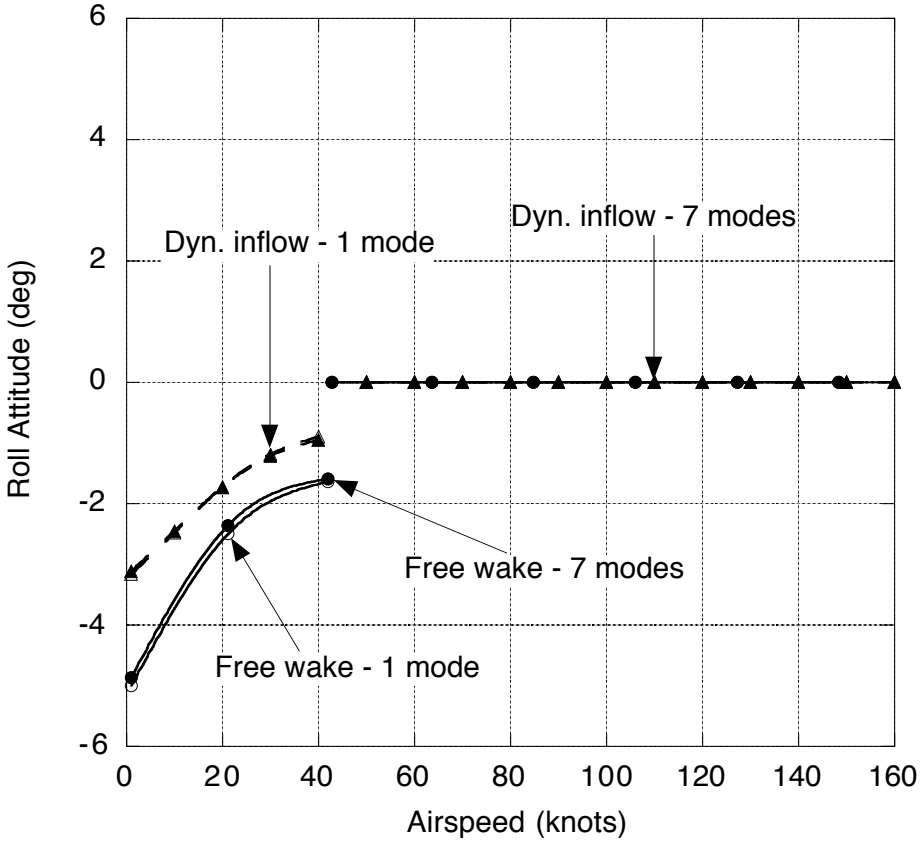

Figure 7.7: Effect of inflow models and blade modeling on aircraft roll attitude for trim versus airspeed for the BO-105 in straight and level flight.

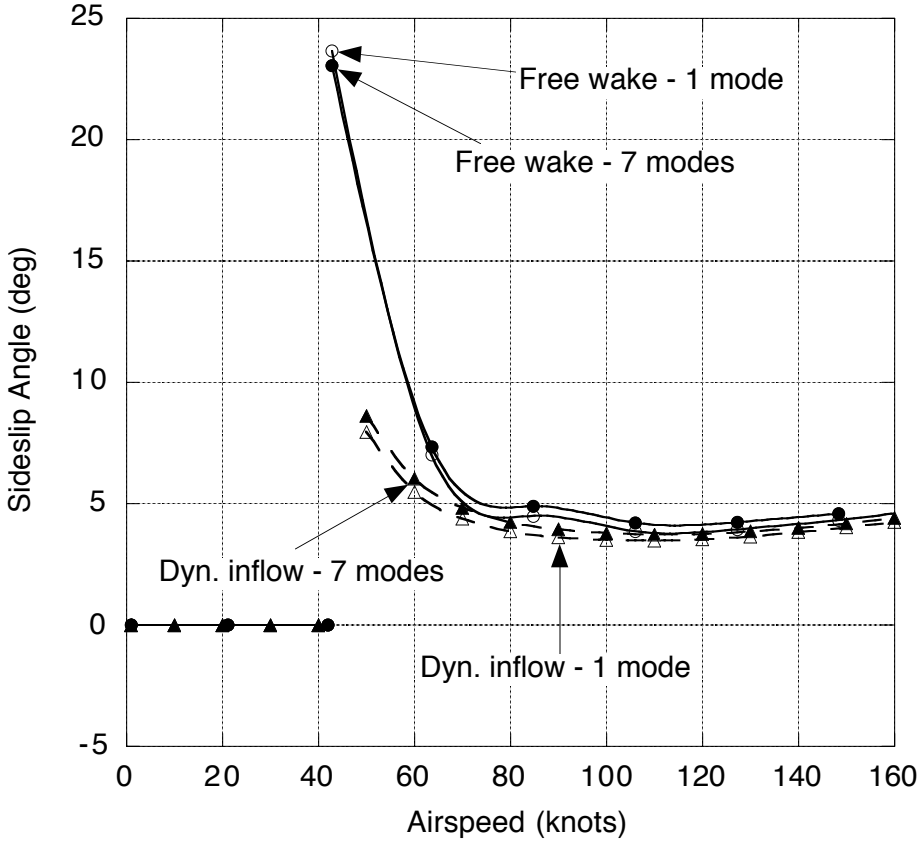

Figure 7.8: Effect of inflow models and blade modeling on aircraft sideslip angle for trim versus airspeed for the BO-105 in straight and level flight.

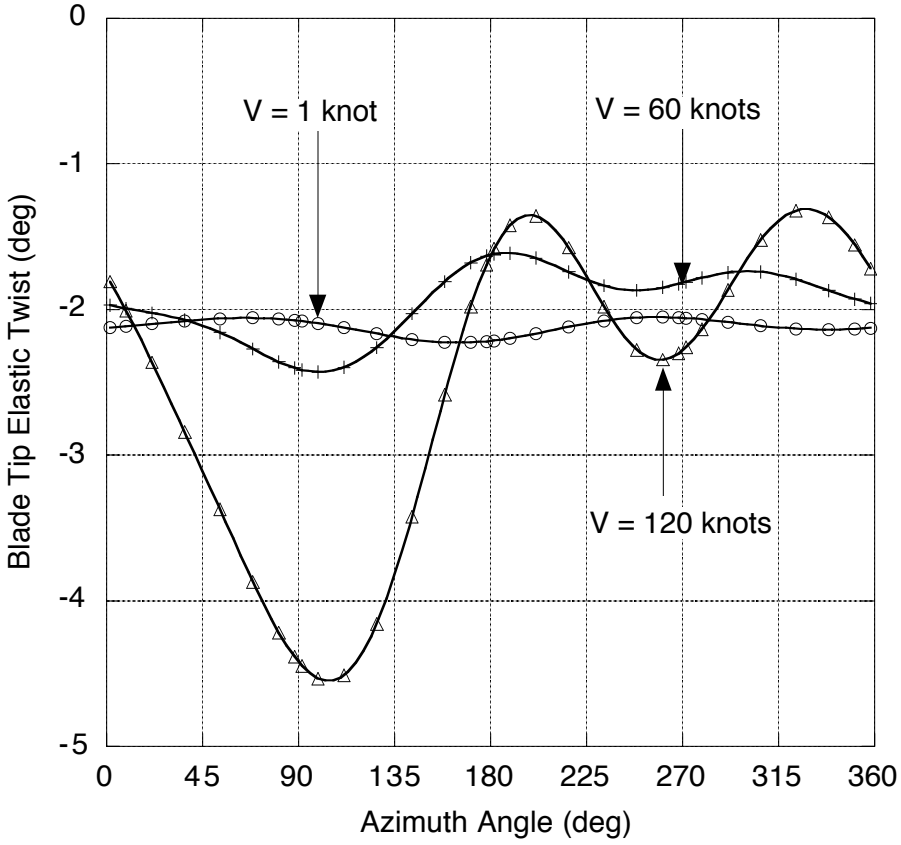

Figure 7.9: Effect of forward speed on blade tip elastic twist versus azimuth angle for the BO-105 with dynamic inflow and the refined blade model.

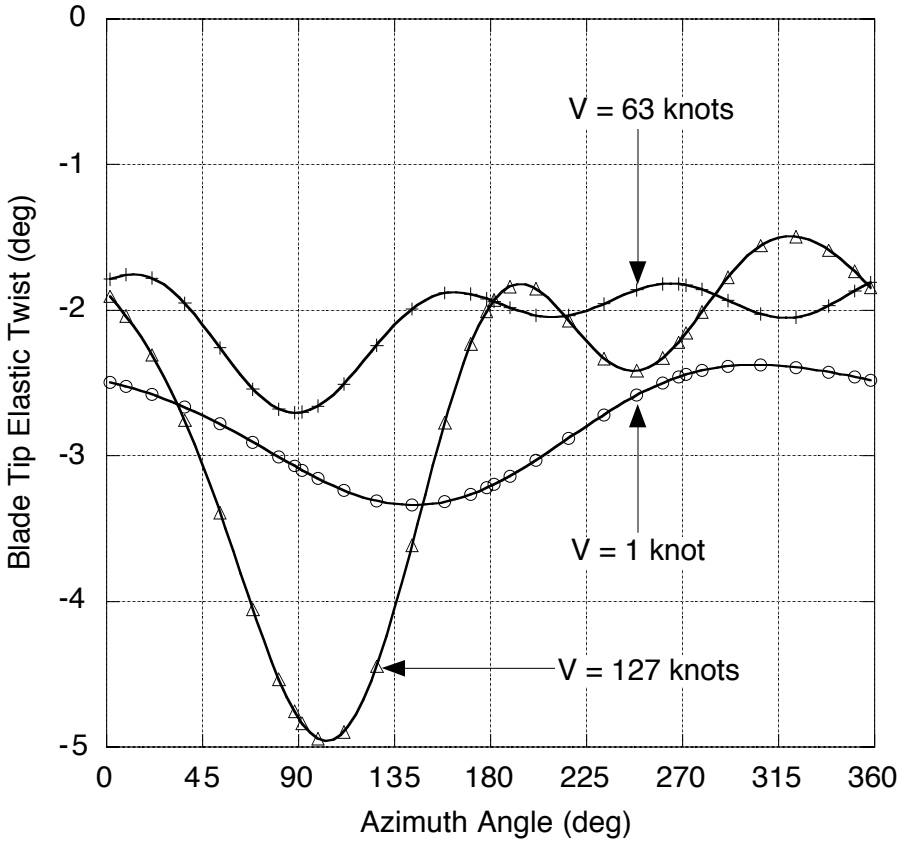

Figure 7.10: Effect of forward speed on blade tip elastic twist versus azimuth angle for the BO-105 with the free wake and the refined blade model.

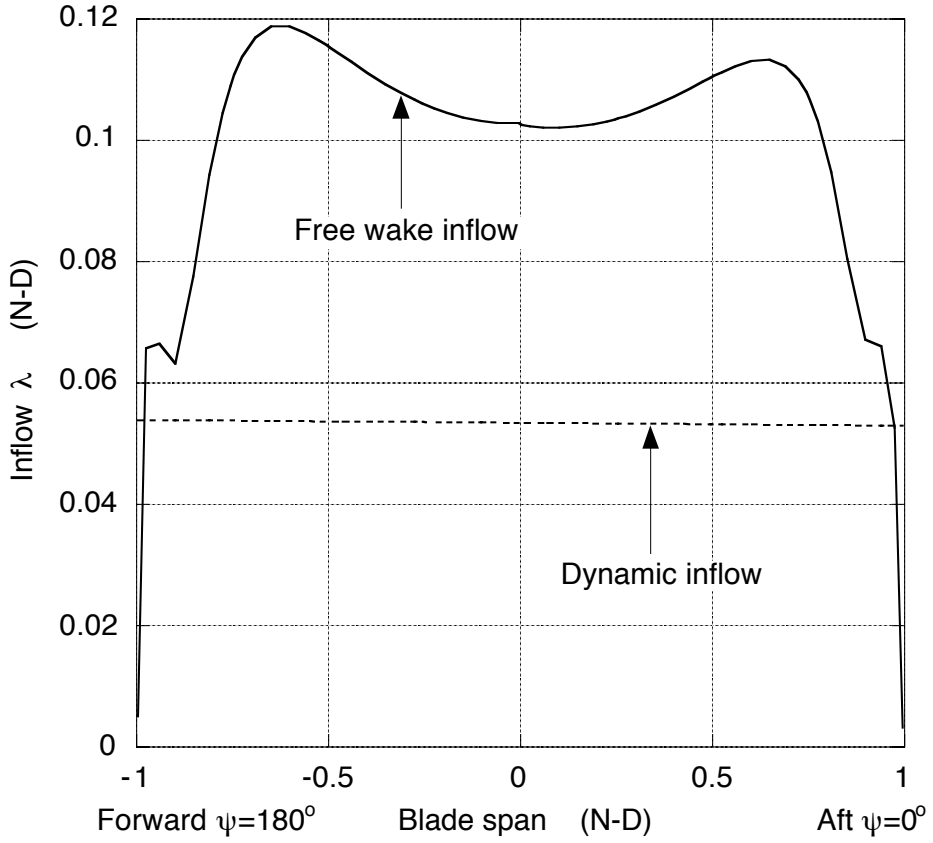

Figure 7.11: Effect of inflow modeling on the longitudinal inflow variation for the BO-105 in hover with the refined blade model.

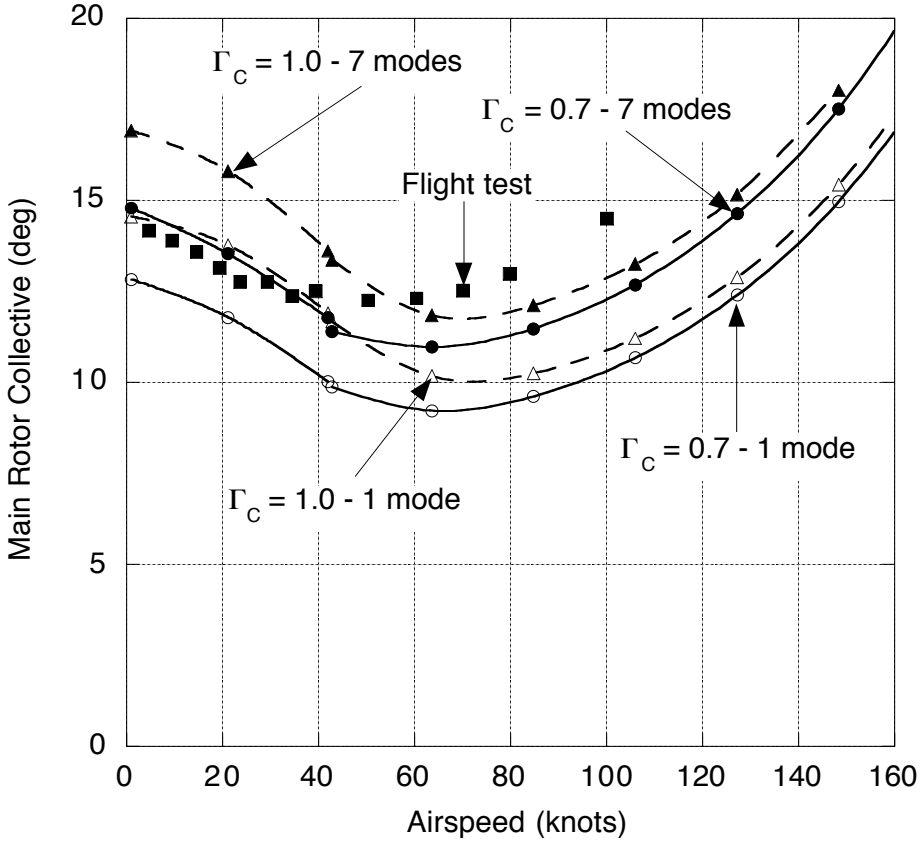

Figure 7.12: Effect of tip vortex strength on main rotor collective pitch required versus airspeed for the BO-105 in straight and level flight.

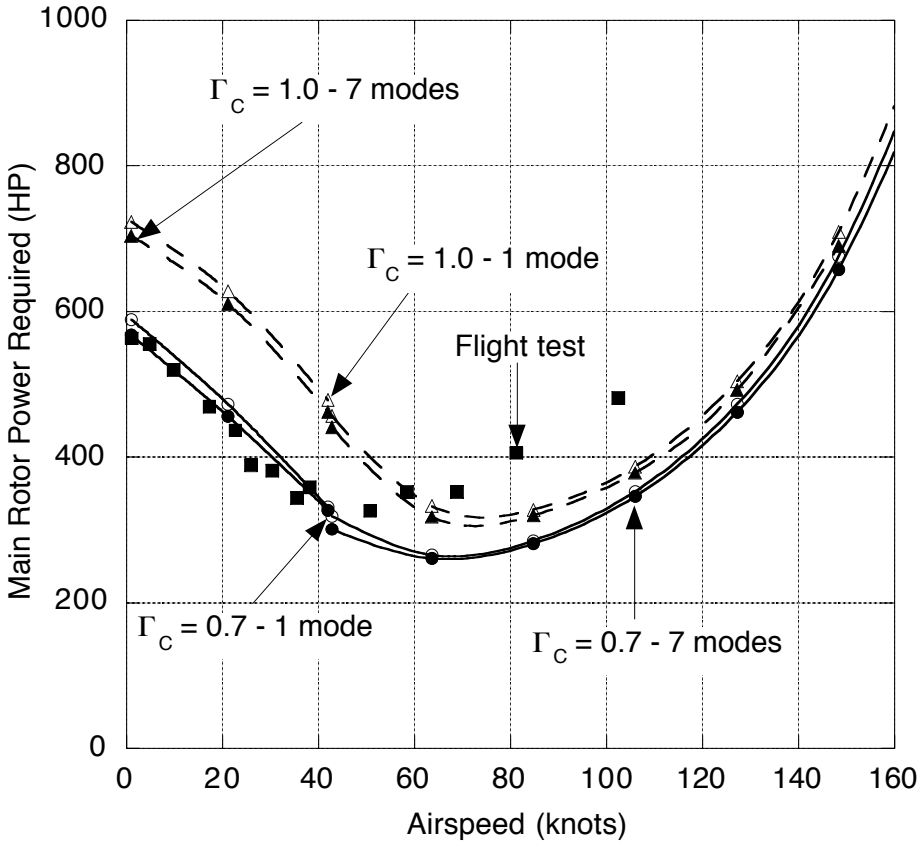

Figure 7.13: Effect of tip vortex strength on main rotor power required versus airspeed for the BO-105 in straight and level flight.

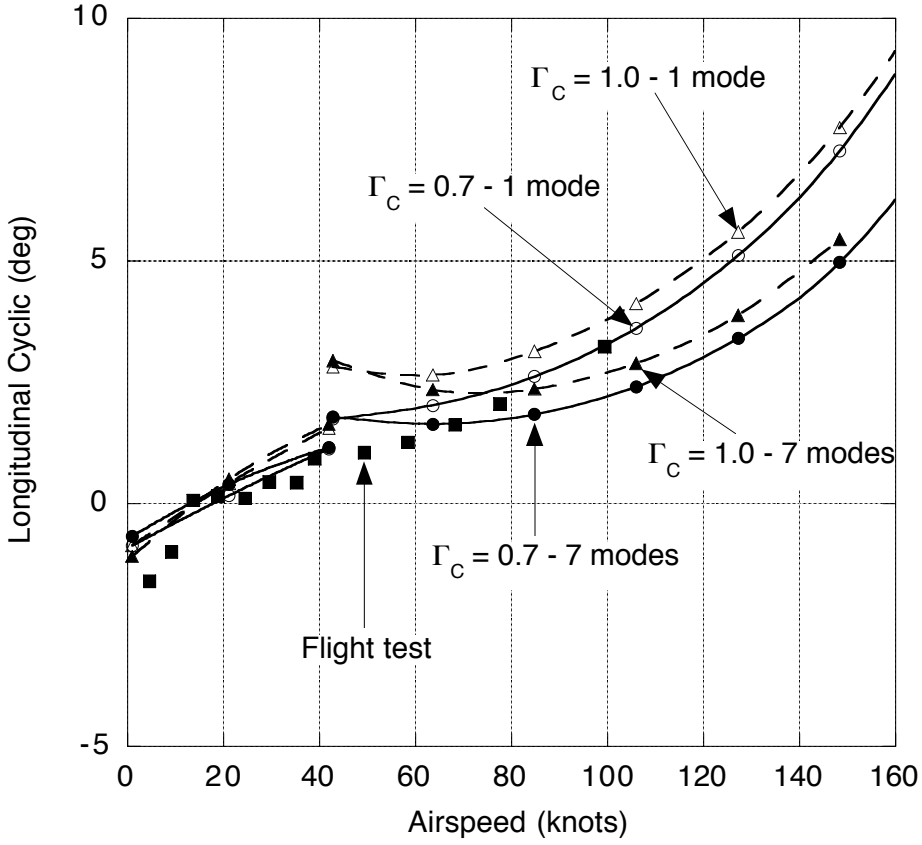

Figure 7.14: Effect of tip vortex strength on longitudinal cyclic pitch required versus airspeed for the BO-105 in straight and level flight.

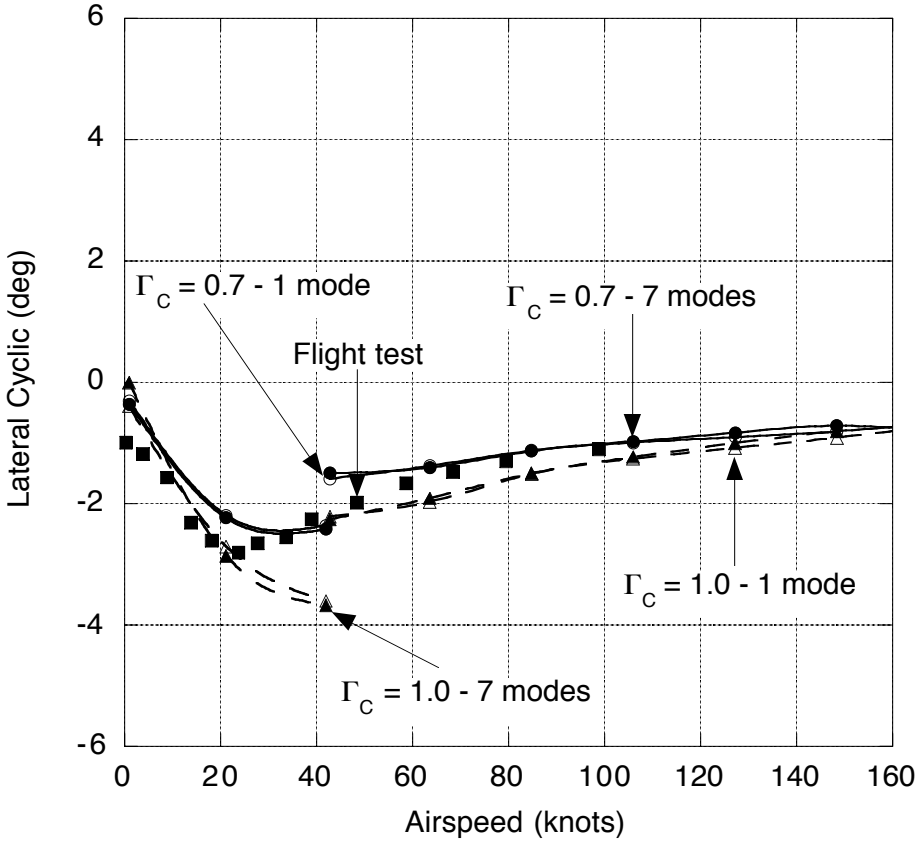

Figure 7.15: Effect of tip vortex strength on lateral cyclic pitch required versus airspeed for the BO-105 in straight and level flight.

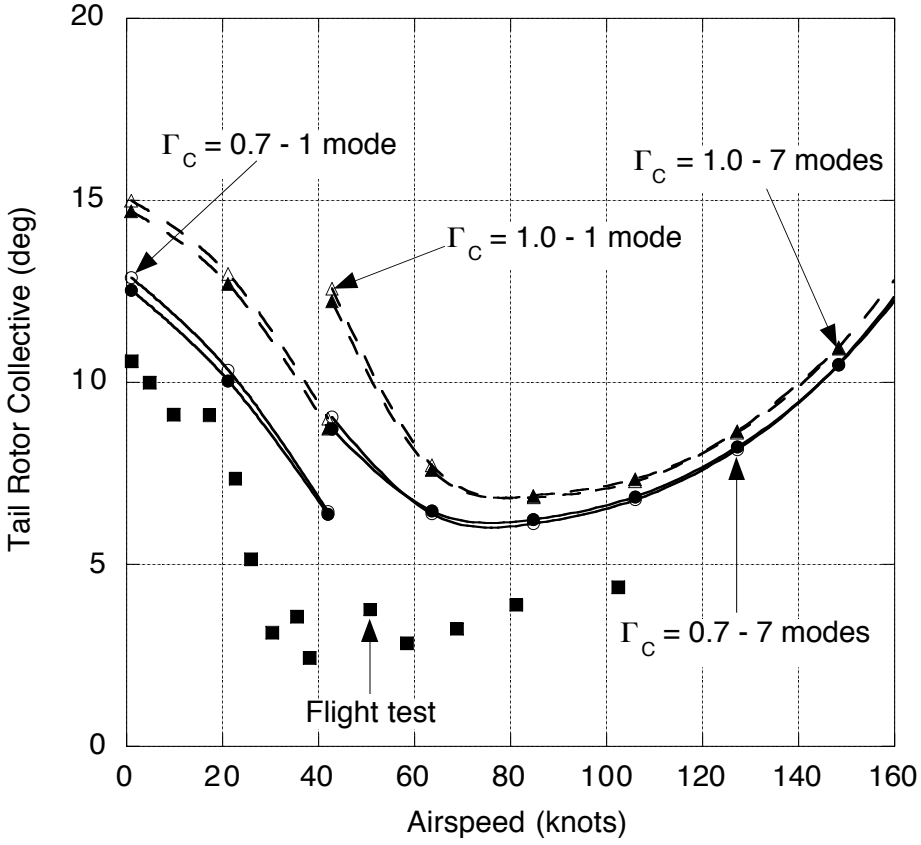

Figure 7.16: Effect of tip vortex strength on tail rotor collective pitch required versus airspeed for the BO-105 in straight and level flight.

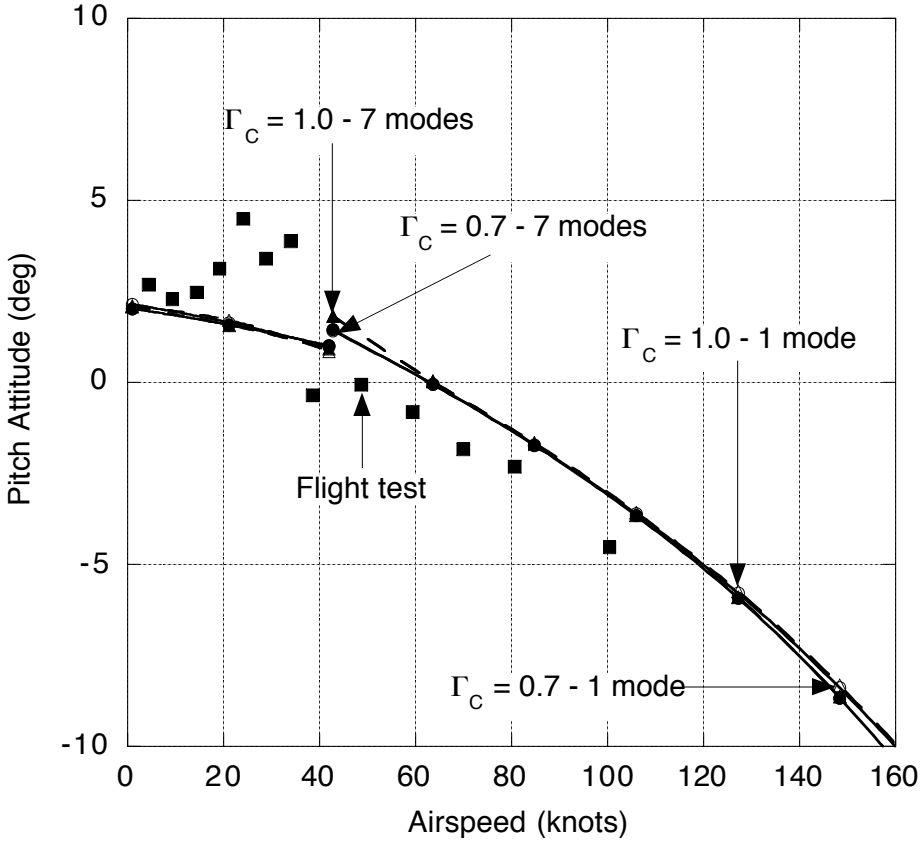

Figure 7.17: Effect of tip vortex strength on aircraft pitch attitude versus airspeed for the BO-105 in straight and level flight.

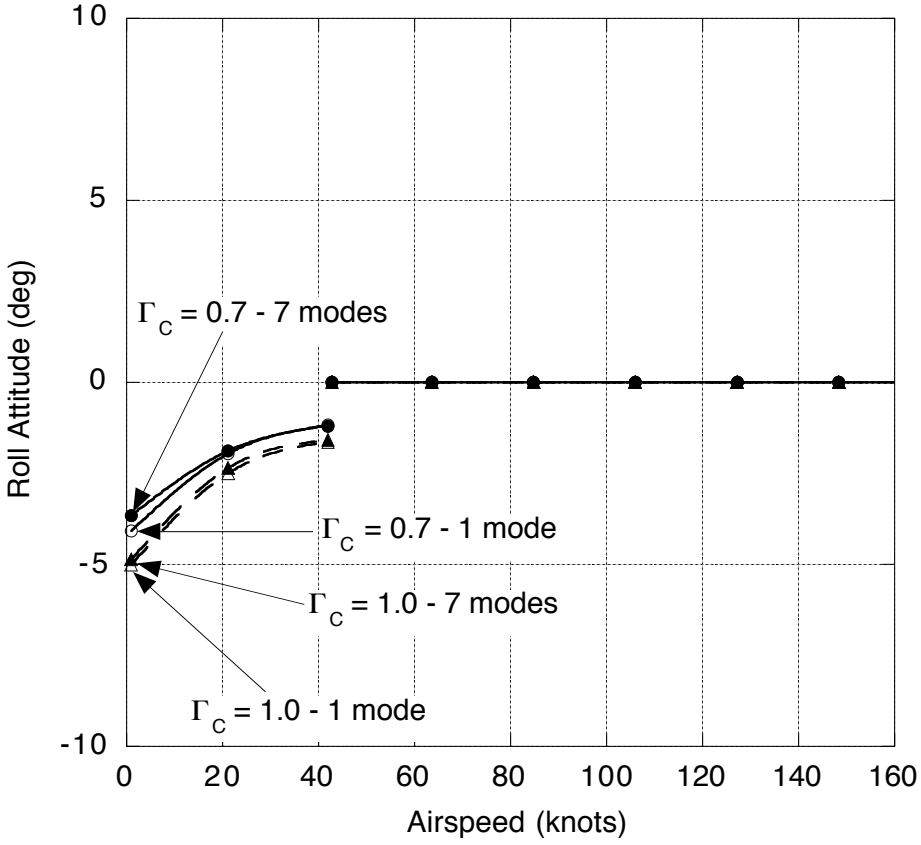

Figure 7.18: Effect of tip vortex strength on aircraft roll attitude versus airspeed for the BO-105 in straight and level flight.

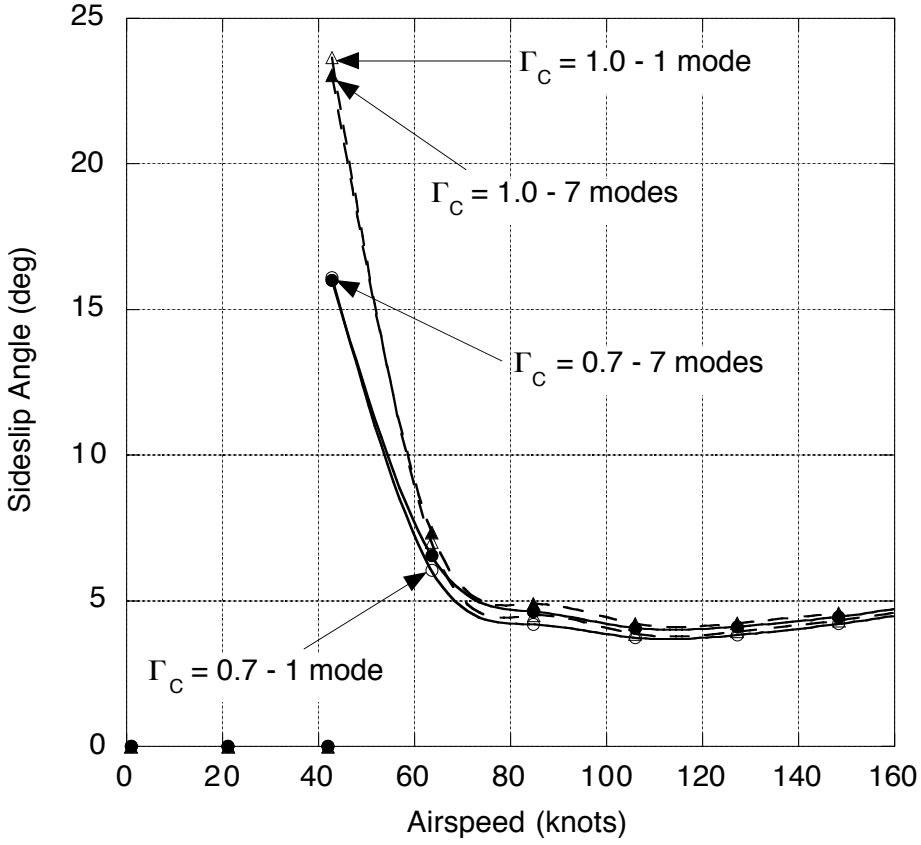

Figure 7.19: Effect of tip vortex strength on aircraft sideslip angle versus airspeed for the BO-105 in straight and level flight.

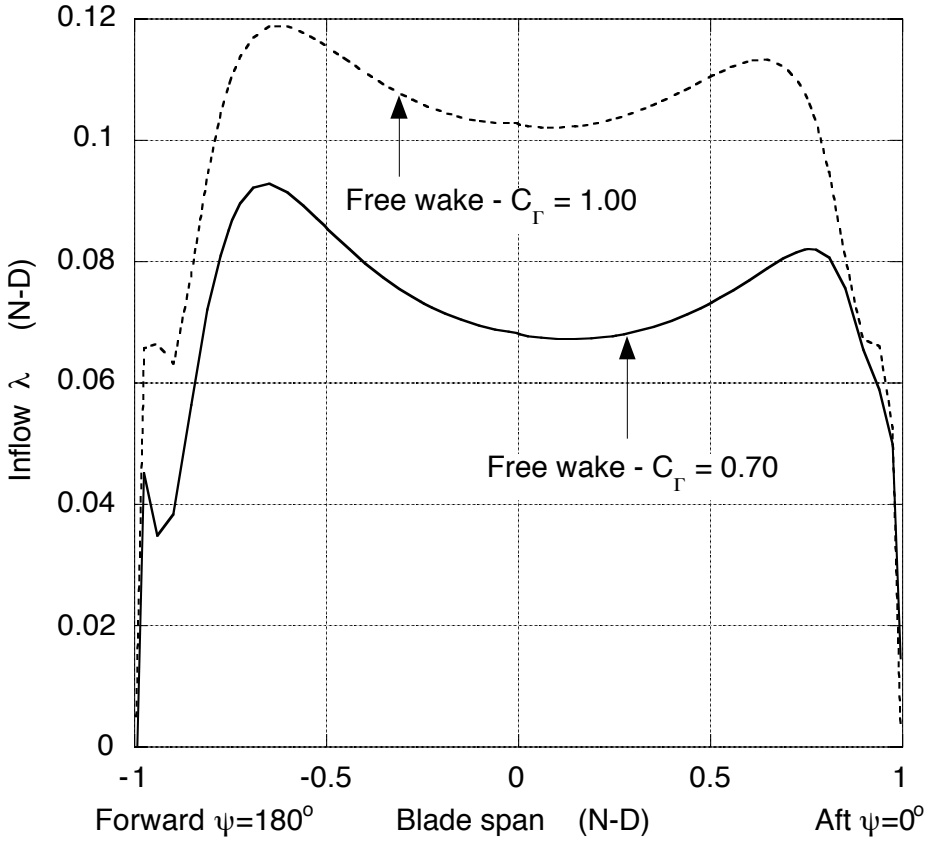

Figure 7.20: Effect of tip vortex strength on the longitudinal inflow variation in inflow for the BO-105 in hover with the refined blade model.

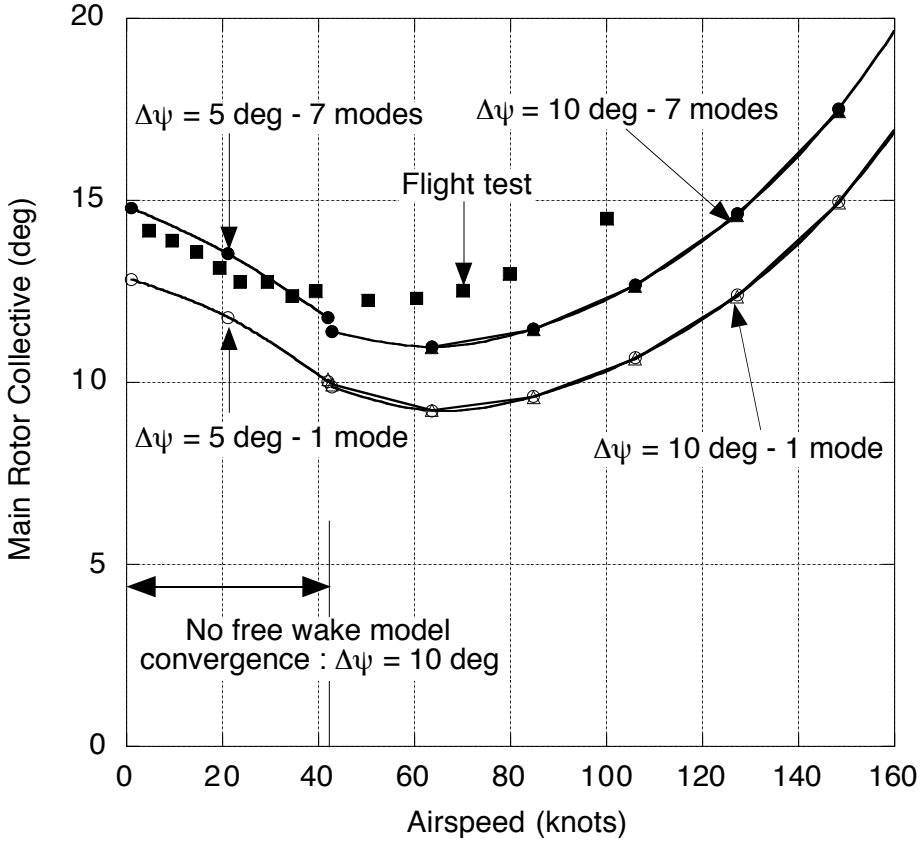

Figure 7.21: Effect of free wake resolution on main rotor collective pitch versus airspeed for the BO-105 in straight and level flight.

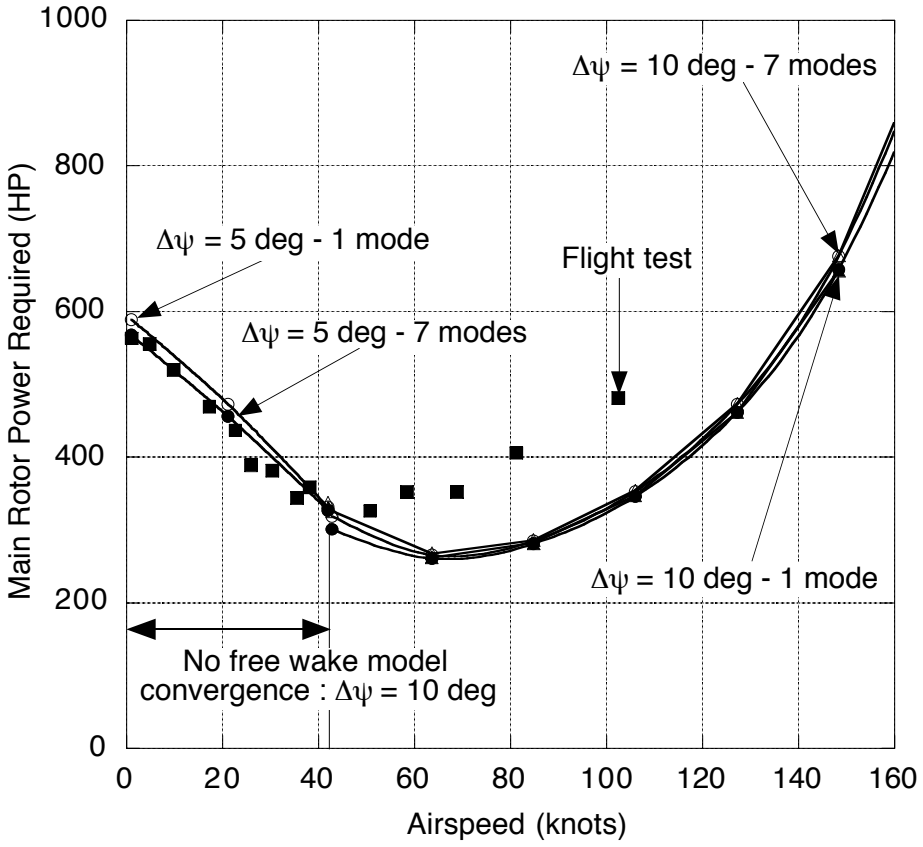

Figure 7.22: Effect of free wake resolution on main rotor power required versus airspeed for the BO-105 in straight and level flight.

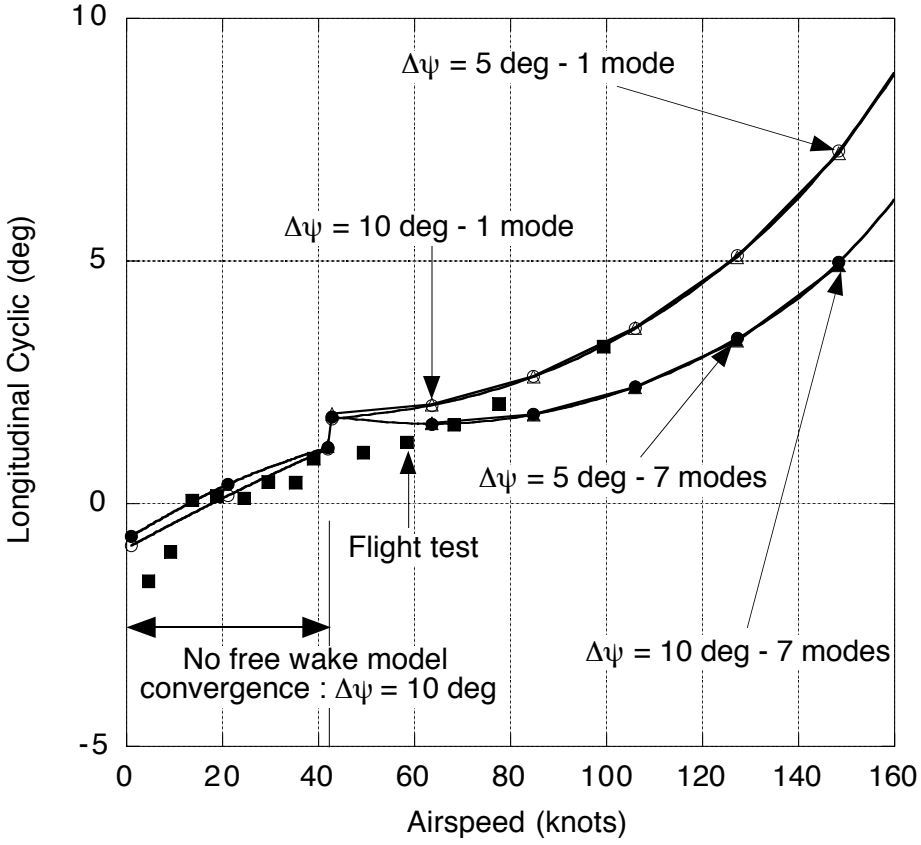

Figure 7.23: Effect of free wake resolution on longitudinal cyclic pitch versus airspeed for the BO-105 in straight and level flight.

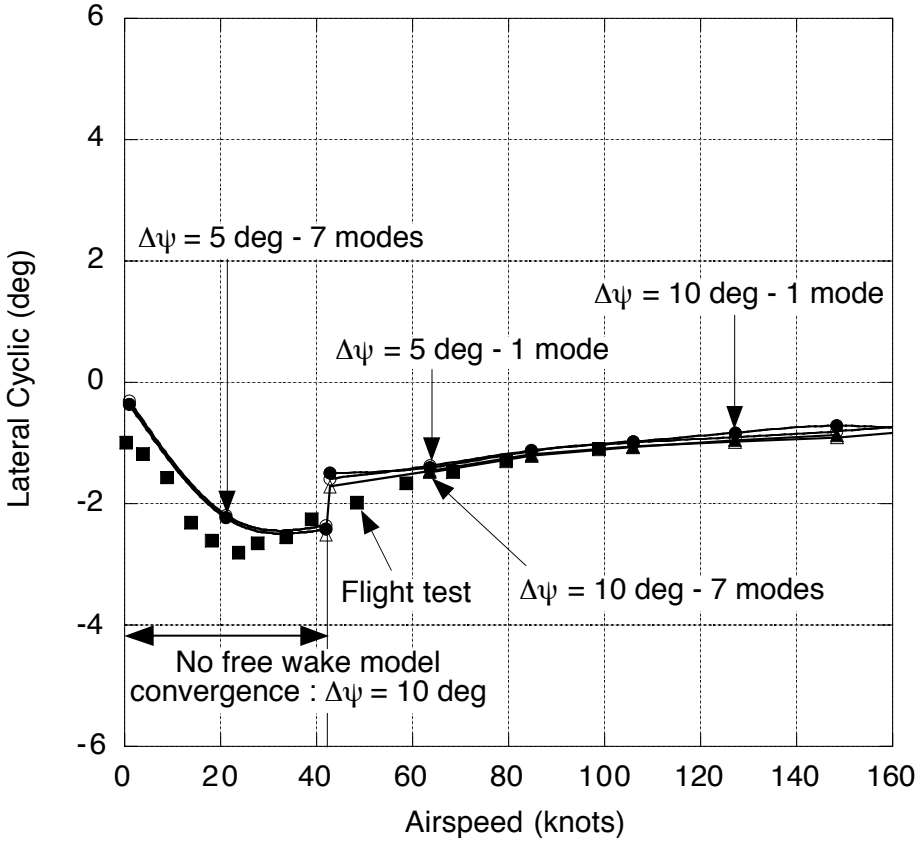

Figure 7.24: Effect of free wake resolution on lateral cyclic pitch versus airspeed for the BO-105 in straight and level flight.

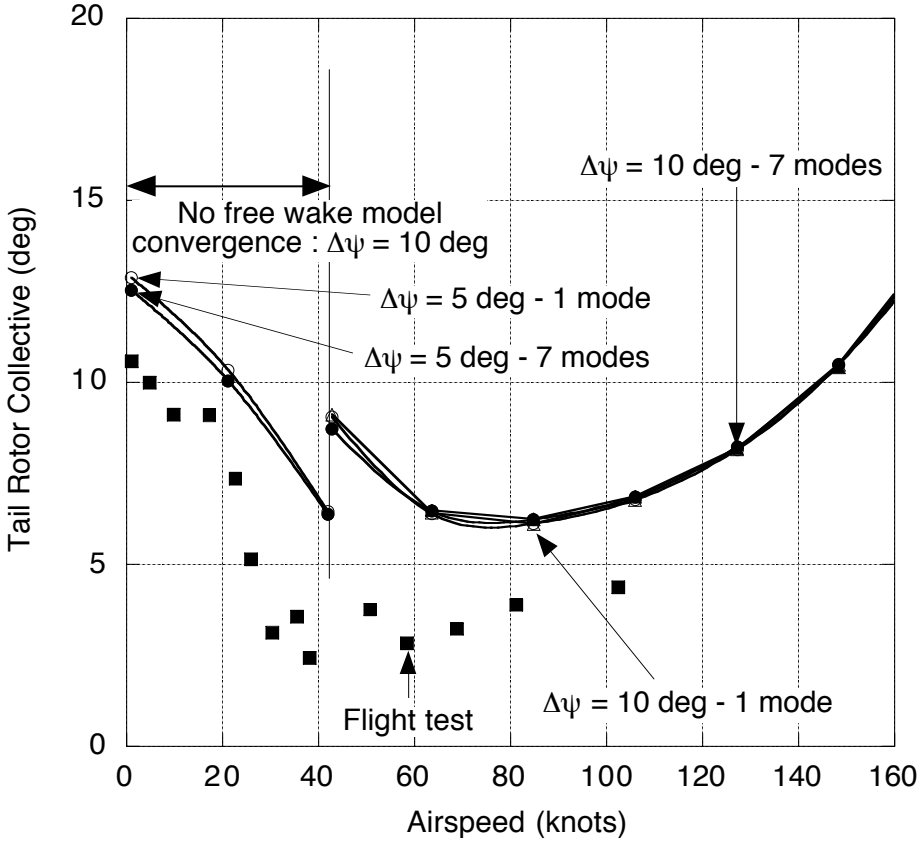

Figure 7.25: Effect of free wake resolution on tail rotor collective pitch versus airspeed for the BO-105 in straight and level flight.

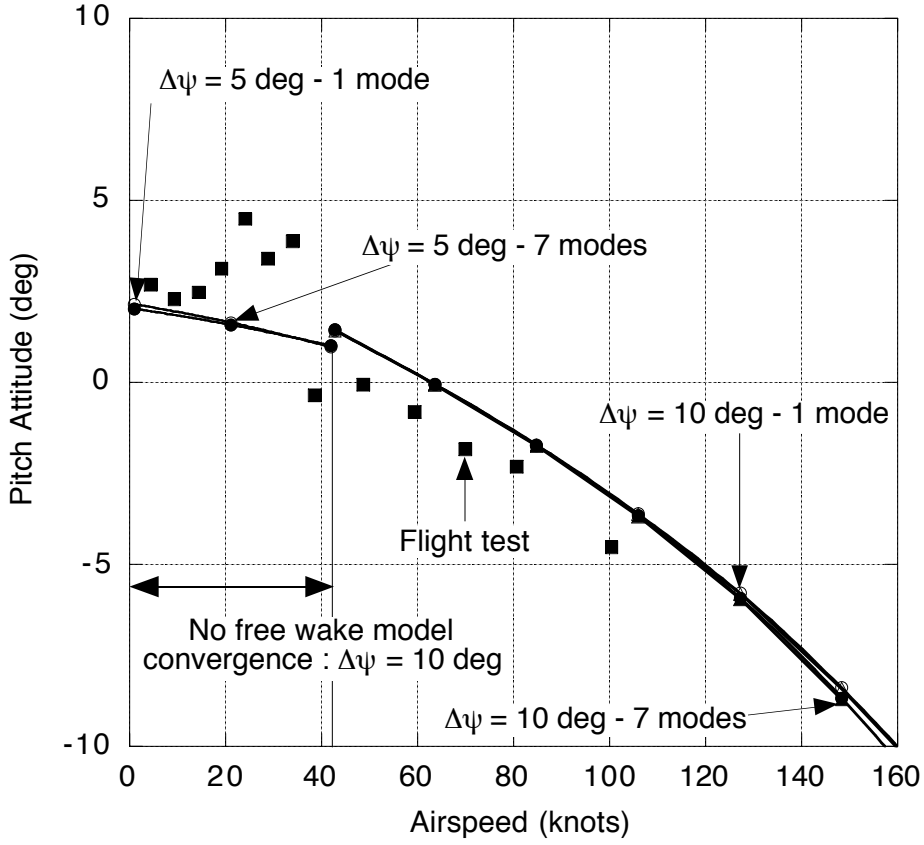

Figure 7.26: Effect of free wake resolution on aircraft pitch attitude versus airspeed for the BO-105 in straight and level flight.

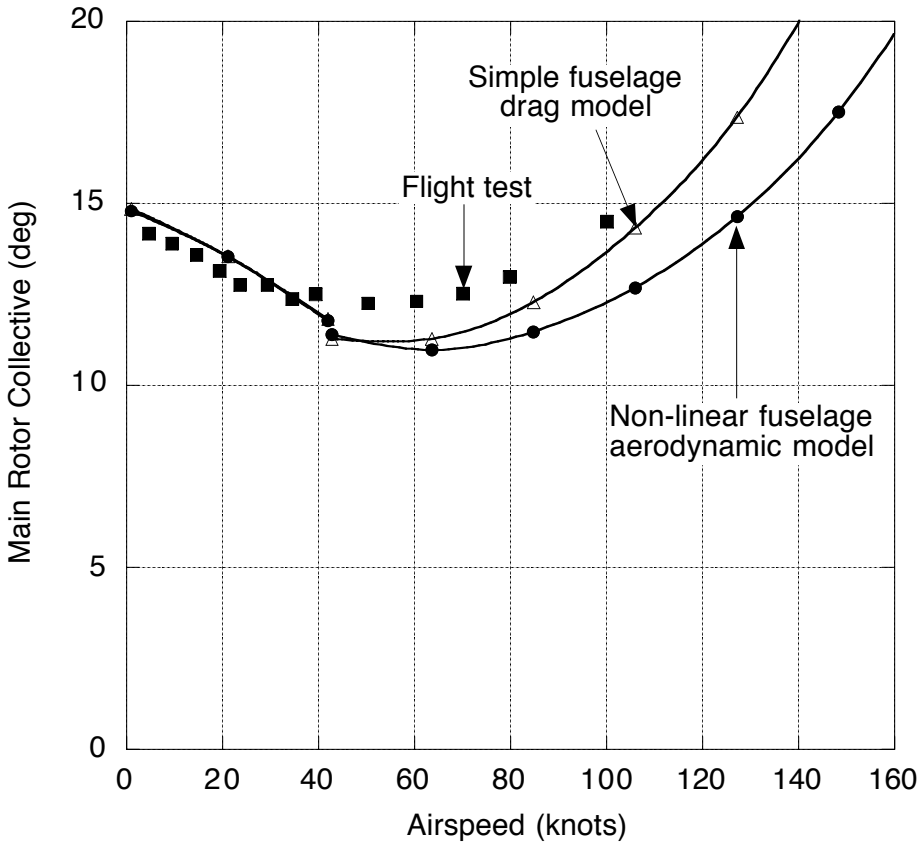

Figure 7.27: Effect of fuselage aerodynamic modeling on main rotor collective pitch versus airspeed for the BO-105 in straight and level flight with the free wake and the refined blade model.

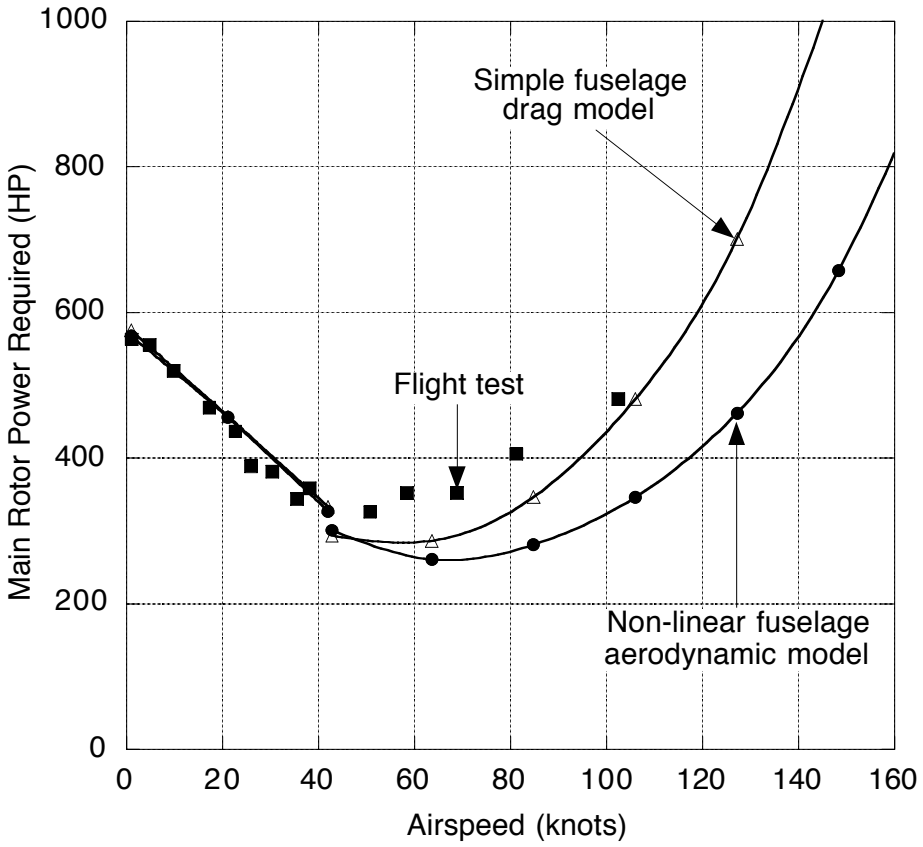

Figure 7.28: Effect of fuselage aerodynamic modeling on main rotor power required versus airspeed for the BO-105 in straight and level flight with the free wake and the refined blade model.

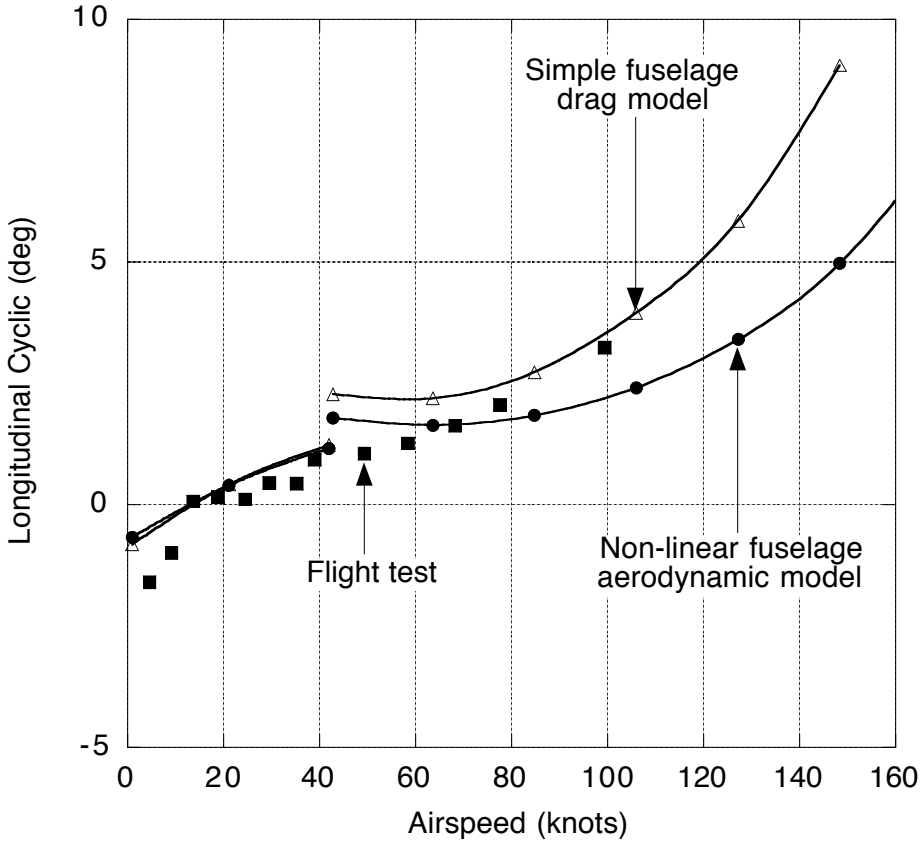

Figure 7.29: Effect of fuselage aerodynamic modeling on longitudinal cyclic pitch versus airspeed for the BO-105 in straight and level flight with the free wake and the refined blade model.

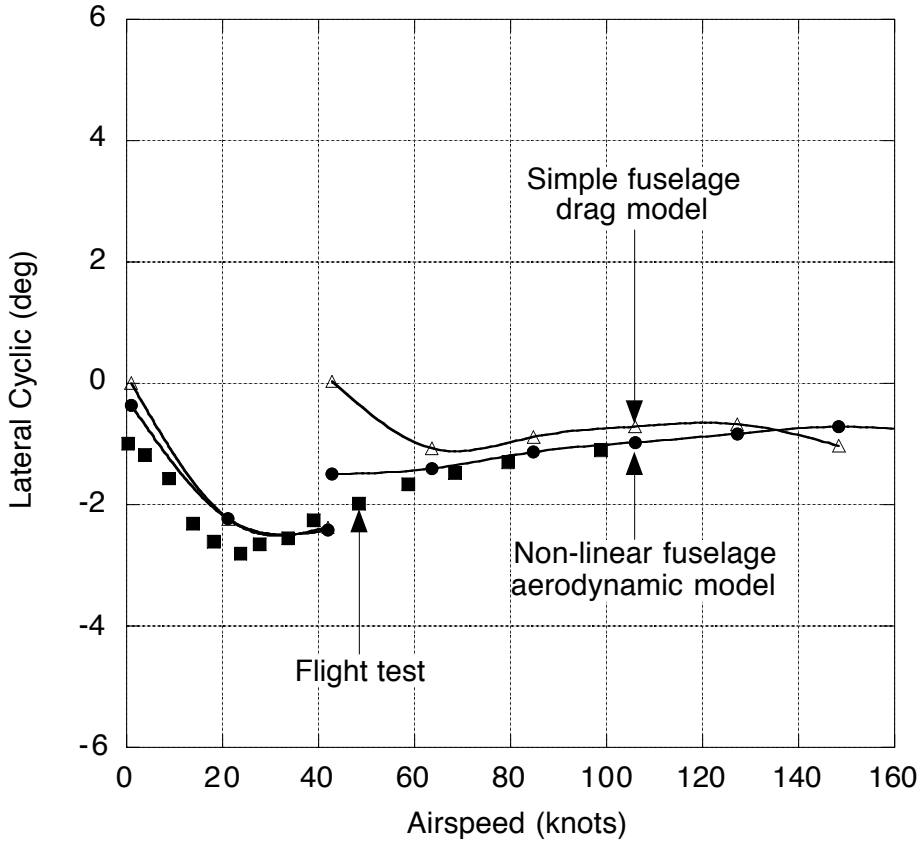

Figure 7.30: Effect of fuselage aerodynamic modeling on lateral cyclic pitch versus airspeed for the BO-105 in straight and level flight with the free wake and the refined blade model.

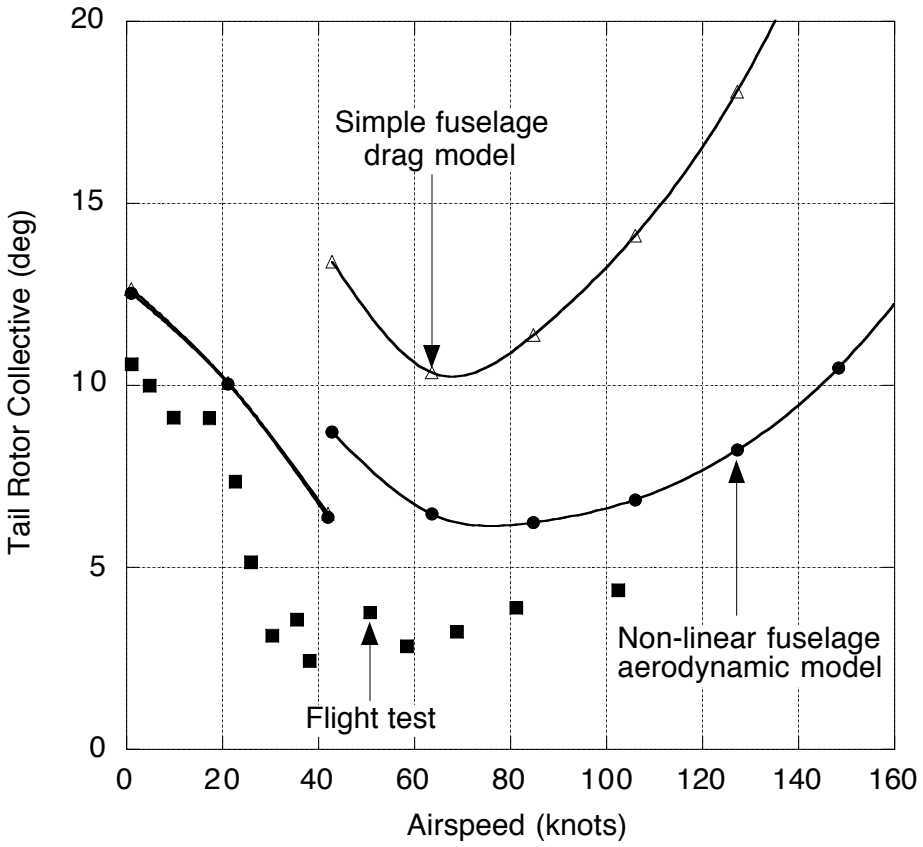

Figure 7.31: Effect of fuselage aerodynamic modeling on tail rotor collective pitch versus airspeed for the BO-105 in straight and level flight with the free wake and the refined blade model.

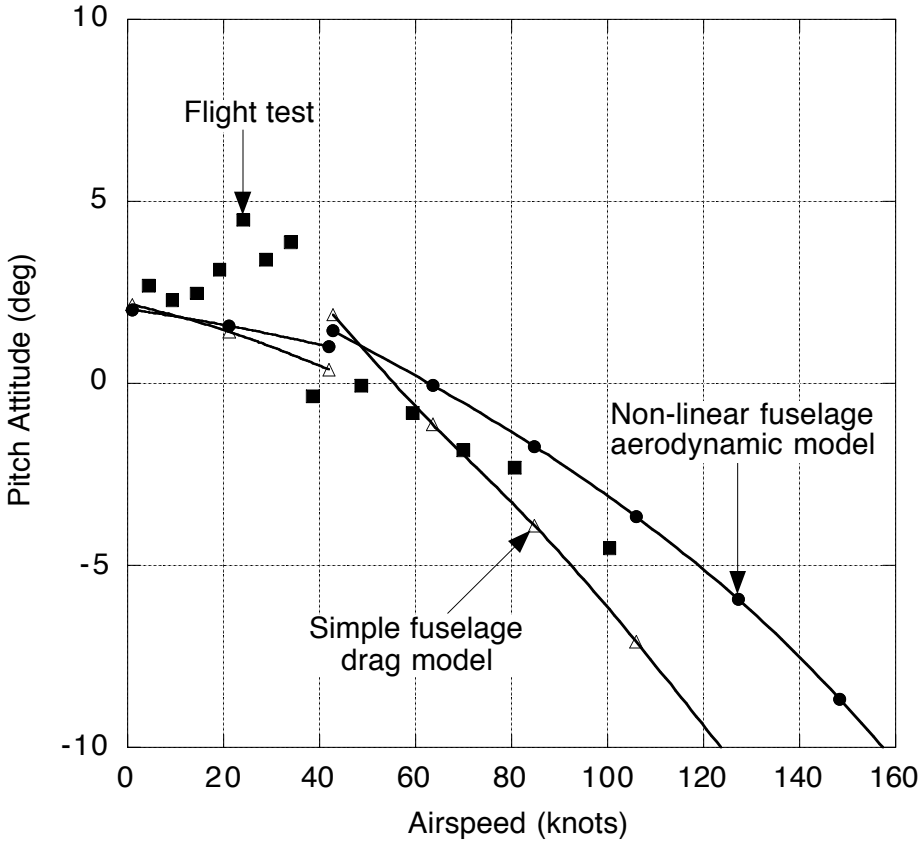

Figure 7.32: Effect of fuselage aerodynamic modeling on aircraft pitch attitude versus airspeed for the BO-105 in straight and level flight with the free wake and the refined blade model.

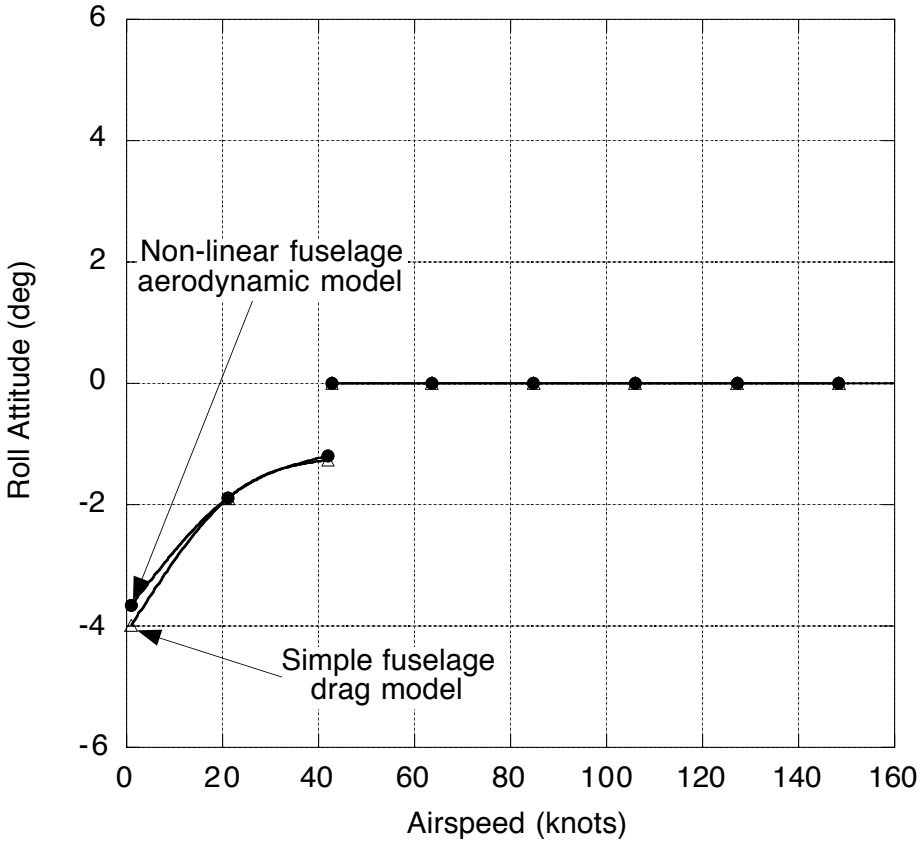

Figure 7.33: Effect of fuselage aerodynamic modeling on aircraft roll attitude versus airspeed for the BO-105 in straight and level flight with the free wake and the refined blade model.

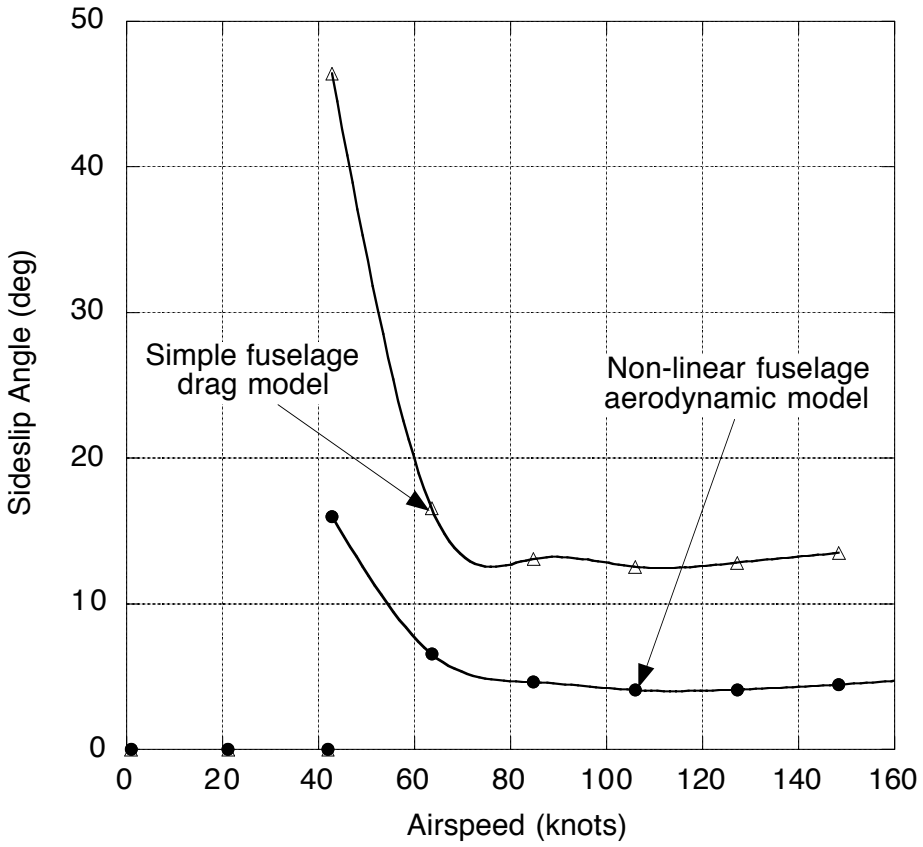

Figure 7.34: Effect of fuselage aerodynamic modeling on aircraft sideslip angle versus airspeed for the BO-105 in straight and level flight with the free wake and the refined blade model.

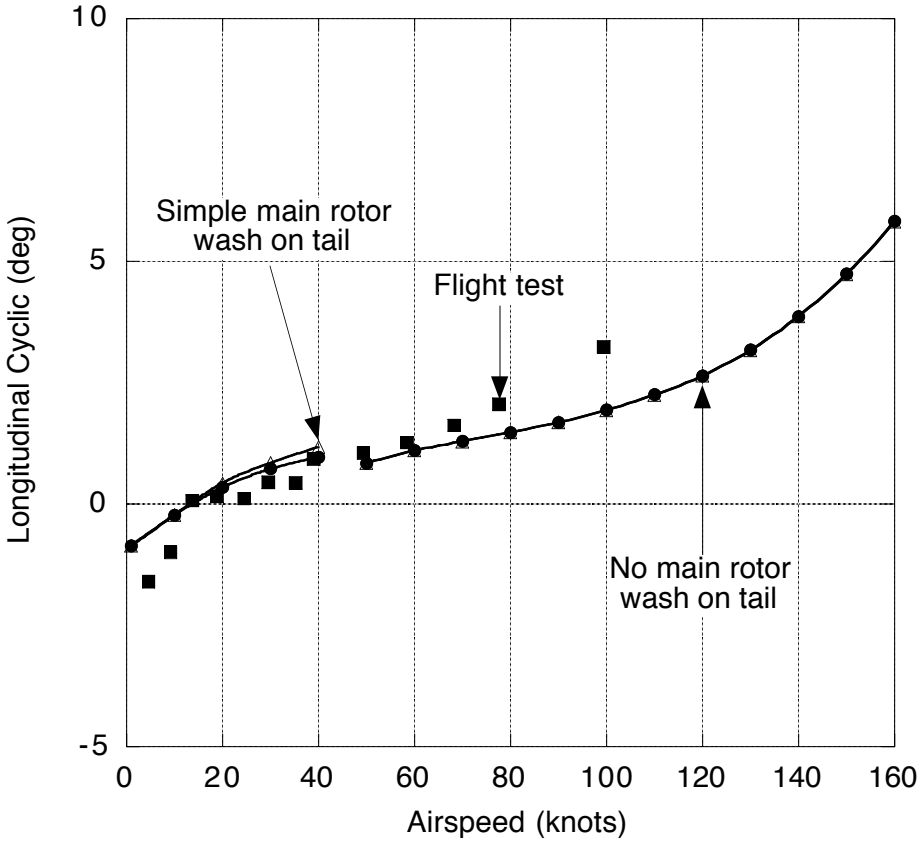

Figure 7.35: Effect of inclusion of main rotor downwash on horizontal tail on longitudinal cyclic pitch versus airspeed for the BO-105 in straight and level flight with dynamic inflow and the refined blade model.

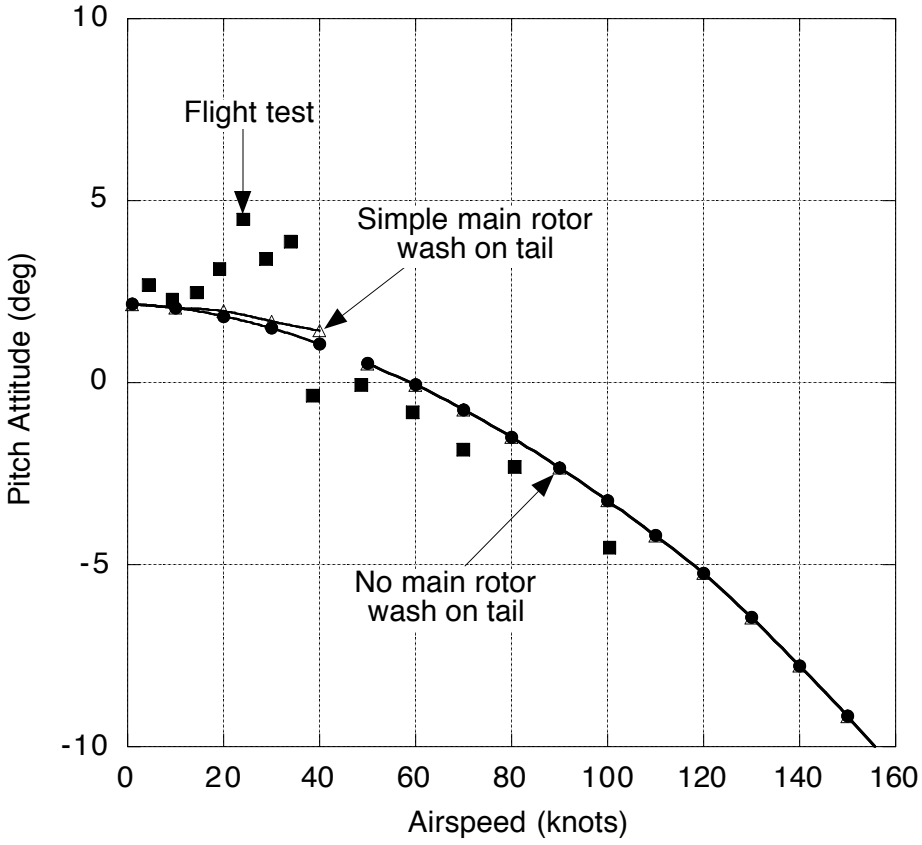

Figure 7.36: Effect of inclusion of main rotor downwash on horizontal tail on aircraft pitch attitude versus airspeed for the BO-105 in straight and level flight with dynamic inflow and the refined blade model.

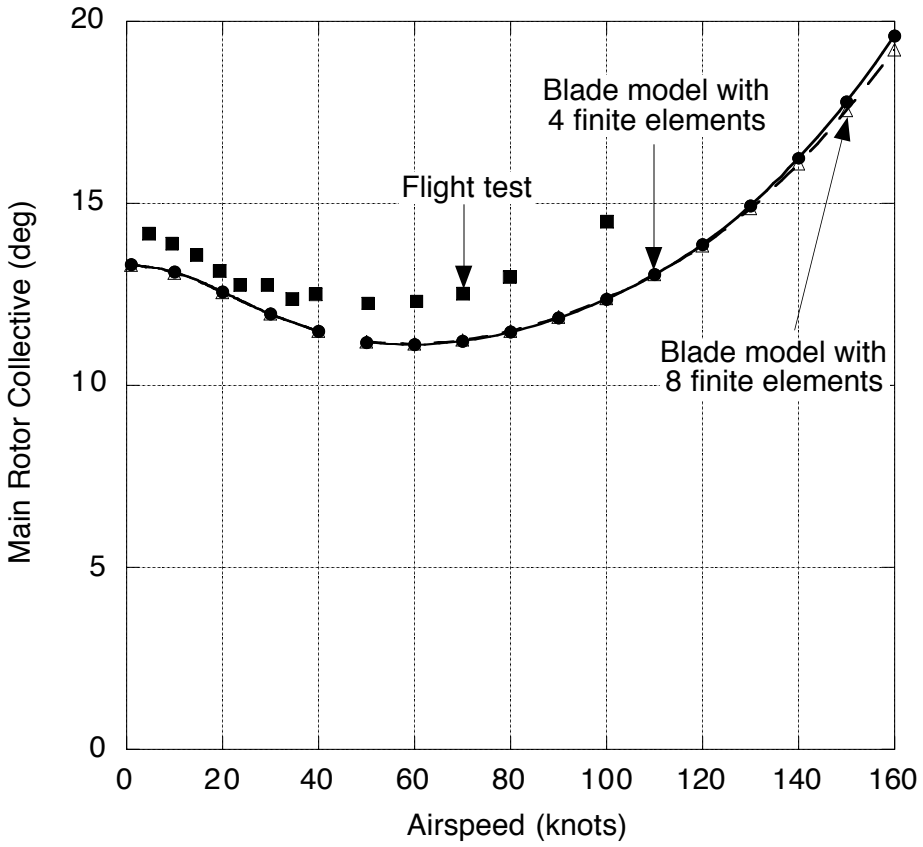

Figure 7.37: Effect of number of finite elements on main rotor collective pitch versus airspeed for the BO-105 in straight and level flight with dynamic inflow and the refined blade model.

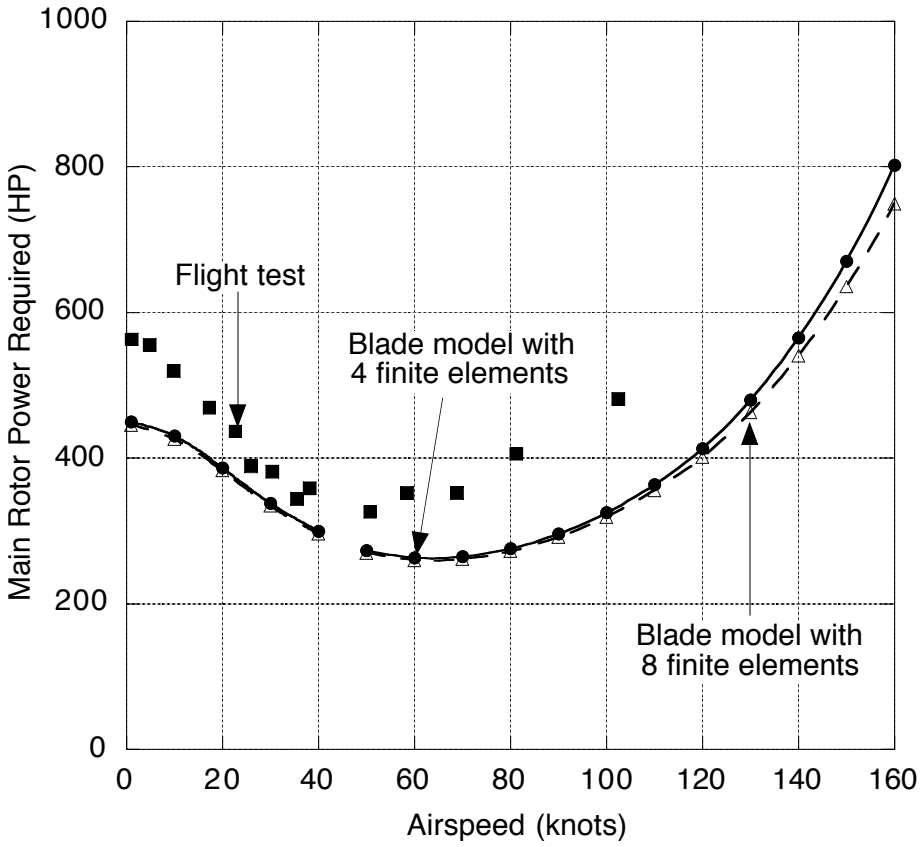

Figure 7.38: Effect of number of finite elements on main rotor power required versus airspeed for the BO-105 in straight and level flight with dynamic inflow and the refined blade model.

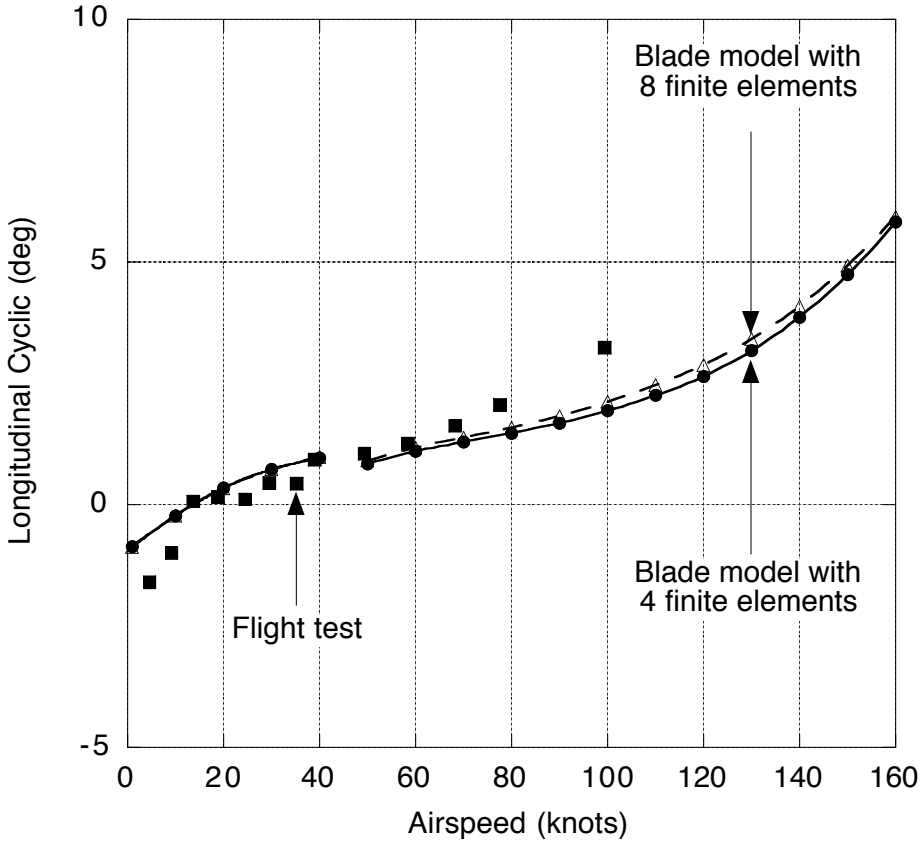

Figure 7.39: Effect of number of finite elements on longitudinal cyclic pitch versus airspeed for the BO-105 in straight and level flight with dynamic inflow and the refined blade model.

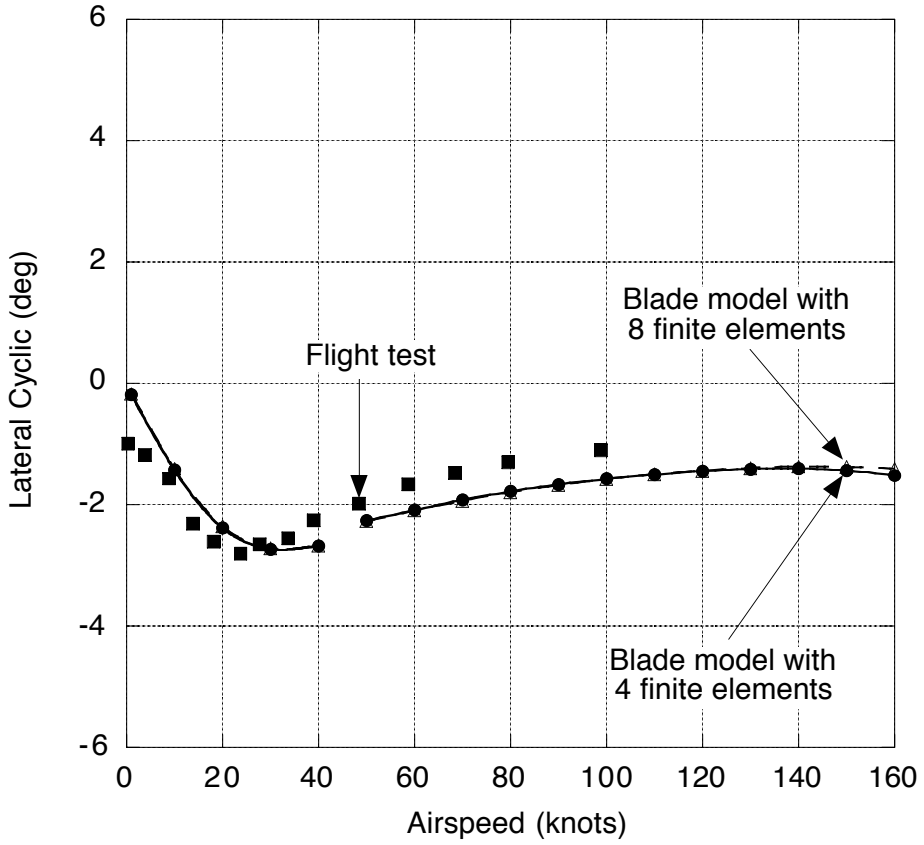

Figure 7.40: Effect of number of finite elements on lateral cyclic pitch versus airspeed for the BO-105 in straight and level flight with dynamic inflow and the refined blade model.

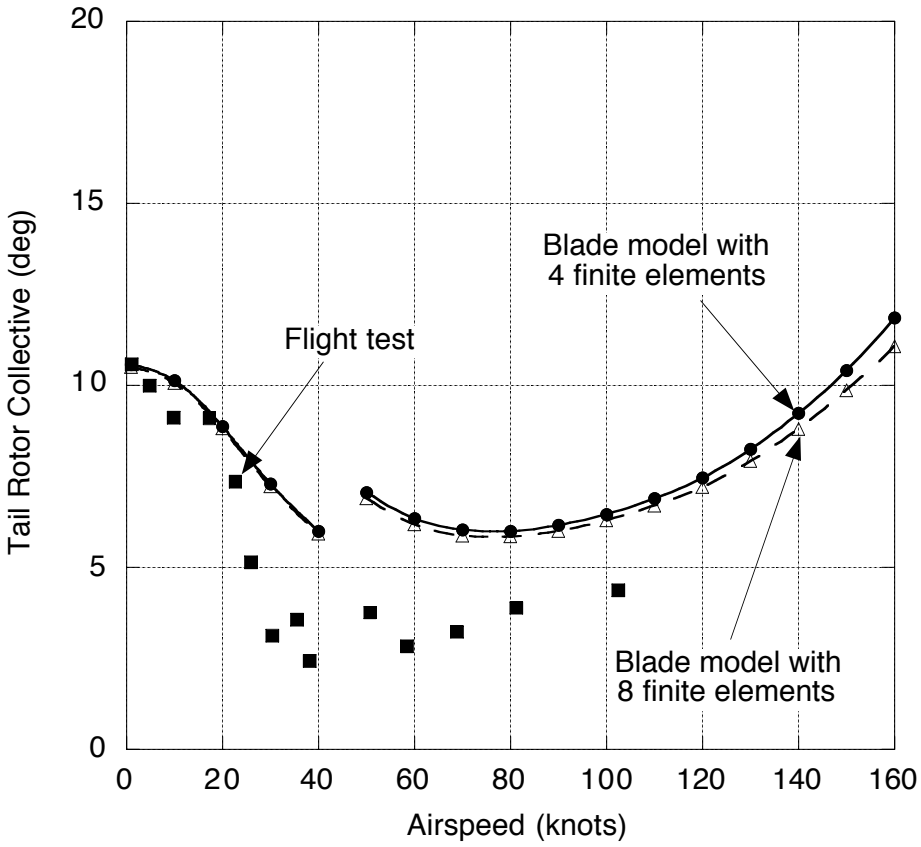

Figure 7.41: Effect of number of finite elements on tail rotor collective pitch versus airspeed for the BO-105 in straight and level flight with dynamic inflow and the refined blade model.

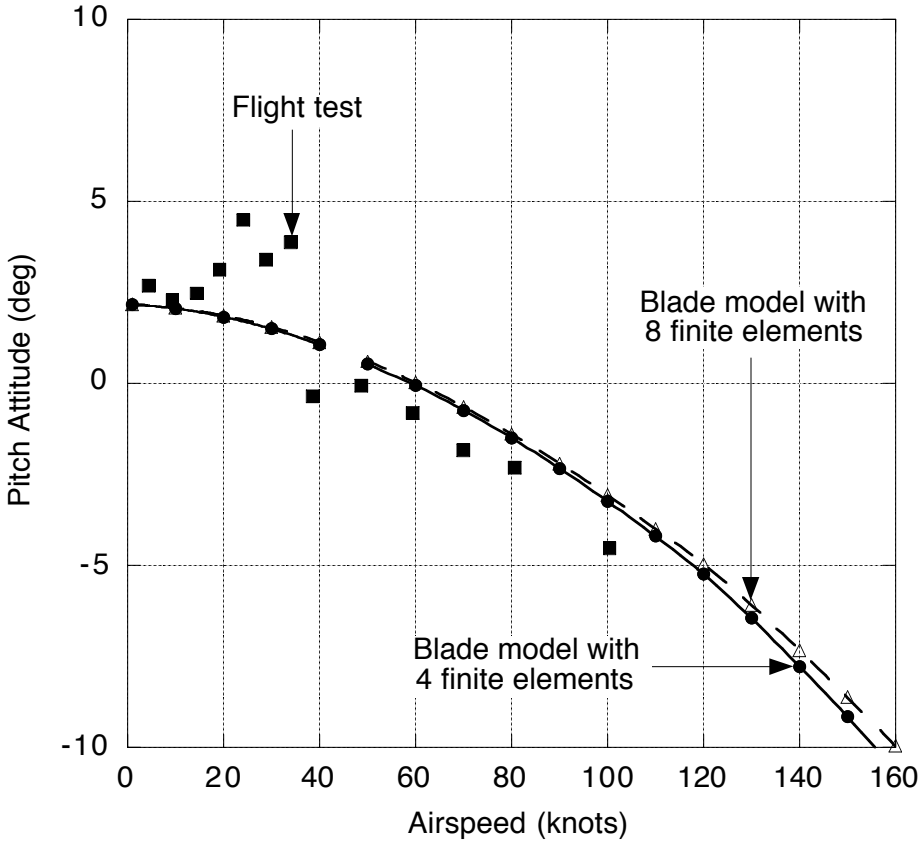

Figure 7.42: Effect of number of finite elements on aircraft pitch attitude versus airspeed for the BO-105 in straight and level flight with dynamic inflow and the refined blade model.

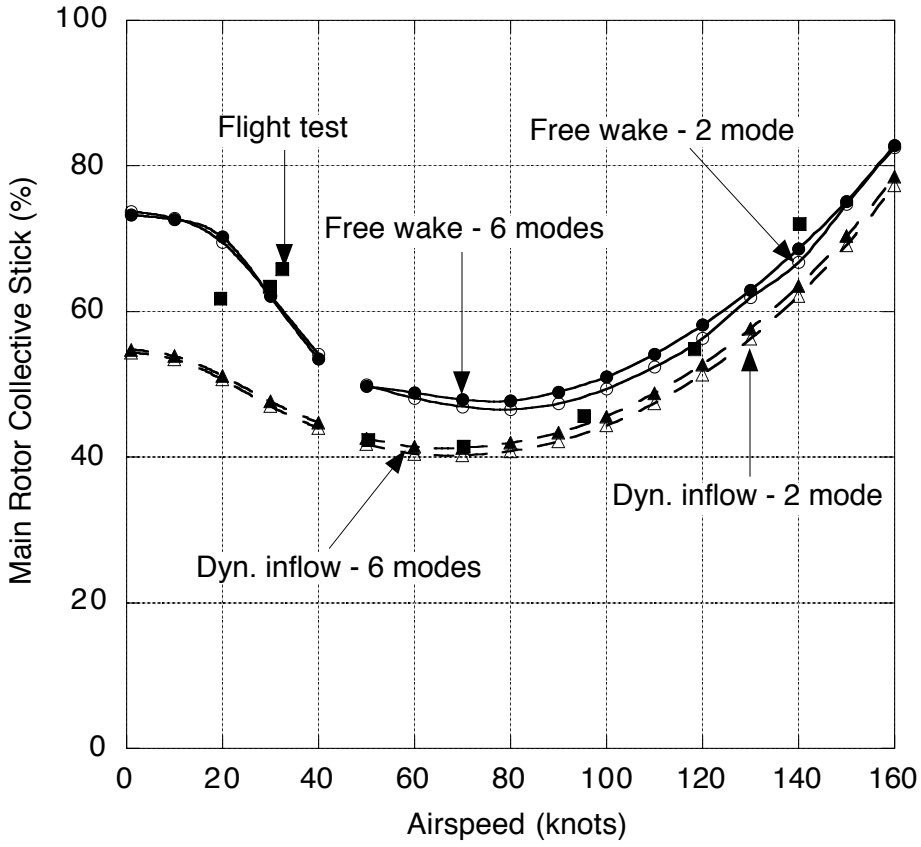

Figure 7.43: Effect of inflow models and blade modeling on main rotor collective stick versus airspeed for the UH-60A in straight and level flight.

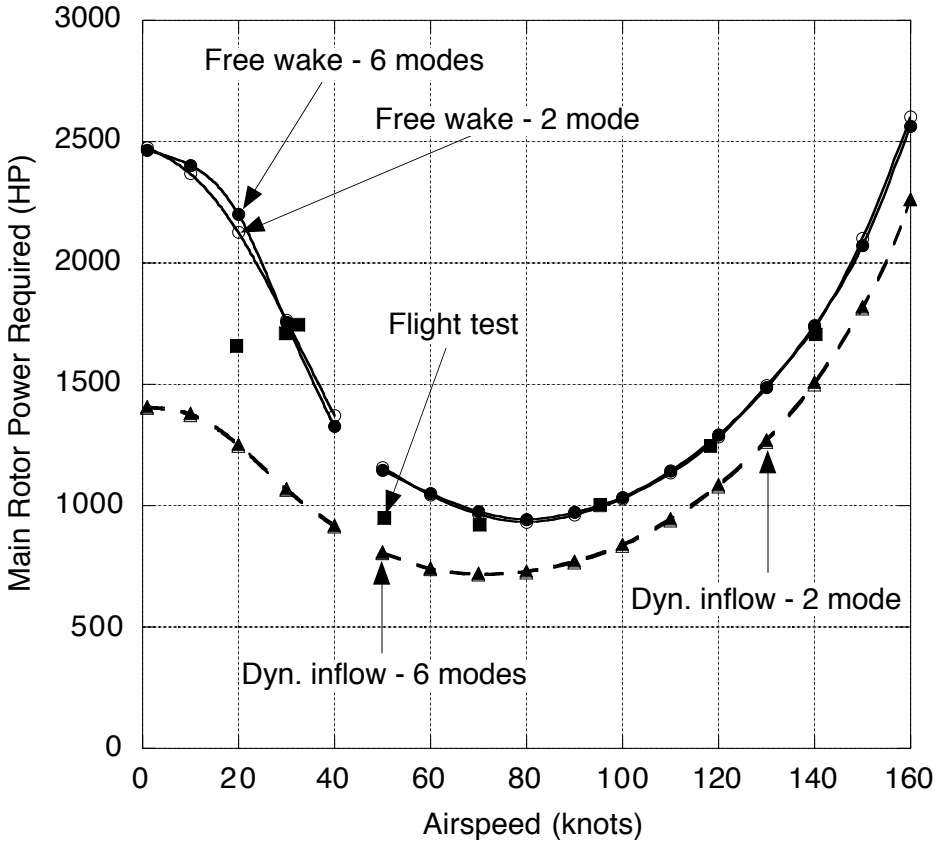

Figure 7.44: Effect of inflow models and blade modeling on main rotor power required versus airspeed for the UH-60A in straight and level flight.

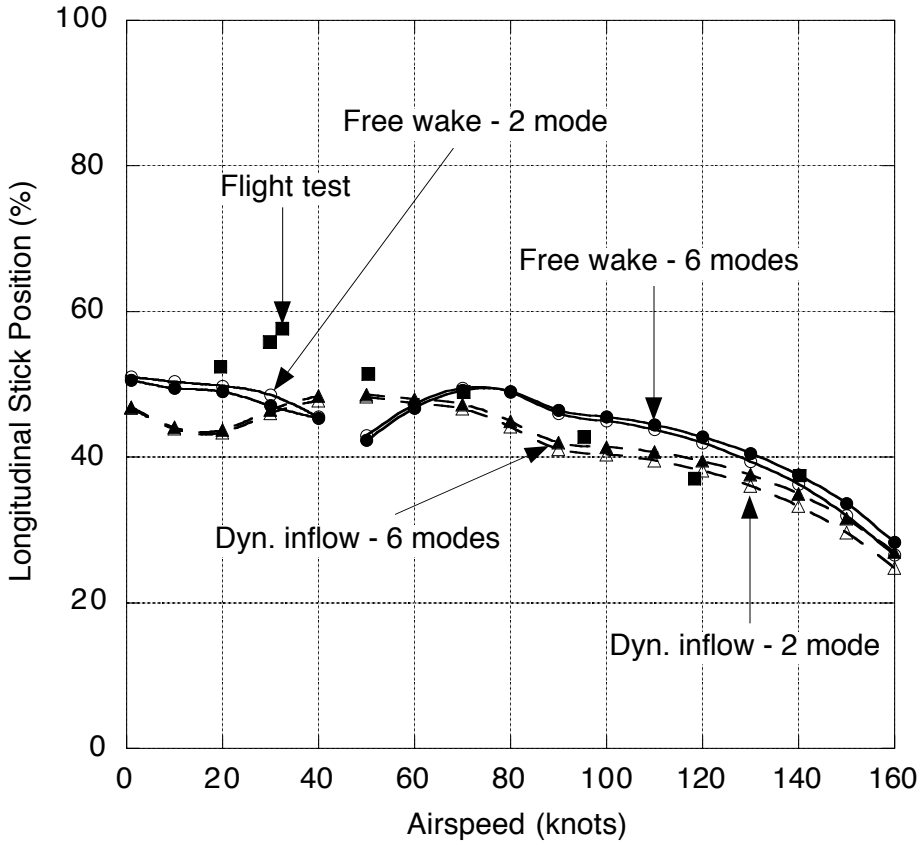

Figure 7.45: Effect of inflow models and blade modeling on longitudinal stick versus airspeed for the UH-60A in straight and level flight.

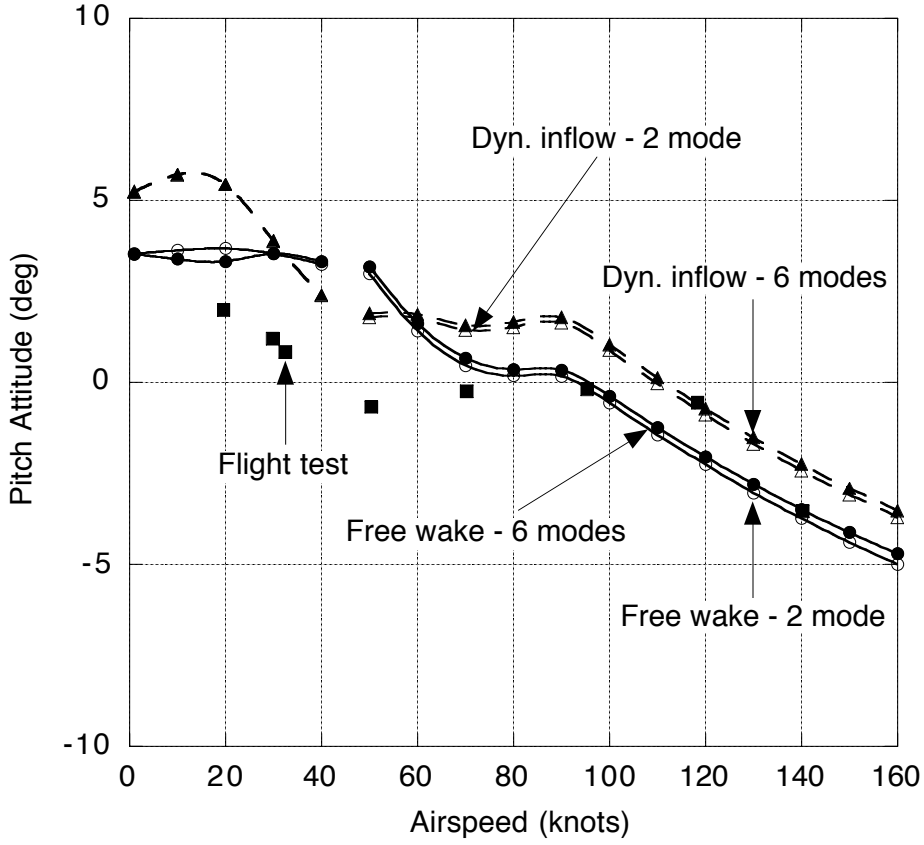

Figure 7.46: Effect of inflow models and blade modeling on aircraft pitch attitude versus airspeed for the UH-60A in straight and level flight.

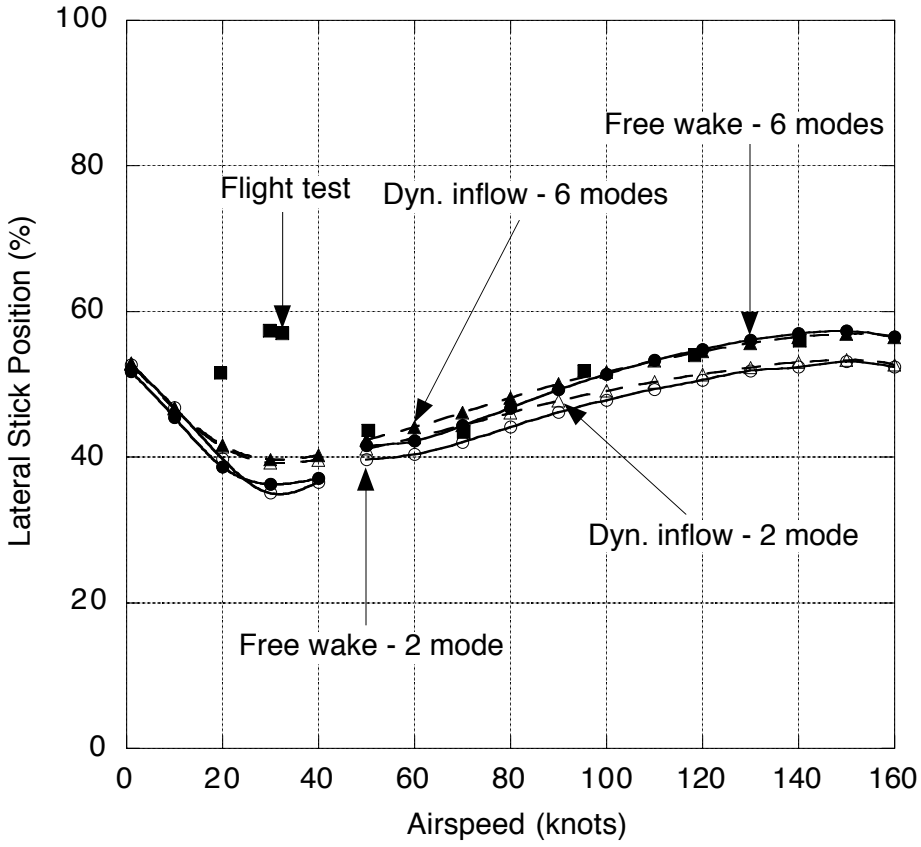

Figure 7.47: Effect of inflow models and blade modeling on lateral stick versus airspeed for the UH-60A in straight and level flight.

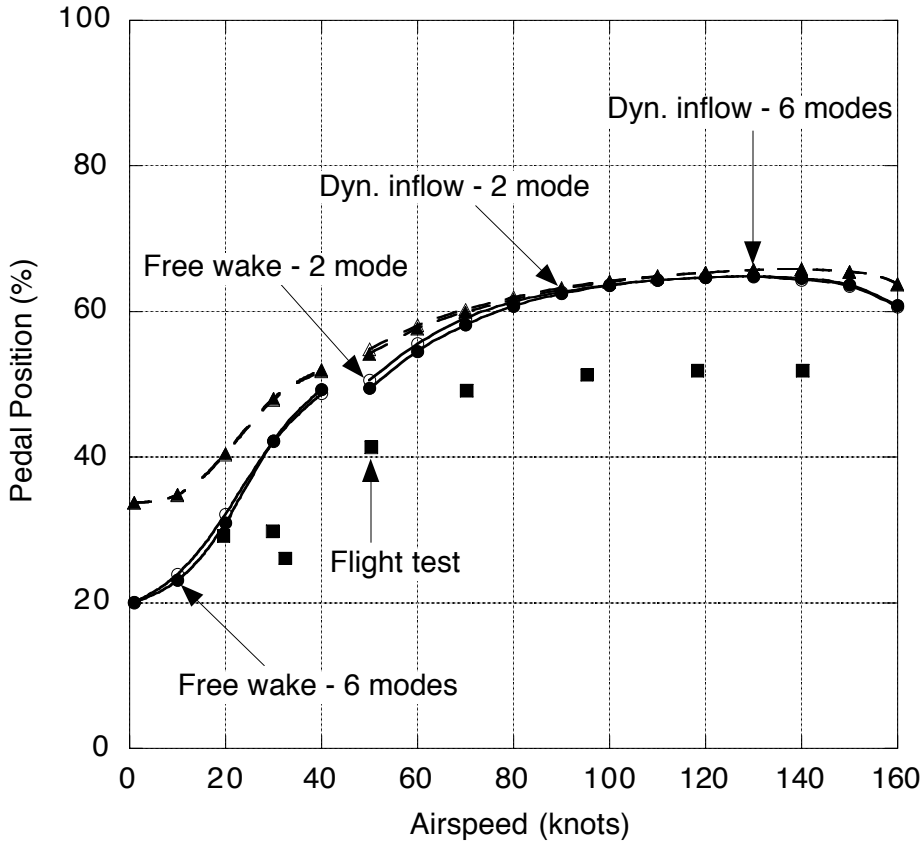

Figure 7.48: Effect of inflow models and blade modeling on pedal position versus airspeed for the UH-60A in straight and level flight.

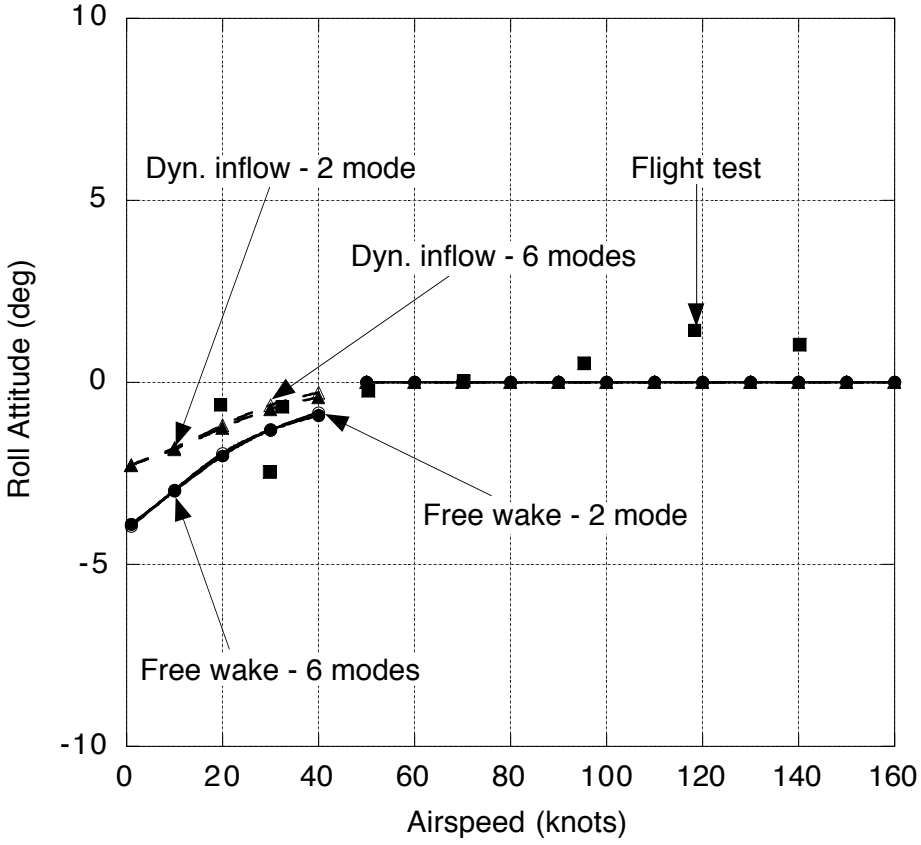

Figure 7.49: Effect of inflow models and blade modeling on aircraft roll attitude versus airspeed for the UH-60A in straight and level flight.

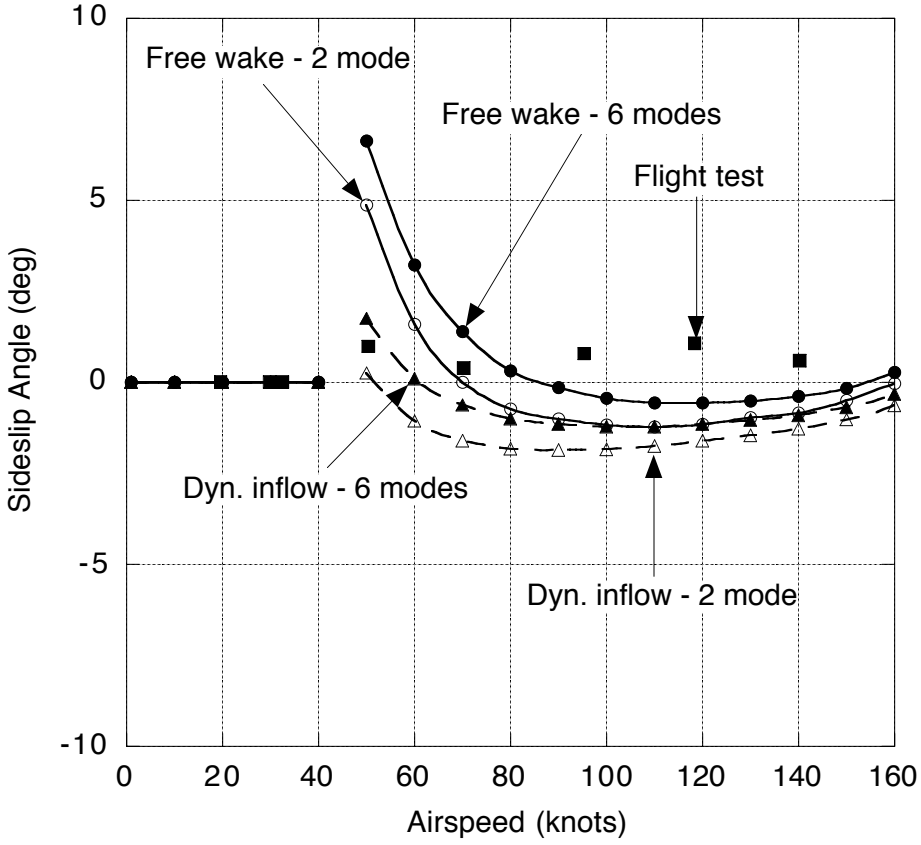

Figure 7.50: Effect of inflow models and blade modeling on aircraft sideslip angle versus airspeed for the UH-60A in straight and level flight.

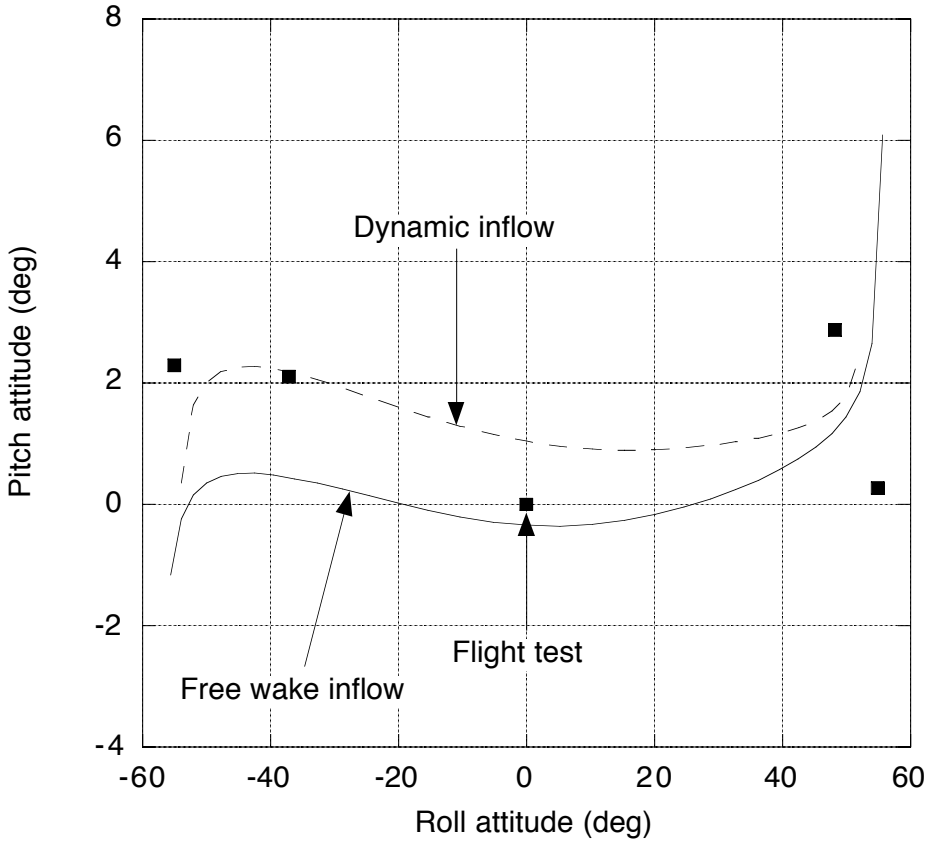

Figure 7.51: Effect of inflow modeling on pitch attitude as a function of roll attitude for the UH-60A in a level coordinated turn at 100 knots.

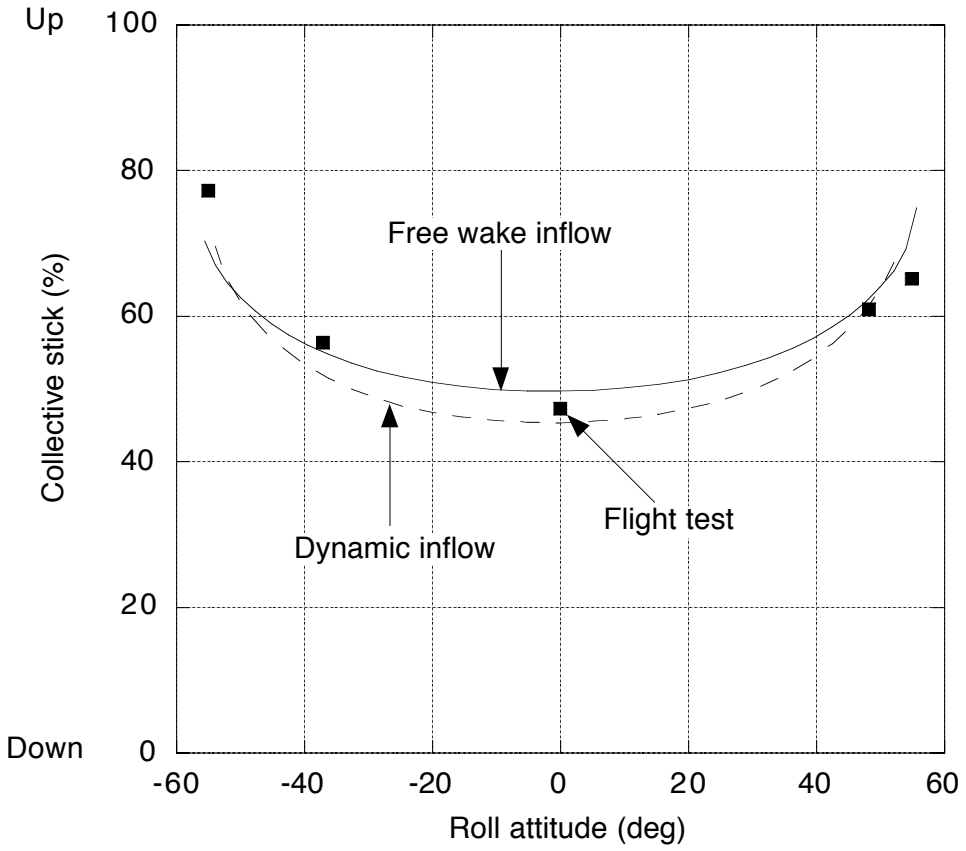

Figure 7.52: Effect of inflow modeling on collective stick position as a function of roll attitude for the UH-60A in a level coordinated turn at 100 knots.

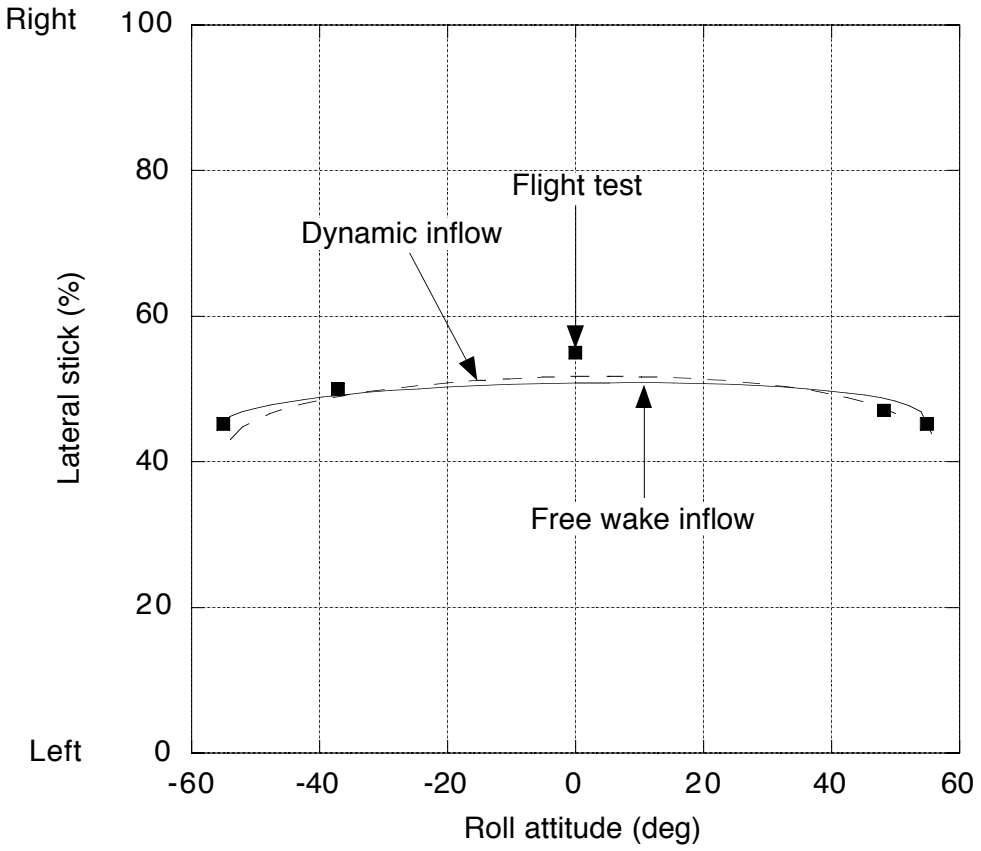

Figure 7.53: Effect of inflow modeling on lateral stick position as a function of roll attitude for the UH-60A in a level coordinated turn at 100 knots.

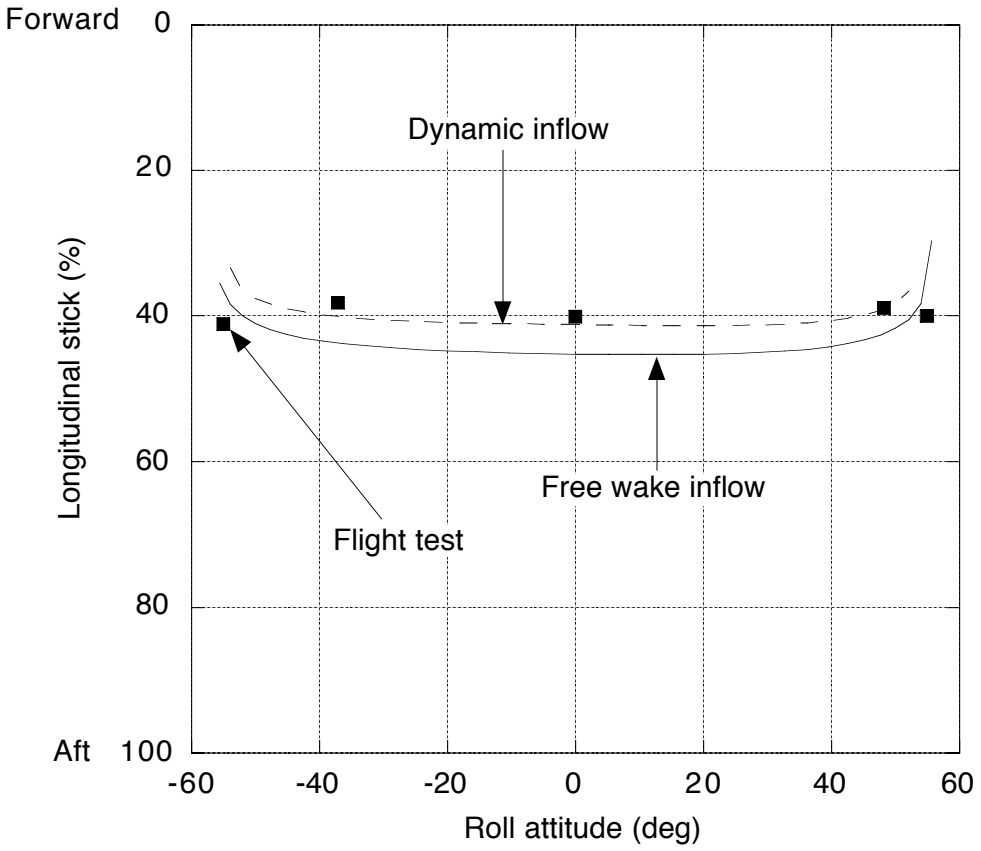

Figure 7.54: Effect of inflow modeling on longitudinal stick position as a function of roll attitude for the UH-60A in a level coordinated turn at 100 knots.

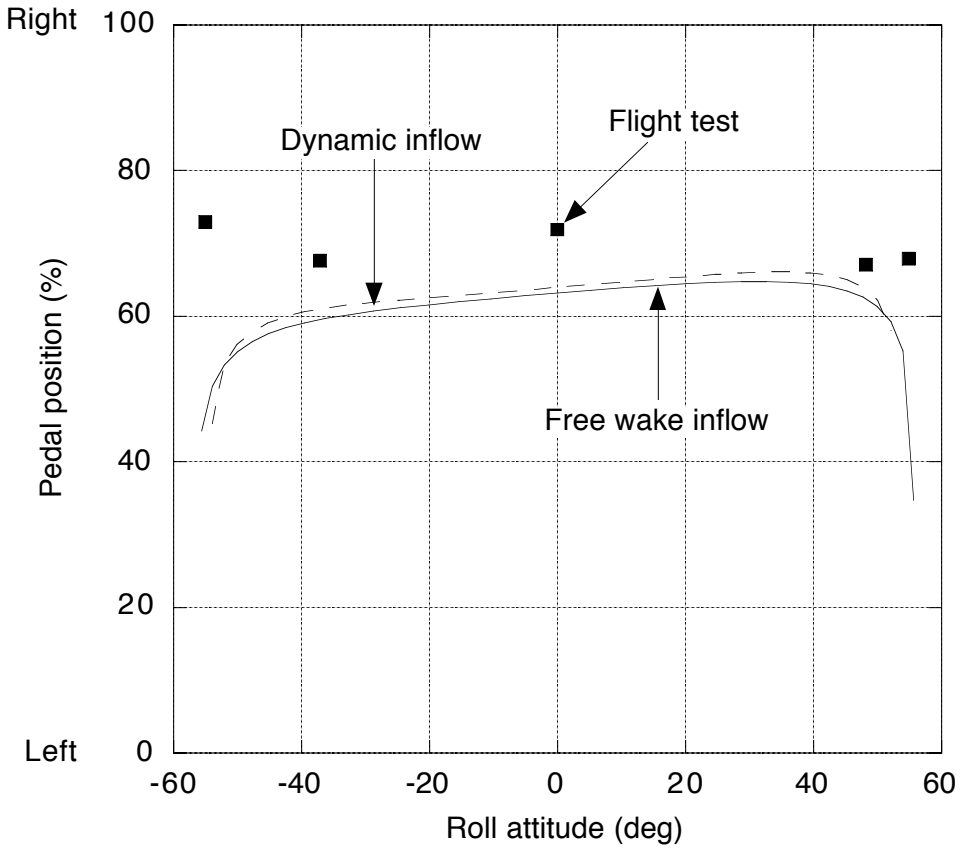

Figure 7.55: Effect of inflow modeling on pedal position as a function of roll attitude for the UH-60A in a level coordinated turn at 100 knots.

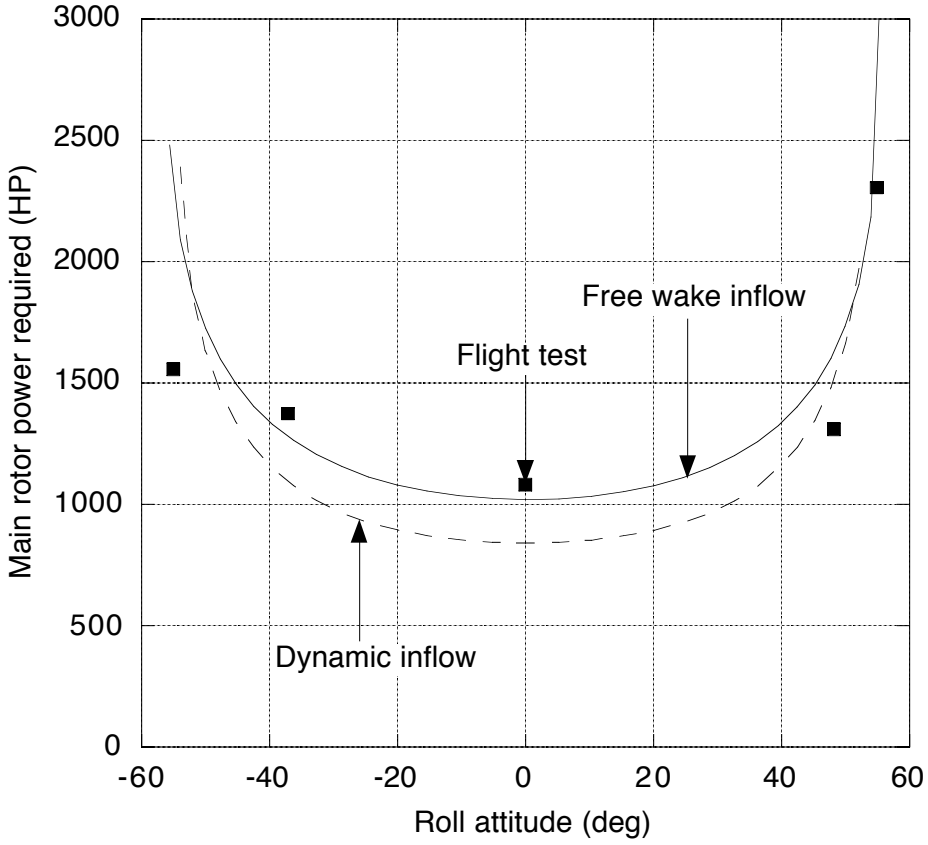

Figure 7.56: Effect of inflow modeling on main rotor power required as a function of roll attitude for the UH-60A in a level coordinated turn at 100 knots.

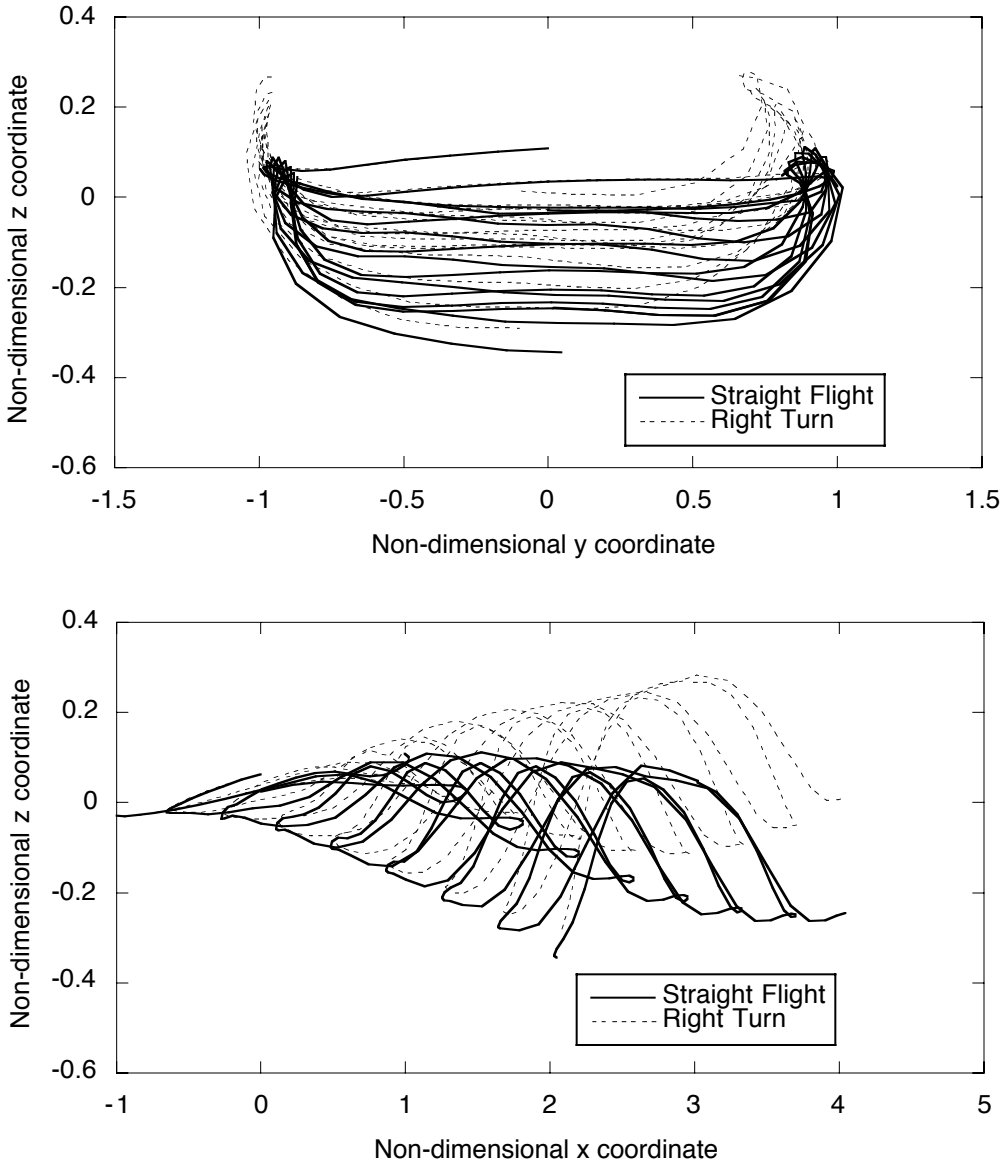

Figure 7.57: Effect of right turn ($\dot{\psi} = 15$ deg/sec) on wake geometry at 100 knots. Top figure shows view of wake from rear. Bottom figure shows view of wake from retreating side.

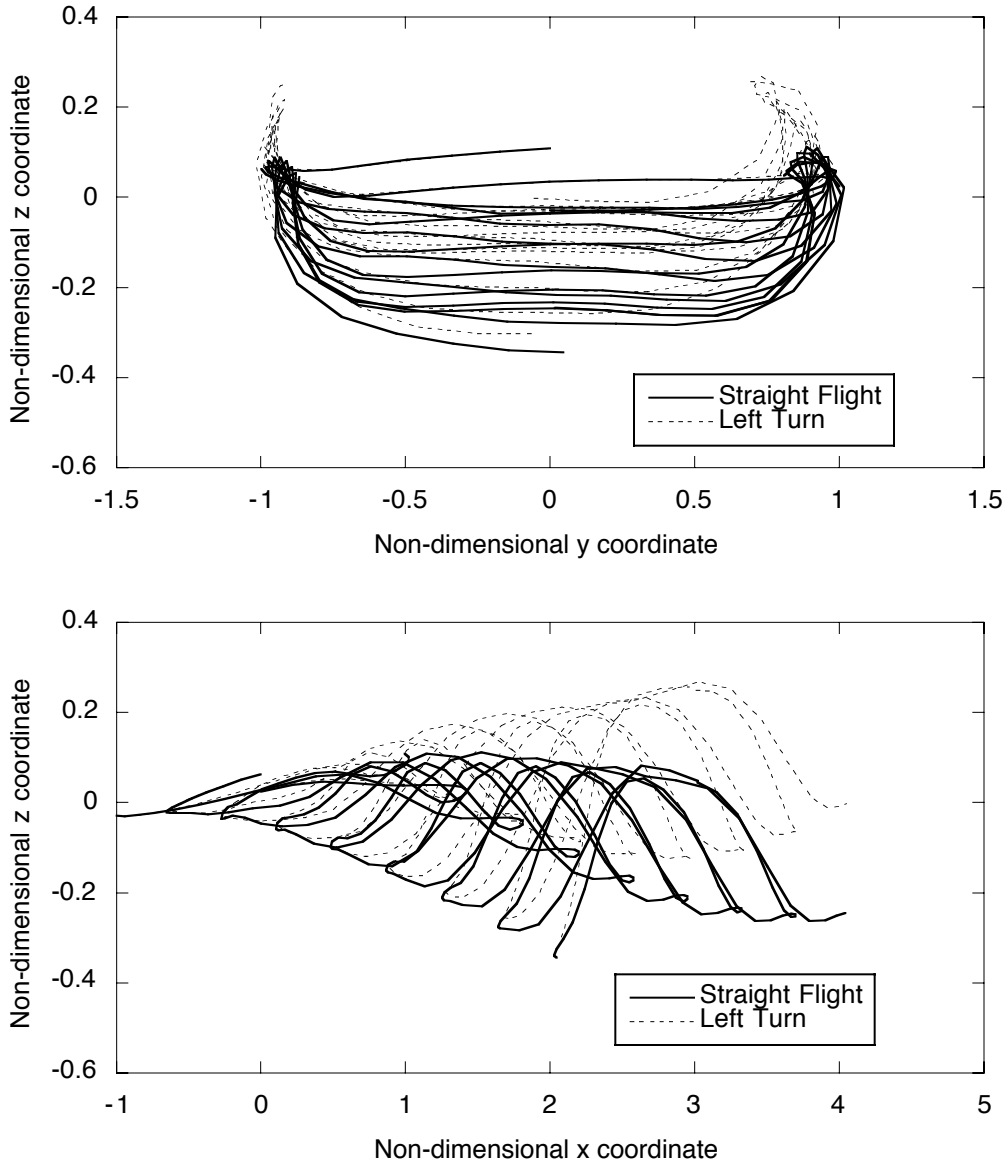

Figure 7.58: Effect of left turn ($\dot{\psi} = -15$ deg/sec) on wake geometry at 100 knots. Top figure shows view of wake from rear. Bottom figure shows view of wake from retreating side.

Chapter 8

Linearized Model Results

This chapter presents results derived from a linear representation of the equations of motion calculated from a given trim condition by numerically perturbing the equations of motion, as described in Chapter 4. These results include poles and frequency responses and are presented for both the UH-60A and BO-105 helicopters in hover as well as in straight and level forward flight. Special attention is given to the off-axis or cross-coupling predictions with the flight simulation model and the effects of inflow and blade modeling on the off-axis frequency responses.

The simulation results are compared to flight test data, where such data are available. The flight tests were typically conducted with frequency sweeps of each of the control axes and the responses of each of the helicopter states were measured. A system identification technique [82] was used to prepare the frequency response data of the amplitude and phase for each input/output pair. A coherence function is defined that is a measure of the accuracy of the flight test data at a particular frequency. The coherence function γ_{xy}^2 is defined as:

$$\gamma_{xy}^2 = \frac{|G_{xy}|^2}{|G_{xx}||G_{yy}|} \tag{8.1}$$

where G_{xx}, G_{yy} and G_{xy} are the input, output and cross-spectral density estimates respectively. The properties of the coherence function as they relate to the current

study are discussed in Ref. [83]. The flight test frequency response results used in this study are considered to be accurate if the coherence function has a value,

$$\gamma_{xy}^2 \geq 0.6 \tag{8.2}$$

The first set of results for this chapter examine the effects of inflow and blade modeling on the system poles and the on-axis and off-axis frequency responses for the UH-60A in hover. Similar sets of results are presented for the UH-60A in forward flight at speeds of 80 and 120 knots. Next, the effects of inflow and blade modeling for the BO-105 in hover and at 80 knots are examined. With respect to the free wake model, the effects of two important modeling parameters are investigated. The effect of the vortex wake resolution is examined in Section 8.5 and the effect of the numerical perturbation size used to calculate the linearized models is considered in Section 8.6. The third inflow model used is an extended momentum theory based dynamic inflow model that includes maneuver induced wake distortions. The effects of this inflow model on the frequency response predictions are presented in Section 8.7. The final set of results consider frequency responses for the UH-60A in level left and right coordinated turns at a forward speed of 100 knots and the effect of inflow modeling on these results is examined. This is followed by a discussion the linearized model results.

8.1 UH-60A in hover

The results in this section refer to the UH-60A articulated rotor helicopter in hover at an altitude of 5250 feet. Details of the modeling parameters of the UH-60A are presented in Section 6.2. The effects of blade and inflow modeling on the pole locations and the frequency responses are examined. The free wake model used is the Bagai-Leishman maneuvering free wake model that captures the effects of steady

maneuvers on the inflow. For the free wake results, the resolution of the vortex wake $\Delta\psi$ is 10 degrees, the total length of each vortex filament ζ_{max} is 720 degrees, and the initial tip vortex strength is equal to the maximum bound circulation along the blade ($C_\Gamma = 1.0$). The other inflow model is the dynamic inflow model of Pitt-Peters that does not include maneuver induced distortions on the wake geometry and inflow. Two different blade models are used in the generation of the numerical results. These are a *simple* blade model that includes only the rigid flap and lag modes, and a *refined* blade model that includes the first six blade modes with the lowest natural frequencies.

8.1.1 Poles

Figures 8.1 and 8.2 show the effect of inflow modeling on the open loop poles of the helicopter mathematical model for the UH-60A in the hover flight condition. The simple blade model with rigid flap and lag degrees of freedom is used. These figures show the imaginary part of the poles on the y-axis plotted against the real part of the pole on the x-axis and for brevity only the positive component of the imaginary parts are shown.

Figure 8.1 has labeled both the rotor and inflow poles. All of the rotor poles appear as complex conjugate pairs with both inflow models. The progressive flap and progressive lag modes have frequencies greater than that of the rotor speed (27 rad/sec) and these modes are not significantly effected by inflow modeling. The reactionless and collective flap modes have frequencies close to that of the rotor speed, and the locations of these modes show only a small effect of inflow modeling. The damping of the regressive and collective lag modes is increased slightly with the addition of the free wake model, while the regressive flap mode shows virtually no effect of inflow modeling. Three additional poles are present with

dynamic inflow that are related to the uniform component and harmonic components of the main rotor inflow dynamics. These poles are not present in the free wake results. This is because the free wake model does not contribute dynamic equations to the mathematical model and so does not contribute any poles. Each of the main rotor inflow poles are stable with the uniform component ($\omega_n = 14$ rad/sec) being the most important for flight dynamics work. The final pole here is for the tail rotor inflow, that is predicted to be more stable with the free wake inflow model than with dynamic inflow.

Figure 8.2 shows the poles of the UH-60A in hover on an enlarged scale so that the fuselage poles are visible. The complex conjugate pair for the dutch roll mode is slightly unstable for dynamic inflow with $\omega_n = 0.6604$ rad/sec and $\zeta = -0.1360$ but is stabilized with the use of the free wake model with $\omega_n = 0.6769$ rad/sec and $\zeta = 0.1938$. The spiral modes of the helicopter appear as a pair of real and negative poles (stable) with both inflow models, and the overall stability of these modes is not effected by inflow modeling. Inflow modeling, however, significantly effects the locations of the poles related to the short period and phugoid modes. The short period mode is a stable complex conjugate pair with dynamic inflow ($\omega_n = 0.5045$ rad/sec and $\zeta = 0.9624$), but exists as two real stable poles with the free wake model ($\omega_n = 0.3645$ rad/sec and $\omega_n = 0.1558$ rad/sec). The phugoid mode is unstable with both the dynamic inflow and free wake models. The free wake shows the phugoid as a complex conjugate pair ($\omega_n = 0.6399$ rad/sec and $\zeta = -0.5466$) while dynamic inflow modeling shows the phugoid as a pair of real poles; one stable ($\omega_n = 0.2168$ rad/sec and $\zeta = 1.0$) and one unstable ($\omega_n = 0.3878$ rad/sec and $\zeta = -1.0$). This phugoid mode for the UH-60A is effected by the coupling of the longitudinal and pitching motions by the 20 degree cant of the tail rotor and the incidence of the horizontal tail, which is 39 degrees in hover. An additional pole is generated at the

origin (not shown) which is a direct consequence of retaining the heading degree of freedom in the mathematical model.

8.1.2 On-axis frequency response

The effects of inflow and blade flexibility modeling on the on-axis frequency response results for the UH-60A in hover are shown in Figures 8.3 through 8.6. The "Dyn. inflow" legend denotes the frequency response results derived from the baseline flight dynamics model that includes the Pitt-Peters dynamic inflow. The "Free wake" legend denotes the frequency response results derived from the new flight dynamics model that includes the Bagai-Leishman maneuvering free wake. Results with the simple blade model are denoted with the "2 modes" legend and results with the refined blade model are denoted with the "6 modes" legend. The curve labeled "Flight test" indicates the data derived from flight test measurements.

Figure 8.3 shows the comparison for the roll rate response, p, to a lateral stick input δ_{lat} for the UH-60A in hover. This figure is typical of those in this section where simulation results generated with both inflow and both blade models are compared to data derived from flight tests. The range of accuracy of the flight test data, based on the coherence function (Eqn. (8.1)), is also indicated in these frequency response figures.

Over the frequency range shown in Figure 8.3 the blade model has essentially no effect on the response predictions both in amplitude and phase. This is seen with both the baseline and new flight dynamics models, where the two curves calculated with dynamic inflow are almost superimposed and the two curves calculated with the free wake model are also almost superimposed. As far as the amplitudes are concerned, the simulation results show a good qualitative agreement with the flight test data, although the gains are slightly over-predicted over much of the frequency

range. For frequencies between 5 and 20 rad/sec the inflow modeling does not effect the gain predictions, while in the lower frequency range between 0.6 to 5 rad/sec the use of the free wake model worsens the over-prediction of the amplitude. Both inflow models capture the frequency of the notch response associated with the regressive lag mode at about 19 rad/sec. The peak corresponding to the lateral body mode of frequency $\omega_n = 0.660$ rad/sec and damping $\zeta = 0.136$ predicted with dynamic inflow is somewhat smoothed out with the free wake model, where this lateral body mode is more highly damped with a frequency of $\omega_n = 0.640$ rad/sec and damping of $\zeta = 0.547$. In the phase portion, for frequencies above 0.8 rad/sec, there is a good agreement between the simulation results and the flight test data, although the phase lag predicted with the free wake model is slightly higher for frequencies up to about 7 rad/sec. Below 0.8 rad/sec the phase predictions with both inflow models are poor, although the coherence estimates indicate that the experimental data are rather unreliable at the low end of the frequency range and it is, therefore, impossible to determine conclusively whether the addition of the free wake model improves the correlation in this frequency range. Also for frequencies below 0.5 rad/sec there is a 180^o phase difference between the results with the free wake and those with dynamic inflow.

The amplitude and phase predictions of the pitch rate response q to the longitudinal stick input δ_{lon} are compared to test data in Figure 8.4. Over the frequency range of accurate flight test data, between 1 and 12 rad/sec, there is an excellent agreement between the simulation results and flight test data in both amplitude and phase. In this frequency range the simulation results are not effected by either the inflow model or the blade model. Large errors remain below a frequency of 1 rad/sec for the amplitude predictions and below 0.8 rad/sec for the phase predictions, although this is outside the range of accurate flight test data and it is impossible to

determine whether the free wake model improves the accuracy of these predictions.

Figure 8.5 shows the vertical acceleration response $\dot{w}$ to a collective stick input δ_{col} in hover. The correlation with flight test data is again quite good, although the amplitudes are slightly over-predicted for frequencies below 8 rad/sec and that the over-prediction is higher with the free wake than with dynamic inflow. This is probably due to the lack of inflow dynamics associated with the free wake model, where a change in the main rotor collective produces a corresponding instantaneous change in the inflow without any inflow dynamics. Because the frequency responses are dynamic responses, the lack of inflow dynamics with the free wake model could be responsible for the over-prediction of the amplitude of the vertical acceleration to a collective stick input. Below a frequency of 1 rad/sec, the phase differences between the simulation results and the flight test data increases steadily to about 90^o at a frequency of 0.1 rad/sec.

Figure 8.6 shows the yaw rate frequency response r to a pedal input δ_{ped}. A good agreement is seen between the simulation results and the flight test data over the frequency range of accurate flight test data. As with the other on-axis frequency responses, there are some significant differences in the phase between the simulation results and flight test data in the low frequency range below about 0.5 rad/sec. Neither the blade model nor inflow model have a significant effect on the yaw rate frequency responses.

The results presented in this section showed the on-axis frequency responses for the UH-60A in the hover flight condition. In general there is a good agreement between the simulation results and the flight test data in the frequency ranges where the flight test data is considered accurate. However, some differences in both the amplitude and phase predictions were observed in the low frequency region below about 0.8 rad/sec. It was also observed that the blade model did not significantly

affect the predictions in the frequency range considered (0.1 to 100 rad/sec). This indicates that the on-axis frequency response characteristics can be predicted with good accuracy using a relatively unsophisticated blade model that includes only the rigid flap and lag modes. The inflow model did, however, have some effect on the on-axis frequency responses, but these effects were in general quite small in the frequency range of importance for flight dynamics work, although the magnitude of the vertical acceleration to collective stick was over-predicted with the free wake model. This was possible a result of the absence of inflow dynamics or unsteadiness associated with the free wake model. The most significant effect of inflow modeling was seen in the low frequency range below about 0.8 rad/sec where some large differences were observed.

8.1.3 Off-axis frequency response

The effects of inflow and blade modeling on the prediction of the off-axis frequency responses for the UH-60A in hover are shown in Figures 8.7 through 8.18. Because a major focus of this study is with respect to the prediction of the off-axis response characteristics and the accuracy of such predictions when compared to flight test data, these comparisons are significant. However the frequency ranges for which the flight test data are considered accurate are generally quite limited for the off-axis responses, and in many cases the flight test data are inaccurate at all frequencies. This limits the comparisons that can be made and conclusions about the accuracy of the predictions.

Figures 8.7 through 8.9 show the pitch rate q, vertical acceleration $\dot{w}$ and yaw rate r responses respectively to a lateral stick input δ_{lat} for the UH-60A in hover. As with the on-axis responses, these figures show only a minor effect of the blade model on the numerical results. The accuracy of the flight test data shown in

these figures are suspect at all frequencies, which limits the extent to which the simulation results can be validated. Given this difficulty, the amplitude of the pitch response is predicted with fair accuracy with both inflow models for frequencies above 2 rad/sec. Below this frequency, the amplitude is over-predicted with both inflow models. This is particularly evident at a frequency of about 0.6 rad/sec where there is a predicted peak corresponding to the lateral phugoid mode that is slightly unstable in hover with both the dynamic inflow and free wake models. A notch type response is seen in the pitch amplitude at about 6.5 rad/sec with dynamic inflow that corresponds to the regressive flap mode with frequency $\omega_n = 5.590$ rad/sec and damping $\zeta = 0.553$. This notch is not seen with the free wake since the regressive flap mode is more highly damped $\zeta = 0.859$ and has a higher frequency $\omega_n = 9.765$ rad/sec. The phase of the pitch response is predicted poorly in the frequency range from 0.6 to 6 rad/sec, and there are also significant effects of inflow modeling in this frequency range. However for frequencies above 6 rad/sec and below 0.6 rad/sec, all of the numerical results show similar phase predictions and correlate well with the test data. The amplitude of the vertical acceleration is significantly improved with the free wake, which shows a good correlation with the flight test data over the entire frequency range. The notch at about 8.5 rad/sec predicted with dynamic inflow is not seen in the free wake results nor in the flight test data. The phase of the vertical acceleration to a lateral control is predicted poorly over the entire frequency range with an average phase discrepancy of about 180°. For the yaw rate response, there is a reasonable agreement between the numerical results and flight test data over most of the frequency range, and an excellent correlation is seen within the frequency range of accurate flight test data from 6 to 12 rad/sec. Below a frequency of about 0.6 rad/sec there is a 180° phase difference between the simulation results with dynamic inflow and those with the free wake.

Figures 8.10 through 8.12 show the roll rate p, vertical acceleration $\dot{w}$ and yaw rate r responses respectively to a longitudinal stick input δ_{lon}. The amplitude of the roll response is predicted higher with the free wake model than with dynamic inflow over most of the frequency range. The phase plot for the roll rate response shows virtually no effect of the inflow model for frequencies above 4 rad/sec, however, some large differences in the phase predictions are seen at frequencies below this value. Also, there is a consistent 180° phase difference between the two sets of inflow results for frequencies below 0.6 rad/sec. The correlation with flight test data for the roll response is poor, but the lack of accurate test data limits this comparison. However, for frequencies below 0.8 rad/sec, the free wake phase results correlate well with the test data, while dynamic inflow results remain 180° out of phase. The magnitude of the vertical acceleration is under-predicted with both inflow models, although the free wake results correlate better with the flight test data. The phase is poorly predicted, with the free wake results being 180° out of phase with the flight test data over most of the frequency range. Again, the free wake and dynamic inflow results show a 180° phase difference in the low frequency range below 0.8 rad/sec.

Figures 8.13 through 8.15 show the roll rate p, pitch rate q and yaw rate r responses respectively to a collective stick input δ_{col}. Each of these responses show that the free wake model over-predicts the amplitude for frequencies below 10 rad/sec when compared to both the dynamic inflow results and the flight test data. The magnitudes however correlate well with the flight test data in the high frequency range above 10 rad/sec and the effects of inflow modeling in this region tend to be small. A similar trend was seen for the on-axis response to a collective stick input (Fig. 8.5) where the amplitude of the vertical acceleration was over-predicted, particularly at low frequencies. This over-prediction of both the on-axis and off-axis responses due to collective inputs is probably due to the lack of inflow dynamics as-

sociated with the free wake model. The phase of the roll rate response is predicted with good accuracy using both inflow models for the frequency range from 0.8 to 12 rad/sec. Below 0.8 rad/sec the dynamic inflow model gives a better correlation with the test data. The phase of the pitch rate response is predicted poorly over the entire frequency range with both inflow models. For the yaw rate response, the flight test data is accurate in the range from 0.6 to 8 rad/sec and the simulation results show an excellent correlation with the flight test data in this region, although the magnitudes are over-predicted with the free wake model. At frequencies below 0.6 rad/sec, the phase predictions are still in good agreement with the test data while the amplitude is significantly over-predicted.

Figures 8.16 through 8.18 show the roll rate p, pitch rate q and vertical acceleration $\dot{w}$ responses respectively to a pedal input δ_{ped}. Over the range of accurate flight test data for the roll rate response, the results obtained with dynamic inflow show a better correlation than those using the free wake. The phase of the roll rate response is predicted well in the low frequency range below 0.4 rad/sec, and in this region the predictions are not significantly effected by inflow modeling. For the pitch rate response, neither the amplitude nor phase are effected by the inflow. The lack of accurate flight test data make these comparisons difficult, but there is, in general, a good agreement between the simulation results and flight test data in the low frequency range below 0.8 rad/sec. The vertical acceleration predictions are in general poor in both magnitude and phase, although the inaccuracies in the flight test data make the comparison difficult.

The results presented in this section showed the off-axis frequency responses for the UH-60A in hover. The quality of the flight test data, based on the coherence function, was in general poor. This limits the comparisons that can be made between the simulation results and flight test data. However, in the frequency ranges where

the flight test data was accurate the correlations were good. The general low quality of the flight test data made it impossible to fully determine the accuracy of the simulation results. A more complete validation of the predicted off-axis responses would require more reliable flight test data.

As with the on-axis responses, the off-axis response predictions are not significantly effected by blade modeling. The inflow model, however, does effect the frequency response results. The largest differences with inflow are seen in the medium to low frequency range. For the phase responses to a longitudinal stick input there is a 180° phase difference between the free wake and dynamic inflow results for frequencies below about 0.8 rad/sec. The off-axis phase predictions to a lateral stick input did not show this phase difference between the dynamic inflow and free wake results at low frequencies. The magnitude responses to a collective stick input were predicted higher with the free wake model than with the dynamic inflow model. This increased gain was probably a result of the lack of inflow dynamics or unsteadiness associated with the free wake model.

8.2 UH-60A in forward flight

This section examines the poles and frequency response results for the UH-60A in straight and level forward flight at an altitude of 5250 feet. The forward speeds of 80 and 120 knots are considered since these are the speeds at which flight test data is available. However this flight test data is only available for the on-axis responses. The modeling configurations are the same as those described in Section 8.1 for the UH-60A in hover. The two inflow models are the Pitt-Peters dynamic inflow model and the free wake model ($\Delta\psi = 10^o$, $\zeta_{max} = 720^o$ and $C_\Gamma = 1.0$). Results with both the simple and refined blade models are presented.

8.2.1 Poles

Figures 8.19 and 8.20 show the effect of inflow modeling on the open-loop (bare airframe) poles for the UH-60A at 80 knots. Figures 8.27 and 8.28 show similar results at 120 knots. At both speeds, the simple blade model with the rigid flap and lag modes is used.

Figures 8.19 and 8.27 show the rotor and inflow poles at speeds of 80 and 120 knots respectively. It should be noted that the tail rotor inflow poles have large negative real values and are off the left side scale of these figures. The poles associated with the main rotor dynamic inflow model move further to the left side with higher frequencies as the speed increases. Therefore, inflow dynamics have a lessening effect on the lower frequency body modes as the speed increases. As for the rotor modes, the poles with the free wake model are in general more highly damped than those with dynamic inflow. This trend is seen at both forward speeds with each of the low frequency rotor modes, namely the reactionless and collective lag modes and the regressive flap mode.

Figures 8.20 and 8.28 show the body modes at 80 and 120 knots respectively. In forward flight, it is somewhat difficult to properly identify the fuselage poles because of large amounts of coupling between the longitudinal and lateral degrees of freedom resulting from, amongst other things, the canted tail rotor. At both speeds, the results show a general low sensitivity of the pole locations to inflow modeling. This is an expected result since inflow modeling plays a lesser roll in the overall dynamics of the helicopter as the speed increases. The dutch roll mode is stable at both 80 and 120 knots and is not significantly effected by inflow modeling, although at 80 knots the damping is reduced from $\zeta = 0.2363$ with the dynamic inflow model to $\zeta = 0.1808$ with the free wake model. The short period mode tends

to become less stable as the speed is increased. With the free wake model, at 80 knots, the short period oscillation is stable ($\omega_n = 0.2865$ rad/sec and $\zeta = 0.2251$) but becomes slightly unstable at 120 knots ($\omega_n = 0.2041$ rad/sec and $\zeta = -0.0016$). The spiral mode, that was a pair of stable real poles in hover, splits and become a stable complex conjugate pair in forward flight. The phugoid instability, that was seen in hover as a complex conjugate pair with the free wake model and as a pair of stable and unstable real poles with dynamic inflow, is seen as a pair of real poles with each inflow model in forward flight. This pair of poles include a stable real pole and a static divergence pole lying on the positive real axis. This unstable pole for the phugoid mode is not significantly effected by the inflow model or the forward speed. The instability of this phugoid mode is related to the positive incidence angle of the horizontal tail, which couples the longitudinal and pitch dynamic motions.

8.2.2 On-axis frequency response

Figures 8.21 and 8.29 show the roll rate response p to a lateral control input δ_{lat} at 80 and 120 knots respectively. At 80 knots (Fig. 8.21), both the amplitude and phase are predicted well at all frequencies except in the low frequency range below 0.5 rad/sec where the amplitude is somewhat under-predicted and there are some differences in the phase. The notch type response and the phase increase associated with the regressive lag mode at about 20 rad/sec are captured well in the numerical results. The same general observations are valid for the 120 knot case, as shown in Figure 8.29. Here the amplitude and phase predictions are very good for frequencies above 0.4 rad/sec. The on-axis response to a lateral control in forward flight only shows a dependency on inflow modeling at very low frequencies below about 0.5 rad/sec. At other frequencies the inflow model has no significant effect.

Figures 8.22 and 8.30 show the pitch rate response q to a longitudinal control

input δ_{lon} at 80 and 120 knots respectively. Neither the amplitude nor the phase predictions are significantly effected by blade or inflow modeling. The amplitudes are predicted accurately over the entire frequency range, except at very low frequencies below about 0.5 rad/sec where the predictions are not as good. Above 0.5 rad/sec both models predict the phase response very accurately. This agreement remains good even to frequencies of 20-30 rad/sec, although the low coherence makes the accuracy of the flight test data above 10 rad/sec somewhat questionable.

Figures 8.23 and 8.31 show the vertical acceleration response $\dot{w}$ to a collective control input δ_{col} at 80 and 120 knots respectively. At 80 knots, the amplitudes are over-predicted by between 5 and 10 dB over the entire range of accuracy of the flight test data. This over-prediction is even higher at lower frequencies, although there is essentially no dependency of the amplitude on inflow or blade modeling. At 120 knots, the amplitude over-predictions are slightly higher than those at 80 knots. Again, there is no dependency of the results on inflow or blade modeling. The phase portions at 80 and 120 knots are poorly predicted with both the dynamic inflow and free wake models over the entire frequency range.

Figures 8.24 and 8.32 show the yaw rate response r to pedal input δ_{ped} at 80 and 120 knots respectively. The frequency response results identified from the flight test data have a very limited range of accuracy. At both speeds the model predictions for both the magnitude and phase are in good agreement with the responses derived from flight test data over this accurate frequency range. The predictions outside the range of accuracy of the test data are not as good, although correlations in these frequency ranges are difficult. The blade model does not effect these results, although there is some dependency on inflow modeling below 1 rad/sec.

The results presented here showed the on-axis frequency responses for the UH-60A in forward flight at 80 and 120 knots. In general, there was a good agreement

between the simulation results and flight test data in the frequency ranges where the flight test data was considered accurate. Outside this range the predictions were not as good, although correlations in these frequency ranges are more difficult because of the questionable accuracy of the flight test data. These frequency response predictions for the UH-60A in forward flight showed very little dependency on blade modeling. The dependency of the responses to inflow modeling decreases as the forward speed increases with a higher sensitivity to inflow modeling in forward flight than in hover.

8.2.3 Off-axis frequency response

Figures 8.25 and 8.33 show the off-axis pitch rate q frequency responses to a lateral stick input δ_{lat} for the UH-60A at forward speeds of 80 and 120 knots respectively. At 80 knots the magnitude predictions with the free wake model are consistently about 8 dB higher than those with dynamic inflow over most of the frequency range. A similar trend is seen for the magnitude predictions at 120 knots, however, the difference is smaller at about 4 dB. The phase results show essentially no dependence on inflow modeling, with all of the phase curves being almost superimposed. This lack of sensitivity of the phase results to inflow modeling is seen at both 80 and 120 knots. There is also little sensitivity in the magnitude and phase predictions to blade modeling. This lack of sensitivity to inflow modeling in forward flight is different from that in hover (Fig. 8.7) where the phase predictions show a dependency on inflow modeling, particularly in the frequency range from 0.7 to 7 rad/sec.

Figures 8.26 and 8.34 show the off-axis roll rate p frequency responses to a longitudinal stick input δ_{lon} at 80 and 120 knots respectively. Both figures show only a small effect of blade modeling on the frequency response results. Although the results with the free wake model and the simple blade model at 120 knots

(Fig. 8.34) show some phase differences from about 0.2 rad/sec to 0.8 rad/sec. The suspicious nature of these predictions could be the results of the way in which the linearized models are calculated with the free wake model and the difficulties in accurately capturing the wake distortion effects. This is discussed further in Section. 8.6. At 80 knots, for frequencies above 1 rad/sec both the magnitude and phase predictions show very little sensitivity to inflow modeling. Below 1 rad/sec the amplitude predictions with the free wake are higher than those with dynamic inflow. The extent of the notch type response predicted with dynamic inflow at about 0.7 rad/sec is significantly smaller with the free wake model. The phase predictions show little sensitivity to inflow modeling over the entire frequency range. At 120 knots, both the amplitude and phase predictions show little sensitivity to blade or inflow modeling. In hover, the phase of the roll rate response to a lateral stick input (Fig. 8.10) did show a sensitivity to inflow modeling for frequencies below 4 rad/sec and also showed a 180^{o} phase difference between the dynamic inflow and free wake model predictions below 0.6 rad/sec. However, at 80 and 120 knots, this sensitivity of the phase to inflow modeling is not seen.

The results presented in this section showed some off-axis frequency responses for the UH-60A at 80 and 120 knots of forward speed. No flight test data were available, which made it impossible to determine the accuracy of the predictions. As with all of the other results for the UH-60A, both in hover and forward flight, it was shown that there is very little dependency of the frequency response predictions on blade modeling. Although, unlike in hover, the off-axis frequency response predictions in forward flight show very little dependency on inflow modeling.

8.3 BO-105 in hover

The results in this section refer to the BO-105 hingeless rotor helicopter in hover at an altitude of 3000 feet. Details of the modeling parameters of the BO-105 are presented in Section 6.1. The effects of blade and inflow modeling on the pole locations and the frequency responses are examined. For the free wake results, the resolution of the vortex wake, $\Delta\psi$, is 5 degrees, the total length of each vortex filament ζ_{max} is 720 degrees, and the initial tip vortex strength is equal to the maximum bound circulation along the blade ($C_\Gamma = 1.0$). The other inflow model is the dynamic inflow model of Pitt-Peters that does not include maneuver induced distortions on the wake geometry and inflow. Two different blade models are used in the generation of the numerical results. These are a *simple* blade model that includes only the first elastic flap mode, and a *refined* blade model that includes the first seven elastic blade modes with the lowest natural frequencies.

8.3.1 Poles

Figures 8.35 and 8.36 show the effects of inflow modeling on the open-loop poles of the helicopter mathematical model for the BO-105 in hover. The model representing the blade motion and flexibility is the refined blade model that includes the seven elastic blade modes with the lowest natural frequencies. Because the BO-105 has a hingeless main rotor and does not incorporate a lag damper, the damping of the lag modes remains fairly low. To ensure that the lag modes remain stable, an additional 1% of critical modal damping is added to the damping of the first lag mode and an additional 0.5% of critical damping is added to that of the second lag mode.

Figure 8.35 shows the effect of inflow modeling on the rotor poles. The highest frequency modes are related to the second elastic torsion and third elastic flap

blade modes and their poles are not significantly effected by inflow modeling. The damping of the second lag mode is predicted higher with the free wake model than with dynamic inflow, but these differences are small. However, because the lag damping is low, the increase in damping with the free wake model is a significant result. The most significant effect of inflow modeling is on the first and second flap modes, and on the first torsional mode. The free wake acts to significantly decrease the frequencies and damping of the first and second flap modes from the results with dynamic inflow. For some of these modes, the damping is reduced to about half of its original value. An exception to this, however, is the regressive flap mode where the damping increases. For the first torsional mode, the damping and frequencies of the poles are significantly increased. As with the second lag mode, the poles related to the first lag mode are effected only a slight amount where the free wake model acts to increase the damping of the first lag mode poles. Again, because the damping of the first lag mode is relatively low, the increased damping of this mode with the free wake is found to be significant.

Figure 8.36 shows the pole locations related to the body modes of the BO-105 in hover. The complex conjugate pair for the phugoid is slightly unstable with dynamic inflow, with $\omega_n = 0.5370$ rad/sec and $\zeta = -0.2488$, and is made more unstable using the free wake inflow model with $\omega_n = 0.6352$ rad/sec and $\zeta = -0.5619$. The dutch roll mode is stabilized with the free wake model from $\omega_n = 0.6753$ rad/sec and $\zeta = 0.1841$ with dynamic inflow to $\omega_n = 0.7333$ rad/sec and $\zeta = 0.5457$ with the free wake. The other two body poles for the BO-105 shown here are related to a spiral mode and a pitch mode. The real part of the spiral mode is reduced and that of the pitch mode is increased with the use of the free wake model. There are also three body modes that are not shown in this figure. The first is the heading mode, which would be located at the origin. The other two are a roll mode and a pitch

mode, which have negative real parts that place them further to the left (stable region) than can be seen on this figure.

8.3.2 On-axis frequency response

The effect of inflow and blade modeling on the on-axis frequency response results for the BO-105 in the hover flight condition are shown in Figures 8.37 through 8.40. Results with both the free wake and dynamic inflow models are included. The dynamic inflow model is the Pitt-Peters model, which does not include maneuvering effects. The free wake results are generated with a vortex wake resolution $\Delta\psi$ of 5 degrees, the total length of each vortex filament ζ_{max} is 720 degrees and the initial tip vortex strength is equal to the maximum bound circulation along the blade ($C_\Gamma = 1.0$). There *simple* and *refined* blade models are used.

Figure 8.37 shows the effect of inflow and blade modeling on the roll rate p response to a lateral control input δ_{lat} for the BO-105 in hover. The effects of blade modeling are most visible at high frequencies above about 60 rad/sec. At about 80 rad/sec there is a peak in the magnitude predictions generated with the refined blade model because of the progressive lag mode. The inflow model has no significant effect on the phase predictions but does effect the magnitude. Here the gain is predicted lower with the free wake than with dynamic inflow for frequencies below 1 rad/sec.

Figure 8.38 shows the pitch rate response q to a longitudinal control input δ_{lon}. The blade model has little effect below about 8 rad/sec. The differences above this frequency result from the inclusion of the first elastic lag mode with the refined blade model. In the frequency range from 0.9 to 6 rad/sec, there is no significant effect of inflow modeling. Below 0.9 rad/sec there is an increased gain predicted with the dynamic inflow model and the differences in the phase when compared with the free

wake predictions.

Figure 8.39 shows the vertical acceleration $\dot{w}$ frequency response to a collective stick input δ_{col}. The predictions here are not sensitive to either the blade model nor the inflow model, with the exception of the notch type response at a frequency of about 35 rad/sec, which is a result of the collective and differential lag modes added with the refined blade model. The yaw rate r response to a pedal input δ_{ped} is shown in Figure 8.40. As with the response to a collective input there is little sensitivity of the response to inflow or blade modeling over most of the frequency range. The only difference is with respect to blade modeling at about 30 rad/sec as a result of the first lag model.

The results presented in this section showed the effect of blade and inflow modeling on the on-axis frequency responses for the BO-105 in hover. The effects of inflow modeling were only seen in the responses to lateral and longitudinal control inputs in the low frequency range below 1 rad/sec. Above this frequency the effects of inflow modeling were minimal. The blade model only effected the results for frequencies above about 15 rad/sec and the differences here were as a result of the inclusion of lag degrees of freedom with the refined blade model.

8.3.3 Off-axis frequency response

The effect of inflow and blade modeling on the prediction of the off-axis frequency responses for the BO-105 in hover is examined in this section. However, due to the lack of flight test data for the off-axis responses, no conclusions about the accuracy of the predictions can be made.

Figure 8.41 shows the pitch rate q response to lateral control input δ_{lat} for the BO-105 in hover. For flight dynamics work, the most important frequency range is generally from about 2 to 20 rad/sec, and this is the region in which the most

significant effects of inflow and blade modeling are seen. Significant phase differences with inflow and blade modeling are evident, but it is not clear which results are most accurate because of the lack of test data. The same types of trends are seen in Figure 8.42, which shows the off-axis roll rate p response to a longitudinal stick input δ_{lon}. Again, there are significant phase differences in the frequency range from 0.8 to 20 rad/sec with the different inflow and blade models.

8.4 BO-105 in forward flight

This section examines the poles and frequency response results for the BO-105 in straight and level forward flight at a forward speed of 80 knots, and at an altitude of 3000 feet. The modeling configurations are the same as those described in Section 8.3 for the BO-105 in hover. The two inflow models used are the Pitt-Peters dynamic inflow model and the free wake model ($\Delta\psi = 5^o$, $\zeta_{max} = 720^o$ and $C_\Gamma = 1.0$). Results with both the simple and refined blade models are presented.

8.4.1 Poles

Figures 8.43 and 8.44 show the effect of inflow modeling on the open-loop poles for the BO-105 in forward flight at 80 knots. The effect of inflow modeling on the rotor poles is shown in Figure 8.43. The change in the pole locations with inflow modeling is significantly less at the 80 knot case than in hover. The first and second lag modes, as well as the third flap and second torsional modes are essentially independent of inflow modeling. The damping of the poles, which is related to the second flap mode, is reduced with the free wake model, while the damping of the poles related to the first torsional mode is increased.

The pole locations for the body modes at 80 knots are shown in Figure 8.44. The phugoid mode is seen as an unstable complex conjugate pair using both inflow

models. The free wake model acts to further destabilize this mode from $\omega_n = 0.2398$ rad/sec and $\zeta = -0.0728$ with dynamic inflow to $\omega_n = 0.1903$ rad/sec and $\zeta = -0.1824$ with the free wake model. The phugoid mode is less unstable at 80 knots than it was in hover. The natural frequency of the dutch roll mode is significantly higher at 80 knots than in hover, and the inflow modeling plays only a minor roll on the location of this pole at 80 knots. The spiral mode, which was stable in hover with both inflow models, remains marginally stable at 80 knots with dynamic inflow, but is seen as a static divergent pole lying on the positive real axis when using the free wake model. The pole related to pitch is seen to be less stable with the addition of the free wake model than with dynamic inflow. As in the hover case, the heading pole at the origin is not shown and the two poles for pitch and roll motion have negative real parts that place them further to the left (stable region) than can be seen on this figure.

8.4.2 On-axis frequency response

This section examines the on-axis frequency response results for the BO-105 at a forward speed of 80 knots and at an altitude of 3000 feet. Figure 8.45 shows a comparison for the roll rate frequency response p to a lateral stick input δ_{lat}. Both the amplitude and phase are predicted well at all frequencies except in the low frequency range below 0.4 rad/sec where the amplitude is somewhat over-predicted and there are some differences in the phase. The blade model does not significantly effect the predictions in the frequency range from 0.4 to 10 rad/sec but does have some effect outside this range. The effect of the regressive lag mode is visible in the results with the refined blade model at about 12 rad/sec but is not seen with the simple blade model results as no lag degrees of freedom are included within this model. The flight test data has phase and amplitude changes from the regressive

lag mode at about 14 rad/sec indicating that the frequency of this mode is slightly under-predicted by the simulation model. The other difference is the peak predicted at about 80 rad/sec from the progressive lag mode, which has low damping but is beyond the frequency range of interest for typical flight dynamics work. The effects of inflow modeling on this on-axis response is small, which is similar to the trend seen for the UH-60A in forward flight.

Figure 8.46 shows the pitch rate response q to a longitudinal control input δ_{lon} at 80 knots. The amplitude predictions are qualitatively in good agreement with the test data over the entire frequency range, although the simulation results are consistently a couple of dB higher. The phase predictions made with the free wake model are in good agreement with the test data over the entire frequency range, and show a significant improvement over the dynamic inflow results for frequencies below 5 rad/sec. The peak in the amplitude associated with the unstable phugoid mode is over-predicted with the dynamic inflow model at a frequency of 2.5 rad/sec with the refined blade model and 3.5 rad/sec with the simple blade model and this peak contributes to the lack of accuracy of the phase with dynamic inflow in this frequency range.

Figure 8.47 shows the vertical acceleration $\dot{w}$ response to a collective control input δ_{col}. The amplitude of the response is over-predicted over the entire frequency range with both inflow models, although qualitatively the predictions agree well with the test data. The phase predictions are not as good as those of the amplitude, although the general trends are similar. A notch type response is visible at about 35 rad/sec corresponding to the collective lag mode. A smaller notch is also visible at about 80 rad/sec corresponding to the progressive lag mode. Apart from these two high frequency effects, the blade model effects the predictions only in the low frequency range, where the effects of blade modeling on the locations of the body

poles cause these changes. The effects of inflow modeling are visible only in the mid to low frequency range below 5 rad/sec.

Figure 8.48 shows the yaw rate response r to a pedal input δ_{ped}. The predictions of both the amplitude and phase are found to be in excellent agreement with the flight test data using both inflow models and both blade models over the frequency range where the test data exist. The response resulting from the collective lag mode at about 32 rad/sec is clearly visible in the predictions using the refined blade model. Apart from this lag mode, the effects of blade and inflow modeling are only visible at frequencies below 0.8 rad/sec and the lack of test data in this region make it difficult to interpret these differences.

8.4.3 Off-axis frequency response

Figure 8.49 and 8.50 show the off-axis frequency of pitch q in response to a lateral input δ_{lat}, and roll p response to a longitudinal input δ_{lon}, respectively. For the pitch rate response to a lateral stick input, as shown in Figure 8.49, neither the free wake model nor the dynamic inflow model give particularly good results for the predictions of either the amplitude or the phase. There are also some significant differences in the predictions with the different blade models. The notch type response at about 2.2 rad/sec made using the free wake model with the refined blade model is "suspicious" and is not seen with the other simulation models nor the flight test data. It should be remembered that the individual perturbations for the states and controls were tailored only for the hover flight condition and not specifically for 80 knots, which probably contributes to these differences. This is discussed further in Section 8.6.

A similar trend is seen in Figure 8.50 which shows the roll rate response to a longitudinal control input. The amplitude predictions made using the free wake

model are lower than those with dynamic inflow and also show a better agreement with the test data. Although the phase predictions are seen to be better with dynamic inflow than with the free wake model.

8.5 Effect of free wake resolution

This section examines the effect of the wake resolution $\Delta\psi$ within the free wake model on the results derived from the linearized models calculated using the free wake. The wake resolution is an important parameter for two main reasons. The first is with respect to computational time. By halving $\Delta\psi$, the computer time required for each iteration of the wake geometry loop increases by a factor of four. The second is that the convergence of the wake geometry loop within the free wake model is particularly sensitive to the wake resolution at certain flight conditions. Convergence of the wake geometry loop is in general more difficult with a coarser wake.

Figures 8.51 and 8.52 show the effect of the free wake resolution on the rotor and body poles for the UH-60A in hover. The wake resolutions are $\Delta\psi = 5^{o}$ and $\Delta\psi = 10^{o}$, respectively. The simple blade model is used for both sets of results because it was previously shown that for the UH-60A in hover, the blade model does not have a significant effect on the linearized results. These results show some effect of the wake resolution on the pole locations, but in each case these difference is small.

Figures 8.53 and 8.54 show the roll p to lateral δ_{lat} and pitch q to longitudinal δ_{lon} on-axis frequency responses, again for the UH-60A in hover. The differences resulting from wake resolution are small and isolated to the low frequency range below 0.6 rad/sec. This frequency range is lower than that generally considered to

be important for flight dynamics work.

Figures 8.55 and 8.56 show the pitch q to lateral δ_{lat} and roll p to longitudinal δ_{lon} off-axis frequency responses. As with the on-axis responses, the effects of wake resolution are only seen at the low frequency region below 0.6 rad/sec and the differences here are smaller than those for the on-axis responses.

These results indicate, for the wake resolutions considered, that the predicted pole locations and both the on and off-axis frequency responses are not dependent on the wake resolution. This conclusion should however be considered carefully because with the coarser wake resolution ($\Delta\psi = 10^{o}$) the convergence of the free wake model is not always possible.

8.6 Effect of numerical perturbation

The linear models generated in the current study describe the small perturbation motion about a given equilibrium position. The linear models are generated by numerically perturbing the equations of motion about this equilibrium position. A central difference approximation to the derivatives is used and the individual elements of the state **A** and control **B** matrices are calculated using Eqs. (4.8) and (4.9). These equations require, amongst other things, a numerical value by which the state and control variables are perturbed. It is the effect of the size of this numerical perturbation that is now examined in this section.

With the dynamic inflow model the perturbation size has little effect on the value of the individual stability and control derivatives that make up the state and control matrices, and also on the resulting frequency responses [56]. The perturbation, however, cannot be arbitrarily large because the equations of motion are non-linear in nature. If the perturbation is too large, then the Taylor series expansion of

the equations (Eqn. (4.1)) is truncated to only include the first derivative or linear terms introduces truncation errors. This still leaves a wide range of perturbation values that can be used, and they span a number of orders of magnitude below the point where truncation errors become an issue. This is, however, not true when the free wake inflow model is used. Here, the circulation loop, which is a double nested loop of the wake geometry and inflow distribution, is contained within the perturbation loop. This is illustrated in Figure 4.2, where the circulation loop is evaluated after each of the positive and negative perturbations of the states and controls are made. Ideally the tolerances of the inner loops would be tighter than those of the outer loops [84], with the tightest tolerance on the innermost loop (wake geometry loop) and the loosest tolerance on the outermost loop (perturbation loop). However this is not possible with the free wake model, where because of the convergence characteristics of the wake geometry loop, the tolerance of the innermost loop is, in general, higher than those of the outer loops. The consequence of this, is that the value of the numerical perturbation used to calculate the individual elements of the state and control matrices must be chosen carefully to fully capture the free wake effects.

Figures 8.57 and 8.58 show the effect of the size of the numerical perturbation of the roll rate Δp on the L_p and M_p stability derivatives for both the BO-105 and UH-60A in hover. Figures 8.59 and 8.60 show similar results of the pitch rate perturbation size Δq on the L_q and M_q stability derivatives. Each of these figures has the stability derivative value on the y-axis plotted as a function of the perturbation size used in the central difference approximation to the derivative (Eqs. (4.8) and (4.9)). The perturbations are made from the pitch and roll rate trim values, which are zero for the straight and level flight case considered. Therefore the perturbation values shown in Figures 8.57 through 8.60 represent the absolute value of the perturbation

and not a relative value.

Three distinct regions are obtained in each of the figures. The first is an erroneous region where the perturbation size is too small and the effects of the free wake geometry and subsequent inflow changes are not captured. This region is labeled "Free wake not activated". When the perturbation size is too small, then the circulation loop (including the wake geometry loop and the circulation-inflow loop) is already converged without the need for further wake geometry and inflow iterations. So the effects of the wake geometry and inflow changes are not captured and the free wake is essentially not activated.

The second is another erroneous region where the perturbation is too large and the errors are related to the fact that the Taylor series is truncated to only include the first derivative or linear terms (Eqn. (4.1)). This region is labeled "Truncation region". This region exists because of the non-linear nature of the mathematical model and when the perturbation size increases, the effects of these non-linearities on the linear approximation becomes more noticeable.

The final region is where the perturbation size is large enough to ensure that the free wake is activated and the effects of the wake distortions on the inflow distribution captured, but not too large that errors resulting from truncation become significant. This region is labeled "Correct region" in Figures 8.57 through 8.60.

The trends seen in these figures with three distinct regions, are typical of those for all of the stability and control derivatives. Namely that the value of the numerical perturbation significantly effects the prediction of the stability and control derivatives. Considering Figure 8.57, which shows the effect of the roll rate perturbation size on the L_p derivative, it is shown that the range of perturbations to be in the "Correct region" is limited for both helicopters and is less than an order of magnitude for the UH-60A. Also, the size and location of this "correct region" is a

function of the helicopter itself because it is different for the BO-105 and UH-60A helicopters. In fact, the location and size of the region for which the perturbation size is correct is dependent on a number of factors, including the helicopter, the state or control derivative being perturbed, the equation being considered, the trim or equilibrium condition, the flight condition, and various free wake model parameters.

These results indicate that the perturbation size used in the calculation of the central difference approximations (such as those in Eqs. (4.8) and (4.9)) required to build the linearized model must be chosen carefully. Further, the selection of the perturbation size used for each state and control variable must be treated separately. Here a relationship between the derivative value and the perturbation size, such as those shown in Figures 8.57 through 8.60, would be constructed and a correct perturbation size selected for each state and control variable. This leads to a complicated and computationally expensive method for the determination of the linearized models that accurately captures the effects of the free wake, including the wake distortions from maneuvers. For the current analysis, this entire procedure has been performed for the BO-105 and UH-60A helicopters only in the hover flight condition. For the calculation of the linearized models in forward flight, the perturbations used are those from the hover flight condition. For this reason any linearized model results in forward flight for both the BO-105 and UH-60A must be considered with care.

Figures 8.61 through 8.68 show the effects on the frequency responses of using an incorrect perturbation size for some of the state variables. For the BO-105 in hover, Figures 8.61 through 8.64 show the on-axis and off-axis frequency responses to lateral and longitudinal control inputs. In each of these figures there are three curves. The first, labeled "Correct perturbations", is generated using the correct perturbation values of all of the state and control variables and represents an accu-

rate frequency response that captures the maneuvering effects associated with the free wake model. The next curve, labeled "Non-linear region", has the two columns of the state matrix related to derivatives of the roll rate p and the pitch rate q generated with perturbations that are too large and in the "Truncation region". Therefore, the columns related to perturbations of p and q are erroneous. The other columns of the state matrix and all of the columns of the control matrix are calculated using the correct perturbations and are identical to those of the "Correct perturbations" linear model. The final curve, labeled "Wake not activated", has the p and q perturbation value being too small to correctly activate the wake and so the columns of the state matrix related to the derivatives with p and q are also erroneous. Again, all of the other columns of the state matrix and the control matrix remain unchanged.

Figures 8.61 and 8.62 show that the on-axis frequency responses are not significantly effected while the off-axis responses, shown in Figures 8.63 and 8.64 so show significant changes. Here, significant magnitude and phase changes are seen for the case in which the free wake is not activated, even though only two columns of the linearized model were changed. Also of significance is that these differences occur in the center of the frequency region that is of most interest in flight dynamics work, namely between 2 and 20 rad/sec. Similar trends are also seen for the UH-60A in hover (Figures 8.65 through 8.68) where again the columns related to the derivatives with p and q were altered. The the UH-60A, the on-axis frequency responses were not significantly affected but there were changes in both the magnitude and phase predictions for the off-axis responses.

It was shown in Figure 8.34 that there were some "suspicious" predictions with the free wake model and the simple blade model for the UH-60A at 120 knots. In particular, the step change in the phase predictions at a frequency of 0.2 rad/sec

is probably the result of an incorrect perturbation size of one or more of the states or controls where the free wake is not being activated correctly. It should be remembered that the perturbation sizes for the states and controls were tailored for the hover flight condition only, and these values were also used to calculate the linearized model results at 120 knots. A further validation of the linearized model results in forward flight would require the tailoring of the perturbation size for each of the states and controls at the particular flight condition. For this precise reason, the results from the linearized models in forward flight must be considered with caution.

The linearized model results with dynamic inflow seem to be fairly independent of the perturbation size used to calculate the linearized models. The same is not true, however, with the free wake model, where the range of valid perturbations required to accurately capture the maneuvering effects associated with the free wake model are relatively small. In certain cases, this range can be as small as a single order of magnitude. In addition, the correct range of perturbation values is dependent on a number of parameters, including the state or control being considered, its numerical value, the particular helicopter, the helicopter configuration, the forward speed, etc. For this study the correct values of the numerical perturbations were tailored for the hover flight condition only. For forward flight, the perturbation sizes used were the same as those from hover and so are not specifically tailored for any forward flight conditions. For this reason the forward flight results presented in this chapter much be considered with care.

8.7 Keller's extended momentum theory

The third inflow model that is considered in this study is the so called "extended momentum theory" model, proposed by Keller [15]. This model includes wake distortion effects from maneuvers through the use of a wake distortion parameter K_R (see Section 2.7). The major difference between this model, which captures wake distortion effects from maneuvers, and the free wake model, which also captures maneuver effects, is that the extended momentum theory model includes inflow dynamics or unsteadiness while the free wake model does not.

Figures 8.69 through 8.72 show the on-axis and off-axis frequency responses to lateral and longitudinal control inputs for the UH-60A in hover. Various values of the wake distortion parameter K_R are used. The dynamic inflow results, that do not include wake distortion effects, can be considered as the case with $K_R = 0.0$. The simple blade model with rigid flap and lag modes is used. Figure 8.69 shows the on-axis roll rate response p to a lateral stick input δ_{lat}. This response is not significantly effected by the K_R value and the agreement with the flight test data is good over the range of accuracy of the test data. The only difference being that the peak corresponding to the dutch roll mode at about 0.6 rad/sec is increased with higher K_R values. The on-axis pitch rate response q to a longitudinal stick input δ_{lon} is shown in Figure 8.70. The effect of the K_R value is small and the agreement with the flight test data is excellent where the test data is considered accurate.

The most significant effects of the inclusion of the wake distortion effects is to the off-axis responses, which are shown in Figures 8.71 and 8.72. Figure 8.71 shows that a substantial improvement in the phase of the pitch rate response q to a lateral stick input δ_{lat} is achieved as the K_R value is increased, although it should be remembered that the flight test data is considered to have limited accuracy over

the entire frequency range. While the dynamic inflow predictions ($K_R = 0.0$) show a 180^o phase difference from the flight test data in the frequency range from 0.9 to 6 rad/sec, the predictions with $K_R = 1.5$ are in phase with the flight test data from about 1.2 to 6 rad/sec. The magnitude predictions do not, however, show the same improvement, although the lack of accurate flight test data make these comparisons difficult.

The off-axis roll rate response p to a longitudinal control input δ_{lon}, shown in Figure 8.72, also has an improved correlation with the inclusion of the wake distortion effects. The phase predictions are improved in the frequency range from 3 to 12 rad/sec, and a better agreement with the flight test data is seen with increasing K_R. However the inclusion of wake distortion effects does not effect the phase in the frequency range from 1 to 3 rad/sec and the correlation in this region is not improved here. The magnitude predictions deteriate somewhat with the wake distortions and the over-predictions increase as the value of K_R is increased.

Similar trends with the inclusion of the wake distortion effects are seen when compared with the BO-105 results. Figures 8.73 through 8.76 show the on-axis and off-axis responses to longitudinal and lateral control inputs for the BO-105 at 80 knots. The refined blade model is used. As with the UH-60A, the on-axis responses are not significantly effected while the off-axis predictions are somewhat improved.

8.8 Discussion of linearized model results

This section contains a discussion of the linearized model results for the BO-105 and UH-60A helicopters presented earlier in this chapter.

The on-axis response results for the BO-105 did not show significant effects of inflow or blade modeling in the frequency range between 2 and 20 rad/sec. At

frequencies lower than 2 rad/sec there were, however, some differences with inflow modeling, which were generally a consequence of the effects of inflow modeling on the rigid body or fuselage modes. At frequencies above 10 rad/sec, blade modeling has some effect on the on-axis predictions because of the additional blade modes included in the refined blade model. In particular, the effects of the inclusion of the first elastic lag mode with the refined blade model effects the frequency responses from about 10 to 80 rad/sec. These trends are seen in both hover and forward flight at 80 knots. With respect to the off-axis response predictions, the inclusion of the free wake model does not improve the correlation with the test data, although the limited amount of flight test data available limited the comparisons to a flight condition of 80 knots only. These off-axis response predictions also showed some sensitivity to blade modeling, particularly in the frequency range from 1 to 8 rad/sec. The third inflow model considered was the extended momentum theory model, proposed by Keller, which includes wake distortion effects from maneuvers. When these results were compared to those with the Pitt-Peters dynamic inflow model, there were only small changes in the on-axis response predictions. In the frequency range from 0.5 to 2 rad/sec, the phase of the on-axis responses were slightly degraded with the wake distortion effects included. However, for the off-axis responses, the correlation for the pitch response to a lateral input was improved with the wake distortion effects included, while it was slightly degraded for the roll response to a longitudinal input.

For the UH-60A, the on-axis frequency responses were, in general, in good agreement with the test data in the frequency range where the flight test data was considered accurate. This was seen in both hover and forward flight. In hover, the on-axis responses to longitudinal and lateral control inputs showed a 180^{o} phase difference between the predictions with the dynamic inflow and free wake inflow models for frequencies below 0.8 rad/sec. This same trend was not seen in forward flight. Again,

in hover the magnitude of the vertical acceleration to a collective control input was over-predicted with the free wake model, as were the magnitudes of the off-axis responses to collective. This over-prediction of the responses to collective is probably resulting from the lack of inflow dynamics or unsteadiness associated with the free wake model, where the change in inflow occurs instantaneously following a change in collective. For the pitch to lateral and roll to longitudinal off-axis responses in hover, there are some improvements in the magnitude predictions with the free wake model, but no real improvements in the phase predictions. Although these correlations should be considered carefully because the accuracy of the flight test data for the off-axis responses is in general quite low. In forward flight, no flight test data for the off-axis responses exists, and so no conclusions about the accuracy of the predicted responses could be made. With the extended momentum theory inflow model, which includes wake distortion effects from maneuvers, there are substantial improvements in the prediction of the phase of the off-axis frequency responses of both the pitch to lateral and roll to longitudinal responses in hover. This trend is not seen in the corresponding amplitude predictions where the amplitudes are somewhat over-predicted with the inclusion of the maneuvering effects in the dynamic inflow model.

These results for the UH-60A indicate that neither inflow nor blade modeling have a significant effect on the on-axis responses in the frequency range of interest for flight dynamics work, that is in the range from 2 to 20 rad/sec. However for the off-axis response predictions the extended momentum theory model gives the best phase correlations, while at the same time degrading the magnitude predictions. The off-axis response predictions were not improved with the free wake model. This seems to indicate, at least for the UH-60A in hover, that the unsteadiness of the inflow is critical for the accurate prediction of the off-axis frequency responses.

The effect of the free wake resolution on the poles and frequency response results was also examined. This free wake parameter has only a small effect on the frequency responses which is visible only in the low frequency range. Here the effect of the wake resolution on the body pole locations, although small, probably causes the changes in the frequency response predictions.

The final effect investigated was that of the perturbation size used in the calculation of the central difference approximation to the first derivatives that make up the linearized model. It was shown that the choice of perturbation size is critical with the free wake model and some rather small changes in this perturbation can have significant effects on the predicted responses. If the perturbation size is too small, then the free wake is essentially not activated and the effects of the free wake distortions from maneuvers are not fully captured. If the perturbation size is too large, then truncation errors become important. This leaves a perturbation region in-between, where the free wake effects are captured accurately. This region is generally quite small and dependent on a number of factors. These include the state or control variable being perturbed, the helicopter and helicopter configuration, flight condition, various free wake parameters, etc. This means that the perturbation size for each state and control variable must be chosen separately and carefully so that the free wake is activated correctly. This must also be done for each helicopter at each flight condition. For this study the perturbation sizes for each of the states and controls to correctly activate the wake were determined for the BO-105 and UH-60A in the hover flight condition only. The values of the perturbation sizes used in forward flight were not specifically examined, but rather, the values from the hover flight condition were used. For this reason, all of the forward flight results presented in this chapter must be considered with care. This is because the use of incorrect perturbation sizes for just one or two states can have significant effects on

the frequency response predictions. For the UH-60A in hover, the use of incorrect perturbations for the pitch and roll rates produced significant phase differences in the off-axis response predictions for frequencies of 2 to 10 rad/sec, which is precisely the frequency range that is of most interest in flight dynamics work.

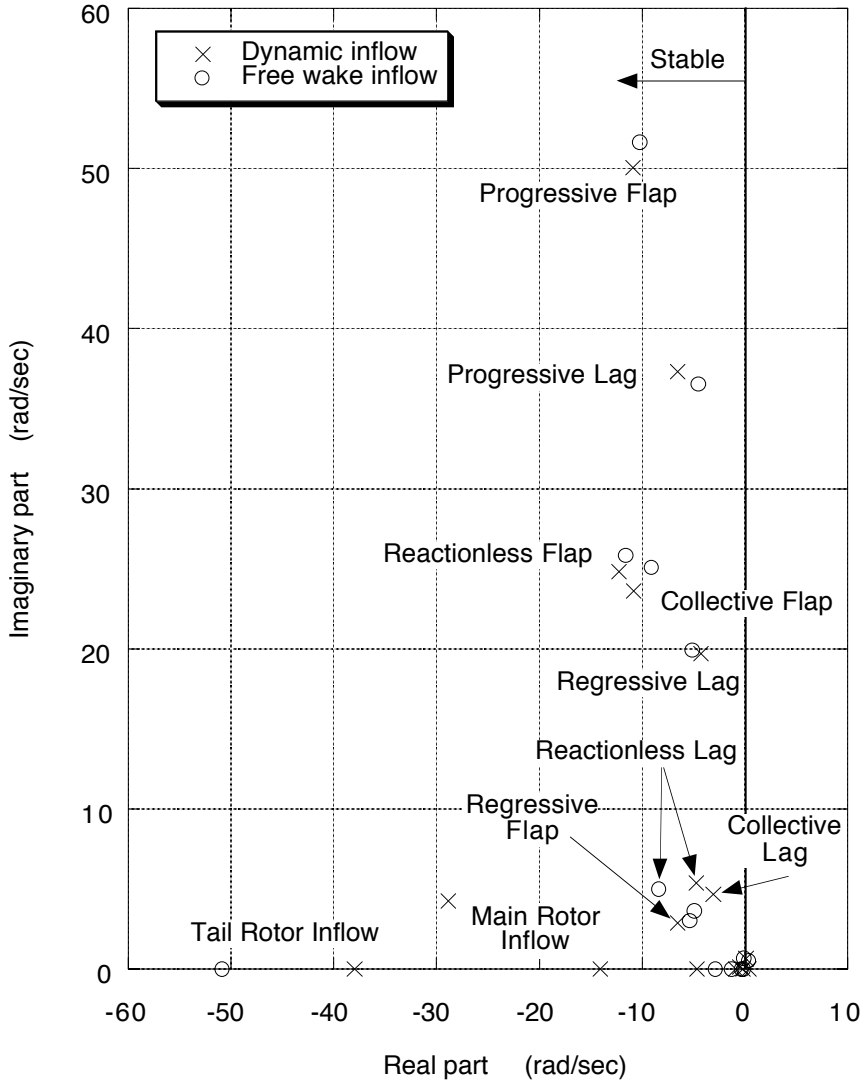

Figure 8.1: Effect of inflow modeling on rotor and inflow poles for the UH-60A in hover with the simple blade model.

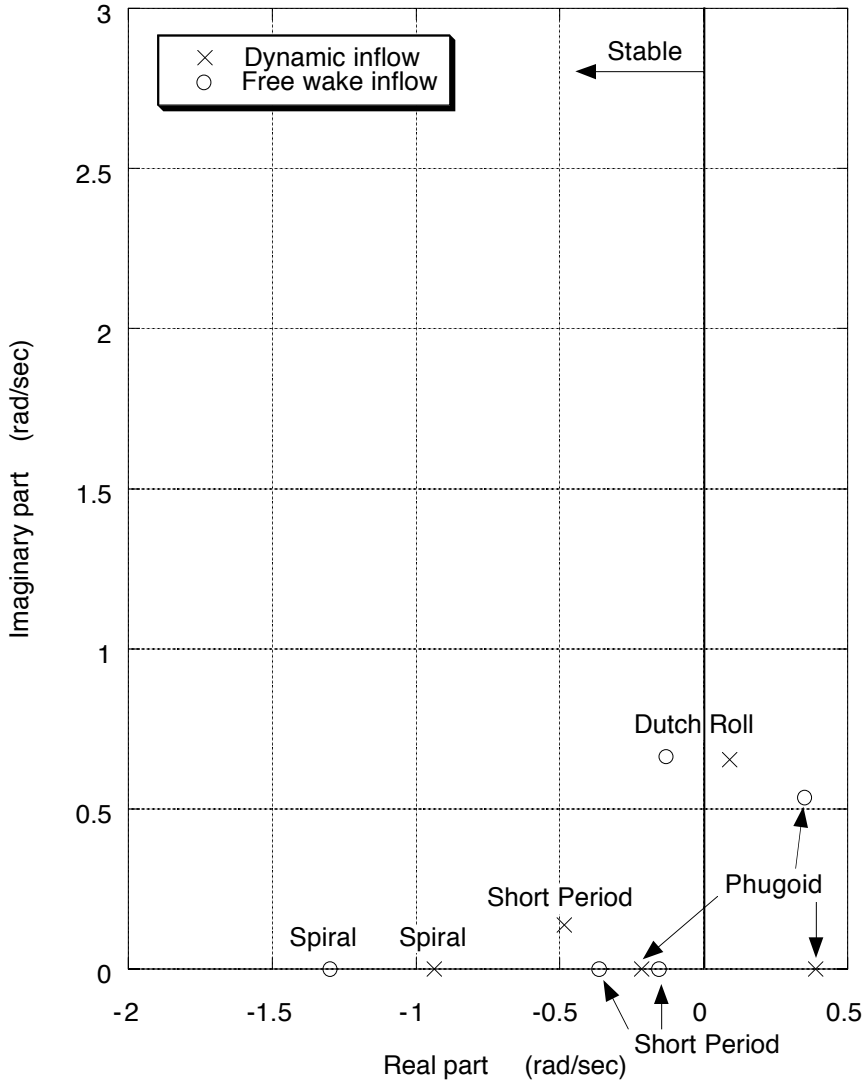

Figure 8.2: Effect of inflow modeling on fuselage poles for the UH-60A in hover with simple blade model.

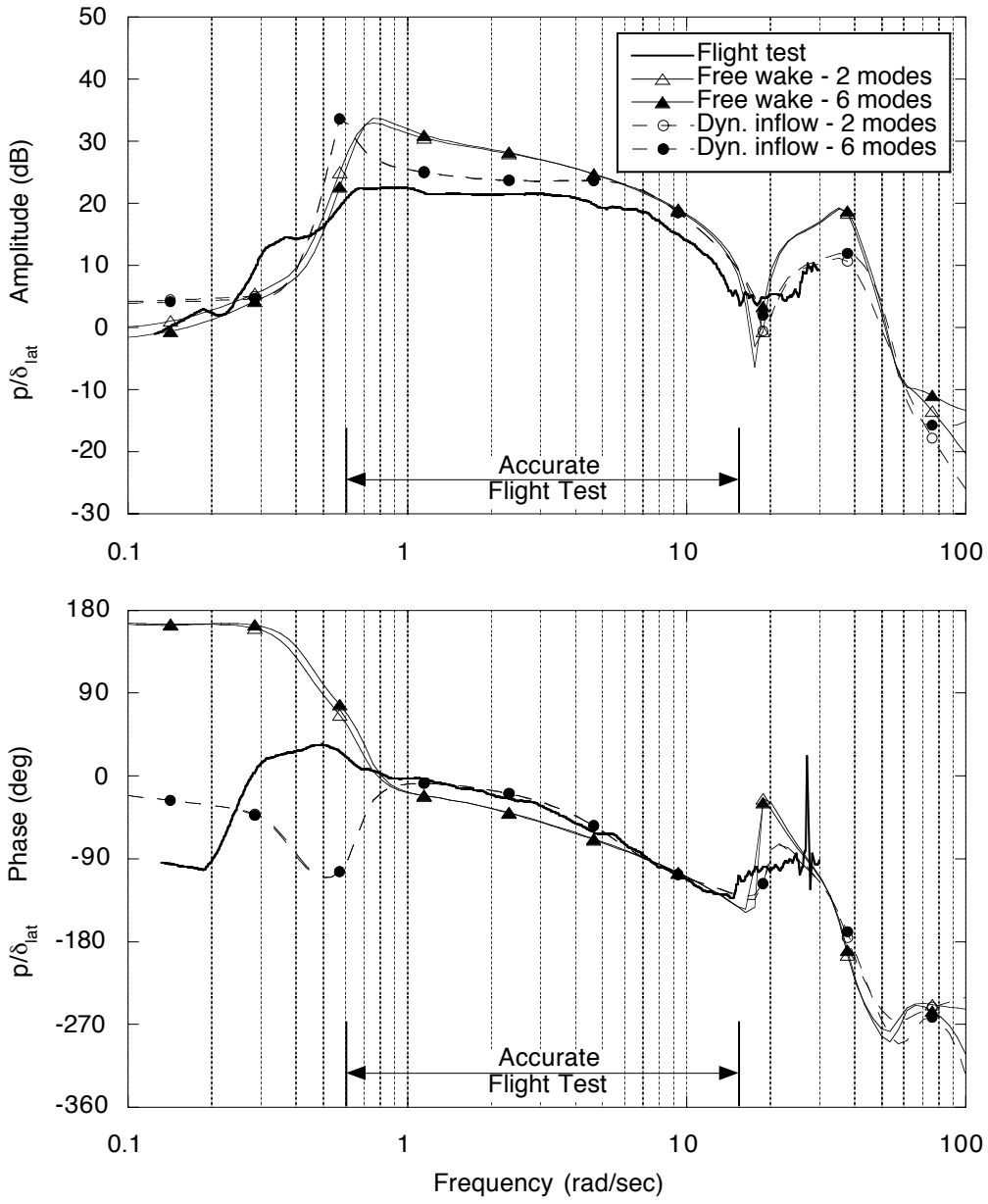

Figure 8.3: Effect of inflow models and blade modeling on the on-axis roll rate frequency response to lateral stick input for the UH-60A in hover.

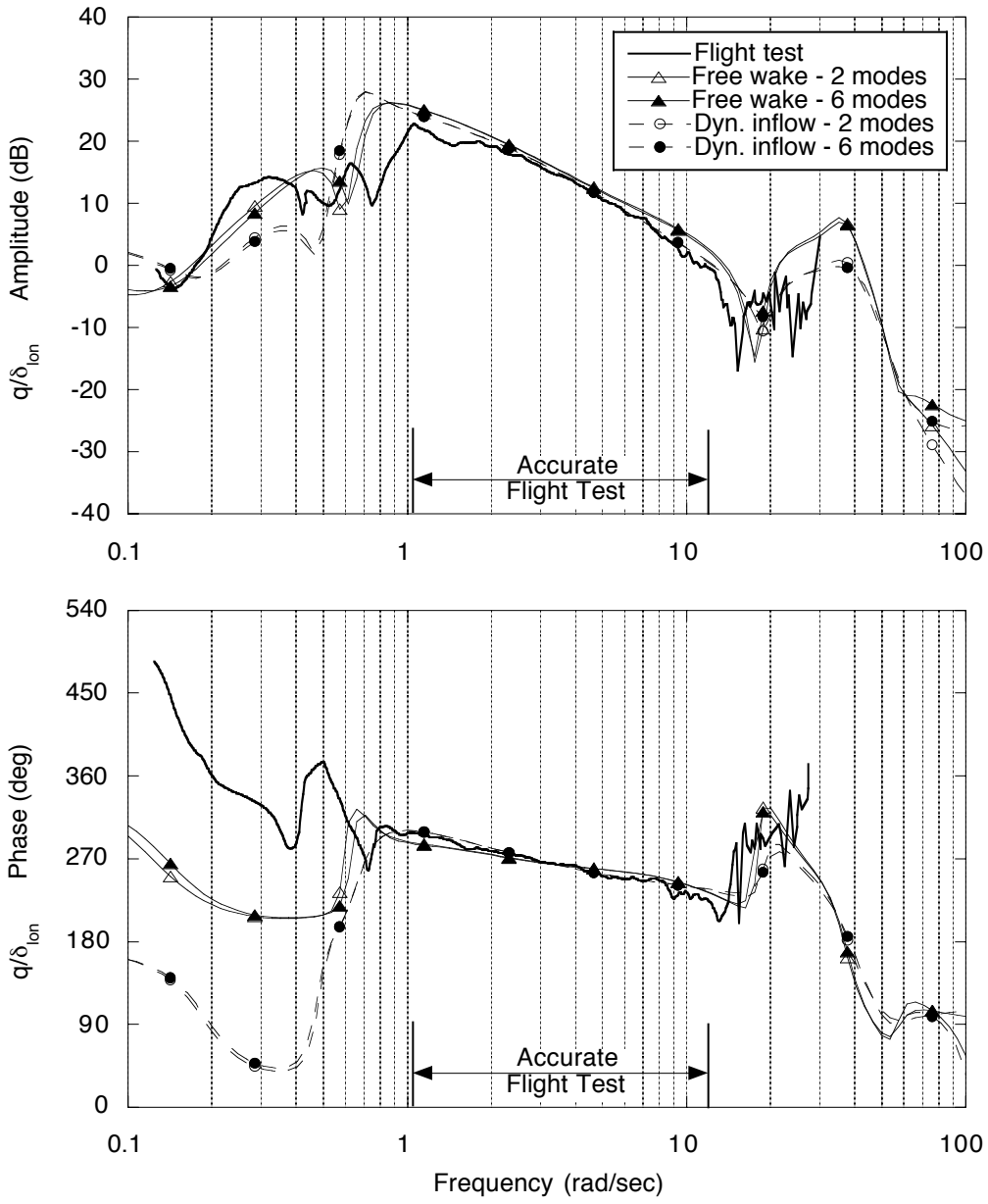

Figure 8.4: Effect of inflow models and blade modeling on the on-axis pitch rate frequency response to longitudinal stick input for the UH-60A in hover.

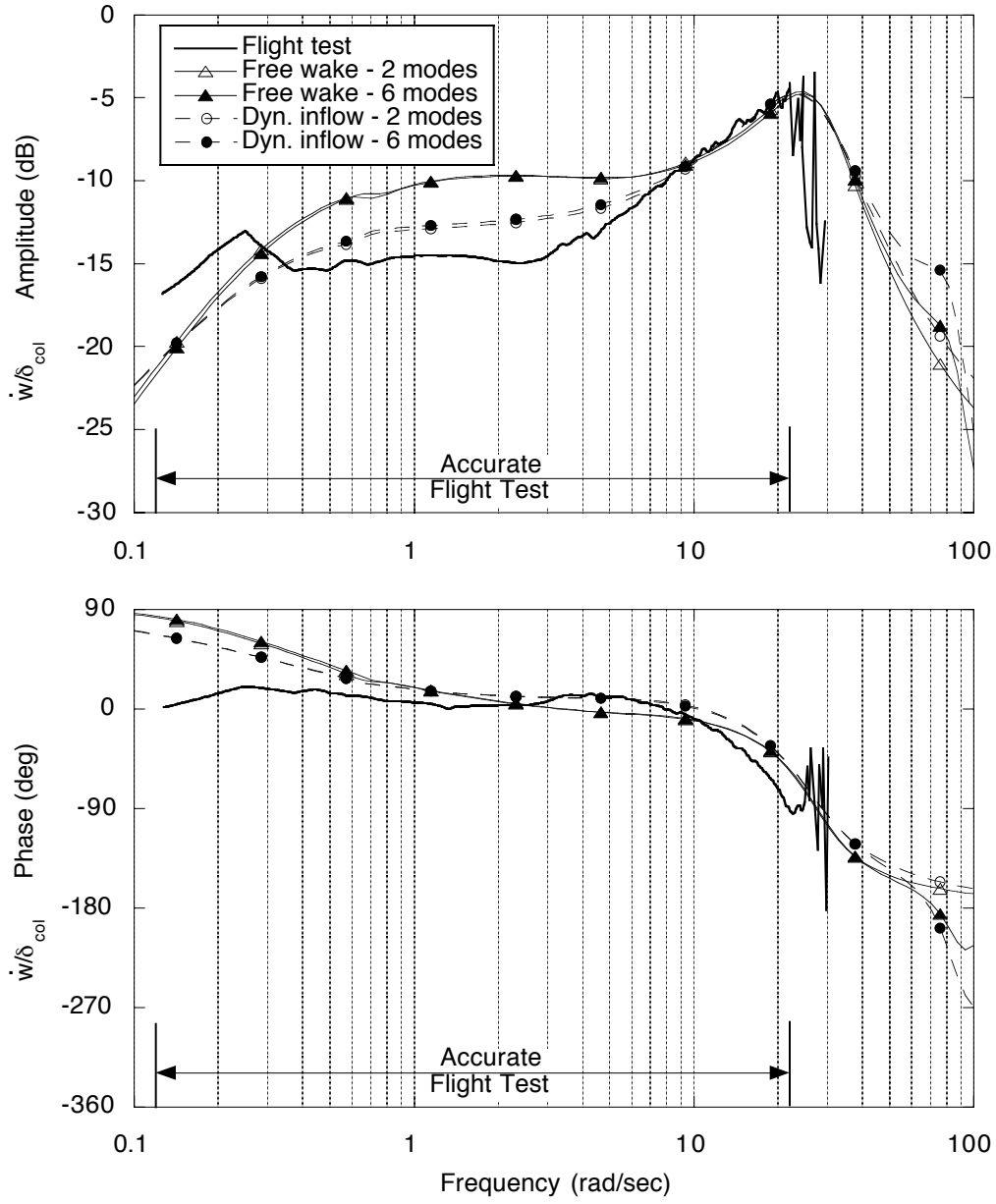

Figure 8.5: Effect of inflow models and blade modeling on the on-axis vertical acceleration frequency response to collective stick input for the UH-60A in hover.

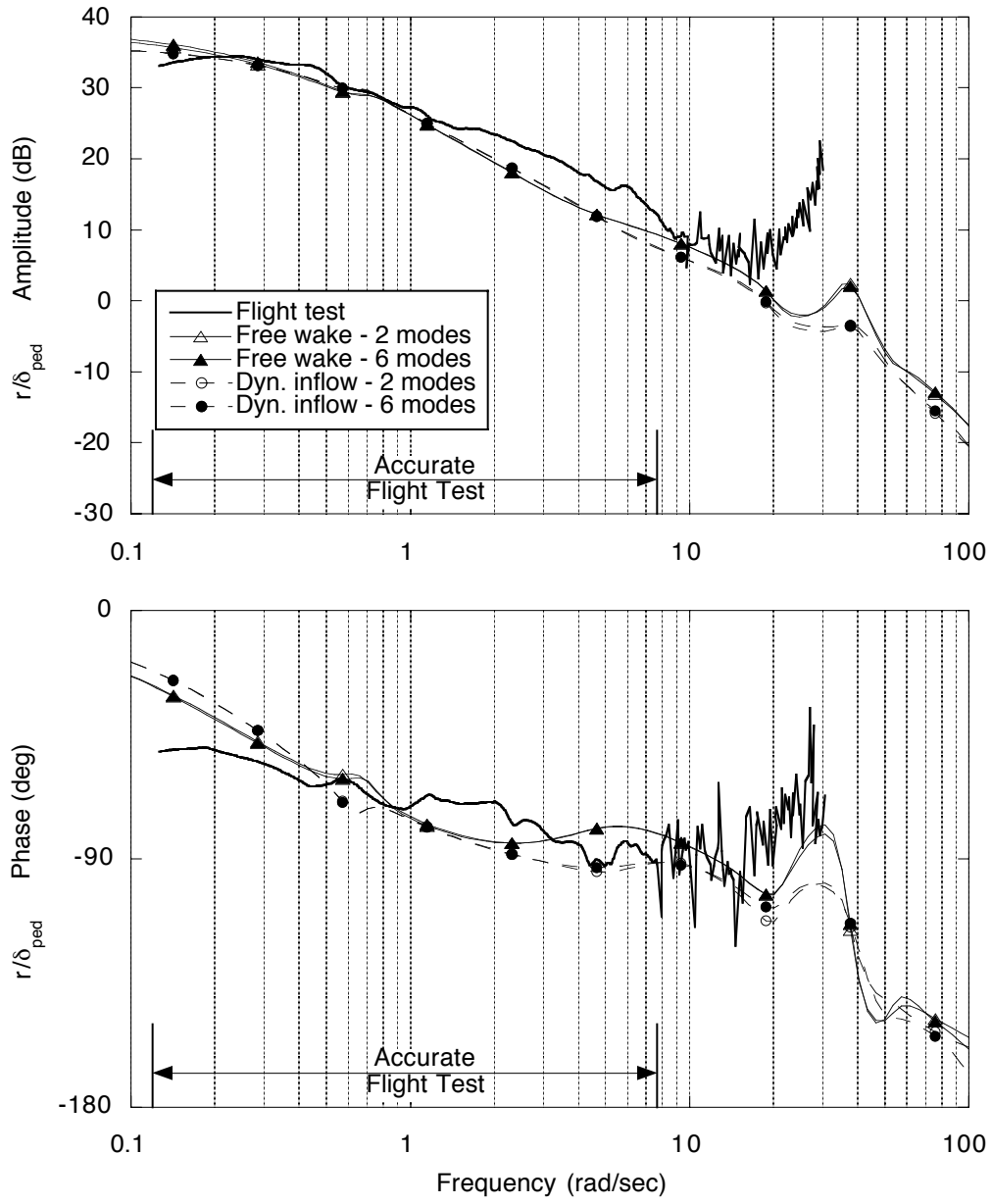

Figure 8.6: Effect of inflow models and blade modeling on the on-axis yaw rate frequency response to pedal input for the UH-60A in hover.

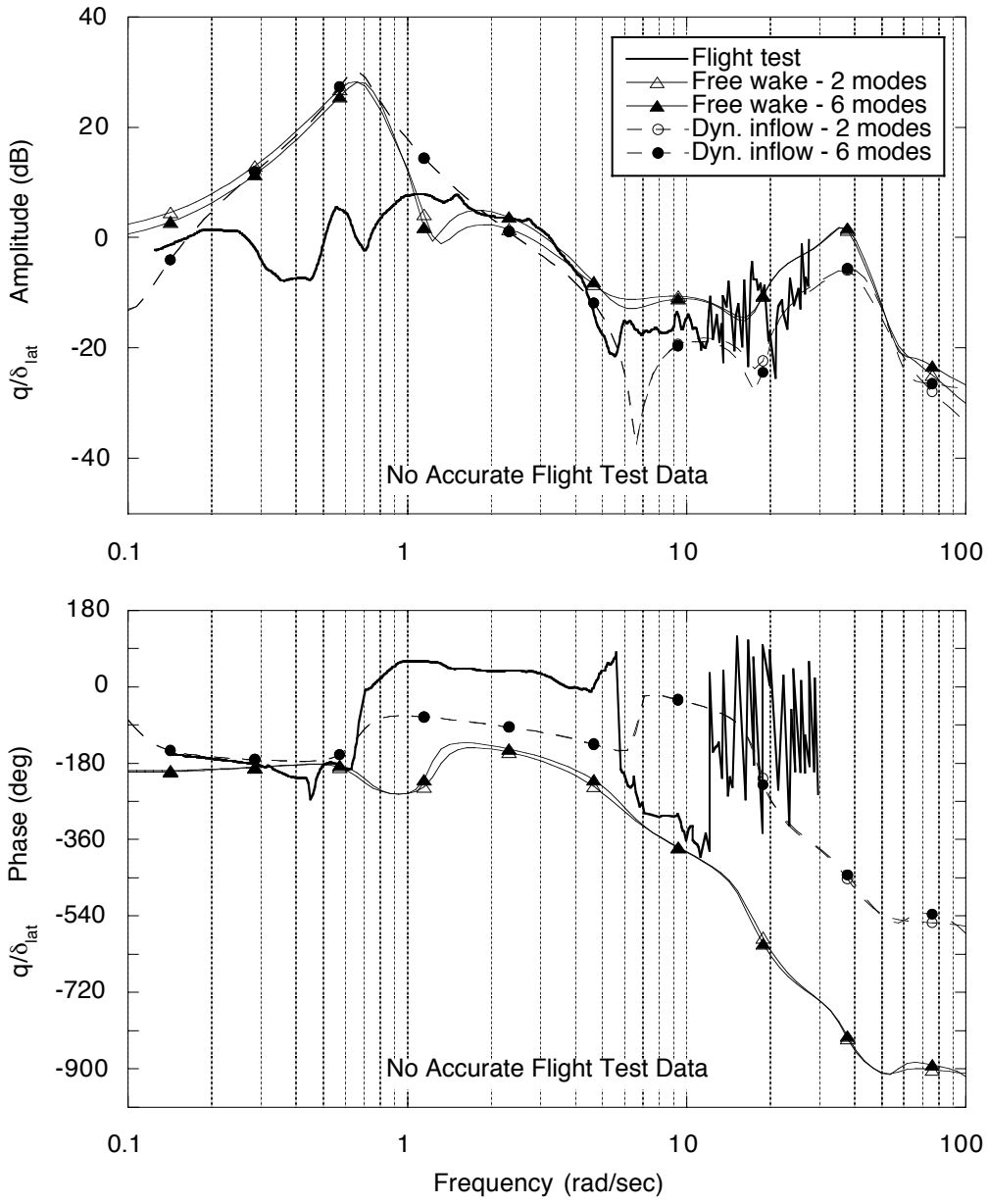

Figure 8.7: Effect of inflow models and blade modeling on the off-axis pitch rate frequency response to lateral stick input for the UH-60A in hover.

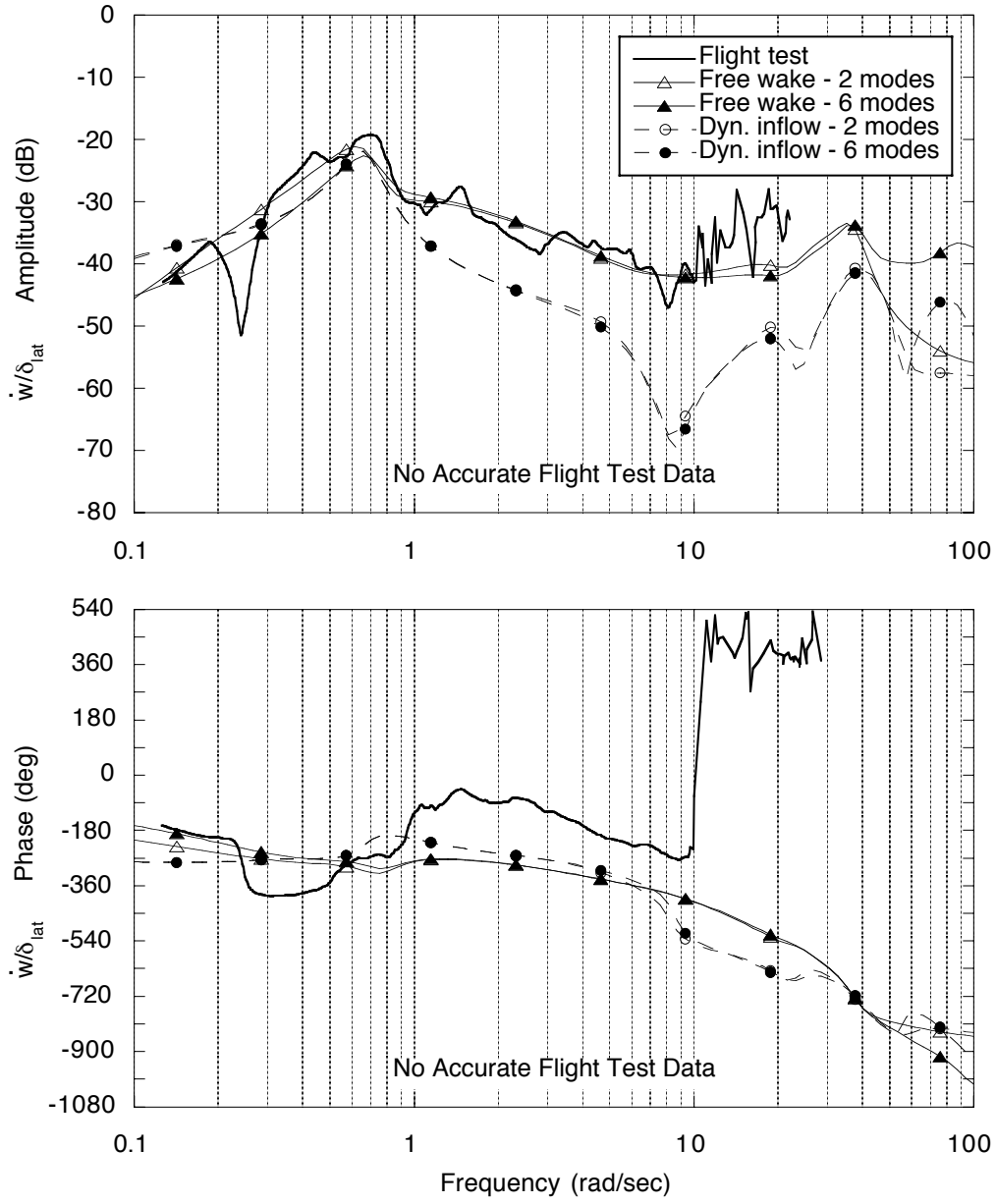

Figure 8.8: Effect of inflow models and blade modeling on the off-axis vertical acceleration frequency response to lateral stick input for the UH-60A in hover.

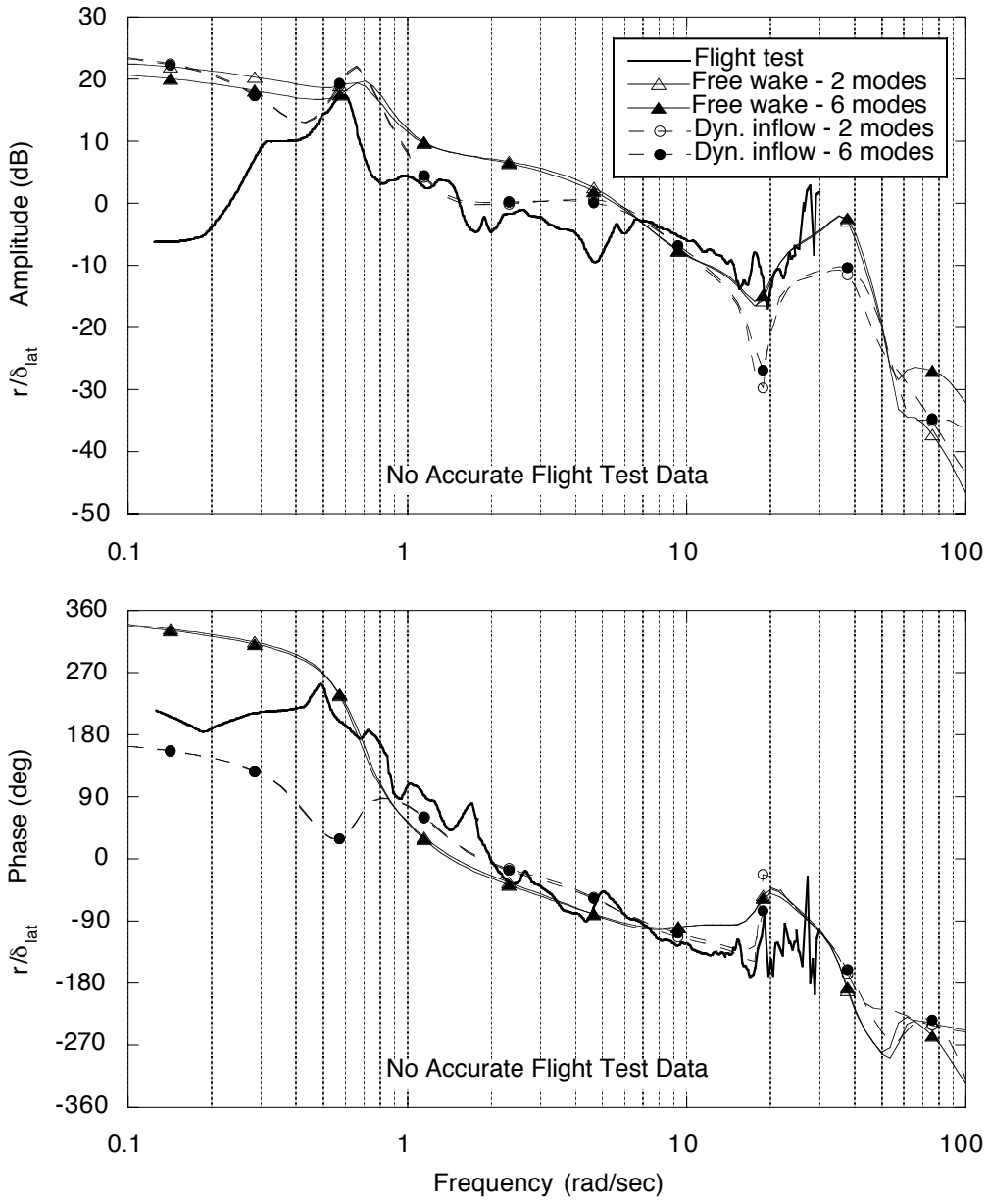

Figure 8.9: Effect of inflow models and blade modeling on the off-axis yaw rate frequency response to lateral stick input for the UH-60A in hover.

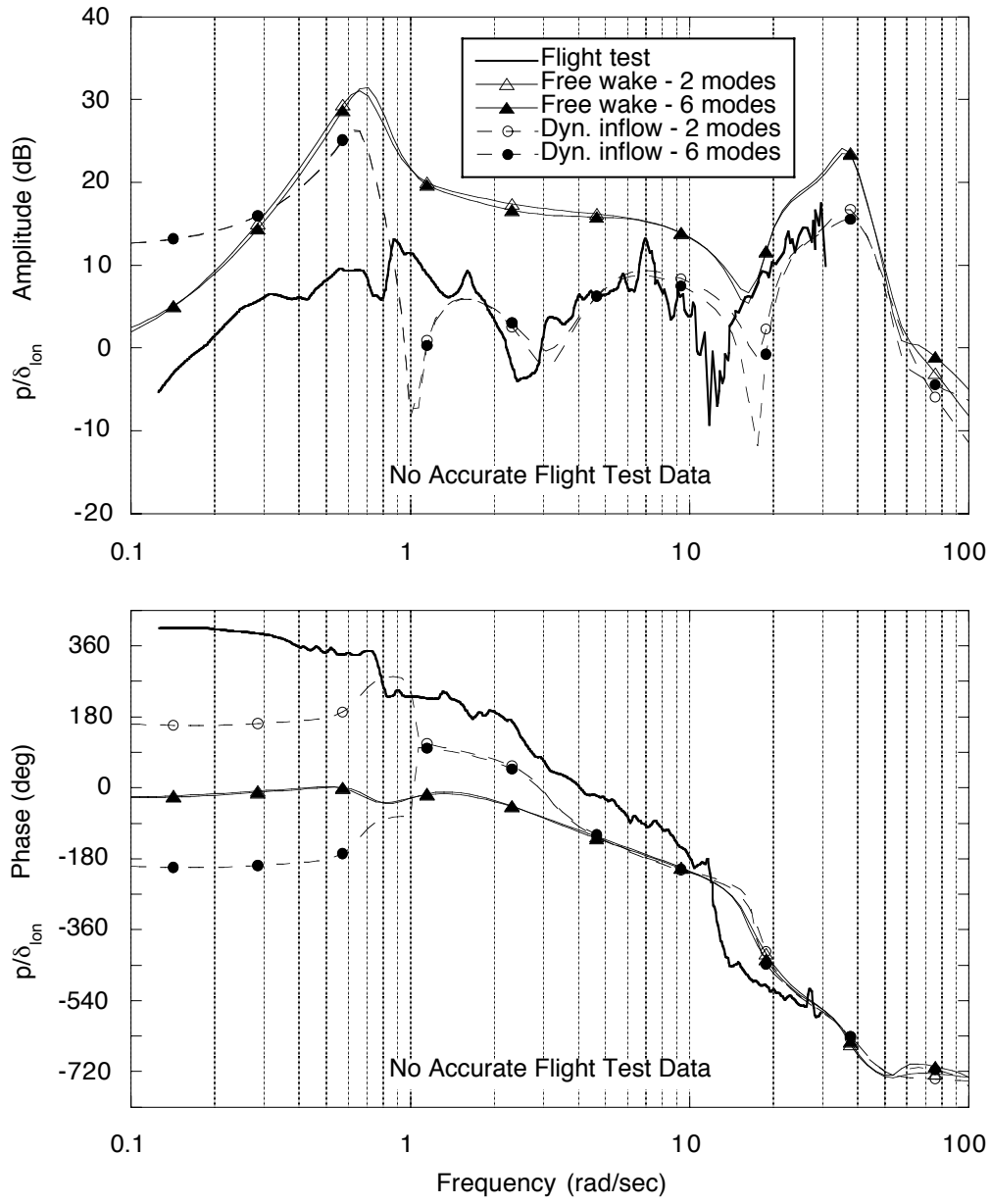

Figure 8.10: Effect of inflow models and blade modeling on the off-axis roll rate frequency response to longitudinal stick input for the UH-60A in hover.

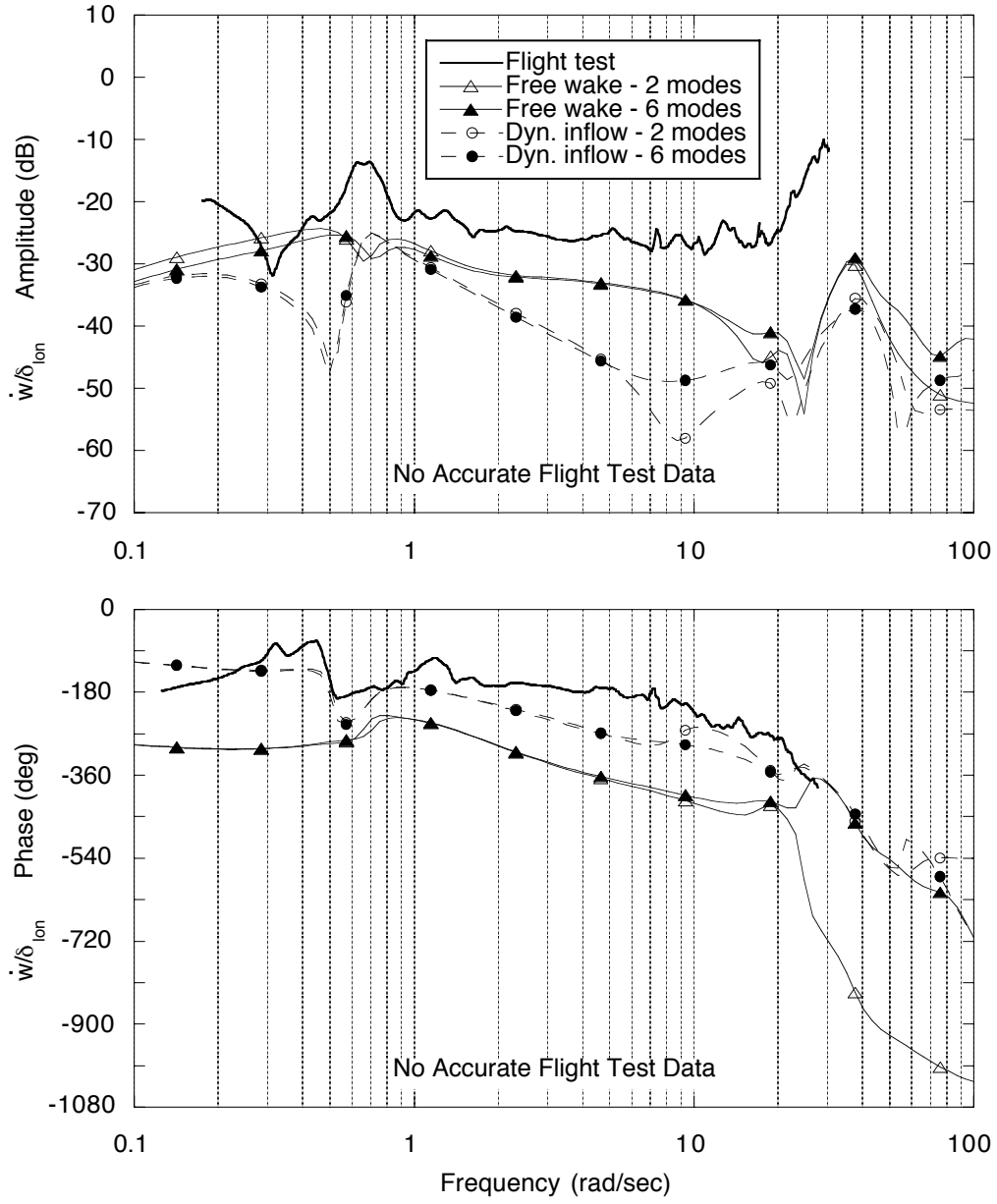

Figure 8.11: Effect of inflow models and blade modeling on the off-axis vertical acceleration frequency response to longitudinal stick input for the UH-60A in hover.

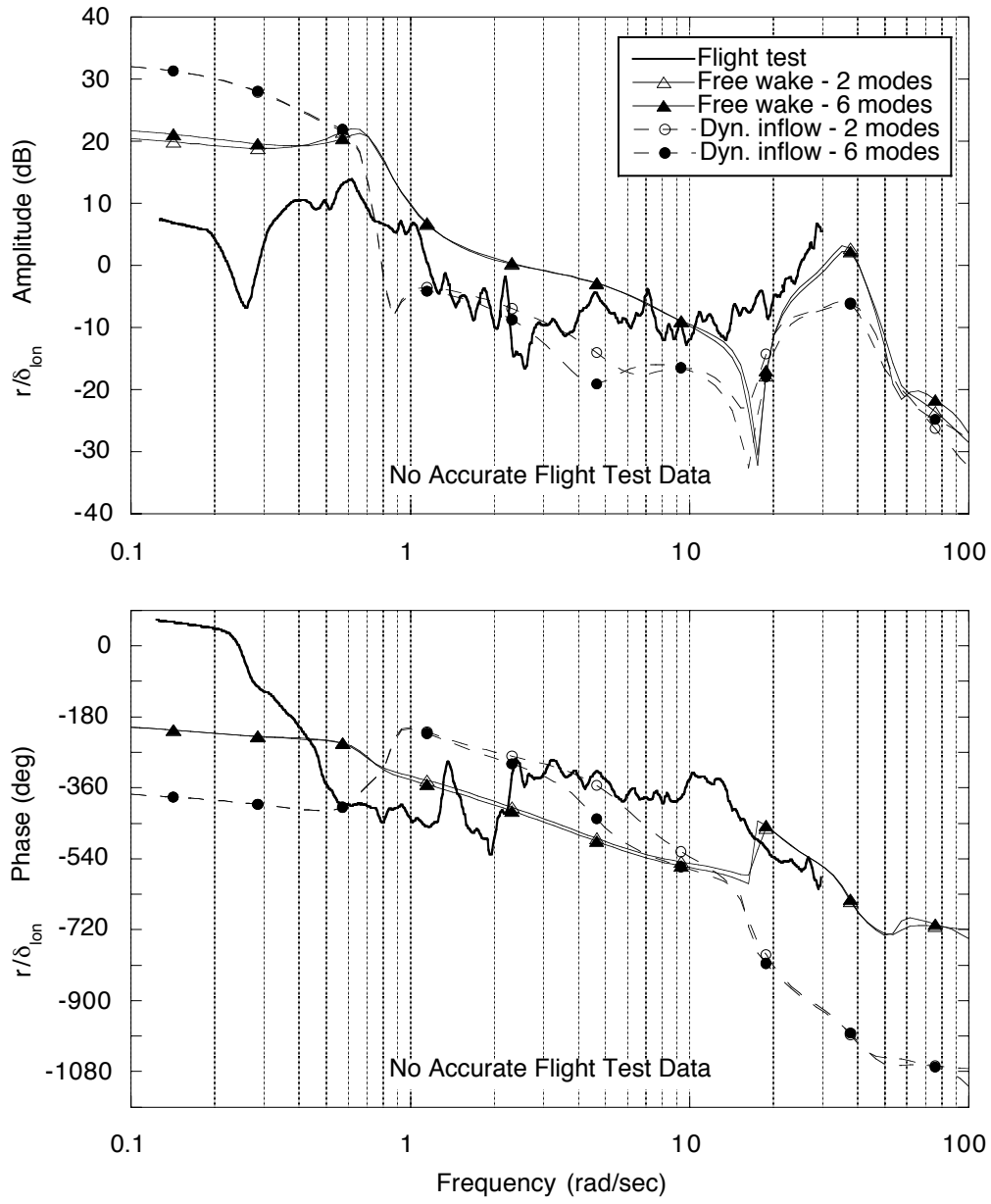

Figure 8.12: Effect of inflow models and blade modeling on the off-axis yaw rate frequency response to longitudinal stick input for the UH-60A in hover.

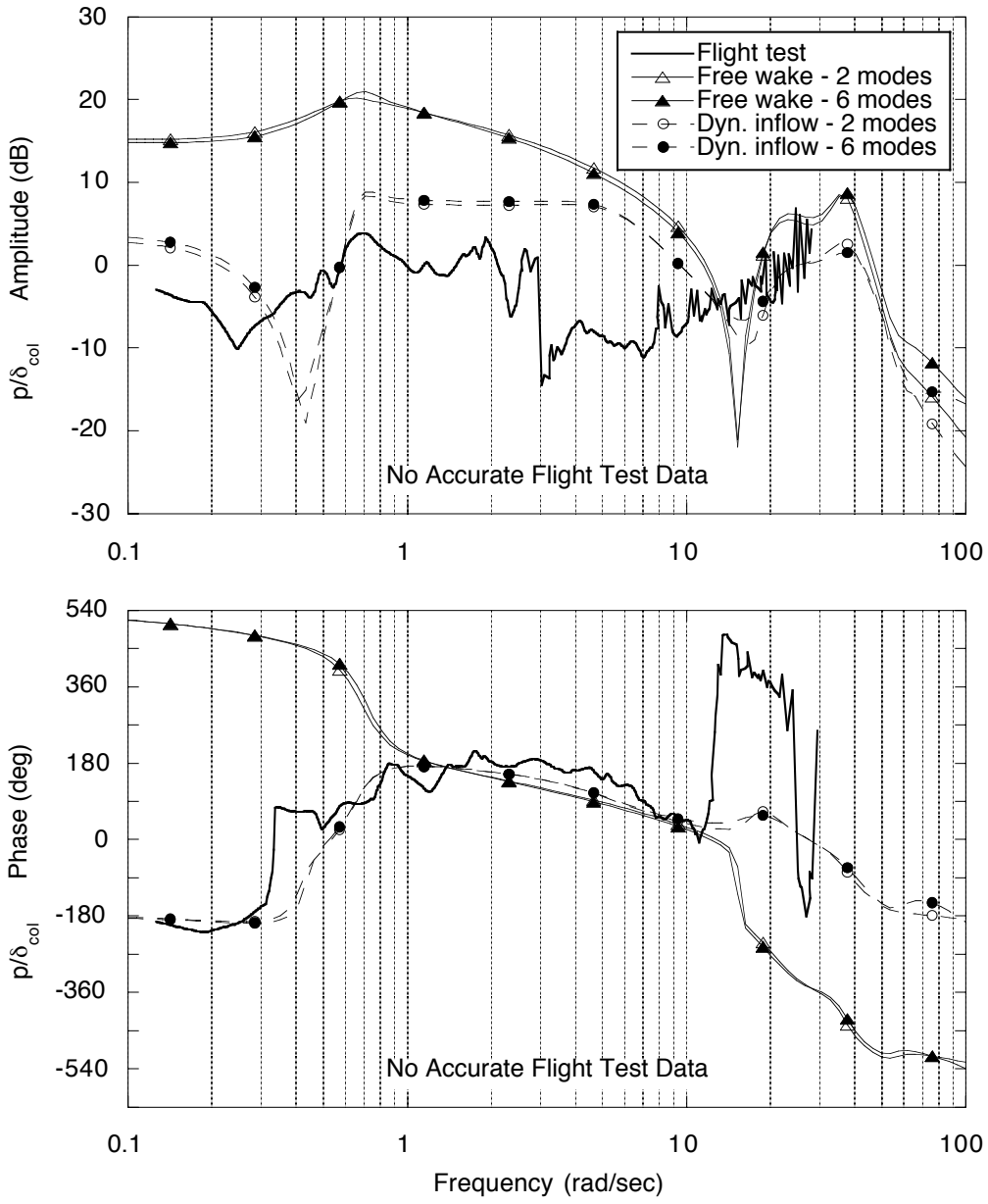

Figure 8.13: Effect of inflow models and blade modeling on the off-axis roll rate frequency response to collective stick input for the UH-60A in hover.

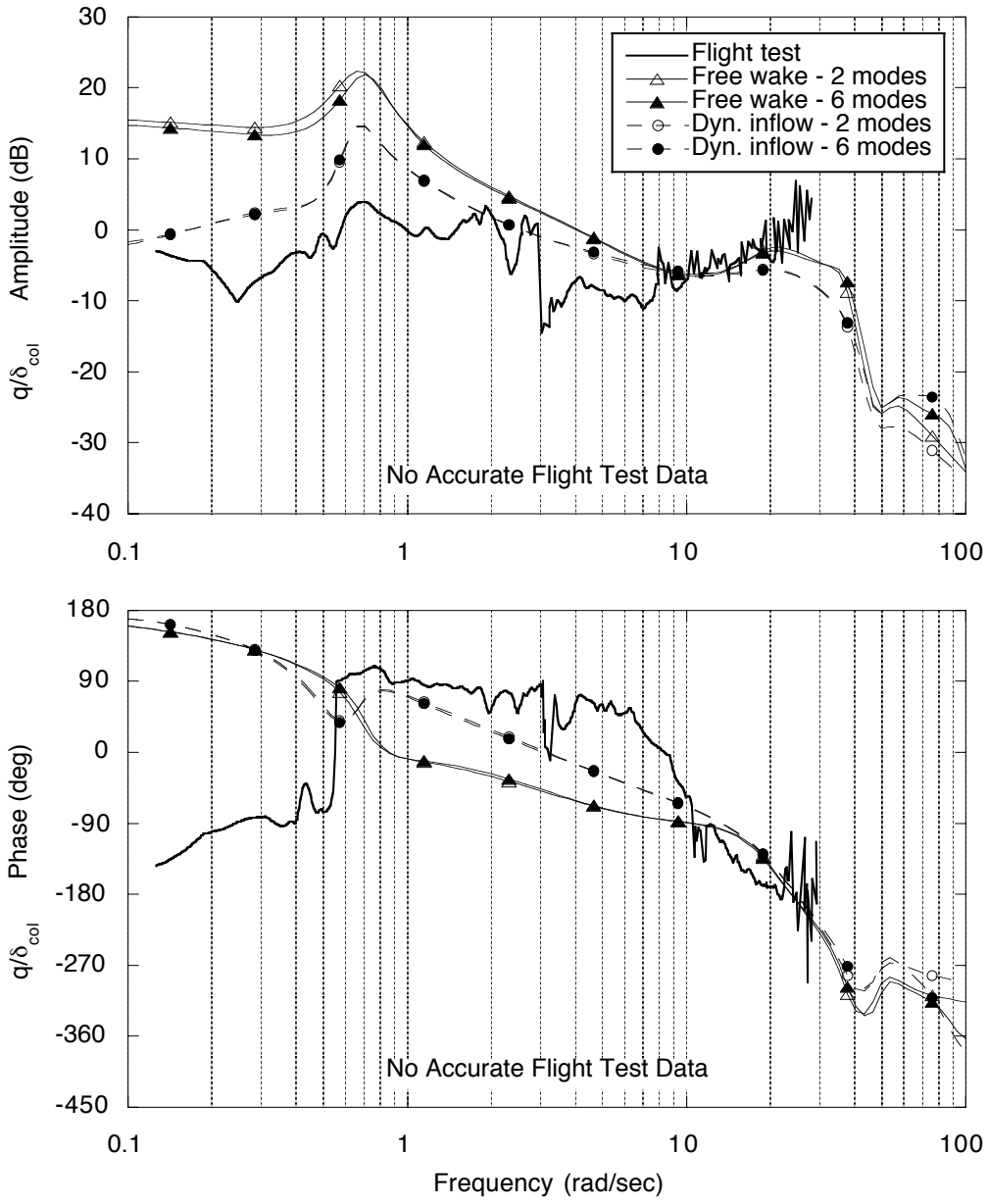

Figure 8.14: Effect of inflow models and blade modeling on the off-axis pitch rate frequency response to collective stick input for the UH-60A in hover.

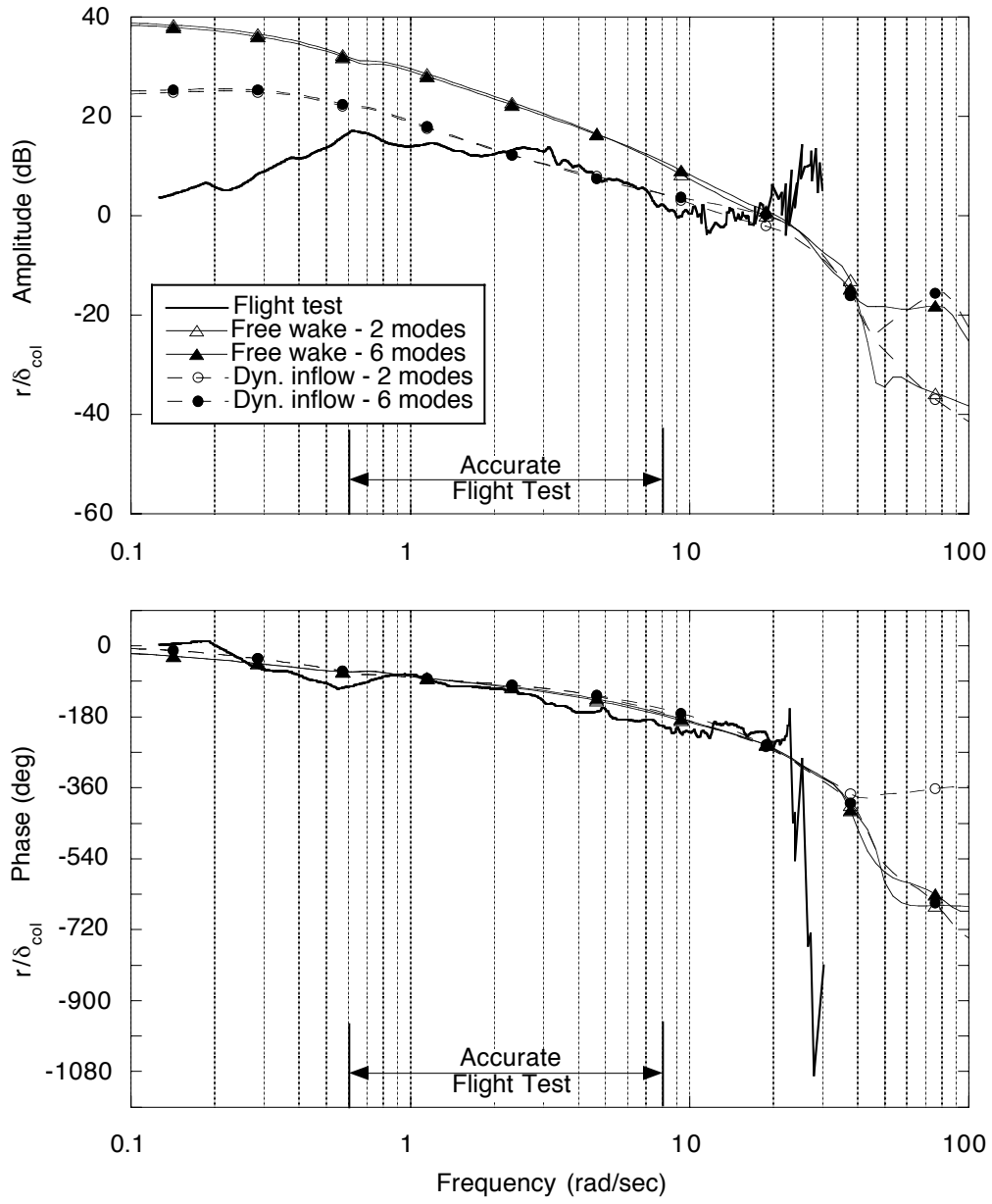

Figure 8.15: Effect of inflow models and blade modeling on the off-axis yaw rate frequency response to collective stick input for the UH-60A in hover.

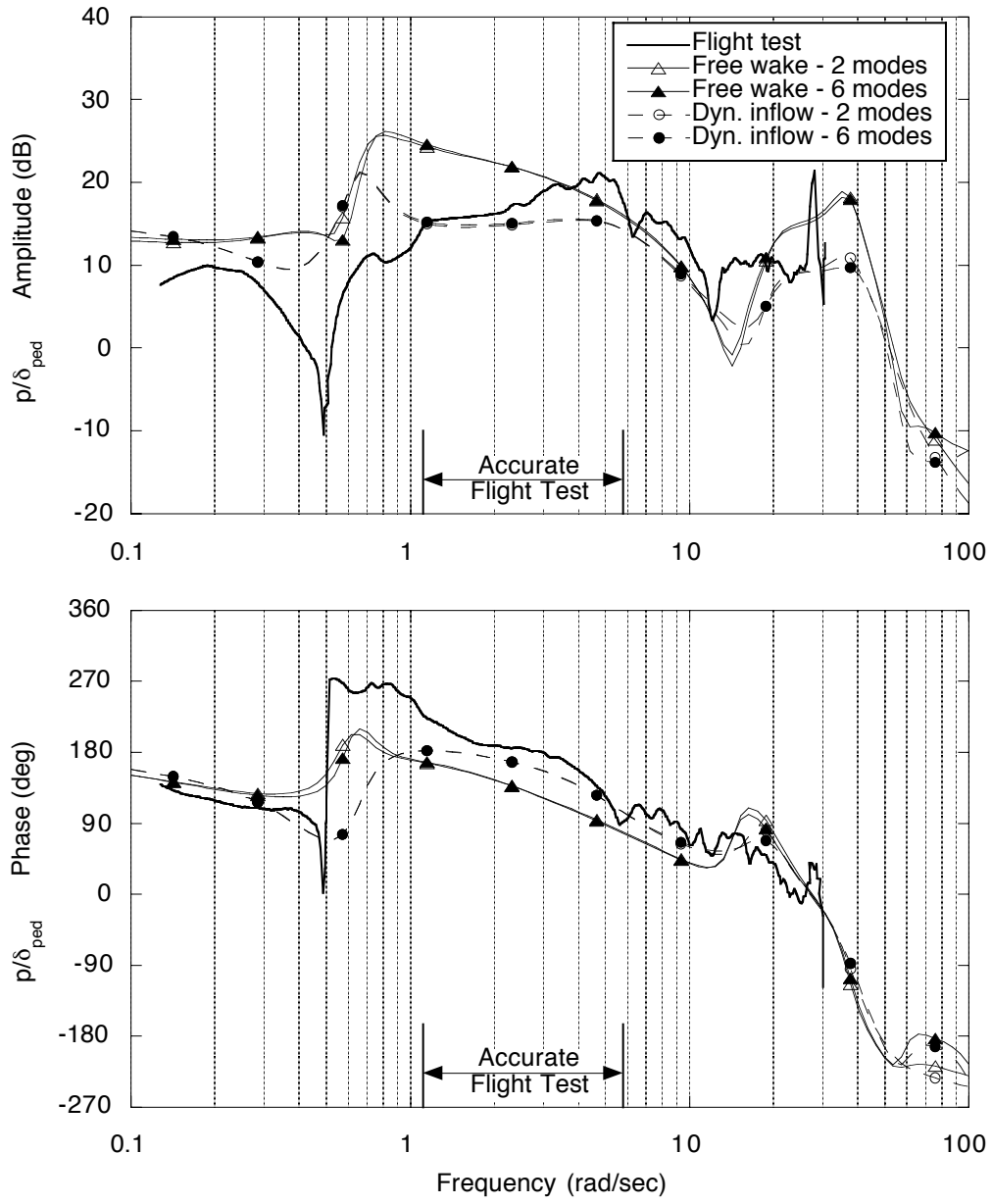

Figure 8.16: Effect of inflow models and blade modeling on the off-axis roll rate frequency response to pedal input for the UH-60A in hover.

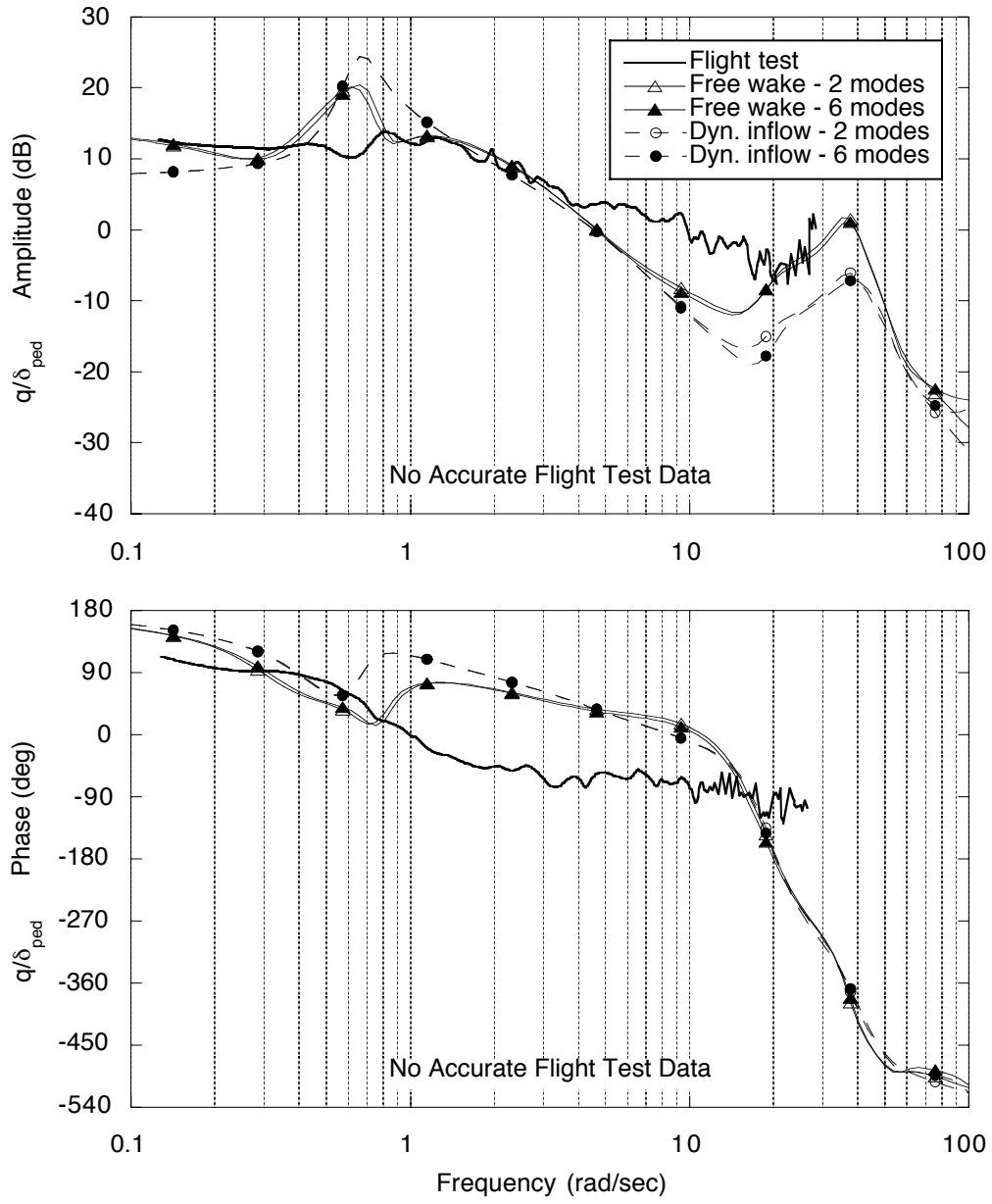

Figure 8.17: Effect of inflow models and blade modeling on the off-axis pitch rate frequency response to pedal input for the UH-60A in hover.

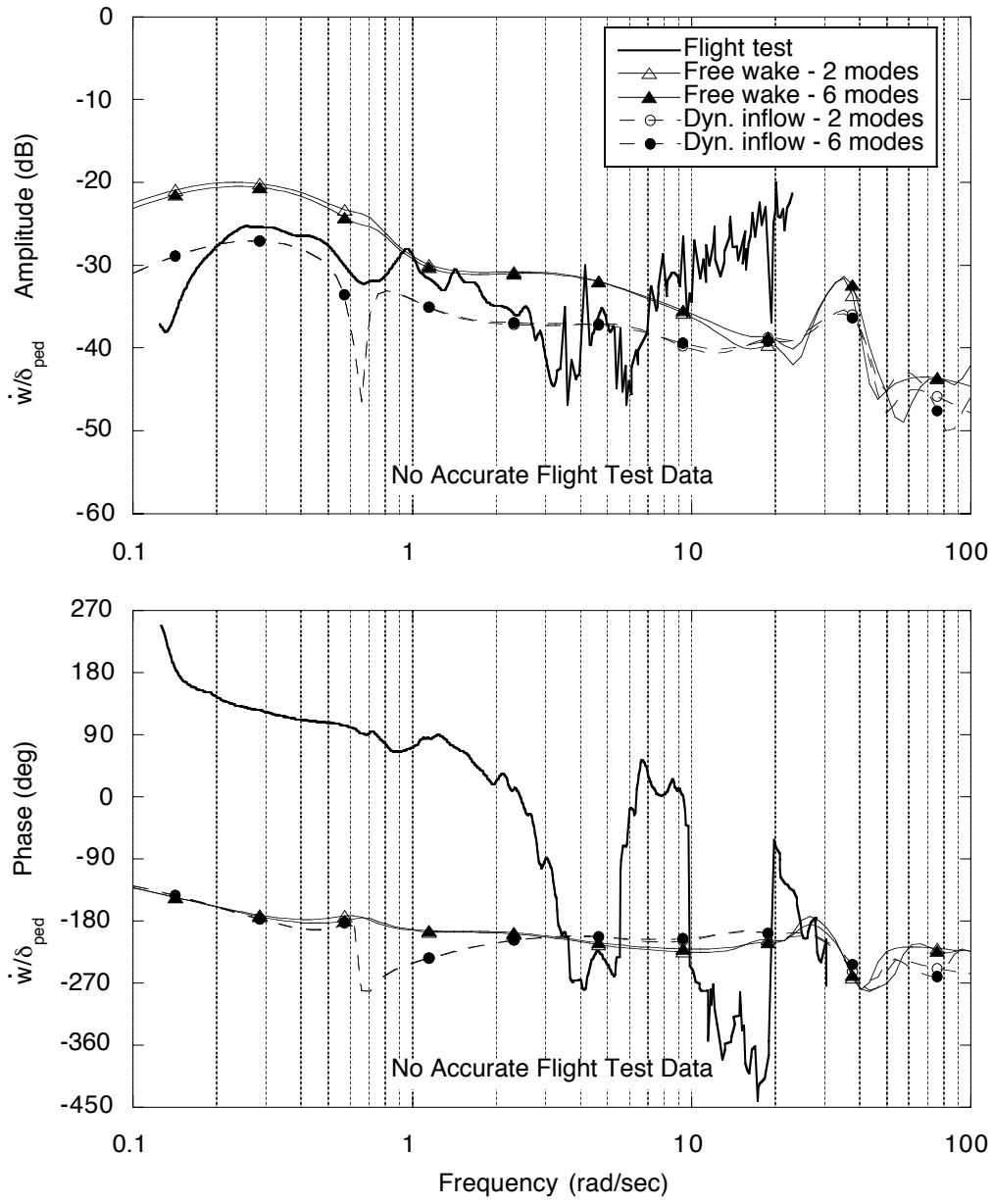

Figure 8.18: Effect of inflow models and blade modeling on the off-axis vertical acceleration frequency response to pedal input for the UH-60A in hover.

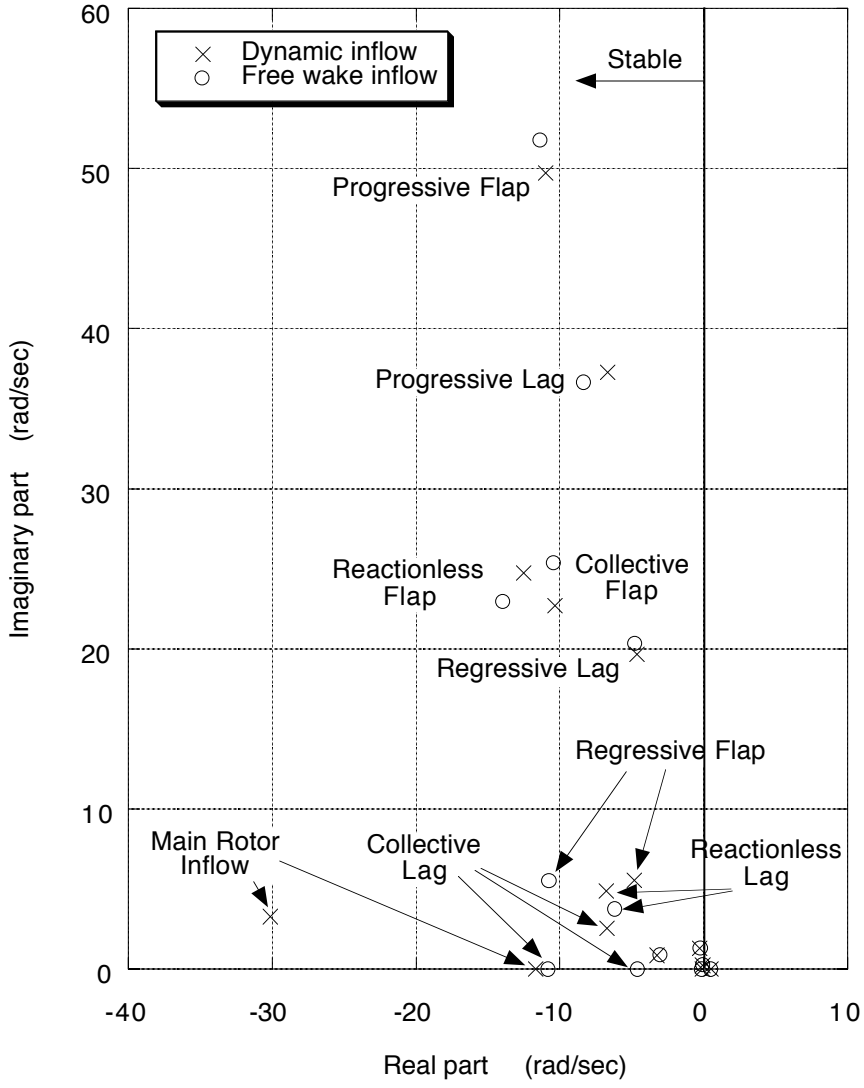

Figure 8.19: Effect of inflow modeling on rotor and inflow poles for the UH-60A at 80 knots with the simple blade model.

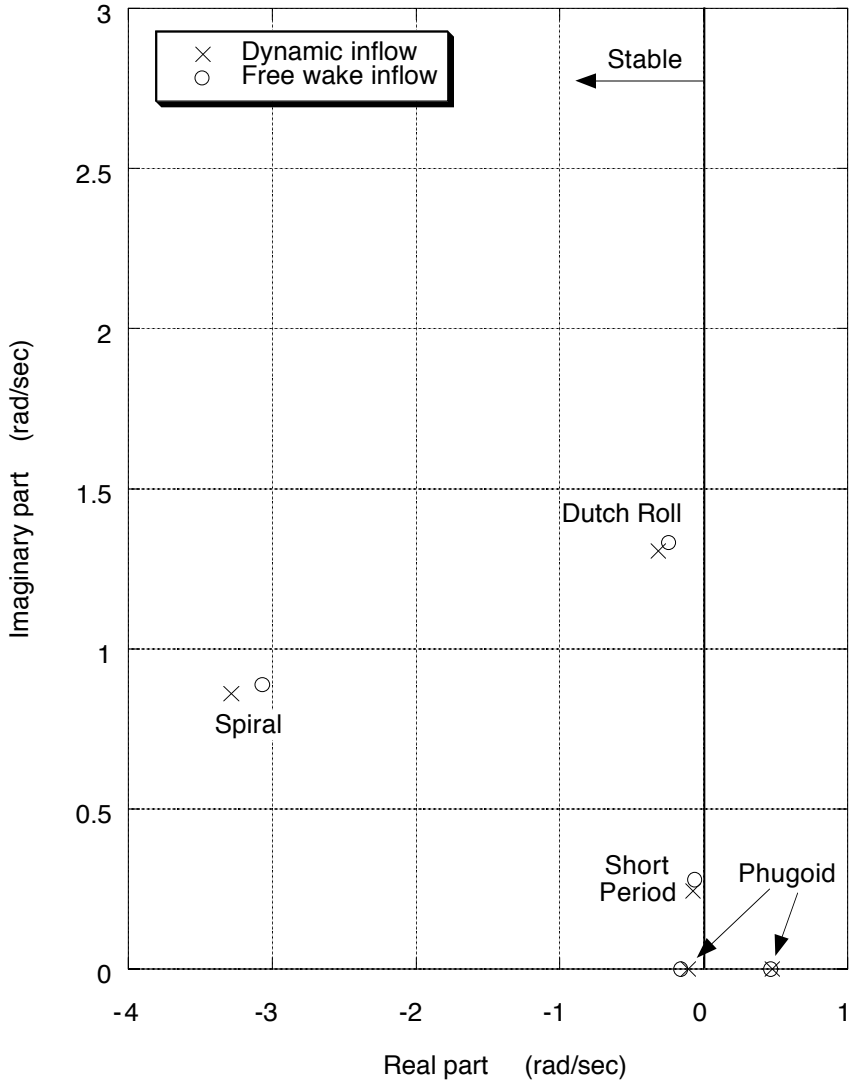

Figure 8.20: Effect of inflow modeling on fuselage poles for the UH-60A at 80 knots with the simple blade model.

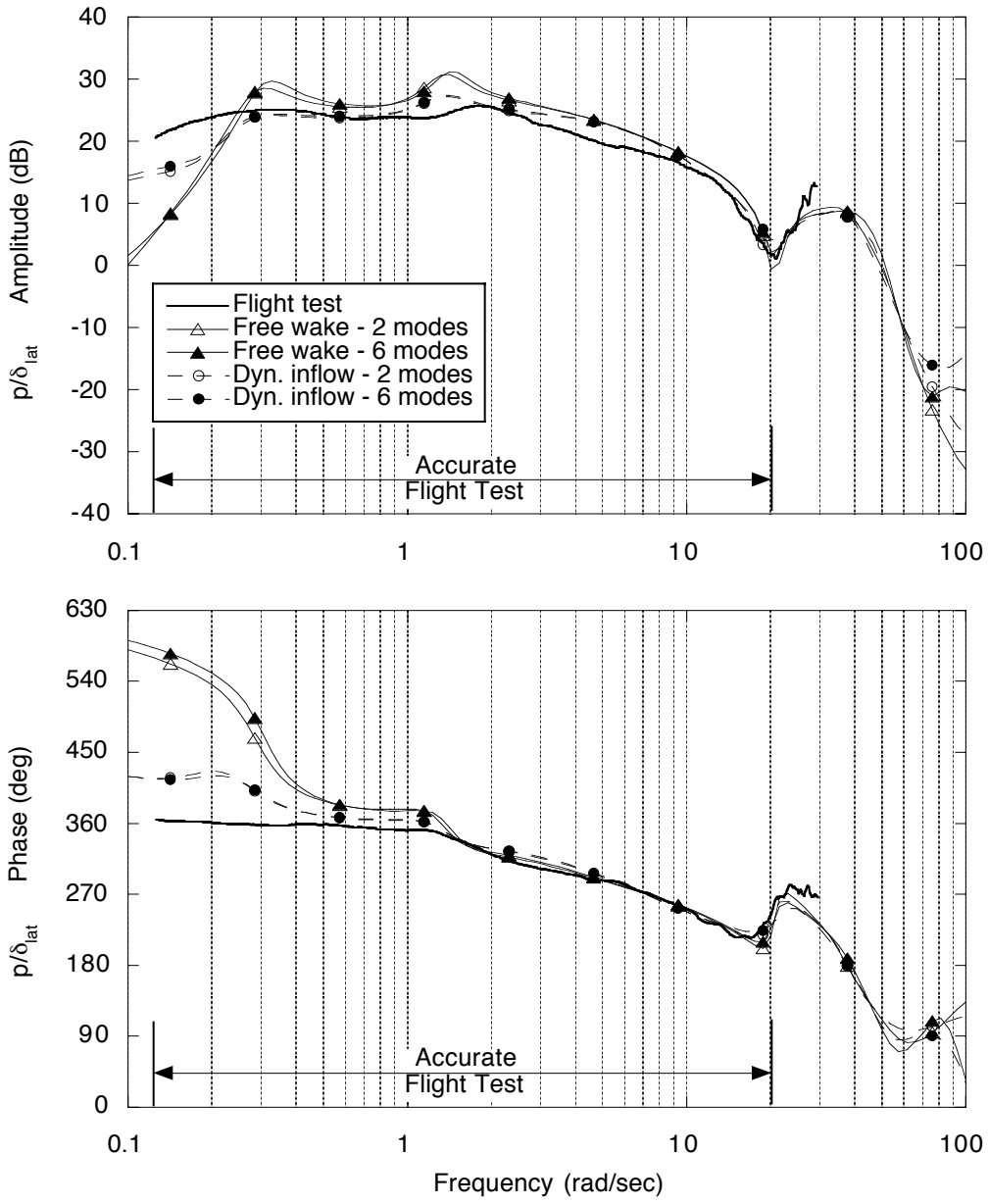

Figure 8.21: Effect of inflow models and blade modeling on the on-axis roll rate frequency response to lateral stick input for the UH-60A at 80 knots.

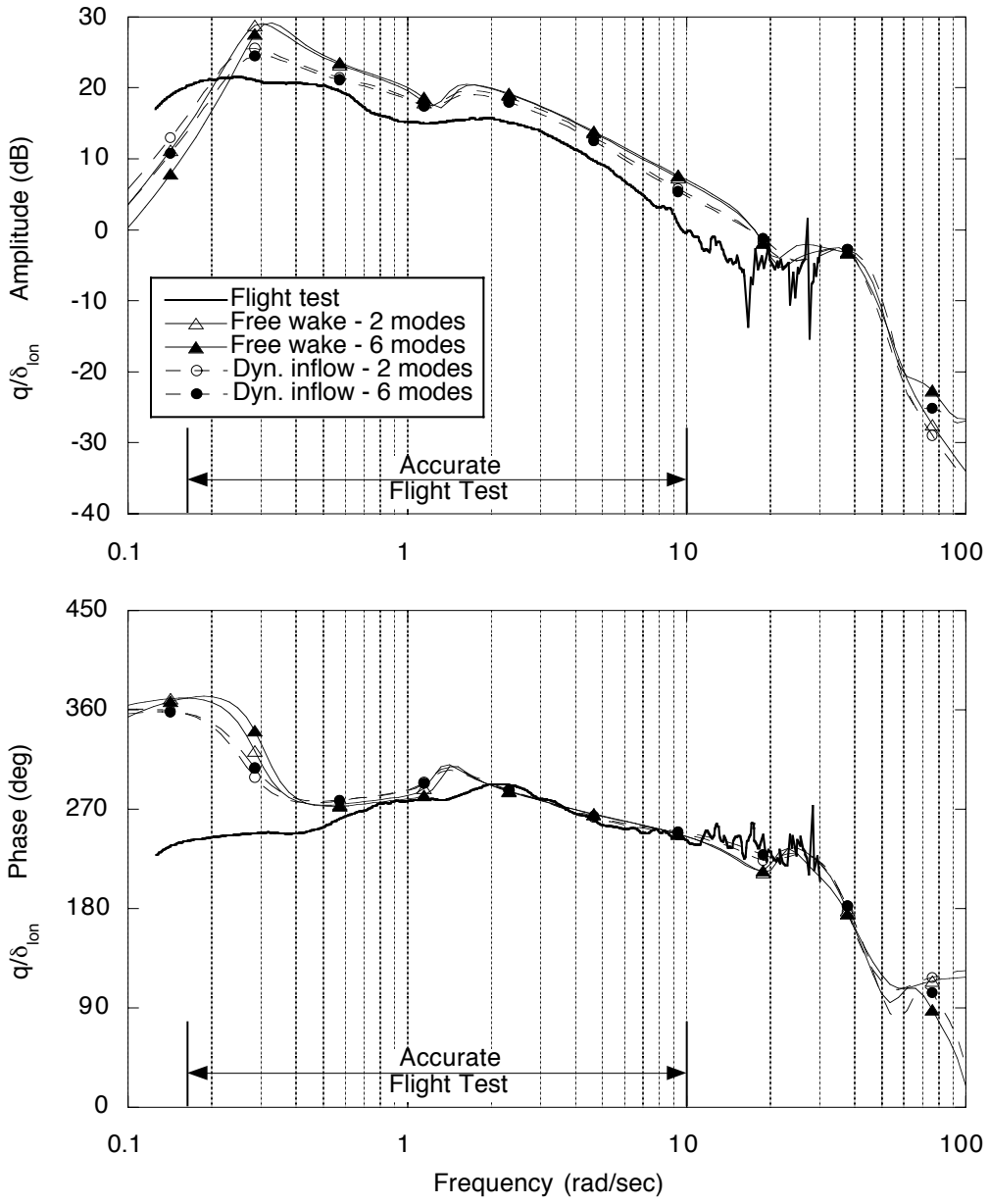

Figure 8.22: Effect of inflow models and blade modeling on the on-axis pitch rate frequency response to longitudinal stick input for the UH-60A at 80 knots.

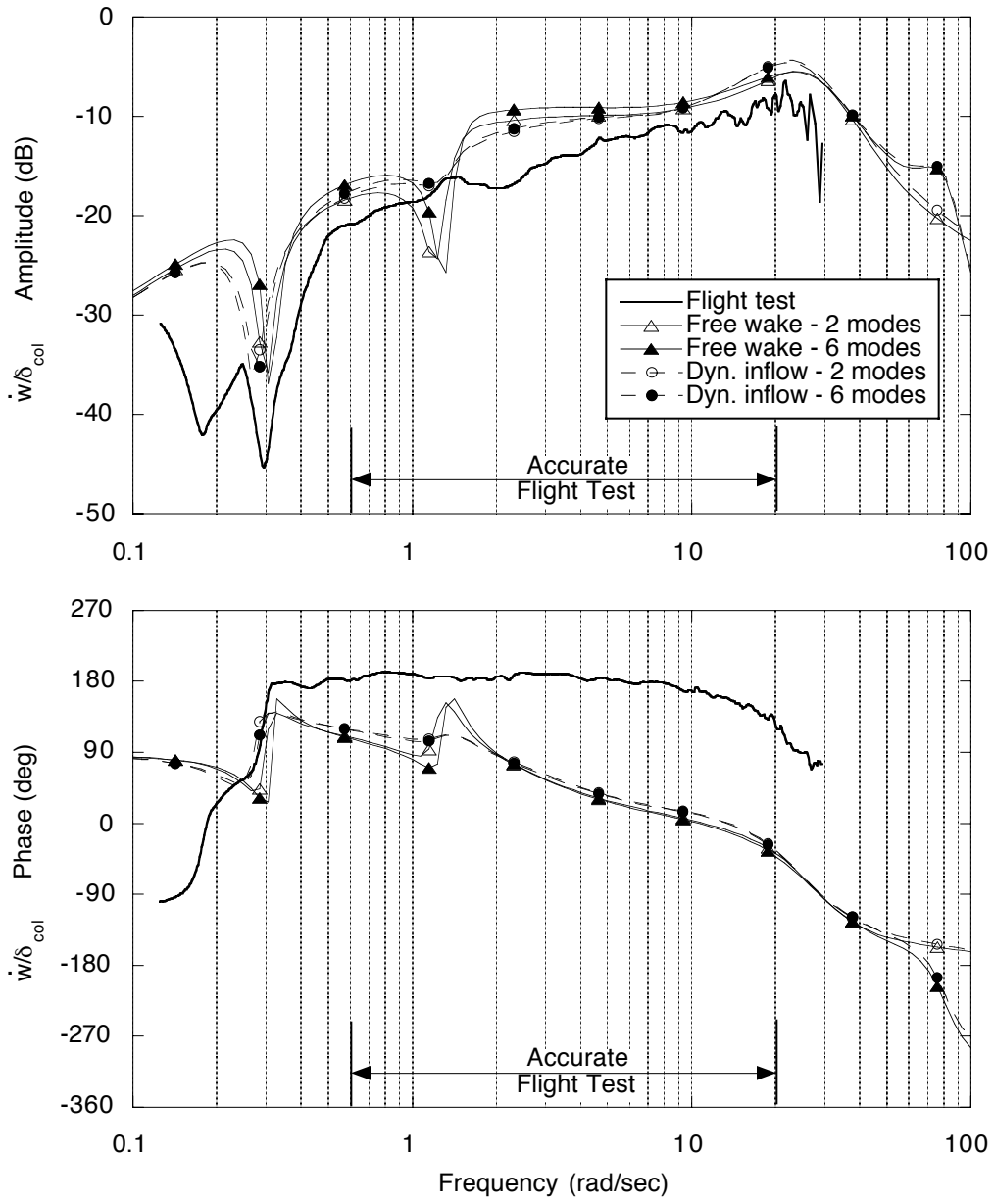

Figure 8.23: Effect of inflow models and blade modeling on the on-axis vertical acceleration frequency response to collective stick input for the UH-60A at 80 knots.

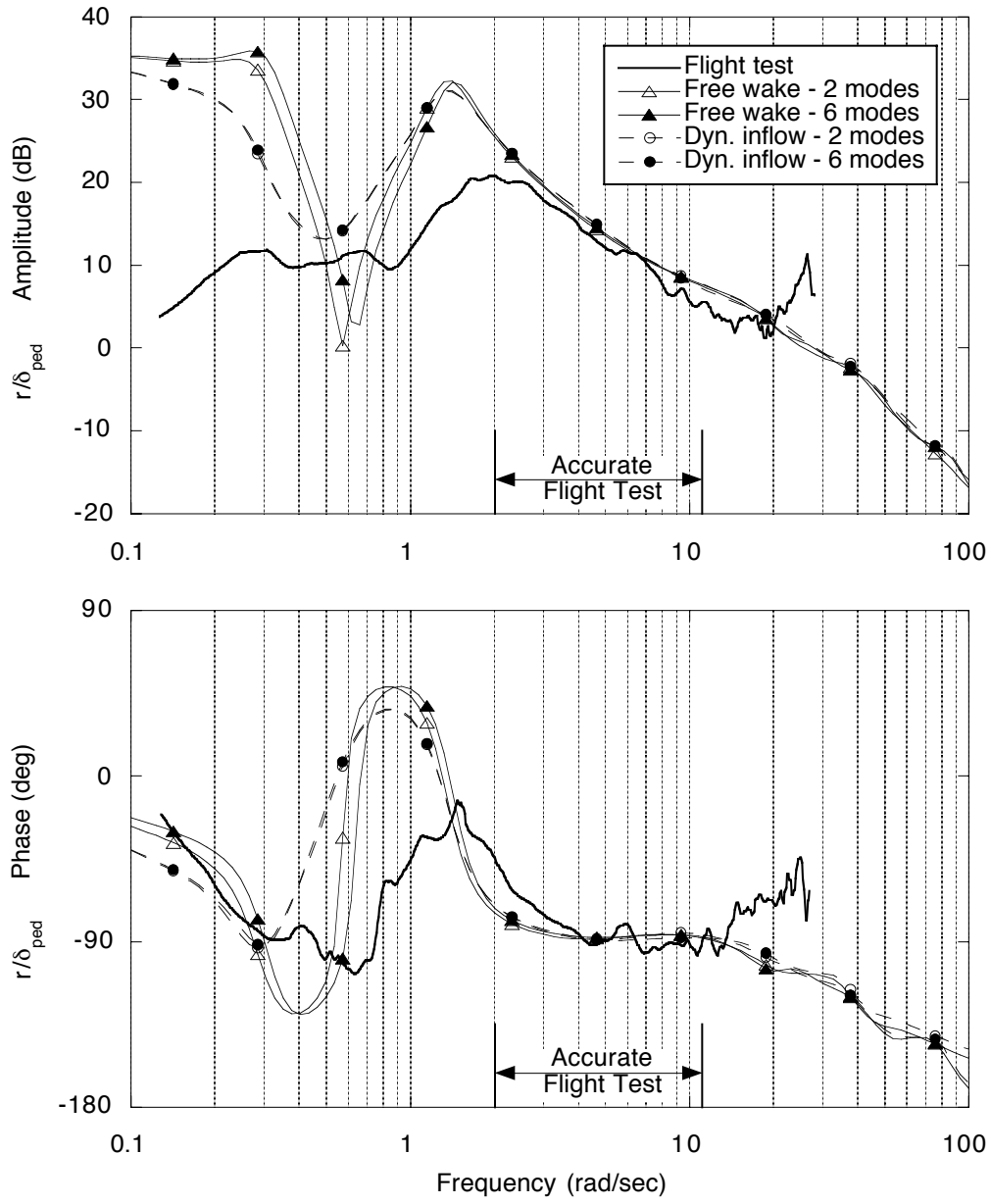

Figure 8.24: Effect of inflow models and blade modeling on the on-axis yaw rate frequency response to pedal input for the UH-60A at 80 knots.

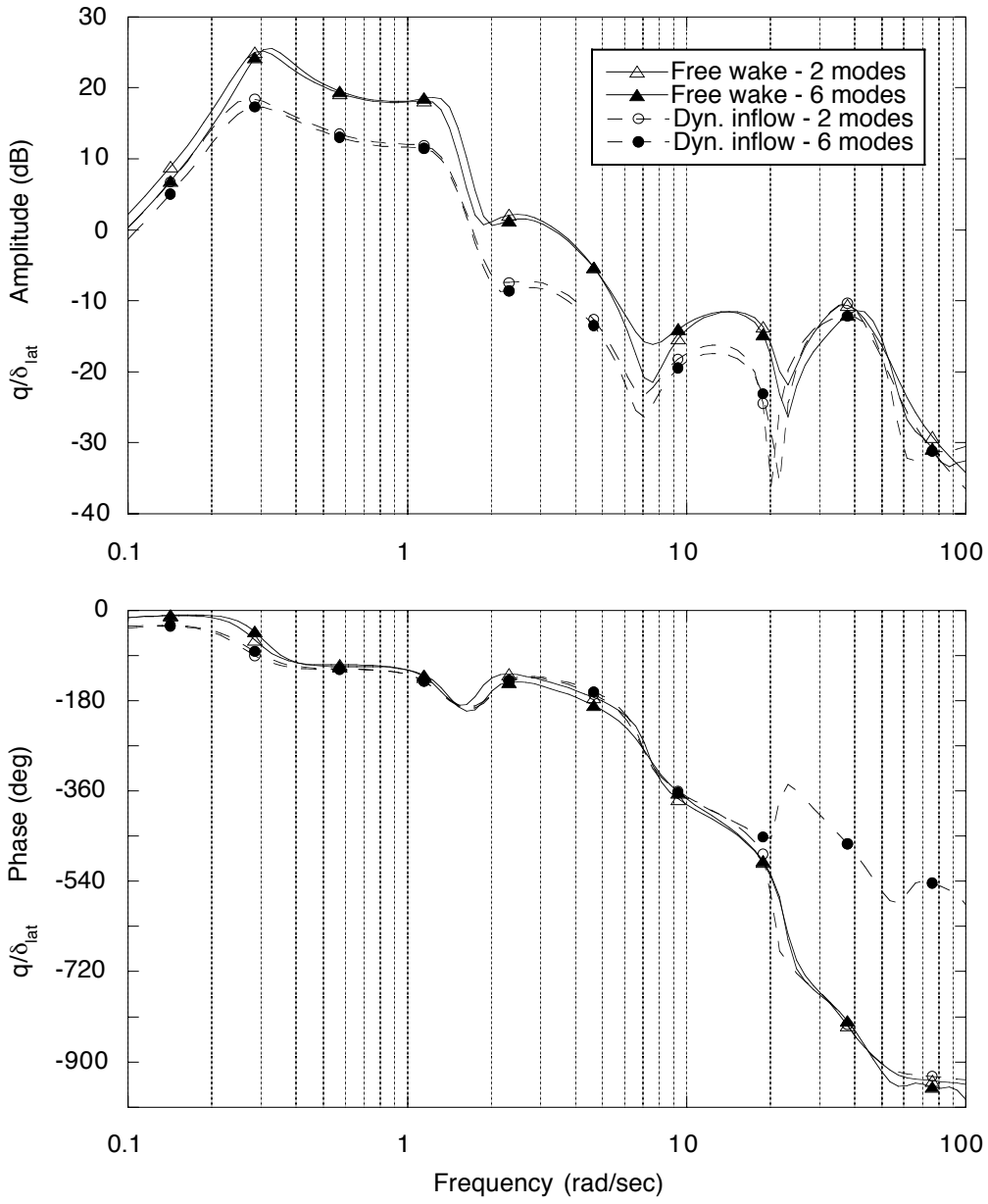

Figure 8.25: Effect of inflow models and blade modeling on the off-axis pitch rate frequency response to lateral stick input for the UH-60A at 80 knots.

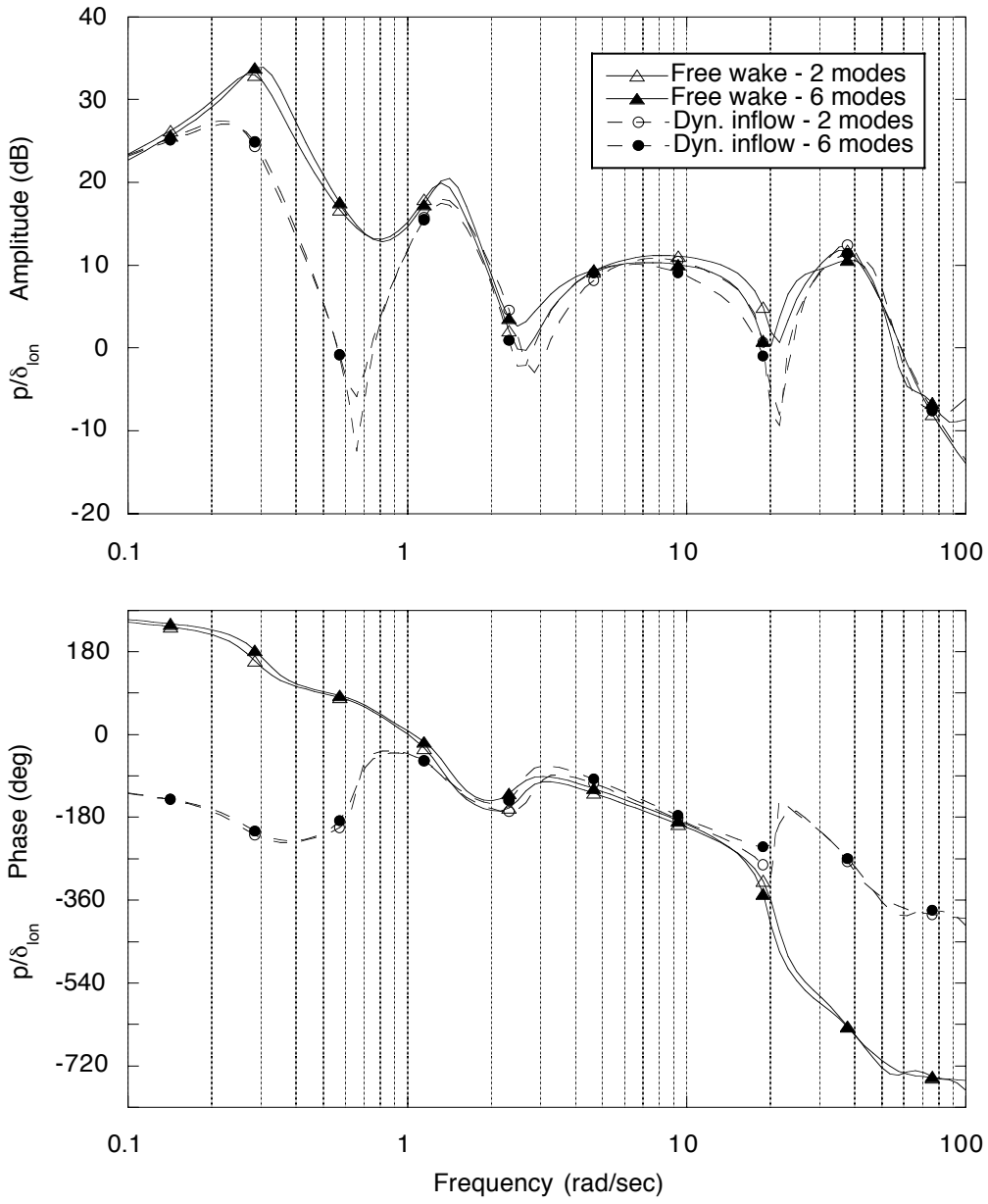

Figure 8.26: Effect of inflow models and blade modeling on the off-axis roll rate frequency response to longitudinal stick input for the UH-60A at 80 knots.

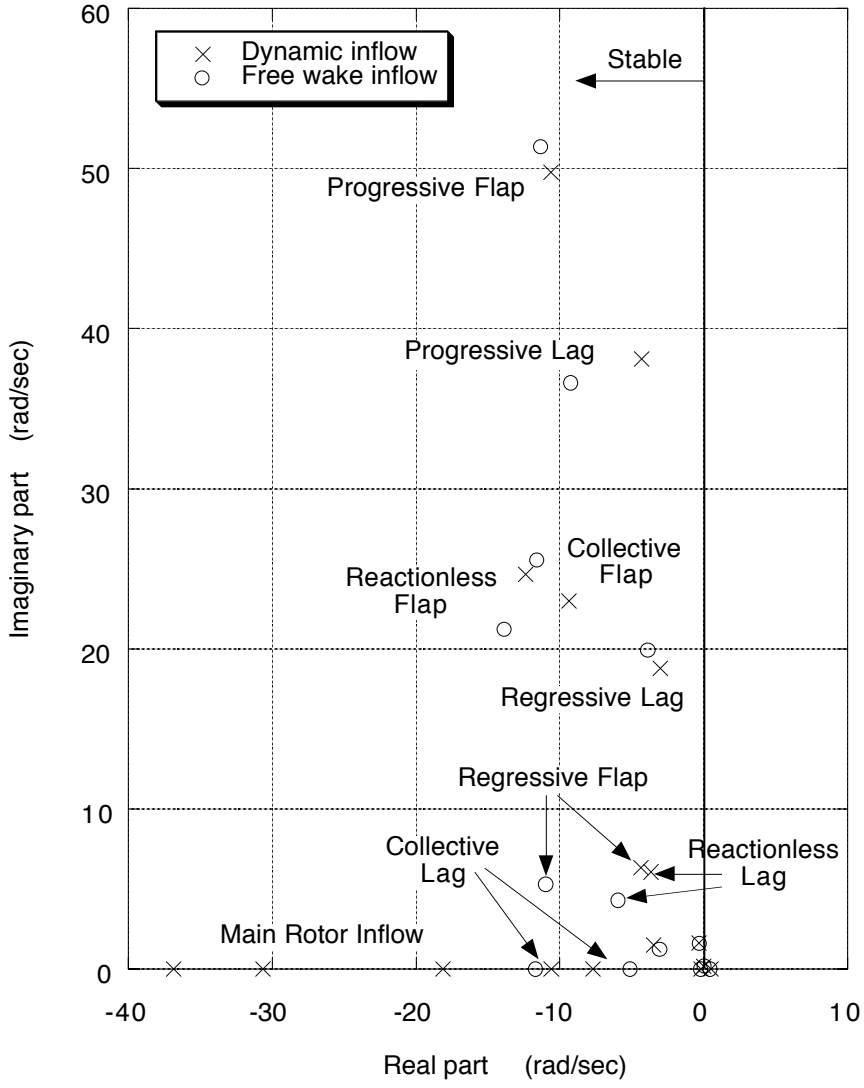

Figure 8.27: Effect of inflow modeling on rotor and inflow poles for the UH-60A at 120 knots with the simple blade model.

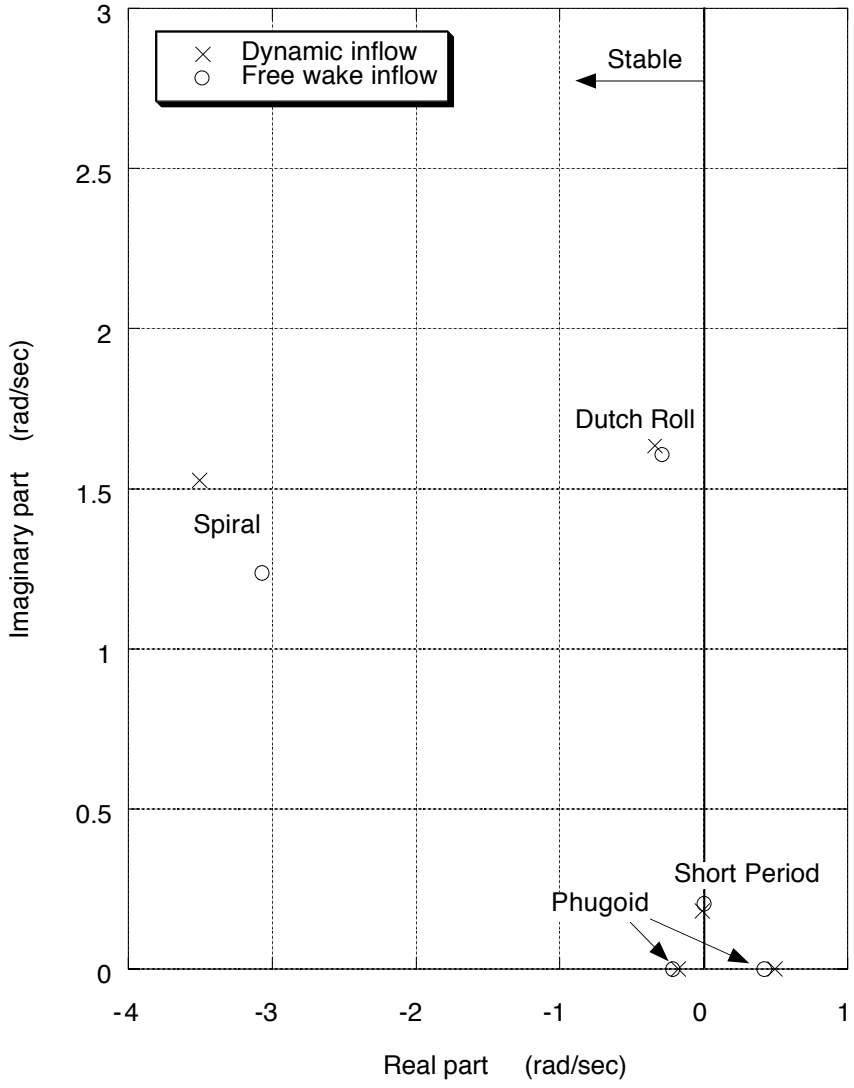

Figure 8.28: Effect of inflow modeling on fuselage poles for the UH-60A at 120 knots with the simple blade model.

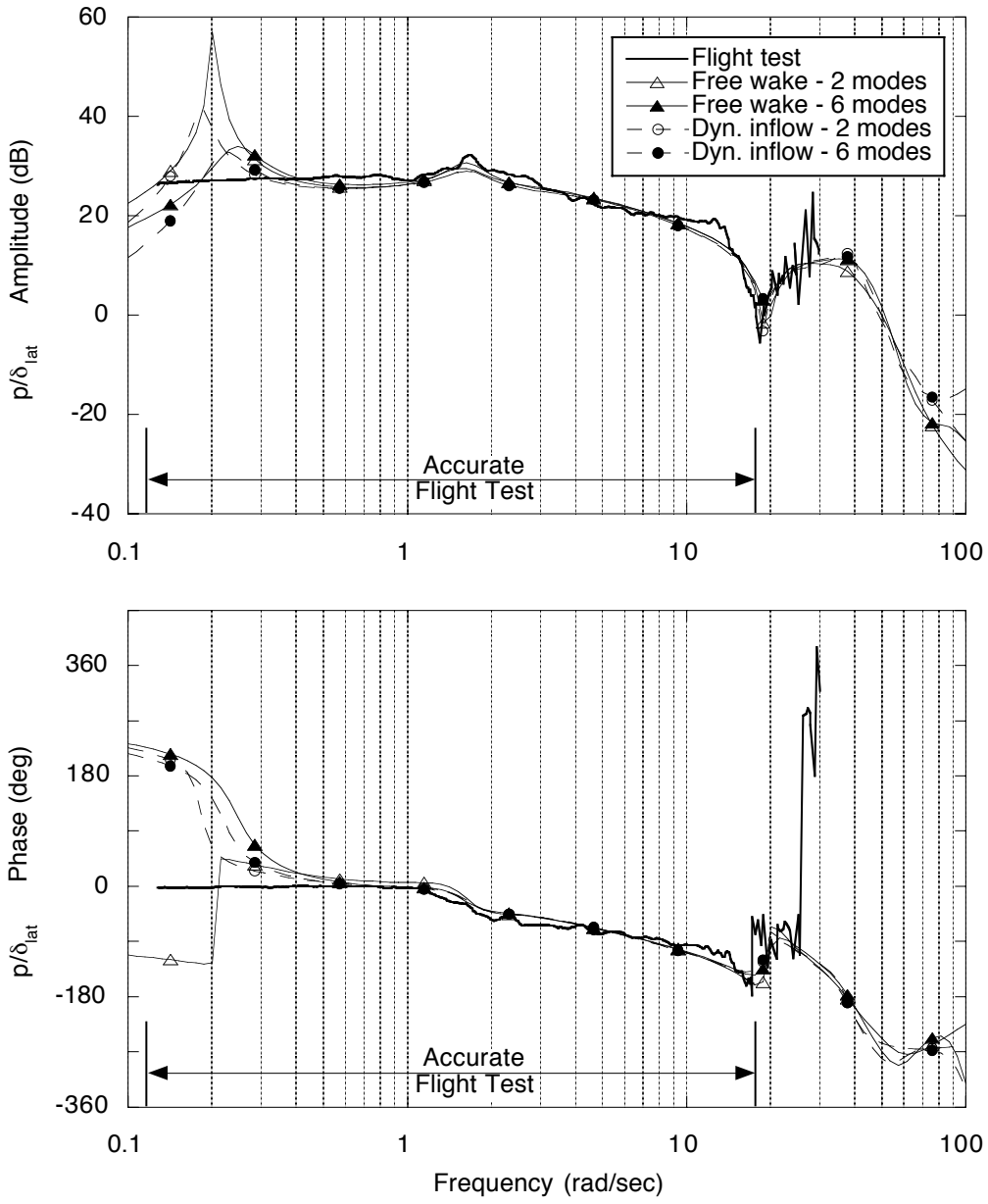

Figure 8.29: Effect of inflow models and blade modeling on the on-axis roll rate frequency response to lateral stick input for the UH-60A at 120 knots.

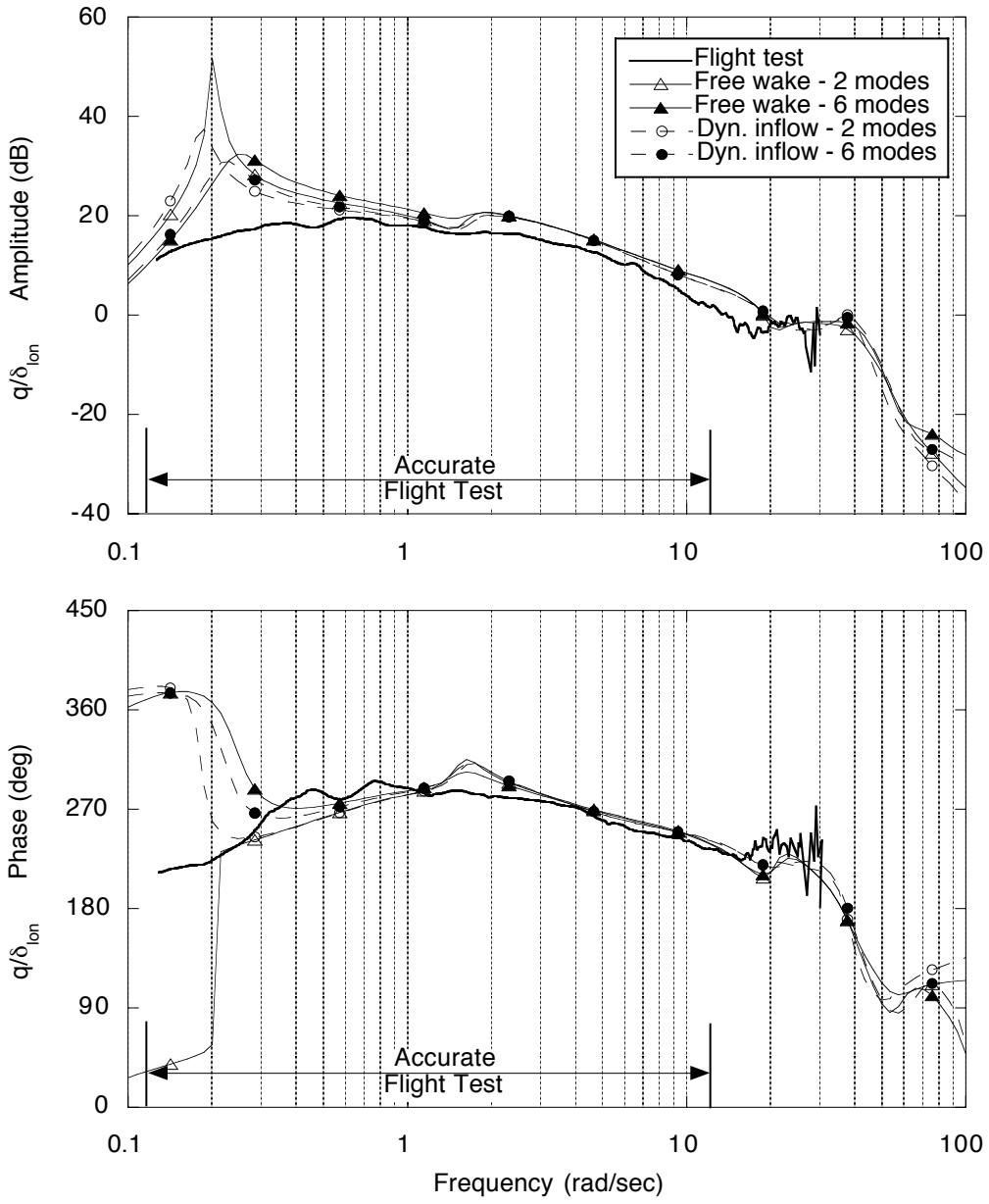

Figure 8.30: Effect of inflow models and blade modeling on the on-axis pitch rate frequency response to longitudinal stick input for the UH-60A at 120 knots.

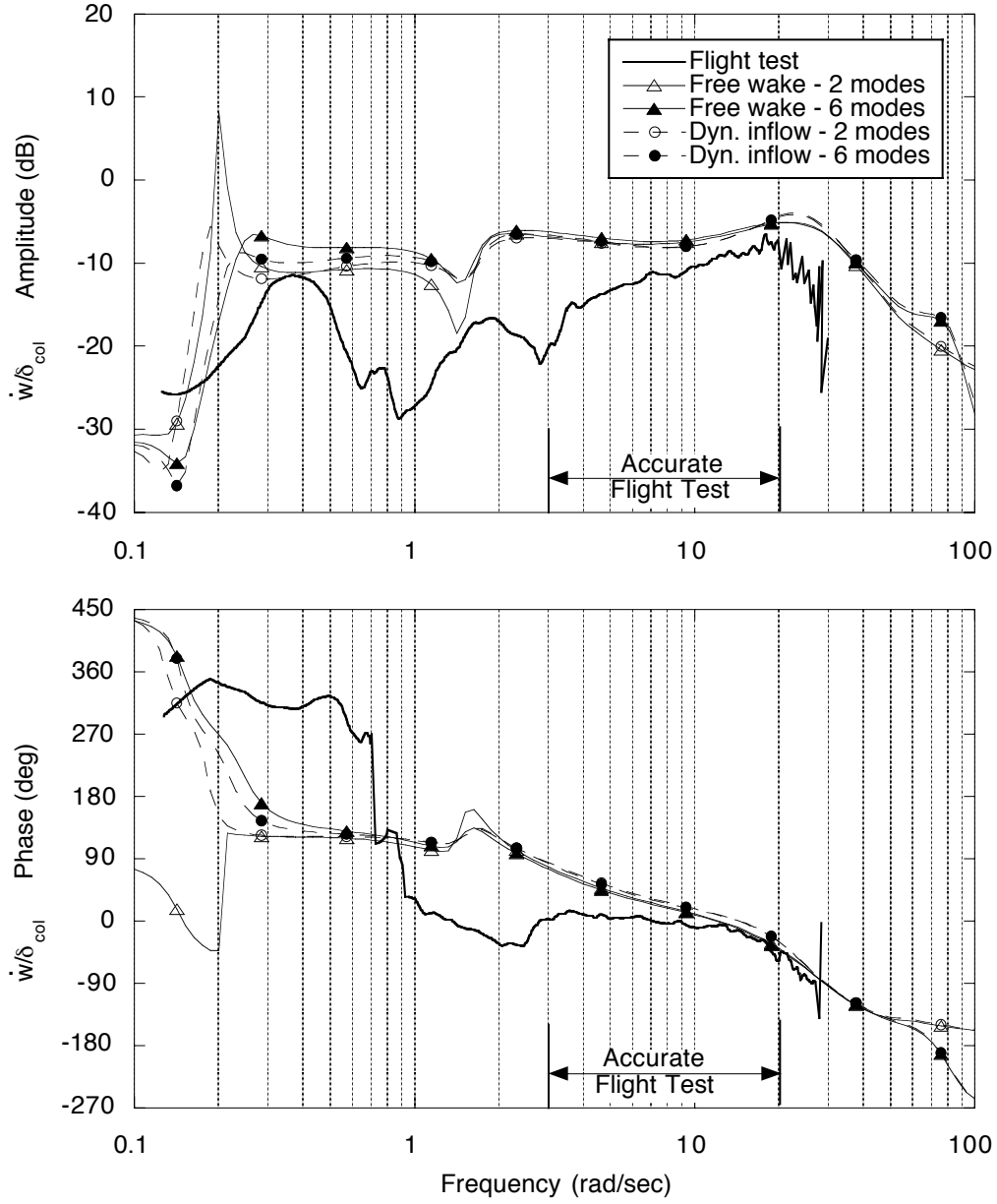

Figure 8.31: Effect of inflow models and blade modeling on the on-axis vertical acceleration frequency response to collective stick input for the UH-60A at 120 knots.

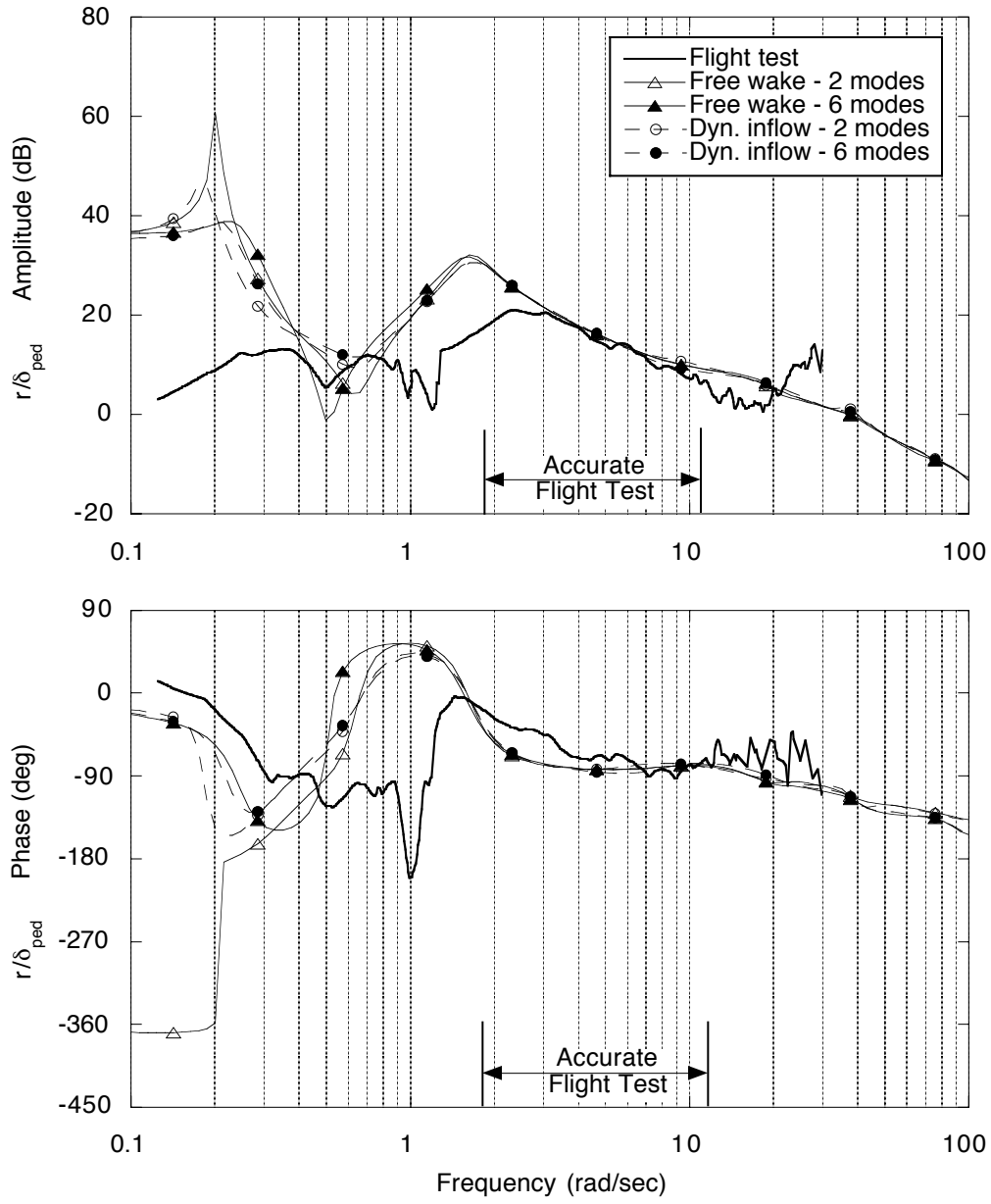

Figure 8.32: Effect of inflow models and blade modeling on the on-axis yaw rate frequency response to pedal input for the UH-60A at 120 knots.

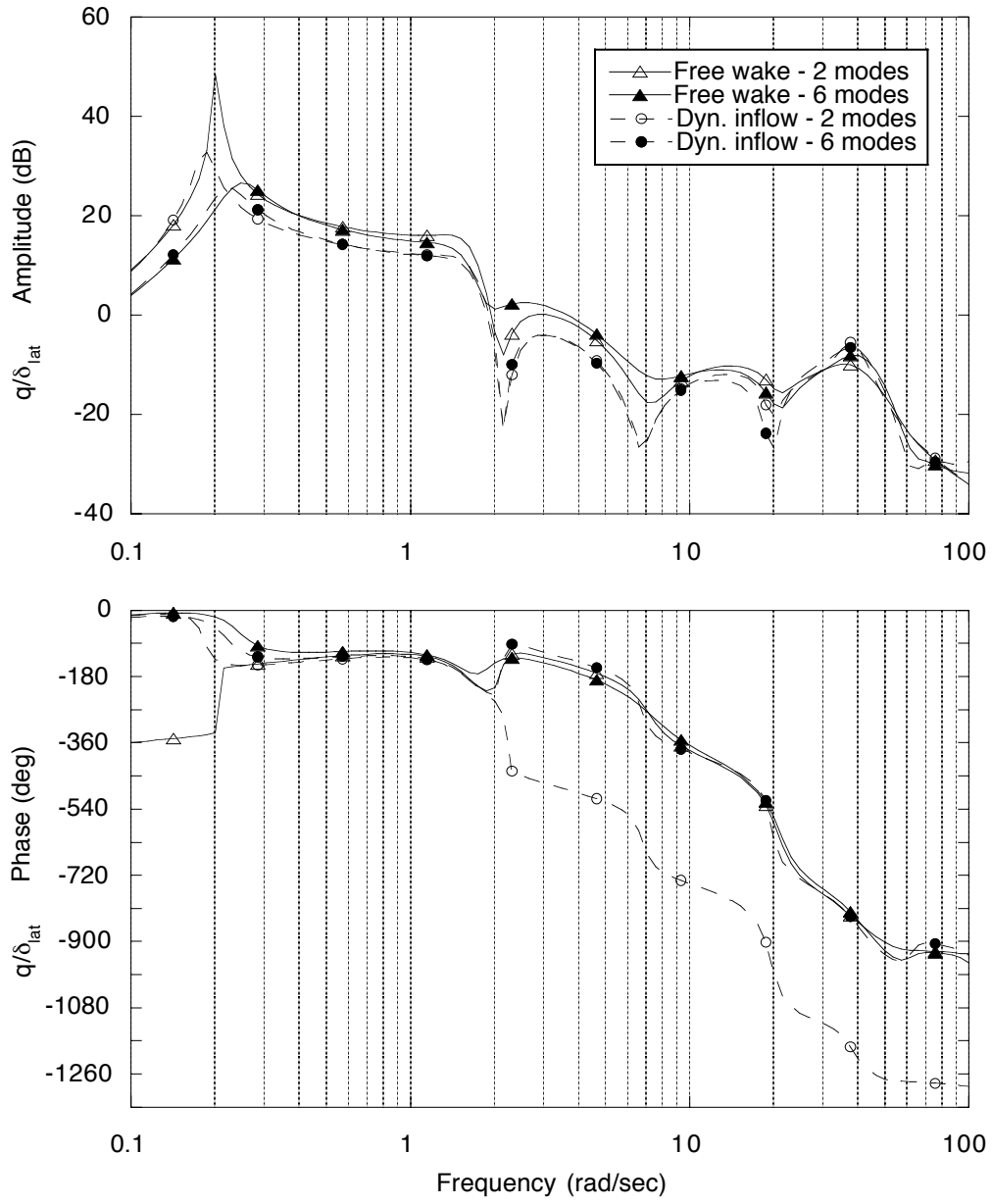

Figure 8.33: Effect of inflow models and blade modeling on the off-axis pitch rate frequency response to lateral stick input for the UH-60A at 120 knots.

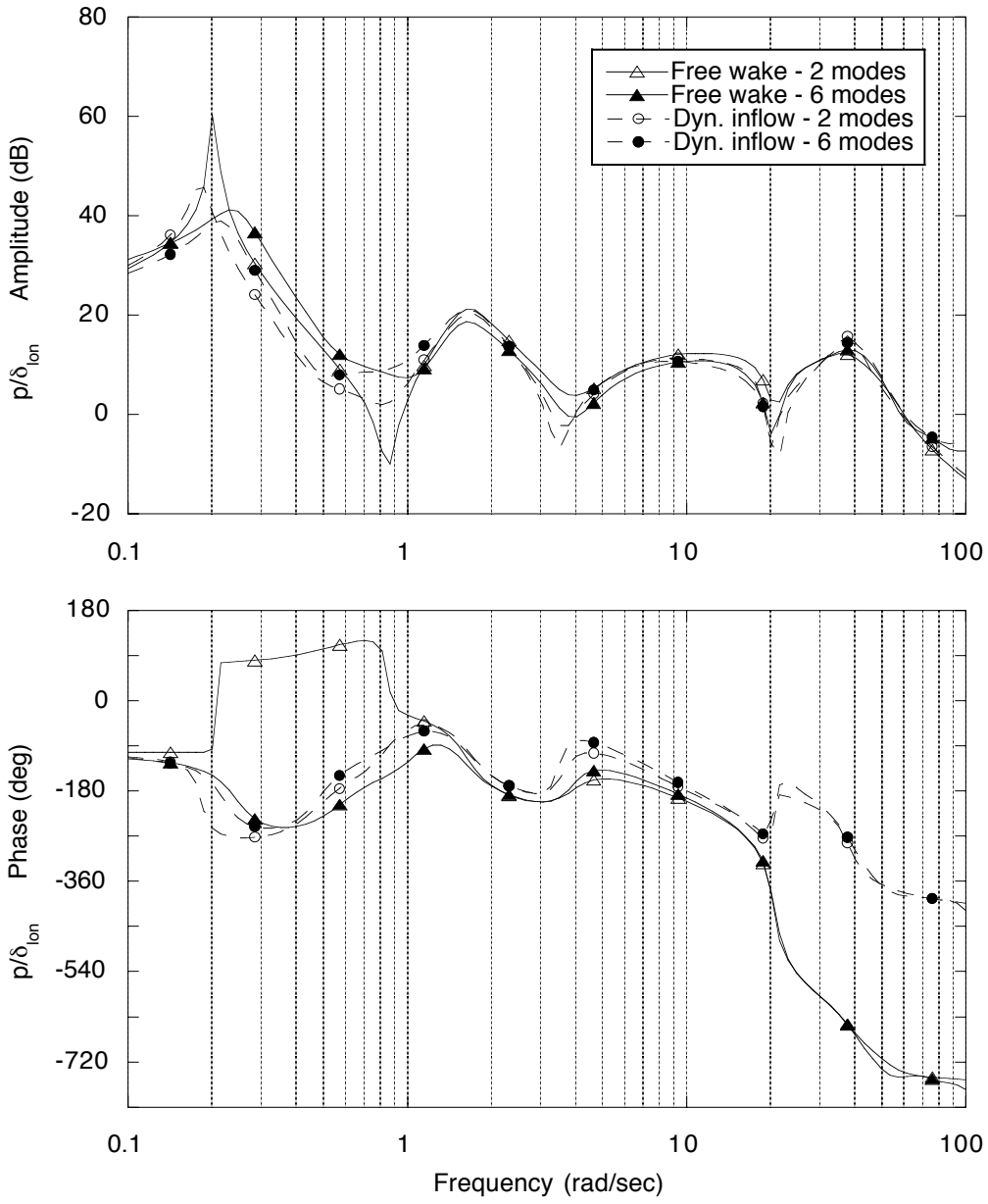

Figure 8.34: Effect of inflow models and blade modeling on the off-axis roll rate frequency response to longitudinal stick input for the UH-60A at 120 knots.

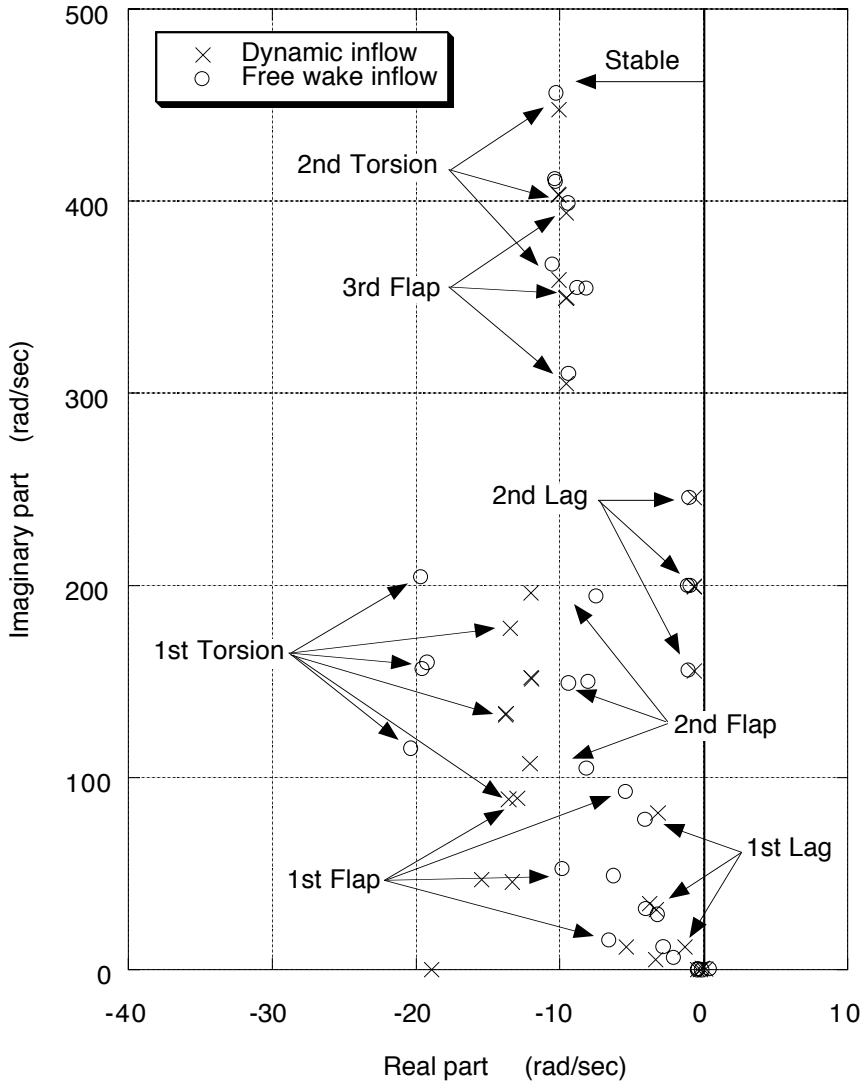

Figure 8.35: Effect of inflow modeling on rotor and inflow poles for the BO-105 in hover with the refined blade model.

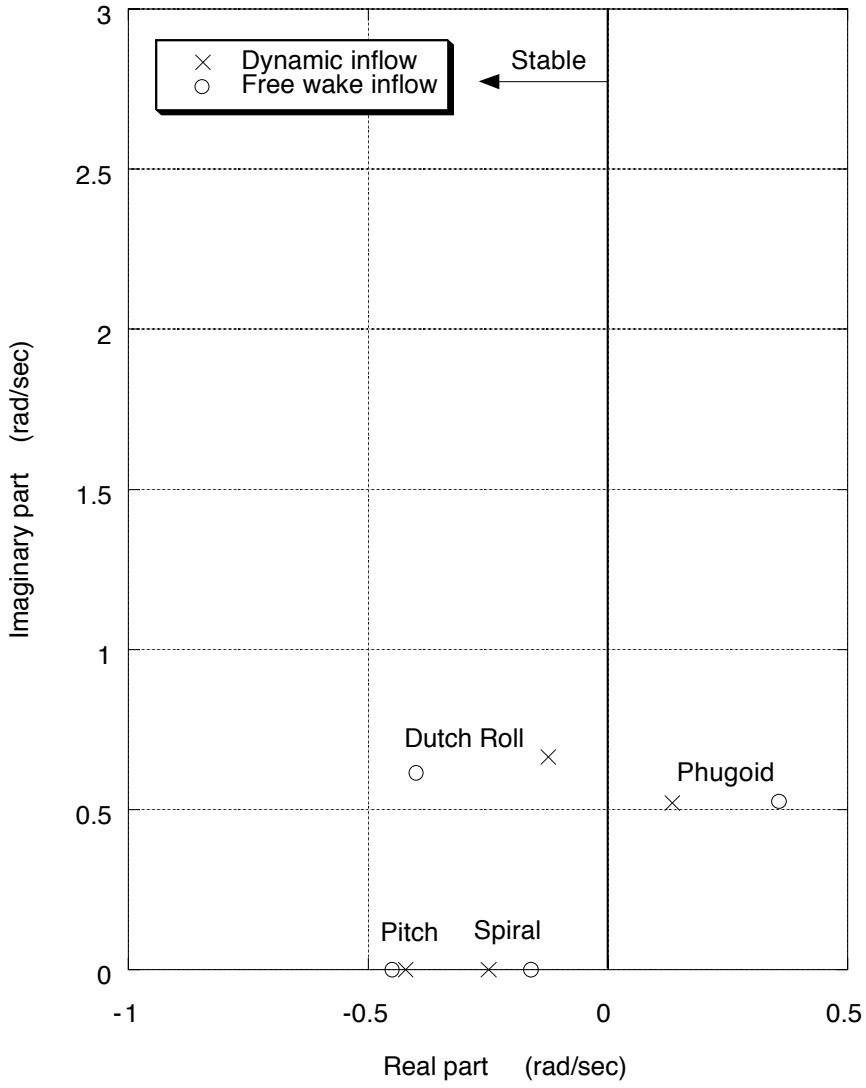

Figure 8.36: Effect of inflow modeling on fuselage poles for the BO-105 in hover with the refined blade model.

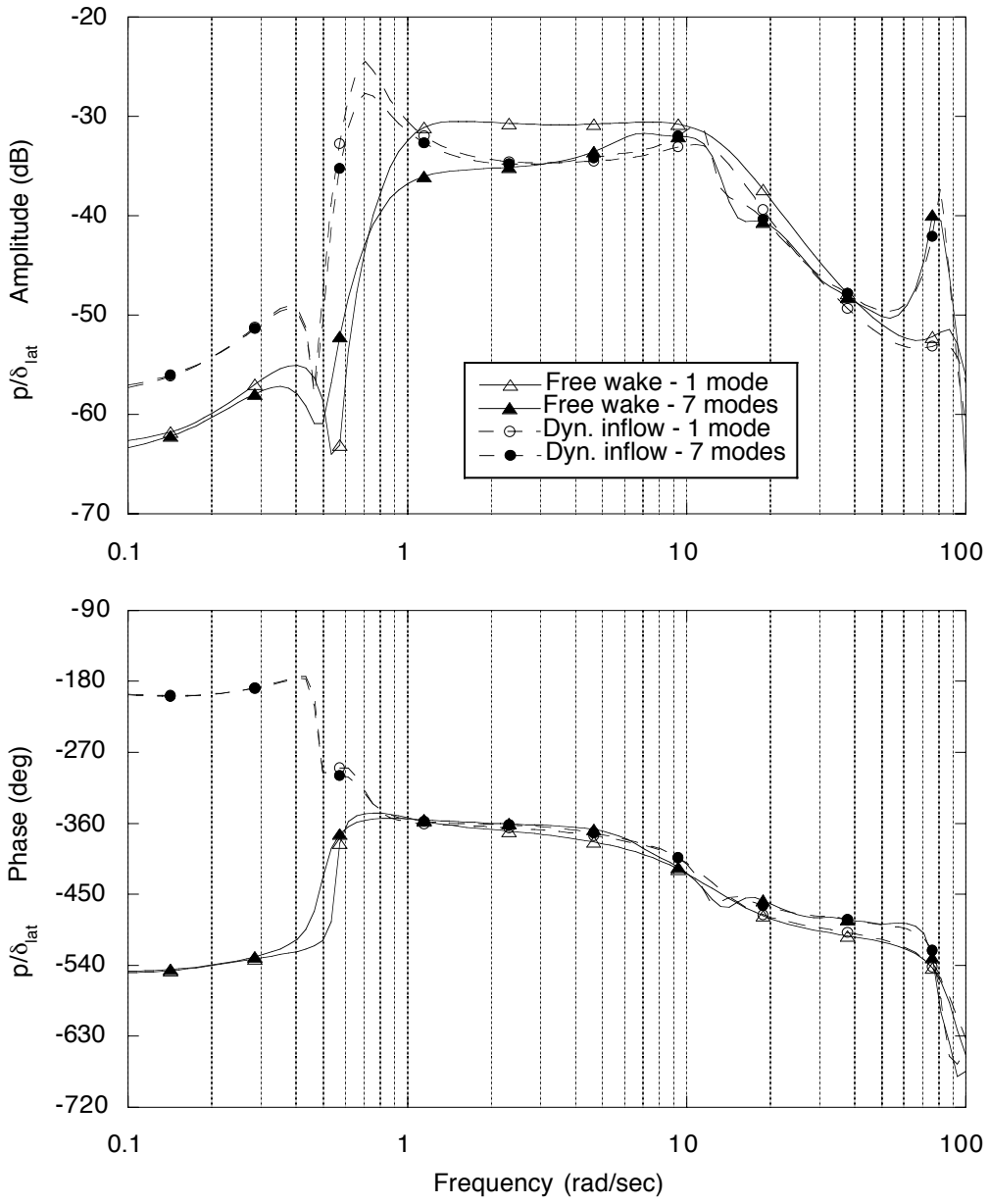

Figure 8.37: Effect of inflow models and blade modeling on the on-axis roll rate frequency response to lateral stick input for the BO-105 in hover.

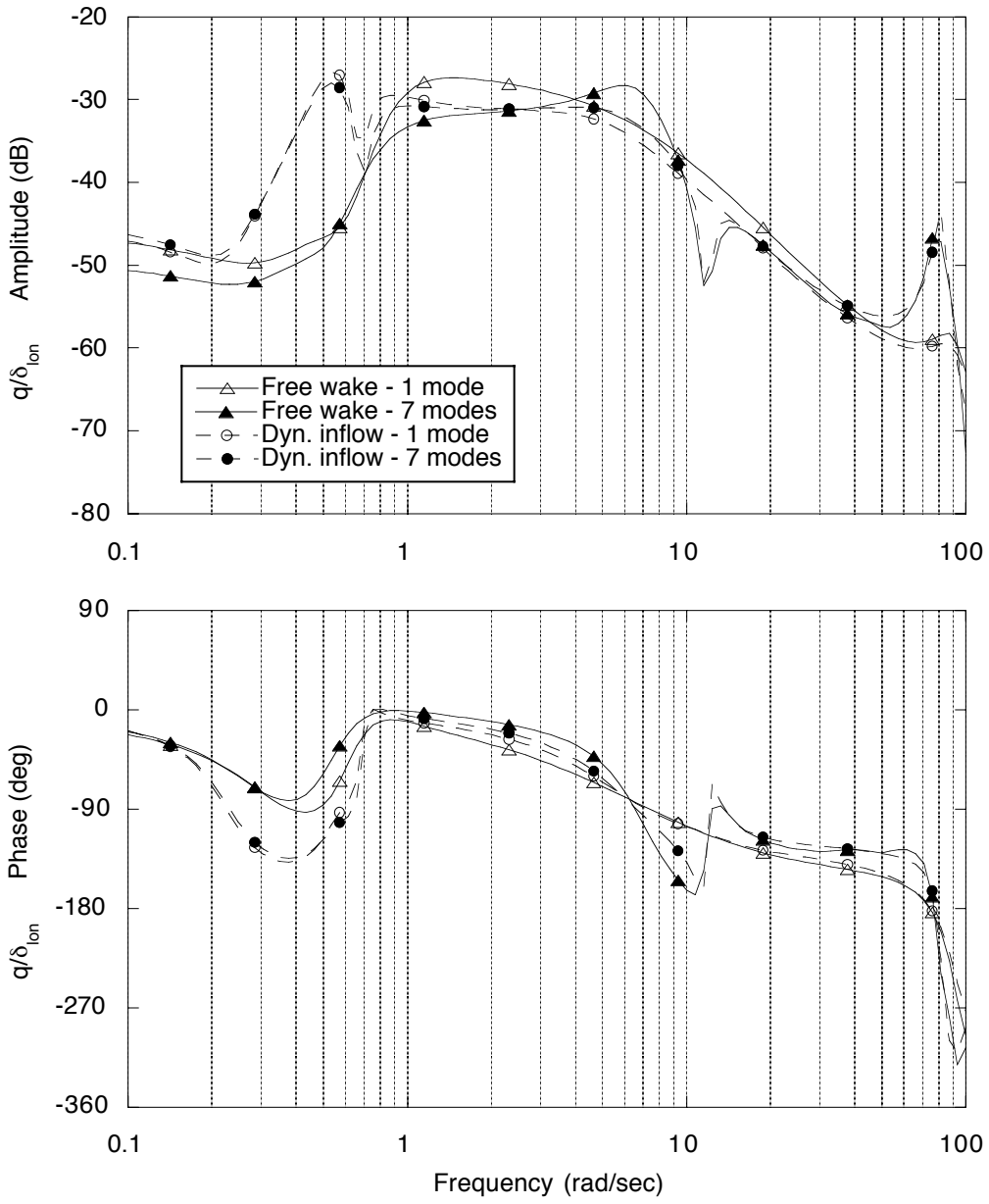

Figure 8.38: Effect of inflow models and blade modeling on the on-axis pitch rate frequency response to longitudinal stick input for the BO-105 in hover.

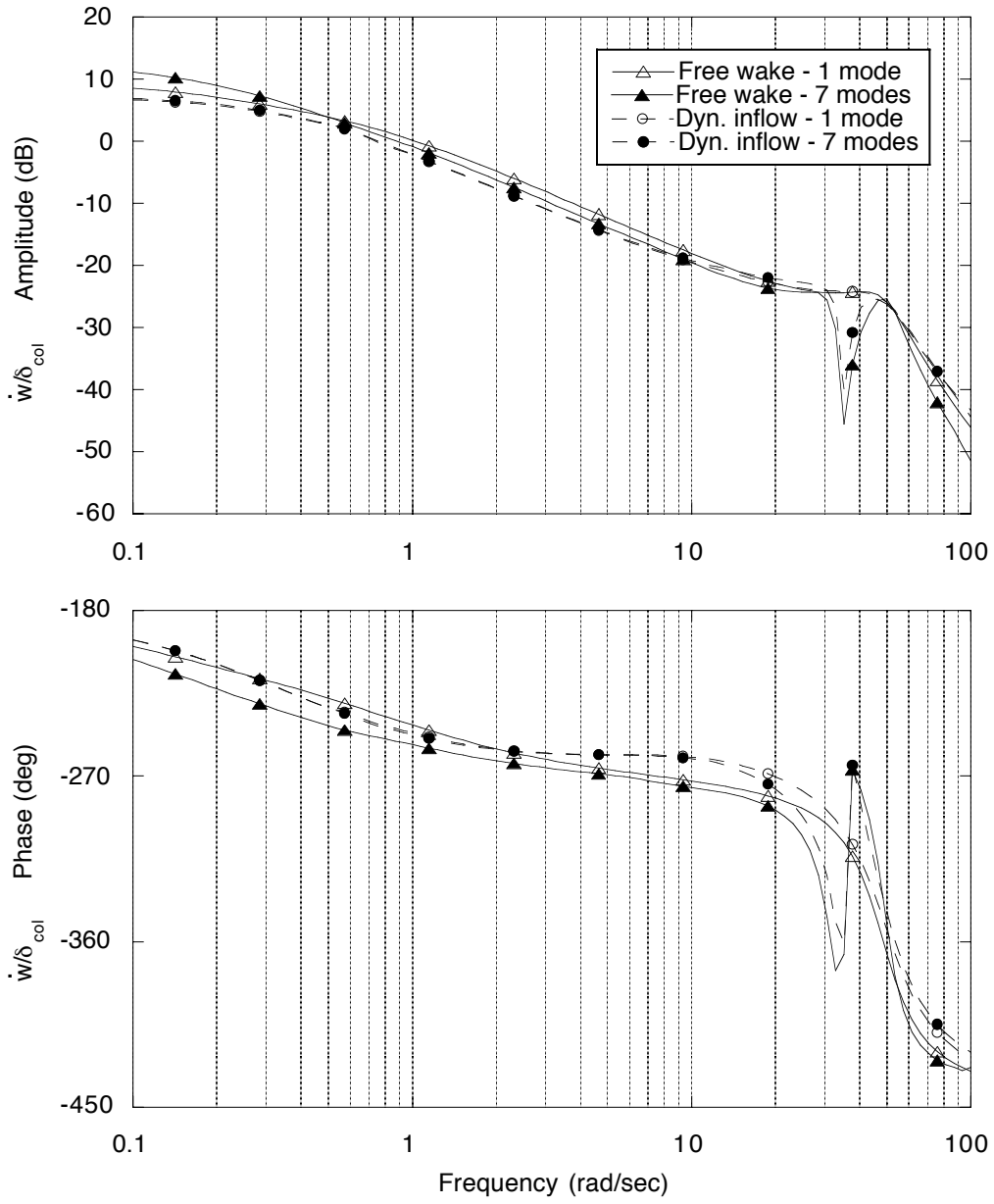

Figure 8.39: Effect of inflow models and blade modeling on the on-axis vertical acceleration frequency response to collective stick input for the BO-105 in hover.

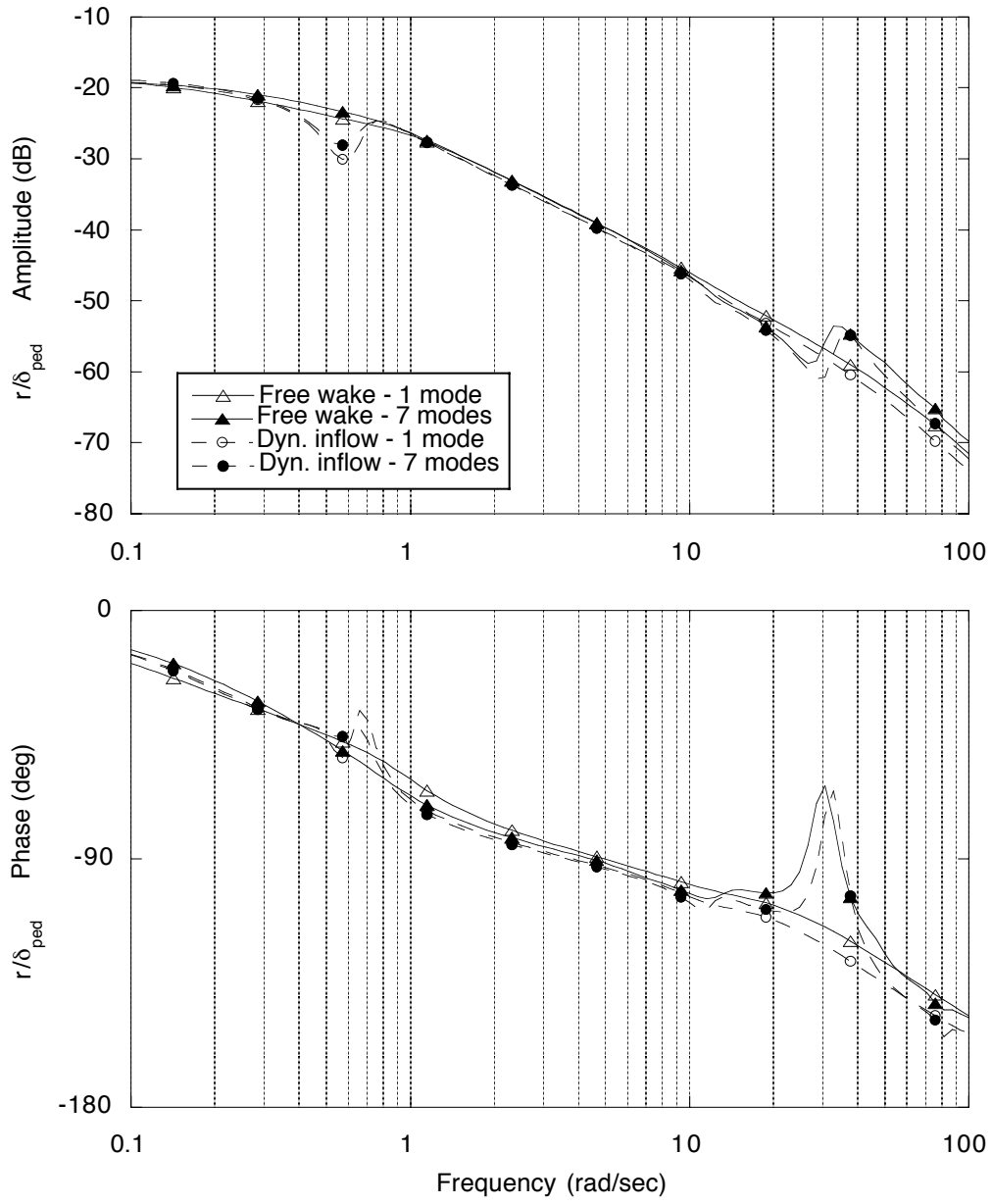

Figure 8.40: Effect of inflow models and blade modeling on the on-axis yaw rate frequency response to pedal input for the BO-105 in hover.

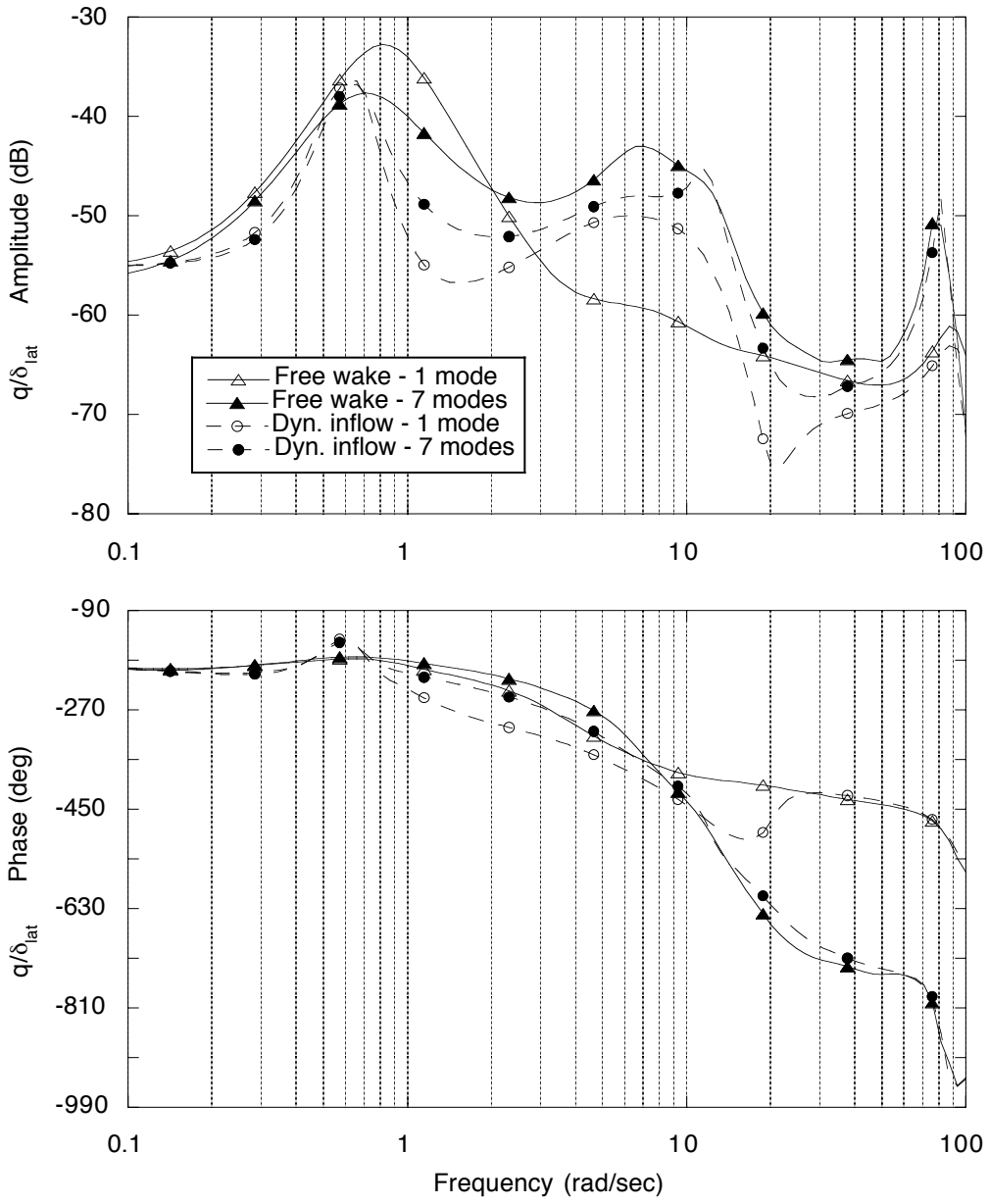

Figure 8.41: Effect of inflow models and blade modeling on the off-axis pitch rate frequency response to lateral stick input for the BO-105 in hover.

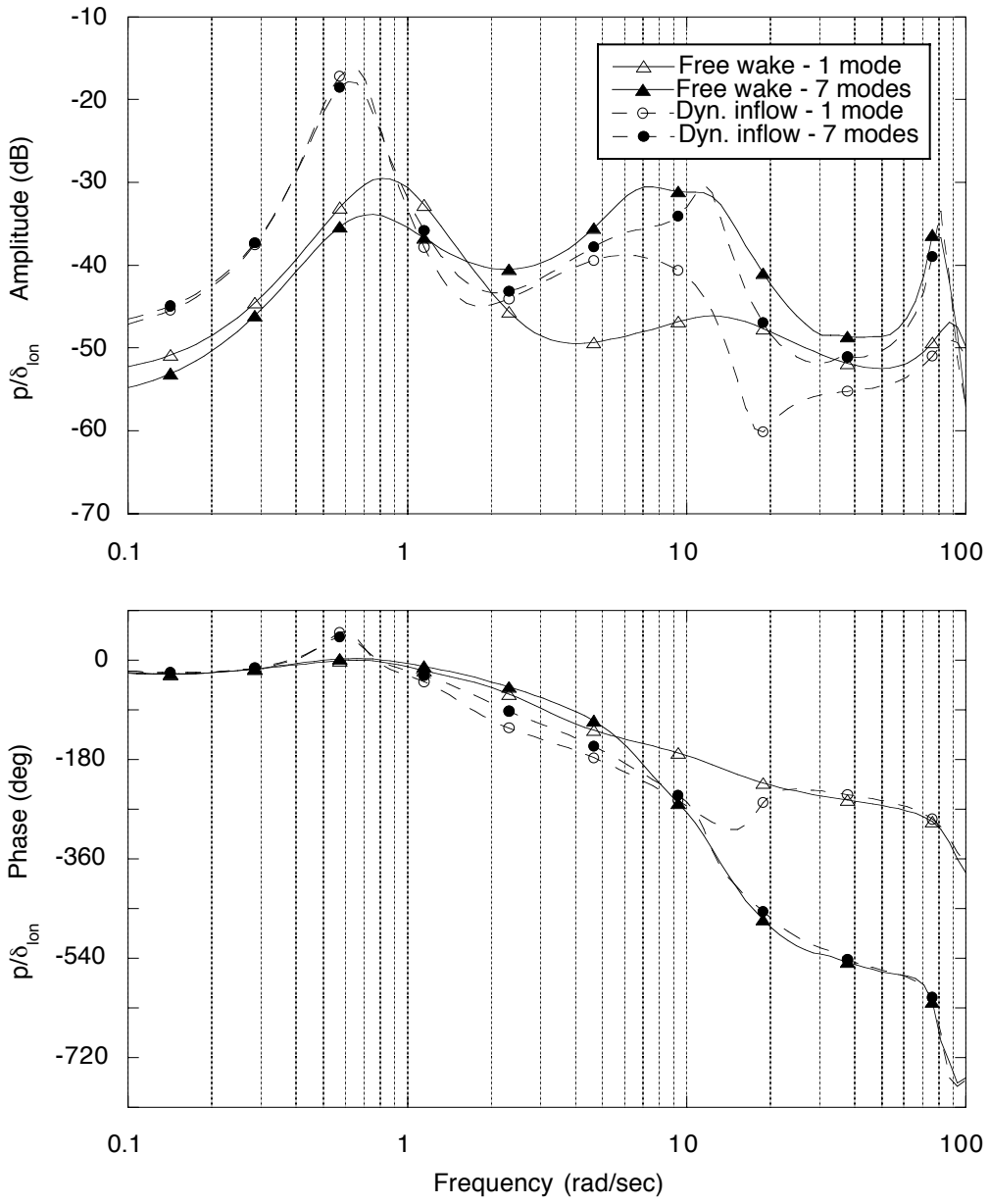

Figure 8.42: Effect of inflow models and blade modeling on the off-axis roll rate frequency response to longitudinal stick input for the BO-105 in hover.

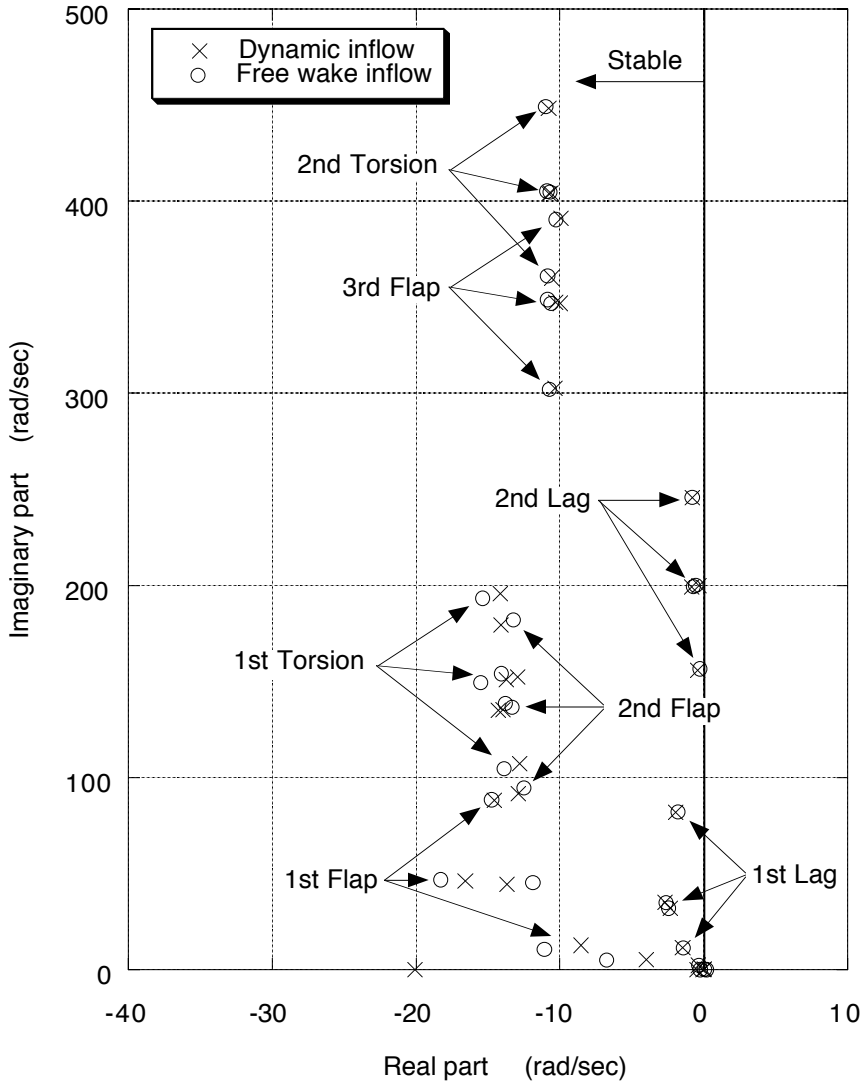

Figure 8.43: Effect of inflow modeling on rotor and inflow poles for the BO-105 at 80 knots with the refined blade model.

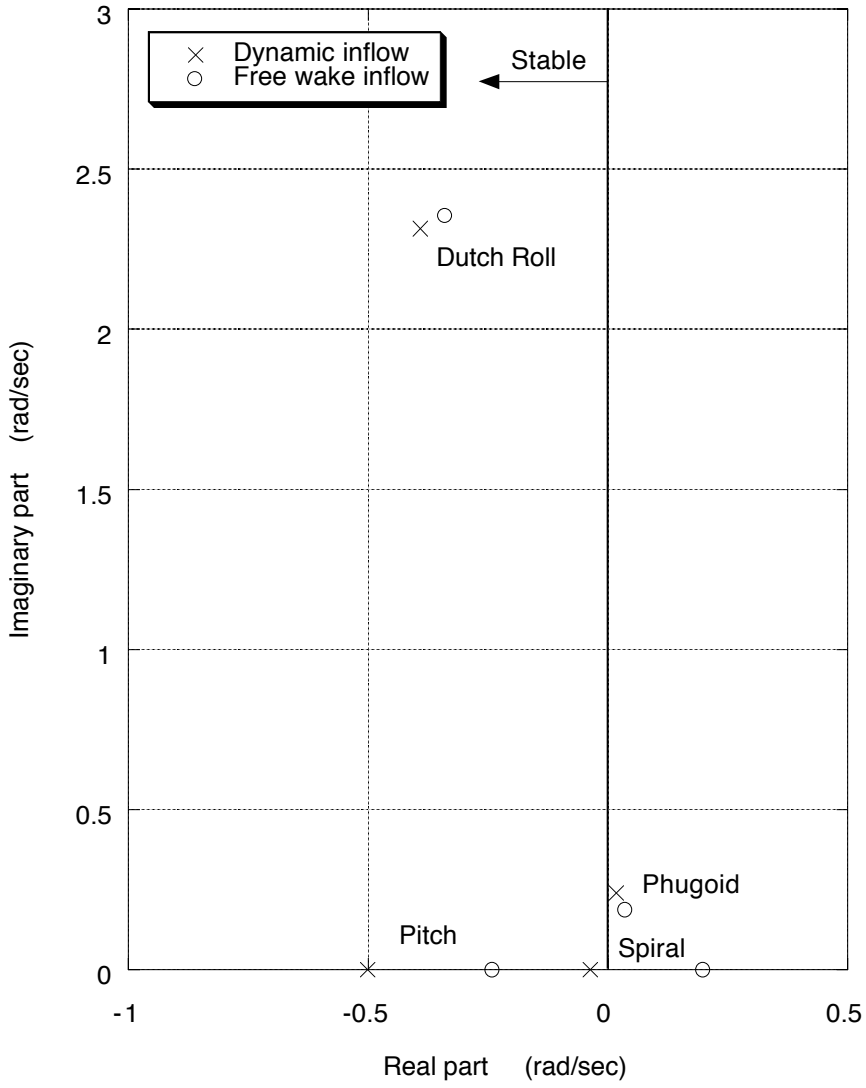

Figure 8.44: Effect of inflow modeling on fuselage poles for the BO-105 at 80 knots with the refined blade model.

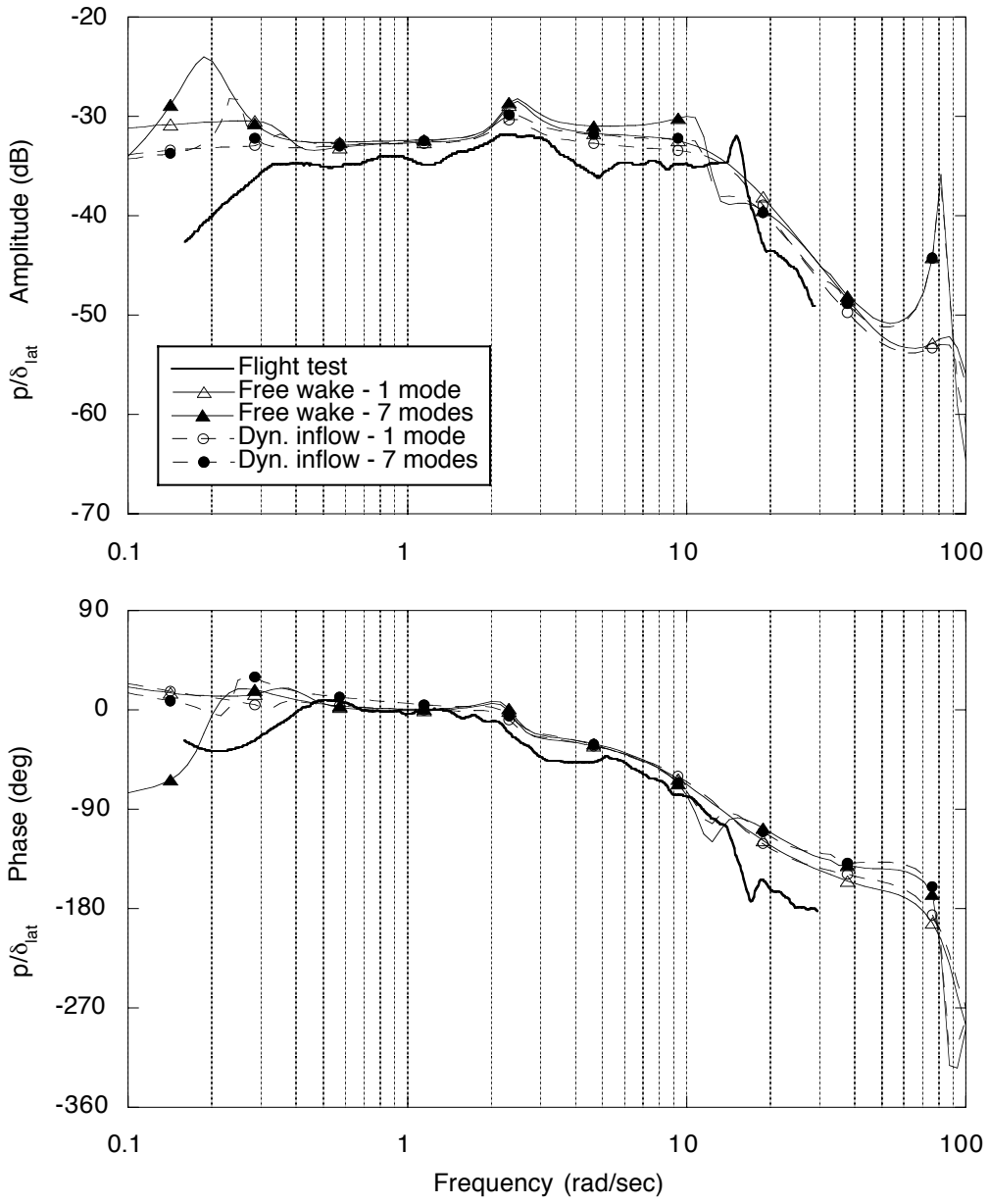

Figure 8.45: Effect of inflow models and blade modeling on the on-axis roll rate frequency response to lateral stick input for the BO-105 at 80 knots.

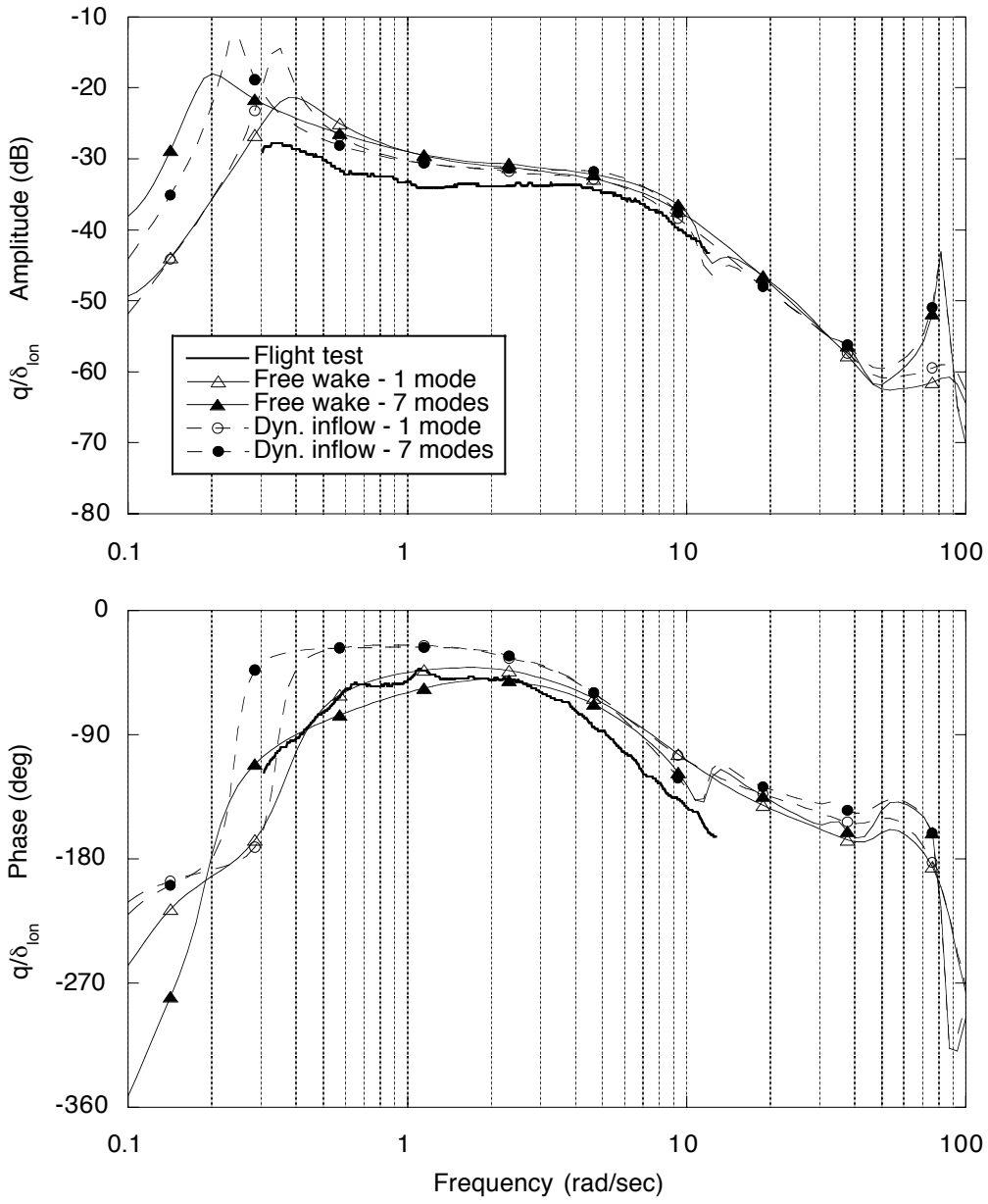

Figure 8.46: Effect of inflow models and blade modeling on the on-axis pitch rate frequency response to longitudinal stick input for the BO-105 at 80 knots.

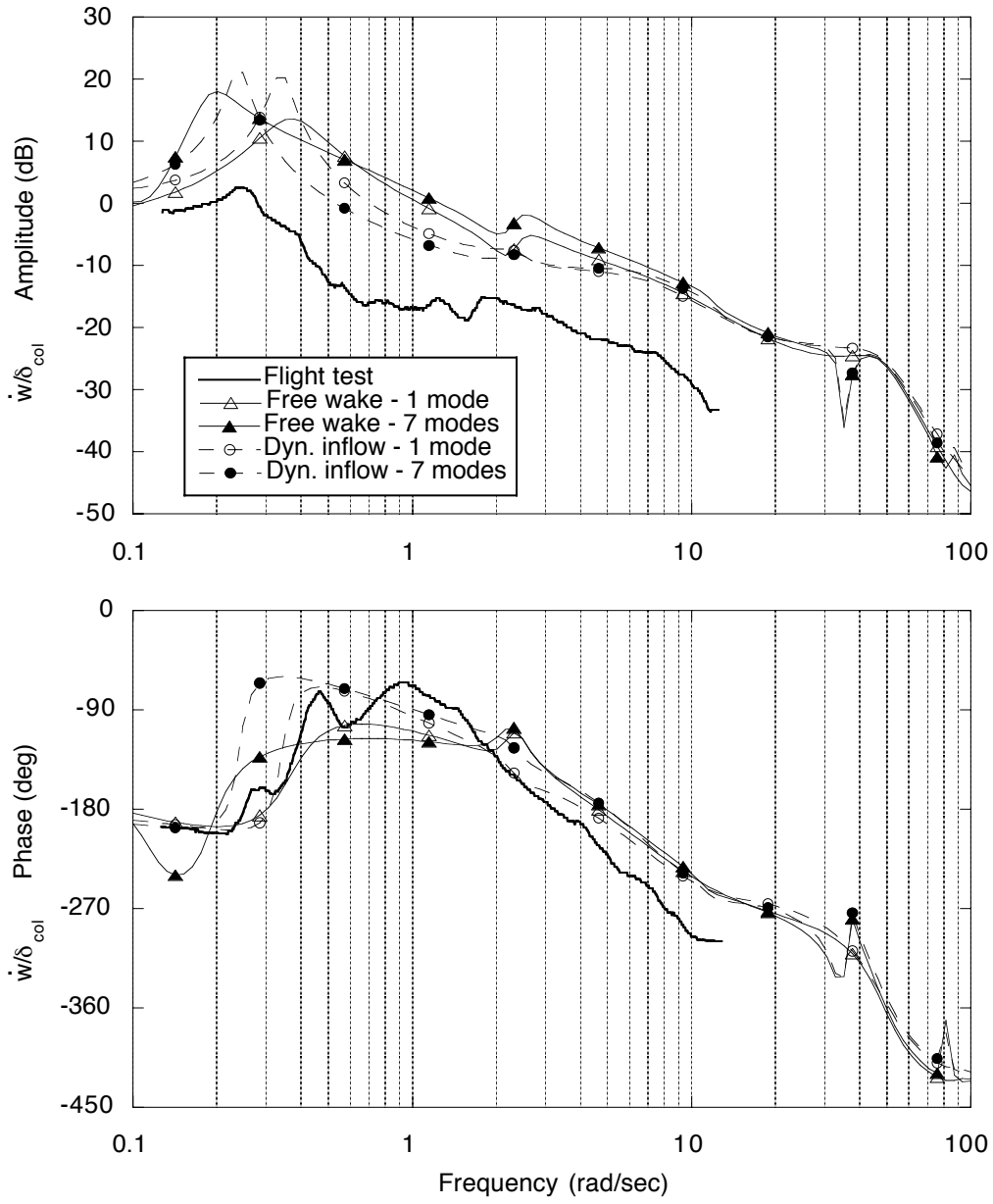

Figure 8.47: Effect of inflow models and blade modeling on the on-axis vertical acceleration frequency response to collective stick input for the BO-105 at 80 knots.

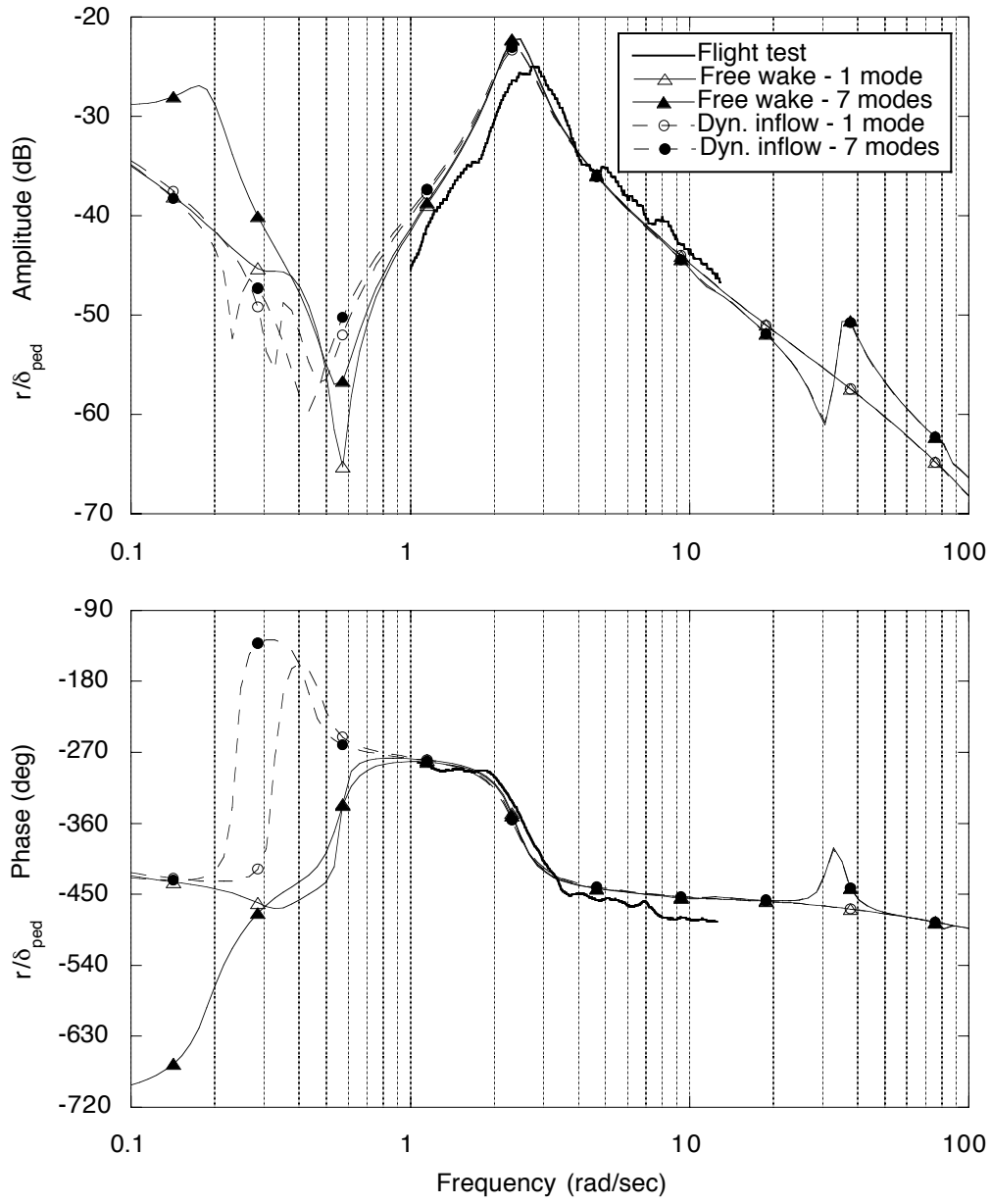

Figure 8.48: Effect of inflow models and blade modeling on the on-axis yaw rate frequency response to pedal input for the BO-105 at 80 knots.

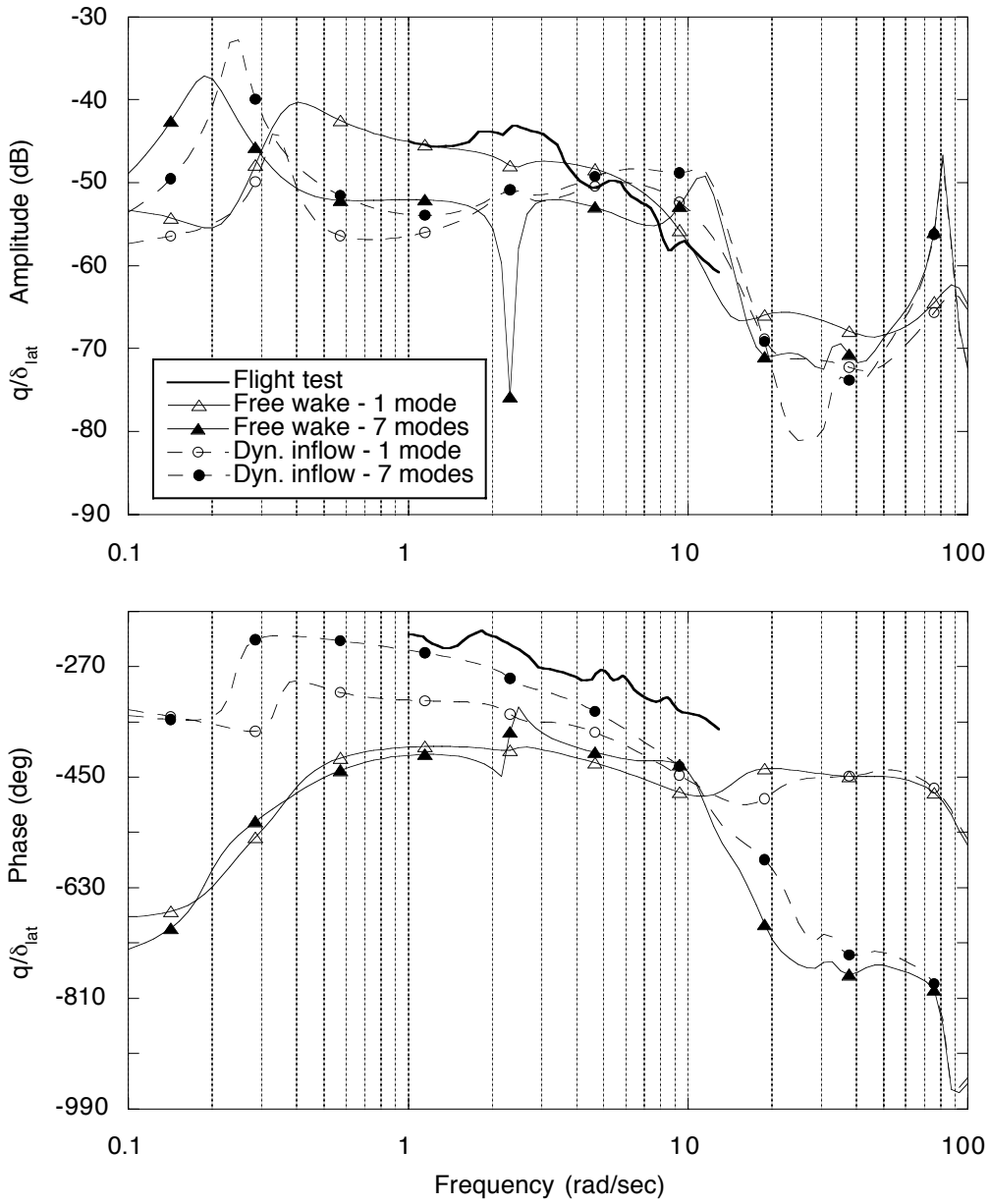

Figure 8.49: Effect of inflow models and blade modeling on the off-axis pitch rate frequency response to lateral stick input for the BO-105 at 80 knots.

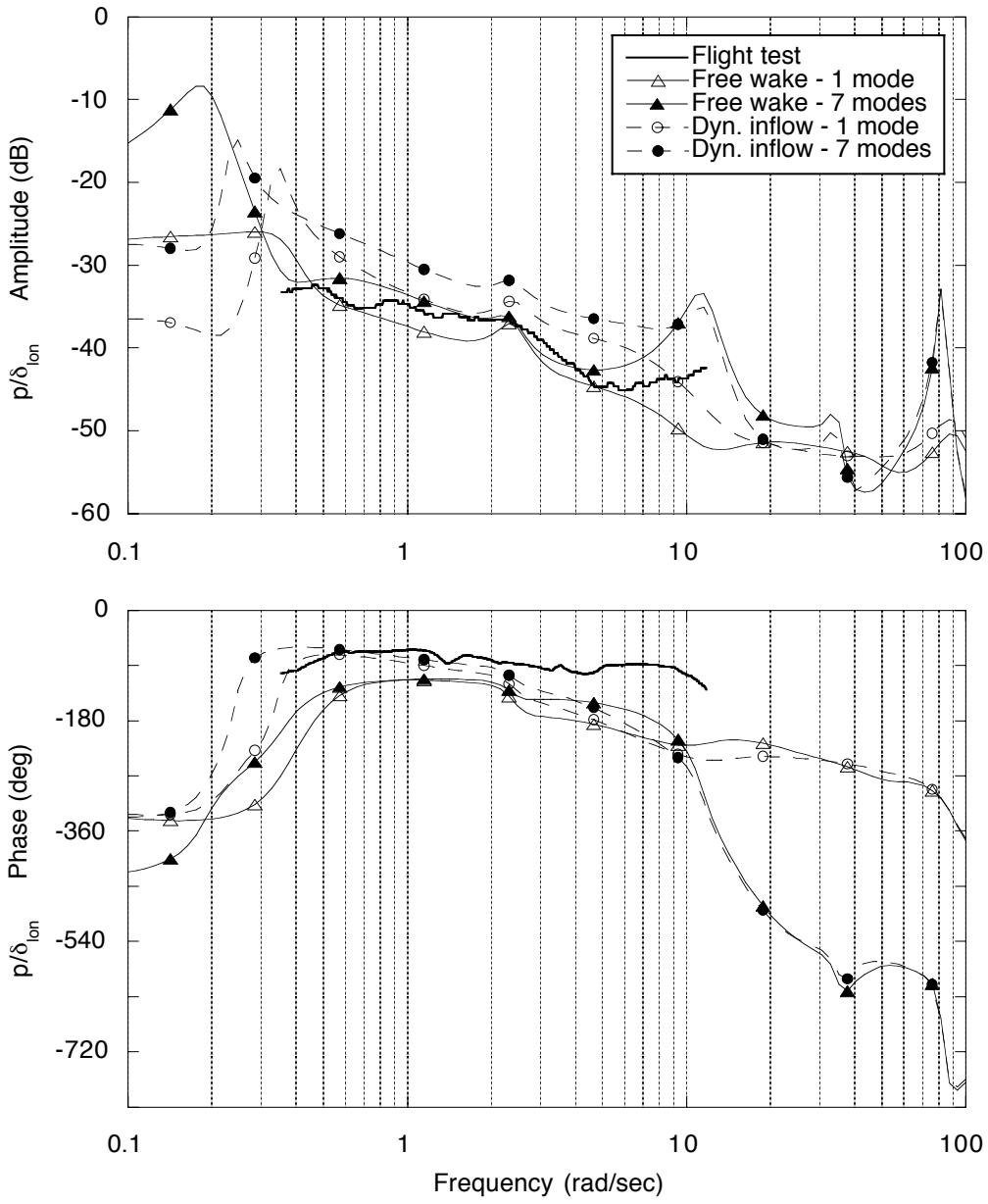

Figure 8.50: Effect of inflow models and blade modeling on the off-axis roll rate frequency response to longitudinal stick input for the BO-105 at 80 knots.

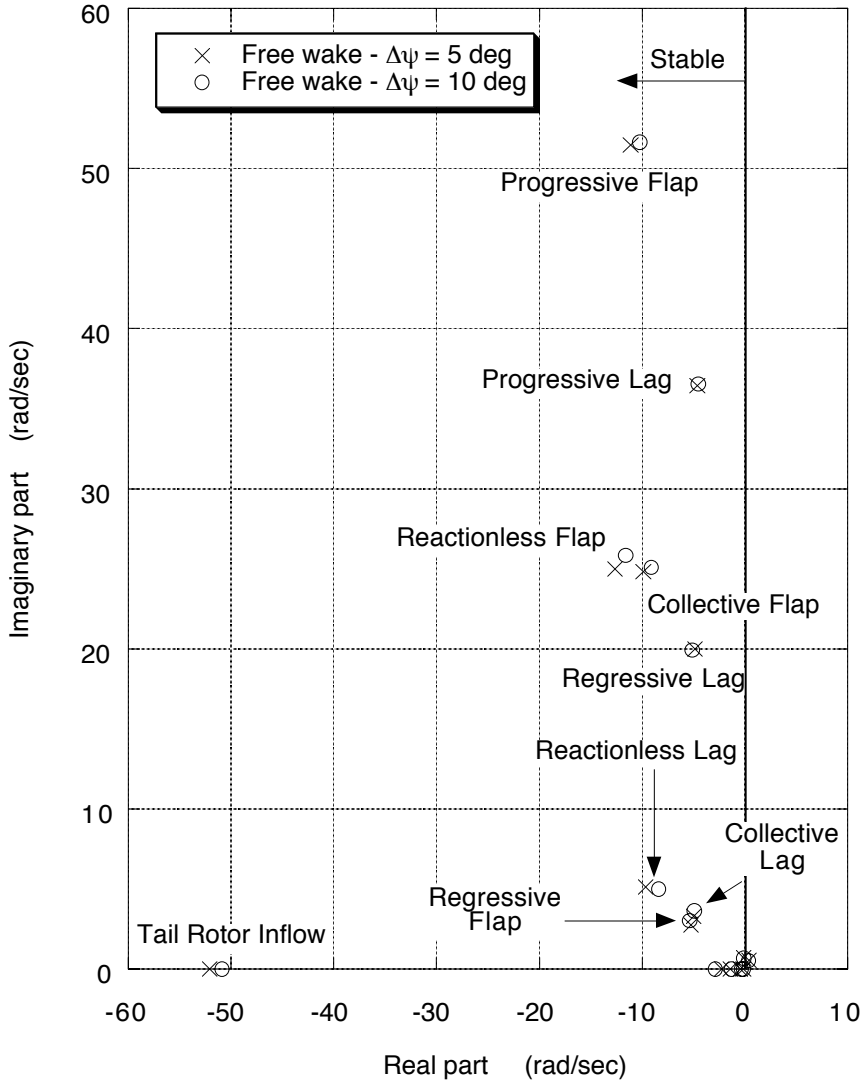

Figure 8.51: Effect of free wake resolution on the rotor poles for the UH-60A in hover with the simple blade model.

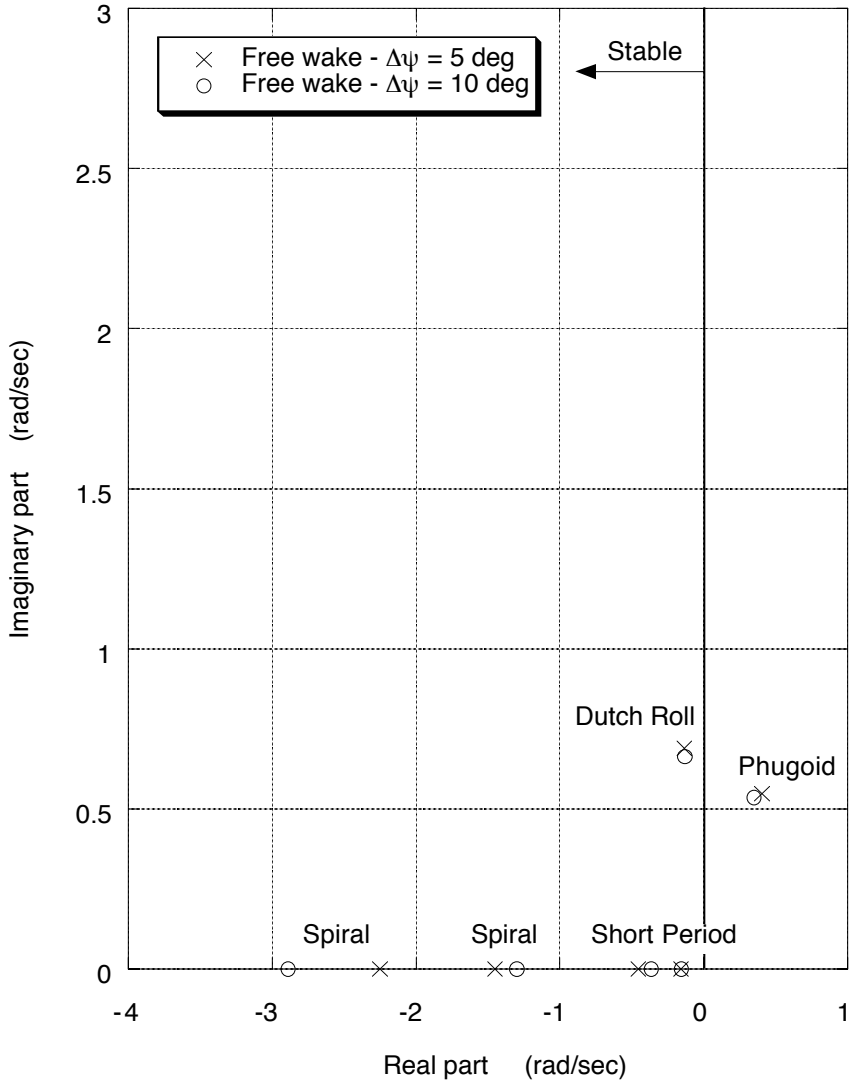

Figure 8.52: Effect of free wake resolution on the fuselage poles for the UH-60A in hover with the simple blade model.

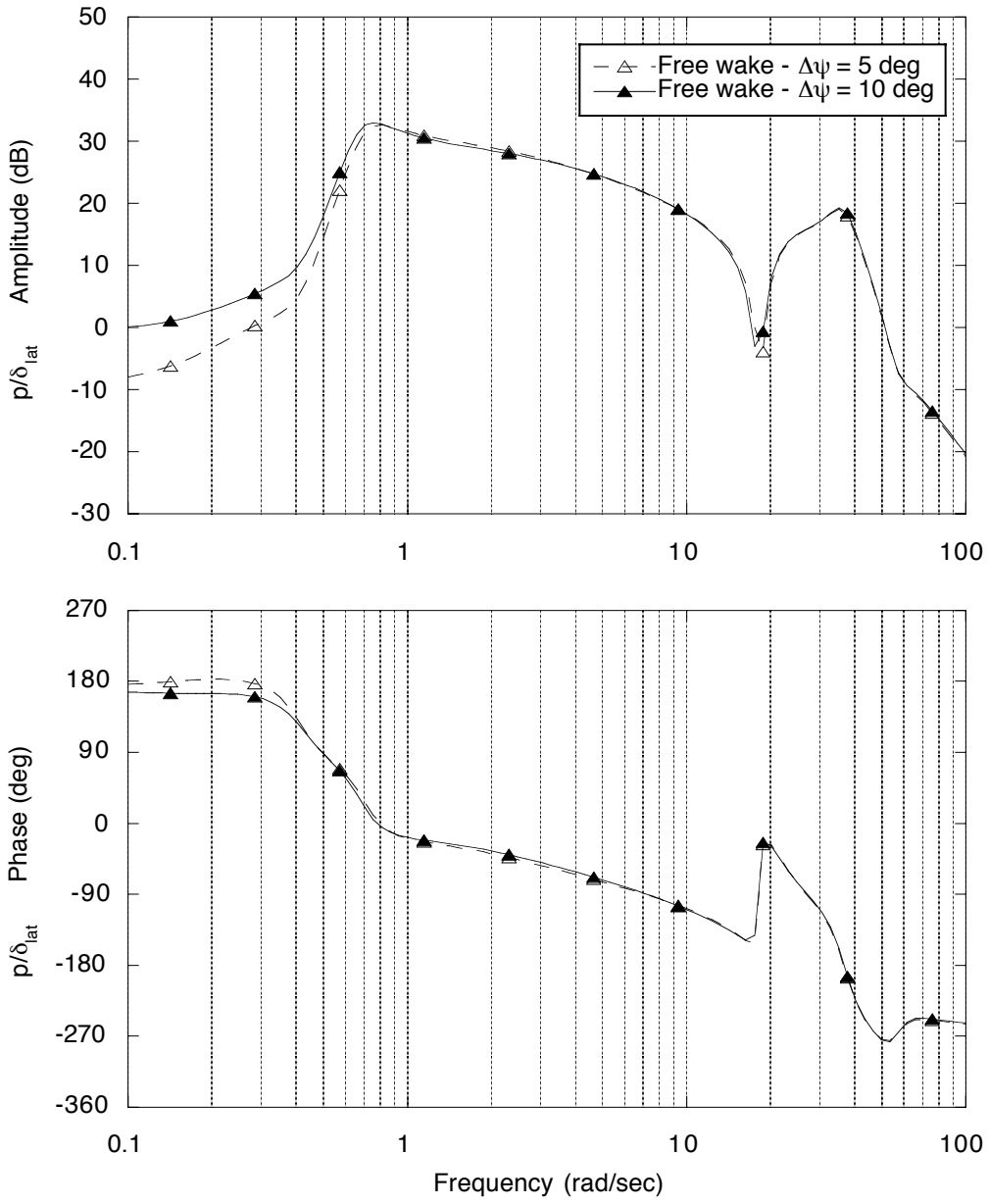

Figure 8.53: Effect of free wake resolution on the roll rate frequency response to a lateral stick input for the UH-60A in hover with the simple blade model.

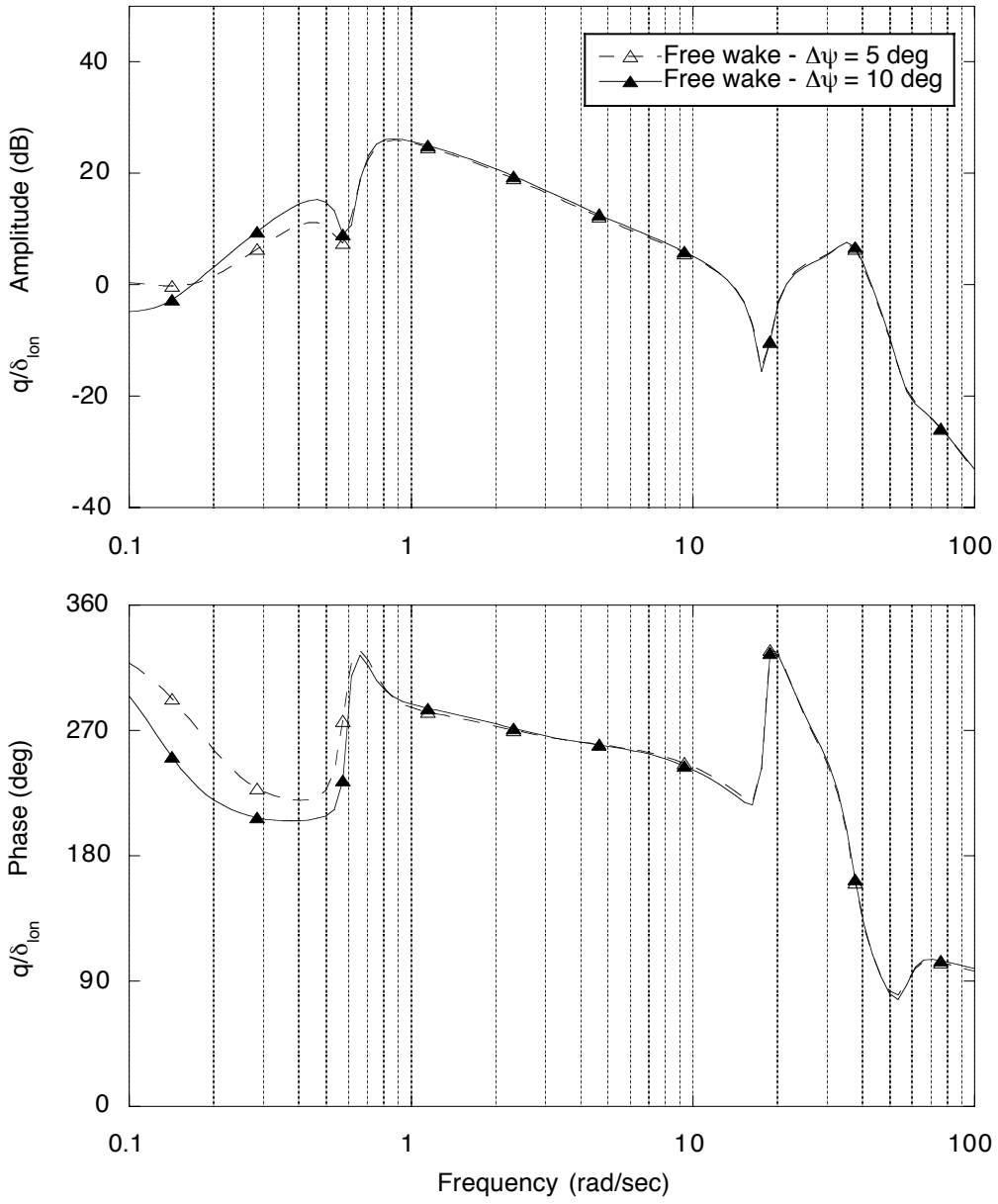

Figure 8.54: Effect of free wake resolution on the pitch rate frequency response to a longitudinal stick input for the UH-60A in hover with the simple blade model.

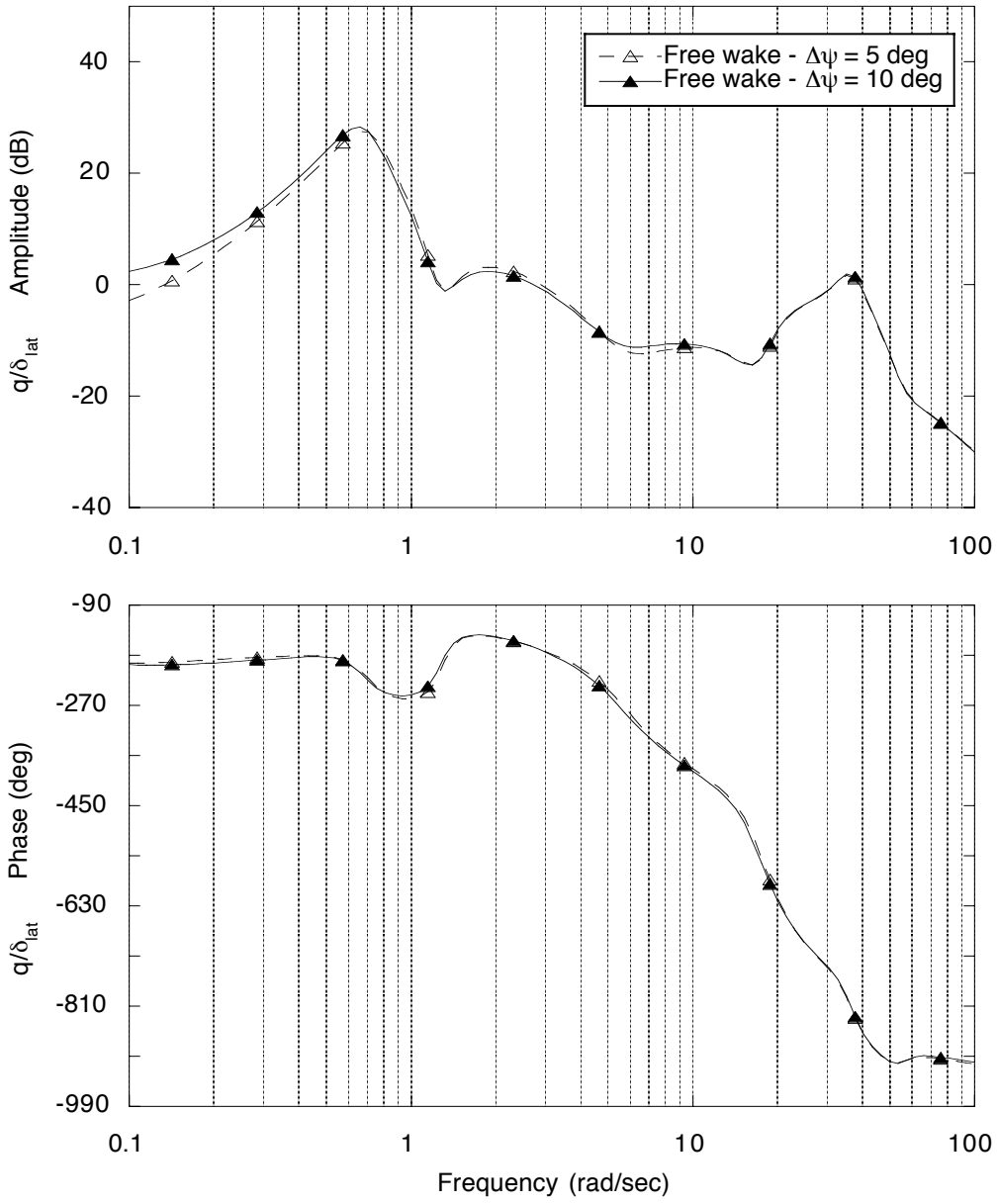

Figure 8.55: Effect of free wake resolution on the pitch rate frequency response to a lateral stick input for the UH-60A in hover with the simple blade model.

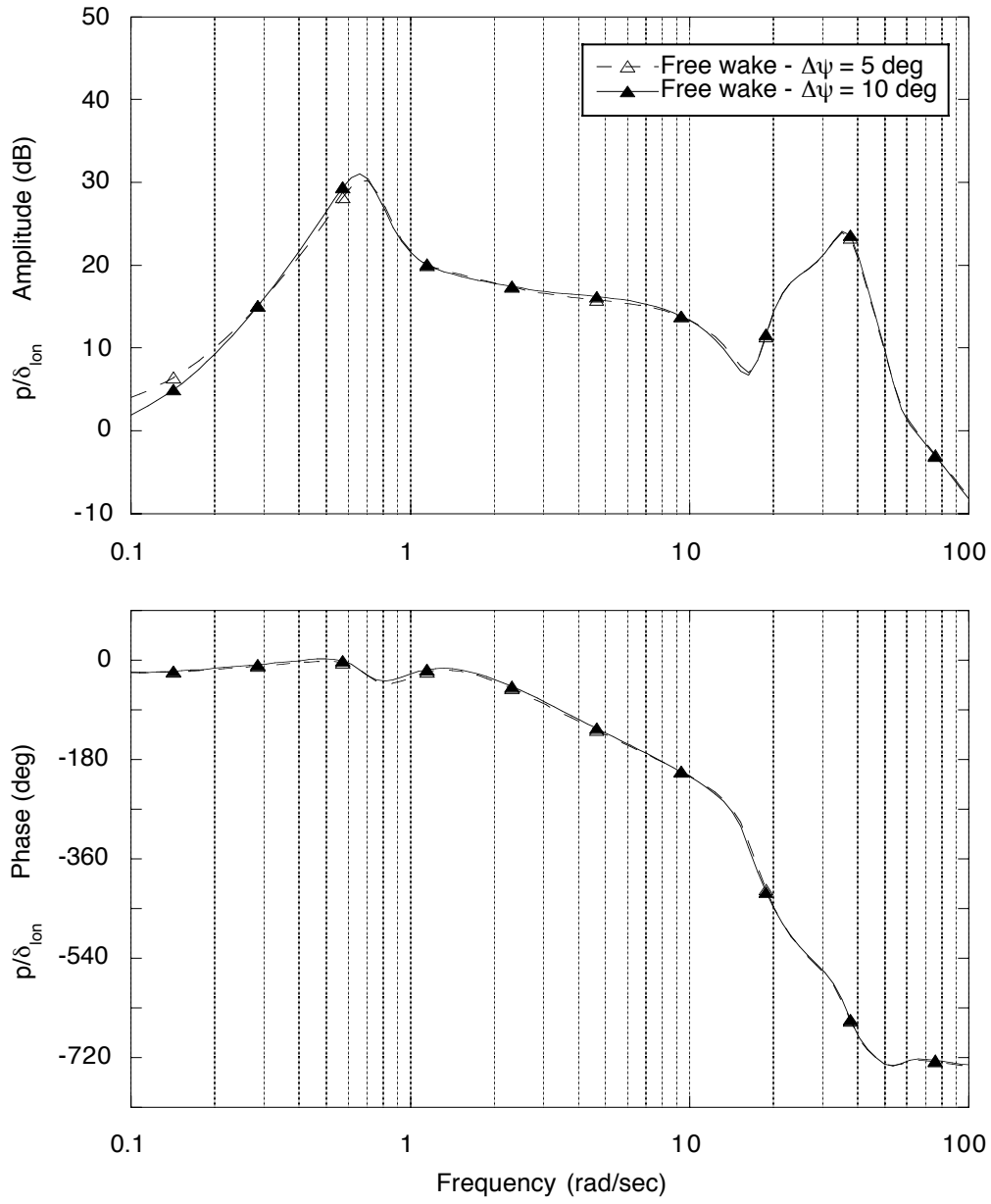

Figure 8.56: Effect of free wake resolution on the roll rate frequency response to a longitudinal stick input for the UH-60A in hover with the simple blade model.

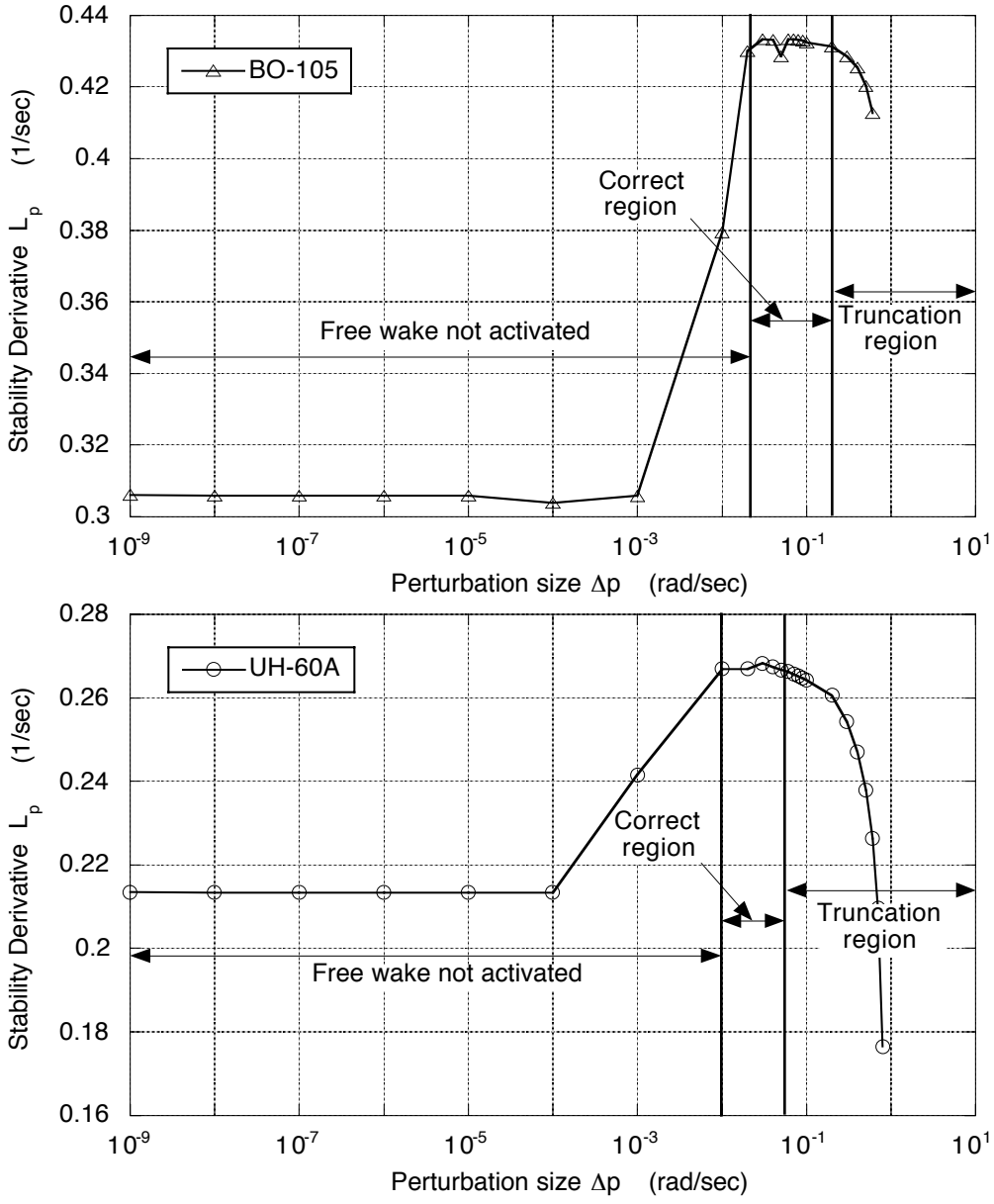

Figure 8.57: Effect of numerical perturbation size on the rolling moment stability derivative to roll rate in hover for the BO-105 (top) and UH-60A (bottom). The simple blade model is used for both aircraft.

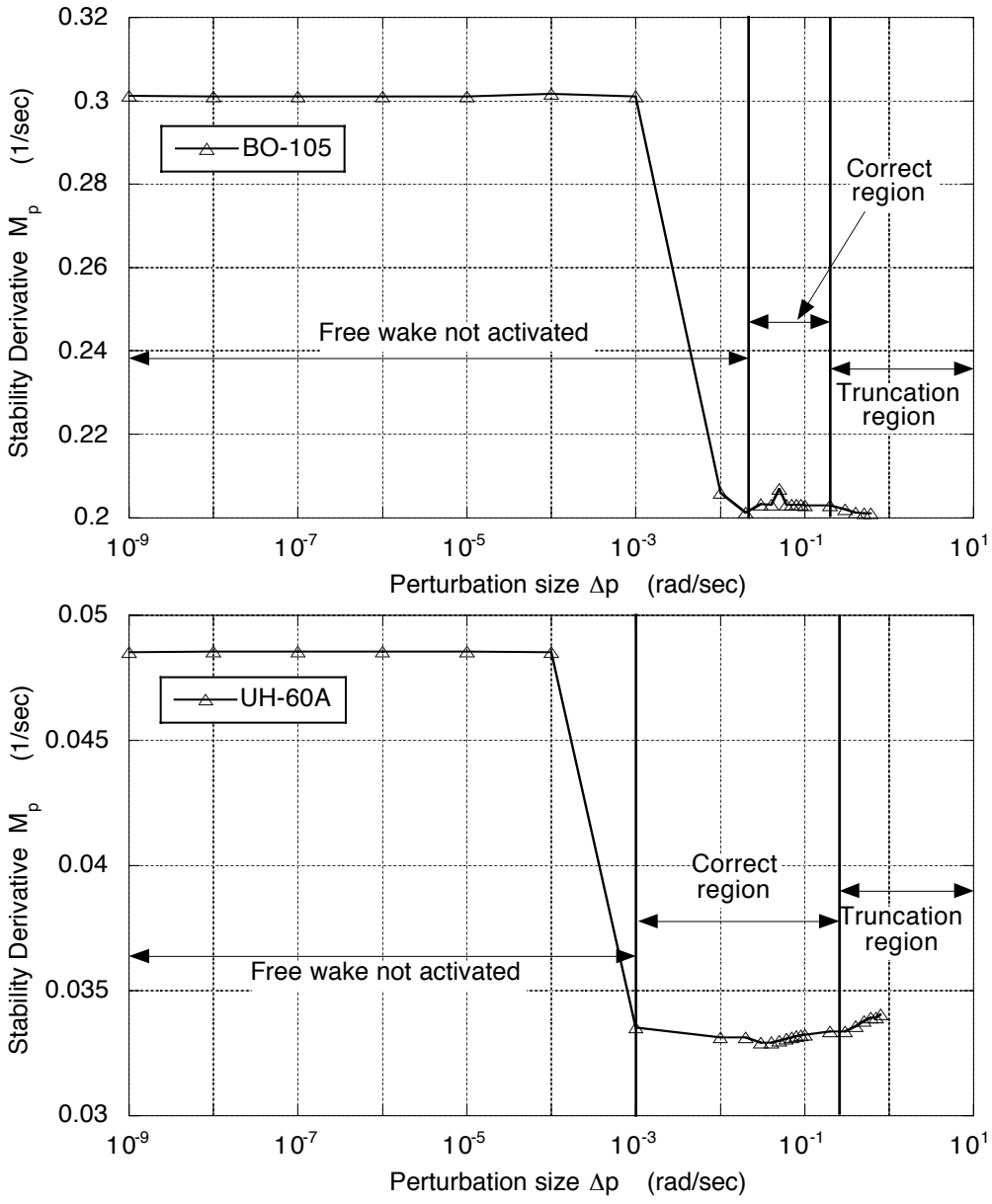

Figure 8.58: Effect of numerical perturbation size on the pitching moment stability derivative to roll rate in hover for the BO-105 (top) and UH-60A (bottom. The simple blade model is used for both aircraft.

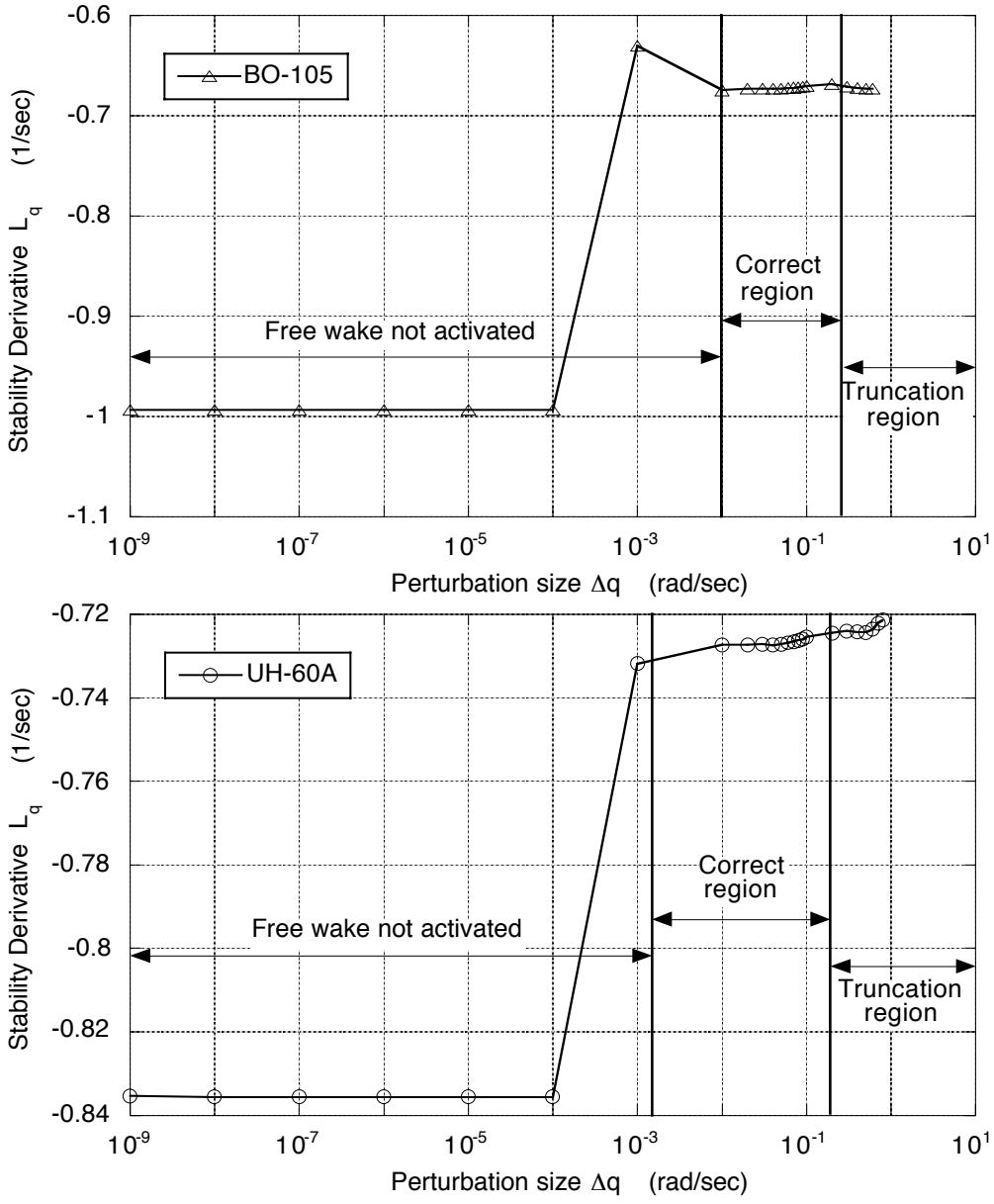

Figure 8.59: Effect of numerical perturbation size on the rolling moment stability derivative to pitch rate in hover for the BO-105 (top) and UH-60A (bottom). The simple blade model is used for both aircraft.

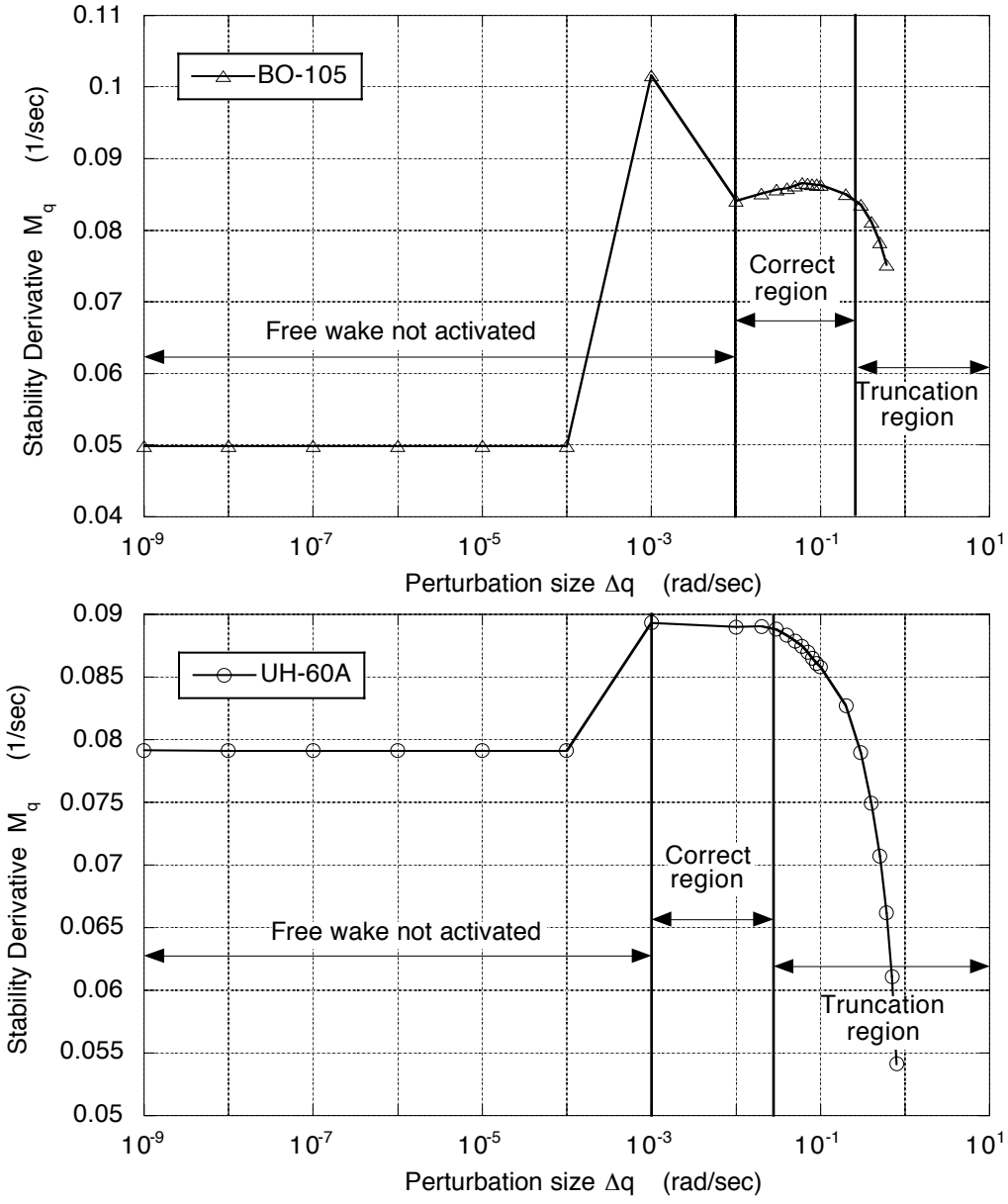

Figure 8.60: Effect of numerical perturbation size on the pitching moment stability derivative to pitch rate in hover for the BO-105 (top) and UH-60A (bottom). The simple blade model is used for both aircraft.

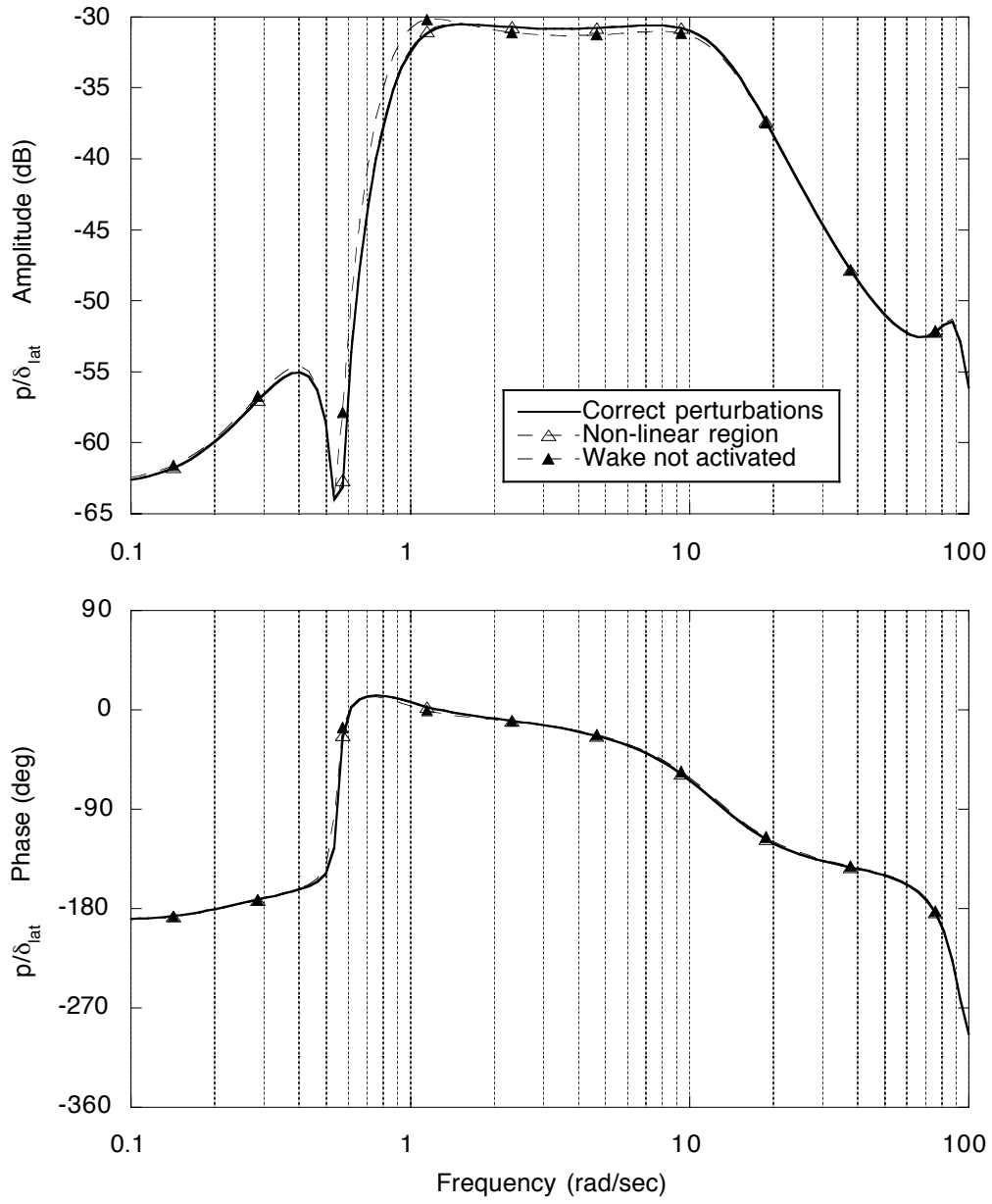

Figure 8.61: Effect of numerical perturbation size on the on-axis roll rate response to a lateral stick input for the BO-105 in hover with the simple blade model.

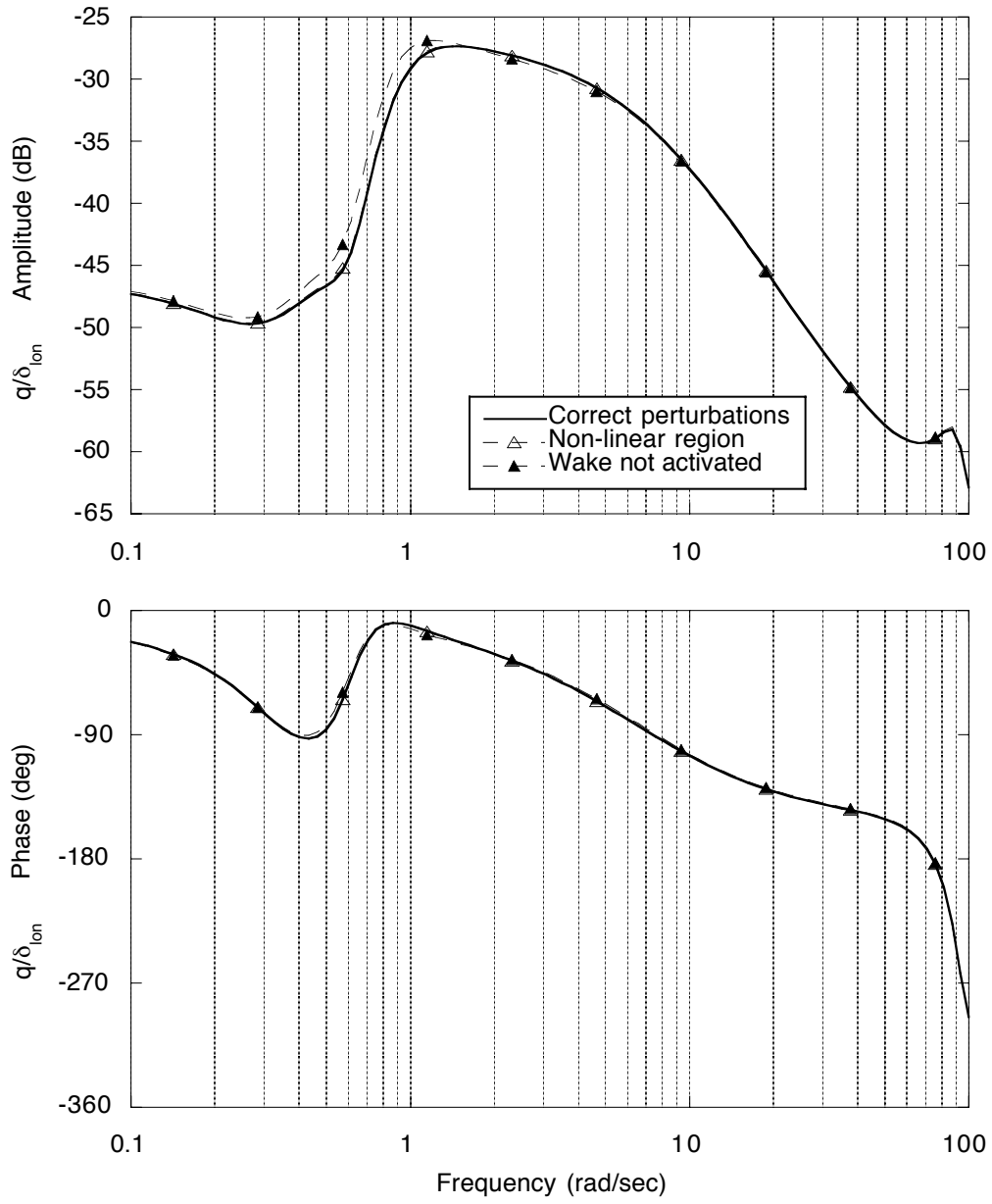

Figure 8.62: Effect of numerical perturbation size on the on-axis pitch rate response to a longitudinal stick input for the BO-105 in hover with the simple blade model.

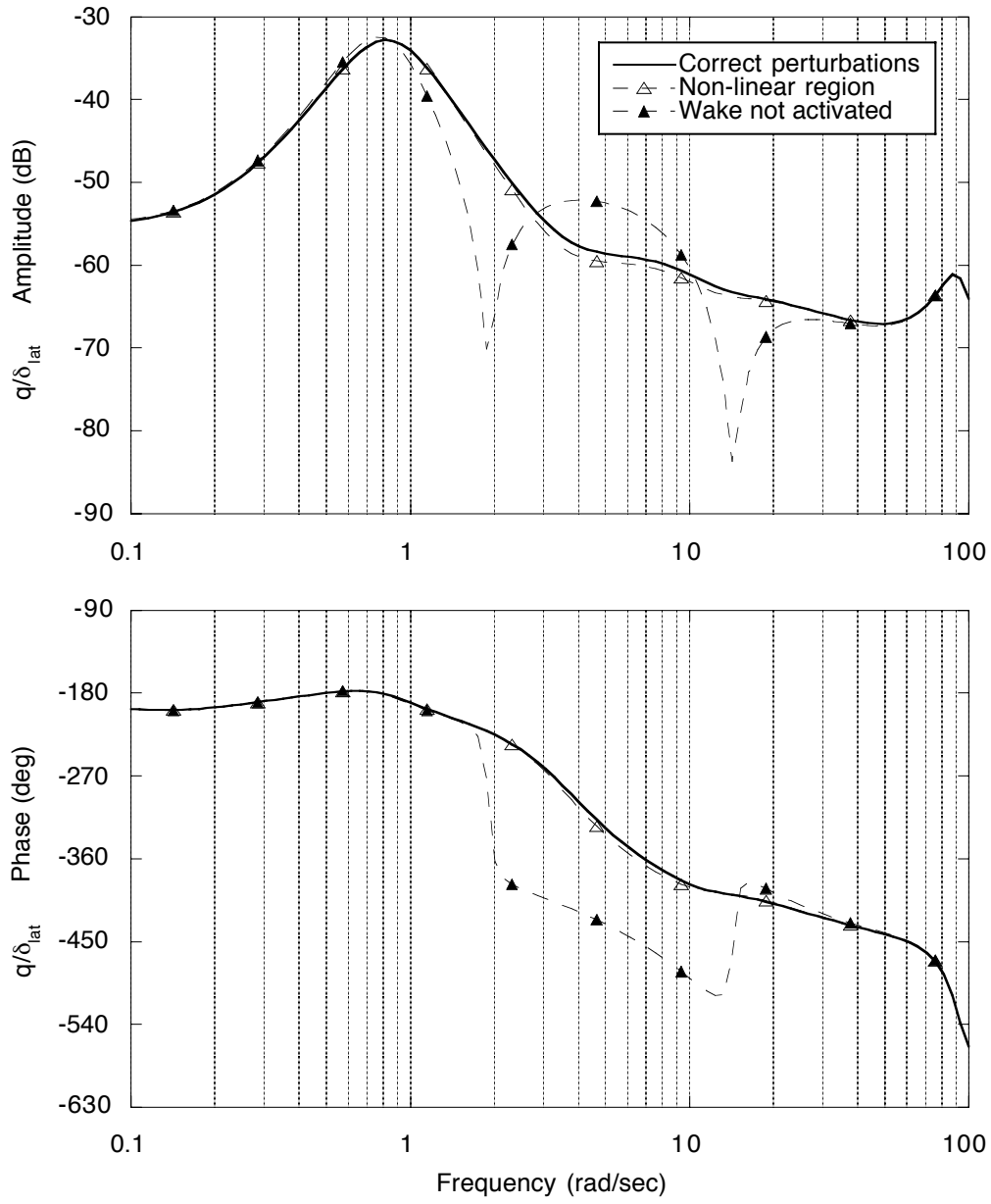

Figure 8.63: Effect of numerical perturbation size on the off-axis pitch rate response to a lateral stick input for the BO-105 in hover with the simple blade model.

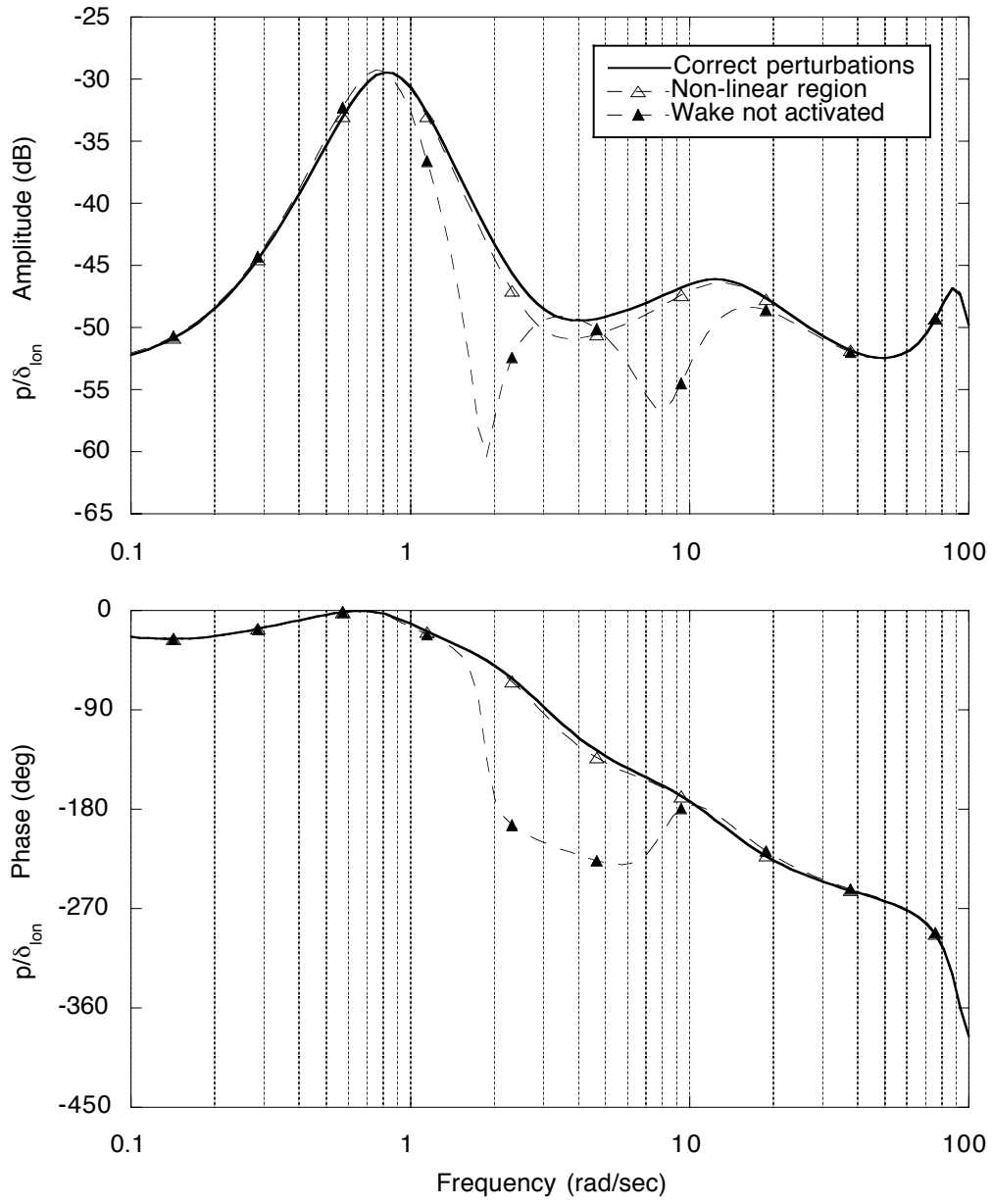

Figure 8.64: Effect of numerical perturbation size on the off-axis roll rate response to a longitudinal stick input for the BO-105 in hover with the simple blade model.

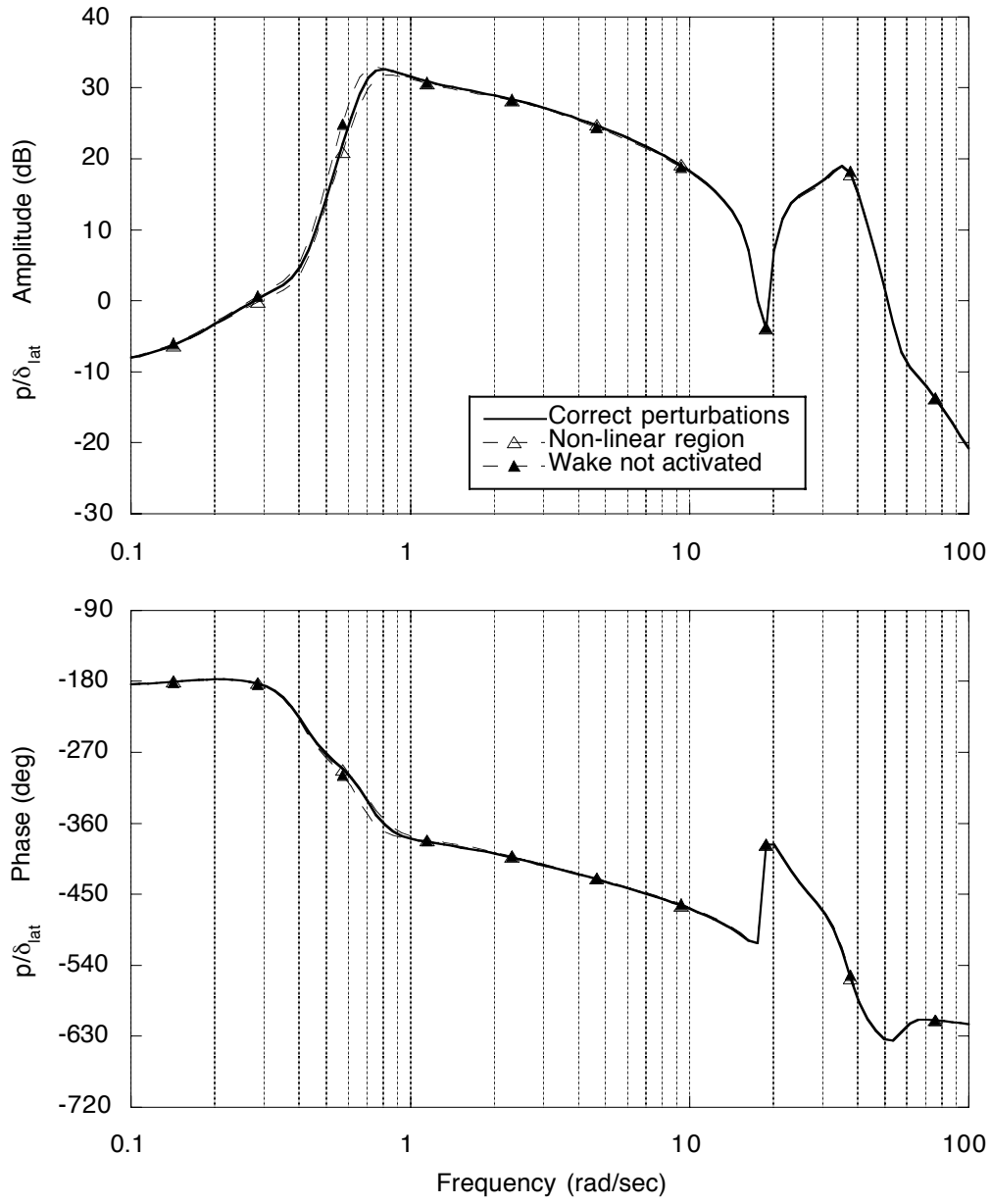

Figure 8.65: Effect of numerical perturbation size on the on-axis roll rate response to a lateral stick input for the UH-60A in hover with the simple blade model.

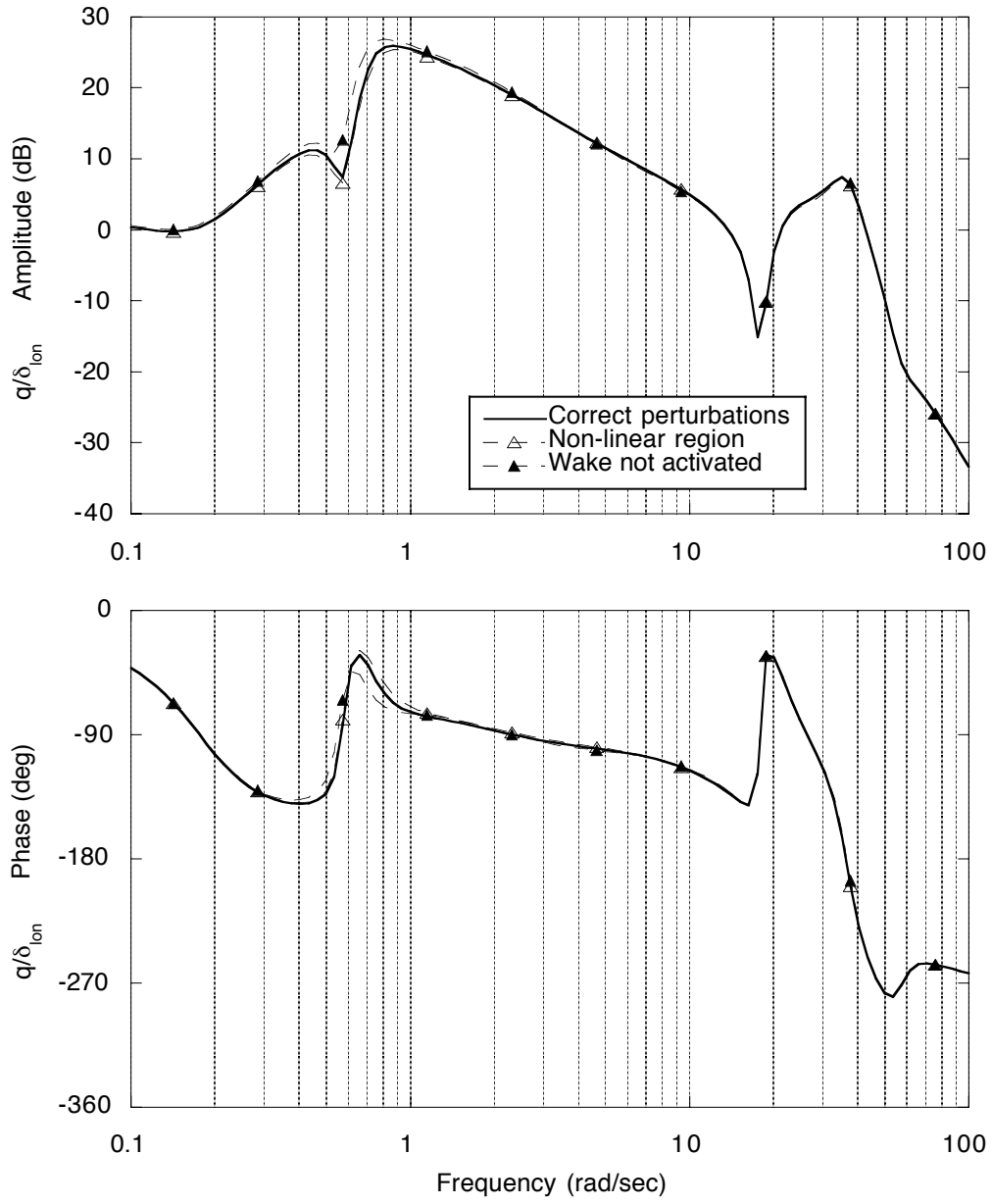

Figure 8.66: Effect of numerical perturbation size on the on-axis pitch rate response to a longitudinal stick input for the UH-60A in hover with the simple blade model.

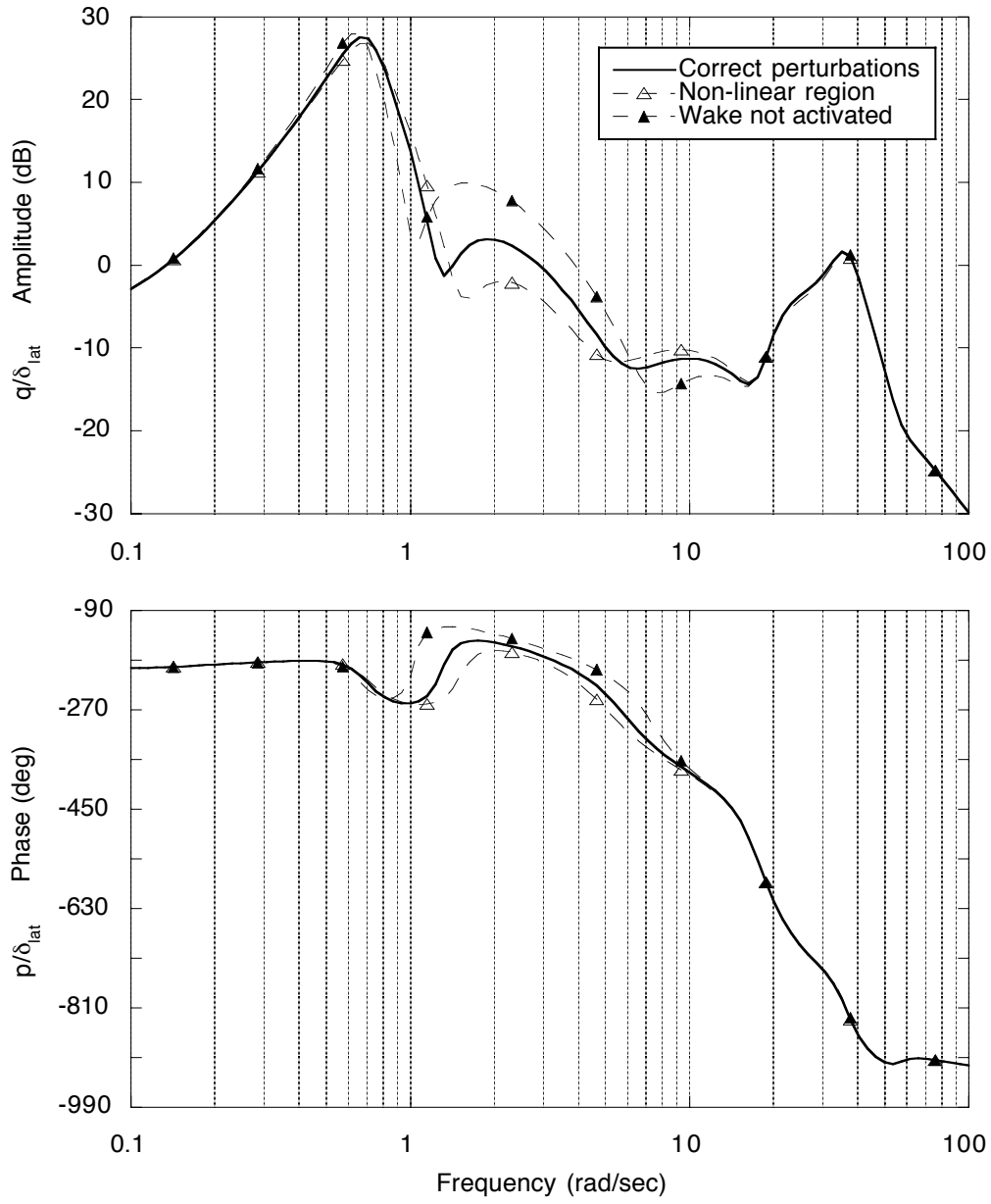

Figure 8.67: Effect of numerical perturbation size on the off-axis pitch rate response to a lateral stick input for the UH-60A in hover with the simple blade model.

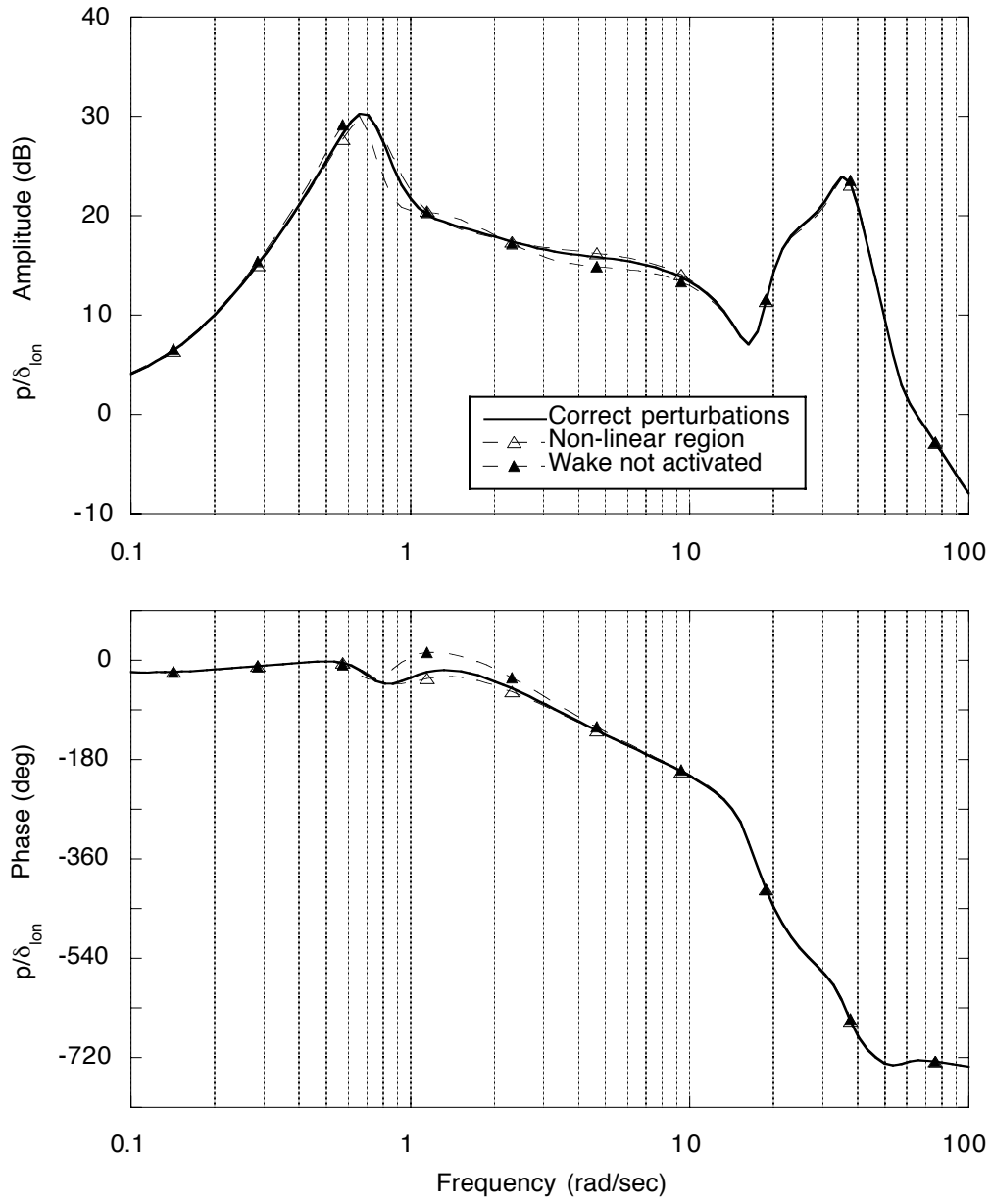

Figure 8.68: Effect of numerical perturbation size on the off-axis roll rate response to a longitudinal stick input for the UH-60A in hover with the simple blade model.

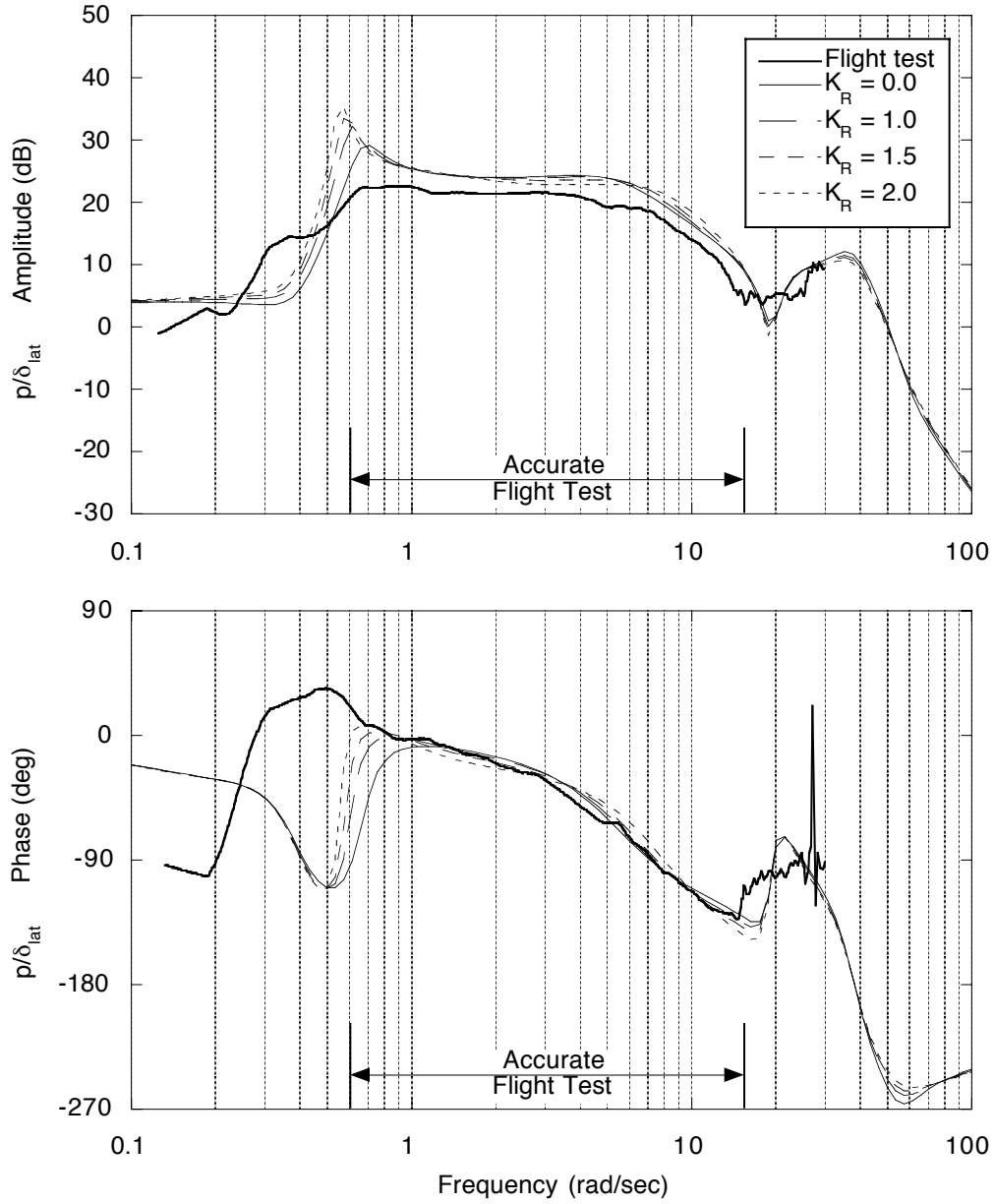

Figure 8.69: Effect of wake distortion parameter K_R within the extended momentum theory model on the on-axis roll rate frequency response to a lateral stick input for the UH-60A in hover with the simple blade model.

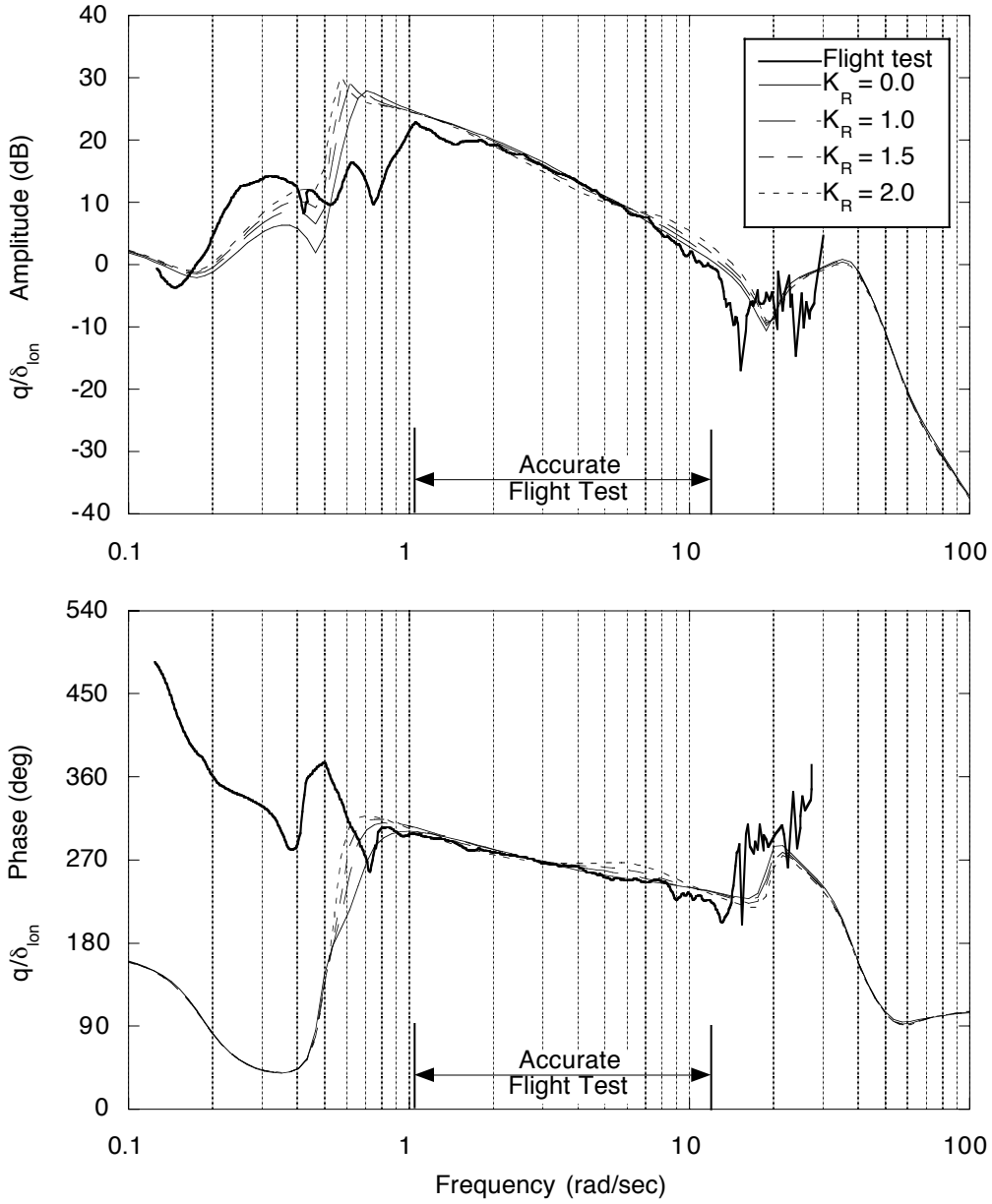

Figure 8.70: Effect of wake distortion parameter K_R within the extended momentum theory model on the on-axis pitch rate frequency response to a longitudinal stick input for the UH-60A in hover with the simple blade model.

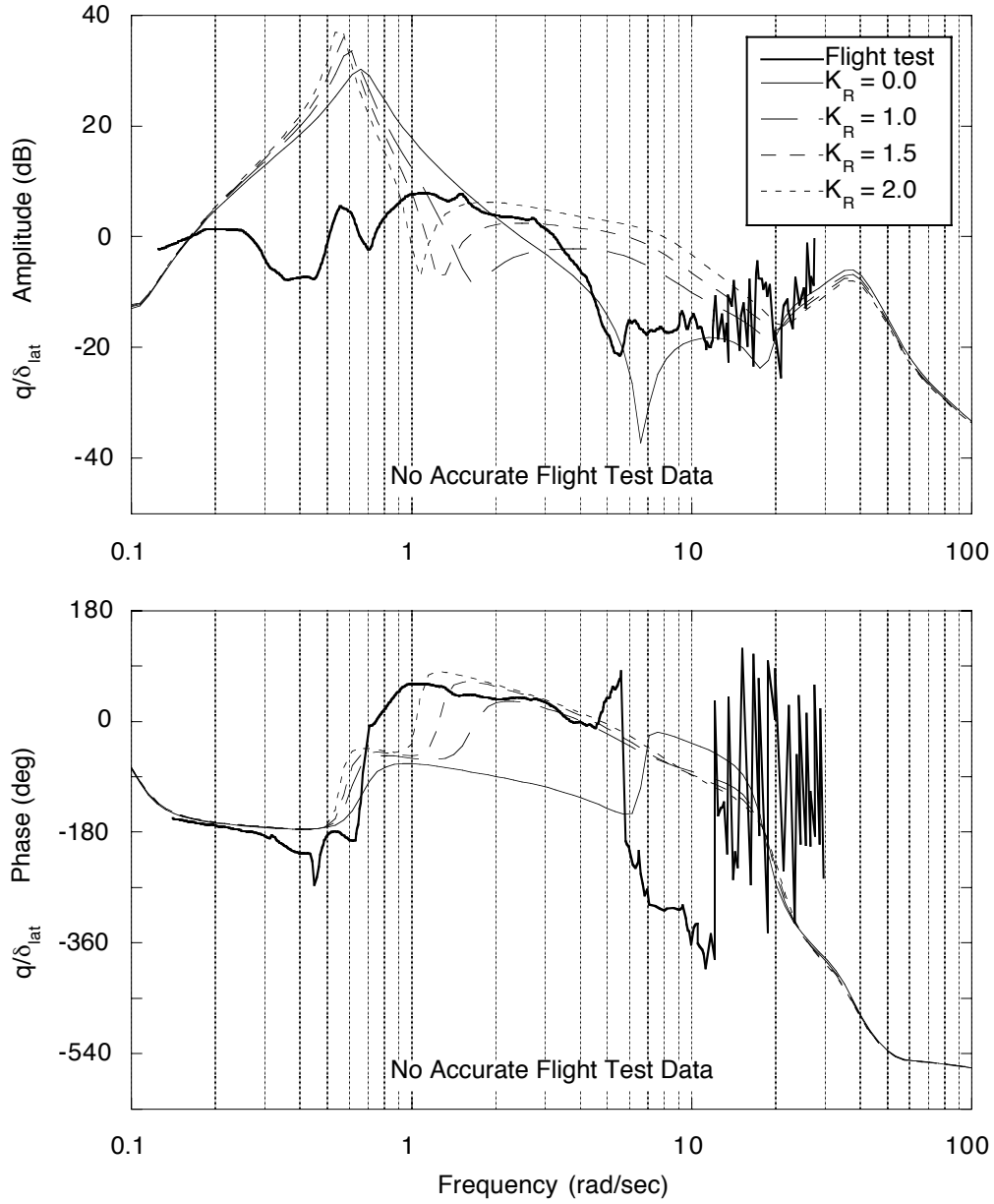

Figure 8.71: Effect of wake distortion parameter K_R within the extended momentum theory model on the off-axis pitch rate frequency response to a lateral stick input for the UH-60A in hover with the simple blade model.

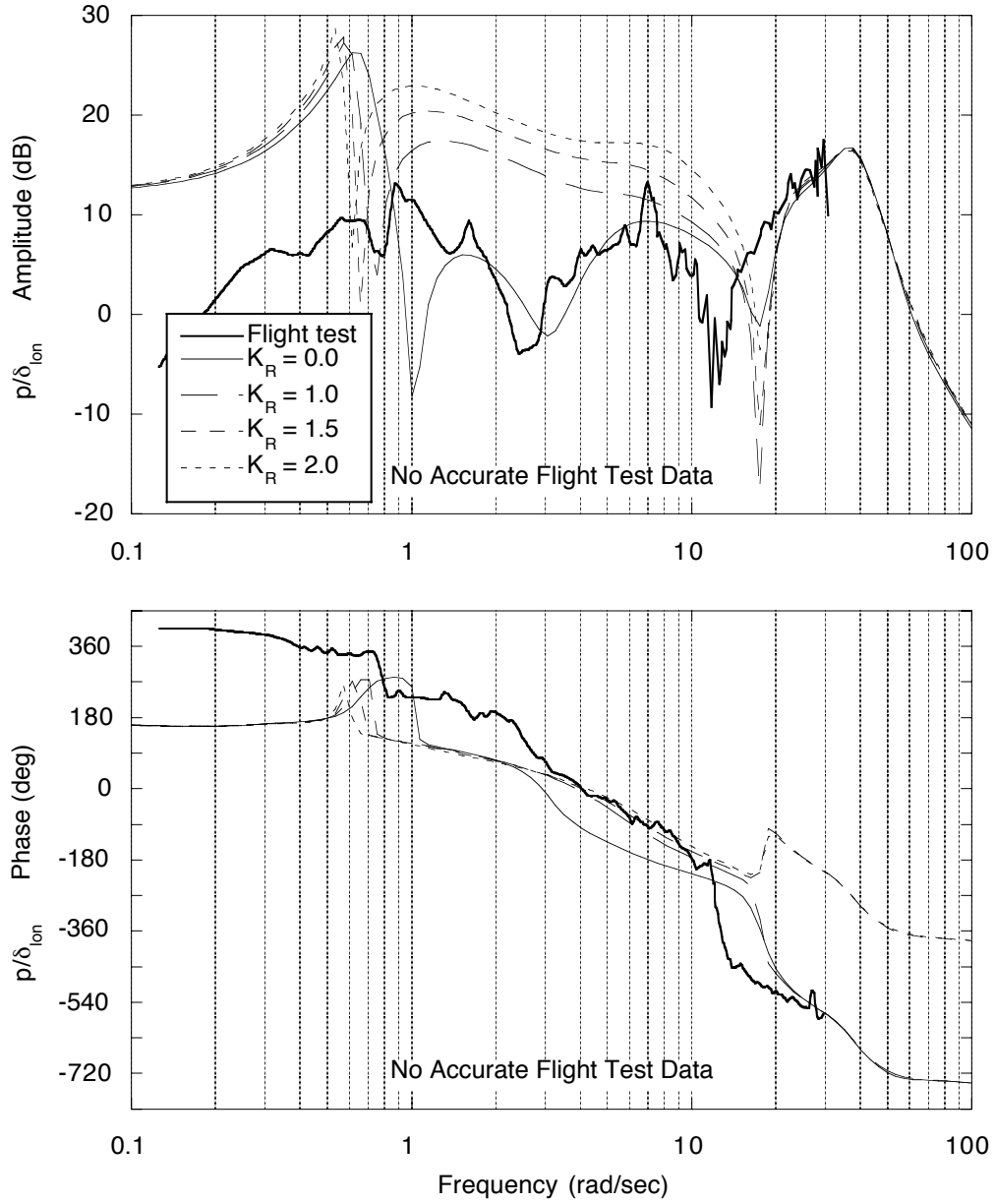

Figure 8.72: Effect of wake distortion parameter K_R within the extended momentum theory model on the off-axis roll rate frequency response to a longitudinal stick input for the UH-60A in hover with the simple blade model.

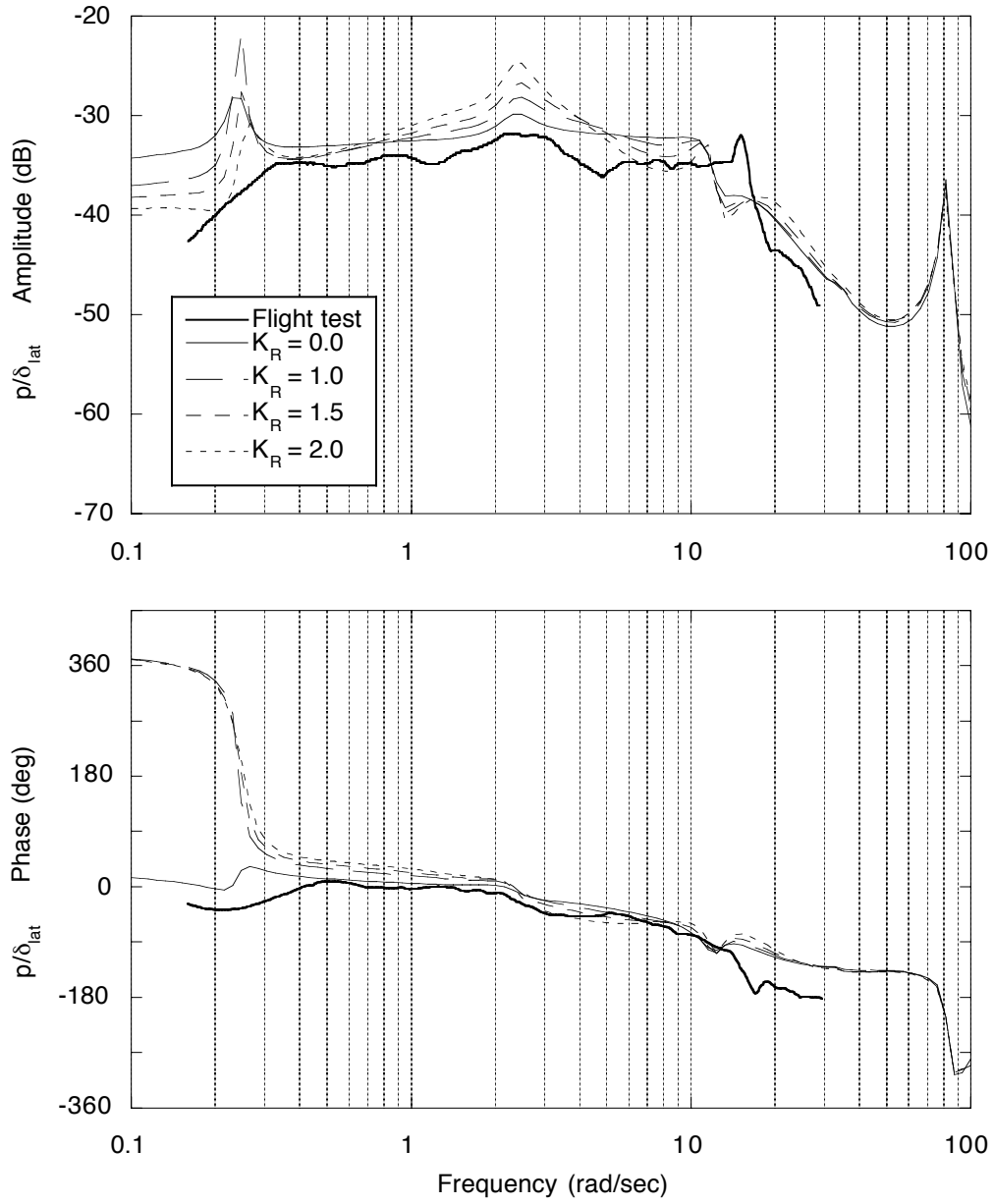

Figure 8.73: Effect of wake distortion parameter K_R within the extended momentum theory model on the on-axis roll rate frequency response to a lateral stick input for the BO-105 at 80 knots with the refined blade model.

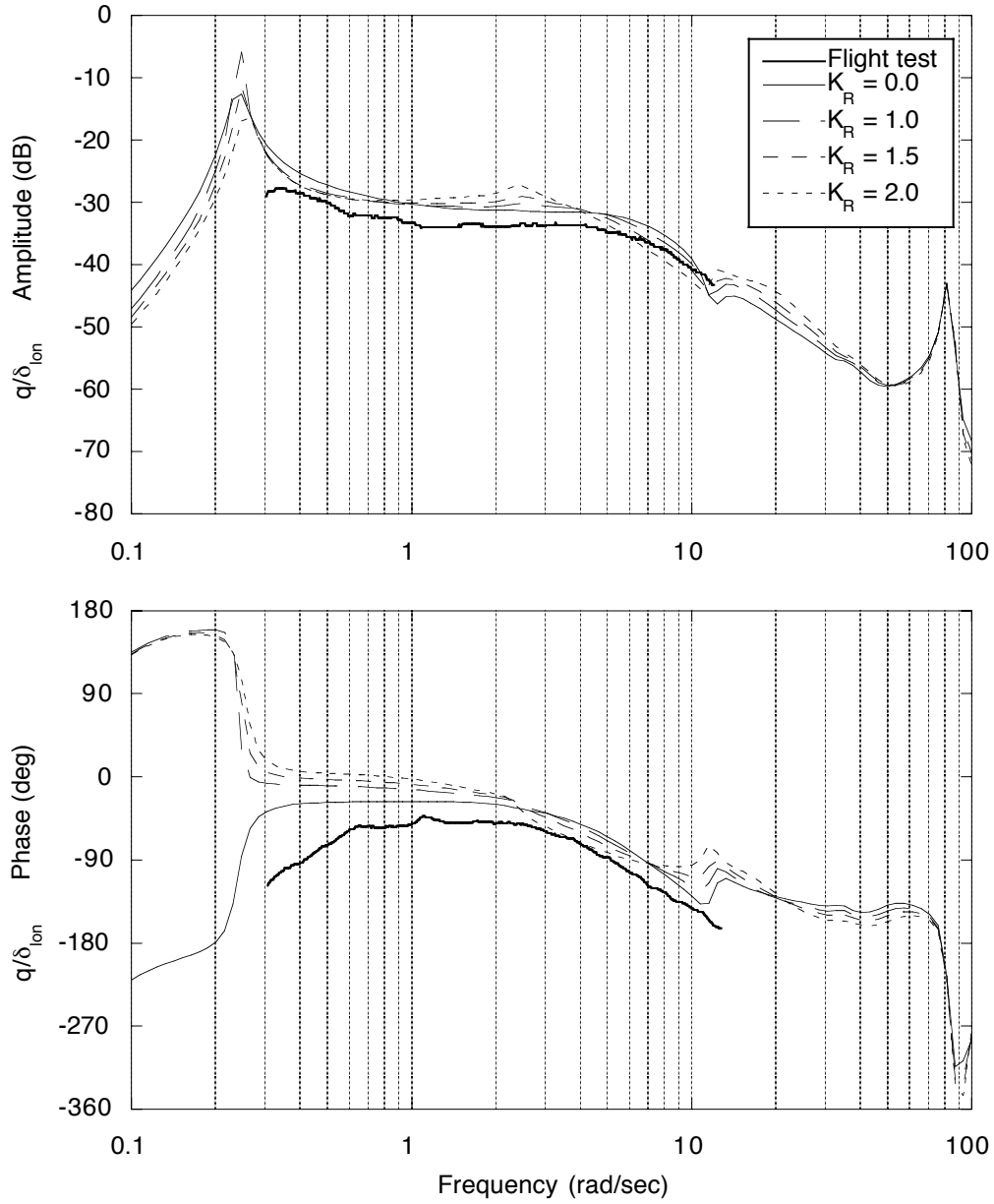

Figure 8.74: Effect of wake distortion parameter K_R within the extended momentum theory model on the on-axis pitch rate frequency response to a longitudinal stick input for the BO-105 at 80 knots with the refined blade model.

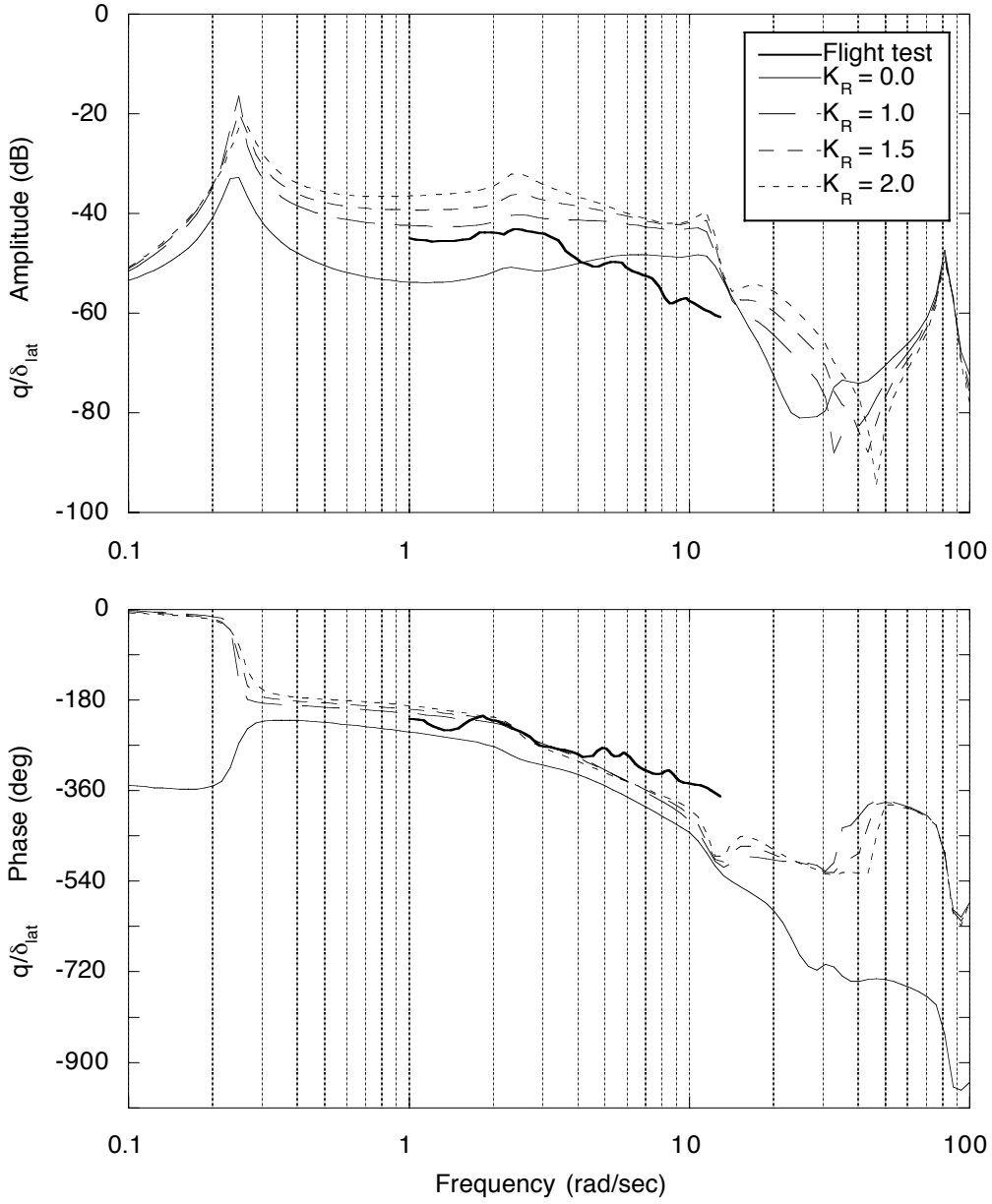

Figure 8.75: Effect of wake distortion parameter K_R within the extended momentum theory model on the off-axis pitch rate frequency response to a lateral stick input for the BO-105 at 80 knots with the refined blade model.

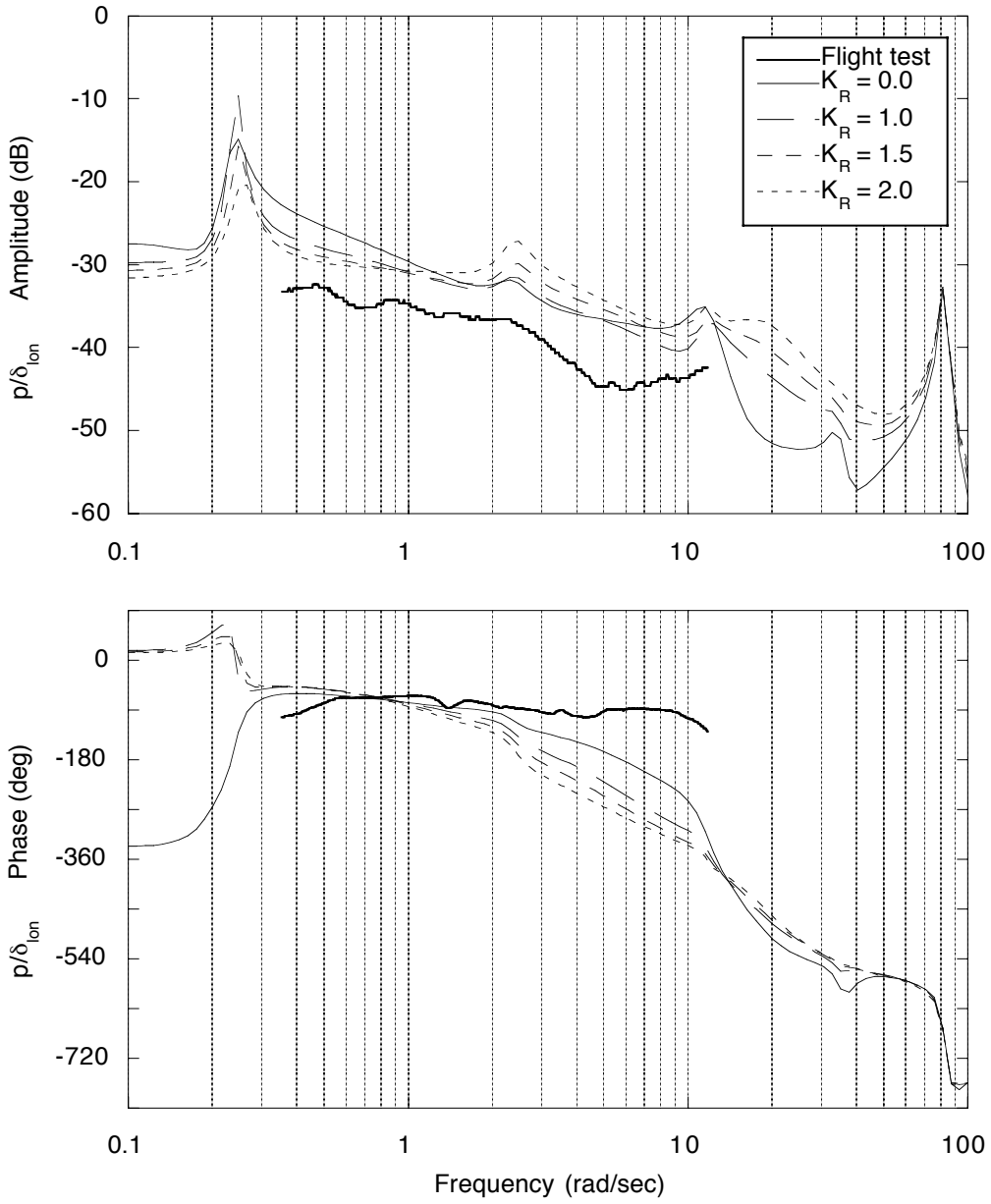

Figure 8.76: Effect of wake distortion parameter K_R within the extended momentum theory model on the off-axis roll rate frequency response to a longitudinal stick input for the BO-105 at 80 knots with the refined blade model.

Chapter 9

Time Integration Results

This chapter presents the dynamic response results calculated with the flight simulation model and includes comparisons with flight test data where such data is available. First, the stick fixed dynamic responses are considered; at a forward speed of 17 knots for the BO-105 and in hover for the UH-60A. Second, the dynamic response to lateral stick maneuvers for both BO-105 and UH-60A helicopters are considered and the simulation results are compared to flight test data. Special attention is given to the off-axis or cross-coupling predictions with the flight simulation model and the effects of inflow and blade modeling on the calculated dynamic responses.

9.1 BO-105 Stick Fixed Dynamic Response

This section presents the results of a simulation for the BO-105 helicopter with the controls held fixed at the calculated trim value. The trim condition is calculated in straight and level flight at a forward speed of 17 knots and an altitude of 250 feet. This flight condition is used for the stick fixed dynamic response because it is the same flight condition as the dynamic response to a lateral stick maneuver considered in Section 9.3. The purpose of the stick fixed simulation is to determine

the amount of drift from the trim conditions as a function of time. For a perfectly trimmed helicopter all the curves should either be straight lines or exactly periodic. The time history results are calculated with the dynamic inflow and free wake inflow models and with the two main rotor blade configurations as discussed previously.

Figures 9.1 and 9.2 show respectively the linear and angular accelerations at the center of gravity of the body as a function of time for the first 0.3 seconds of the time integration. This corresponds to about 2-1/4 rotor revolutions. These linear and angular accelerations are proportional to the resultant forces and moments at the center of mass of the helicopter. Both the simple and refined blade models are used, with the simple blade model results denoted by "1 mode" and the refined blade model results with "7 modes". These figures show the vibrational characteristics at the center of mass of the helicopter for each of the inflow and blade models. The magnitude of the accelerations predicted using the free wake inflow model are at least an order of magnitude higher than those predicted using a momentum theory based dynamic inflow model, and the highest periodic accelerations are predicted with the refined blade model.

Focusing on the linear accelerations, Figure 9.1 also shows that the magnitude of the vertical acceleration is higher than in the longitudinal and lateral directions. This is a result of the higher main rotor loads in the vertical direction. Figure 9.2 shows that the roll acceleration is higher than the pitch and yaw accelerations. This is because the roll inertia is lower than the pitch and yaw inertias. For the models that include the free wake, including coupled flap-lag-torsion dynamics (refined blade model), higher vibrations are predicted at the center of gravity than the simpler blade model with the fundamental flap mode only. The reason for this is that the higher harmonics of inflow with the free wake excites higher blade modes, which results in higher accelerations at the center of mass of the body.

The mathematical model of this study was not validated for vibratory load calculations. However, the general trends appear to be consistent with the results presented in Ref. [85], namely, that the predicted vibratory loads increase with the introduction of a free wake model, and with a more sophisticated flexible blade modeling.

From a flight dynamics point of view, it should be noted that the predictions of the model with the free wake are not exactly periodic. Therefore, the average linear and angular accelerations of the aircraft are not equal to zero, and a slow drift away from trimmed conditions should be expected. Figures 9.3 through 9.5 show such a drift for the linear and angular velocities and fuselage attitudes respectively. The calculations were performed for 45 rotor revolutions, corresponding to just over 6 seconds of simulation time. The results obtained using the dynamic inflow model are also shown in the figures. It is clearly seen that the linear and angular velocities and angular attitudes calculated with the free wake model slowly deviate from trim, whereas the results with the dynamic inflow model remain almost perfectly trimmed. These deviations are larger with the refined blade model. The roll rate p (Fig. 9.4) calculated with the free wake and refined blade model builds up to 2-3 degrees per second within the first few rotor revolutions. This is in part because of the higher angular accelerations in the roll direction with the free wake model and the refined blade model. All the other linear and angular velocities build up more slowly.

The results of Figures 9.3 through 9.5 indicate the starting point for the integration is not an exact trim condition. The algebraic trim procedure used in the present analysis is based on the same mathematical model as the free flight response simulation, and does enforce, among other conditions, force and moment equilibrium on average over one rotor revolution. Furthermore, the linear and angular velocities and the fuselage attitudes are assumed to be constant (the angular rates

are assumed to be zero for straight flight). This algebraic trim procedure does not, however, explicitly enforce periodicity of the states at the end of one revolution of time integration. Also, the time dependency of the blade motions is approximated in the trim calculations by a truncated Fourier series, whereas the free flight response calculations do not contain any such approximation. Therefore, there are small differences between the trim and the free flight response solutions with fixed controls, which result in the slow drift of the latter shown in Figures 9.3 through 9.5.

This is not significant when the dynamic inflow model is used, because the predicted accelerations are small. It only becomes an issue with the free wake model because of the higher predicted accelerations. An alternative to the algebraic trim is a periodic trim procedure that explicitly enforces periodicity. In a periodic trim condition, the helicopter returns to its original state after the equations of motion are integrated for each rotor revolution. This allows for the linear and angular velocities and fuselage attitudes to vary through the time integration as long as they return to their original values after each rotor revolution. This procedure was described in Ref. [77], where it was called "Phase II" trim, and it was used to refine the results of an algebraic trim procedure ("Phase I" trim) identical to that used in the present study. In Ref. [77] no benefits were observed, but the results referred to an articulated, rigid blade, and dynamic inflow was used. A periodic trim procedure may be more appropriate when a free wake inflow model, as well as blade flexible modes, is used.

There are two additional numerical issues that arise with the inclusion of the free wake model that are not seen using the baseline flight dynamics model with the dynamic inflow model. The first of these is related to the strategy of updating the inflow distribution when the free wake model is used. In this case, the inflow distribution is updated only at the start of each rotor revolution and is held fixed

for that particular rotor revolution. Therefore, any disturbances that occur within the rotor revolution have no effect on the inflow until the next rotor revolution. Furthermore the helicopter state at the start of each rotor revolution is used to calculate the inflow distribution, which leads to the assumption that, for the free wake model calculations, this helicopter state represents a steady-state condition at which a steady-state inflow is calculated. This is illustrated in Figure 9.6, which shows the angular velocities at the center of gravity of the body as a function of time for the first 0.3 seconds of time integration. The free wake model is evaluated at the trim condition to obtain the inflow distribution to start the calculation of the dynamic response. This inflow distribution is now fixed and used to integrate the equations of motion for one rotor revolution, or to about 0.14 seconds (shown in Fig. 9.6). At this point the helicopter state is assumed to be steady state for the purposes of re-evaluating the free wake model and producing a new inflow distribution. It is seen that at the start of the second rotor revolution the angular velocities are no longer zero, as in trim, and will effect the resulting inflow distribution.

The second numerical issue is related to the difference in the treatment of the main rotor inflow calculations between the trim and time integration phases of the simulation. As described in Section 3.2.2, a one-dimensional linear interpolation is required to convert the values of the inflow from the equidistant azimuthal locations used in the free wake model to the non-equidistant azimuthal locations used in the flight dynamics model trim calculations. However, during the time history calculations, no such interpolation is required because the azimuthal points used in the free wake and are the same as those used in the flight dynamics model. The result of this is that the inflow distribution resulting from trim and the inflow distribution used to start the numerical time integration will be slightly different as a direct result of the linear interpolation. This difference in inflow distributions

also contributes to the drift from the trim condition when the stick fixed dynamic response is considered.

9.2 UH-60A Stick Fixed Dynamic Response

This section presents the results of a simulation for the UH-60A helicopter with the controls held fixed at the calculated trim value. The trim condition is calculated in straight and level flight at a forward speed of 1 knot (representative of hover) and an altitude of 5250 feet. This flight condition is the same as that used for the dynamic response to a lateral stick maneuver as considered in Section 9.4. As with the BO-105 dynamic response, the purpose of the stick fixed simulation is to determine the amount of drift from the trim conditions as a function of time. The time history results are calculated with the dynamic inflow and free wake inflow models, and with the two main rotor blade configurations used for the UH-60A.

Figures 9.7 and 9.8 show the linear and angular accelerations at the center of gravity of the body as a function of time for the first 0.6 seconds of the time integration, which corresponds to about 2-1/2 rotor revolutions. These figures show the vibrational characteristics at the center of mass of the helicopter, and these linear and angular accelerations are proportional to the forces and moments at the center of mass. The figures show that the accelerations predicted using the free wake inflow model are of similar magnitudes to those predicted using a momentum based dynamic inflow model. However, while in each case the vibrations predicted with the dynamic inflow model are centered around zero, the vibrations predicted with the free wake model are either not centered at zero or drift away from this zero center within the first couple of rotor revolutions. As with the BO-105, including more modes in the modal coordinate transformation with the refined blade model

predicts higher vibrations at the center of gravity. It is also noted that these vibrational accelerations calculated for the UH-60A (Figs. 9.7 and 9.8) in the near hover flight condition are significantly lower than those of the BO-105 (Figs. 9.1 and 9.2). The lower vibrational accelerations with the UH-60A are in part a result of the lower cyclic variations in blade loading in hover as compared to forward flight. Also, the articulated hub of the UH-60A does not transfer blade flap and lag moments directly though to the center of mass of the body, where as the articulated hub of the BO-105 does transfer these flap and lag moments directly through to the hub. Therefore, the hub configuration is also important in looking at vibrational characteristics at the center of mass of the body.

Figures 9.9 through 9.11 show the linear and angular velocities and fuselage attitudes respectively for 45 rotor revolutions, corresponding to just over 10 seconds of simulation time. As with the BO-105 results, it is clearly seen in these figures that the linear and angular velocities and angular attitudes calculated with the free wake model slowly deviate from trim, whereas the results with the dynamic inflow model remain almost perfectly trimmed. The drift from trim is slower to develop for the UH-60A from the near hover flight condition than for the BO-105 at 17 knots of forward speed as a result of the lower vibrational accelerations associated with the UH-60A in near hover. The drift in trim for the dynamic response of the UH-60A in near hover and the numerical issues related to the calculation of the dynamic responses are the same as those for the BO-105, as described in Section 9.1.

9.3 BO-105 Lateral Maneuver Results

This section presents results of a free flight simulation, for a mostly lateral cyclic maneuver at 17 knots. Simulation results for the BO-105 are compared with flight

test data. The control deflections that define the maneuver are shown in Figure 9.12. The maneuver is part of a series of test flights carried out for system identification purposes [86]. The control excursions are relatively small, and the response of the helicopter is mostly in a linear range of the flight simulation model.

9.3.1 Effect of blade and inflow modeling

Figure 9.13 shows the roll and pitch rate predictions obtained using the dynamic inflow model with the simple and refined blade models. The dynamic inflow model is the Pitt-Peters three-state dynamic inflow model, as implemented in Ref. [7]. This model does not include maneuver-induced effects on the wake geometry and inflow, and therefore is representative of straight flight conditions only. These results show a typical trend already observed by other investigators, namely that the roll rate (on-axis) response is predicted accurately while the pitch rate (off-axis) response is predicted poorly. The off-axis response predictions are not improved with the refined blade model including 7 flexible blade modes. Figure 9.14 shows the fuselage pitch and roll attitude changes from trim calculated with the dynamic inflow model. The roll attitude (on-axis) change is predicted with a fair accuracy while the pitch attitude (off-axis) change is predicted with significantly less accuracy.

Figure 9.15 shows the roll and pitch rate predictions obtained using the maneuvering free wake model with both the simple and refined blade models. The results with the refined blade model show that the on-axis response p is accurately predicted. The off-axis response q is also predicted with reasonable accuracy. The agreement for the initial pitch acceleration, which is indicated by the slope of the pitch rate response for t of about 1.5 seconds, is excellent. The same is true for t of about 3 seconds, when the helicopter responds to the reversal of the lateral cyclic input. Before the application of the first lateral cyclic input, i.e., for $t \leq 1.5$

seconds, the predicted pitch rate response slowly drifts away from zero. This is a consequence of the trim methodology, as mentioned in Section 9.1.

The other curves in Figure 9.15 have been obtained using the simple blade model, that is, representing blade flexibility with just the first flap mode. The on-axis response p tends to be over-predicted, although it remains in phase with the lateral input. The off-axis response q, on the other hand, is predicted poorly. The initial nose-up motion is missed almost completely, and good agreement is recovered only after 3-4 seconds. Figure 9.16 shows the fuselage pitch and roll attitude changes from trim with the free wake model. With the refined blade model, both the roll attitude (on-axis) and pitch attitude (off-axis) changes are predicted accurately with the refined blade model and the free wake. With the simple blade model, the roll attitude change is over-predicted and the pitch attitude change is initially predicted in the opposite direction to the flight test results.

All of these results show a substantial improvement in the prediction of the pitch rate (off-axis) response with the free wake model when compared to the dynamic inflow model results, however this improvement is only observed when the refined blade model that includes coupled flap-lag-torsion dynamics of the rotor blades. The improvements are not seen with the simple blade model with only the fundamental blade flap mode. To examine the effect of the blade model on the simulation responses, the conditions for trim are first examined.

Figures 9.17 and 9.18 show the circulation distributions corresponding to trim ($t = 0$) at 17 knots with the simple blade model, and the dynamic inflow and free wake models respectively. With the dynamic inflow model (Figure 9.17) there is an almost linear distribution of circulation from the blade root to tip with the peak circulation values observed at the blade tips with a value between 100 and 150 ft^2/sec. With the free wake model (Figure 9.18) a similar linear distribution of

circulation from the blade root to tip is observed, although a slight bias towards the blade tips is observed. The variation in circulation along the length of the blades is higher with the free wake model than with dynamic inflow where the peak values of circulation with the free wake model are at the blade tips with values between 250 and 300 ft^2/sec.

Figures 9.19 and 9.20 show the change or perturbation in circulation with the inclusion of the additional blade flexibility associated with the refined blade. These contour plots are generated with dynamic inflow and the free wake model respectively. These circulation changes are generated by subtracting the baseline circulation distributions with the simple blade model from those generated with the refined blade model, and represent the change in bound circulation that is observed when including the additional blade flexibility associated with the refined blade model. With dynamic inflow, the effect of the inclusion of the additional blade flexibility (Figure 9.19) is to decrease the circulation in the tip region and to increase the circulation over the inner portion of the rotor disk. This redistribution of circulation is in part a result of the nose down elastic blade twist (about two degrees from the blade root to tip) associated with the refined blade model. This elastic twist therefore acts to move the mean bound circulation inboard and offloads the blade tips to a certain degree. A similar trend is seen in the free wake model results (Figure 9.19) where the tip region is somewhat off-loaded by moving the mean bound circulation inboard when the refined blade model is used. However, where the change with dynamic inflow was virtually independent of azimuth angle, the change with the free wake model increases the bound circulation over the inboard portions of the blade more on the advancing side than on the retreating side.

There are two effects that contribute to the change in the circulation distributions with the different blade models. The first is that the refined blade model includes

elastic twist of the blades where the simple model does not. This was mentioned earlier. The second is that the blade model effects the trim solution. It was shown in Figure 7.1 that there was about a two degree increase in the trim collective pitch required when the refined blade model was used, and this also effects the circulation distribution.

Figure 9.21 shows respectively the rear and side views of the wake geometries for the trim condition at 17 knots calculated with the simple and refined blade models. A small amount of wake roll-up becomes visible near the end of the wake on both the advancing and retreating sides of the disk even at this near hover flight condition of 17 knots. The two wake geometries are essentially the same except for a slight vertical offset. This offset is due to the higher blade tip flap displacements that are calculated with the refined blade model. Because the origin in the wake geometry plots is located at the rotor hub, the higher blade flap angles with the refined blade model are seen as a vertical displacement of the tip vortices.

Figure 9.22 shows the inflow distribution for trim at 17 knots with dynamic inflow and the refined blade model. This figure shows a linear distribution of inflow over the rotor disk with a mostly longitudinal variation. The lowest value of about 0.012 being near the front of the disk and the highest value of about 0.076 being near the rear of the disk. Even at this relatively low speed of 17 knots, there is a significant longitudinal variation of inflow from the front to the rear of the disk, with the lowest value at the front of the disk being about one-sixth the magnitude of the peak value at the rear.

Figure 9.23 shows the inflow distribution for trim at 17 knots with the free wake and refined blade models. This figure shows that the inflow over much of the disk (except for a region at the front) is between 0.08 and 0.12, which is significantly higher than that predicted with dynamic inflow. The inflow over the front of the

disk drops sharply and a small upwash is observed at the blade tips from azimuth angles of about 100 to 260 degrees. This upwash is observed only at the very tip of the blades and is a result of the blow back of the wake at this speed, as shown in Figure 9.21.

The differences in the simulation results with varying blade and inflow models start just after the lateral stick is first applied at about 1.5 seconds. By $t = 1.7$ seconds, the maximum roll rate (on-axis) response is reached and differences in the pitch rate (off-axis) responses are visible. The point between the 12th and 13th rotor revolutions, or about 1.7 seconds, is examined further to determine the source of the differences in the off-axis response.

Figure 9.24 shows the change in the inflow distribution from the trim condition at 17 knots to the start of the 13th rotor revolution as calculated with the dynamic inflow model. This inflow change is calculated by subtracting the inflow at the trim condition from the inflow at the start of the 13th rotor revolution of time integration. This figure shows a mostly longitudinal change in the inflow which produces a mostly longitudinal change in the lift distribution over the rotor disk. Because the response of the rotor lags the lift change by slightly under 90 degrees, this longitudinal change in lift results in a lateral change in the rotor response which contributes to a lateral response of the helicopter. This helps to explain the poor off-axis response predictions with the dynamic inflow model that does not include maneuver-induced effects, which is because the inflow changes contribute to the lateral response and not to the longitudinal response of the helicopter.

Figure 9.25 shows the rear and side views of the actual wake geometries at the 1st and 13th rotor revolutions predicted with the free wake model. The refined blade model is used for the generation of these results. At the 13th rotor revolution, the roll rate is about 11 deg/sec and the pitch rate is about -2 deg/sec. Looking at the

view of the wake geometry from the rear, a slight elongation of the vortex wake on the retreating side is visible that is a result of the pitch and roll rates at this point in the maneuver. There is also a smaller contraction of the wake on the advancing side.

Figure 9.26 shows the difference in inflow generated with these two wake geometries, with the inflow from the wake at $t = 0$ used as the baseline. This inflow change is calculated by subtracting the inflow at $t = 0$ from the inflow at the start of the 13th rotor revolution. Looking at the retreating side, the stretching of the vortex wake resulting from the pitch and roll rates moves the vortex filaments further from the rotor disk, which in turn lowers the inflow in this region. This inflow change is clearly visible in Figure 9.26. The decrease in inflow increases the lift in this region. Conversely, on the advancing side the effect of the pitch and roll rates is a contraction of the vortex wake, which moves the vortex filaments closer to the rotor and produces an increase in the inflow. This increase in inflow decreases the lift on the advancing side. Because the response of the rotor lags the lift change by slightly under 90 degrees, the decrease in lift on the advancing side causes the rotor to flap down at the front, and the increase in lift on the retreating side causes the rotor to flap up at the rear. This change in flapping causes a nose down tilt of the rotor disk and a corresponding nose down pitching moment. This lateral change in inflow, which causes a longitudinal change in blade response, was not seen with the dynamic inflow model and helps to explain the more accurate prediction of the off-axis response generated with the free wake and refined blade models.

Figure 9.27 shows the change in inflow from trim at $t = 0$ to the 13th rotor revolution made using the simple blade model. This figure shows an increase in inflow on the advancing side and a decrease in inflow on the retreating side, which is similar to the inflow changes seen in Figure 9.26 with the refined blade model. With

the simple blade model, the inflow changes required to improve the prediction of off-axis response are present, but the improvements in the off-axis response are not seen. Therefore, this suggests that the prediction of the off-axis dynamic response to pilot inputs is a truly aeroelastic problem, which requires both a free wake model that includes wake distortions resulting from maneuvers and flexible blade models that include coupled flap, lag and torsional degrees of freedom.

9.3.2 Effect of wake resolution

The wake resolution is composed of two free wake parameters. These are the vortex filament discretization resolution $\Delta\zeta$, and the azimuthal discretization resolution $\Delta\psi$ (see Section 2.9). For this study these have the same value and are collectively referred to as the wake resolution. For the free wake results shown in Figure 9.15 the wake resolution $\Delta\psi$ is 5 degrees and the total length of each filament is 720 degrees. Figure 9.28 shows the effect of reducing the free wake resolution, i.e., increasing $\Delta\psi$, on the accuracy of the prediction of roll and pitch rate responses. The results shown in Figure 9.28 are generated with wake resolutions of $\Delta\psi = 5^o$, as in Figure 9.15, and $\Delta\psi = 10^o$. The refined, 7-mode blade model is used for both cases. It is seen that the roll rate p is predicted well using both vortex wake resolutions, with the finer resolution providing a slightly better accuracy. For the pitch rate q predictions, the coarser discretization still gives reasonably good results, but the finer discretization is noticeably more accurate. These results indicate that the accurate prediction of dynamic responses to pilot inputs requires, amongst other things, a careful selection of the free wake resolution from both computational and accuracy points of view.

9.3.3 Effect of maneuver-induced wake distortions

The Bagai-Leishman free wake model used in this study is capable of capturing the changes in wake geometry caused by the maneuver [13]. Figure 9.29 attempts to separate the effects of these maneuver-induced wake geometry changes on the pitch and roll rate predictions. The refined, 7-mode blade model is used. Wake resolution and maximum wake age are the same as in Figure 9.15, that is, $\Delta\psi = 5^o$ and the total length of each filament is 720 degrees. The "Free wake (zero rates)" legend indicates the results obtained by arbitrarily setting to zero the roll and pitch rates provided to the free wake as inputs; although not completely rigorous, this effectively removes the maneuvering effects from the free wake model. These roll and pitch rates are set to zero only for the calculation of the free wake geometry and in all the other portions of the model p and q retain their correct value. The results show that the roll rate response p is not significantly affected. On the other hand, there is some worsening of the off-axis correlation, and the magnitude of the pitch response tends to be under-predicted. Therefore, the changes in wake geometry from the maneuver need to be taken into account for a good prediction of the off-axis response, although they do not appear to be important for the on-axis predictions.

To try to determine where these differences in the pitch rate response p come from, the results corresponding to the start of the 13th rotor revolution were examined. Recall that in the simulation of a given rotor revolution, the wake geometry and associated inflow is that obtained at the end of the previous rotor revolution and is held fixed through the current rotor revolution. Therefore the point at the end of the 12th rotor revolution is marked on the plots in Figure 9.29. This is the time at which differences in the pitch rate response q start to become visible and is also close to the time at which the highest value of the roll rate p, following the

initial lateral cyclic control input, is reached. The inclusion of maneuvering effects on the free wake geometry should be most visible at this time.

Figure 9.30 shows respectively a rear and side view of the wake geometries during the 13th rotor revolution of the maneuver. The roll and pitch rates are about 9 deg/sec and 3 deg/sec respectively. The thin dashed lines in these figures shows the geometry of the wake with the maneuvering effects removed by setting $p = q = 0$ for the free wake calculations. The thick solid lines show the geometry of the wake with the free wake maneuvering effects correctly modeled. The geometries of the two wakes are very similar. Although there is a small contraction of the wake on the advancing side, that is, the vortices are closer together, and elongation on the retreating side resulting from the inclusion of the positive (advancing side down) roll rate on the wake geometry. This similarity of the wake geometries with and without maneuvering effects is not surprising considering that the values of the roll and pitch rates are themselves quite small. However, the differences in the pitch rate response (Fig. 9.29) with and without the maneuvering effects show that even this small difference in the wake geometries can have a noticeable effect on the off-axis response prediction.

Figure 9.31 shows the "perturbation" in inflow from the wake geometry changes resulting from the inclusion of maneuvering effects. This perturbation is defined as the inflow distribution generated with the maneuvering effects included minus the inflow distribution that does not include those effects. This essentially isolates the effects of maneuver-induced changes in wake geometry on the inflow distribution. However, it should be pointed out that, because p and q are set to zero only for the calculation of the wake distortions resulting from the maneuver and nowhere else, the changes in inflow resulting from the kinematics of the maneuver are still retained in both cases; for example, in both cases a nose-up pitching motion will

generate a downwash on the front of the disk, and an upwash on the rear.

The inflow perturbation just defined, and shown in Figure 9.31, essentially corresponds to an additional downwash on the advancing side and an additional upwash on the retreating side. This translates into lower angles of attack, lower lift, and lower flapping moments on the advancing side; with the reverse being true on the retreating side. Because of the delay in the flapping response of the rotor, this in turn translates into an increase in longitudinal flapping (tip path plane tilting down over the nose), and helps explain the stronger nose down pitch rate achieved at this point in the time history calculations with the maneuver-induced wake distortions included (see Figure 9.29).

9.3.4 Effect of inflow dynamics

This section examines the effects of inflow dynamics or unsteadiness on the roll and pitch rate responses to mostly a lateral maneuver for the BO-105 at 17 knots. The dynamic inflow model is used with varying levels of wake unsteadiness. The inflow equation takes the form

$$k[M]\dot{\lambda} + [K]\lambda = \mathbf{C} \tag{9.1}$$

where $k = 1$ gives the correct inflow dynamics as in the Pitt-Peters dynamic inflow model. For values of k less than 1, the dynamic effects are reduced and the inflow changes more quickly than with $k = 1$. For very small values of k, the dynamic effects are effectively removed, and the inflow model becomes quasi-steady. For values of k greater than 1, the dynamic effects are enhanced by effectively increasing the fluid inertia. The result of the enhanced dynamics is that the inflow changes more slowly with time. For the case with very large k, the inflow would effectively be constant and invariant with time. While this procedure is not rigorous, it does show the effects of changing the inflow dynamics or unsteadiness on the predicted responses.

Figure 9.32 shows the effect of inflow dynamics on the prediction of the roll and pitch rate responses to the mostly lateral stick maneuver. The refined blade model is used for all of the predictions. With dynamic inflow, the "Baseline" refers to the results with $k = 1$, "Dynamics reduced" refers to the results with $k < 1$, and "Dynamics enhanced" refers to the results with $k > 1$. This figure shows that the on-axis response is significantly over-predicted when the dynamics or unsteadiness associated with inflow are reduced. This over-prediction of the on-axis response with reduced inflow dynamics also leads to some changes in the pitch rate prediction.

9.3.5 Comparison with Keller's extended momentum theory

The other inflow model that is investigated in this study is an "extended momentum theory" model, proposed by Keller [15], which includes additional inflow terms proportional to pitch and roll rates (see Section 2.7). This model is characterized by a wake distortion parameter K_R that is determined based on a simplified vortex wake analysis (or may be identified from flight test data). The value proposed by Keller for hover was 1.5. Other studies have determined different values for this parameter, from 0.75 to 1.75 [63], with the specific values depending on the theory used. Figure 9.33 compares results obtained using various values of the wake distortion parameter K_R with results obtained with the dynamic inflow model and with flight test data. The dynamic inflow results can be considered as the case $K_R = 0$. The 7-mode, refined blade model was used. The modification to the dynamic inflow model proposed by Keller is strictly only valid in the hover flight condition; here it is used in a near hover flight condition, i.e., 17 knots. Figure 9.33 shows that the on-axis roll rate response p is not significantly changed with the inclusion of the wake distortion effects. On the other hand, the off-axis correlation is noticeably improved

with the addition of the wake distortion effects. The best overall correlation with test data seems to occur when using $K_R = 1.5$.

Figure 9.34 shows the change in the inflow distribution from the trim condition to the point at the start of the 13th rotor revolution. The extended momentum theory with $K_R = 1.5$ and the refined blade models are used. This inflow change is calculated by subtracting the trim inflow from the inflow at the start of the 13th rotor revolution. Recall that a similar inflow change with the dynamic inflow model that does not include maneuver-induced effects (Fig. 9.24) showed a mostly longitudinal change in the inflow, which contributes mostly to the lateral response of the helicopter. Using the extended momentum theory and $K_R = 1.5$, the linear inflow change (Fig. 9.34) is both in the longitudinal and lateral directions. Focusing on the lateral change in inflow, this figure shows an increase in inflow on the advancing side and a decrease in inflow on the retreating side. This translates into a nose-down, or negative, pitching moment. This explains the improvement in the prediction of the initial off-axis response to the lateral maneuver.

Finally, Figure 9.35 compares the results obtained with the maneuvering free wake model and with the extended dynamic inflow and $K_R = 1.5$. Both results are generated with the 7-mode refined blade model. The on-axis roll rate response is predicted with good accuracy with both inflow models. Yet the free wake model predicts the off-axis pitch rate response more accurately. Keller's model, as a linear inflow model, cannot be used for the prediction of vibratory loads, however, it does capture the main features of the off-axis response, and is computationally far more efficient than the free wake model. Therefore, for typical flight dynamic simulations, using an extended dynamic inflow model such as Keller's, with the K_R constant calibrated using a more accurate maneuvering free wake model, appears to be the most cost-effective strategy.

9.4 UH-60A - Lateral Maneuver

This section presents results of a free flight simulation, for a mostly lateral stick maneuver for the UH-60A in hover at an altitude of 5250 feet. The simulation results for the UH-60A are compared with flight test data. The control deflections that define the maneuver are shown in Figure 9.36. The control deflections for this maneuver are relatively small to ensure that the response of the helicopter is mostly in the linear range of the flight simulation model.

9.4.1 Effect of inflow and blade modeling

Figure 9.37 shows the roll and pitch rate predictions obtained using the dynamic inflow model with the simple and refined blade models. The dynamic inflow model is the Pitt-Peters model, which does not include maneuver-induced effects on the wake geometry and inflow, and so is only representative of straight flight and level conditions. These results are typical of those with dynamic inflow modeling, where the roll rate (on-axis) response is predicted with good accuracy but the pitch rate (off-axis) response is predicted poorly. With respect to blade modeling, the results here for the UH-60A show a similar trend to those of trim and linearization where the predictions are fairly insensitive to blade modeling.

It is worth pointing out that the off-axis response predictions seem to initially start in the correct direction before moving in the opposite direction to the flight test data. However, this occurs in the region essentially before the lateral control is first applied (Figure 9.37). The small negative pitch rate that builds up in the first 0.8 seconds results from the small amount of negative or forward longitudinal stick over this time.

Focusing on the flight test data shown in Figure 9.37, the roll rate response

to the mostly lateral stick input is relatively small with a peak value less than 10 deg/sec. Also, the off-axis or pitch rate response is less than 2 deg/sec. for the entire 4 seconds of the time history. For responses of such small magnitudes, effects such as rotor-fuselage aerodynamic interactions (which are not modeled here) may affect significantly the actual responses. Because the off-axis response is small, it may be somewhat difficult to obtain good correlations.

Figure 9.38 shows the roll and pitch rate responses obtained using the maneuvering free wake model, and with both the simple and refined blade models. These results are generated with a vortex wake resolution $\Delta\psi$ of 10°, the total length of each vortex filament ζ_{max} is 720°, and the initial tip vortex strength is equal to the maximum bound circulation along the blade ($C_\Gamma = 1.0$). Both the pitch and roll rate responses are found to be independent of blade modeling, although the drift in the pitch rate response is higher with the refined blade model than with the simple blade model. This is a result of the higher vibrational accelerations associated with the refined blade model. The on-axis response is over-predicted and the off-axis response is predicted poorly.

The over-prediction of the roll rate has a significant effect on the pitch rate predictions and contributes to the lack of accuracy of the pitch rate predictions. However, there appears to be no improvement in the initial pitch rate response to the lateral control using the maneuvering free wake model even before the roll rate is over-predicted.

There are some possible explanations for this over-prediction of the on-axis response and the lack of accuracy in the off-axis response predictions. First, the coupling between the longitudinal and lateral motions for the UH-60A is not being correctly captured with the free wake model during the lateral maneuver.

Second there is a lack of inflow dynamics or unsteadiness associated with the

free wake model. It was shown that the off-axis frequency response predictions were not improved with the free wake model that includes maneuver-induced effects but not inflow dynamics or unsteadiness. However, improvements were seen with the extended momentum theory inflow model that includes wake distortion effects.

The third explanation is related to the blade modeling. For the current study the UH-60A rotor is modeled with straight blades that have no sweep in the tip region. This limits the coupling between the pitch and flap degrees of freedom in the simulation model, which may be important for the correct prediction of the dynamic responses. For the BO-105, it was shown that the inclusion of the torsional degrees of freedom with the refined blade model significantly reduced the over-prediction of the on-axis response and led to similar improvements in the off-axis response predictions.

Each of these possible explanations for the lack of accuracy of the prediction of the UH-60A dynamic responses is now treated in turn in the next three sections.

9.4.2 Effect of free wake modeling

This section examines the effects of the free wake resolution and the maneuver-induced wake distortions as possible sources for the lack of accuracy in the prediction of the off-axis responses. For the free wake results shown in Figure 9.38 the wake resolution $\Delta\psi$ is 10° and the total length of each vortex filament ζ_{max} is 720°. Figure 9.39 shows the effect of increasing the wake resolution, i.e., decreasing $\Delta\psi$, on the accuracy of the prediction of the roll and pitch rate responses. In comparing the results generated with a wake resolution of 5° and those with $\Delta\psi = 10°$, it is seen that the roll rate is over-predicted with both wake resolutions. For the pitch rate predictions, there is also no effect of wake resolution on the predicted responses. Although for the case with the courser wake and the refined blade model, the free

wake model fails to converge after about 1.6 seconds of simulation time.

The other effect that is investigated in this section is whether the coupling between the longitudinal and lateral motions resulting from the wake distortion effects on the inflow distribution is being accurately captured. To determine if the maneuver effects are being accurately captured, the results corresponding to the 7th rotor revolution are examined. Recall that in the simulation of a given rotor revolution, the wake geometry and associated inflow is that obtained at the end of the previous rotor revolution and is held fixed through the current rotor revolution. The point at the start of the 7th rotor revolution, t=1.39 sec., is close to the point of the maximum roll rate response and the effect of the maneuver induced wake distortions on the inflow should be apparent. Figure 9.40 shows the change in the inflow from the start of the maneuver, at t=0 sec., to the start of the 7th rotor revolution, at t=1.39 sec. This inflow change is calculated by taking the inflow at t=1.39 sec. and subtracting the inflow at t=0. The results show a general increase in inflow on the advancing or starboard side of the rotor and a general decrease in inflow on the retreating or port side. This translates into a lateral change in the lift distribution, which causes a nose down longitudinal tilt of the rotor disk resulting from the inflow change. This is in the correct direction to improve the off-axis response predictions, but such improvements are not seen in the present results.

In conclusion, the results presented in this section indicate that the correct effects of maneuver-induced wake distortions are being captured by the free wake model, yet these do not translate into significant improvements in the off-axis response predictions.

9.4.3 Effect of inflow dynamics

This section examines the effects of inflow unsteadiness on the roll and pitch rate responses to mostly a lateral maneuver for the UH-60A in hover. The dynamic inflow model is used with varying levels of wake dynamics with various values of k in Eqn. (9.1), as described in Section 9.3.4.

Figure 9.41 shows the effect of inflow dynamics on the prediction of the roll and pitch rate responses to the mostly lateral stick maneuver for the UH-60A in hover. The simple blade model is used because the predictions with both the dynamic inflow and free wake models were found to be fairly insensitive to blade modeling. With dynamic inflow, the "Baseline" refers to the results with $k = 1$, "Dynamics reduced" refers to the results with $k < 1$, and "Dynamics enhanced" refers to the results with $k > 1$. This clearly shows that the on-axis response is significantly over-predicted when the dynamics associated with inflow are reduced. This over-prediction of the on-axis response with reduced inflow dynamics leads to higher positive pitch rate predictions from about t=2 sec. Even though the over-prediction of the roll rate with reduced inflow dynamics is not as large as that with the free wake model, these results do suggest that the lack of inflow dynamics contributes to the over-prediction of the roll rate response with the free wake model. The over-prediction of the roll rate response also leads to inaccuracies in the off-axis pitch rate responses. For the UH-60A, improvements in the off-axis response predictions first require accurate on-axis response predictions and this seems to require the inclusion of inflow dynamics.

9.4.4 Effect of tip sweep

This section examines the effect of including a swept tip to the modeling of the UH-60A rotor blades on the dynamic response. The current rotor blade model does

not have the capability of accurately modeling the swept tip region. For the results presented in this section the swept tip region is implemented as an offset of the center of gravity location from the elastic axis of the straight blade. This is not a rigorous method for the inclusion of a swept tip with the current inertial model, and leads to an inaccurate prediction of the inertial loads in the lag direction. This has implications for the lag dynamics of the blade, along with the torque and power calculations. So that this does not become an issue with the swept tip included, only the flap and torsional degrees of freedom are included.

For the UH-60A in hover, Figure 9.42 shows the roll and pitch rate responses to the mostly lateral maneuver. The curve denoted with the "Dyn. inflow - 2 modes" legend is generated with dynamic inflow and the simple blade model that includes only the rigid flap and lag modes with no tip sweep. The curve denoted with the "Free wake - 2 modes" legend again uses the simple blade model with no tip sweep but inflow is modeled using the free wake. The final curve denoted with the "Free wake - Swept tip" legend uses the free wake inflow model and a blade model that includes the rigid and first elastic flap modes and the first elastic torsion mode, and also includes a swept tip. For the on-axis roll rate response, there is essentially no effect of the inclusion of the swept tip with the free wake, and the on-axis response is still over-predicted. For the off-axis response, there are improvements to be found with the addition of the tip sweep. This improvement is apparent from t=0.9 sec. where the control is first applied, and the off-axis response shows the same trend as the flight test data until about t=1.4 sec. At this point the over-prediction of the on-axis response significantly affects the off-axis response.

The results of this section showed that the inclusion of the swept tip with the free wake model leads to the accurate prediction of the initial off-axis response direction. However, the over-prediction of the on-axis response with the straight

(unswept) blade is not improved with the swept tip. This over-prediction of the on-axis response ultimately leads to the off-axis response being predicted inaccurately. The results found here agree with those of the BO-105 (Section 9.3) where the inclusion of additional blade modes (particularly torsion) was critical for the accurate prediction of the off-axis response.

9.4.5 Comparison with Keller's extended momentum theory

This section examines the effects of the extended momentum theory on the dynamic response predictions for the UH-60A. This inflow model includes maneuver-induced wake distortions through the wake distortion parameter K_R and also retains inflow dynamics. Figure 9.43 compares the results with flight test data obtained using K_R values of 0 and 1.5 and the simple and refined blade models. Notice that the blade model does not effect either the on-axis or off-axis responses. The inclusion of the wake distortion effects leads to some small changes in the on-axis response, but more significantly, shows that the off-axis response is predicted in the correct direction, as least initially. The improvements are seen from t=1.1 sec., where the roll rate has built up sufficiently to effect the inflow and lead to improvements in pitch rate predictions, to t=1.6 sec., where the predictions and test data start to diverge.

The results presented in this section showed that improvements in the off-axis response predictions can be achieved using an extended momentum theory inflow model that includes maneuver induced wake distortions. In addition, these improvements can also be achieved using a relatively unsophisticated blade model that includes only the rigid flap and lag modes.

9.5 Discussion of time integration results

This section contains a discussion of the time integration results presented in this chapter for the responses to stick-fixed simulations and to lateral control maneuvers for the BO-105 and UH-60A helicopters.

The results for the stick-fixed simulations showed that it was possible to obtain realistic values of the vibratory loads through the incorporation of the maneuvering free wake model, although no validation of the vibratory loads prediction was carried out. These stick-fixed responses also showed a slow drift away from the trim condition as the simulation proceeded. This indicated that the trim calculations must be carried out much more accurately when using a free wake model, rather than when a dynamic inflow type model is used. The algebraic trim procedure used in the current study enforces, among other things, force and moment equilibrium where the average forces and moments over a single rotor revolution are zero, but does not explicitly enforce periodicity. This is not significant with a dynamic inflow type model but becomes an issue with the free wake model because of the higher acceleration predictions. A shooting type procedure that explicitly enforces periodicity may prove to be necessary for the calculation of the trim condition when using the free wake inflow model.

For the BO-105, the free flight on-axis responses to pilot pitch and roll inputs can be predicted with good accuracy with a relatively unsophisticated model. Here neither the refined blade model not the free wake model are required. It is also possible to predict the off-axis responses from first principles, that is, without empirically derived correction factors and without assumptions about the wake geometry. This, however, requires sophisticated modeling with both a refined flexible blade model and a free wake model that includes the wake distortions caused by the maneuvers.

The BO-105 results also confirmed that the free wake model used is this study can be effectively used for the prediction of free-flight dynamic response even though the free wake model is only rigorously valid for steady, trimmed conditions. Most of the features of the off-axis response can be captured using a dynamic inflow theory extended to account for maneuver-induced wake distortions, and for a fraction of the cost of using a free wake model. Probably the most cost-effective strategy for the BO-105 response predictions (if vibratory loads are not required) is to calibrate such an inflow theory using the more accurate free wake based model, and use the inflow theory in all of the calculations.

For the UH-60A, the conclusions are somewhat different. The on-axis responses to pilot inputs can be predicted accurately with a traditional dynamic inflow model but are significantly over-predicted with the free wake model. In addition, the off-axis response predictions were not improved with the maneuvering free wake model regardless of the blade model. A contributing factor to this is the over-prediction of the on-axis response, however the off-axis responses to the initial lateral control is in the incorrect direction, even before the on-axis response is over-predicted.

An investigation into the effects of inflow dynamics on the predicted on-axis response seem to suggest that the over-prediction of the on-axis response with the free wake model is partially a result to the lack of inflow dynamics associated with the free wake. The inflow dynamics, however, did not seem to directly effect the off-axis response predictions. The effects were indirect and related to the over-prediction of the on-axis response. An investigation of the inflow distribution produced by the maneuvering free wake model showed that the inflow changes required to improve the prediction of the off-axis response were present. However, these maneuver-induced inflow changes did not lead to improvements in the off-axis response predictions. A third investigation was carried out for the UH-60A that examined the effect on the

off-axis response of including a swept tip. Although not implemented rigorously, the inclusion of the tip sweep did not reduce the over-prediction of the on-axis response when using the free wake model. However, improvements in the initial off-axis response predictions to the pilot control inputs were seen with the accurate qualitative and quantitative predictions. A short time after the initial control input, the predictions become less satisfactory because of the over-prediction of the on-axis response.

The accurate prediction of the on-axis response to pilot control inputs for the UH-60A seems to be highly dependent on the modeling of inflow dynamics. The off-axis response seems to be less dependent on the inflow dynamics and more on the blade modeling where the modeling of the swept tip is required. Here the flap-torsion coupling introduced by the swept tip appears to be critical.

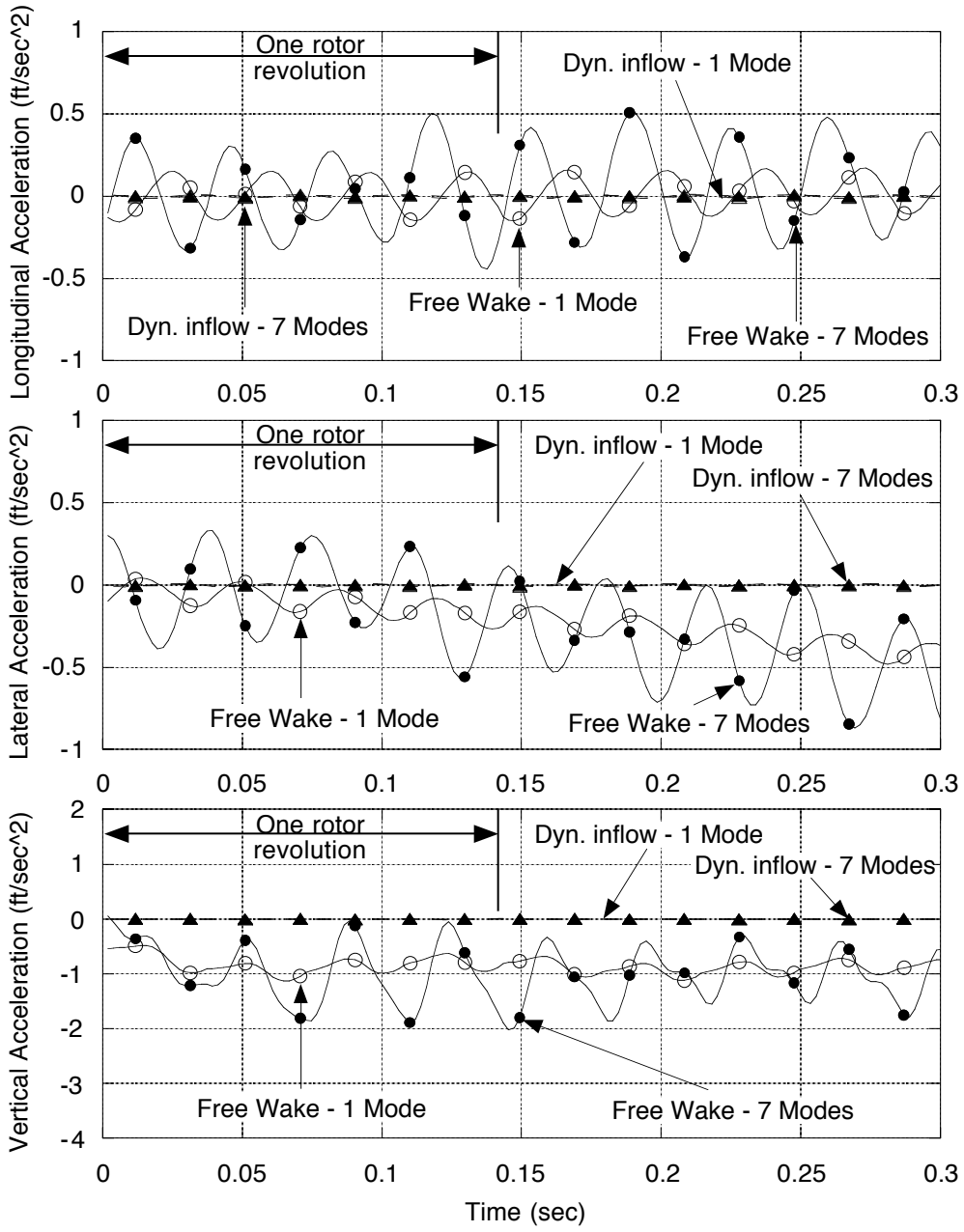

Figure 9.1: Effect of inflow models and blade modeling on linear accelerations at the computed trim conditions for the BO-105 at a forward speed of 17 knots.

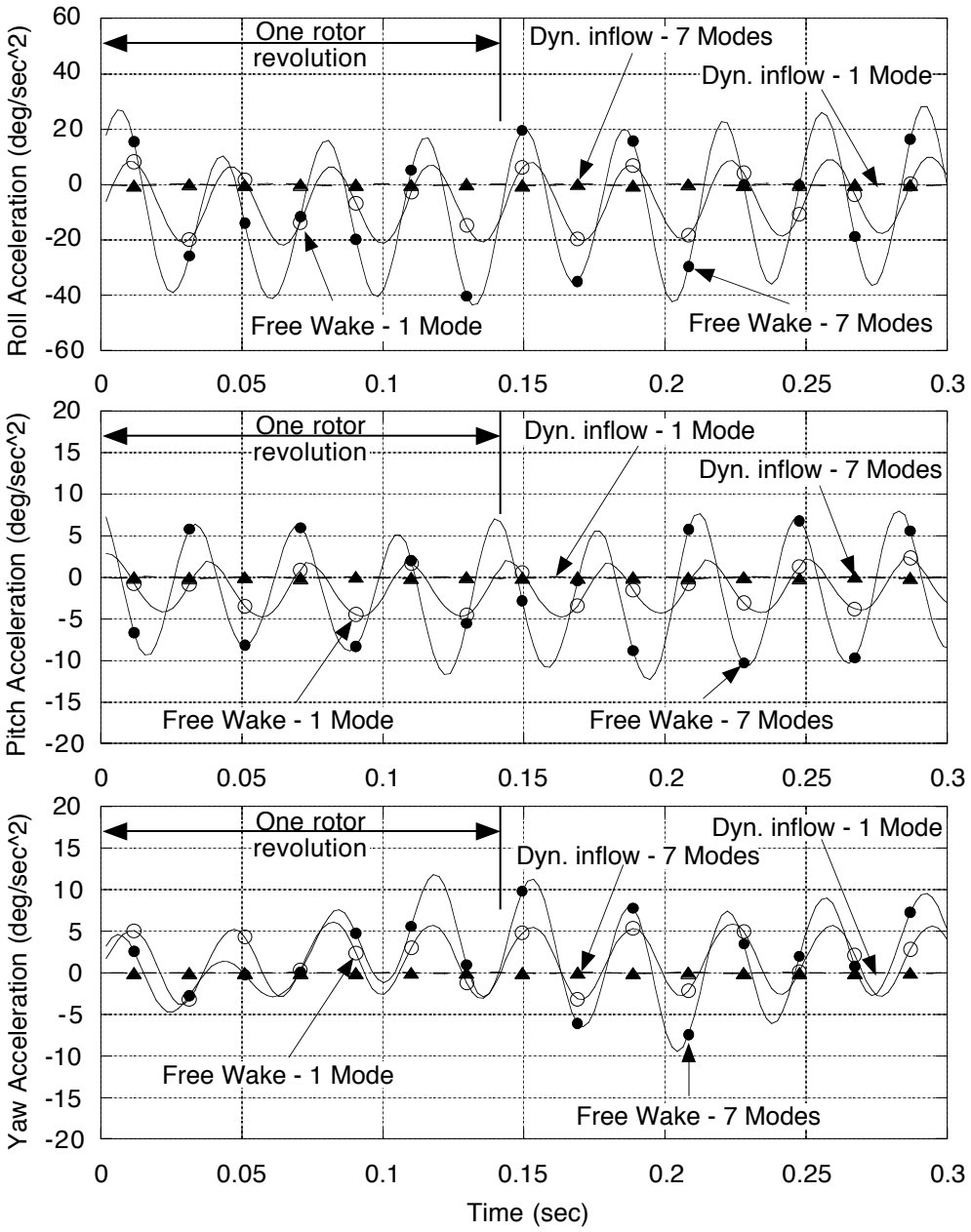

Figure 9.2: Effect of inflow models and blade modeling on roll, pitch and yaw accelerations at the computed trim conditions for the BO-105 at a forward speed of 17 knots.

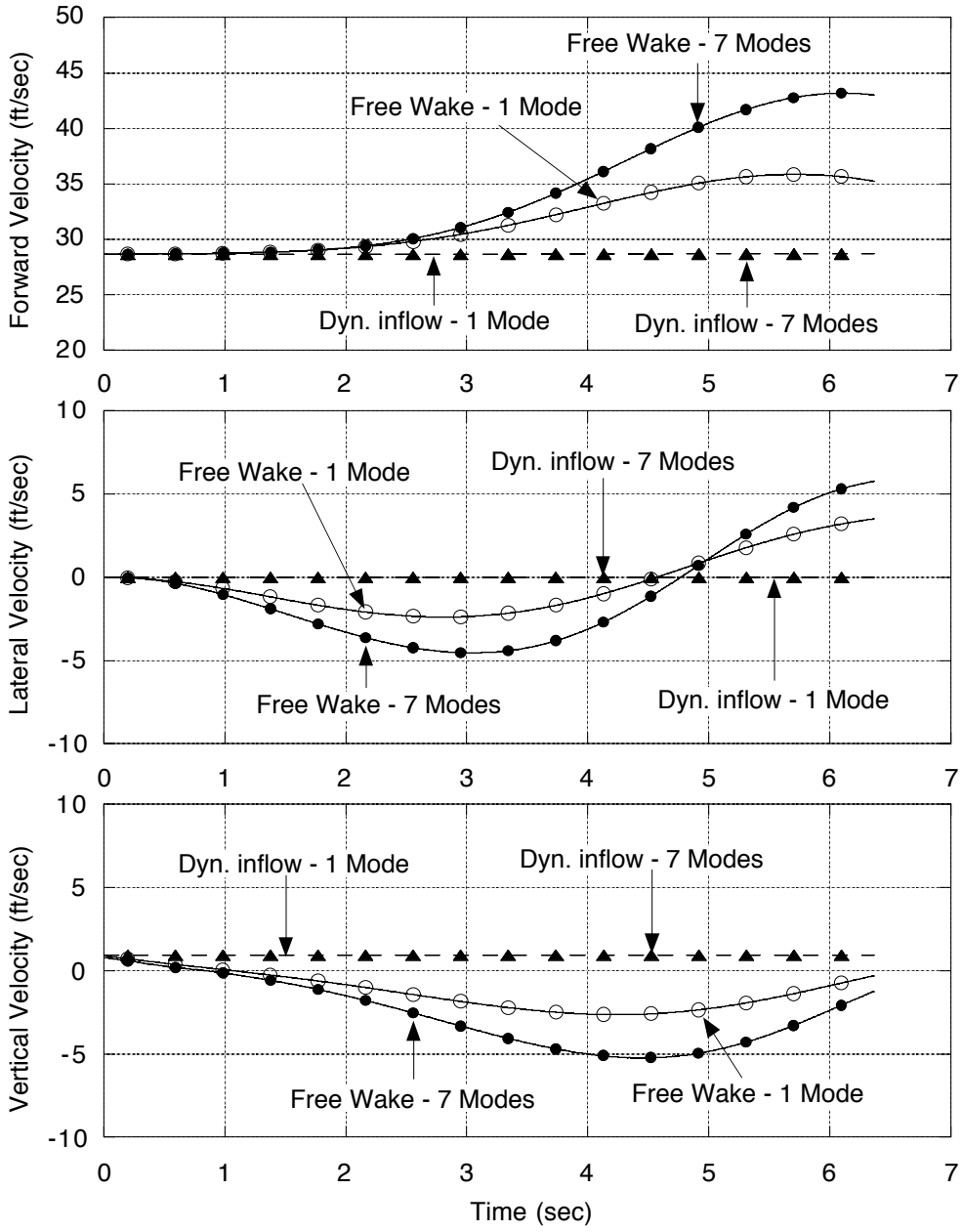

Figure 9.3: Effect of inflow models and blade modeling on velocity components from the computed trim conditions for the BO-105 at a forward speed of 17 knots.

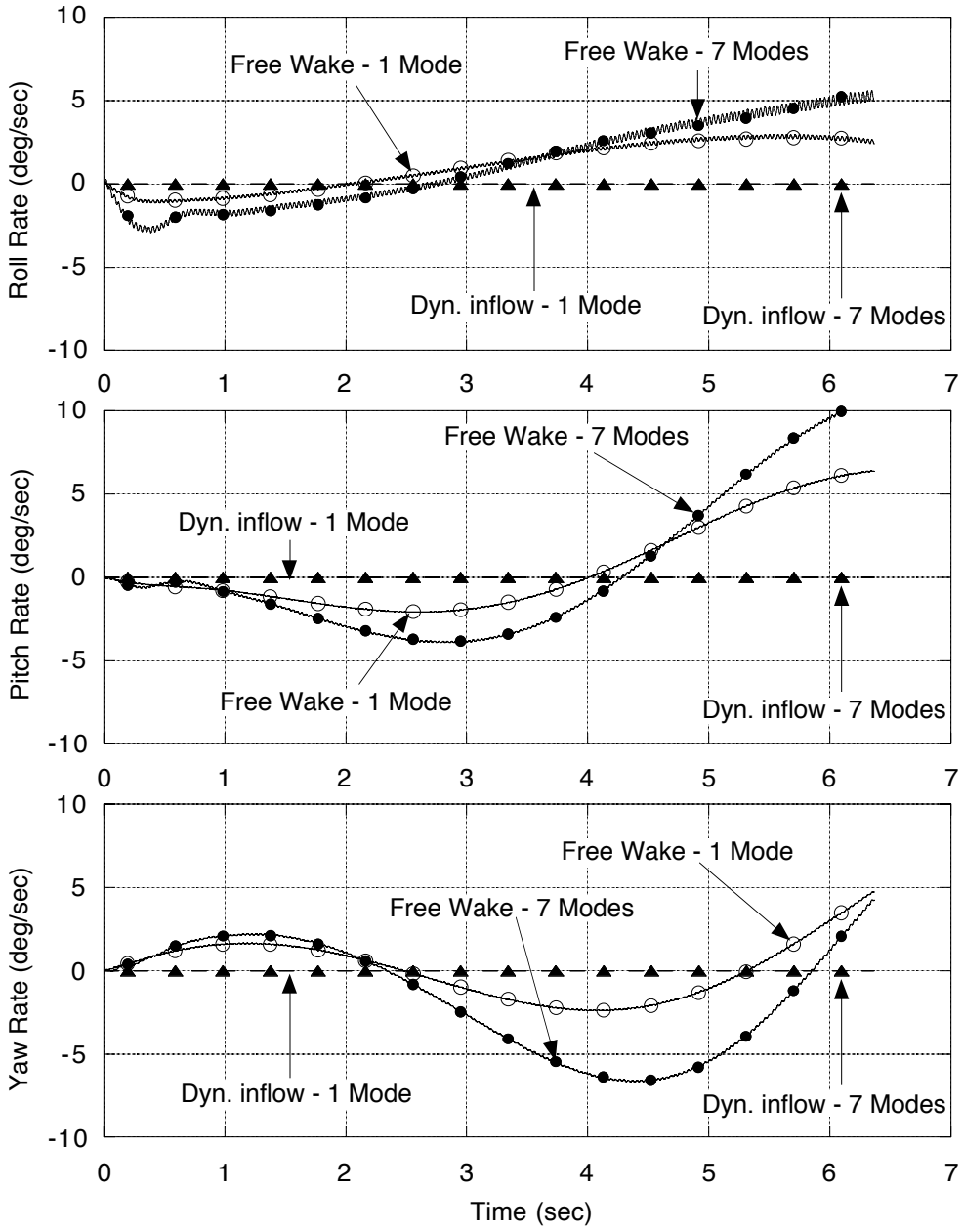

Figure 9.4: Effect of inflow models and blade modeling on roll, pitch and yaw rates from the computed trim conditions for the BO-105 at a forward speed of 17 knots.

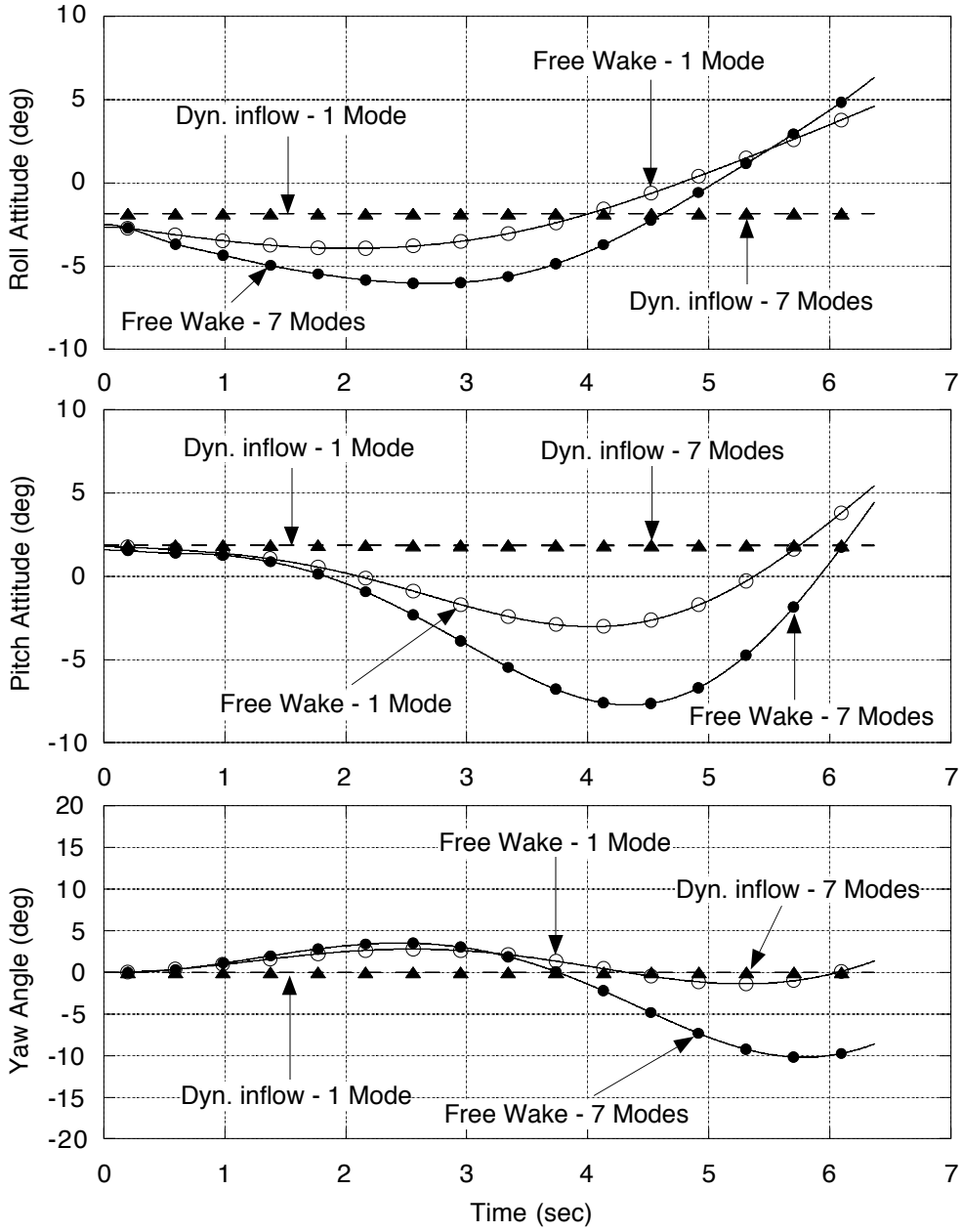

Figure 9.5: Effect of inflow models and blade modeling on roll, pitch and yaw attitudes from the computed trim conditions for the BO-105 at a forward speed of 17 knots.

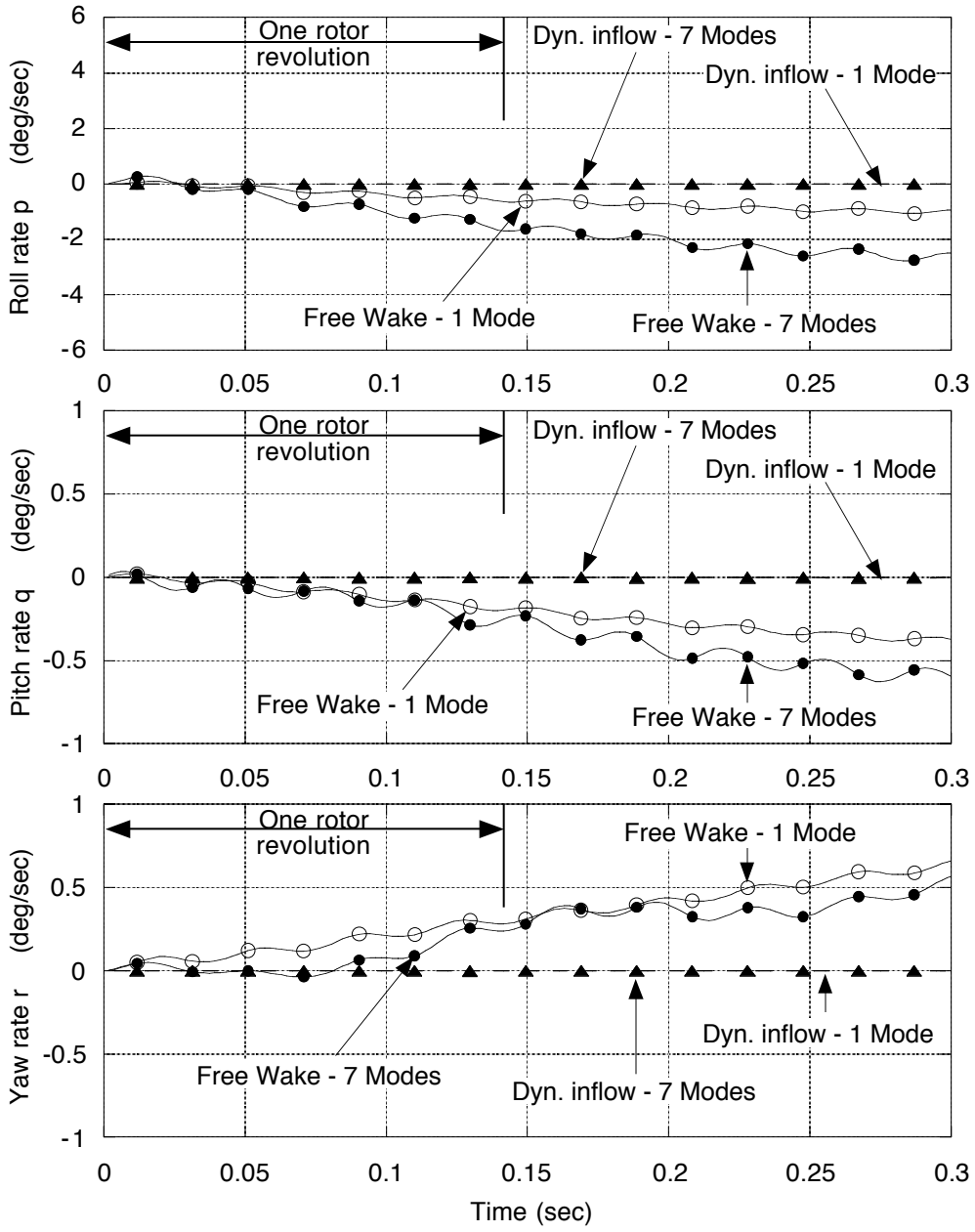

Figure 9.6: Effect of inflow models and blade modeling on roll, pitch and yaw rates from the computed trim conditions for the BO-105 at a forward speed of 17 knots.

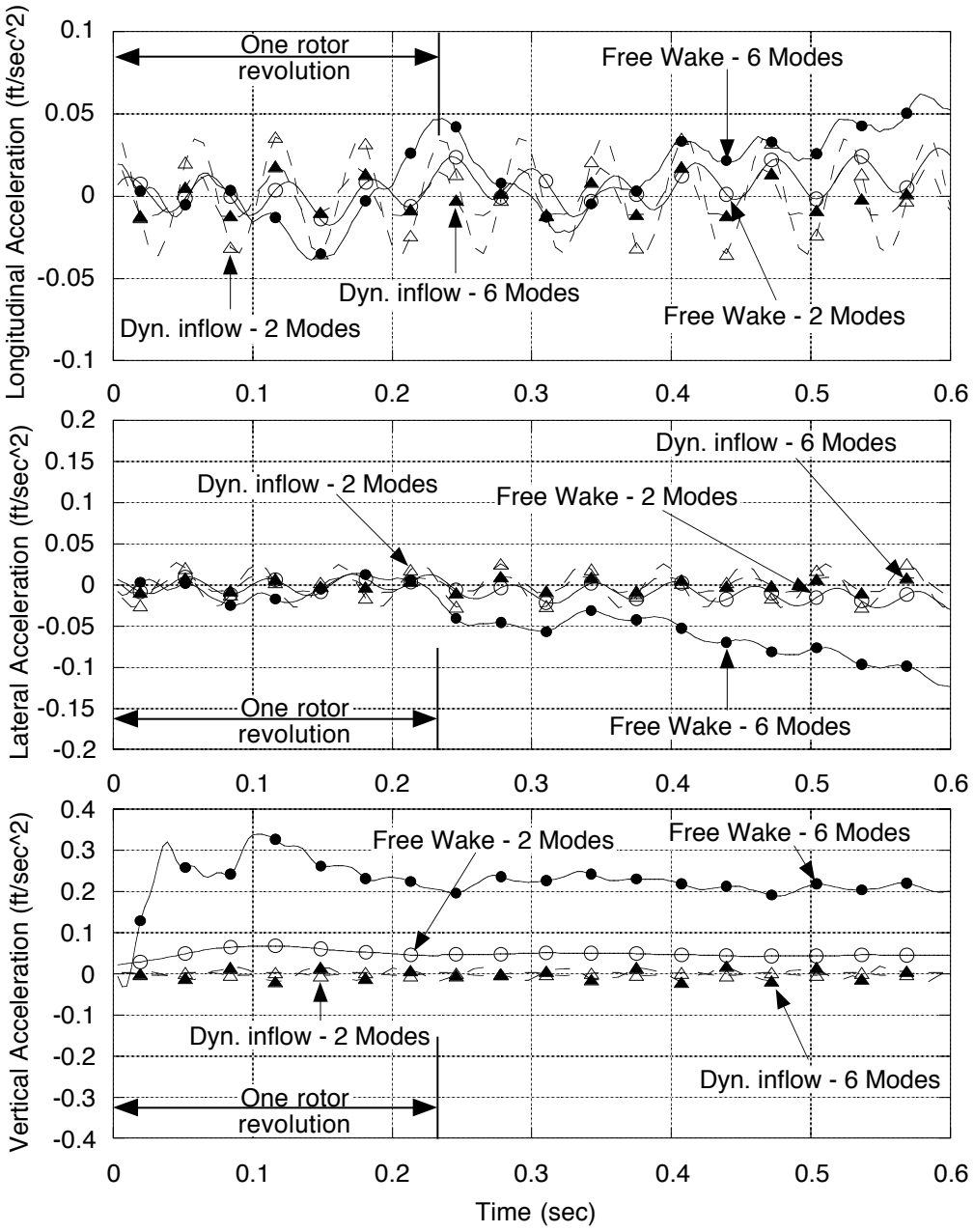

Figure 9.7: Effect of inflow models and blade modeling on linear accelerations from the computed trim conditions for the UH-60A in hover.

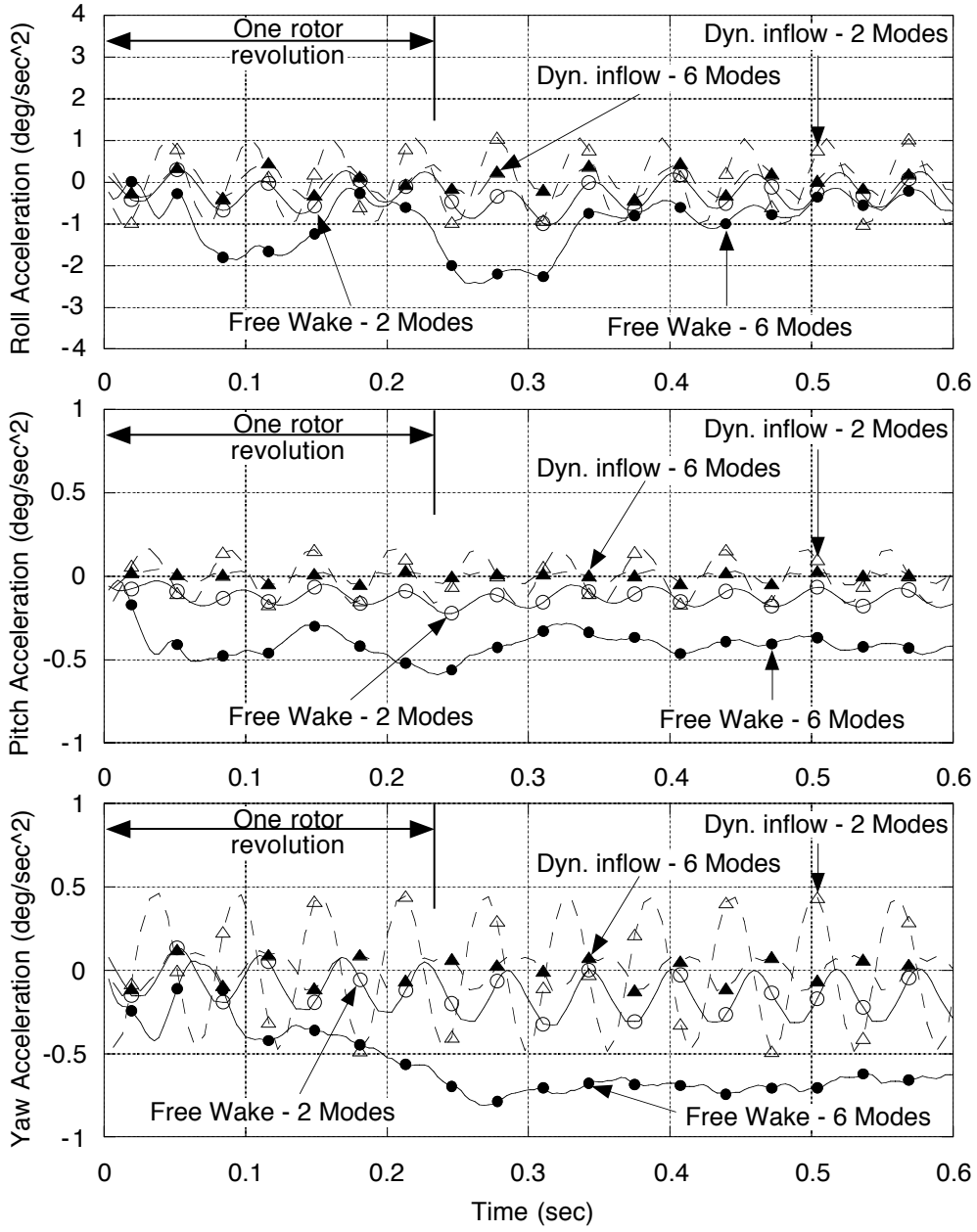

Figure 9.8: Effect of inflow models and blade modeling on roll, pitch and yaw accelerations from the computed trim conditions for the UH-60A in hover.

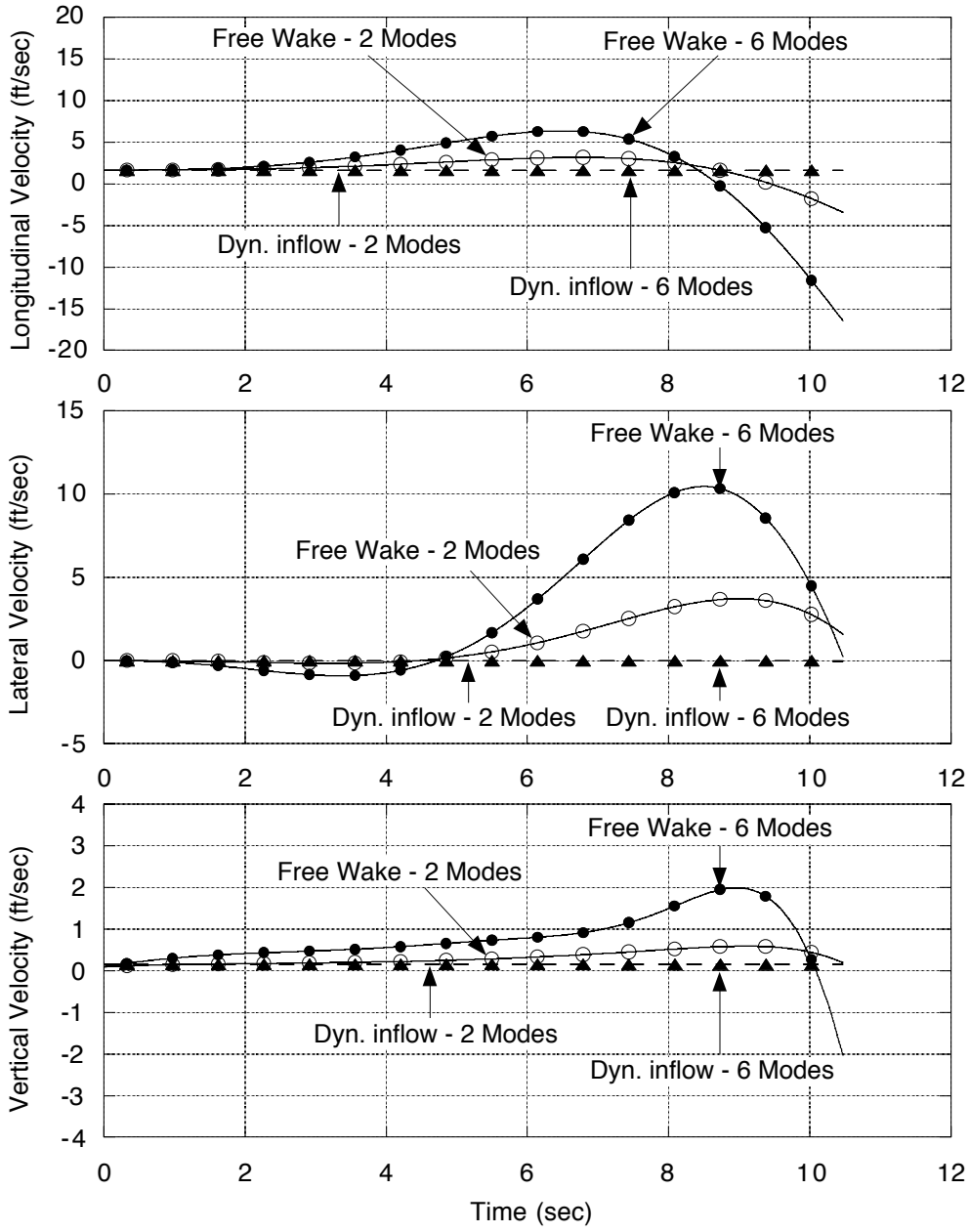

Figure 9.9: Effect of inflow models and blade modeling on velocity components at the computed trim conditions for the UH-60A in hover.

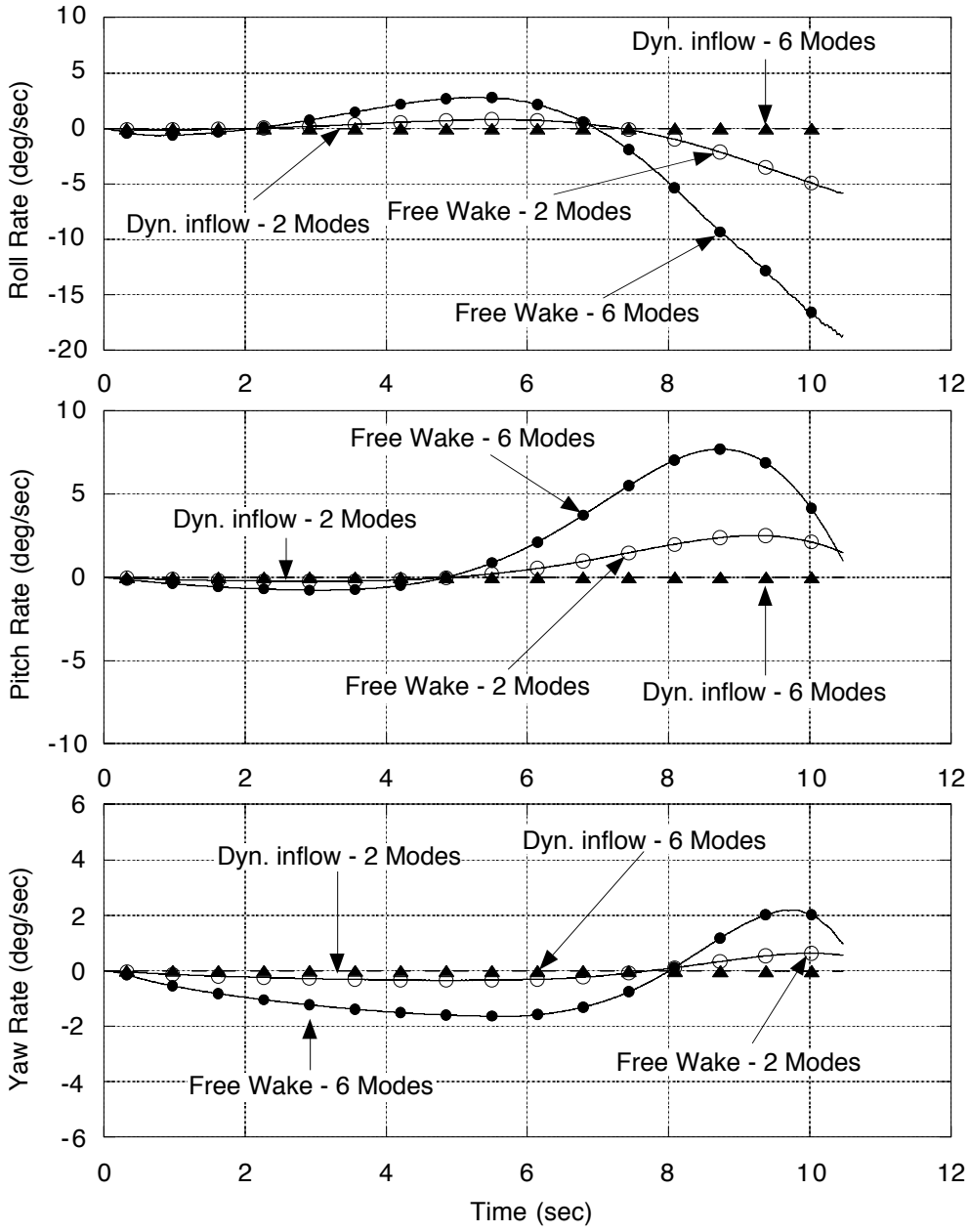

Figure 9.10: Effect of inflow models and blade modeling on roll, pitch and yaw rates at the computed trim conditions for the UH-60A in hover.

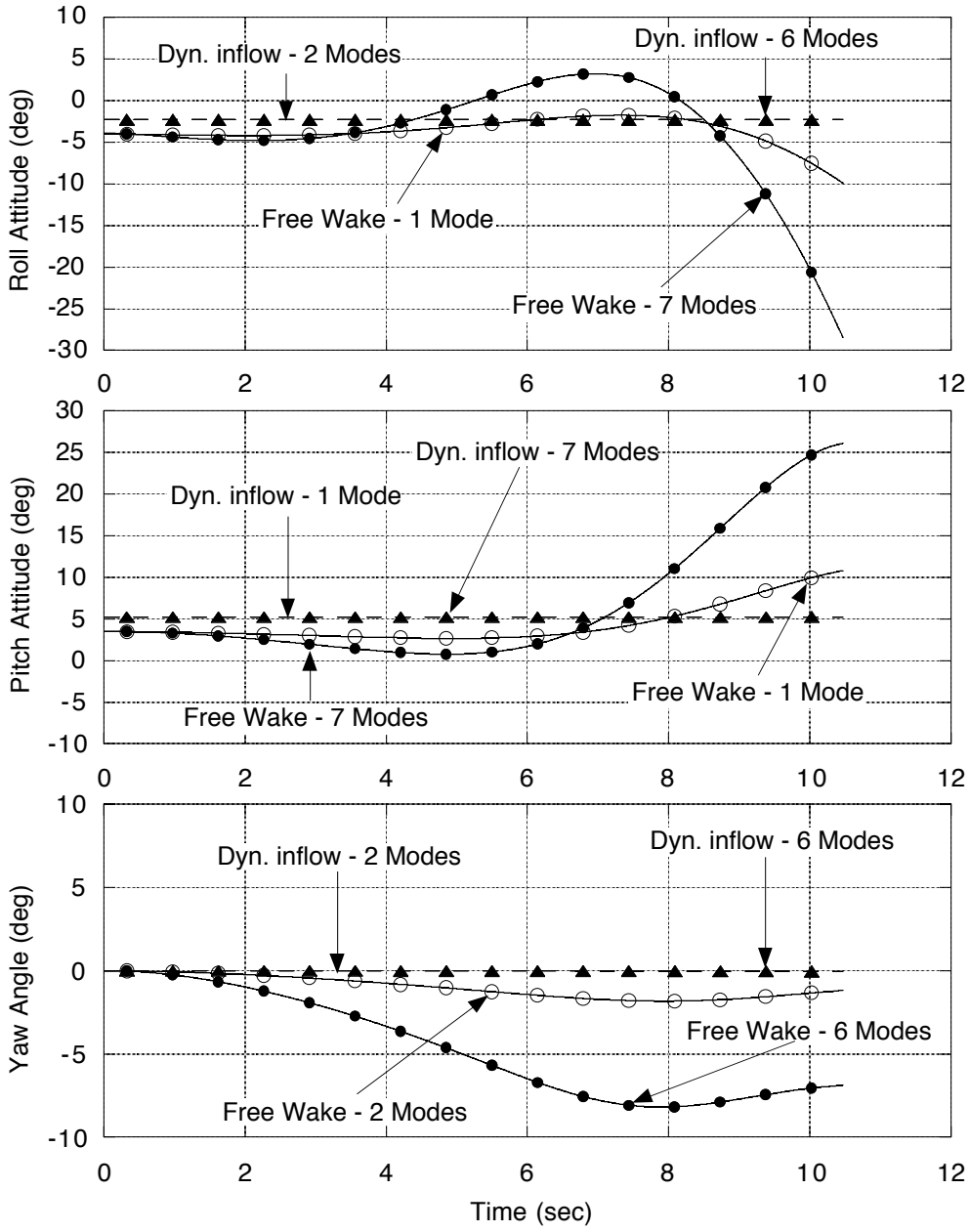

Figure 9.11: Effect of inflow models and blade modeling on roll, pitch and yaw attitudes at the computed trim conditions for the UH-60A in hover.

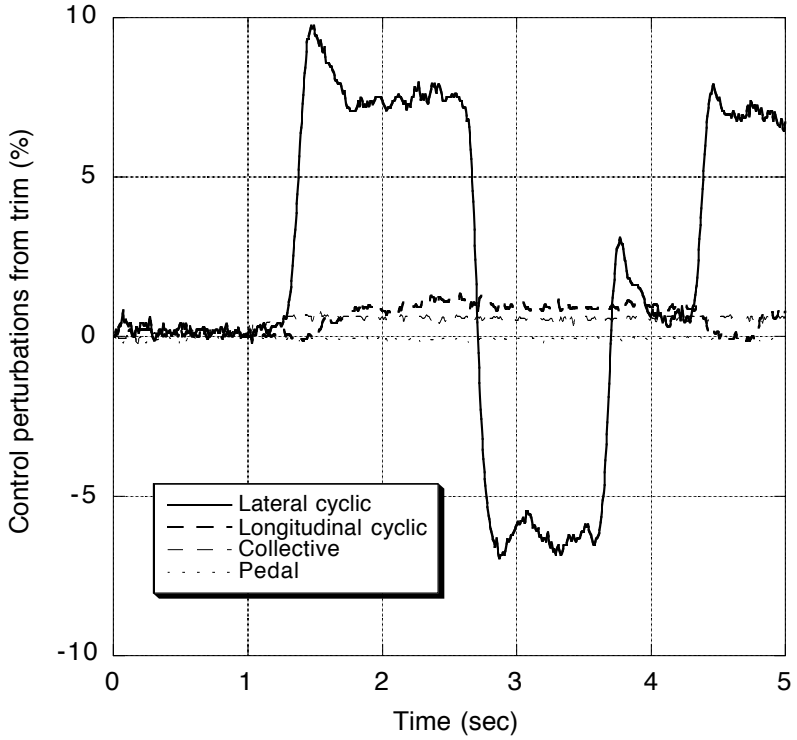

Figure 9.12: Control deflections from trim for the selected maneuver for the BO-105 in straight and level flight at 17 knots.

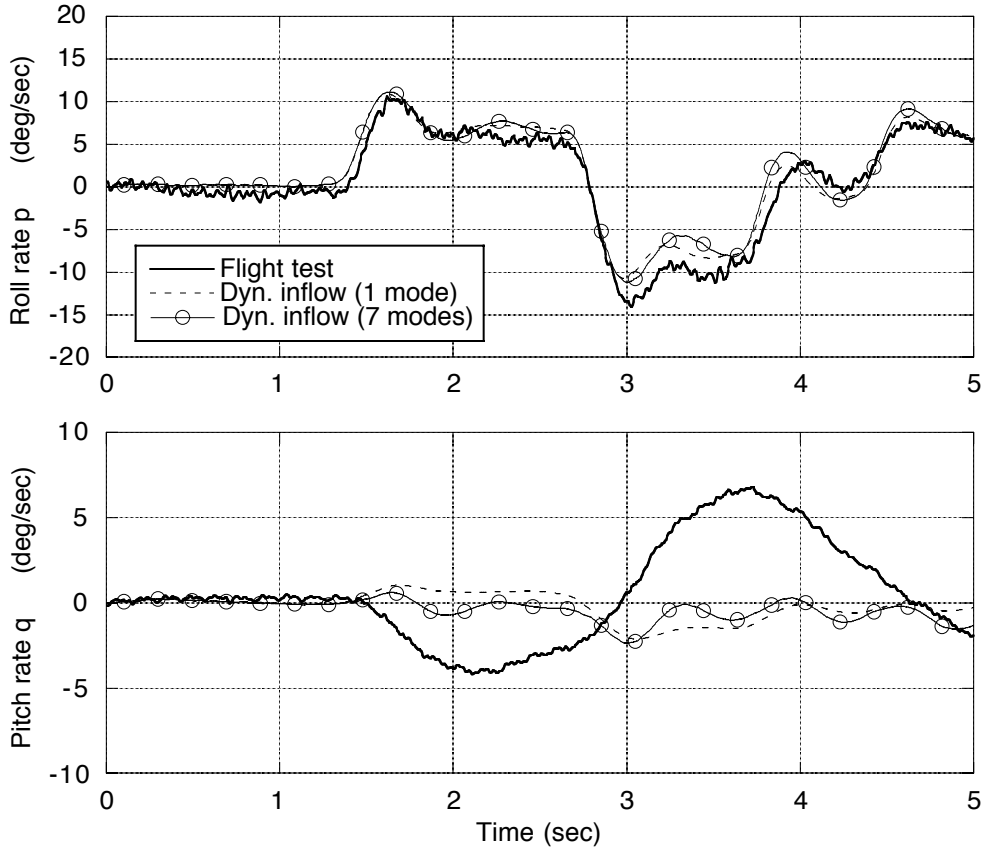

Figure 9.13: Effect of number of blade modes on the roll and pitch rate responses for the BO-105 with the dynamic inflow model (without maneuver-induced effects).

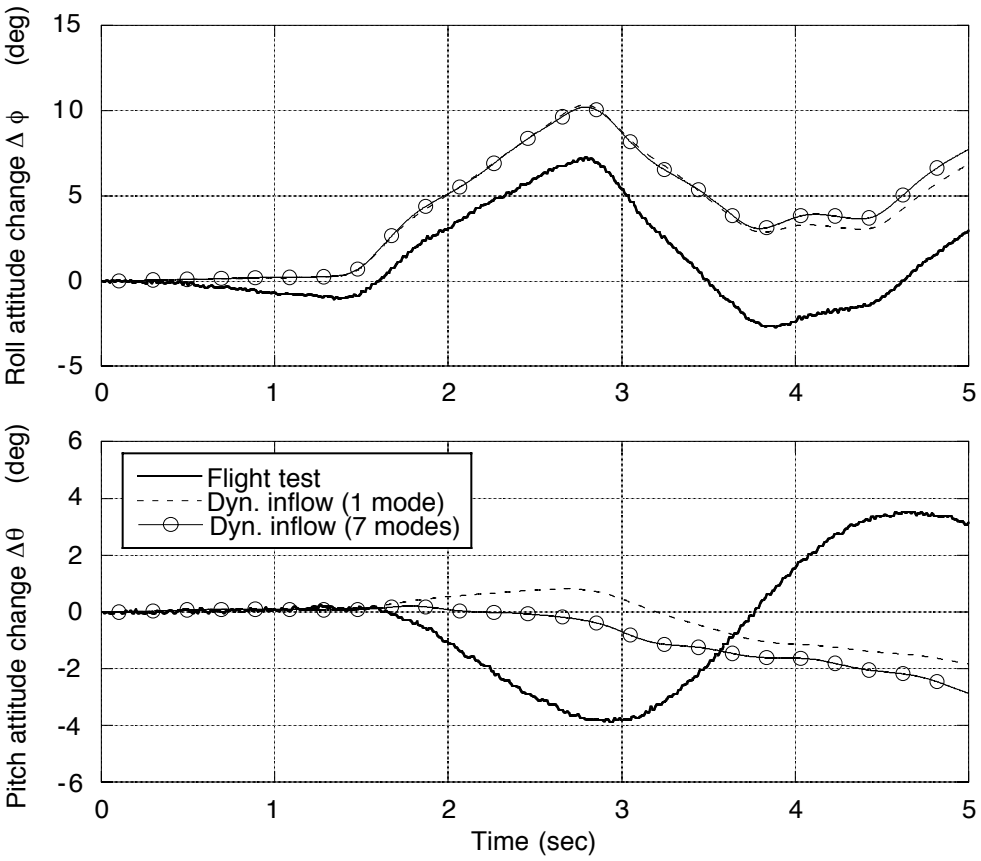

Figure 9.14: Effect of number of blade modes on the roll and pitch attitudes for the BO-105 with the dynamic inflow model (without maneuver-induced effects).

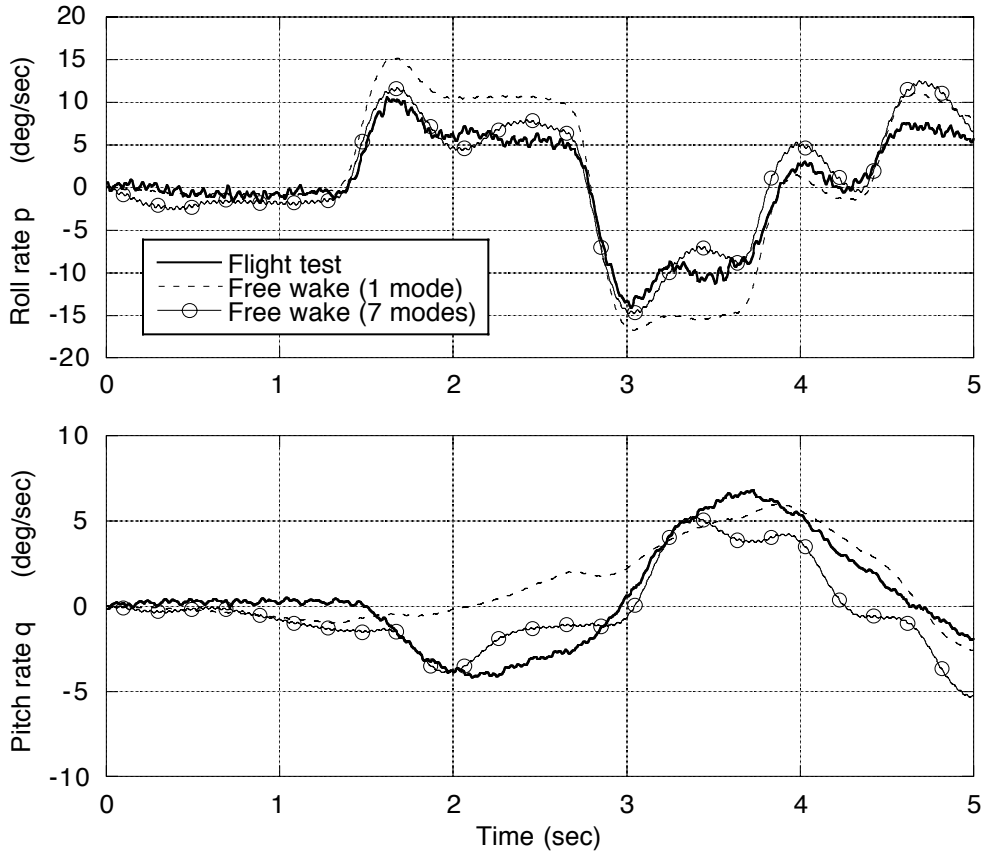

Figure 9.15: Effect of number of blade modes on the roll and pitch rate responses for the BO-105 with the free wake model.

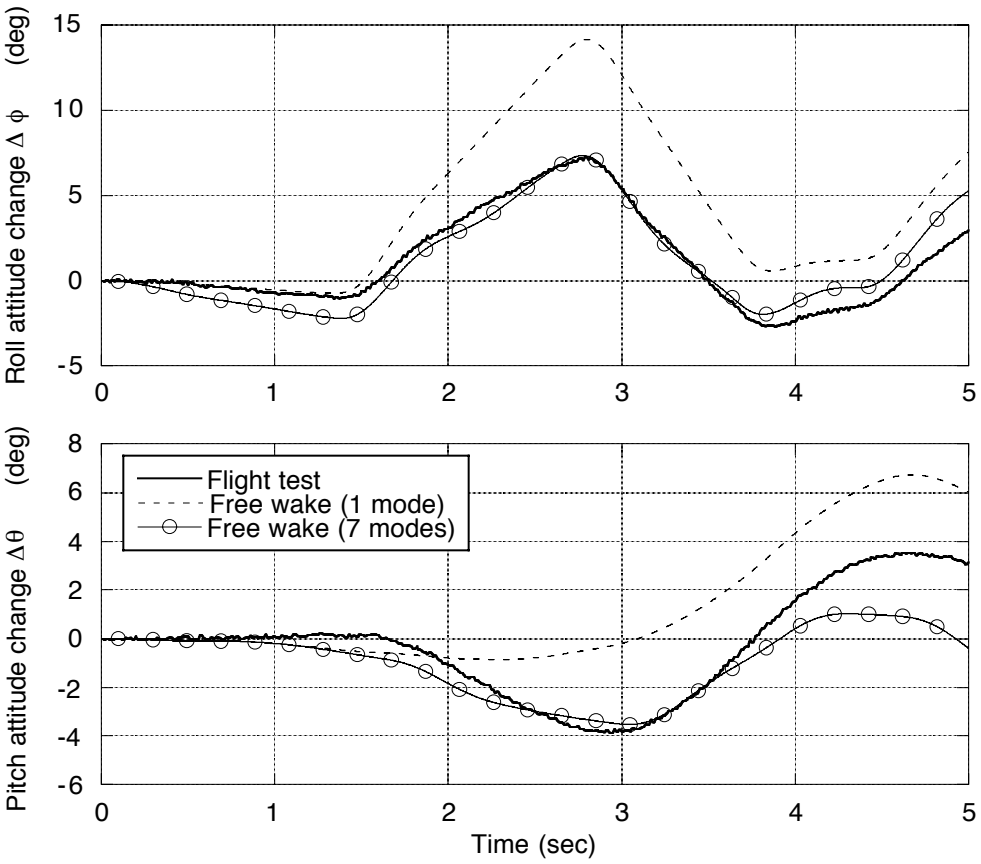

Figure 9.16: Effect of number of blade modes on the roll and pitch attitudes for the BO-105 with the free wake model.

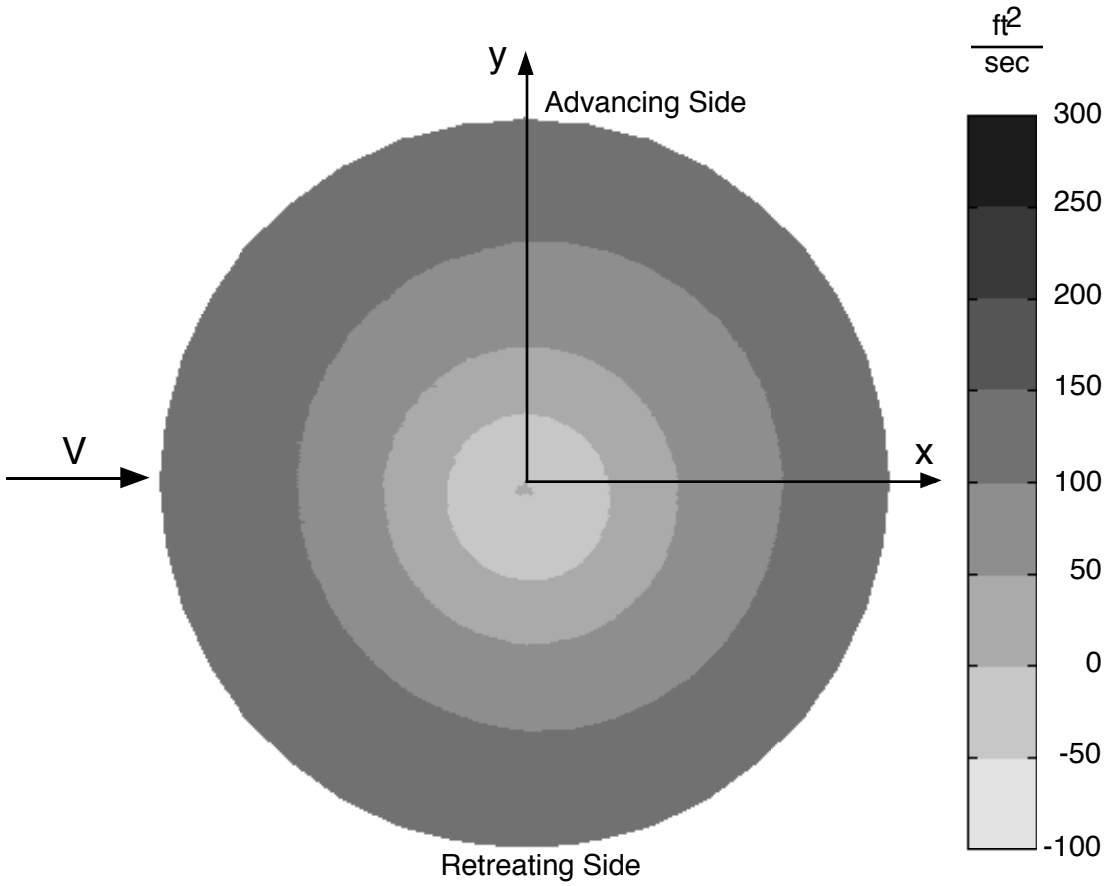

Figure 9.17: Circulation distribution for the trimmed flight condition for the BO-105 at 17 knots with dynamic inflow and simple blade model.

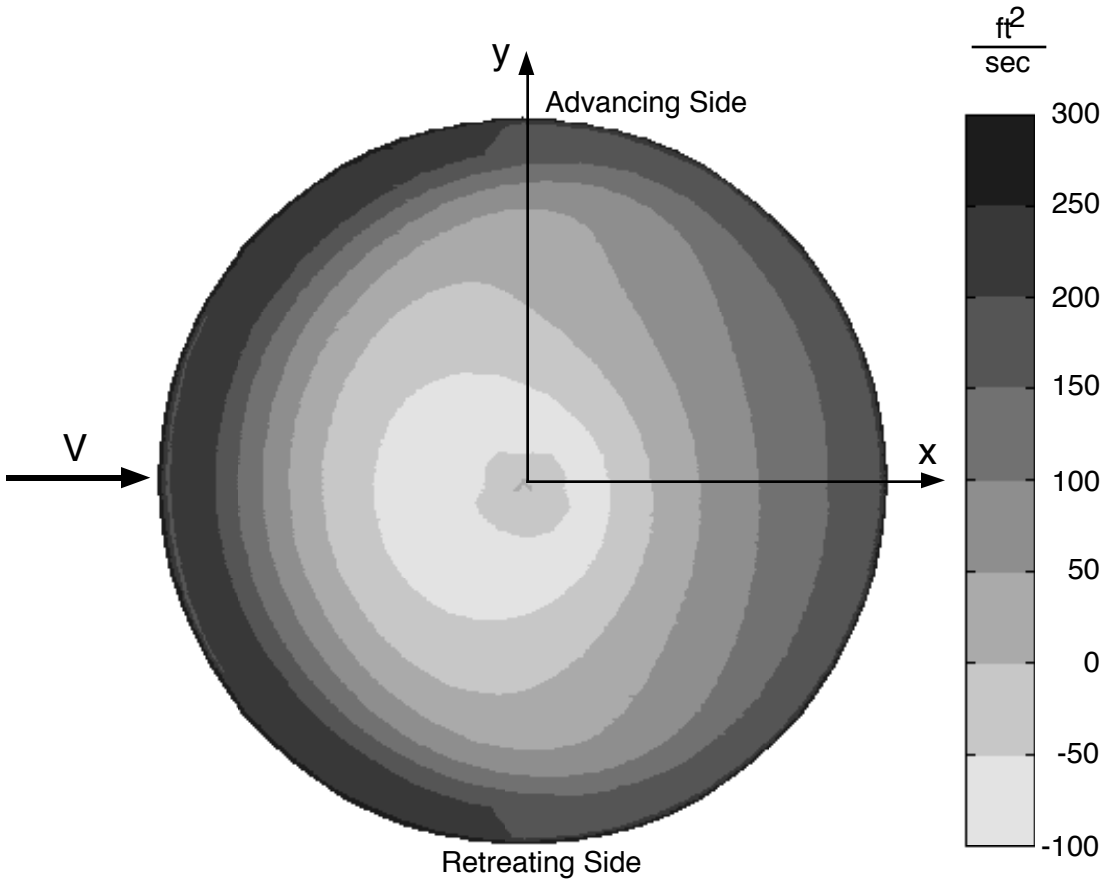

Figure 9.18: Circulation distribution for the trimmed flight condition for the BO-105 at 17 knots with the free wake and simple blade model.

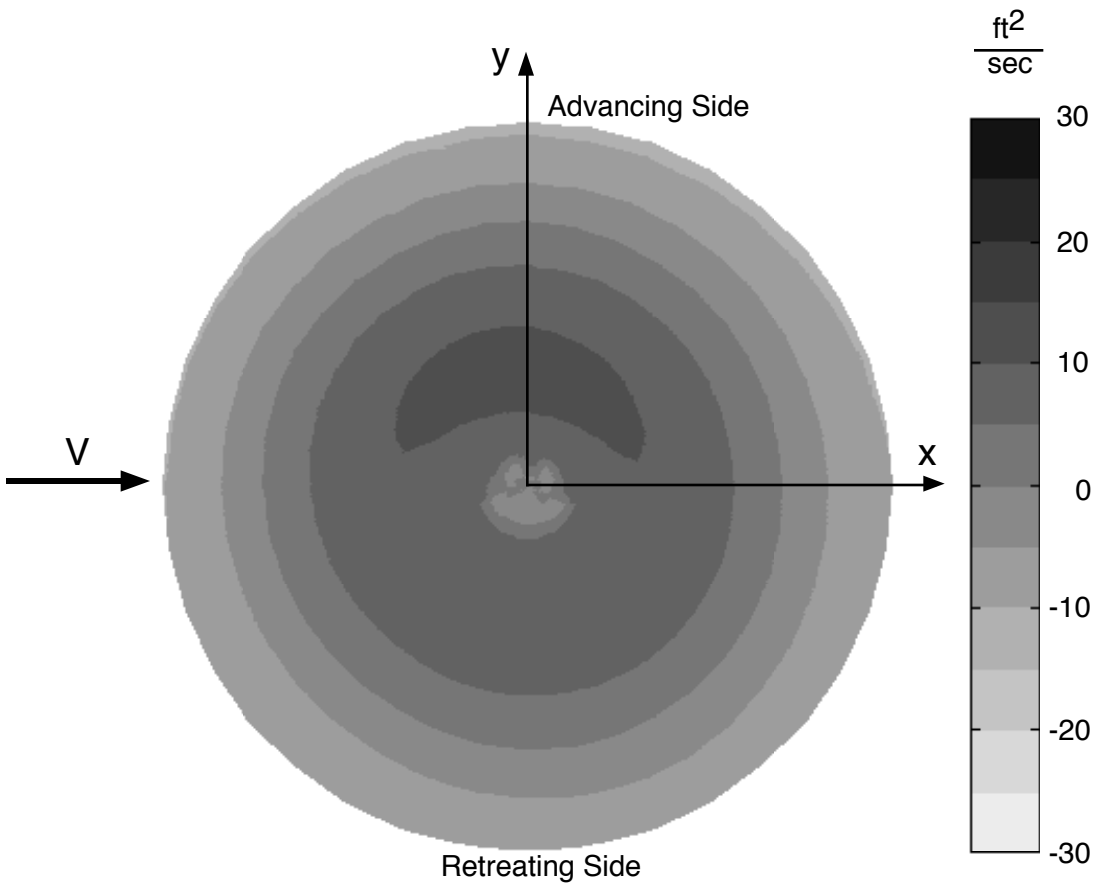

Figure 9.19: Effect of blade model on circulation distribution for trim at 17 knots for the BO-105 with dynamic inflow. Baseline with simple blade model.

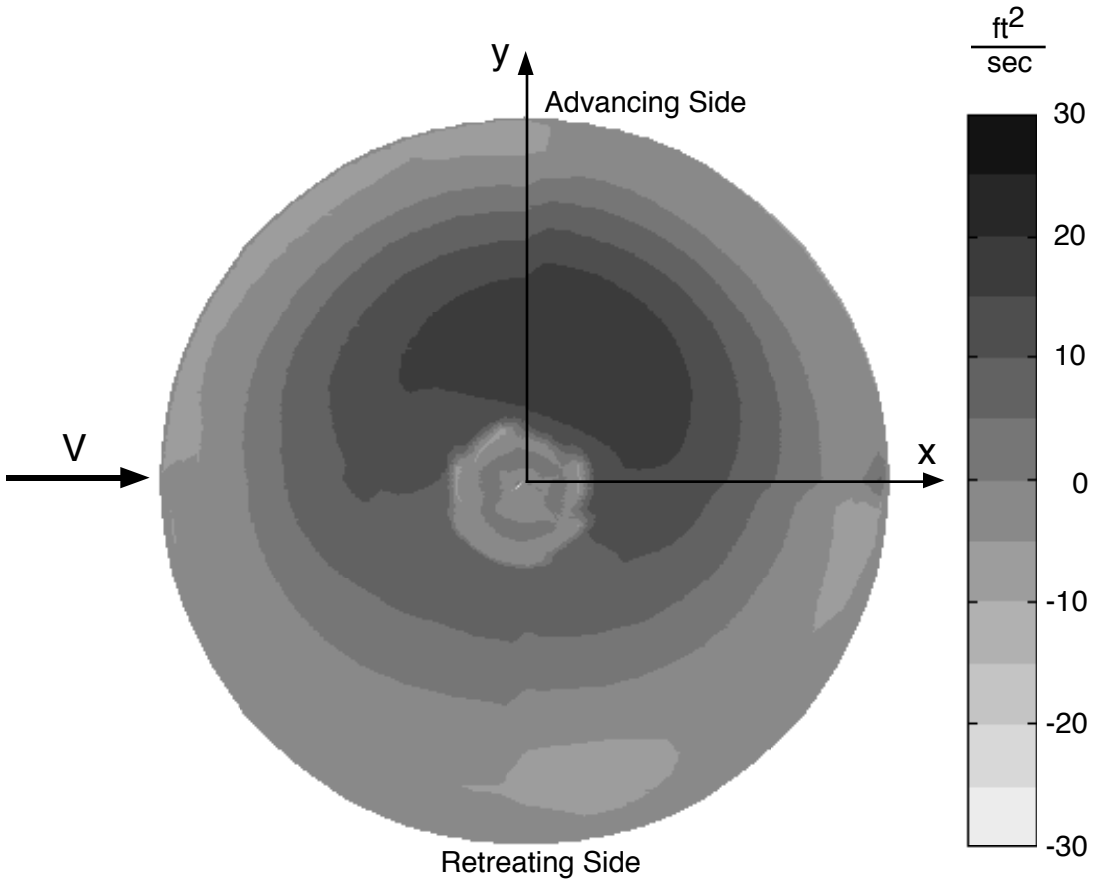

Figure 9.20: Effect of blade model on circulation distribution for trim at 17 knots for the BO-105 with the free wake model. Baseline with simple blade model.

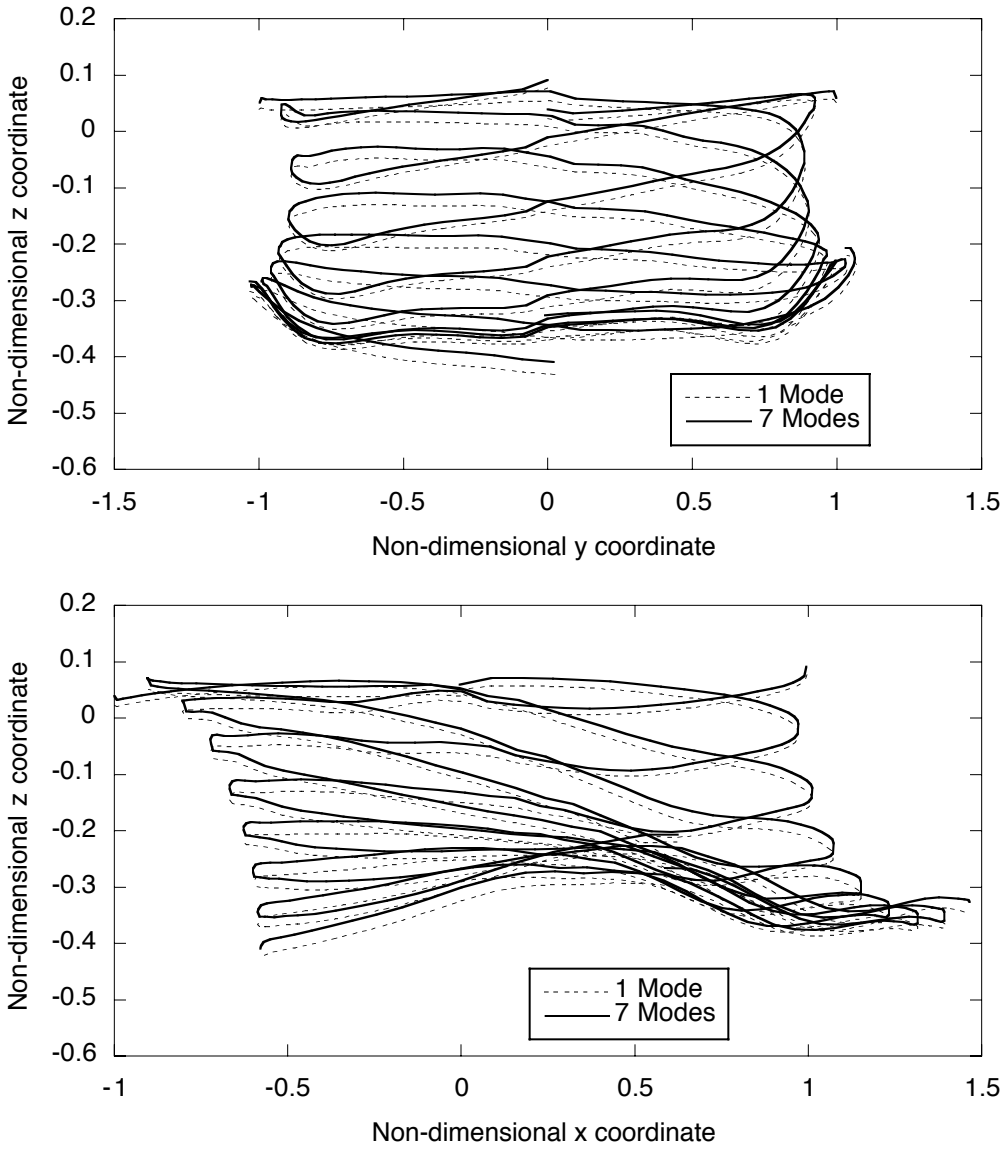

Figure 9.21: Effect of blade model on trim wake geometry at 17 knots for the BO-105 with the free wake.

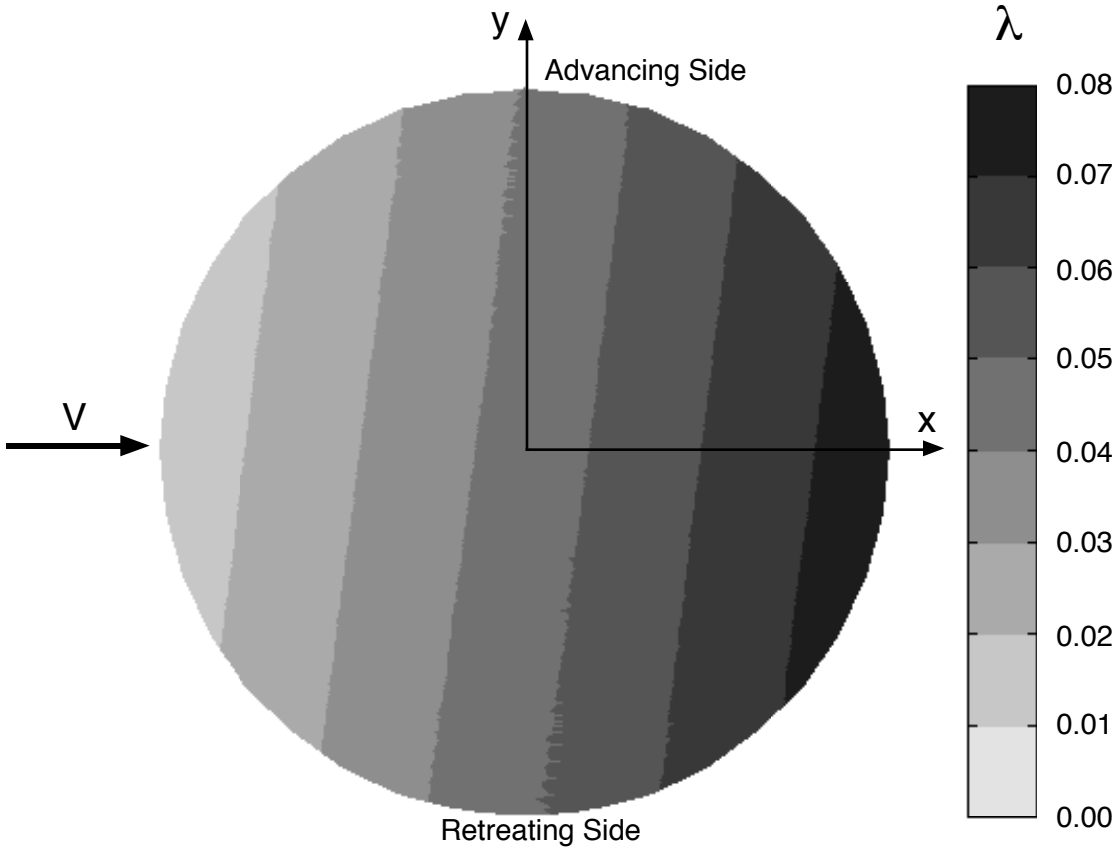

Figure 9.22: Inflow distribution for trim at 17 knots for the BO-105 with dynamic inflow and the refined blade model.

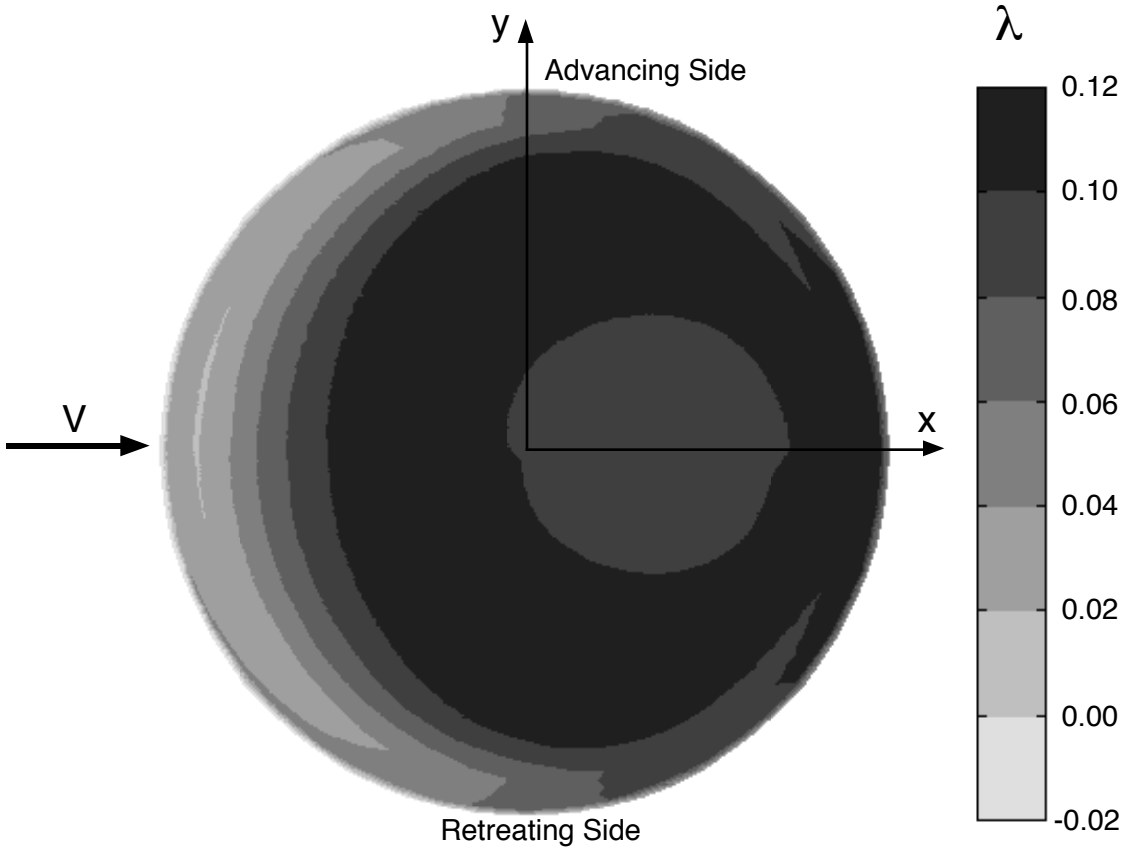

Figure 9.23: Inflow distribution for trim at 17 knots for the BO-105 with the free wake and the refined blade model.

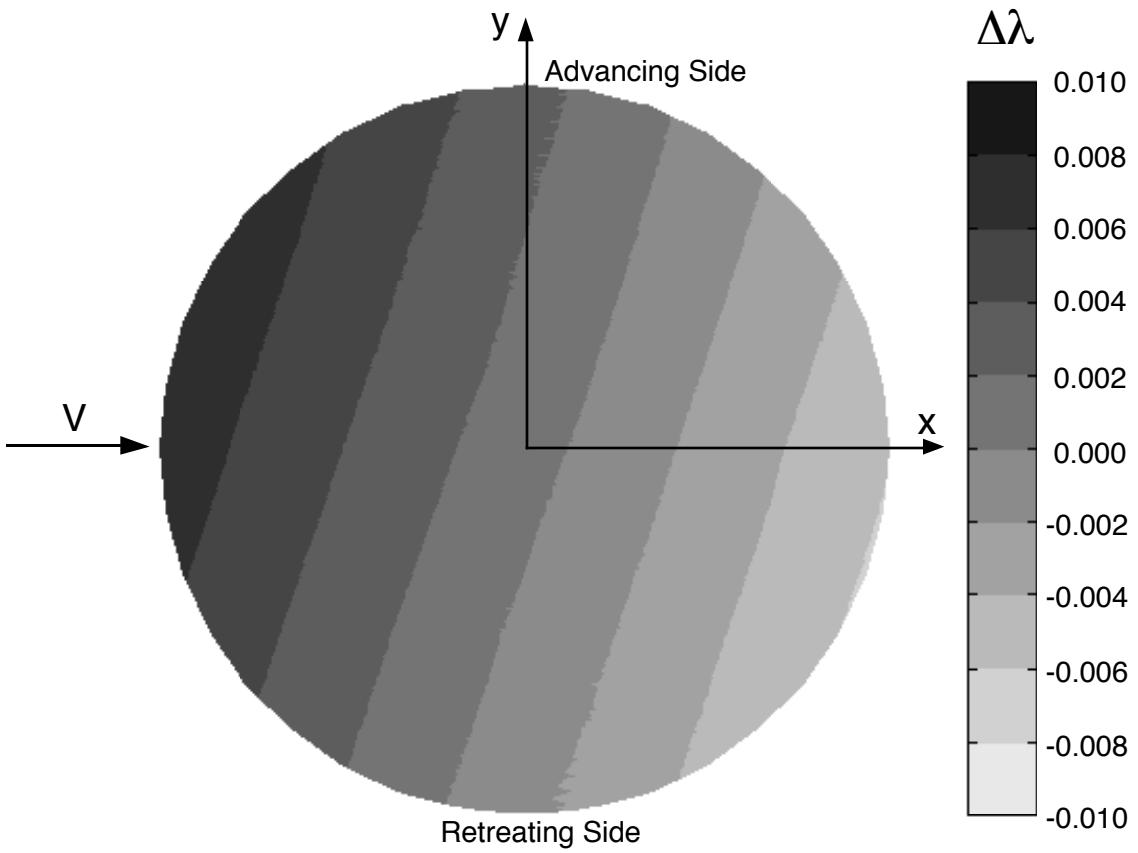

Figure 9.24: Change in inflow distribution from trim condition at 17 knots to the point at the start of the 13th rotor revolution for the BO-105 with dynamic inflow and the refined blade model. Baseline is trim inflow.

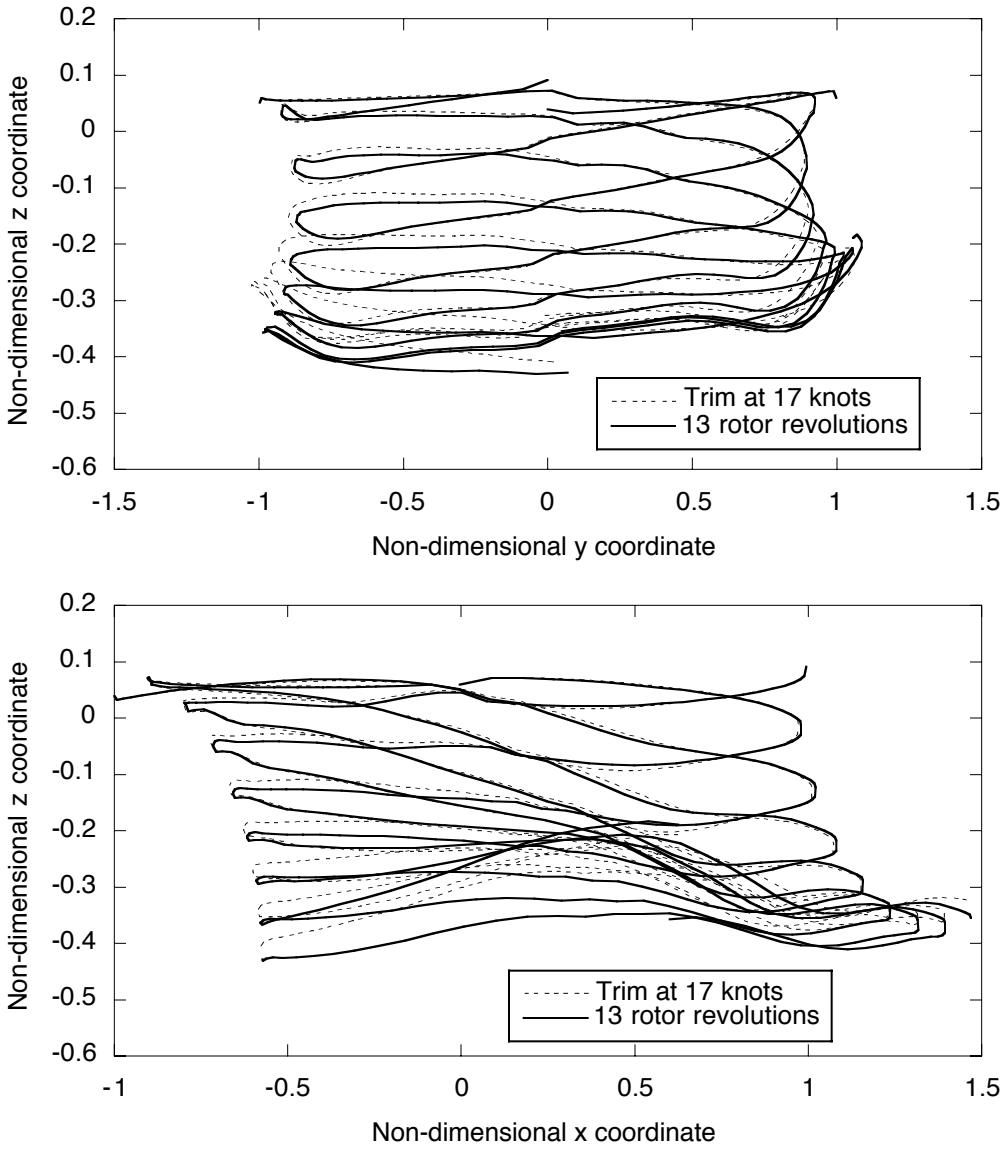

Figure 9.25: Effect of blade model of wake geometry 13 rotor revolutions into the maneuver for the BO-105 with the free wake.

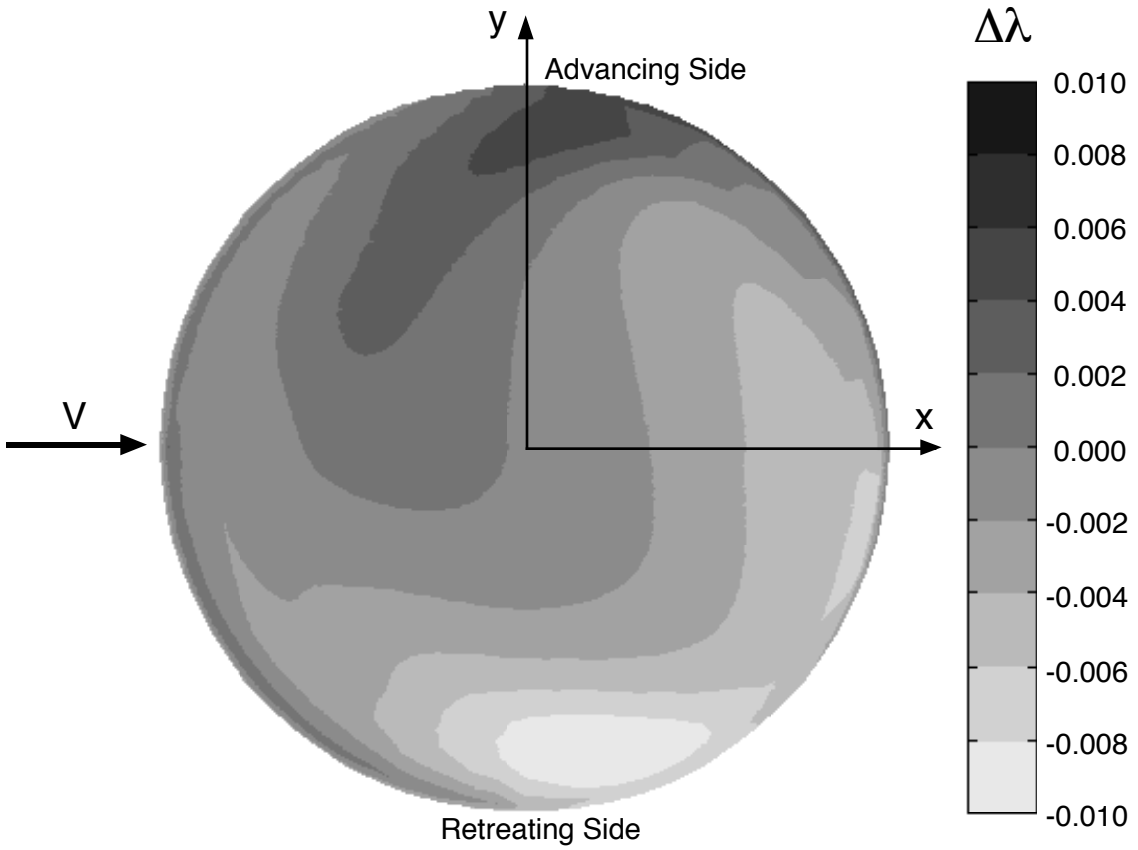

Figure 9.26: Change in inflow distribution from trim condition at 17 knots to the point at the start of the 13th rotor revolution for the BO-105 with the free wake and the refined blade model. Baseline is trim inflow.

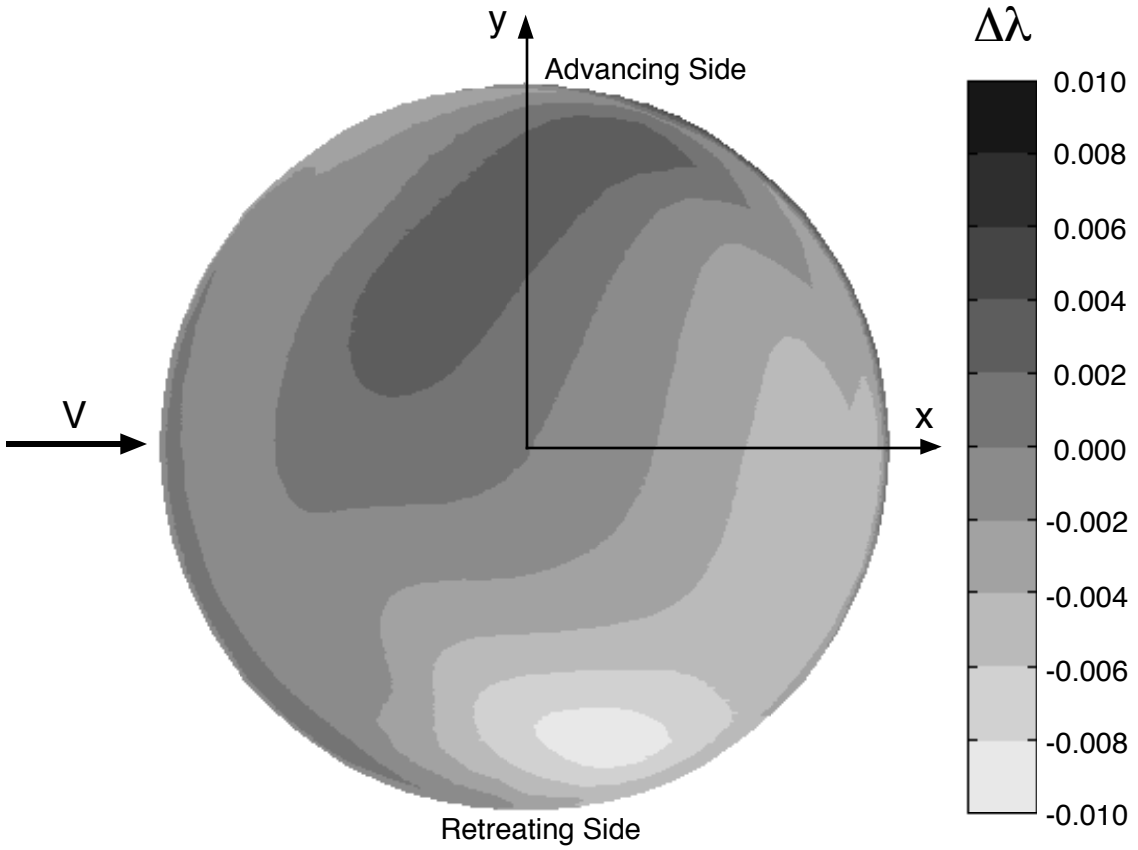

Figure 9.27: Change in inflow distribution from trim condition at 17 knots to the point at the start of the 13th rotor revolution for the BO-105 with the free wake and the simple blade model. Baseline is trim inflow.

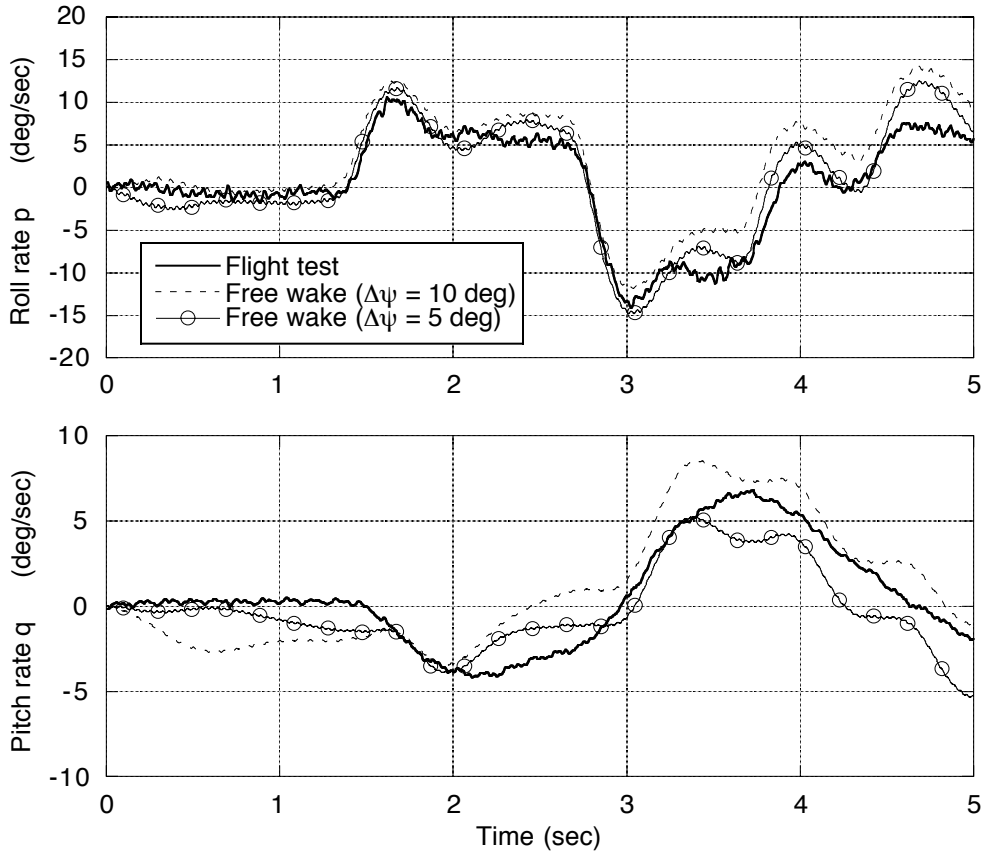

Figure 9.28: Effect of the free wake resolution $\Delta\psi$ on the roll and pitch rate response for the BO-105 with the free wake and refined blade model.

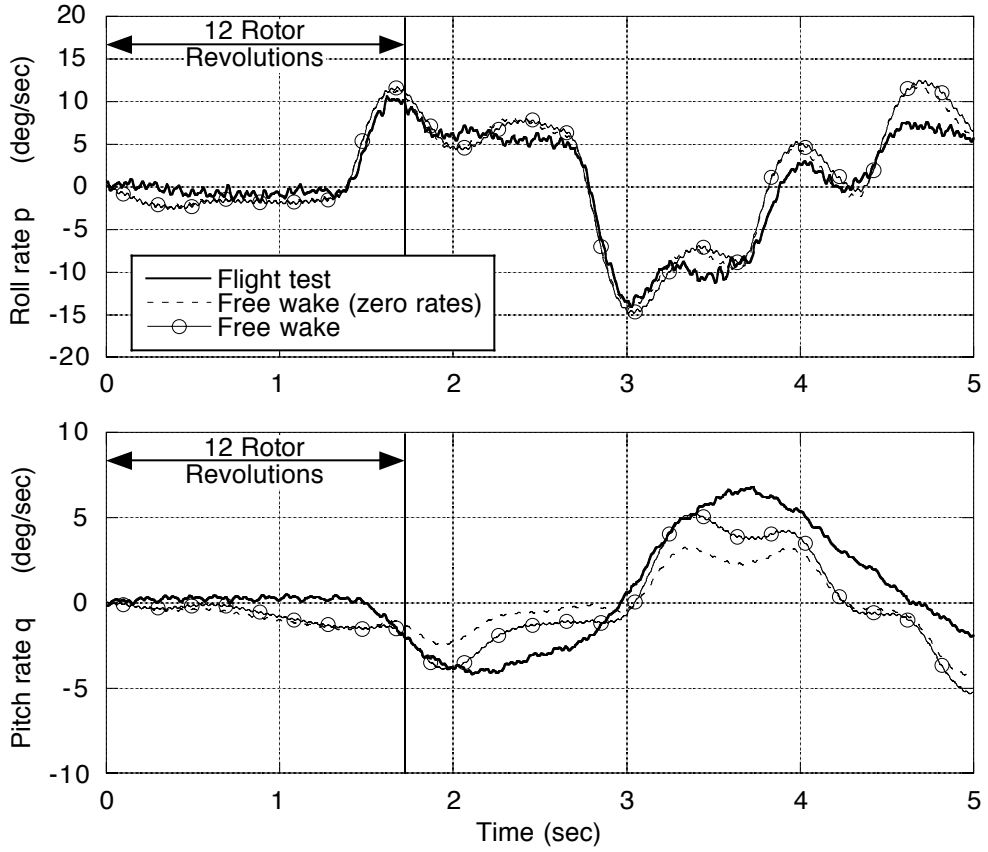

Figure 9.29: Effect of maneuver-induced wake distortions on the roll and pitch rate response for the BO-105 with the free wake and the refined blade model.

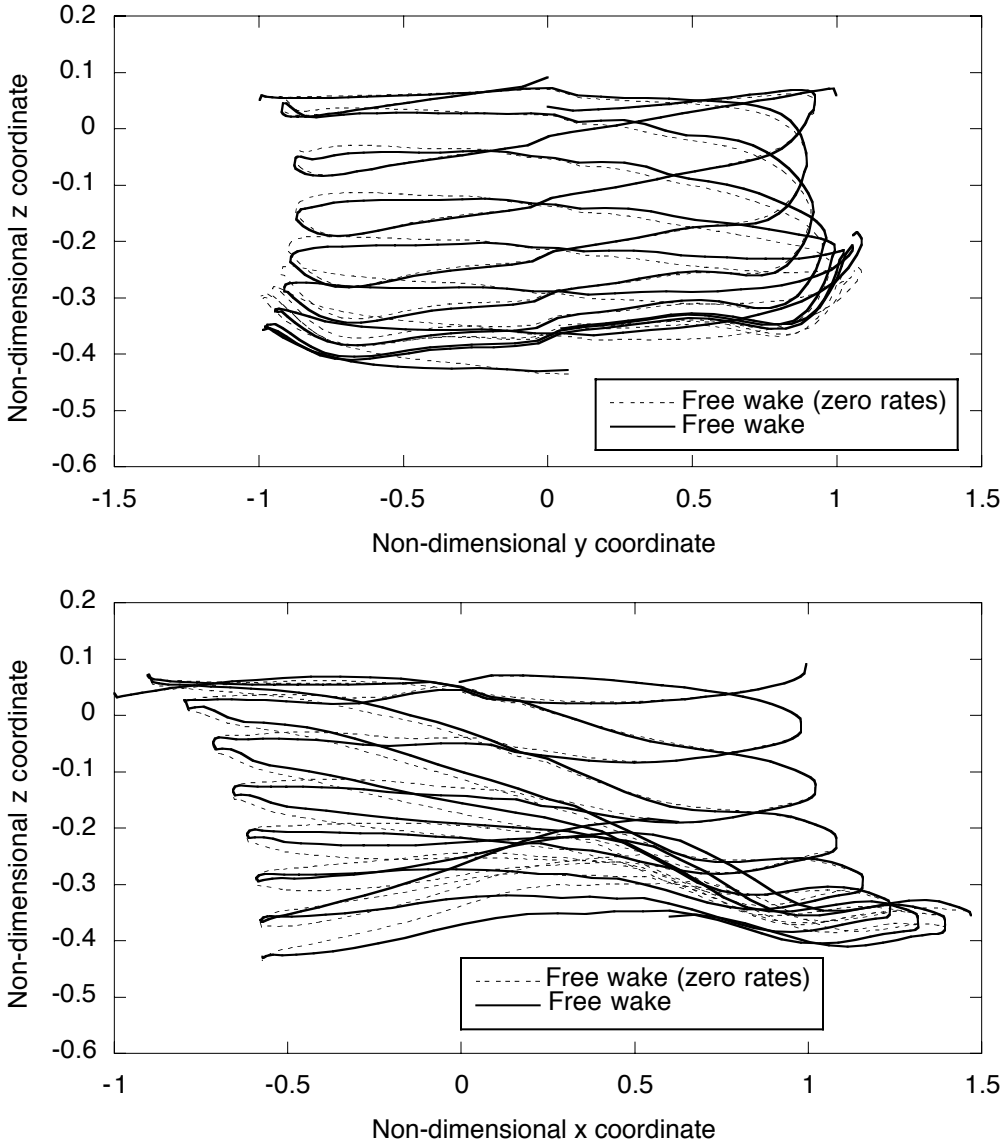

Figure 9.30: Effect of inclusion of maneuver-induced wake distortions within the free wake model on the wake geometry at 17 knots for the BO-105.

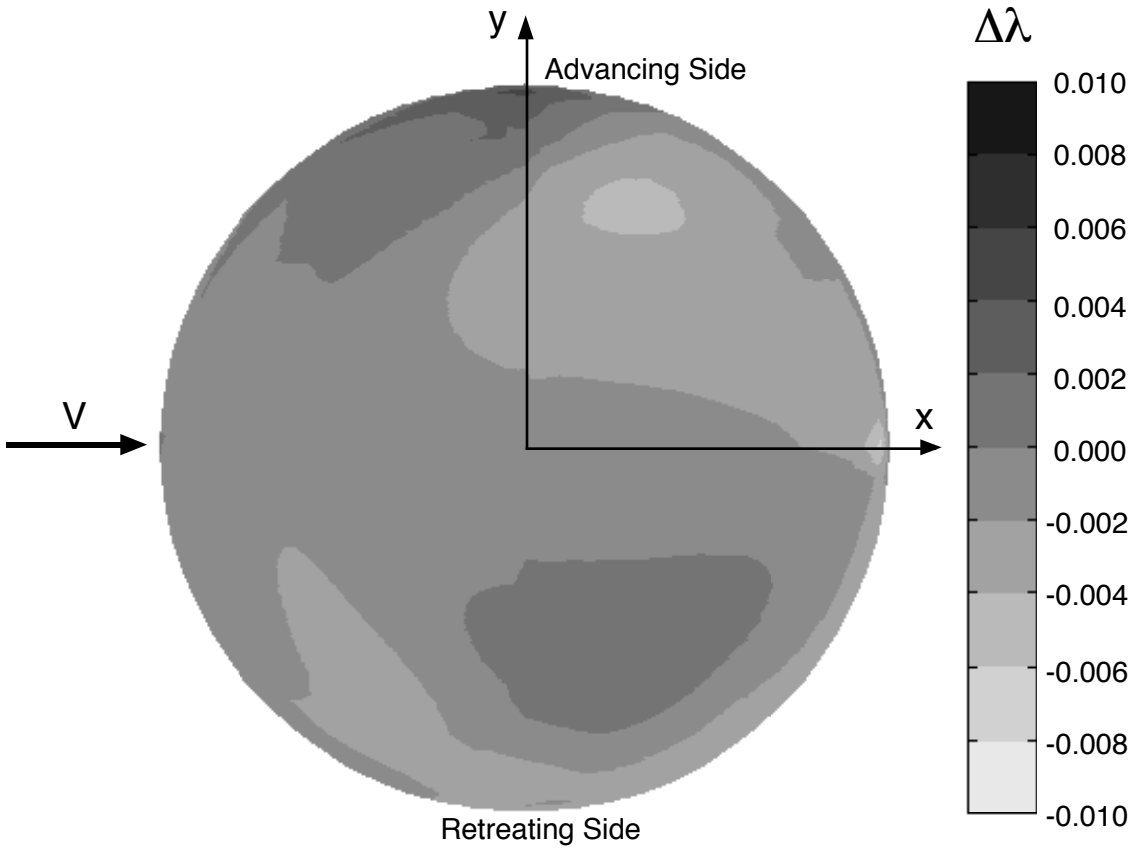

Figure 9.31: Change in inflow with the inclusion of maneuver-induced wake distortions within the free wake model at 13 rotor revolutions into the maneuver for the BO-105. Baseline with no maneuver-induced wake distortions.

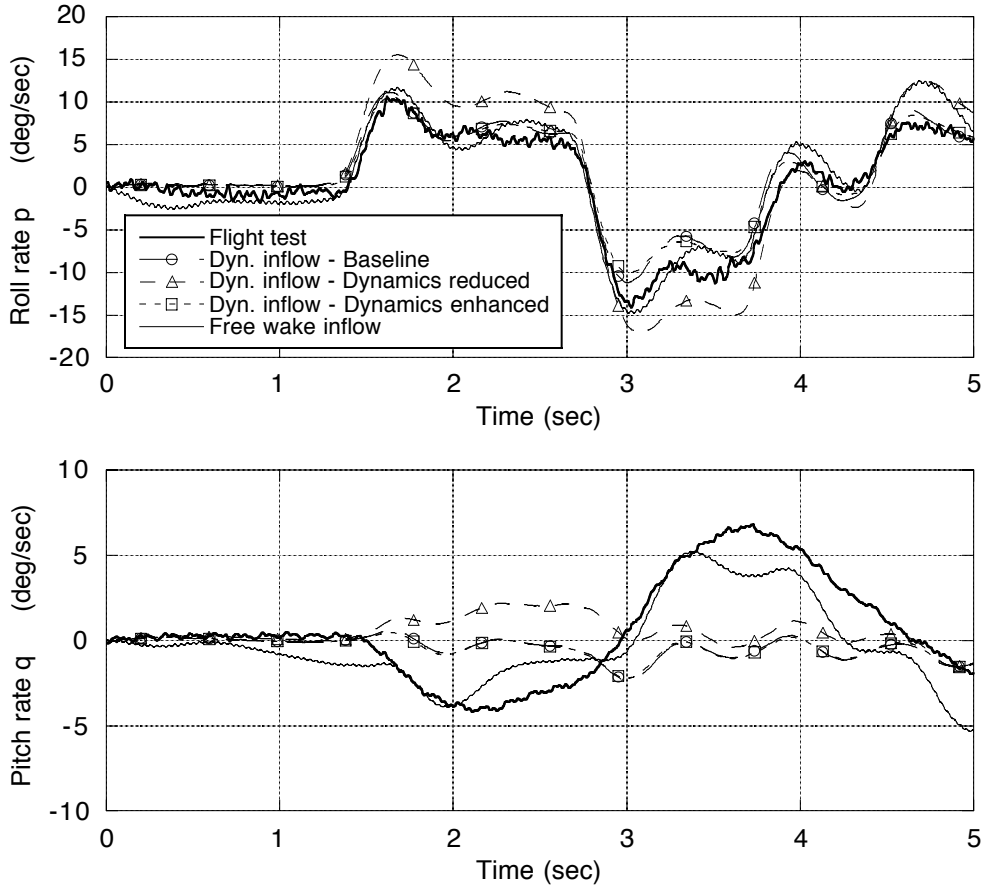

Figure 9.32: Effect of inflow dynamics or unsteadiness on the roll and pitch rate responses to the lateral maneuver for the BO-105 at 17 knots.

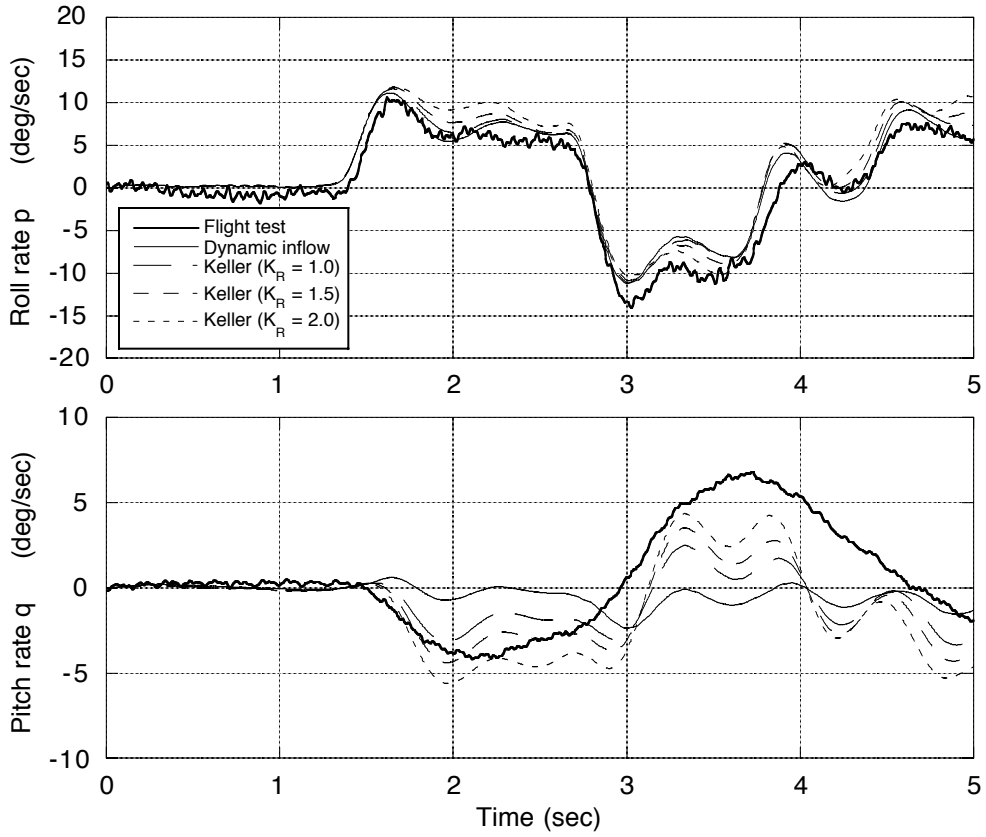

Figure 9.33: Effect of wake distortion parameter K_R within the extended momentum theory model on the roll and pitch rate responses for the BO-105 with the refined blade model.

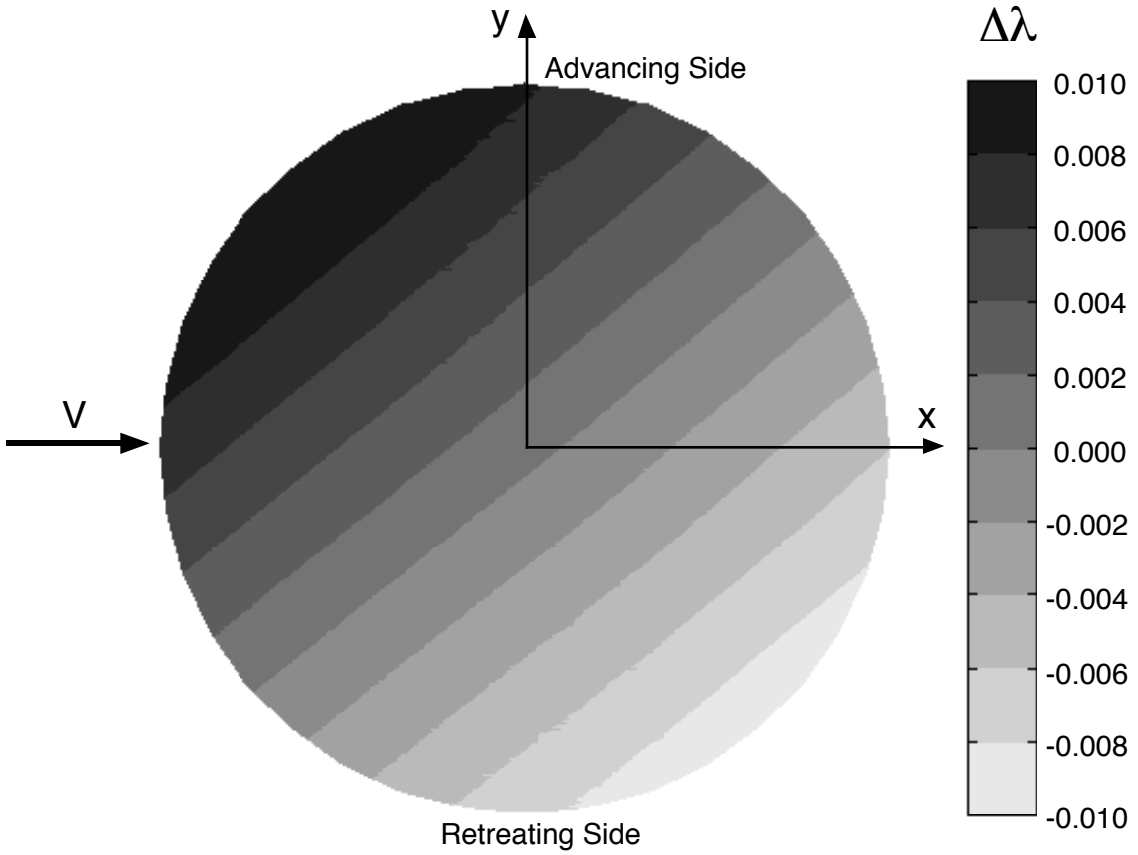

Figure 9.34: Change in inflow with the inclusion of maneuver-induced effects with $K_R = 1.5$ at the 13th rotor revolution for the BO-105 with the refined blade model. Baseline with dynamic inflow and no maneuver-induced effects.

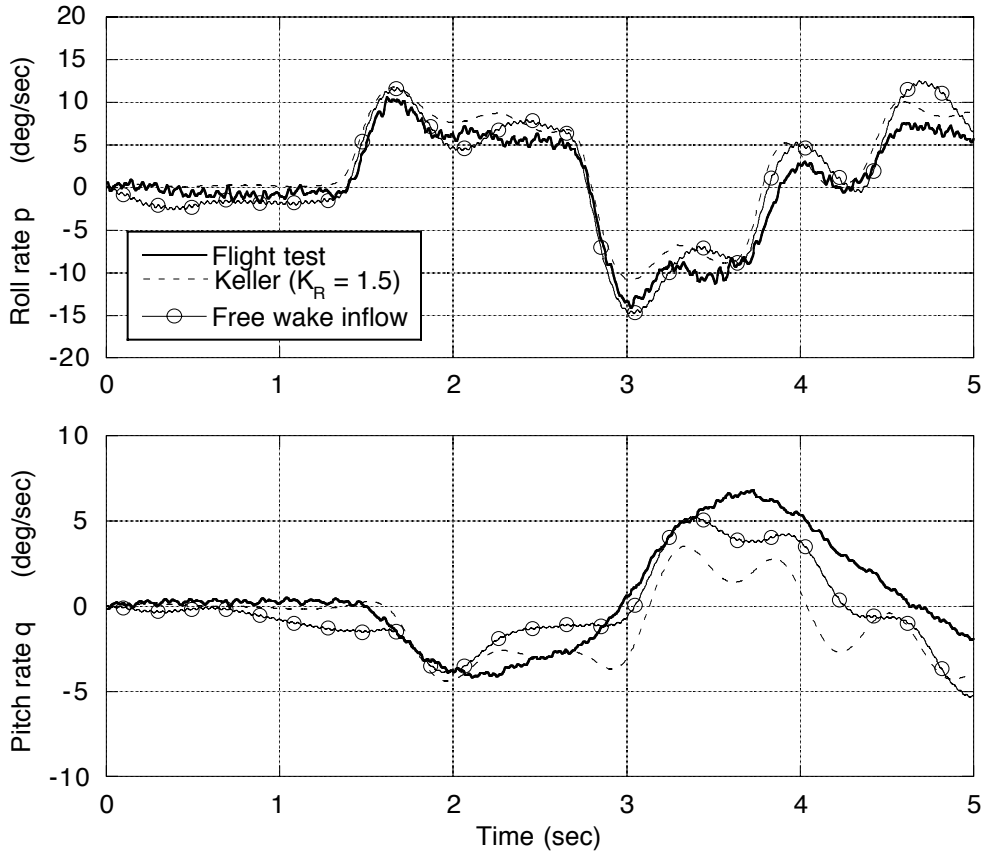

Figure 9.35: Effect of inflow model on roll and pitch rate responses for the BO-105 with the refined blade model.

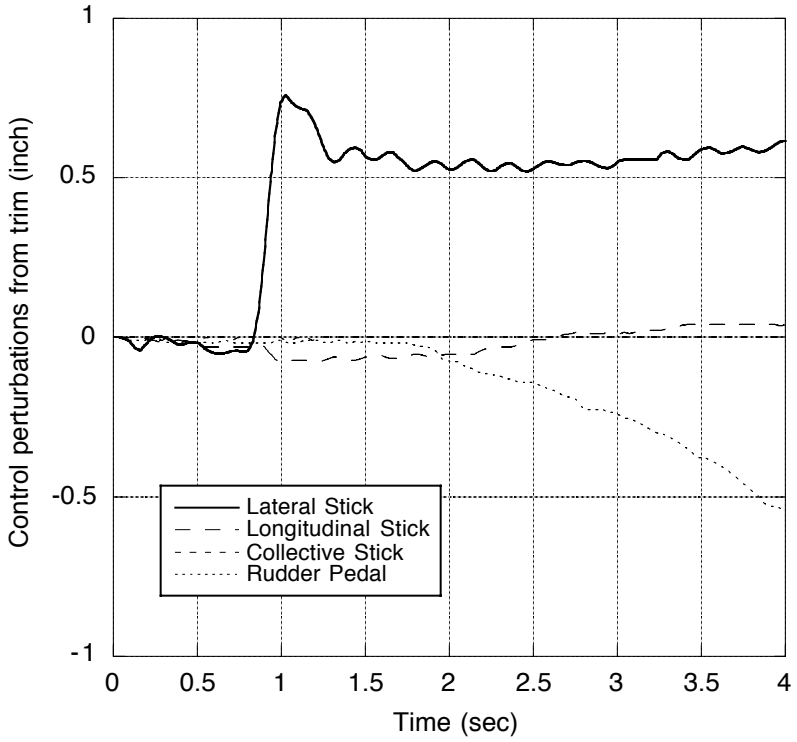

Figure 9.36: Control deflections from trim for the selected maneuver for the UH-60A in hover.

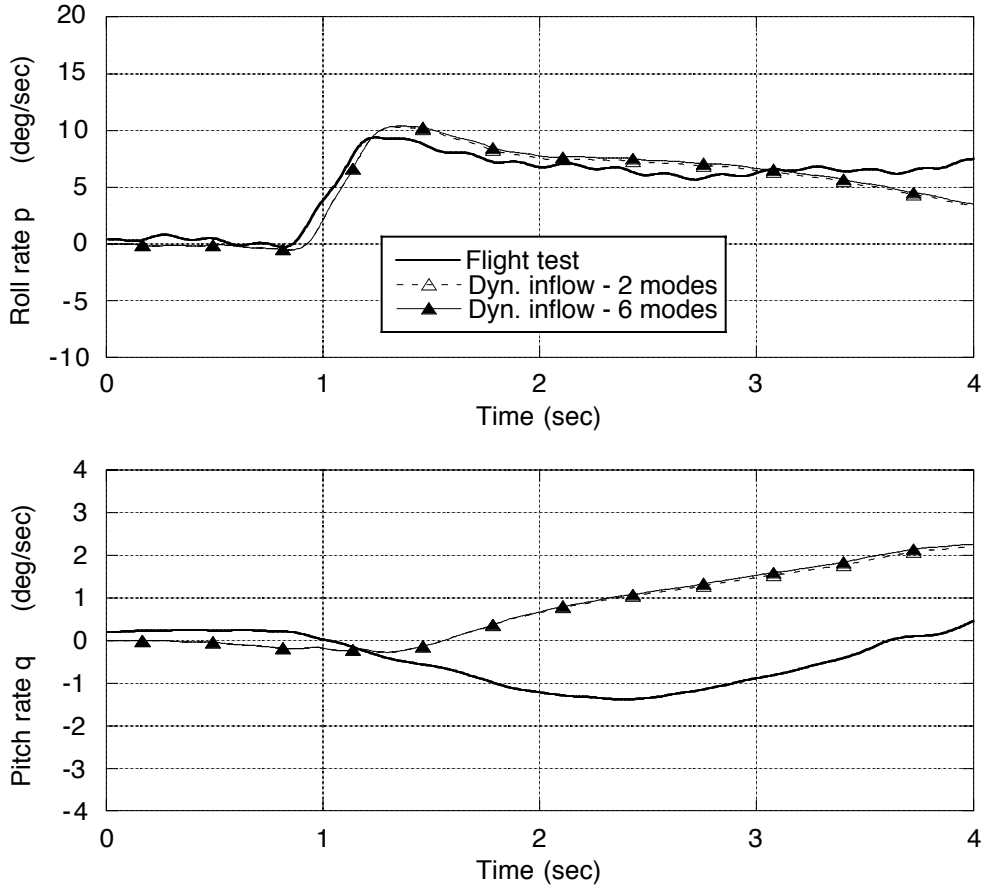

Figure 9.37: Effect of blade modeling on the roll and pitch rate responses to the lateral maneuver for the UH-60A from hover with dynamic inflow.

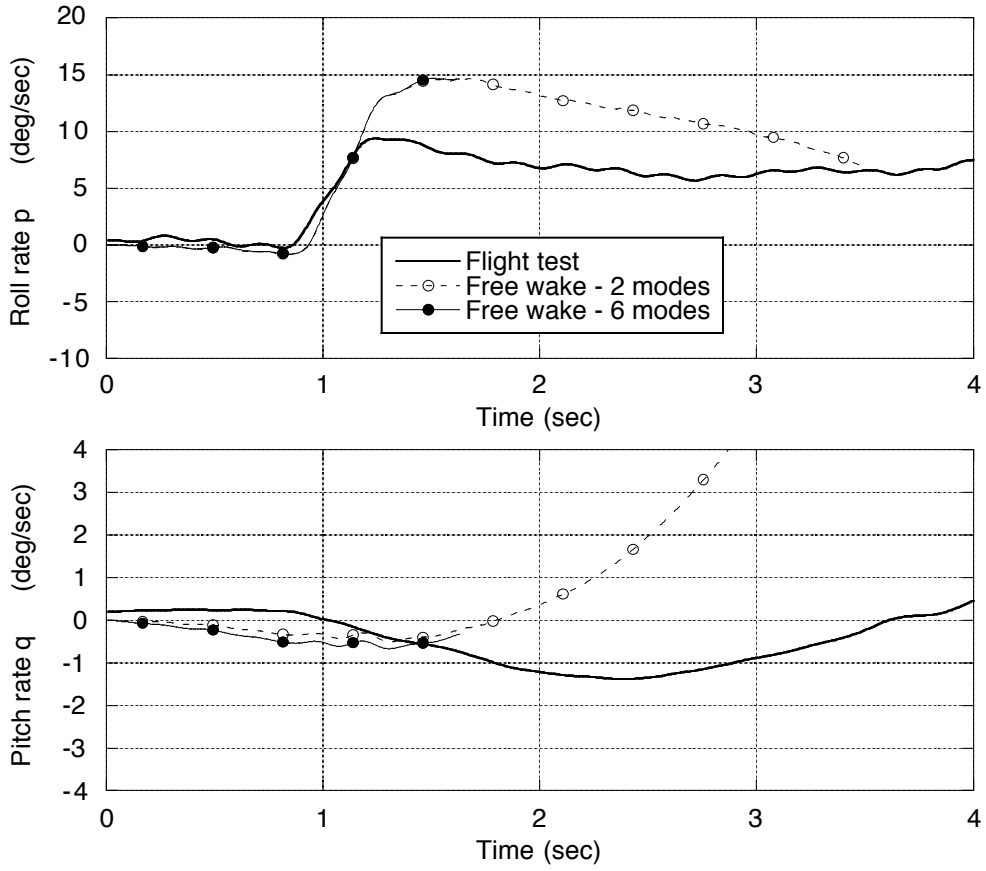

Figure 9.38: Effect of blade modeling on the roll and pitch rate responses to the lateral maneuver for the UH-60A from hover with the free wake and $\Delta\psi = 10$ degrees.

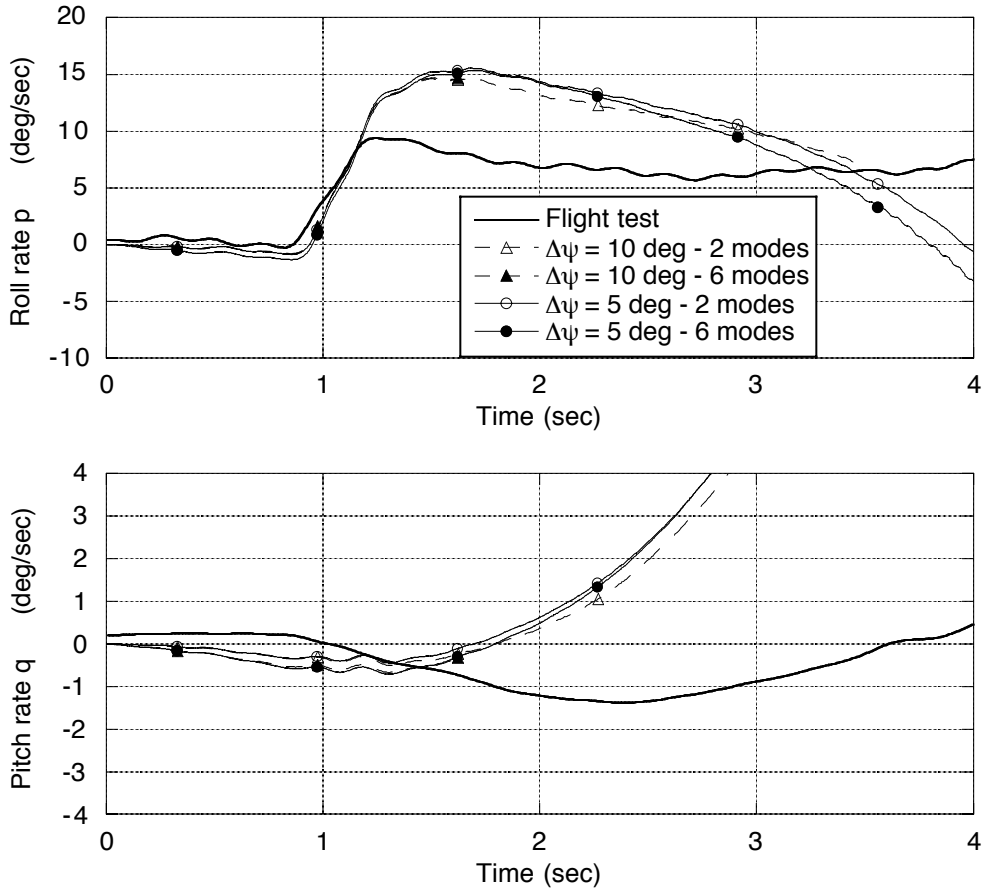

Figure 9.39: Effect of free vortex wake resolution on the roll and pitch rate responses to the lateral maneuver for the UH-60A from hover.

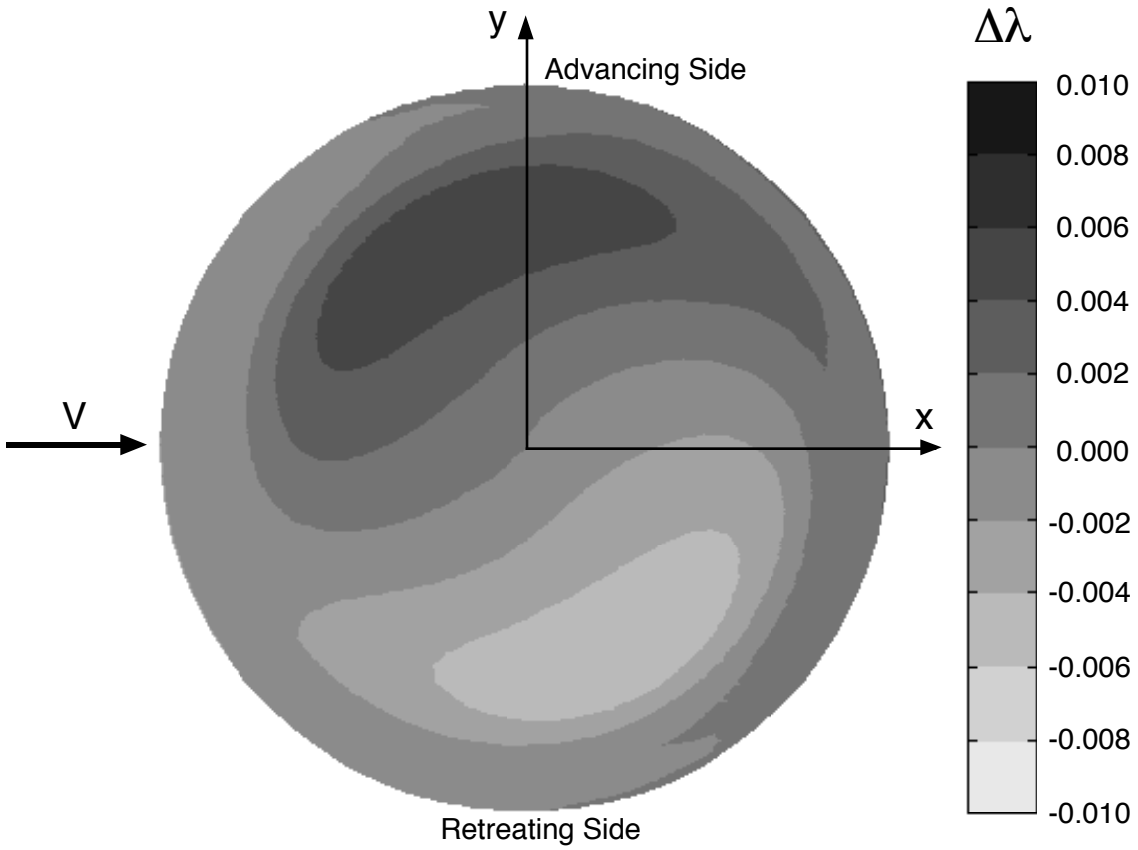

Figure 9.40: Change in inflow distribution from hover to the start of the 7th rotor revolution for the UH-60A from hover with the refined blade model. Baseline is trim inflow.

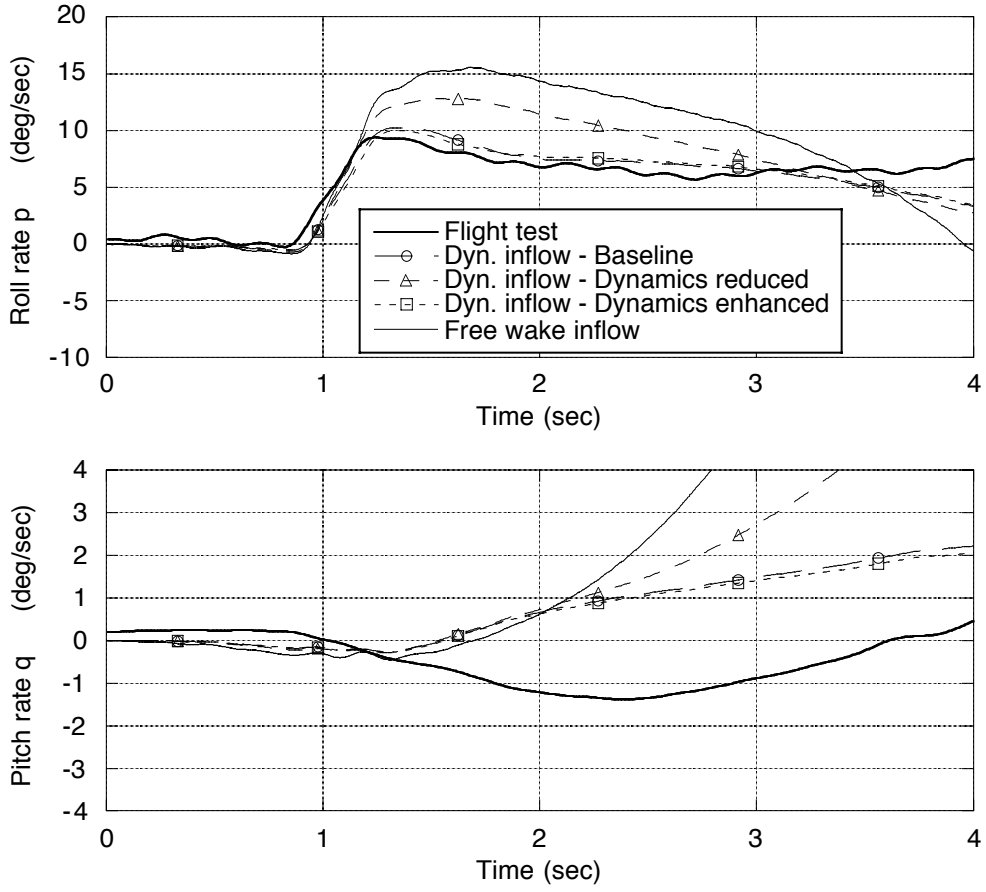

Figure 9.41: Effect of inflow dynamics or unsteadiness on the roll and pitch rate responses to the lateral maneuver for the UH-60A from hover.

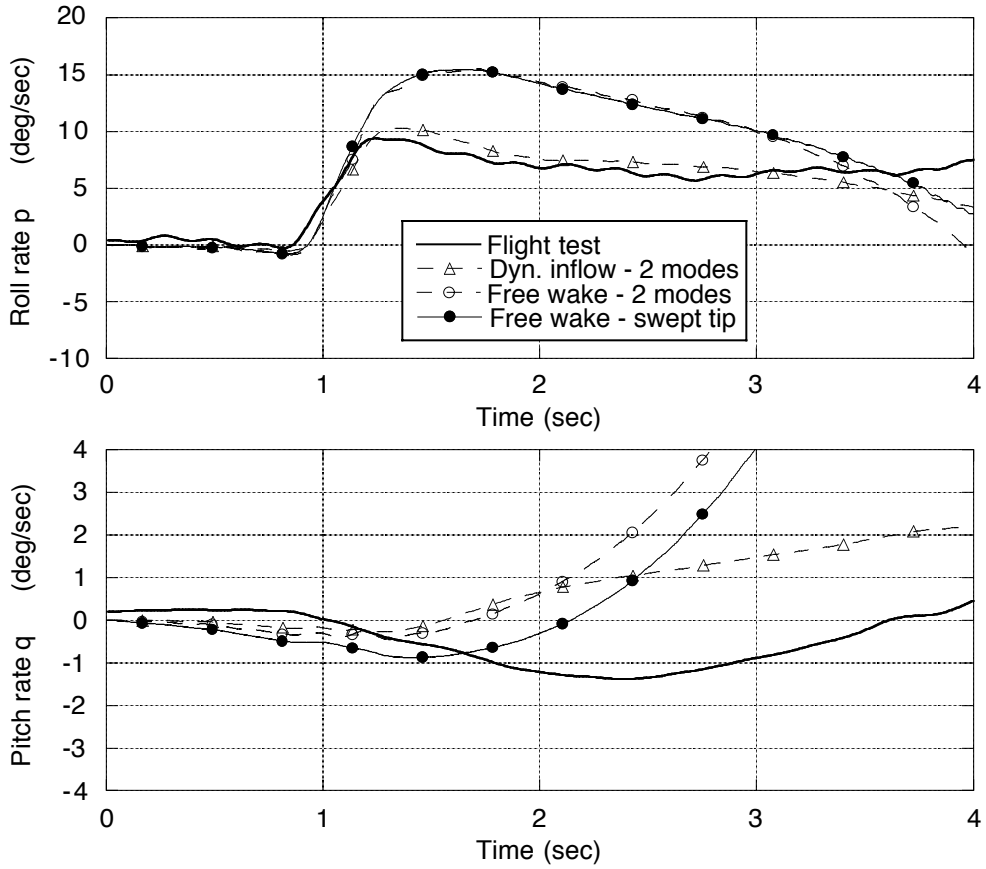

Figure 9.42: Effect of inclusion of tip sweep roll and pitch rate responses to the lateral maneuver for the UH-60A from hover with the free wake. Blade model with tip sweep includes two flap modes and one torsion mode.

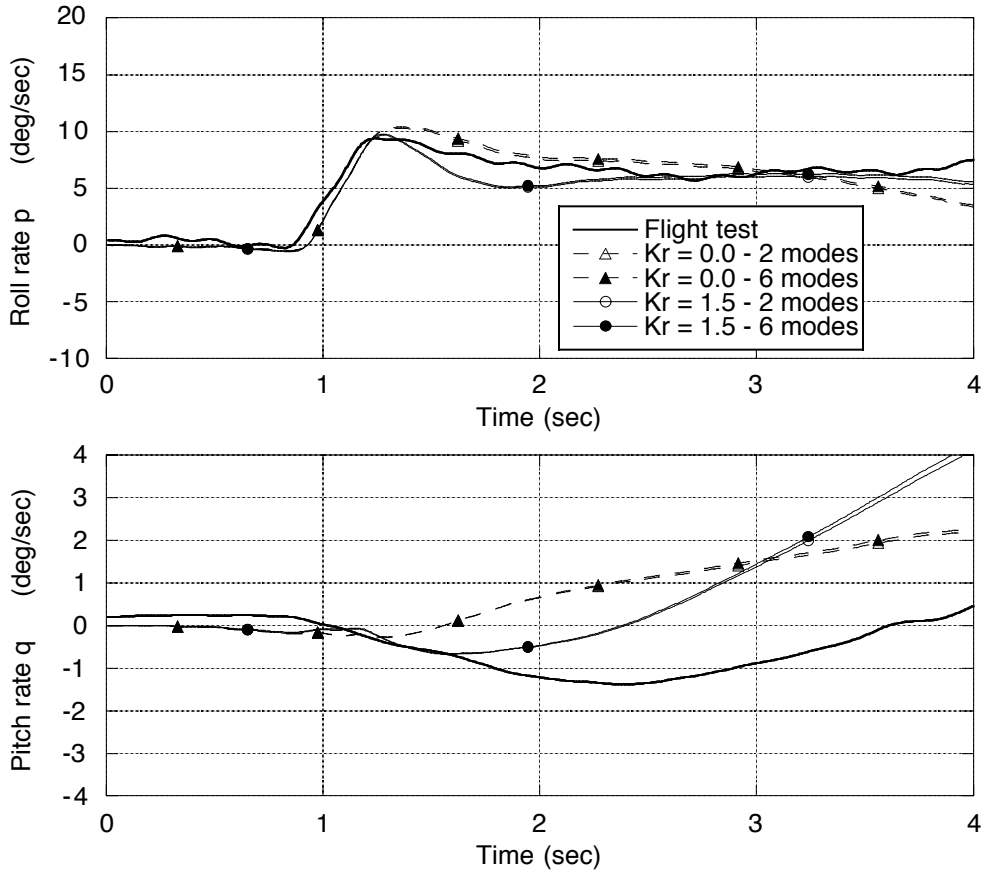

Figure 9.43: Effect of wake distortion parameter K_R within the extended momentum theory model on the roll and pitch rate responses for the UH-60A with the refined blade model.

Chapter 10

Summary and Conclusions

A coupled rotor-fuselage flight dynamic model has been developed that includes a maneuvering free wake model and a coupled flap-lag-torsion flexible blade model. The model has been used to investigate effects of inflow and blade modeling on the prediction of various flight dynamic characteristics for both articulated and hingeless rotor helicopters. The inclusion of the free wake model required new numerical procedures for the calculation of trim equilibrium positions, for the extraction of high-order, constant coefficient linear equations, and for the calculation of free flight time history responses to arbitrary pilot inputs.

With respect to the extraction of high-order linearized models using the free wake, it should be kept in mind that the free wake has no predefined states or equations that can be perturbed, and therefore no inflow dynamics is modeled. The new linearization procedure indirectly perturbs the free wake model when the perturbations of each of the state and control variables are performed. Therefore, the effects of the free wake equations are included within the resulting linearized models without the addition of state variables. However, no unsteadiness or dynamics associated with the inflow is rigorously modeled.

With respect to the calculation of the dynamic time responses with the free

wake, which is rigorously valid for a steady flight condition only, the assumption is made that a "steady state" condition exists each time the free wake model inflow is calculated. The new time integration procedure stops the integration of the equations of motion at specific intervals of the integration, at which time the inflow is updated using the free wake model.

Results were presented for two distinct configurations: an articulated rotor configuration based on the UH-60A and a hingeless rotor configuration based on the BO-105. For both of these configurations, results were presented for trim, stability poles, frequency responses and dynamic time history responses to pilot inputs. The effects of inflow and blade modeling on each of the particular results were presented, and the simulation results were compared with actual flight test data where such data were available. The effects of turn rate and turn direction on the trim state and frequency response characteristics were studied for the UH-60A. This new model provided a valuable tool for the investigation of the effects of inflow and blade modeling on specific helicopter responses. In particular, an investigation of the off-axis response or cross-coupling was performed, and it was possible to draw specific conclusions regarding the level of modeling sophistication required in flight dynamics codes to improve the accuracy of the off-axis predictions.

Based on the results presented in this dissertation, the following conclusions can be drawn:

1. The use of the free wake model significantly improves the predictions of the helicopter trim state for both configurations considered. This was especially true in low speed flight and hover. The most significant improvements were seen in the predictions of the main rotor collective and power required by the rotor, which were significantly under-predicted when using dynamic inflow.

These improvements can be explained by the higher average main rotor inflow generated with the free wake model than that of the dynamic inflow model. As the forward speed increases, the predicted trim state becomes less sensitive to inflow modeling. In high speed forward flight, the type of inflow model does not have a significant effect on the accuracy of the predictions.

2. The initial tip vortex strength was found to have a significant effect on the trim state of the helicopter. The parameter C_Γ is the ratio of the initial tip vortex strength to the maximum bound circulation along the blade. The best correlations with test data were achieved with $C_\Gamma = 0.7$ for the BO-105 and $C_\Gamma = 1.0$ for the UH-60A. At present, the physical mechanisms involved in the formation of the trailed vortex are not fully understood, and so the parameter C_Γ must be derived empirically. The resolution of the vortex wake does not effect the predicted trim state. However, the wake resolution significantly affects the convergence characteristics of the wake model. With low wake resolution, wake convergence proved difficult at low speeds unless longer tip vortices were retained in the wake simulation.

3. Using the free wake model, the linearized models extracted from the full set of non-linear equations were found to be particularly sensitive to the numerical perturbation used in the central difference approximation to the derivatives that make up the linear model. The range of perturbations that can be used to correctly capture the free wake effects are, in general, quite small. Careful selection of the values of the numerical perturbations is therefore required.

4. The on-axis frequency responses were not significantly affected by inflow modeling in the frequency range of interest for flight dynamics applications, and the correlations with flight test data were, in general, good. The extended

momentum theory inflow model, which includes maneuver induced wake distortions while retaining inflow dynamics, showed the best predictions of the off-axis frequency responses. The addition of the free wake model did not improve the off-axis response predictions. The probable reason for this is the lack of inflow dynamics or unsteadiness associated with the free wake model.

5. For the BO-105, the free flight on-axis response to pilot inputs can be predicted with good accuracy with a relatively unsophisticated model; neither a free wake nor a refined flexible blade model are required. It is also possible to predict the off-axis response from first principles, that is, without empirically derived correction factors and without assumptions on the wake geometry. To do so, however, requires a more sophisticated modeling capability. Both a free wake model that includes the wake distortions caused by the maneuver and a refined flexible blade model must be used.

6. For hingeless rotor helicopters, it appears that most features of the off-axis response can be captured by using a dynamic inflow theory extended to account for maneuver-induced wake distortions, and for a fraction of the cost of using a free wake model. The most cost-effective strategy, for typical flight dynamic analyses and if vibratory loads are not required, is probably to calibrate such a theory using the more accurate free wake-based model, and then use it in all further calculations.

7. For the UH-60A, the free flight dynamic responses to pilot inputs appear to be sensitive to inflow dynamics. While dynamic inflow models accurately predict the on-axis response, the use of the free wake model leads to the on-axis response being over-predicted. This over-prediction was not affected by blade modeling while the lack of inflow dynamics or unsteadiness associated with

the free wake model was shown to contribute to the on-axis response over-prediction. The lack of accuracy of the on-axis response predictions for the UH-60A using the free wake leads to similar differences in the off-axis response. Although, the inclusion of the swept tip region leads to some improvements in the off-axis response predictions, at least initially. Further investigation is therefore required into the dynamic responses of the UH-60A.

Appendix A

Multiblade Coordinate Transformation

The multiblade coordinate transformation is used to transform the state vector from the rotating frame to the fixed frame and vice versa. Specifically, the multiblade coordinate transformation involves a conversion of the portions of the state vector that correspond to the rotor degrees of freedom.

From Eqn. (3.53) the state vector in the rotating frame is partitioned into a rigid body part, an inflow part and a main rotor part, as follows (for the baseline case with the dynamic inflow model):

$$\mathbf{y} = \left\{ \begin{array}{c} \mathbf{y}_B \\ \mathbf{y}_I \\ \mathbf{y}_R \end{array} \right\} \tag{A.1}$$

where the rigid body $\mathbf{y}_B$ and inflow $\mathbf{y}_I$ parts are given in Eqs. (3.54) and (3.65) respectively.

For a four-bladed rotor and $N_{\rm m}$ blade modes used in the modal coordinate transformation, the main rotor partition of the state vector $\mathbf{y}_R$ is

$$\begin{aligned} \mathbf{y}(\psi)_R \;\; = \;\; & [q_1^1 \; q_2^1 \; q_3^1 \; q_4^1 \; \dot{q}_1^1 \; \dot{q}_2^1 \; \dot{q}_3^1 \; \dot{q}_4^1 \\ & \ldots q_1^{N_{\rm m}} \; q_2^{N_{\rm m}} \; q_3^{N_{\rm m}} \; q_4^{N_{\rm m}} \; \dot{q}_1^{N_{\rm m}} \; \dot{q}_2^{N_{\rm m}} \; \dot{q}_3^{N_{\rm m}} \; \dot{q}_4^{N_{\rm m}}]^\top \end{aligned} \tag{A.2}$$

In the non-rotating frame of reference the state vector for a four-bladed rotor and N_{m} blade modes is

$$\begin{aligned}\mathbf{y}_{NR}(\psi) &= [u\ v\ w\ p\ q\ r\ \phi_F\ \theta_F\ \psi_F\ \lambda_0\ \lambda_s\ \lambda_c\ \lambda_t\ q_0^1\ q_{1c}^1\ q_{1s}^1\ q_2^1\ \dot{q}_0^1\ \dot{q}_{1c}^1\ \dot{q}_{1s}^1\ \dot{q}_2^1 \\ &\quad \ldots q_0^{N\mathrm{m}}\ q_{1c}^{N\mathrm{m}}\ q_{1s}^{N\mathrm{m}}\ q_2^{N\mathrm{m}}\ \dot{q}_0^{N\mathrm{m}}\ \dot{q}_{1c}^{N\mathrm{m}}\ \dot{q}_{1s}^{N\mathrm{m}}\ \dot{q}_2^{N\mathrm{m}}]^\top\end{aligned} \tag{A.3}$$

where $q_0^k, q_{1c}^k, q_{1s}^k$, and q_2^k are respectively the collective, longitudinal, lateral, and differential portion of the generalized coordinate of the k-th rotor mode.

The transformation from the rotating frame to the non-rotating frame is

$$\mathbf{y} = \mathbf{T}\mathbf{y}_{NR} \qquad \mathbf{y}_{NR} = \mathbf{T}^{-1}\mathbf{y} \tag{A.4}$$

where $\mathbf{T}$ is the multiblade coordinate transformation matrix from the non-rotating frame to the rotating frame.

The matrix $\mathbf{T}$ can be partitioned in the same way as the state vector (Eqn. (A.1))

$$\mathbf{T} = \begin{bmatrix} \mathbf{T}_B & 0 & 0 \\ 0 & \mathbf{T}_I & 0 \\ 0 & 0 & \mathbf{T}_R \end{bmatrix} \tag{A.5}$$

where

$$\mathbf{T}_B = [I] \qquad (\text{size} = 10 \times 10) \tag{A.6}$$

$$\mathbf{T}_I = [I] \qquad (\text{size} = 3 \times 3) \tag{A.7}$$

and

$$\mathbf{T}_R = \begin{bmatrix} \mathbf{T}_f & & 0 \\ & \ddots & \\ 0 & & \mathbf{T}_f \end{bmatrix} \tag{A.8}$$

where the number of diagonal blocks ($\mathbf{T}_f$) is equal to the number of blade modes used in the modal coordinate transformation.

The block matrix is

$$\mathbf{T}_f = \begin{bmatrix} 1 & \cos\psi & \sin\psi & -1 & 0 & -\Omega\sin\psi & \Omega\cos\psi & 0 \\ 1 & -\sin\psi & \cos\psi & 1 & 0 & -\Omega\cos\psi & -\Omega\sin\psi & 0 \\ 1 & -\cos\psi & -\sin\psi & -1 & 0 & \Omega\sin\psi & -\Omega\cos\psi & 0 \\ 1 & \sin\psi & -\cos\psi & 1 & 0 & \Omega\cos\psi & \Omega\sin\psi & 0 \\ 0 & 0 & 0 & 0 & 1 & \cos\psi & \sin\psi & -1 \\ 0 & 0 & 0 & 0 & 1 & -\sin\psi & \cos\psi & 1 \\ 0 & 0 & 0 & 0 & 1 & -\cos\psi & -\sin\psi & -1 \\ 0 & 0 & 0 & 0 & 1 & \sin\psi & -\cos\psi & 1 \end{bmatrix} \tag{A.9}$$

The perturbation matrices in the non-rotating frame ($\mathbf{A}_{NR}$ and $\mathbf{B}_{NR}$) can be obtained from the perturbation matrices in the rotating frame ($\mathbf{A}$ and $\mathbf{B}$) through the transformations

$$\mathbf{A}_{NR} = \mathbf{T}^{-1}(\mathbf{A}\mathbf{T} - \dot{\mathbf{T}}) \tag{A.10}$$

$$\mathbf{B}_{NR} = \mathbf{T}^{-1}\mathbf{B} \tag{A.11}$$

The multiblade transformation is also used to transform the derivative state vector from the rotating frame to the non-rotating frame. This transformation only effects the portions of the derivative vector related to the rotor degrees of freedom.

As in Eqn. A.1, the derivative vector in the fixed frame is partitioned into a rigid body part, and a main rotor part, as follows (with the inflow part removed since the transformation is only used when the free wake model is used):

$$\dot{\mathbf{y}} = \left\{ \begin{array}{c} \dot{\mathbf{y}}_B \\ \dot{\mathbf{y}}_R \end{array} \right\} \tag{A.12}$$

For a four bladed rotor and N_{m} blade modes used in the modal coordinate transformation, the main rotor portion of the derivative vector $\dot{\mathbf{y}}_R$ is:

$$\begin{aligned} \mathbf{y}(\psi)_R = [&\dot{q}_1^1\ \dot{q}_2^1\ \dot{q}_3^1\ \dot{q}_4^1\ \ddot{q}_1^1\ \ddot{q}_2^1\ \ddot{q}_3^1\ \ddot{q}_4^1 \\ &\ldots \dot{q}_1^{N_{\mathrm{m}}}\ \dot{q}_2^{N_{\mathrm{m}}}\ \dot{q}_3^{N_{\mathrm{m}}}\ \dot{q}_4^{N_{\mathrm{m}}}\ \ddot{q}_1^{N_{\mathrm{m}}}\ \ddot{q}_2^{N_{\mathrm{m}}}\ \ddot{q}_3^{N_{\mathrm{m}}}\ \ddot{q}_4^{N_{\mathrm{m}}}]^\top \end{aligned} \tag{A.13}$$

The transformation from the rotating to non-rotating frames is:

$$\dot{\mathbf{y}}_{NR} = \mathbf{T}_{d1}\dot{\mathbf{y}} + \mathbf{T}_{d2}\mathbf{y} \tag{A.14}$$

where $\mathbf{T}_{d1}$ and $\mathbf{T}_{d2}$ are the multiblade coordinate transformation matrices and are given by:

$$\mathbf{T}_{d1} = \begin{bmatrix} \mathbf{T}_B & 0 \\ 0 & \mathbf{T}_{R1} \end{bmatrix} \tag{A.15}$$

$$\mathbf{T}_{d2} = \begin{bmatrix} 0 & 0 \\ 0 & \mathbf{T}_{R2} \end{bmatrix} \tag{A.16}$$

where

$$\mathbf{T}_B = [I] \qquad (\text{size} = 10 \times 10) \tag{A.17}$$

and

$$\mathbf{T}_{R1} = \begin{bmatrix} \mathbf{T}_g & & 0 \\ & \ddots & \\ 0 & & \mathbf{T}_g \end{bmatrix} \tag{A.18}$$

$$\mathbf{T}_{R2} = \begin{bmatrix} \mathbf{T}_h & & 0 \\ & \ddots & \\ 0 & & \mathbf{T}_h \end{bmatrix} \tag{A.19}$$

where the number of diagonal blocks ($\mathbf{T}_g$ and $\mathbf{T}_g$) is equal to the number of blade modes used in the modal coordinate transformation.

The block matrices are (for a four-bladed rotor)

$$\mathbf{T}_g = \frac{1}{4} \begin{bmatrix} 1 & 1 & 1 & 1 & 0 & 0 & 0 & 0 \\ 2C_1 & 2C_2 & 2C_3 & 2C_4 & 0 & 0 & 0 & 0 \\ 2S_1 & 2S_2 & 2S_3 & 2S_4 & 0 & 0 & 0 & 0 \\ 1 & -1 & 1 & -1 & 0 & 0 & 0 & 0 \\ 0 & 0 & 0 & 0 & 1 & 1 & 1 & 1 \\ -2\Omega S_1 & -2\Omega S_2 & -2\Omega S_3 & -2\Omega S_4 & 2C_1 & 2C_2 & 2C_3 & 2C_4 \\ 2\Omega C_1 & 2\Omega C_2 & 2\Omega C_3 & 2\Omega C_4 & 2S_1 & 2S_2 & 2S_3 & 2S_4 \\ 0 & 0 & 0 & 0 & 1 & -1 & 1 & -1 \end{bmatrix} \tag{A.20}$$

$$\mathbf{T}_h = \frac{1}{4} \begin{bmatrix} 0 & 0 & 0 & 0 & 0 & 0 & 0 & 0 \\ -2\Omega \sin\psi_1 & -2\Omega \sin\psi_2 & -2\Omega \sin\psi_3 & -2\Omega \sin\psi_4 & 0 & 0 & 0 & 0 \\ 2\Omega \cos\psi_1 & 2\Omega \cos\psi_2 & 2\Omega \cos\psi_3 & 2\Omega \cos\psi_4 & 0 & 0 & 0 & 0 \\ 0 & 0 & 0 & 0 & 0 & 0 & 0 & 0 \\ 0 & 0 & 0 & 0 & 0 & 0 & 0 & 0 \\ L_1(\psi_1) & L_1(\psi_2) & L_1(\psi_3) & L_1(\psi_4) & 0 & 0 & 0 & 0 \\ L_2(\psi_1) & L_2(\psi_2) & L_2(\psi_3) & L_2(\psi_4) & 0 & 0 & 0 & 0 \\ 0 & 0 & 0 & 0 & 0 & 0 & 0 & 0 \end{bmatrix} \tag{A.21}$$

where

$$C_1 = \cos(\psi_1) \tag{A.22}$$

$$C_2 = \cos(\psi_2) \tag{A.23}$$

$$C_3 = \cos(\psi_3) \tag{A.24}$$

$$C_4 = \cos(\psi_4) \tag{A.25}$$

$$S_1 = \sin(\psi_1) \tag{A.26}$$

$$S_2 = \sin(\psi_2) \tag{A.27}$$

$$S_3 = \sin(\psi_3) \tag{A.28}$$

$$S_4 = \sin(\psi_4) \tag{A.29}$$

$$L_1(\psi) = -2\dot{\Omega}\sin\psi - 2\Omega^2\cos\psi \tag{A.30}$$

$$L_2(\psi) = 2\dot{\Omega}\cos\psi - 2\Omega^2\sin\psi \tag{A.31}$$

Bibliography

[1] Bagai, A. and Leishman, J. G., "Rotor Free-Wake Modeling using a Relaxation Technique – Including Comparisons with Experimental Data," *Proceedings of the 50th Annual American Helicopter Society Forum*, Washington D.C., May 1994.

[2] Anon., "Handling Qualities Requirements For Military Rotorcraft," U.S. Army AVSCOM Aeronautical Design Standard, ADS-33C, Aug. 1989.

[3] Howlett, J. J., "UH-60A Black Hawk Engineering Simulation Program - Volume II - Mathematical Model," NASA CR-166309, Dec. 1981.

[4] Ballin, M. G. and Dalang-Secretan, M. A., "Validation of the Dynamic Response of a Blade-Element UH-60 Simulation Model in Hovering Flight," *Proceedings of the 46th Annual American Helicopter Society Forum*, Washington D.C., May 1990.

[5] Kim, F. D., Celi, R., and Tischler, M. B., "High-Order State Space Simulation Models of Helicopter Flight Mechanics," *Journal of the American Helicopter Society*, Vol. 38, No. 4, Oct. 1993, pp. 16–27.

[6] Pitt, D. M. and Peters, D. A., "Theoretical Prediction of Dynamic Inflow Derivatives," *Vertica*, Vol. 5, No. 1, 1981, pp. 21–34.

[7] Peters, D. A. and HaQuang, N., "Dynamic Inflow for Practical Applications," *Journal of the American Helicopter Society*, Vol. 33, No. 4, Oct. 1988, pp. 64–68.

[8] Turnour, S. R. and Celi, R., "Modeling of Flexible Rotor Blades for Helicopter Flight Dynamics Applications," *Journal of the American Helicopter Society*, Vol. 41, No. 1, Jan. 1996, pp. 52–66; Correction in Vol. 41, No. 3, Jul 1996, pp. 191–194.

[9] Celi, R., "Helicopter Rotor Blade Aeroelasticity in Forward Flight with an Implicit Structural Formulation," *AIAA Journal*, Vol. 30, No. 9, Sept. 1992, pp. 2274–2282.

[10] Peters, D. A., Boyd, D. D., and He, C. J., "Finite-State Induced-Flow Model for Rotors in Hover and Forward Flight," *Journal of the American Helicopter Society*, Vol. 34, No. 4, Oct. 1989, pp. 5–17.

[11] Peters, D. A. and He, C. J., "Correlation of Measured Induced Velocities with a Finite-State Wake Model," *Journal of the American Helicopter Society*, Vol. 36, No. 3, July 1991, pp. 59–70.

[12] Leishman, J. G. and Nguyen, K. Q., "State Space Representation of Unsteady Airfoil Behavior," *AIAA Journal*, Vol. 28, No. 5, May 1990, pp. 836–844.

[13] Bagai, A., Leishman, J. G., and Park, J., "Aerodynamic Analysis of a Helicopter in Steady Maneuvering Flight Using a Free-Vortex Rotor Wake Model," *Journal of the American Helicopter Society*, Vol. 44, No. 2, April 1999, pp. 109–120.

[14] Shamie, J. and Friedmann, P. P., "Effect of Moderate Deflections on the Aeroelastic Stability of a Rotor Blade in Forward Flight," *Proceedings of the 3rd Annual European Rotorcraft and Powered Lift Aircraft Forum*, Aixen-Provence, France, Sept. 1977.

[15] Keller, J. D., "An Investgation of Helicopter Dynamic Coupling Using an Analytical Model," *Journal of the American Helicopter Society*, Vol. 41, No. 4, Oct. 1996, pp. 322–330.

[16] Keller, J. D. and Curtiss, H. C. Jr., "Flight Dynamic Simulation of Hingeless Rotor Helicopters Including a Maneuvering Free Wake Model," *Presented at the 54th Annual American Helicopter Society Forum*, Washington D.C., May 1998.

[17] Arnold, U. T. P., Keller, J. D., Curtiss, H. C. Jr., and Riechert, G., "The Effect of Inflow Models on the Predicted Response of Helicopters," *Journal of the American Helicopter Society*, Vol. 43, No. 1, Jan. 1998, pp. 25–36.

[18] Ormiston, R. A., Rutkowski, M. J., Ruzicka, G. C., Saberi, H., and Jung, Y., "Comprehensive Aeromechanics Analysis of Complex Rotorcraft Using 2GCHAS," *Proceedings of the American Helicopter Society Aeromechanics Specialists Conference*, San Fransisco, California, Jan. 1994.

[19] Yen, J. G., Corrigan, J. J., Schillings, J. J., and Hsieh, P. Y., "Comprehensive Analysis Methodology at Bell Helicopter: COPTER," *Proceedings of the American Helicopter Society Aeromechanics Specialists Conference*, San Fransisco, California, Jan. 1994.

[20] Johnson, W., "A Comprehensive Analytical Model of Rotorcraft Aerodynamics and Dynamics, Volume I: Theory Manual, Volume II: User's Manual," Johnson Aeronautics, Palo Alto, CA, 1988.

[21] Johnson, W., "Technology Drivers in the Development of CAMRAD II," *Proceedings of the American Helicopter Society Aeromechanics Specialists Conference*, San Fransisco, California, Jan. 1994.

[22] Shultz, L. A., Panda, B., Tarzanin, F. J., Derham, R. C., Oh, B. K., and Danone, L., "Interdisciplinary Analysis For Advanced Rotors – Approach, Capabilities and Status," *Proceedings of the American Helicopter Society Aeromechanics Specialists Conference*, San Fransisco, California, Jan. 1994.

[23] DuVal, R., "A Real-Time Blade Element Helicopter Simulation for Handling Qualities Analysis," *Proceedings of the 15th Annual European Rotorcraft Forum*, Amsterdam, The Netherlands, Sept. 1989.

[24] Bir, G. S., Chopra, I., Ganguli, R., Ganguli, R., Smith, E. C., Vellaichamy, S., Wang, J., Kim, K. C., Chan, W. Y., Nixon, M. W., Kimata, N. W., Smith, J. A., Torok, M., and Nguyen, K. Q., "University of Maryland Advanced Rotorcraft Code (UMARC)," Theory Manual, Center for Rotorcraft Education and Research, University of Maryland, College Park, MD, July 1994.

[25] Bir, G. and Chopra, I., "Status of University of Maryland Advanced Rotorcraft Code (UMARC)," *Proceedings of the American Helicopter Society Aeromechanics Specialists Conference*, San Fransisco, California, Jan. 1994.

[26] Dress, J. M., "A Theory of Airflow Through Rotors and Its Application to some Helicopter Problems," *Journal of the Helicopter Association of Great Britian*, Vol. 3, No. 2, July 1949.

[27] Scully, M. P., "A Model of Computing Helicopter Vortex Wake Distortion," Massachusetts Institde of Technology, Aeroelastic Research Laboratory, Report ASRL TR-138-1, Cambridge, MA, June 1967.

[28] Peters, D. A. and Hohenemser, K. H., "Application of the Floquet Transition Matrix to the Problems of Lifting Rotor Stability," *Journal of the American Helicopter Society*, Vol. 16, No. 2, April 1971, pp. 25–33.

[29] Kaplan, W., *Operational Methods of Linear Systems.* Addison Wesley, 1962.

[30] He, C. J. and Lewis, W. D., "A Parametric Study of Real-Time Mathematical Modeling Incorporating Dynamic Wake and Elastic Blades," *Proceedings of the 48th Annual American Helicopter Society Forum*, Washington D.C., May 1992.

[31] Choi, K., He, C. J., and Du Val, R. W., "Comprehensive Comparisons of Rotormap and Blade Element Models," *Journal of the American Helicopter Society*, Vol. 44, No. 1, Jan. 1999, pp. 42–49.

[32] Ballin, M. G., "Validation of a Real-Time Engineering Simulation of the UH-60A Helicopter," NASA TM-88360, 1987.

[33] Turnour, S. R., Flight Dynamics Modeling of Hingeless and Bearingless Rotor Helicopters, Ph.D. Dissertation, Department of Aerospace Engineering, University of Maryland, College Park, MD, 1996.

[34] Johnson, W., "Recent Developments in the Dynamics of Advanced Rotor Systems," *Vertica*, Vol. 10, No. 1, 1986, (Part I), and Vol. 10, No. 2, 1986, (Part II).

[35] Ormiston, R. A., Warmbrodt, W. G., Hodges, D. H., and Peters, D. A., "Rotorcraft Aeroelastic Stability," *Proceedings of the NASA/Army Rotorcraft Tech-*

nology Conference, Vol. I - Aerodynamics, Dynamics and Aeroelasticity, NASA Conference Publication 2495, Feb. 1988.

[36] Friedmann, P. P., "Helicopter Rotor Dynamics and Aeroelasticity – Some Key Ideas and Insights," *Vertica*, Vol. 14, No. 1, 1990, pp. 101–121.

[37] Chopra, I., "Perspectives in Aeromechanical Stability of Helicopter Rotors," *Vertica*, Vol. 14, No. 4, 1990, pp. 457–508.

[38] Millott, T. A., Friedmann, P. P., and Yuan, K. A., "Correlation Studies for Hingeless Rotors in Forward Flight Using 2GCHAS," *Journal of the American Helicopter Society*, Vol. 43, No. 3, July 1998, pp. 257–262.

[39] Greenberg, J. M., "Airfoil in Simusoidal Motion in a Pulsating Stream," NACA-TN 1326, 1947.

[40] Ganguli, R., Chopra, I., and Weller, W. H., "Comparison of Calculated Rotor Hub Loads With Experimental Data," *Journal of the American Helicopter Society*, Vol. 43, No. 4, Oct. 1998, pp. 312–318.

[41] Srinivas, V., "The UM Free Wake Model in UMARC," Report UM-AERO 95-26, University of Maryland, College Park, MD, 1995.

[42] Milgram, J., Chopra, I., and Straub, F., "Rotors With Trailing Edge Flaps: Analysis and Comparison With Experimental Data," *Journal of the American Helicopter Society*, Vol. 43, No. 4, Oct. 1998, pp. 319–332.

[43] Chunduru, S. J., Subramamian, S., and Goankar, G. H., "Dynamic Stall and Wake Effects on Trim and Stability of Hingeless Rotors with Experimental Correlation," *Journal of the American Helicopter Society*, Vol. 42, No. 4, Oct. 1997, pp. 370–382.

[44] Nagabhushanam, J. and Gaonkar, G. H., "Hingeless-Rotor Aeromechanical Stability in Axial and Forward Flight With Wake Dynamics," *Journal of the American Helicopter Society*, Vol. 44, No. 3, July 1999, pp. 222–233.

[45] Torok, M. S. and Chopra, I., "Hingeless Rotor Aeroelastic Stability Analysis With Refined Aerodynamic Modeling," *Journal of the American Helicopter Society*, Vol. 36, No. 4, Oct. 1991.

[46] Milgram, J. and Chopra, I., "Air Resonance of Hingeless Rotor Helicopters in Trimmed Forward Flight," *Journal of the American Helicopter Society*, Vol. 39, No. 4, Oct. 1994, p. ????

[47] Gaonkar, G. H. and Peters, D. A., "Effectiveness of Current Dynamic-Inflow Models in Hover and Forward Flight," *Journal of the American Helicopter Society*, Vol. 31, No. 2, April 1986, pp. 47–57.

[48] Gaonkar, G. H. and Peters, D. A., "Review of Dynamic Inflow Modeling for Rotorcraft Flight Dynamics," *Vertica*, Vol. 12, No. 3, 1988, pp. 213–242.

[49] Chen, R. T. N., "A Survey of Nonuniform Inflow Models for Rotorcraft Flight Dynamics and Control Applications," *Proceedings of the 15th Annual European Rotorcraft Forum*, Amsterdam, The Netherlands, Sept. 1989.

[50] Bagai, A., Contributions to the Mathematical Modeling of Rotor Flow-Fields Using a Pseudo-Implicit Free-Wake Analysis, Ph.D. Dissertation, Department of Aerospace Engineering, University of Maryland, College Park, MD, 1995.

[51] Landgrebe, A. J., "The Wake Geometry of a Hovering Helicopter Rotor and Its Influence on Rotor Performance," *Journal of the American Helicopter Society*, Vol. 17, No. 4, Oct. 1972, pp. 3–15.

[52] Miller, W. O. and Bliss, D. B., "Direct Periodic Solutions of Rotor Free Wake Calculations By Inversion of a Linear Periodic System," *Proceedings of the 46th Annual American Helicopter Society Forum*, Washington D.C., May 1990.

[53] Hoad, D. R., Althoff, S. L., and Elliott, J. W., "Rotor Inflow Variability with Advance Ratio," *Proceedings of the 44th Annual American Helicopter Society Forum*, Washington D.C., June 1988.

[54] Ghee, T. A. and Elliott, J. W., "The Wake of a Small-Scale Rotor in Forward Flight Using Flow Visualization," *Journal of the American Helicopter Society*, Vol. 40, No. 3, July 1995, pp. 52–65.

[55] Chen, R. T. N. and Jeske, J. A., "Kinematic Properties of the Helicopter in Coordinated Turns," NASA Technical Papers 1773, April 1981.

[56] Kim, F. D., Formulation and Validation of High-Order Mathematical Models of Helicopter Flight Dynamics, Ph.D. Dissertation, Department of Aerospace Engineering, University of Maryland, College Park, MD, 1991.

[57] Chen, R. T. N., "Flight Dynamics of Rotorcraft in Steep High-g Turns," *Journal of Aircraft*, Vol. 21, No. 1, Jan. 1984.

[58] Spence, A. M. and Celi, R., "Coupled Rotor-Fuselage Dynamics and Aeroelasticity in Turning Flight," *Journal of the American Helicopter Society*, Vol. 40, No. 1, Jan. 1995, pp. 47–58.

[59] Celi, R., "Steady Stall and Compressibility Effects on Hingeless Rotor Aeroelasticity in High-g Turns," *Vertica*, Vol. 14, No. 4, 1990, pp. 509–530.

[60] Celi, R., "Helicopter Rotor Dynamics in Coordinated Turns," *Journal of the American Helicopter Society*, Vol. 36, No. 4, Oct. 1991, pp. 39–47.

[61] Rosen, A. and Isser, A., "A New Model of Rotor Dynamics During Pitch and Roll of a Hovering Helicopter," *Journal of the American Helicopter Society*, Vol. 40, No. 3, July 1995, pp. 17–28.

[62] Basset, P. M., "Modeling of the Dynamic Inflow on the Main Rotor and the Tail Components in Helicopter Flight Mechanics," *Proceedings of the 22nd Annual European Rotorcraft Forum*, Brighton, UK, Sept. 1996.

[63] Basset, P. M. and Tchen-Fo, F., "Study of the Rotor Wake Distortion Effects on the Helicopter Pitch-Roll Cross-Coupling," *Proceedings of the 24nd Annual European Rotorcraft Forum*, Marseilles, France, Sept. 1998.

[64] von Grünhagen, W., "Dynamic Inflow Modeling for Helicopter Rotors and Its Influence on the Prediction of Crosscoupling," *Proceedings of the American Helicopter Society Aeromechanical Specialists' Conference*, Fairfield County, CT, Oct. 1995.

[65] Mansur, M. H. and Tischler, M. B., "An Empirical Correlation Method for Improving Off-Axis Response in Flight Mechanics Helicopter Models," *Journal of the American Helicopter Society*, Vol. 43, No. 2, April 1998, pp. 94–102.

[66] Bagai, A. and Leishman, J. G., "Rotor Free-Wake Modeling using a Pseudo-Implicit Technique – Including Comparisons with Experimental Data," *Journal of the American Helicopter Society*, Vol. 40, No. 3, July 1995, pp. 29–41.

[67] McRuer, D., Ashkenas, I., and Graham, D., *Aircraft Dynamics and Automatic Control*. Princeton University Press, 1973. pp. 203–295.

[68] Rosen, A. and Friedmann, P. P., "Nonlinear Equations of Equilibrium for Elastic Helicopter or Wind Turbine Blades Undergoing Moderate Deflections," NASA CR-159478, Dec. 1978.

[69] Weissinger, J., "The Lift Distribution of Swept-Back Wings," NASA TM-1120, March 1947.

[70] Friedmann, P. P. and Straub, F. K., "Application of the Finite Element Method to Rotary-Wing Aeroelasticity," *Journal of the American Helicopter Society*, Vol. 25, No. 1, Jan. 1980.

[71] Bailey, F. J. Jr., "A Simplified Theoretical Method of Determining the Characteristics of a Lifting Rotor in Forward Flight," NACA Rep. 716, 1941.

[72] Bhagwat, M. J. and Leishman, J. G., "Correlation of Helicopter Rotor Tip Vortex Measurements," *AIAA Journal*, Vol. 38, No. 2, 2000, pp. 301–308.

[73] Dosanjh, D. S., Gasparek, E. P., and Eskinazi, S., "Decay of a Viscous Trailing Vortex," *The Aeronautical Quarterly*, Vol. 3, No. 3, 1962, pp. 167–188.

[74] Bagai, A. and Leishman, J. G., "Rotor Free-Wake Modeling using a Pseudo-Implicit Relaxation Algorithm," *Proceedings of the 12th AIAA Applied Aerodynamics Conference*, Colorado Springs, Colorado, June 1994.

[75] Bagai, A. and Leishman, J. G., "Flow Visualization of Compressible Vortex Structures using Density Gradient Techniques," *Experiments in Fluids*, Vol. 15, 1993, pp. 431–442.

[76] Lamb, S. H., *Hydrodynamics*. Cambridge University Press, 6th ed., 1932.

[77] Kim, F. D., Celi, R., and Tischler, M. B., "Forward Flight Trim Calculation and Frequency Response Validation of a High-Order Helicopter Simulation Model," *Journal of Aircraft*, Vol. 30, No. 6, Nov.-Dec. 1993, pp. 854–863.

[78] More, J. J., Garbow, B. S., and Hillstrom, K. E., *User's Guide for MINPACK-1.* Argonne National Laboratory, Report ANL-80-74, Aug. 1980.

[79] Staley, J. A., "Validation of Rotorcraft Flight Simulation Program Through Correlation with Flight Data for Soft-In-Plane Hingeless Rotors," USAAMRDL-TR-75-50, Jan. 1976.

[80] Padfield, G. D., McCallum, A. T., Haverdings, H., Dequin, A. M., Haddon, D., Kampa, K., Basset, P. M., and von Grünhagen, W., "Predicting Rotorcraft Flying Qualities Through Simulation Modelling. A Review of Key Results from Garteur AG06," *Proceedings of the 21st Annual European Rotorcraft Forum*, Saint-Petersburg, Russia, Aug. 1995.

[81] Abbott, W. Y., Benson, J. O., Oliver, R. G., and Williams, R. A., "Validation Flight Test of UH-60A for Rotorcraft Systems Integration Simulator (RIRS)," Report No. USAAEFA-79-24, U.S. Army Aviation Engineering Flight Activity, July 1982.

[82] Tischler, M. B. and Cauffman, M. G., "Frequence-Response Method for Rotorcraft System Identification with Applications to the BO-105 Helicopter," *Proceedings of the 46th Annual American Helicopter Society Forum*, Washington D.C., May 1990.

[83] Tischler, M. B., "Frequency Response Identification of XV-15 Tilt-Rotor Aircraft Dynamics," NASA Technical Memorandum 89428, May 1987.

[84] Celi, R., "Recent Applications of Design Optimization to Rotorcraft – A Survey," *Journal of Aircraft*, Vol. 36, No. 1, Jan.-Feb. 1999, pp. 176–189.

[85] Hansford, R. E. and Vorwald, J., "Dynamics Workgroup On Rotor Vibratory Loads Prediction," *Journal of the American Helicopter Society*, Vol. 43, No. 1, Jan. 1998, pp. 76–87.

[86] Kaletka, J. and Gimonet, B., "Identification of Extended Models from BO-105 Flight Test Data for Hover Flight Condition," *Proceedings of the 21st Annual European Rotorcraft Forum*, Saint-Petersburg, Russia, Aug. 1995.